National Nanotechnology Infrastructure Network

Research Experience for Undergraduates (NNIN REU) Program

International Research Experience for Graduates (NNIN iREG) Program

International Research Experience for Undergraduates (NNIN iREU) Program

2013 Research Accomplishments

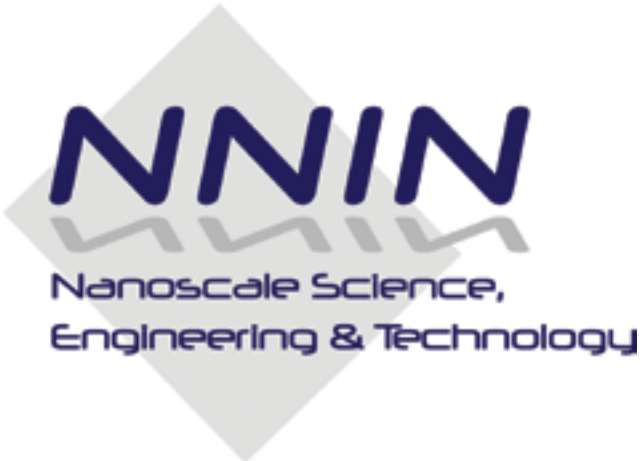

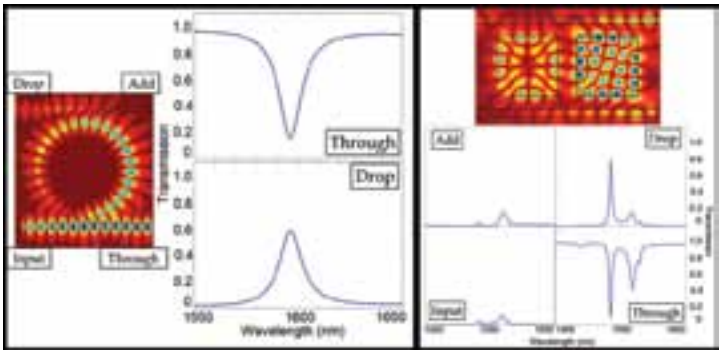

Silicon Nanophotonic Add-Drop Filter Based on High-Q Square Resonant Cavities; Emily Donahue, pages 174-175

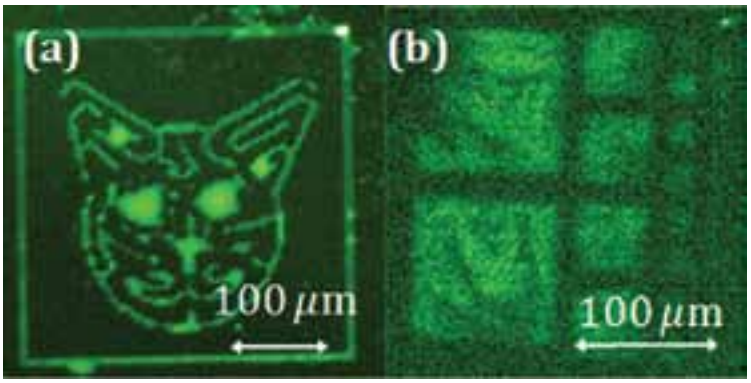

Deposition of the Immobilization Layer 3-Aminopropyltriethoxysilane on GaN for Extremophile-Based Biosensors; Tiffany Huang, pages 218-219

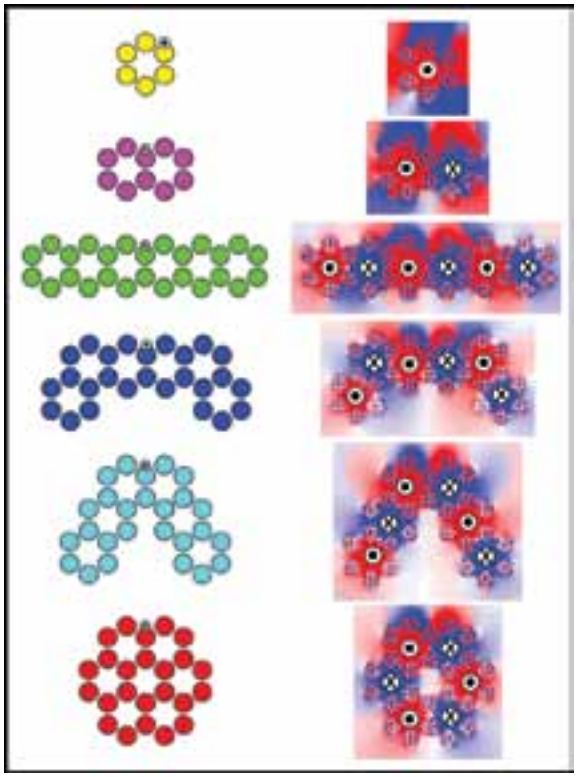

Understanding Magnetic Plasmon Mode Mixing Using Electron Energy Loss Spectroscopy; Harrison J. Goldwyn, pages 194-195

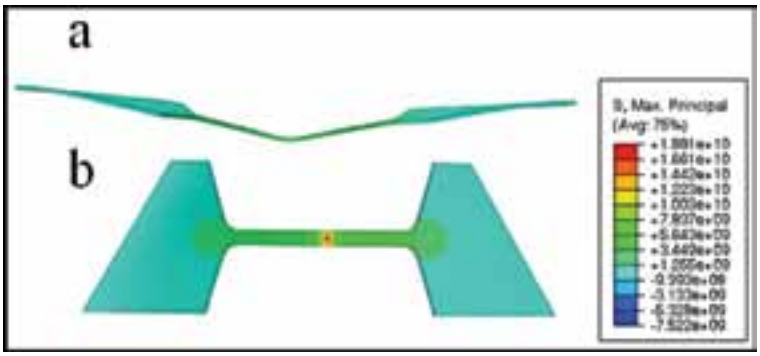

Determination of Strength Degradation Mechanisms of Native Oxide on Silicon Nanostructures; Rafael Jesus Haro, pages 122-123

Conformable Conducting Polymer Electrodes used with an Ionic Liquid Gel for Electroencephalography; Camryn Johnson, pages 18-19

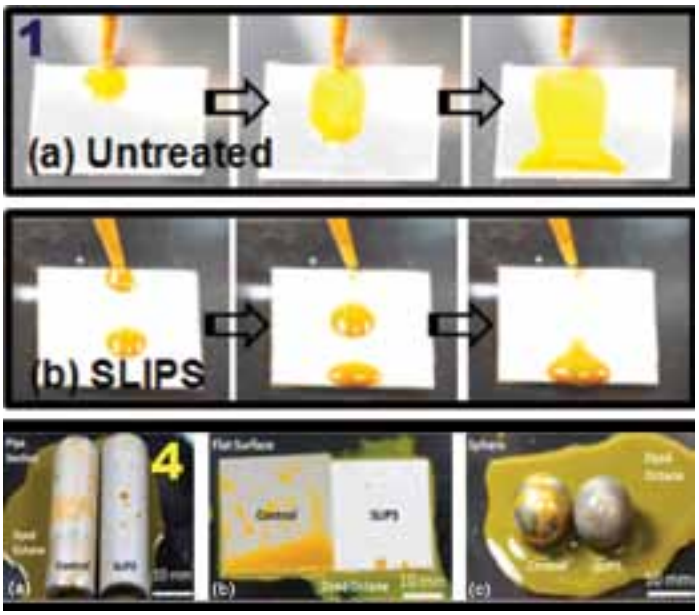

Developing Bioinspired Slippery Coating on Industrial Steels; Keiko Kato, pages 126-127

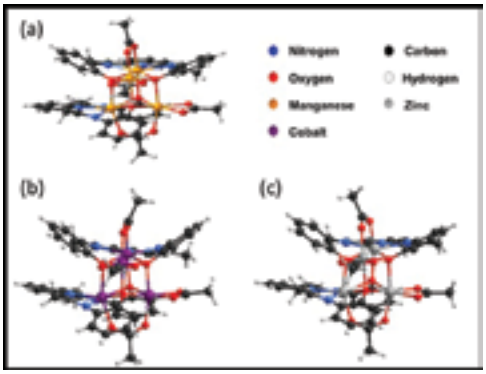

Synthesis and Covalent Attachment of {M4} Polynuclear Metallic Complexes....; Christopher A. Nakamoto, pages 70-71

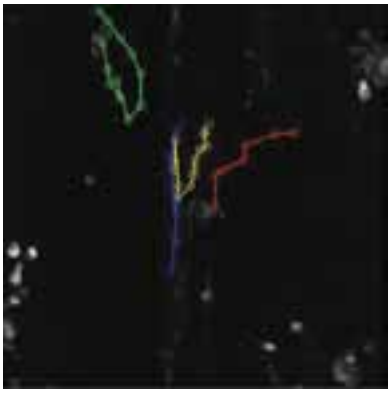

Curved Functionalized Microfluidic Channels...; Ang Li, pages 32-33

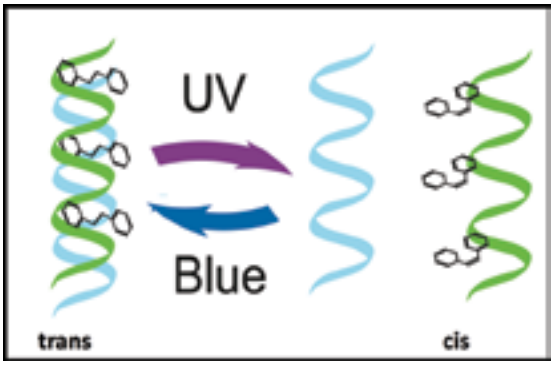

Azobenzene Functionalized DNA for Light-Induced DNA Stringency; Hannah Zeitler, pages 78-79

National Nanotechnology Infrastructure Network
Research Experience for Undergraduates Program

2013 Research Accomplishments

The National Nanotechnology Infrastructure Network (NNIN) is an integrated partnership of fourteen user facilities, supported by the National Science Foundation. NNIN provides opportunities for nanoscience and nanotechnology research, including support in fabrication, synthesis, characterization, modeling, design, computation, and hands-on training in an open environment. The NNIN members includes:

- ***ASU NanoFab, Arizona State University***
- ***Cornell NanoScale Facility, Cornell University***
- ***Nanotechnology Research Center, Georgia Institute of Technology***
- ***Center for Nanoscale Systems, Harvard University***
- ***Howard Nanoscale Science and Engineering Facility, Howard University***
- ***Penn State Nanofabrication Facility, The Pennsylvania State University***
- ***Stanford Nanofabrication Facility, Stanford University***
- ***UCSB Nanofabrication Facility, University of California, Santa Barbara***
- ***Colorado Nanofabrication Laboratory, University of Colorado, Boulder***
- ***Lurie Nanofabrication Facility, University of Michigan***
- ***Minnesota Nano Center, University of Minnesota***
- ***Microelectronics Research Center, The University of Texas at Austin***
- ***NanoTech User Facility, University of Washington***
- ***Nano Research Facility, Washington University at St. Louis***

http://www.nnin.org/

Biological Applications, pages 2-57

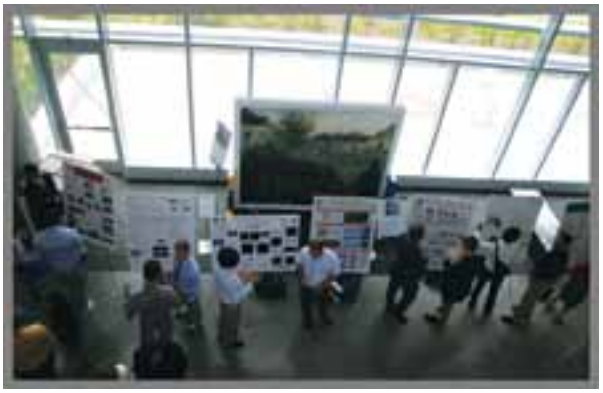

Effects of Cellular Architecture on MDA-MB-231 Breast Cancer Cell Motility ... 26

Ted Kocher, *Biological Systems Engineering, University of Nebraska-Lincoln NNIN REU Site: University of Minnesota-Twin Cities*

Microfluidics for the Study of Breast Cancer ... 28

Lisa Kriegh, *Biosystems Engineering, Oklahoma State University . . . . NNIN REU Site: Arizona State University*

Design of Synthetic Protein Membranes Using Droplet Microfluidics ... 30

Corey Landry, *Biological Engineering, Louisiana State University . . . . NNIN REU Site: Harvard University*

Curved Functionalized Microfluidic Channels for the Study of Cell Dynamics ... 32

Ang Li, *Department of Biomedical Engineering, Georgia Institute of Technology. . . . . . . NNIN REU Site: Harvard University*

Identifying the Biomechanical Effects of UV Resistant Molecules and Nanoparticles on Human Skin ... 34

Sarah Nainar, *Biochemistry, Washington & Jefferson College . . . . NNIN REU Site: Stanford University*

Fabrication of Nano Ion Pumps for Retinal and Neural Prosthesis ... 36

Zachary Pritchard, *Chemical and Biomolecular Engineering, Georgia Institute of Technology. . . . . NNIN REU Site: UCSB*

Differentiation of Human Mesenchymal Stem Cells to Schwann Cells on Electrospun Nanofibers ... 38

Shelby Pursley, *Biological Engineering, Louisiana State University. . . . . . NNIN REU Site: Georgia Institute of Technology*

Electrohydrodynamic Jet Printing on Hydrogel Substrates for Cell Culturing Applications ... 40

Audre Ramey, *Mechanical Engineering, University of Portland. . . . . . .NNIN REU Site: University of Michigan, Ann Arbor*

Surface Ligand Density Dependence of Collective Cell Migration on Photoactivatable Self Assembled Monolayers ... 42

Radu Reit, *Biomedical Engineering, Georgia Institute of Technology . . . . NNIN iREU Site: NIMS, Japan*

Micro-Scale Microbial Fuel Cell: Petroleum Biosensing ... 44

Anne Showalter, *Biological Chemistry, Culver-Stockton College. . . . . NNIN REU Site: Arizona State University*

Dynamics of Bacterial Quorum Sensing in Microfluidic Devices ... 46

Peter Youpeng Su, *Chemical and Biomolecular Engineering, University of California, Berkeley NNIN REU Site: Georgia Tech*

Fabrication of Flexible, Implantable Probes for in vivo Recording of Neural Activity ... 48

Brianna Thielen, *Engineering, Harvey Mudd College . . . . .NNIN iREU Site: Saint-Étienne et Gardanne, France*

The Study of Disposable Substrates in Surface Acoustic Wave Devices ... 50

Christine Truong, *Physics, Polytechnic Institute of New York University. . . . NNIN REU Site: The Pennsylvania State University*

The Impact of MEMS-Produced Micro-Electrode Material Coating on Dental Plaque Biofilm Growth ... 52

Katherine Warthen, *Bioengineering, Montana State University . . . . . .NNIN REU Site: University of Michigan, Ann Arbor*

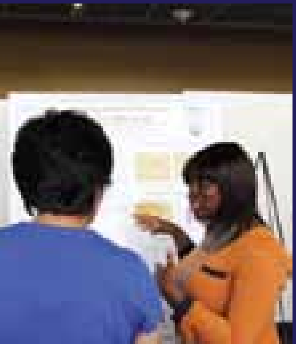

Chemistry, pages 58-79

Electronics, pages 80-101

Materials, pages 102-161




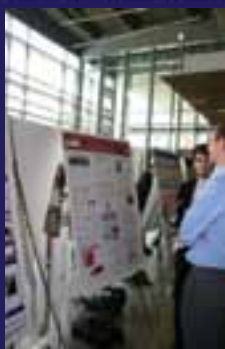

Mechanical Devices, pages 162-169

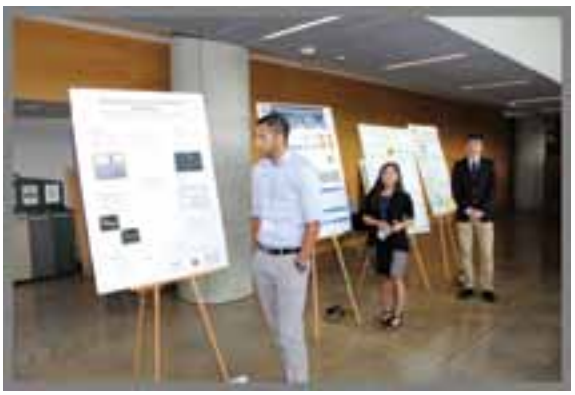

Optics & Opto-Electronics, pages 170-191

Fabricating Dual-Sided Micro Lenses and High Frequency Talbot Diffraction Gratings Using Binary Masks. 170

***Bradlee Kyle Beauchamp**, Engineering Physics, Rose-Hulman Institute of Technology . . . . . NNIN REU Site: University of Colorado*

Infrared Filtering via Sub-Wavelength Gratings for Hyperspectral Imaging ... ... .172

***Arthur Bowman, III**, Physics, Wayne State University . . . . . NNIN REU Site: University of Michigan, Ann Arbor*

Silicon Nanophotonic Add-Drop Filter Based on High-Q Square Resonant Cavities 174

***Emily Donahue**, Engineering Physics, Cornell University . . . . . NNIN REU Site: University of Colorado, Boulder*

Voltage-Tunable Plasmonic Metamaterials Based on Stark Tunable Intersubband Polaritons. 176

***Priyanka Gaur**, Brain and Cognitive Sciences, MIT . . . . . NNIN REU Site: The University of Texas at Austin*

Silicon Nanowires for Optical Light Trapping in Solar Cells 178

***Christopher Green**, Applied Physics, Lock Haven University . . . . . NNIN REU Site: Arizona State University*

Optical and Electrical Studies of Metal:Semiconductor Nanocomposites for Nanophotonics... 180

***Stephen D. March**, Electrical Engineering, Iowa State University . . . . . NNIN REU Site: The University of Texas at Austin*

Stabilizing Fiber Optic Pressure Sensor Measurements by Fabricating an Enclosed Photonic Crystal Cavity. 182

***Jacqueline Ong**, General Engineering, Harvey Mudd College . . . . . NNIN REU Site: Stanford University*

Surface Scatterers on Slab-Wave Guides for Uniform Bacteria Growth 184

***Brandon Thomas Pereyra**, Mechanical Engineering, Binghamton University . . . . . NNIN REU Site: Cornell University*

XPS Analysis of Sulfide and Aluminum Nitride Based Buffer Layers for Epitaxial Zinc Oxide Growth. 186

***Jacob M. Rothenberg**, Physics, University of Rochester . . . . . NNIN iREU Site: NIMS, Japan*

Influence of the Type of Wetting Layer on the Contact Resistance in Metal-Graphene Ohmic Contacts. 188

***Yuki Sunayama**, Graduate School of Engineering, University of Shiga, Japan NNIN iREG Site: University of Colorado, Boulder*

**Graphene-Based Electro-Optic Modulator Fabrication .. ..

Physics & Nanostructure Physics, pages 192-209

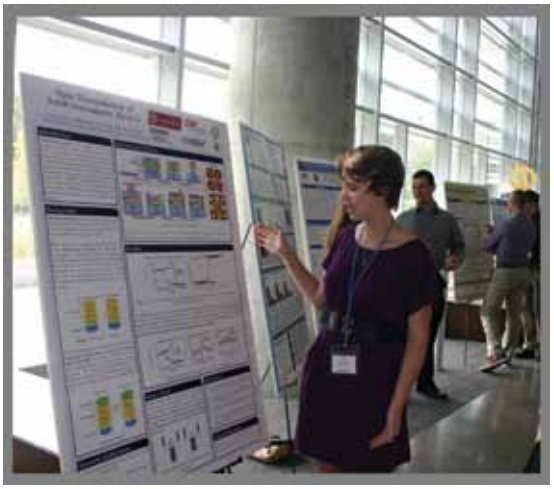


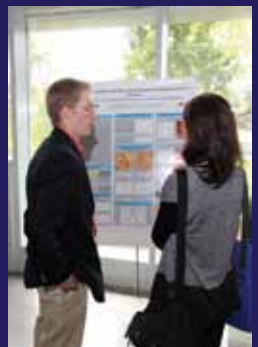

Process & Characterization, pages 210-229

Societal & Ethical Issues of Nanotechnology, pages 230-233

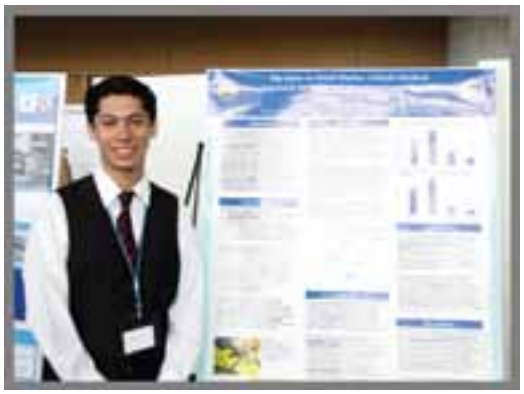

Cover Background:

Daichi Oka, Carbon Coated Tin-Seeded Silicon Nanowires for Lithium-Ion Battery Anodes, NNIN iREG Site: The University of Texas at Austin. Full report, page 148.

NNIN on Seeded Hydrogel Surface:

Audre Ramey, Electrohydrodynamic Jet Printing on Hydrogel Substrates for Cell Culturing Applications, NNIN REU Site: University of Michigan. Full report, page 40.

Chromium-Doped Particles:

Deanna Lanigan, Improvement of Lithium Ion Batteries with Selected Dopants, NNIN REU Site: WUSTL. Full report, page 132.

2013 NNIN REU Research Accomplishments

2013 NNIN REU Research Accomplishments

The 2013 NNIN REU interns at the network convocation held at the Georgia Institute of Technology in August.

Welcome to the 2013 edition of NNIN REU Research Accomplishments! This publication reflects the hard work of the undergraduate researchers, as well as the dedication and commitment of their mentors, the NNIN site staff, REU coordinators, and the principal investigators.

Our summer program brings undergraduates from colleges and universities across the U.S. into some of the nation's leading academic nanofabrication laboratories for an intensive ten-week research experience. The participants are trained in safe laboratory practices, learn the essential scientific background for their project, and then perform independent research in nanotechnology, under the guidance of their mentor. For many of the students, the NNIN REU is their first experience when the answer, or even the existence of an answer, is not yet known. The summer experience provides the students with a sample of what life for them could be like as a graduate student in applied science or engineering, both in and outside the clean room. For many, the NNIN REU Program helps them to decide to pursue a career in research and development.

During the summer of 2013, 91 students participated in our Research Experience for Undergraduates (REU) Program. From the previous summer's NNIN REU Program, 16 students were selected to participate in NNIN's International Research Experience for Undergraduates (iREU) Program in France, Germany and Japan. In addition, nine graduate students from Japan participated in our research exchange (iREG) program at seven of our sites.

NNIN is committed to making all three of these programs a significant experience for the participants, by focusing on advanced research and knowledge, seeking strong mentors and staff support, exposing the students to a professional research environment, and having high expectations for the summer research projects, as well as for the presentations at the final convocation. The students' exposure to a wider variety of research conducted by their peers and the other nanofab users across diverse disciplines of science and engineering provides a significant complementary experience.

I would like to thank all of the NNIN REU staff, graduate student mentors, and faculty for their contributions to the success of this year's programs. Particular thanks are due to Ms. Melanie-Claire Mallison and Dr. Lynn Rathbun for their contributions to organizing the logistics of these programs. In addition, I am grateful to Ms. Leslie O'Neill and Dr. Nancy Healy for organizing the network-wide convocation in August at Georgia Tech in Atlanta, Georgia.

I wish all our program participants the best for their future careers, whether in science, engineering, or other disciplines. I hope you will build on this summer's experience and I look forward to hearing from you on your future successes!

Roger T. Howe
Director, NNIN
rthowe@stanford.edu

The 2013 NNIN REU Program @ ASU NanoFab, Arizona State University, Tempe, AZ

The 2013 NNIN REU Program @ Cornell NanoScale Science and Technology Facility, Cornell University, Ithaca, NY

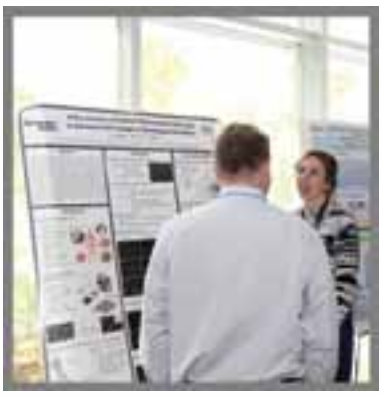

The 2013 NNIN REU Program @ Nanotechnology Research Center, Georgia Institute of Technology, Atlanta, GA

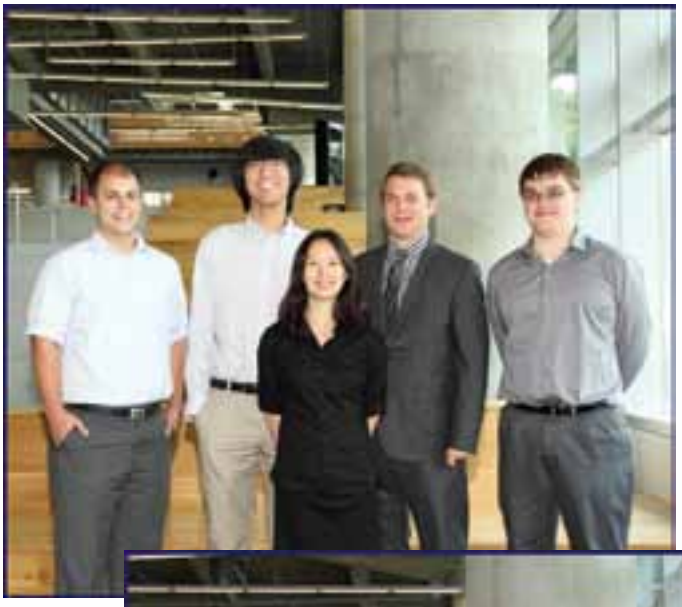

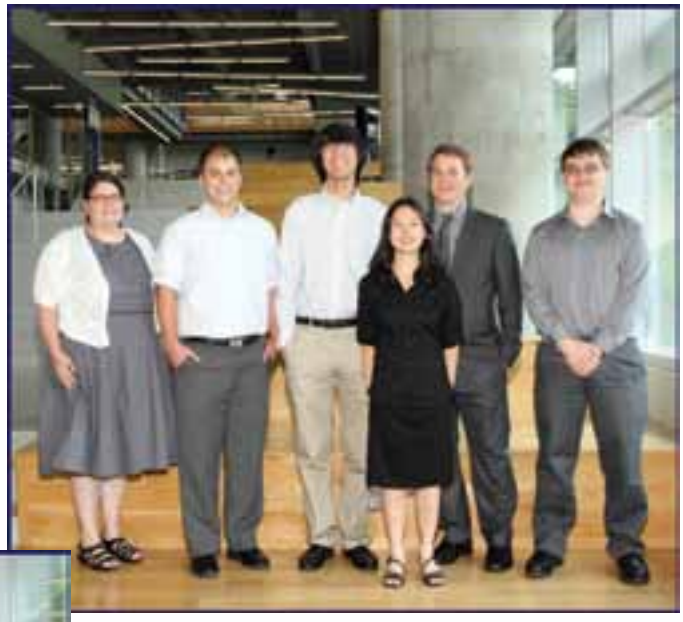

The 2013 NNIN REU Program @ Center for Nanoscale Systems, Harvard University, Cambridge, MA

The 2013 NNIN REU Program @ Howard Nanoscale Science and Engineering Facility, Howard University, Washington, DC

The 2013 NNIN REU Program @ Penn State Nanofabrication Lab, The Pennsylvania State University, University Park, PA

The 2013 NNIN REU Program @ Stanford Nanofabrication Facility, Stanford University, Stanford, CA

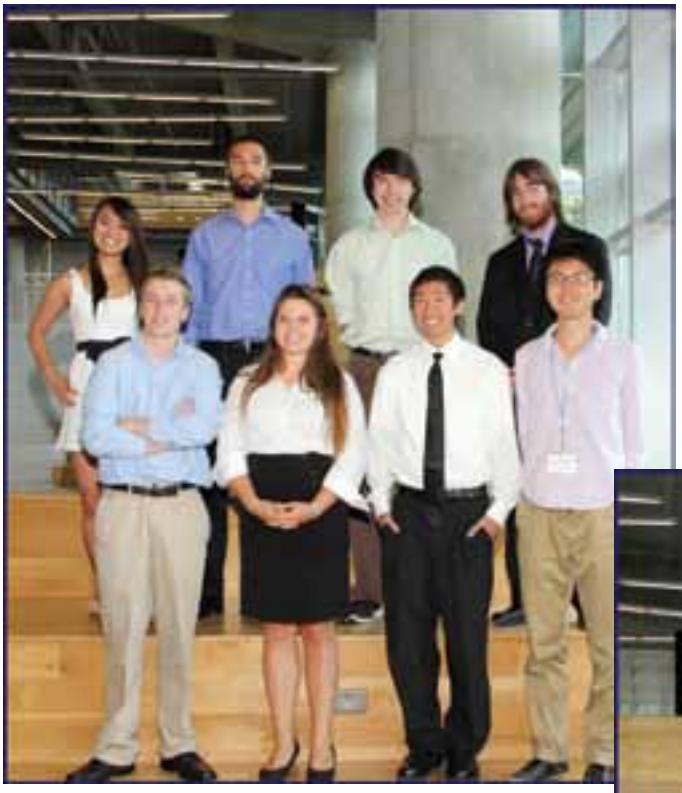

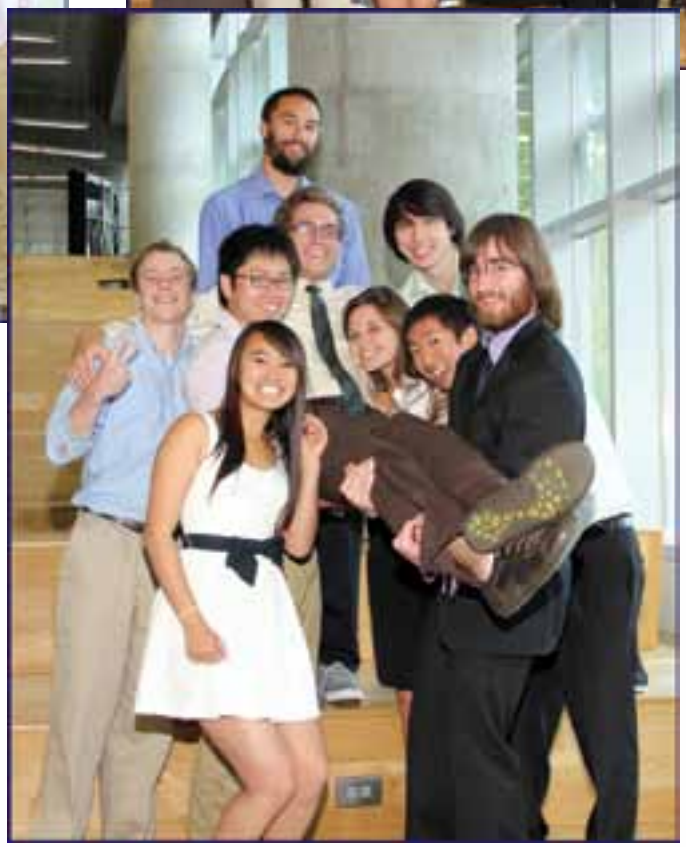

The 2013 NNIN REU Program @ UCSB Nanofabrication Facility, University of California, Santa Barbara, CA

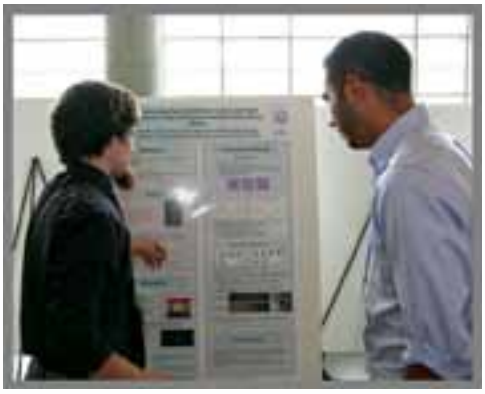

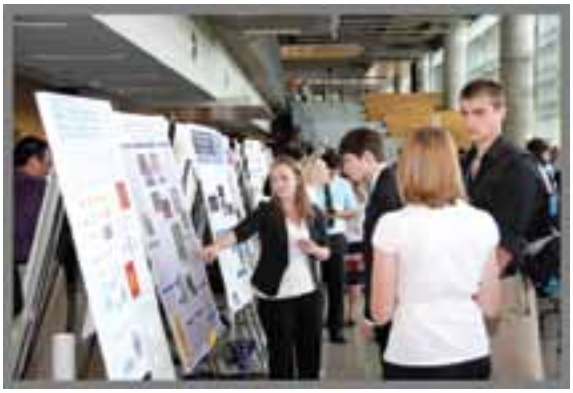

The 2013 NNIN REU Program @ Colorado Nanofabrication Laboratory, University of Colorado, Boulder, CO

The 2013 NNIN REU Program @ Lurie Nanofabrication Facility, University of Michigan, Ann Arbor, MI

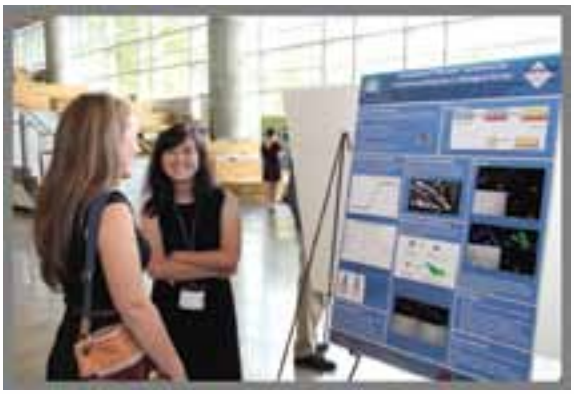

The 2013 NNIN REU Program @ Minnesota Nano Center, University of Minnesota-Twin Cities, Minneapolis, MN

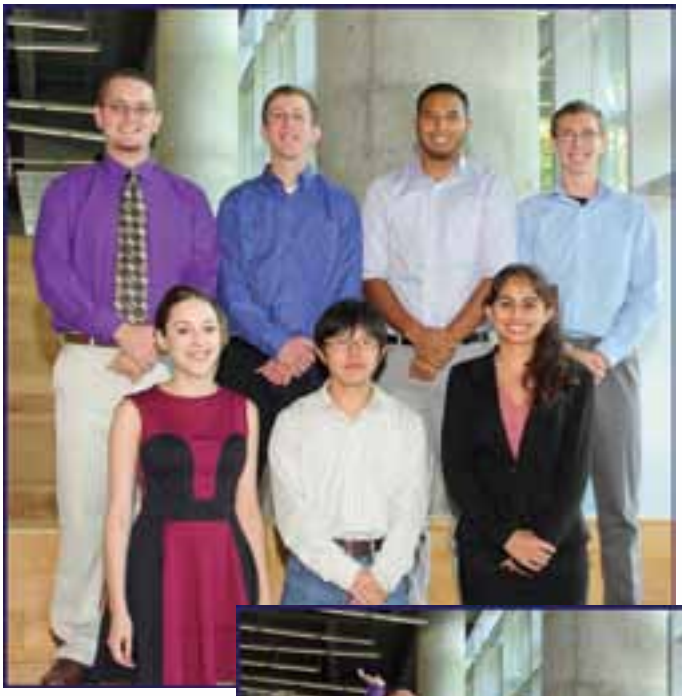

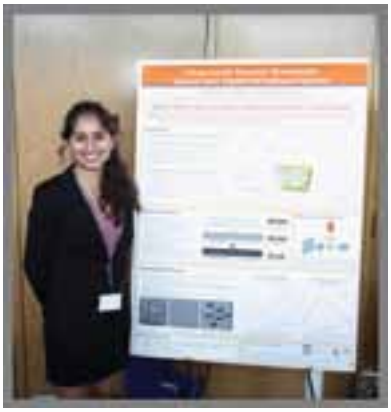

The 2013 NNIN REU Program @ Microelectronics Research Center, The University of Texas, Austin, TX

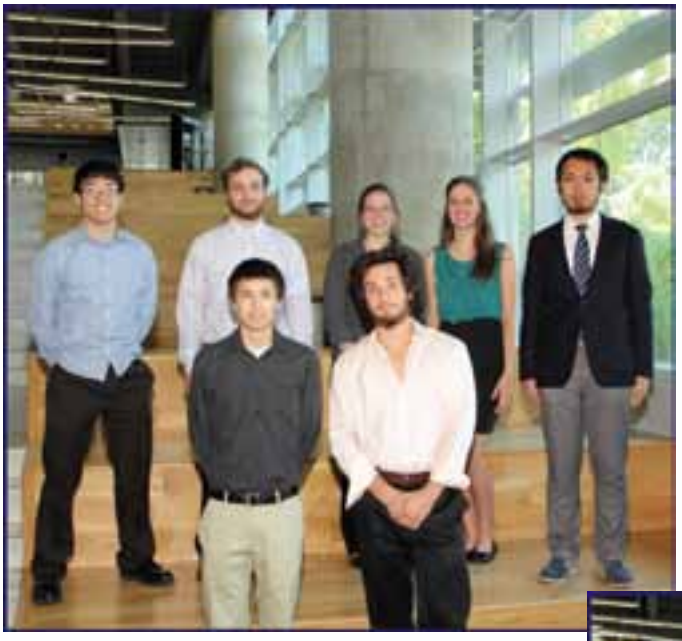

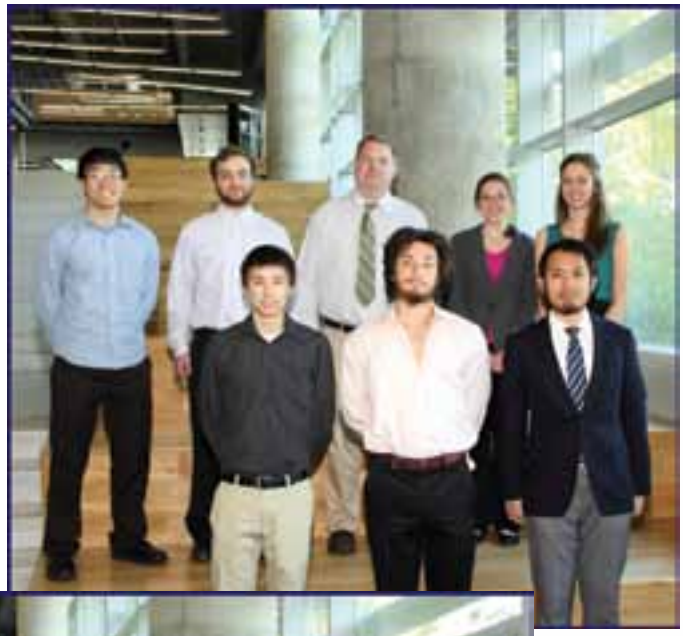

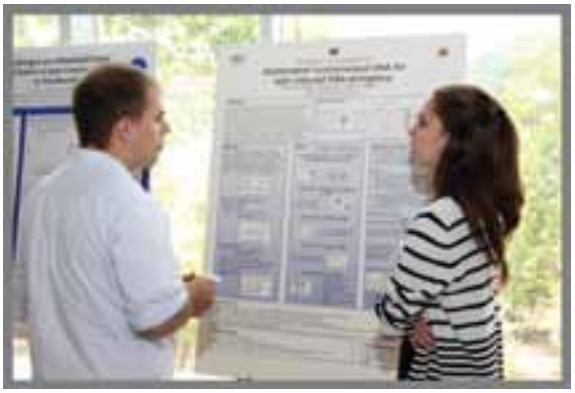

The 2013 NNIN REU Program @ NanoTech User Facility, University of Washington, Seattle, WA

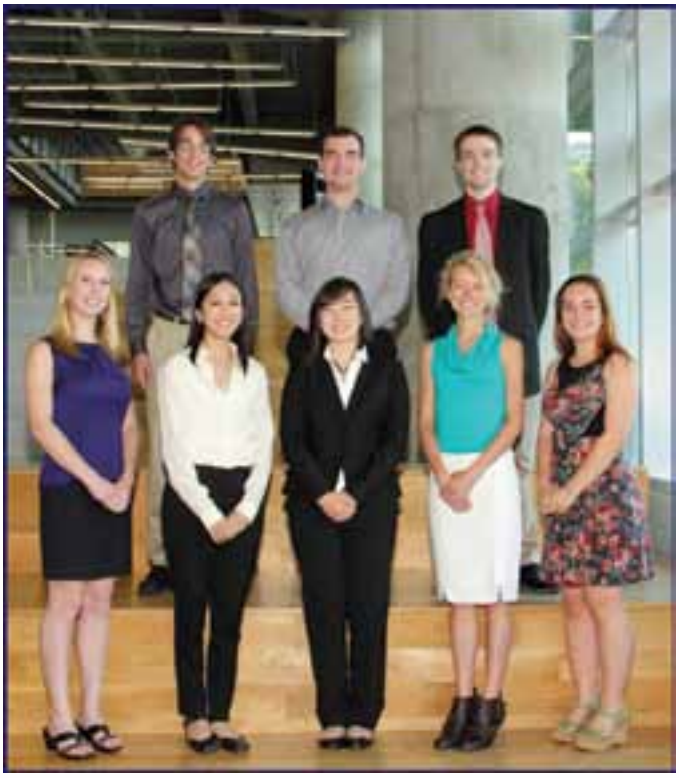

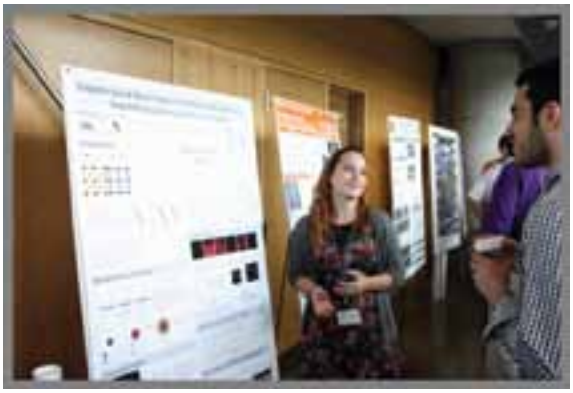

The 2013 NNIN REU Program @ Nano Research Facility, Washington University in St. Louis, St. Louis, MO

The 2013 NNIN iREG Program

The 2013 NNIN iREU Program

Commonly Used Abbreviations & Their Meanings

μl . . . .microliter
μm . . . .micron, micrometer
μN . . . .micro-Newtons
μs . . . .microsecond
< . . . .is less than
> . . . .is greater than
~ . . . .approximately
Ω . . . .ohm
1D . . . .one dimensional
2D . . . .two dimensional
2DEG . . . .two dimensional electron gas
3D . . . .three dimensional
3DOM carbon . . . ..three-dimensionally ordered macroporous carbon
^{4}He helium-4
a-Si . . . .amorphous silicon
A&M . . . .Agricultural & Mechanical
AC . . . .alternating current
AFM . . . .atomic force microscopy/microscope
Ag . . . .silver
agLDL . . . .aggregated low-density lipoproteins
$AgNO_3$ . . . .silver nitrate
AgSR . . . .silver-alkanethiolate
AIC . . . .aluminum-induced crystallization
Al . . . .aluminum
Al_2O_3 . . . .aluminum oxide
ALD . . . .atomic layer deposition
AlGaN . . . .aluminum gallium nitride
AM . . . .amplitude modulation
APD . . . .avalanche photodiode
APS . . . .advanced photon source
Ar . . . .argon
ARC . . . .anti-reflective coating
ArF . . . .argon fluoride
As . . . .arsenic
AST . . . .aspartate transaminase
atm . . . .standard atmosphere (as a unit of pressure)
ATRP . . . .atom transfer radical polymerization
Au . . . .gold
AuNPs . . . .gold nanoparticles
BAM . . . .bisphenol aminomethyl
BCL_3 . . . .boron trichloride
BDM . . . .2,3-butanedione monoxime
BES . . . .bioelectrochemical system
BHJ . . . .bulk heterojunction
Bi . . . .bismuth
BioSAXS . . . .biological small angle x-ray scattering
BN . . . .boron nitride
BOE . . . .buffered oxide etch
BOX . . . .buried oxide layer
BPB . . . .bisphenol base
BPF . . . .bisphenol F
BSA . . . .bovine serum albumin
BST . . . .barium strontium titanate
BTO . . . .barium titanate
C . . . .carbon
C . . . .centigrade
C-V . . . .capacitance-voltage
C_3N_4 . . . .carbon nitride
C_4F_8 . . . .octafluorocyclobutane, or perfluorocyclobutane
$CaCO_3$ . . . .calcium carbonate
CAD . . . .computer-aided design
CCS . . . .continuous compositional spreads

Cd .. ..cadmium

CdS. .. ..cadmium sulfide

CdSe.. .. ..cadmium selenide

CDW . .. .charge-density-wave

Ce .. ..cerium

CF_4 . .. .carbon tetrafluoride or tetrafluoromethane

CFD .. ..computational fluid dynamics

CFMA .. ..carbon-fiber microelectrode amperometry

CH_4. .. ..methane

CHESS . .. .Cornell High Energy Synchrotron Source

CHF_3.. .. ..trifluoromethane

CIGS . .. .copper indium gallium diselenide

CION. .. ..colloidal iron oxide nanoparticles

Cl. .. ..chlorine

Cl_2 .. ..chlorine gas

Cl_2/SF_6.. .. ..chlorine sulfur hexafluoride

cm .. ..centimeter

CMOS .. ..complementary metal oxide semiconductor

CMOSFET . .. .complementary metal oxide field effect transistor

CMP .. ..chemical mechanical polishing

CNL .. ..charge neutrality level

CNTFET.. .. ..carbon nanotube field-effect transistor

Co .. ..cobalt

CO_2. .. ..carbon dioxide

COF .. ..covalent organic framework

CoFeAl. .. ..cobalt iron aluminum

CoP. .. ..cobalt porphyrin

CPC .. ..colloidal photonic crystal

CPD .. ..contact potential difference

Cr. .. ..chromium

CRDS .. ..cavity ring-down spectrometer

CTC .. ..circulating tumor cell

CTC .. ..composite thermal capacitors

CTL .. ..confinement tuning layer

Cu .. ..copper

Cu_2ZnSnS_4.. .. ..copper zinc tin sulfide

$CuAlO_2$. .. ..copper aluminum oxide

CVD .. ..cardiovascular disease

CVD .. ..chemical vapor deposition

CW . .. .continuous wave

CXRF .. ..confocal x-ray fluorescence microscopy

DARPA. .. ..Defense Advanced Research Projects Agency

DC .. ..direct current

DCB .. ..double cantilever beam

DCE 1,2-dichloroethane

DCM . .. .dichloromethane

de novo . .. .Latin expression meaning “from the beginning,” “afresh,” “anew,” “beginning again.”

DEP .. ..dielectrophoresis

DFT .. ..density functional theory

DFT .. ..discrete Fourier transform

DH-PSF .. ..double helix point-spread function

DI .. ..de-ionized

DIC. .. ..differential interference contrast

DMF.. .. ..dimethyl formamide

DNA.. .. ..deoxyribonucleic acid

DNP .. ..dynamic nuclear polarization

DODAB .. ..dimethyl dioctadecyl ammonium bromide

DPPC. 1,2-dipalmatoyl-sn-glycero-3-phosphocholine

DPPG .. ..1,2-dimyristoyl-sn-glycero-[phospho-rac-(1-glycerol)]

DRAM.. .. ..dynamic random access memory

DRIE .. ..deep reactive ion etch

dsDNA.. .. ..double-stranded DNA

DUV .. ..deep ultraviolet

e-beam.. .. ..electron beam lithography

E. coli .. ..*Escherichia coli*

EB .. ..exchange bias

EBID . .. .electron beam induced deposition

EBL .. ..electron beam lithography

ECD .. ..electrochemical detectors

ECM.. .. ..extracellular matrix

EDS .. ..energy dispersive spectroscopy

EDTA .. ..ethylenediaminetetraacetic acid

EELS . .. .electron energy loss spectroscopy

EG .. ..ethylene glycol

EIS.. .. ..electrochemical impedance spectroscopy

EMCCD .. ..electron multiplying charge coupled device

EO .. ..electro-optic

EOT .. ..equivalent oxide thickness

EPICs .. ..electronic photonic integrated circuits

EPR .. ..enhanced permeability and retention

Er. .. ..erbium

ErAs .. ..erbium arsenide

ESM .. ..effective screening medium

EUV .. ..extreme ultraviolet

ex vivo .. ..Latin for "out of the living" --
that which takes place outside an organism

F .. ..fluorine

FcCOOH . .. .ferrocenecarboxylic acid

FDMA .. ..fluorinated perfluorodecyl methacrylate

FDMNES .. ..finite-difference method approach
to predicting spectroscopic transitions

Fe. .. ..iron

FeDRAM. .. ..ferroelectric dynamic random access memory

FEM .. ..finite element method

FES. .. ..functional electrical stimulation

FESEM. .. ..field-emission scanning electron
microscopy/microscope

FET. .. ..field-effect transistor

FFTs .. ..fast Fourier transforms

fg . .. .femto gram

FIB . .. .focused ion beam

FIR . .. .far infrared

fJ.. .. ..femto Joules

FLT . .. .field-like torque

FM.. .. ..frequency modulation

FMR .. ..ferromagnetic resonance

FOTS. .. ..fluorosilane, tridecafluoro-
1,1,2,2-tetrahydrooctyltrichlorosilane

FRAP. .. ..fluorescence recovery after photobleaching

FRET. .. ..fluorescence resonance energy transfer

FTIR.. .. ..Fourier transform infrared spectroscopy

FWM . .. .four-wave mixing

Ga .. ..gallium

GaAs . .. .gallium arsenide

GaAsN.. .. ..gallium arsenide nitride

GaInNAs . .. .gallium indium nitride arsenide

GaN .. ..gallium nitride

GaP. .. ..gallium phosphide

GaSb.. .. ..gallium antimonide

GASP .. ..growth advantage in stationary phase

GB .. ..glass bead

GBLMA .. ..α-gamma butyrolactone methacrylate

GC .. ..gas chromatograph

GC-C-IRMS.. .. .. ..gas chromatography combustion
isotope ratio mass spectrometry

Ge .. ..germanium

GEDI μdevices. .. ..geometrically enhanced differential
immunocapture microdevices

GFET. .. ..graphene field effect transistor

GHz .. ..gigahertz

GI .. ..gastrointestinal

GMFI. .. ..gross mean fluorescence intensity

GMR . .. .giant magnetoresistance

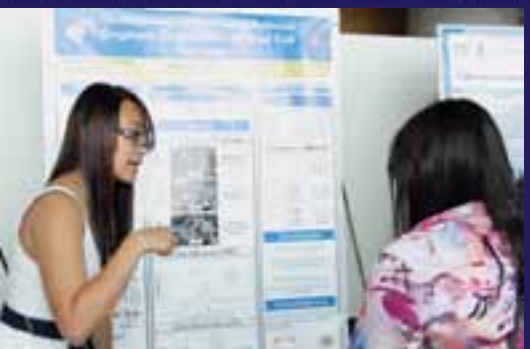

GNR .. ..gold nanorod

GNR .. ..graphene nanoribbons

GPa. .. ..gigapascal

GPC .. ..gel permeation chromatography

GPS .. ..global positioning system

GRIN. .. ..gradient refractive index

GUI .. ..graphical user interface

GVD .. ..group-velocity dispersion

h .. ..hours

H.. .. ..hydrogen

H-NMR .. ..hydrogen-1 nuclear magnetic resonance spectroscopy

H_2O_2 .. ..hydrogen peroxide

HAMA.. .. ..hydroxyl adamantyl methacrylate

$HAuCl_4$. .. ..chloroauric acid

hBN .. ..hexagonal boron nitride

hcp.. .. ..hexagonal close packing

HCP1. .. ..Heme Carrier Protein 1

He .. ..helium

HEMTs. .. ..high electron mobility transistors

HF .. ..hydrofluoric acid

HFEs . .. .hydrofluoroethers

HfO_2 .. ..hafnium dioxide

Hg .. ..mercury

high-κ .. ..high dielectric constant

HMDS .. ..hexamethyldisilazane

HMGB.. .. ..high-mobility group box protein

HOMO-LUMO .. ..highest occupied molecular orbital & lowest unoccupied molecular orbital

HOPG .. ..highly oriented pyrolytic graphite

HRS .. ..high resistance state

HRTEM .. ..high-resolution transmission electron microscopy

HS-ssDNA.. .. ..thiol terminated single stranded DNA

HSQ .. ..hydrogen silsesquioxane

HSQ/FOx .. ..negative electron beam resist hydrogen silsesquioxane

Hz .. ..Hertz

I-V .. ..current-voltage

I/O .. ..input/output

IC. .. ..integrated circuit

ICP . .. .inductively coupled plasma

ICP-MS .. ..inductively coupled plasma mass spectroscopy

ICP-RIE .. ..inductively coupled plasma reactive ion etcher

IFVD . .. .impurity free vacancy diffusion

IID .. ..impurity induced disordering

IIEI . .. .ion implant enhanced interdiffusion

In . .. .indium

in situ. .. ..Latin phrase which translated literally as 'in position' -- to examine the phenomenon exactly in place where it occurs

in vitro .. ..Latin for "within glass" -- refers to studies in experimental biology that are conducted using components of an organism that have been isolated from their usual biological context in order to permit a more detailed or more convenient analysis than can be done with whole organisms.

in vivo .. ..Latin for "within the living" -- experimentation using a whole, living organism

InAlN .. ..indium aluminum nitride

InAs .. ..indium arsenide

InAs NWs .. ..indium arsenide nanowires

InGaAsN . .. .indium gallium arsenide nitride

InP .. ..indium phosphide

IPA.. .. ..isopropyl alcohol

IPE.. .. ..Ion & Plasma Equipment, Inc.

IPT.. .. ..in-plane torque

IR. .. ..infrared

IRMS. .. ..isotope ratio mass spectrometry

IrO_2 or IrO_x. .. ..iridium oxide

ISFET .. ..ion-sensitive field effect transistor

ITO. .. ..indium tin oxide
κ .. ..dielectric constant
K.. .. ..Kelvin (a unit of measurement for temperature)
kDa. .. ..kilodaltons
KFM.. .. ..Kelvin force microscopy
kg. .. ..kilogram
kHz. .. ..kilohertz
KOH.. .. ..potassium hydroxide
KPFM .. ..Kelvin probe force microscopy
L/D. .. ..length-to-diameter ratio
La .. ..lanthanum
LAO .. ..lanthanum aluminum oxide
LED .. ..light-emitting diode
LER .. ..line edge roughness
Li. .. ..lithium
LO .. ..local oscillator
low-κ. .. ..low dielectric constant
LPCVD .. ..low pressure chemical vapor deposition
lpm . .. .liter per minute
LRS .. ..low resistance state
LSPR. .. ..localized surface plasmon resonance
Lu .. ..lutetium
LWGs .. ..liquid-core/liquid-cladding waveguides
LWR.. .. ..line width roughness
m . .. .minutes
M-OPTG . .. .microring-based optical pulse-train generator
MACE.. .. ..metal-assisted chemical etching
MAMA. .. ..methyl adamantyl methacrylate
MBE.. .. ..molecular beam epitaxy
MCBJ .. ..mechanically controllable break junction
MD. .. ..molecular dynamics
ME.. .. ..magnetoelectric
MEG.. .. ..maleimide-ethylene glycol disulfide
MEMs .. ..microelectromechanical systems
MFC .. ..microbial fuel
MFMR.. .. ..microfabricated micro-reactors
MgO .. ..magnesium oxide
MGs .. ..molecular glasses
MHz .. ..megahertz
micron .. ..micrometer, aka μm
MIFIS .. ..metal-insulator-ferroelectric-insulator-semiconductor
min . .. .minutes
ml .. ..milliliter
mm . .. .millimeter
mM. .. ..millimolar
MMA-MAA.. .. .. ..methyl-methacrylate-co-methacrylic acid
mmHg .. ..millimeters of mercury; unit of pressure measurement
MnO_2 NPs .. ..manganese oxide nanoparticles
Mo .. ..molybdenum
MOCVD.. .. ..metal oxide chemical vapor deposition
MONOS .. ..metal/oxide/nitride/oxide/semiconductor
MOS.. .. ..metal oxide semiconductor
MoS_2.. .. ..molybdenum disulfide
MOSFET. .. ..metal oxide semiconductor field effect transistor
MOVPE .. ..metal organic vapor phase epitaxy
MPM . .. .multiphoton microscopy
MQCA.. .. ..magnetic quantum-dot cellular automata
MQW .. ..multiple quantum well
MRA.. .. ..multifunction reconfigurable antenna
MRAM. .. ..magnetic random access memory
MRFM.. .. ..magnetic resonance force microscopy
MRI .. ..magnetic resonance imaging
ms .. ..millisecond
MSM . .. .metal-semiconductor-metal
MTJ .. ..magnetic tunneling junction



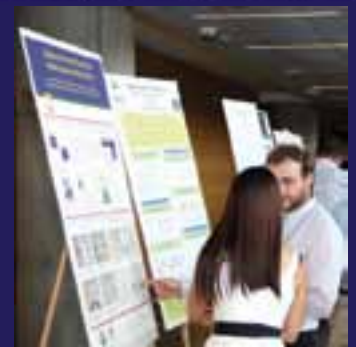


mTorr. .. ..millitorr

mV.. .. ..millivolt

MVD . .. .molecular vapor deposition

MWNT. .. ..multiwalled carbon nanotube

MΩ. .. ..megaohms

N.. .. ..nitrogen

N_2 .. ..nitrous oxide

nA .. ..nanoAmperes

NaCl.. .. ..sodium chloride

NASA .. ..National Aeronautics & Space Administration

Nb .. ..niobium

Nb_3Sn .. ..triniobium-tin

NEMs .. ..nanoelectromechanical systems

NEXAFS. .. ..near edge x-ray absorption fine structure

NH_4F. .. ..ammonium fluoride

Ni. .. ..nickel

NIR. .. ..near-infrared

nL .. ..nanoliter

nm .. ..nanometer

NMP.. .. ..n-methyl-2-pyrrolidone

NMR . .. .nuclear magnetic resonance microscopy / spectroscopy

NNIN iREG .. ..National Nanotechnology Infrastructure Network International Research Experience for Graduates (NNIN iREG) Program

NNIN iREU .. ..National Nanotechnology Infrastructure Network International Research Experience for Undergraduates (NNIN iREU) Program

NNIN REU. .. ..National Nanotechnology Infrastructure Network Research Experience for Undergraduates (NNIN REU) Program

NORIS.. .. ..nanometrology optical ruler imaging system

NPR .. ..nonlinear polarization rotation

NPs. .. ..nanoparticles

NPs. .. ..nanopores

ns. .. ..nanosecond

NSF .. ..National Science Foundation

NSOM.. .. ..near-field scanning optical microscopy

NSSP. .. ..nanostructured semipolar

NV.. .. ..nitrogen-vacancy

NVM . .. .non-volatile memory

NW FETs. .. ..nanowire field-effect transistors

O.. .. ..oxygen

OFET. .. ..organic field effect transistor

OLED .. ..organic light-emitting diode

ONO.. .. ..oxide/nitride/oxide

OPS .. ..optical particle sizer

OPV .. ..organic photovoltaic cells

OTFT. .. ..organic thin-film transistor

P/E.. .. ..program/erase

Pa. .. ..Pascals

PAB .. ..post-apply bake

PaC. .. ..Parylene C

PAMAM.. .. ..polyamidoamine

PANOMs. .. ..planarized aperatures for near-field optical microscopy

Pb .. ..lead

PBG .. ..photonic bandgap

PBPK. .. ..physiologically-based pharmacokinetic

PbS . .. .lead sulfide

PBS .. ..phosphate-buffered saline

PbSe .. ..lead selenide

PC .. ..persistent current

PC .. ..photocurrent

PCB .. ..printed circuit board

PCBM .. ..[6,6]-phenyl-C61-butyric acid methyl ester, a fullerene derivative

PCM.. .. ..phase change material

PCN .. ..photonic crystal nanocavity

Pd .. ..palladium

PD .. ..photodetector

PDMS .. ..polydimethylsiloxane

PE-GNR .. ..polyelectrolyte gold nanorod

PEB .. ..post-exposure bake

PEC .. ..photoelectrochemical

PECVD .. ..plasma enhanced chemical vapor deposition

PEDOT:PSS .. ..poly(3,4-ethylenedioxythiophene): poly(styrenesulfonate)

PEG .. ..polyethylene glycol

PEI.. .. ..poly(ethyl imine)

PFM .. ..piezo-response force microscopy

pH .. ..a measure of the activity of hydrogen ions (H+) in a solution and, therefore, its acidity.

Ph.D. . .. .doctorate of philosophy

PhC. .. ..photonic crystal

PID . .. .proportional-integral-derivative

PL .. ..photoluminescence

pL .. ..picoliter

PLD .. ..pulsed laser deposition

PLGA .. ..poly(lactic-*co*-glycolic) acid

PMGI. .. ..poly(methyl glutarimide)

PMMA.. .. ..poly(methyl methacrylate)

PmPV .. ..poly(m-phenylenevinylene-*co*-2,5-dioctoxy-p-phenylenevinylene)

poly-Si.. .. ..polycrystalline silicon

POP .. ..polyolefin plastomer

PPM .. ..photolithographic phase masks

PS .. ..polystyrene

PSL. .. ..polysterene latex

PSMO .. ..praseodymium strontium manganite

PSμM .. ..phase separation micro-molding

Pt . .. .platinum

Pt/Ir .. ..platinum/iridium

PTX .. ..paclitaxel

PV .. ..photovoltaic

PVA .. ..poly-vinyl alcohol

PVC .. ..polyvinyl chloride

PVD .. ..physical vapor deposition

PVDF .. ..polyvinylidene fluoride

PVP .. ..polyvinylpyrrolidone

Py .. ..permalloy, $Ni_{81}Fe_{19}$

PZT. .. ..lead zirconate titanate ($PbZr_{0.52}Ti_{0.48}O_3$)

Q.. .. ..quality factor

QD.. .. ..quantum dots

QW. .. ..quantum well

QWI .. ..quantum well intermixing

RA.. .. ..resistance-area

Re number.. .. ..Reynolds number

RF .. ..radio frequency

RF MEMS.. .. ..radio frequency microelectromechanical systems

RFID . .. .radio frequency identification

RIE. .. ..reactive ion etch

RMS or rms .. ..root mean square

RNA.. .. ..ribonucleic acid

ROS .. ..reactive oxygen species

RPEVCD. .. ..remote plasma-enhanced chemical vapor deposition

RRAM.. .. ..resistive random access memory

RTA .. ..rapid thermal anneal

RTD .. ..resistance temperature device

s .. ..seconds

S .. ..sulfur

SA-MOVPE.. .. .. ..selective area metal organic vapor phase epitaxy

SABC .. ..surface active block copolymers

SAED .. ..selected area electron diffraction

SAMs .. ..self-assembled monolayers

Sb .. ..antimony

SBH .. ..Schottky barrier height

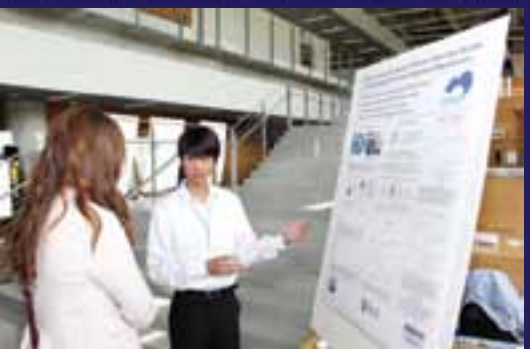

Sc. .. ..scandium
SCAN .. ..single-chromatin analysis at the nanoscale
sccm .. ..standard cubic centimeters per minute
$scCO_2$ .. ..supercritical carbon dioxide
SCOFET.. .. ..single crystal organic field effect transistor
SCORE. .. ..SNARE Complex Reporter
SDS .. ..sodium dodecyl sulfate
Se. .. ..selenium
sec .. ..seconds
SECM .. ..scanning electrochemical microscopy
SEM .. ..scanning electron microscopy/microscope
SERS. .. ..surface enhanced Raman spectroscopy
SF_6.. .. ..sulfur hexafluoride
SFLS . .. .supercritical fluid-liquid-solid
SH .. ..second harmonic
Si . .. .silicon
Si_3N_4.. .. ..silicon nitride
SiAlON .. ..silicon aluminum oxynitride
SiC.. .. ..silicon carbide
SiH_4 .. ..silane
SiN . .. .silicon nitride
SiNWs.. .. ..silicon nanowires
SiO_2 .. ..silicon dioxide
SIROF.. .. ..sputtered iridium oxide film
SLBs.. .. ..supported lipid bilayers
SLG .. ..single-layer graphene
SLM .. ..spatial light modulator
SLUG .. ..superconducting low-inductance undulatory galvanometer
SMS .. ..single molecule spectroscopy
Sn .. ..tin
SnO_2.. .. ..tin oxide
SNPs.. .. ..silver nanoparticles
SNR .. ..signal-to-noise ratio
SOFC. .. ..solid oxide fuel cells
SOI . .. .silicon-on-insulator
SPCM .. ..scanning photocurrent microscopy
SPD .. ..switching phase diagram
SPR .. ..surface plasmon resonance
Sr_2RuO_4 .. ..strontium ruthenate
$SrTiO_3$ .. ..strontium titanate
ssDNA.. .. ..single-stranded deoxyribonucleic acid
ST-FMR .. ..spin torque ferromagnetic resonance
STEM .. ..scanning transmission electron microscopy/microscope
STJ . .. .superconducting tunnel junction
STM .. ..scanning tunneling microscopy/microscope
STO .. ..strontium titanate
STT. .. ..spin-transfer torques
STT-MRAM.. .. .. ..spin-transfer torque magnetic random access memory
SVA .. ..solvent vapor annealing
t-BOC .. ..*tert*-butoxycarbonyl
Ta. .. ..tantalum
Ta_2O_5 . .. .tantalum pentoxide
TaN. .. ..tantalum nitride
TAO_x . .. .tantalum oxide
TCO .. ..transparent conducting oxide
Te. .. ..tellurium
TE .. ..transverse electric
TEC .. ..thermionic energy converter
TEM .. ..transmission electron microscopy/microscope
TER .. ..transepithelial resistance
TFM .. ..traction force microscopy
TFT. .. ..thin-film transistor
T_g. .. ..glass transition temperature
TH .. ..third harmonic
THz .. ..terahertz

Ti . .. .titanium

TiN . .. .titanium nitride

TiO_2 .. ..titanium dioxide

TIR-FRET .. ..total internal reflection - fluorescence resonance energy transfer

TLM .. ..transfer length measurement

TM.. .. ..transverse magnetic

TMAH.. .. ..tetramethylammonium hydroxide

TMOS .. ..tetramethylorthosilicate

TMR.. .. ..tunneling magnetoresistance

TO .. ..thermo-optic

TO .. ..torsional oscillator

TO .. ..transformation optics

TPoS.. .. ..thin-film piezoelectric-on-substrate

TRT .. ..thermal release tape

TSVs . .. .through silicon vias

TTD .. ..transverse translational diversity

TTV .. ..total thickness variation

TXM.. .. ..transmission x-ray microscopy

UHV.. .. ..ultra-high vacuum

UV.. .. ..ultraviolet

UV-Vis . .. .ultraviolet-visible

V.. .. ..vanadium

V.. .. ..voltage

VA-CNT .. ..vertically aligned carbon nanotube

vdW .. ..van der Waals

VLS .. ..vapor-liquid-solid

VSM.. .. ..vibrating sample magnetometry

W. .. ..tungsten

WDM .. ..wavelength-division multiplexing

We number . .. .Weber number

WGM .. ..whispering gallery mode

XeF_2 .. ..xenon difluoride

XMCD.. .. ..x-ray magnetic circular dichroism

XPM.. .. ..cross-phase modulation

XPS .. ..x-ray photoelectron spectroscopy

XRD .. ..x-ray diffraction

XRR .. ..x-ray reflectivity

YBCO .. ..yttrium-barium-copper-oxide

YBS .. ..y-branch switch

ZMW. .. ..zero-mode waveguide

ZnO .. ..zinc oxide

ZnO:Al . .. .zinc aluminum oxide

ZnS. .. ..zinc sulfide or zinc-blende

Zr. .. ..zirconium

ZrO_2 .. ..zirconium dioxide

ZTO .. ..zinc tin oxide

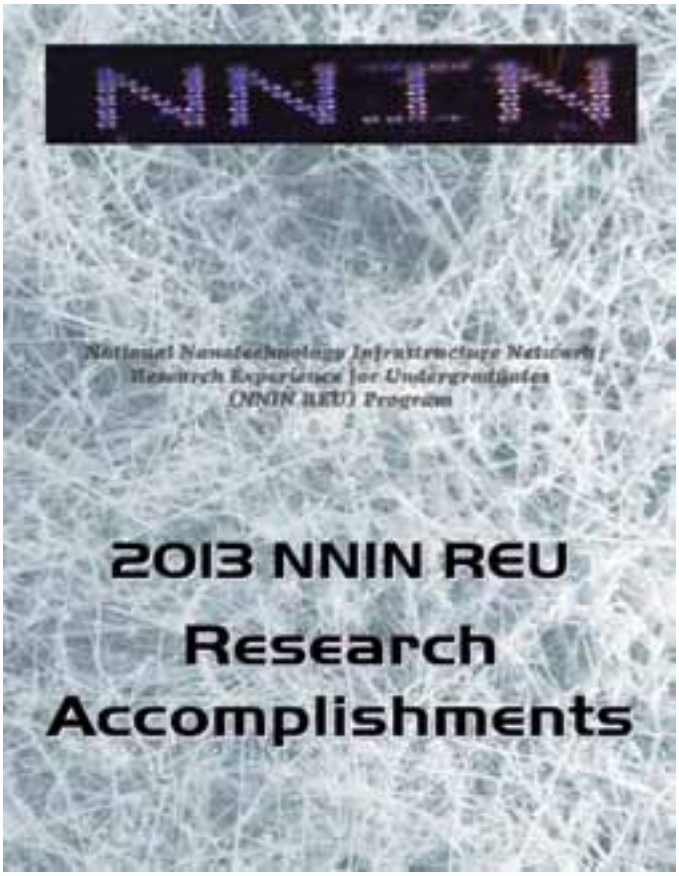

The 2013 NNIN REU Research Accomplishments are also online as secure PDF files at

http://nnin.org/reu/past-years/2013-nnin-reu-program

The photographs in the TOC&INTRO were provided by the NNIN REU and iREU interns, and NNIN staff.

The site photographs were taken by James Griffin.

This book is printed on 10% post-consumer paper, using soy-based inks. Please do your part to reduce, reuse, and recycle.

The National Nanotechnology Infrastructure Network is grateful for the financial assistance of the following corporations:

Agilent Technologies

Analog Devices

Applied Materials

Canon

Daihen Corporation

Ericsson

IBM Corporation

Infineon

Intel Corporation

NEC Corporation

Qualcomm

Renesas Electronics Corporation

Robert Bosch Corp.

SIX Semicondutores

STMicroelectronics

Texas Instruments, Incorporated

Toshiba

National Nanotechnology Infrastructure Network

Research Experience for Undergraduates (NNIN REU) Program

International Research Experience for Graduates (NNIN iREG) Program

International Research Experience for Undergraduates (NNIN iREU) Program

2013 NNIN REU Research Accomplishments

Binding of DU145 Prostate Tumor Cancer Cells to Silicon Carbide

Ayobami Adeleke
Chemistry, Delaware State University

NNIN REU Site: Howard Nanoscale Science and Engineering Facility, Howard University, Washington, DC
NNIN REU Principal Investigator: Dr. Tina Brower-Thomas, Engineering, Architecture, and Computer Sciences, Howard University
NNIN REU Mentor: Dr. Paulette Furbert-Harris, College of Medicine, Howard University
Contact: aadeleke11@students.desu.edu, tina.browerthomas@howard.edu, pfurbert-harris@howard.edu

Introduction:

Prostate cancer occurs in men worldwide. The risk factors vary among different ethnic groups. Prostate cancer has been detected in European and American men more so than in East and South Asian men [1]. DU145, one of the three "classical" cell lines of prostatic cancer, was isolated by K.R. Stone et al. from a wound in the brain of a patient with metastatic carcinoma of the prostate and a three year history of lymphocytic leukemia. The cell line is not detectably hormone sensitive and does not express prostate specific antigen (PSA) [2].

The long-term goal of this study is to explore an alternative technique to differentiate biological cells on silicon carbide substrates by their electrical properties using scanning tunneling microscopy (STM) and a probe technique. To this extent, the specific objective of this project was to examine the binding of metastatic DU145 prostate cancer cells to different types of silicon carbide (SiC): 3C-SiC grown on Si, 6H-SiC, and highly doped (HD) 6H-SiC to determine the most effective binding substrate.

SiC is biocompatible and is utilized in many biomedical applications such as stents, orthopedic implants, in drug delivery and tissue engineering [3]. For applications such as tissue engineering it is important to examine the binding potential and proliferative capabilities of cells as they develop into tissue on SiC substrates. The 3C, 6H and HD 6H poly types of silicon carbide were considered because of their electrical conductivity between that of metals and insulating materials [4]. Depending on their crystal structure and if the material is doped, then poly types have high thermal conductivity and high electron mobility that may be useful in a bio-electronic device.

The number 3 in 3C refers to the three-bilayer periodicity of the stacking structure and the letter C denotes the cubic symmetry of the crystal; similarly, the number 6 in 6H refers to the six-bilayer periodicity of the stacking structure and H denotes the hexagonal symmetry of the crystal.

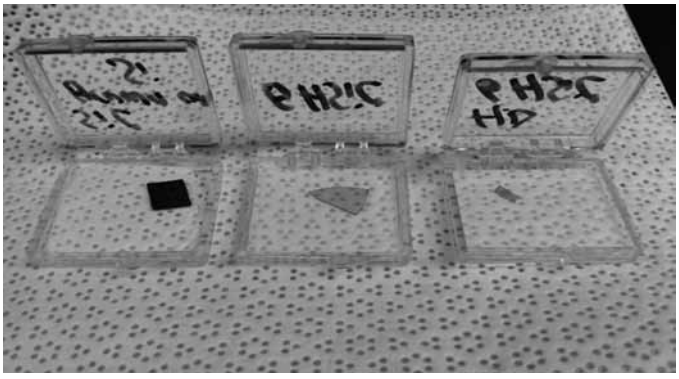

Figure 1: Substrates from left to right: 3C-SiC grown on Si, 6H-SiC, and highly doped 6H-SiC.

Experimental Procedure:

Substrate Preparation. The substrates shown in Figure 1 were cleaned by ultrasonic bath using soap, water, acetone, and methanol sequentially for three minutes each. Cleaned substrates were placed in a dust free cloth lined container.

Tumor Cell. DU145 was purchased from American Type Culture Collection (ATCC). The cells were cultured in complete Roswell Park Memorial Institute (RPMI) 1640 media {5% fetal bovine serum, gentamycin (50mg/ml), penicillin/ streptomycin (5,000 units / 5,000 mg/ml)} in a humidified atmosphere of 5% CO_2 and 95% air.

Binding of Cells to SiC Substrates. DU145 cells were harvested, either from a frozen sample by quick thaw or from trypsin-treated cultures. The cells were counted and adjusted to various concentrations. Substrates were placed into the wells of a 6-well culture plate; 2 ml of cells were added to each well. The plate was incubated overnight at 37°C in 5% CO_2. An Olympus IX71 inverted microscope with an Olympus DP70 camera was used to confirm binding and sizes of the cells on the substrate. Optical microscope mages of the cells bound to 6H and HD 6H-SiC are shown in Figure 2.

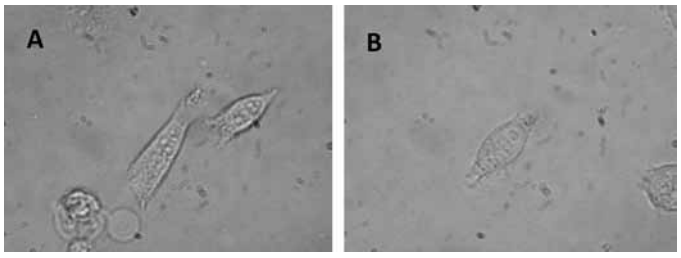

Figure 2: DU145 cells at 5 × 10^4 cells/ml on [A] 6H-SiC, and [B] highly doped 6H-SiC.

Fixing of DU145 Tumor Cells to SiC Substrates. Substrates with DU145 cells were placed into individual wells of a six well plate; 2 ml of methanol was added to each well. After five minutes, the substrates were bathed in water. Five minutes later, the substrates were placed in an empty well and allowed to dry. Atomic force microscopy (AFM) was used to obtain three-dimensional high resolution images of the cells [5].

Experimental Design. Three different experiments (trials) were executed with various concentrations of DU145 cells to determine; 1) the optimal cell concentration for the examination of individual cells, and 2) the most effective substrate for binding cells.

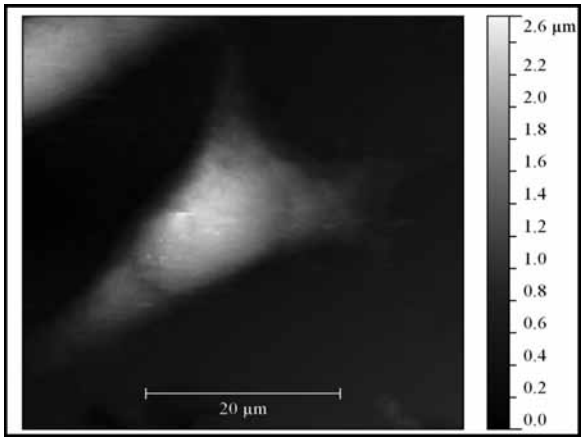

Figure 3: AFM image of luminal-like cells fixed to 6H-SiC.

Results and Conclusions:

A procedure for preparing samples that would allow for the discrimination of cells in a heterogeneous mixture of cells that could be used in STM and the probe technique was developed using the DU145 cell line. Luminal-like cells with a width and length of 44.091 μm and 6.452 μm, respectively, were observed on 6H-SiC and HD 6H-SiC while binding on 3C-SiC was undetermined because of its lack of transparency. The optimum concentration of cells was determined to be 5×10^4 cells/ml. Highly doped 6H-SiC was the better substrate for observing the cells' morphologically.

Future Work:

We plan to apply STM and the probe technique to measure electrical properties (i.e. current-voltage curves) of the cells as an alternative method to differentiate biological materials.

Acknowledgements:

I would like to acknowledge Dr. Tina Brower-Thomas, Ph.D. (Howard University), Dr. Gary Harris, Ph.D. (Howard University), Dr. Paulette Furbert-Harris, Ph.D. (Howard University Cancer Center and Department of Microbiology), Dr. Kim M. Lewis, Ph.D. (Rensselaer Polytechnic Institute), Mr. James Griffin, Mr. Crawford Taylor, Dr. William Rose, Howard Nanoscale Science and Engineering Facility, the National Nanotechnology Infrastructure Network Research Experience for Undergraduates (NNIN REU) Program, the National Science Foundation, and NIH MARC U*STAR Program 2-T34-GM008250-20A2.

References:

[1] http://www.news-medical.net/health/

[2] Wang, S., et al. "Highly Efficient Capture of Circulating Tumor Cells by Using Nanostructured Silicon Substrates with Integrated Chaotic Micromixers," Angew. Chem. Int. Ed. Engl., 50, 3084-3088 (2011).

[3] Schmehl, J. M., Harder, C., Wendel, H.P., et al. "Silicon Carbide Coating of Nitinol Stents to Increase Antithrombogenic Properties and Reduce Nickel Release," Cardiovascular Revascularization Medicine, 9, 255-262, (2008).

[4] H. Morkoç, "Large-band-gap SIC, III-V Nitride, and II-VI ZnSe-based Semiconductor Device Technologies," J. Appl. Phys., 76, 1363-98, 1994.

[5] Kada, G., Kienberger, F., and Hinterdorfer, P., "Atomic Force Microscopy in Bionanotechnology," Nanotoday, 3, 12-19 (2008).

Characterization of Polymer Films on Silicon Photonics Devices for Blood Analysis

Alexandra S. Benson
Chemistry, Hope College

NNIN REU Site: NanoTech User Facility, University of Washington, Seattle, WA
NNIN REU Principal Investigator: Daniel M. Ratner, Ph.D., Bioengineering, University of Washington
NNIN REU Mentor: James T. Kirk, Bioengineering, University of Washington
Contact: alexandra.benson@hope.edu, dratner@uw.edu, jtk8@u.washington.edu

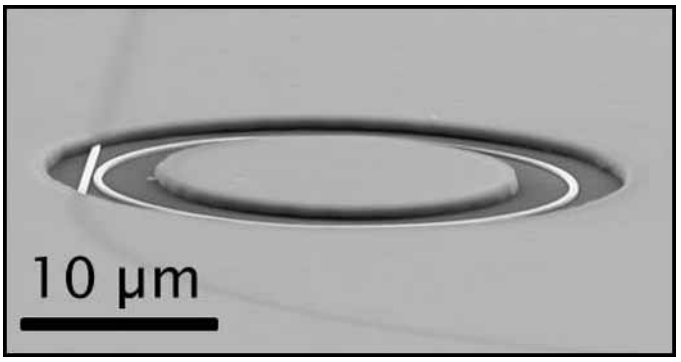

Figure 1: Silicon microring resonator on insulating oxide with fluoropolymer coating.

Introduction:

Silicon photonic devices employ nano- and microscale silicon features as optical guides to direct light in applications such as high-speed telecommunications and biosensing. The microring resonator, an archetypal silicon photonic device, consists of an optical waveguide fabricated in close proximity to a silicon ring (see Figure 1) [1]. Light at a resonant wavelength dependent on ring dimensions and effective refractive index couples into the ring; in biosensing applications, waveguides are modified using surface chemistry to facilitate selective binding of biomaterials from complex media such as blood. With any biological binding event, a shift in resonant wavelength is detected due to a change in the local refractive index at the waveguide surface. Surface protein fouling of these biosensors has been observed upon use in clinical samples, but growth of zwitterionic polymer films through atom-transfer radical polymerization (ATRP) minimizes non-specific binding events while enabling chemical immobilization of capture elements for biosensing [2].

Here, we developed a reliable protocol for the characterization of these polymer films using atomic force microscopy (AFM) to correlate topographical film quality and surface roughness with the ability of modified sensors to inhibit protein fouling. The reproducibility of the polymer film quality was essential for the potential use of these devices in clinical applications, particularly in antibody/antigen binding for performing serologic and phenotypic analysis of biologic samples.

Experimental Procedure:

Silicon microring resonators fabricated by Genalyte in arrays on chips on insulating oxide were piranha-cleaned using a 50:50 solution of 30% H_2O_2 and concentrated H_2SO_4. The chips were oven-dried for several hours prior to overnight solution functionalization with a silane initiator in toluene. Using carboxybetaine methacrylate (CBMA) as the monomer for ATRP, a batch polymerization scheme was employed to produce thin polymer films. Characterization of the polymer film was performed on several chips from different polymerization batches using AFM. Both 5 μm and 3 μm scans were obtained of the waveguide and cladding to measure the average height and large-scale topography of the features on substrates both with and without polymer. Small-scale scans were also obtained in regions near the waveguide at a size scale of 1 μm in order to compare surface roughness and morphology among the bare chips and various batches of polymerization. Polymer film thickness measurements were also deduced from bare silicon substrates used as control surfaces. This was done by scanning regions in which the polymer film had been scratched away down to the silicon surface. All of these measurements were obtained in tapping mode with an OTESPA tip in air or a FESP tip in water.

Results and Conclusions:

AFM was used to measure the polymer film thickness in a scratched region of an unpatterned silicon substrate (see Figure 2). While the numbers obtained via AFM were comparable to those determined using ellipsometry, the data was not within error. Therefore, it is necessary to further develop the protocol for determining film thickness using AFM before it can be used exclusively for this characterization on the microring resonator chips. Something besides ellipsometry is necessary to determine film thickness on the chips due to the complicated architecture and small sample size of the microrings.

Further characterization of the polymer film was performed using AFM in order to correlate topographical data with quantitative data regarding protein fouling. In Figures 3 and 4, images of the topography of the polymer film from two identical batches of polymerization are juxtaposed with graphs

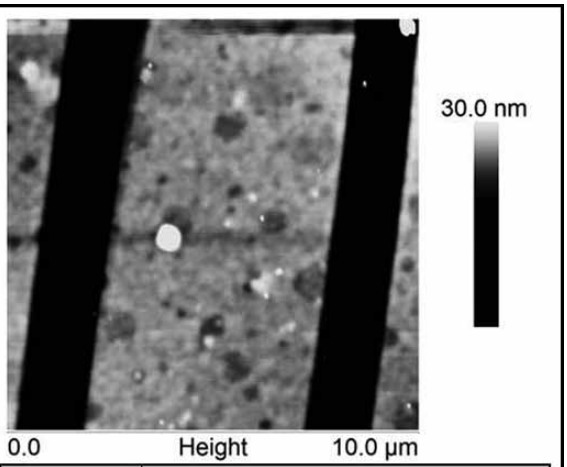

Method	Average Polymer Film Thickness (nm)
AFM	23.1 ± 1.3
Ellipsometry	26.74 ± 0.25

Figure 2: AFM image of scratched region of silicon substrate after first polymerization batch.

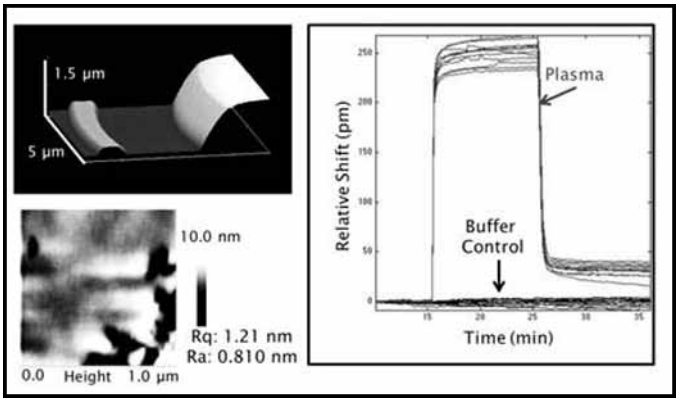

Figure 3: AFM and protein fouling data from first polymerization batch.

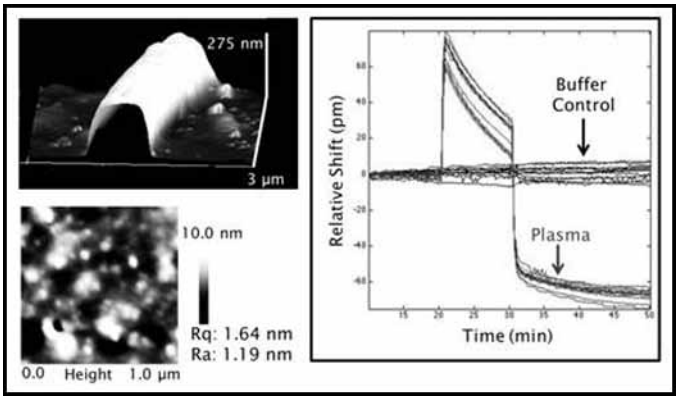

Figure 4: AFM and protein fouling data from second polymerization batch.

concerning the quantity of protein fouling. In Figure 3, the AFM image of the topography of the surface shows that it is smooth with some defects indicated by darker regions. This correlates with the graph that shows that the surface is not to non-fouling standards but does show a lower amount of protein fouling than a bare silicon substrate. In Figure 4, however, the graph shows unexpected results that could be due to a loss of polymer from the surface upon flowing plasma over the chips. This is supported by the AFM data showing that there are large features on the surface of the chip. AFM has been useful to relate the small-scale surface features to the quantitative protein fouling data and will be useful in the further optimization of the batch polymerization process.

Future Work:

The goal is to further optimize the procedure for the characterization of chips with polymer coating using AFM in order to use it more exclusively as a technique for determining polymer thickness on the microring chips for which ellipsometry is not possible. AFM will also be used in a characterization protocol to assist in the optimization of polymer film growth for minimizing protein fouling on the chips. Further, functionalization of the terminal ends of the polymer film will allow for specific immobilization of elements in complex media for detecting biological analytes.

Acknowledgements:

I would like to thank the Ratner lab, especially Dr. Dan Ratner and Jim Kirk, for their support and guidance contributing to my learning throughout my time on the project. My thanks also go out to Dr. Shaoyi Jiang's lab for assistance with the batch polymerization and the Nanotech User Facility at the University of Washington for instrumentation use. Gratitude must also be given to the site coordinator at the University of Washington, Mack Carter. Funding sources included the NSF-funded National Nanotechnology Infrastructure Network Research Experience for Undergraduates (NNIN REU) Program, and NSF Biophotonics Grant Nos. 0930411 and 1264174.

References:

[1] Iqbal, M., et al.; IEEE Journal of Selected Topics in Quantum Electronics, 16, 654 (2010).

[2] Kirk, J.T.; Brault, N.D.; Baehr-Jones, T.; Hochberg, M.; Jiang, S.; Ratner, D.M.; Biosensors and Bioelectronics, 42, 100 (2013).

Developing Nanoscale Electrodes for Sensitive Detection of Brain Cell Activities

Dara Bobb-Semple
Chemistry, Stony Brook University

NNIN REU Site: Stanford Nanofabrication Facility, Stanford University, Stanford, CA
NNIN REU Principal Investigator: Prof. Bianxiao Cui, Chemistry, Stanford University
NNIN REU Mentor: Allister McGuire, Chemistry, Stanford University
Contact: dara.bobb-semple@stonybrook.edu, bcui@stanford.edu

Abstract:

Vertical nanopillar electrode arrays have garnered much attention due to their applications in the study of the electrical behavior of neurons. Previous methods for measuring neuronal activity include the use of planar multielectrode arrays (MEAs); however, neuronal mobility and inefficient neuron-electrode interactions on flat substrate surfaces make it difficult to monitor the activity of specific neurons over extended periods of time. Vertical nanopillar arrays serve as neuron traps by effectively pinning the neurons and also offer a non-invasive measurement technique, thus allowing for long-term study. The aim of this work is to develop a novel electrode device composed of a patterned MEA fabricated on quartz and glass substrates using photolithography and subsequently electrodepositing vertically aligned Au nanopillars of varying diameters (200-600 nm) on the MEA. Using optical microscopy and scanning electron microscopy, it was noted that the specified quality and morphology of the devices were maintained throughout processing.

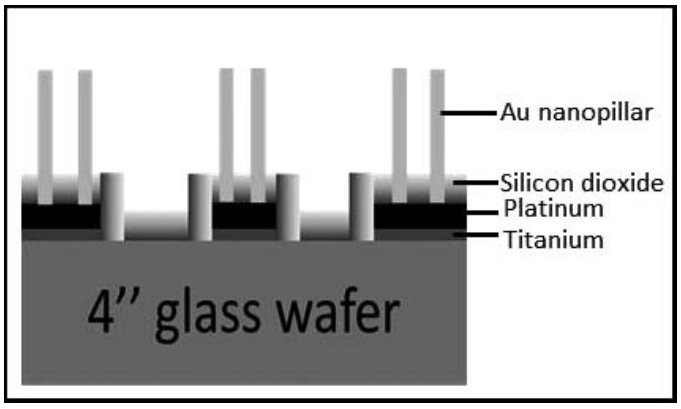

Figure 1: Representation of the vertical nanopillar electrode device.

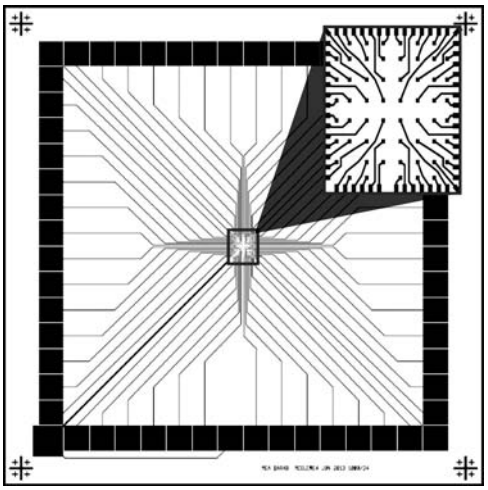

Figure 2: Electrode design pattern.

Introduction:

One of the main problems in measuring action potentials (AP) of neurons is neuronal mobility. Syntheses of many current nanostructures used to address this problem involve complex procedures and loading the neurons can be difficult and time consuming [1]. Other methods to control migration include the use of chemical modification or patterned deposition of proteins to promote neuron-electrode adhesion; however, it is difficult to control how many neurons are attached to each electrode [1].

Accurate AP measurements require efficient coupling of the measuring electrode and cell membrane. Intracellular methods such as patch clamping provide accurate measurements but are invasive and therefore reduce cell life, limiting recording times to only a few hours [2]. Extracellular techniques such as multielectrode arrays (MEAs) have lower signal quality due to the infrequent one-to-one neuron-electrode interactions [2].

Combining the extracellular and intracellular measurement technologies of multielectrode arrays and vertically aligned nanopillars, respectively, provides a non-invasive technique for accurate AP measurements. Vertical nanopillar arrays serve as low throughput intracellular recording electrodes, effectively pinning the neurons for long-term studies [2]. Previous work by Xie et al. has shown that neuritic protrusions wrap the nanopillars with a thin layer of membrane to improve interactions [1]. It is also proposed that vertical nanopillars serve as focal adhesion substrates, allowing for stronger anchorage of the cell matrix than on flat surfaces leading to preferential adhesion of neurons to the nanopillars [1].

In this work, MEA devices are designed and fabricated on glass and quartz substrates. These substrates allow for observation of the nanopillars and neurons on top of the device using optical microscopy. Vertically aligned gold nanopillars are electrodeposited on the surface of the MEA (Figure 1). Gold

is chosen because it is a good conductor, unreactive in most aqueous reagents and has good self-assembly chemistry for surface functionalization. This device will allow for both long-term and multiplexed measurements of the AP of individual neurons at the synapse.

Experimental Procedure:

Two masks with multiple square die, each of edge length 20 mm were designed (Figure 2) and used to pattern four-inch quartz and glass wafers with electrode (10 nm Ti/100 nm Pt) leads and pads using standard photolithography methods. The sizes of the inner contact pads were varied to facilitate variation in nanopillar diameter. The substrate's surface was passivated with a 1.8 μm SiO_2 layer deposited by low pressure chemical vapor deposition. A reactive ion etch was used to expose the outer contact pads of the device for wiring bonding during packaging. The wafer was diced into pieces. A simple electrical test was performed for each piece to confirm electrical connection using a digital multimeter. Electron-beam lithography was used to make holes of diameter 200-600 nm to facilitate pillar growth. A 24K pure gold solution (Gold Plating Services) maintained at 65ºC was used for electroplating.

Results and Discussion:

Optical microscopy and SEM images show that the MEAs maintained the features of the original design (Figure 3 and 4) with clear lines and only small changes (1-2 μm) in feature size. These changes were expected since the device fabrication involved several processing steps. The electrical test confirmed all MEA devices were functioning as expected, indicating that the passivation layer had been successfully etched away from the surface of the outer contact pads.

Attempts to etch through the oxide following e-beam lithography were unsuccessful because the layer of e-beam resist used was too thin. The high etch rate of the resist led to significant reduction in oxide thickness, creating a surface that was not conducive to nanopillar growth. Nevertheless, dummy devices were used to confirm the gold plating conditions.

Conclusions and Future Work:

Patterned MEAs were successfully designed and fabricated using standard photolithography techniques. However, additional work needs to be done in optimizing the technique used in preparing the MEA surface for nanopillar growth. Once these challenges are overcome, nanopillar arrays of varying diameters (200-600 μm) will be electrodeposited on the MEA. In the future, we also hope to vary nanopillar shape and composition to determine how these properties affect action potential measurements in neurons. These nanopillar electrode devices have the potential to serve as high-sensitivity probes for detecting membrane potentials at the synapse level which will help in understanding the long term behavior of neuronal circuits and thus provide insight into the mechanics of the brain.

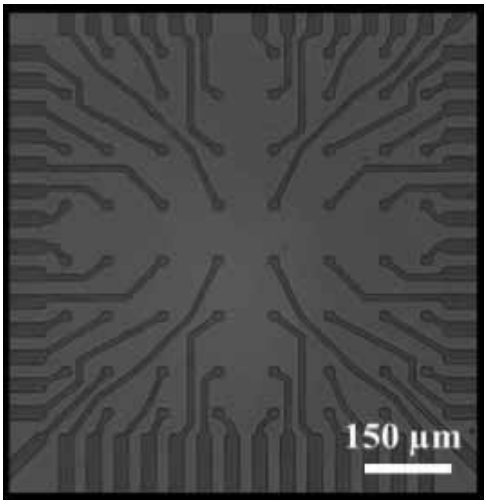

Figure 3: Optical microscopy image showing the center of the MEA, where nanopillar arrays will be grown.

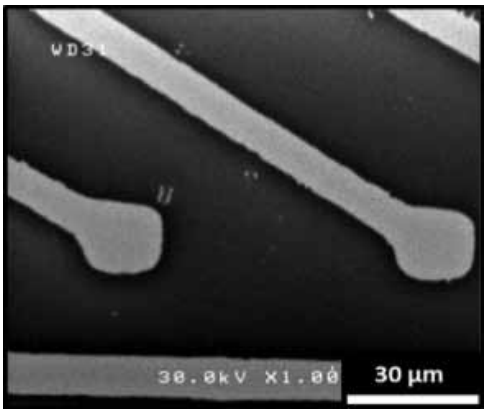

Figure 4: SEM of inner contact pad of the MEA device.

Acknowledgements

Thanks to Professor Bianxiao Cui, Allister McGuire, and the Cui group, Dr. Michael Deal, Maureen Baran, Janee Johnson, SNF staff, the NNIN REU Program, NSF, and CIS.

References:

[1] Xie, C., et al. Nano Lett. Noninvasive neuron pinning with nanopillar arrays 10, 4020-4024 (2010).

[2] Xie, C., et al. Nature Nanotech. Intracellular recording of action potentials by nanopillar electroporation 7, 185-190 (2012).

Delivery of Immunosuppressive DNA Drug for Treatment of Autoimmune Diseases

Colin Burns-Heffner
Bioengineering, Clemson University

NNIN iREU Site: National Institute for Materials Science (NIMS), Tsukuba, Ibaraki, Japan
NNIN iREU Principal Investigator: Dr. Hanagata Nobutaka, National Institute of Materials Science (NIMS)
NNIN iREU Mentor: Hiromi Morita, National Institute of Materials Science (NIMS)
Contact: cburnsh@clemson.edu, hanagata.nobutaka@nims.go.jp, hiromi.morita@nims.go.jp

Abstract:

The focus of this project was drug delivery methods for delivering various deoxyribonucleic acid (DNA) fragments to treat autoimmune disease. A cationic liposome was successfully used to transfect the DNA drugs into the mouse fibroblast cells, significantly reducing the immune response to large B-DNA molecules. The cationic liposomes have some limitations when utilized in other cell types, so other nanoparticle drug delivery methods involving silica nanoparticles were explored. Our experiments have shown that silica nanoparticles are ineffective carriers for these types of DNA drugs.

Introduction:

In autoimmune diseases, large DNA fragments such as the body's own "self" DNA can stimulate an immune response, attacking your own cells. Small DNA fragments, however, do not elicit such a response, so these small fragments can be administered to a patient to occupy the receptors, stopping cells from responding to self-DNA fragments. When the naked DNA fragments were added to cells, there was a small immune suppression effect. In order to increase this effect, a more efficient drug delivery method had to be developed. Three different drug delivery methods were tested: cationic liposomes, silica nanoparticles coated in positively charged PEI, and streptavidin-coated silica nanoparticles bound to biotin-labeled DNA fragments. Experiments involving the two types of silica nanoparticles showed that both failed to suppress the immune response. This demonstrated that silica nanoparticles are an ineffective method of delivering the DNA drugs to cytosolic receptors.

Experimental Procedure:

We first transfected different DNA fragments into cells using a cationic liposome. Single-strand and double-strand versions of three types of DNA fragment were combined with lipofectamine, a cationic liposome, and transfected into cells in a 24-well plate. In each well, 10 μg of the DNA drug were added. After waiting one hour, 10 μg of B-DNA/lipofectamine were added into all of the wells. After 24 hours, the supernatant was collected from each well and tested to see the concentration of two cytokines (IL-6 and IFN-β). A greater amount of these cytokines indicates a strong immune response, while a lesser amount means that the DNA drug suppressed the immune response. To measure the cytokine concentrations, a process called enzyme-linked immunosorbent assay (ELISA) was used. This process uses antibodies to bind to the cytokines, creating a color assay that can then be read by a plate reader. The absorbance levels were compared to a standard curve, revealing the concentrations of the two types of cytokines.

After that experiment was finished, we employed a similar technique to test the silica nanoparticle coated with PEI. First, we made the DNA drug/nanoparticle complex. A silica/PEI solution was prepared with 0.05% PEI and 10 mg of silica nanoparticles. This was mixed for one hour and centrifuged at 150,000G for 30 minutes. The pellet was re-suspended in 5 mL of water. Three tubes were then prepared: one with double-stranded CpG, one with single-stranded CpG, and one control with only silica and PEI. In each, 1 mg of silica nanoparticles and 80 μg of DNA were mixed with water for a total volume of 1 mL. The three tubes were then placed in a rotating machine for one hour, centrifuged at 150,000G for 30 minutes, and re-suspended in 1 mL of water. Once the silica/PEI/CpG complex was finished, they were transfected into cells and the cytokine levels were measured in the same manner described above.

The next experiment involved streptavidin-coated silica nanoparticles bound to biotin-labeled CpG. The silica/streptavidin nanoparticles were first washed in a wash buffer, mixing 400 μl of the silica/streptavidin nanoparticle with 1 mL of wash buffer and centrifuging at 5,000 rpm for five minutes, discarding the supernatant, and re-suspending the pellet in 400 μl of wash buffer. Three tubes were then prepared: one with double-stranded CpG, one with single-stranded CpG, and one control with only silica/streptavidin nanoparticles. In the two tubes containing DNA, 80 μg of either single or double-stranded CpG were mixed with 2.5 mg of silica/streptavidin nanoparticles for a final volume of 200 μl. Once the silica/streptavidin/CpG-biotin complexes were finished, they were transfected into cells and the cytokine levels were measured using ELISA, as described previously.

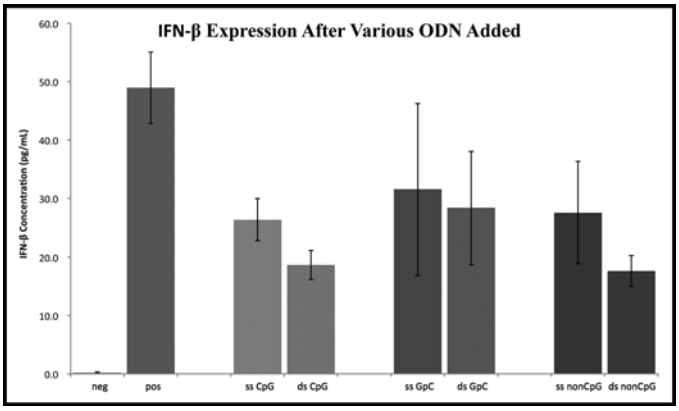

Figure 1: Cytokine suppression effect of DNA drugs with cationic liposome delivery method.

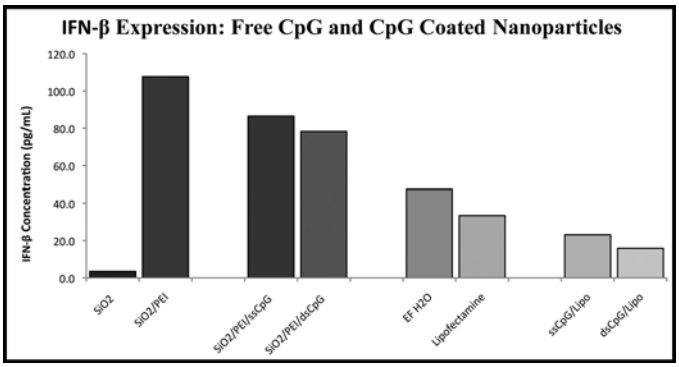

Figure 2: Cytokine suppression effect of DNA drugs with silica/PEI nanoparticle delivery method.

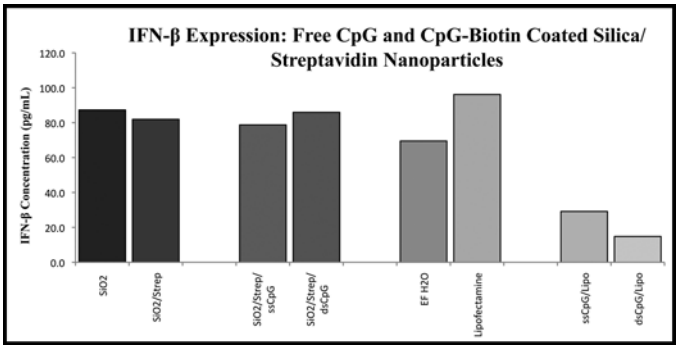

Figure 3: Cytokine suppression effect of DNA drugs with silica/streptavidin/ CpG-Biotin delivery method.

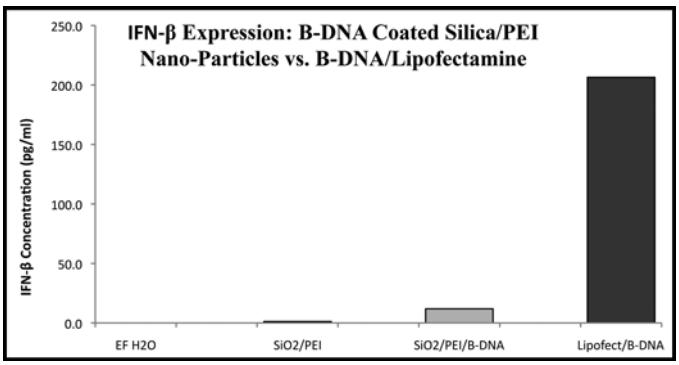

Figure 4: Cytokine expression after silica/PEI/B-DNA nanoparticle delivery method vs. cationic liposome/B-DNA delivery method.

When these silica-based delivery methods failed to suppress the immune response, one last experiment was conducted to confirm a hypothesis on why they were failing. Instead of binding the DNA drug to the silica/PEI nanoparticle, transfecting that into the cells, and then adding the B-DNA (to aggravate the immune system), the B-DNA was bound to the silica/PEI nanoparticle and then transfected into the cells. To make the silica/PEI/B-DNA complex, the same silica/PEI procedure described above was used, only the B-DNA was substituted for CpG.

Results and Conclusions:

The only drug delivery method that effectively suppressed the immune response was the cationic liposome, as can be seen in Figure 1. Double-stranded CpG showed 62% suppression in IFN-β and 74% suppression in IL-6. The two silica nanoparticle delivery methods showed no suppression. Figure 2 shows that PEI actually created an even greater cytokine output than the controls. In Figure 3, it can be seen that cells treated with the silica/streptavidin/CpG nanoparticles had the same cytokine production as the controls.

From this data, it was hypothesized that the silica nanoparticles were getting stuck in the endosomes of cells when taken up by endocytosis, so the DNA drugs weren't able to access the receptors in the cytosol. This was tested by transfecting silica/PEI/B-DNA nanoparticles into cells, and the cytokine outputs seen in Figure 4 support this hypothesis, as even the B-DNA wasn't able to get to the cytosolic receptors and elicit an immune response. From this data, it can be concluded that silica nanoparticles are ineffective carriers of DNA drugs when targeting receptors in the cytosol.

Acknowledgements:

Dr. Hanagata Nobutaka, Hiromi Morita, National Nanotechnology Infrastructure Network International Research Experience for Undergraduates (NNIN iREU) Program.

Cisplatin-Based Metal Organic Framework Nanoparticles for Targeted Drug Delivery and Tumor Imaging

Samantha Renee Corber
Physics, Chemistry, Washburn University

NNIN REU Site: Nano Research Facility (NRF), Washington University in St. Louis, St. Louis, MO
NNIN REU Principal Investigator: Prof. Samuel Achilefu, Radiology, Washington University in St. Louis School of Medicine
NNIN REU Mentor: Dr. Rui Tang, Radiology, Washington University in St. Louis School of Medicine
Contact: samantha.corber@washburn.edu, achilefus@mir.wustl.edu, tangr@mir.wustl.edu

Abstract:

Nanoscale metal organic framework (NMOF) particles are nanoparticles composed of an amorphous framework constructed from an organic linker ligand and a metal ion. These nanoparticles are excellent candidates for use in drug delivery due to their biodegradability, tunable size and high loading capacity. In this study, we synthesized novel NMOFs based on the anti-cancer drug cisplatin with high payload (83%). A targeted near-infrared (NIR) molecular probe was also incorporated into this nanoparticle to achieve NIR imaging capability and targeted drug particle delivery. The anticancer effect of the nano-construct was demonstrated on cancer cells and the targeted delivery of this nano-theranostic agent was evaluated both *in vitro* and *in vivo*.

Introduction:

Metal organic frameworks are materials composed of metal ions coordinated with organic linker ligands. When shrunk down to the nanoscale, the potential for drug delivery applications arise [1]. The drug can be directly loaded into the porous in the framework or alternatively the framework can be constructed with the drug acting as the organic linker. By building the framework from the drug itself, one can increase the payload of the particle while decreasing the overall unwanted material. However, not all drugs can be used in the framework directly in this fashion. For example, a stringent requirement is that the metal ions should form the framework with the desired drug.

In this project, we constructed MOF nanoparticles based on the anti-cancer drug cisplatin with a simple nanoprecipitation method. Different nanoparticle sizes were obtained when using different precipitation procedures. To achieve the controlled drug delivery and imaging capability, we coated the amorphous prodrug nanoparticle with polymer and silica shells, at the same time, an integrin targeted imaging probe LS301 was incorporated to achieve the targeted tumor imaging. The morphologies and sizes were characterized via electron microscopes and dynamic light scattering. *In vitro* and *in vivo* studies were also conducted to confirm the targeted imaging capability and therapeutic effect.

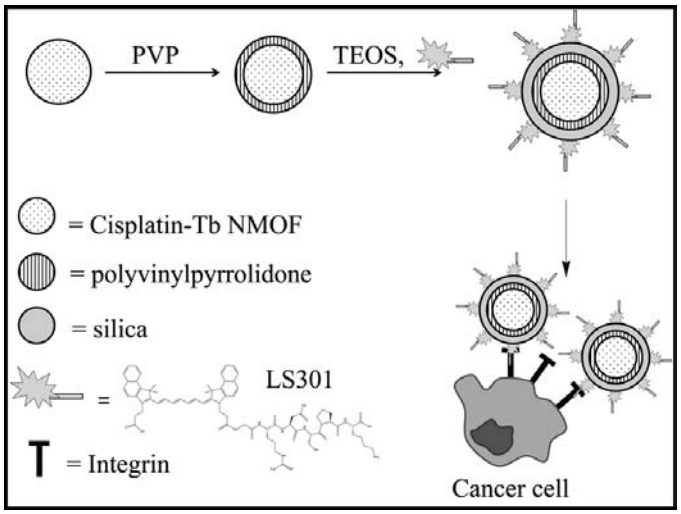

Figure 1: Coating scheme for nanoscale metal organic framework particles.

Experimental Procedure:

A disuccinatocisplatin (DSCP) salt was first synthesized [1]. Methanol was added to the mixture of DSCP prodrug NPs with terbium salt to form the NMOF construct through the nanoprecipitation process [2]. By modifying method to precipitate the prodrug NPs, we were able to obtain particles with different sizes. Polyvinylpyrrolidone (PVP) and silica shells were coated onto this NMOF construct subsequently to achieve the controlled the drug release. At the same time, NIR imaging probe cypate-cyclic GRD (LS301) [3] was also incorporated into the nano-construct to make it capable for targeted tumor imaging (Figure 1).

Results and Conclusions:

The particles were characterized by scanning electron microscopy (SEM), transmission electron microscopy (TEM), and dynamic light scattering (DLS) to determine the morphology and size. Figure 2a shows a SEM image of NP1-uncoated, and

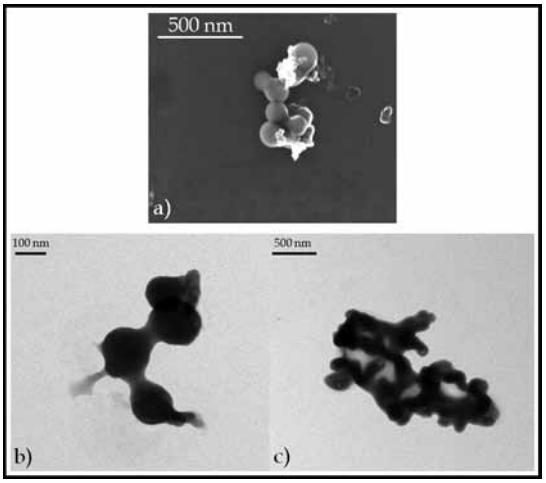

Figure 2: a) SEM image of NP1-uncoated. b) TEM image of NP2-uncoated. c) TEM image of NP1-silica/probe.

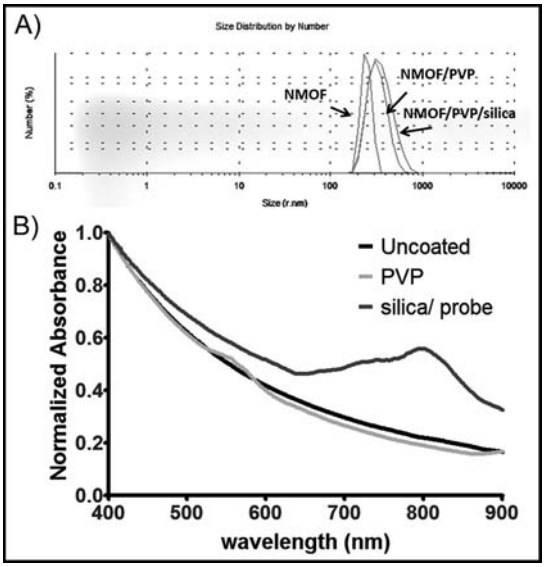

Figure 3: a) Graph of size distribution of uncoated, PVP coated and silica/probe coated NP1 determined by DLS. b) Normalized absorbance of bare, PVP and silica/probe coated NP1.

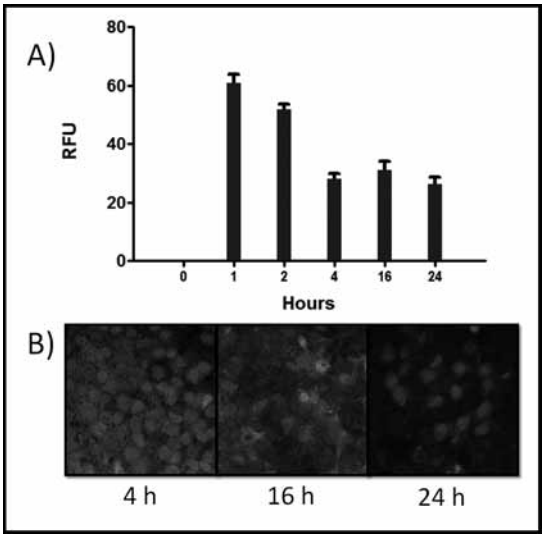

Figure 4: a) Relative fluorescence of cells at various time points during the internalization study. b) Representative images of the fluorescence of LS301 and nuclear stain during internalization at various time points.

Figure 2b and c shows a TEM image of NP2-uncoated and NP1-silica/probe. The DLS results demonstrating the change in size as a function of time during the coating procedure can be seen in Figure 3a. The absorption (Figure 3b) and emission spectra were recorded on a spectrophotometer and spectrofluorometer, respectively for NP1 uncoated, PVP-coated and silica coated NPs. NP1-silica/probe sample exhibited an emission peak around 800 nm that indicates the targeted imaging probe LS301 was successfully incorporated into the nano-construct.

The internalization of the silica-probe coated NP1 was investigated in A431 cancer cells. The relative fluorescence of the NMOF particles at different time point is shown in Figure 4. The high intensity of fluorescence after one hour shows that NP1 rapidly internalized in the cells. Following this peak intensity, the fluorescence intensity gradually decreased with time until it plateaued after four hours. This decrease in fluorescence was probably caused intracellular degradation of the particles, which was accompanied by the drug release. The observed fluorescence enhancement at one hour incubation could be attributed to sequestration of the dye in the silica shell [4]. Subsequent degradation of the silica shell resulted in the release of the LS301 molecular probe, with the attendant loss of fluorescence enhancement by the silica shell.

Conclusions and Future Work:

To summarize, we successfully synthesized a high payload cisplatin-based NMOF anti-cancer drug construct with targeted tumor imaging capability. The controlled drug delivery and targeted tumor imaging were demonstrated in both *in vitro* and *in vivo* studies. In the future, more drugs or co-drug will be examined to form this kind of NMOF construct to explore the better drug delivery and therapeutic effect.

Acknowledgements:

I am very grateful to my PI Prof. Samuel Achilefu and mentor Dr. Rui Tang for their guidance and patience throughout this project. I would also like to thank the NRF for programming and instrument training and assistance. Finally, I would like to thank the NNIN REU Program for the opportunity and NSF for funding.

References:

[1] Huxford, R.C., Rocca, J.D., and Lin,W. Curr. Opin. Chem. Biol. 2011, 14(2), 262-268.

[2] Reiter, W.J., Pott, K.M., Taylor, K.M.L., and Lin, W. J. Am. Chem. Soc. 2008, 130, 11584-11584.

[3] Achilefu, S., Bloch, S., Markiewicz, M.A., Zhong, T., Ye, Y., Dorshow, R.B., Chance, R.C., and Liang, K. Proc. Natl. Acad. Sci. U. S. A. 2005, 102, 7976-7981.

[4] Kim, J.S., et al. Nanomedicine 2012, 7(2), 219-229.

System Automation for High Throughput Biosensor

Dakota Nevans Crisp
Physics and Engineering Physics: Electrical Applications, Southeast Missouri State University

NNIN REU Site: Microelectronics Research Center, The University of Texas, Austin, TX
NNIN REU Principal Investigator: Dr. Ray T. Chen, Electrical and Computer Engineering, University of Texas at Austin
NNIN REU Mentor: Dr. Swapnajit Chakravarty, Omega Optics, Inc.
Contact: dncrisp1s@semo.edu, raychen@uts.cc.utexas.edu, swapnajit.chakravarty@omegaoptics.com

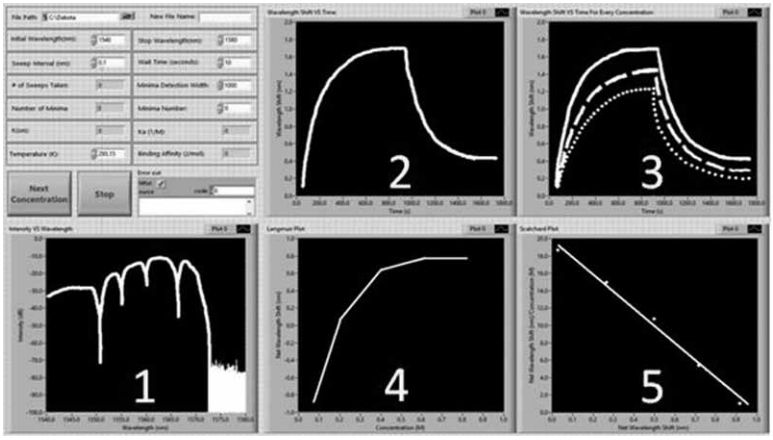

Figure 1, left: Screen shot of LabVIEW program made to automate data collection and analysis. Synthesized data was placed into the graphs in order to demonstrate how the program would operate while making biosensing measurements. (1) Transmission spectrum of each laser sweep. (2) Resonance Wavelength vs. Time. (3) Resonance Wavelength vs. Time for each sample concentration. (4) Net Red Shift vs. Concentration. (5) Scatchard linear regression of Net Red Shift vs. Concentration. Note the net red shifts in (2) and (3).

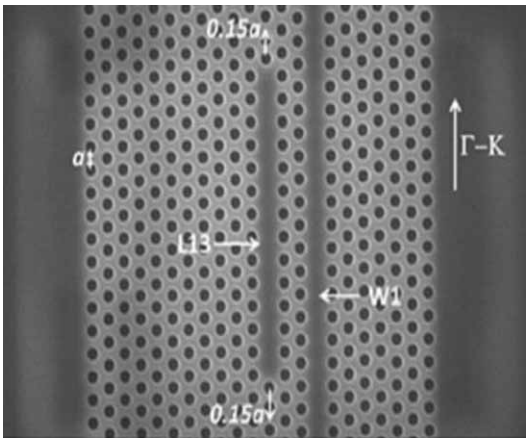

Figure 2, right: SEM showing an L13 microcavity coupled to a W1 PC waveguide [1].

Abstract and Introduction:

Photonic crystal (PC) microcavities have demonstrated the highest sensitivities among label free, chip based, optical biosensors. These high sensitivities coupled with the study of binding kinetics have important implications in the fields of biomarker and drug discovery for pharmaceutical industries. Chip based biosensors permit miniaturization, leading to the possibility of economical personal diagnostic assays for detecting biomarkers of cancer [1].

A holistic approach for studying binding kinetics requires studying the effects on the biosensor of several samples with various biomolecule concentrations. Real-time data acquisition, concentration modification, and sample/sensor interaction control was automated using LabVIEW. See Figure 1 for the front panel of our program showing synthesized data, which delivered a step by step procedure of analysis.

Multiplexed biosensor devices have the ability to detect multiple biomolecules by functionalizing their conjugate pair (receptor) onto the microcavities of the different arms of the multiplexed device. See Figure 2 for basic device structure. Bovine serum albumin (BSA) is commonly used to block non-specific binding, thus securing the specificity of the device. As a function of time, biomolecules will bind to their respective receptor, change the index of refraction, and appropriately induce a red shift for the resonance wavelength of the transmission spectrum. Upon red shift saturation, a buffer wash is introduced. Upon buffer saturation, a net red shift is produced, denoting the difference between the final resonance wavelength and the initial resonance wavelength. A Scatchard regression of the plot of net red shift versus biomolecule concentration produces a line whose absolute value of the slope is Ka; ΔG can be found by using the Gibb's free energy equation for the inverse of the Ka.

Experimental Procedure:

Troubles with biomolecule contamination lead to the characterization of our automation program to be preformed allowing the biosensor to detect changes in molar concentration of sugar water. Fiber optic cables were coupled with the gratings of our biosensor. The input and output cables were connected to a tunable laser and photodetector, respectively. Initially, 40 μL of deionized water was introduced to the sensor. After

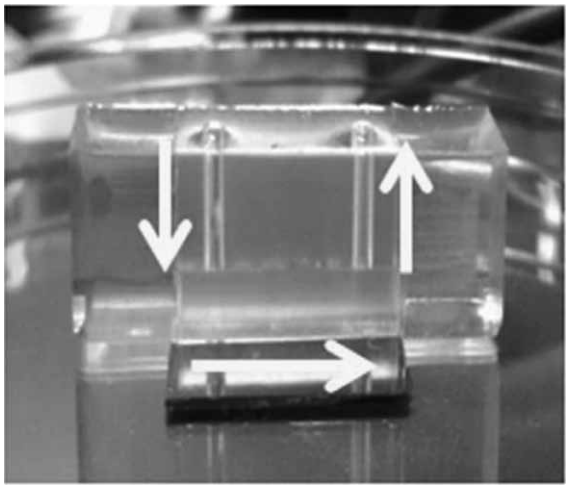

Figure 3: Enclosed microfluidic channel mold fitted onto a sensor. This design allowed for dynamic sample flow/interaction with the waveguide and microcavites.

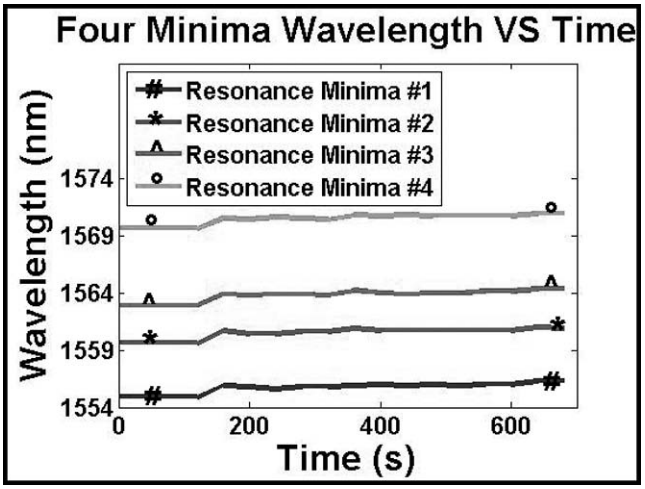

Figure 4: Plot of all four resonance wavelengths versus time with increasing molar concentration of sugar water. Overall red shifts are detected for each resonance minima.

160 seconds, 5 μL of 200 M sugar water was added on top of the deionized water every 80 seconds. The idea was to slowly increase the molar concentration of the sample without making noticeable changes to the sample size.

Before microfluidics could be implemented into our biosensing, characterization had to be made. An enclosed microfluidic channel mold was bonded to a dummy wafer with UV-curing optical adhesive. See Figure 3. The dummy wafer was used because it perfectly matched the device the mold would be used with in the future, but would save ruining actual devices. Two syringes fitted to two syringe pumps were connected with a "Y"-joint, whose output was connected to the input of the microfluidic channel. The output of the microfluidic channel was lead to a waste receptacle. Using an additional, independent program to automate syringe pump control, adhesive application techniques, adhesive strength, and maximum flow rate were then tested. Thorlabs NOA61 and NOA81 optical adhesives were used.

Results and Conclusions:

Our biosensing automation program worked successfully using chemical sensing. A real-time plot showing the change in resonance wavelength versus time and easy control over the setup was demonstrated. See Figure 4.

A maximum flow rate of 1 mL/min was achieved with the NOA81 optical adhesive. It was determined that the NOA61 optical adhesive had too weak of a bond strength to be used in conjunction with our microfluidic pressure conditions. The syringe pump control program worked successfully. A new mold with input and output ports in the horizontal direction rather than the vertical direction was submitted to our local machine shop. This design should further reduce pressure inside the mold, lessening the chances of leaking and contaminating the stage. Due to time constraints, a mold of this design was not able to be tested during this internship.

Future Work:

The next step would be to integrate the syringe pump control program with the data collection and analysis program. This would create a singular program that would control almost every aspect of the experiment all from one panel. Furthermore, once the biomolecule problem is fixed, biosensing will resume. The singular program can then be used to begin taking data and studying binding kinetics in order to determine Ka and ΔG.

Acknowledgements:

I would like to personally thank the National Nanotechnology Infrastructure Network Research Experience for Undergraduates (NNIN REU) Program for this fantastic opportunity. Credit also goes to the National Science Foundation (NSF) for funding NNIN. Finally, I would like to thank my PI, Dr. Ray Chen, my mentor, Dr. Swapnajit Chakravarty, and the graduate students in my research team for all of the help and guidance over the summer.

References:

[1] Chakravarty, S.; Lai, W.; Zou, Y.; Drabkin, H.; Gemmill, R.; Simon, G.; Chin, S.; Chen, R. T.; Biosensors and Bioelectronics 43 (2013) 50-55.

Engineering Three-Dimensional Biological Scaffolds Using a Modified Rotary Jet Spinning System

John Phillip Ferrier, Jr.
Physics/Mathematics (Double Major), University of Central Arkansas

NNIN REU Site: Center for Nanoscale Systems, Harvard University, Cambridge, MA
NNIN REU Principal Investigator: Prof. Kevin Kit Parker, Disease Biophysics Group, Harvard University
NNIN REU Mentor: Dr. Sung Jin Park, Disease Biophysics Group, Harvard University
Contact: jpferrierjr@gmail.com, kkparker@seas.harvard.edu, sjinpark@seas.harvard.edu

Abstract:

Protein fibers with nanoscale diameters comprise the extracellular space in tissues and organs in the body. Current tissue engineering approaches often fail to recapitulate the three-dimensional nanoscale geometry of extracellular matrix fibers. Here, we have designed and developed modifications to a rotary jet spinning (RJS) system for fabricating nanofibers. Traditionally, the RJS produces two-dimensional sheets of polymer nanofibers at high speeds by solution extrusion through a perforated reservoir. Due to the nanometer thickness of the elongated polymer droplets, the nanofibers quickly dry and solidify and then are collected on a mandrel. The focus of this project is to engineer an automated nanofiber production and mandrel collection system in order to (a) easily create anisotropic scaffold tissue, and (b) generate small three-dimensional basic organ structures. The RJS system was constructed with multiple points of actuation for precise control, a computer program that allows for various parameter inputs to alter the fabrication process, a specially made support structure, and a custom designed interfacing circuit to allow for digital controls over high-voltage inputs and outputs. Currently, the RJS system is nearing the completion of its engineering process. With these modifications, we will be able to replicate the three-dimensional nanostructures of tissues and organs.

Introduction:

Advancements in biological research have created a demand for new substrates to be utilized for cellular development and testing. New biological scaffolds are needed to test cell dynamics in a three-dimensional environment and provide a structure for tissue development. This new structure would allow for more effective techniques in tissue experimentation *in vitro* [1]. It was hypothesized that the structure of these biological scaffolds could be engineered using the process of rotary jet spinning (RJS) [2]. This process can be visualized in Figure 1.

Figure 1: Rotary jet spinning (RJS) nanofiber extrusion.

Experimental Procedure:

The configured RJS system produced thin sheets of the scaffold nanofibers. The process needed to be changed to include a more accurately controlled environment and a nanofiber collection system to build three-dimensional biological scaffolding. The leading idea involved using a rotating mandrel collection system that could be motioned linearly through the developing thin sheets of nanofibers. This design allowed for varying speeds of collection and different scaffold structures. *Figure 2 has been removed from this report*.

This RJS system was designed to be run by computer program that interfaced with the motor controls of actuating part of

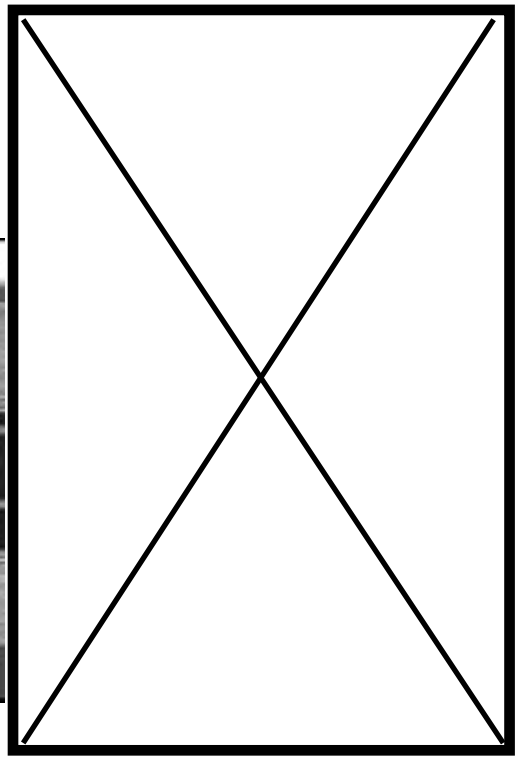

the system. In order to accurately design the interface, the respective motors needed to be chosen. For the center RJS motor that produces the nanofibers, an 80,000 rpm Nakanishi motor was selected to allow for a large range of centrifugal forces to aid in the development of smaller nanofibers. A Maxon motor was chosen for the collection mandrel. The Maxon motor can achieve speed rates up to 6,000 rpm, but it was reduced to 2,285 rpm to keep the collected nanofibers from being spun off of the mandrel.

Figure 3: RJS system program Graphical User Interface (GUI).

Figure 4: Center RJS system motor with mandrel.

The linearly actuating motor is used to move the collection mandrel through the nanofiber extrusion zone for collection. Different speeds of the linear motor cause the collection process to produce various scaffold structures. To allow for a wide range of scaffolding options, a high-speed/high-torque system was needed. For this task, a Misumi linear stepper motor actuator was chosen.

Results and Conclusions:

The program for the system was written in LabView with a simple Graphical User Interface (GUI) that displays the proper operation of the system to the end user as seen in Figure 3. To interface between the computer program and motor controls, a circuit was constructed to translate the digital signals of the computer into high-voltage signals and controls over the motors.

With the parts that were received, the RJS system center motor was constructed, as seen in Figure 4. When the center motor and the collection mandrel motor were connected to the main circuit board and tested, both worked in accordance to their respective operations in the program. These two were the only ones tested since the linear motor had still not been received.

Future Work:

The RJS system requires the integration of the linear motor system. After this is complete, the system can be tested operationally. The RJS system was designed with many variables in the system set to constant rates. This was done for simplicity in the engineering process. After the RJS system has been completely assembled and tested, an upgraded version has been devised that allows for the set variables to be varied both automatically through the operating program and manually. This will allow the system to fully test differing extrusion and collection scenarios to pinpoint optimum nanofiber extrusion techniques for building ideal anisotropic biological scaffolding for different solutions.

Acknowledgments:

I would like to thank my principal investigator, Prof. Kevin Kit Parker, for opening his lab and giving me the opportunity to learn. I'd also like to thank my mentor, Dr. Sung Jin Park, for his guidance and support. A special thanks is needed for Matthew Hemphill, Grant Gonzales, and Josue Goss for their help around the lab and great advice. I would like to thank Harvard University, the School of Engineering and Applied Science, the Disease Biophysics Group, Dr. Kathryn Hollar, Ms. Melanie-Claire Mallison, the National Nanotechnology Infrastructure Network Research Experience for Undergraduates (NNIN REU) Program, and the National Science Foundation (NSF) for the opportunity to receive this experience.

References:

[1] Geisse, N.A., Feinberg, A.W., Kuo, P., Sheehy, S., Bray, M.A., and Parker, K.K. "Micropatterning Approaches for Cardiac Biology." Micro- and Nanoengineering of the Cell Microenvironment: Technologies and Applications. A.Khademhosseini, M.Toner, J.T.Borenstein, S.Takayama, editors. Boston: Artech House; 2008:341-357.

[2] Badrossamay, M.R., McIlwee, H.A., Goss, J.A., and Parker, K.K. "Nanofiber assembly by RJS." Nanoletters. 2010;10:2257-2261.

Fabrication of Nanofluidic Devices for DNA Confinement

Suman Gunasekaran
Engineering Sciences, Harvard University

NNIN REU Site: Minnesota Nano Center, University of Minnesota-Twin Cities, Minneapolis, MN
NNIN REU Principal Investigator: Prof. Kevin Dorfman, Chemical Engineering and Material Science, University of Minnesota
NNIN REU Mentor: Dr. Julian Sheats, Chemical Engineering and Material Science, University of Minnesota
Contact: sumangunasekaran@college.harvard.edu, dorfman@umn.edu, jtsheat@umn.edu

Abstract:

Confining deoxyribose nucleic acid (DNA) in a nanochannel affords the elongation necessary for DNA barcoding, a promising genomic mapping technique. Therefore, our objective was to fabricate nanofluidic devices that would allow for efficient confinement of genomic DNA. To limit DNA sticking to the channel walls, fused silica, an inherently hydrophilic material, was used as the device substrate. After overcoming many fabrication hurdles, these nanofluidic devices were successfully fabricated; however, DNA sticking to the nanochannels proved to be a significant issue during device loading. Scanning electron microscopy (SEM) images of the nanochannels indicated that channel roughness was likely the cause. The fabrication process was further refined, in regards to electron-beam lithography, to minimize this roughness.

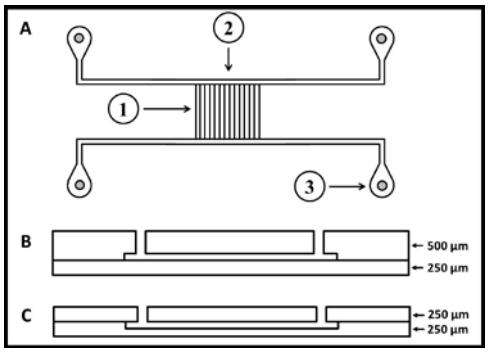

Figure 1: A) Device layout: 1. Nanochannels, 2. Microchannels, 3. Through holes. B) Cross-section of device design. C) Cross-section of initial device design, which did not bond well due to warping.

Introduction:

Accurate, low-cost genome sequencing will have broad implications in a wide variety of fields such as personalized medicine [1]. Next-generation sequencing methods have made tremendous strides over the past decade in accuracy and read length. However, these 'short read' shotgun sequencing methods possess inherent limitations for entire genome sequencing. Repetitive genomic regions, which account for half of the human genome, cannot be directly mapped [2], and technologies that rely on ensemble measurements are unable to detect rare genomic variations [3].

Confining genomic DNA to a nanochannel can afford numerous sequence analysis techniques without the need for amplification or DNA fragmentation. If DNA can be loaded into a channel ~ 50 nm wide, the DNA molecules cannot fold back on themselves and are forced by physical confinement to be in an elongated, linearized state [3]. If the DNA is fluorescently labeled at specific sequences, the confined DNA creates a distinct optical pattern, resembling a barcode that provides a large-scale view of the genomic DNA. This technique known as DNA barcoding provides a scaffold for *de novo* construction of sequence data obtained from next-generation sequencing methods, allowing for entire genome sequencing [1].

Thus the objective of the project was to establish a robust method for fabricating nanofluidic devices that effectively confine genomic DNA. Specifically, we wanted to use fused silica, which is inherently hydrophilic, as the substrate material to limit DNA sticking to the nanochannel walls [3].

Device Fabrication:

The nanofludic devices were fabricated on 10 cm diameter, 500-μm-thick fused silica wafers. Each device contained of an array of nanochannels between two parallel microchannels with reservoirs for loading (Figure 1). To fabricate the nanochannels, electron-beam lithography was used. Since fused silica is an insulating material, 30 nm of aluminum was deposited on the wafers to prevent charging. An electron beam resist layer was spin-coated on top of this aluminum layer, and standard techniques were used to define, develop, and etch the device patterns. This process produced channels 60 nm deep and 50-150 nm wide (depending on the predetermined electron beam exposure level). The microchannels and reservoirs were patterned by contact photolithography and were etched by a wet and dry etch sequence. Sandblasting was then used to establish the through holes on the back of the wafer. After thorough cleaning, the etched wafer was physically pressed onto a 250-μm-thick wafer and fusion-bonded overnight.

Initial attempts to fabricate the devices using two 250-μm-thick wafers (Figure 1) were unsuccessful because it was difficult to establish a good bond between the wafers. Analysis indicated that significant warping in the wafers, most likely due to undesired etching, was the possible cause.

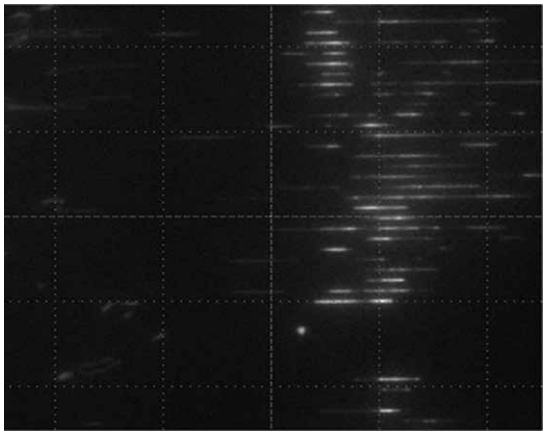

Figure 2: Fluorescently dyed λ-DNA in nanochannels. Bright areas are locations of DNA sticking.

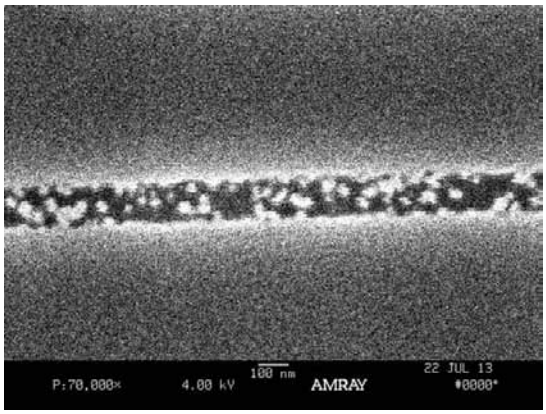

Figure 3: SEM image of channel obtained from initial fabrication procedure.

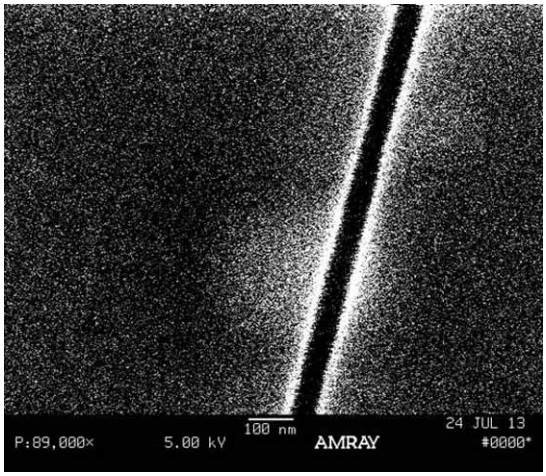

Figure 4: SEM image of channel obtained from modified fabrication procedure.

Device Evaluation:

The device was filled with 2.5X tris, borate, ethylenediaminetetraacetic acid (TBE) aqueous buffer containing B-mercaptoethanol (5% w/w), ascorbic acid (0.07% w/w), and polyvinylpyrrolidone (0.01% w/w). Genomic DNA from virus phage λ, dyed with fluorescent label YOYO-1, was pipetted into the reservoir, pumped through the microchannel, and subsequently forced into the nanochannels by an applied voltage. However, as DNA moved through the nanochannels, a large portion of the DNA was sticking to the channel walls (Figure 2).

SEM micrographs of the device indicated that there was significant roughness on the bottom and sides of the nanochannels which is most likely the reason for the DNA sticking (Figure 3). To reduce channel roughness, the electron-beam lithography process was modified by depositing the 30 nm aluminum layer above the electron beam resist instead of below it. This modification allowed for a more complete removal of the aluminum layer, thereby creating a cleaner fused silica etch. Nanochannels produced following this protocol were significantly smoother (Figure 4); however, more analysis and testing is needed to confirm that channel roughness has been reduced.

Future Work:

After establishing a robust fabrication procedure that produces smooth channel walls, the next step would be to load DNA into the nanochannels to determine if the modified procedure has reduced DNA sticking. These nanofluidic devices will be used to further our understanding of how confined DNA behaves, which will ultimately help enable better genomic mapping technologies.

Acknowledgments:

I thank Dr. Julian Sheats, Prof. Kevin Dorfman, and the staff of the University of Minnesota Nanofabrication Center for helping with the project, and the NNIN REU Program and the NSF for financial support.

References:

[1] Lam, E.T., et al. Genome mapping on nanochannel arrays for structural variation analysis and sequence assembly. Nature Biotechnology, 30, 771-776 (2012).

[2] Treangen, T.J. and Salzberg, S.L. Repetitive DNA and next-generation sequencing: computational challenges and solutions. Nature Reviews Genetics, 13, 36-46 (2012).

[3] Reisner W., et al. DNA confinement in nanochannels: physics and biological applications. Reports on Progress in Physics, 75, 10 (2012).

Conformable Conducting Polymer Electrodes used with an Ionic Liquid Gel for Electroencephalography

Camryn Johnson
Biological Engineering Major, Louisiana State University at Baton Rouge

NNIN iREU Site: Centre Microélectronique de Provence, Ecole Nationale Supérieure des Mines de Saint Etienne, France
NNIN iREU Principal Investigator: Dr. George Malliaras, Department of Bioelectronics, Centre Microélectronique de Provence, Ecole Nationale Supérieure des Mines de Saint Etienne
NNIN iREU Mentor: Pierre Leleux, Department of Bioelectronics, Centre Microélectronique de Provence, Ecole Nationale Supérieure des Mines de Saint Etienne
Contact: cjoh197@lsu.edu, malliaras@emse.fr, leleux@emse.fr

Introduction:

Electroencephalography (EEG) is a non-invasive and relatively inexpensive diagnostic tool that typically uses metallic electrodes on the surface of the scalp to measure electrical activity in the brain. Commercial silver/silver chloride (Ag/AgCl) electrodes used in EEG require a liquid electrolyte to decrease the electrode-skin impedance. This electrolyte not only often dries out quickly, preventing recording over longer time periods, but it also can sometimes cause short circuits if it leaks between two electrodes in a high density electrode array [1].

One path to improving EEG electrodes is having a flexible electrode, which improves the contact with the skin and thus decreases the electrode-skin impedance [2]. In a similar effort, conducting polymers are also being researched as a material to be used due to their flexibility, high conductivity, rough surface area (and thus lower impedance), and biocompatibility [3]. Additionally, polymerized ionic liquids are appealing for use as a quasi-solid-state electrolyte in combination with an electrode because they do not run or dry out, solving two of the main problems with electrolytes currently used in EEG [4].

In this project, we improved upon current electrodes by decreasing the electrode-skin impedance and improving time stability using a combination of a conformal substrate, conducting polymer, and an ionic liquid gel. We show that the ionic liquid gel improves the performance and time stability compared to commercial electrodes.

Experimental Procedure:

Figure 1 illustrates the fabrication process for the devices. Gold electrodes were patterned using a standard shadow mask evaporation process onto a two-micron layer of Parylene C. We then insulated the electrodes with two additional layers of Parylene C. Subsequently, standard photolithography was used to expose only the electrode sites to etching. Following etching, the conducting polymer poly(3,4-ethylenedioxythiophene): poly(styrenesulfonate) — PEDOT:PSS — was spun over the entire wafer. The top layer of Parylene C was removed from the electrodes and contact pads, leaving the remaining Parylene C to insulate only the interconnects. This process yields conformal electrodes with a thickness of only 4 μm.

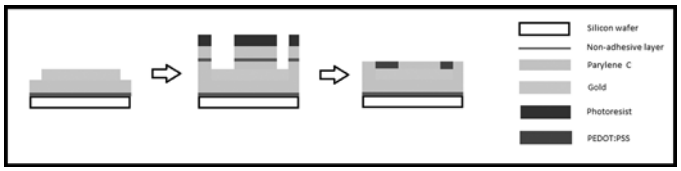

Figure 1: The fabrication process for the electrodes.

Figure 2: A demonstration of the device's conformability. (See full-color version on inside cover.)

The holder was laser-cut out of Kapton®, and gold was then deposited. This holder was attached to the thin electrode, preventing it from curling up into itself and providing a more stable contact pad than the delicate Parylene C. Figure 2 demonstrates the flexibility of the device.

The ionic liquid gel was made using an ionic liquid (1-ethyl-3-methylimidazolium ethyl sulfate), a monomer (poly(ethylene glycol) diacrylate), and a photo initiator. It was then coupled with the electrode as a quasi-solid-state electrolyte.

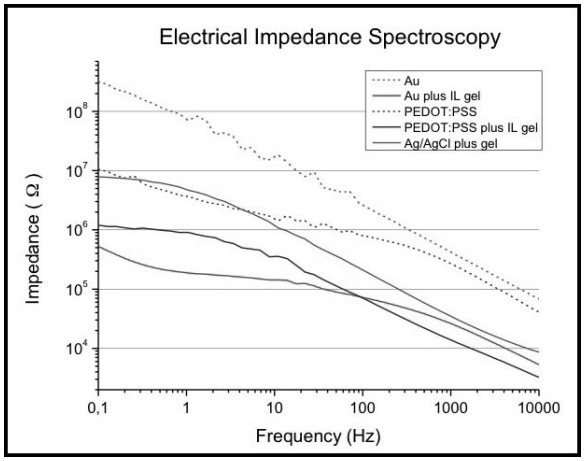

Figure 3: Electrical impedance spectroscopy done on electrodes with gold only, PEDOT:PSS only, gold plus an ionic liquid gel, PEDOT:PSS plus an ionic liquid gel, and commercial Ag/AgCl with a gel.

Results:

We tested the impedance of the ionic liquid gel on electrodes, along with several different controls. We fabricated electrodes with PEDOT:PSS only, gold only, PEDOT:PSS plus the ionic liquid gel, and gold plus the ionic liquid gel. We also tested a commercially available Ag/AgCl electrode used for clinical purposes. Figure 3 shows the electrical impedance spectroscopy for each of these electrodes. The electrode with only PEDOT:PSS demonstrated a better impedance than the gold only, the electrode that performed the worst. The increased surface area of the PEDOT:PSS provides an increased capacitance, thus lowering the impedance. The ionic liquid gel significantly improved the performances of both the gold and the PEDOT:PSS electrodes to a range similar to commercially available electrodes.

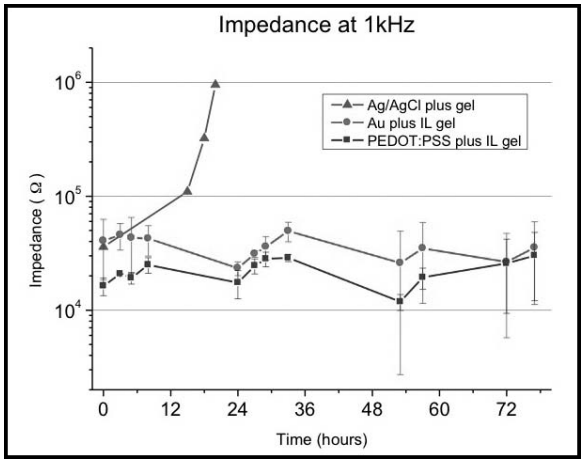

Figure 4: Electrode-skin impedances measured at 1 kHz for electrodes with gold plus an ionic liquid gel, PEDOT:PSS plus an ionic liquid gel, and commercial Ag/AgCl with a gel.

Figure 4 shows the impedance at 1 kHz measured for gold electrodes with the ionic liquid gel, PEDOT:PSS electrodes with the ionic liquid gel, and commercial Ag/AgCl electrodes with a commercial gel over three days. All three electrodes began in approximately the same range, but while the impedance of the commercial electrode steadily increased, the impedance of both the PEDOT: PSS and gold electrodes with the ionic liquid gel maintained relatively consistent low impedance. Both the electrodes with the ionic liquid gel remained at a steady low impedance over three days, while the commercial Ag/AgCl electrode quickly dropped off in performance after only one day. Although both the PEDOT: PSS and the gold electrodes with the ionic liquid gel are in approximately the same range, the PEDOT: PSS electrodes exhibited more stability in performance.

Conclusions:

In conclusion, we developed a process for the fabrication of conducting polymer EEG electrodes with a thickness of only 4 μm. These electrodes are incredibly conformal, improving their recording quality and decreasing their electrode-skin impedance. We also used an ionic liquid gel coupled with these electrodes, which further reducing their impedance. We showed that the ionic liquid gel did not dry out, even over three days, compared to the commercially available gel. This provides a means of recording data with EEG over extended periods of time, which is often a necessity. The gel also functions as a solid-state electrolyte, resulting in less chance of leakage and a short circuit. This solves two of the biggest problems clinicians face when using EEG. These improvements to current electrodes could provide a path to better and more accurate EEG recordings, meaning clinicians could rely less heavily on more invasive diagnostic techniques.

Acknowledgements:

This work was supported by funding from the National Nanotechnology Infrastructure Network International Research Experience for Undergraduates (NNIN iREU) Program, the National Science Foundation, and EMSE-CMP. Special thanks to my PI, Dr. George Malliaras, and my mentor, Pierre Leleux.

References:

[1] L.-D. Liao, I.-J. Wang, S.-F. Chen, J.-Y. Chang, C.-T. Lin, Sensors (Basel, Switzerland) 2011, 11, 5819-34.

[2] J.-Y. Baek, J.-H. An, J.-M. Choi, K.-S. Park, S.-H. Lee, Sensors and Actuators A: Physical 2008, 143, 423-429.

[3] N. K. Guimard, N. Gomez, C. E. Schmidt, Progress in Polymer Science 2007, 32, 876-921.

[4] J. Lu, F. Yan, J. Texter, Progress in Polymer Science 2009, 34, 431-448.

Development of Microfluidic Devices for Use in Immunophenotyping

Meghan Kazanski
Biomedical Engineering, University of Rochester

NNIN REU Site: Lurie Nanofabrication Facility, University of Michigan, Ann Arbor, MI
NNIN REU Principal Investigator: Jianping Fu, Mechanical Engineering, University of Michigan, Ann Arbor
NNIN REU Mentors: Weiqiang Chen and Xiang Li, Mechanical Engineering, University of Michigan, Ann Arbor
Contact: mkazansk@u.rochester.edu, jpfu@umich.edu, wqchen@umich.edu, xngli@umich.edu

Abstract:

Immunophenotyping presents significant promise in the diagnosis and prognosis of immune system disorders. While a means of detection of diseases including HIV/ AIDS, tuberculosis and sepsis, current methods (flow cytometry and enzyme-linked immunosorbent assay or ELISA), lack specificity, as well as time and sample-volume efficiency. Microfluidic devices may present the solution to such limitations. Through the integration of a high-porosity, polydimethylsiloxane (PDMS) microfiltration membrane (PMM), with a microfluidic microfiltration platform, microbead filtration may be used to achieve antigen-specific cellular isolation. The PMM was fabricated via semiconductor microfabrication techniques including traditional lithography and reactive ion etching (RIE). The silicon molds for components of the microfiltration platform were fabricated using photolithographic techniques, followed by deep reactive ion etching (DRIE). The PDMS components were then fabricated via soft lithography and layered to construct a complete device for microfiltration and chemiluminescence assay application for highly sensitive subpopulation characterization. This microfluidic device may drastically reduce time, costs and inaccuracies of immunophenotyping, yielding more efficient detection, evaluation, and treatment of disorders.

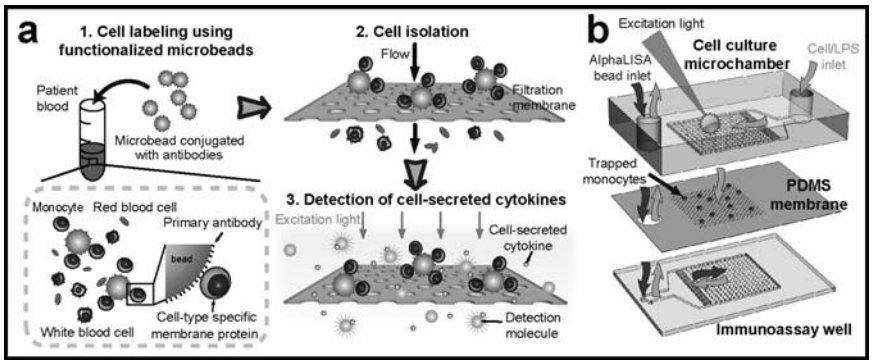

Figure 1: The proposed PMM-integrated device.

Introduction:

The immune system has various leukocyte constituents within the blood, maintaining particular functions in disease combating. Infections and other obstructions cause abnormalities amongst constituents, characterized in the numbers, proportions or functional responses of leukocyte subpopulations. For example, human immunodeficiency virus (HIV) causes $CD4^+$ T cell depletion. Thus, the identification of disproportionately-low $CD4^+$ T cells and overall T-cell proportions provide an indication of acquired immunodeficiency syndrome (AIDS) [1]. Immunophenotyping technology is used to identify qualitative abnormalities in immune cell subpopulations for use in diagnosis and prognosis. The current challenge in the design of immunophenotyping devices is overcoming the time, cost, and sample-size inefficiencies, while increasing characterization specificity. A microfluidic device is proposed with the integration of a high-porosity PMM within a microfluidic chamber, consisting of cell culture and immunoassay components (see Figure 1). The PMM is designed for efficient bioparticle separation. Microbeads are coated with cell-specific antibodies, resulting in the selective capture of the cell subpopulations via bonding of cell surface proteins to beads. Pore diameters are designed to trap only bead-subset groups above the PMM. The PMM was fabricated with traditional lithography and RIE [2], then layered between microchamber components [1]. This device will isolate cell subsets and characterize populations using a no-wash chemifluorescence assay (AlphaLISA) [3].

Experimental Methods:

PMM Micromachining. PMM fabrication was completed using a surface micromachining technique for soft materials [2]. A silicon wafer was O_2-plasma activated and silanized with (tridecafluoro-1,1,2,2,-tetrahydrooctyl)-1-trichlorosilane vapor for later PMM release. The PDMS prepolymer was prepared with a 1:10, curing agent: base monomer ratio, spun onto silanized wafers at 7,000 rpm for 30 s, then cured at 60°C overnight. The PDMS surface was plasma activated for 5 min, with coating of AZ 9260 photoresist immediately following. A soft-bake process at 90°C for 10 min and traditional exposure

and development followed. The wafers were processed with RIE using SF_6 and O_2 mixtures to anisotropically pattern PDMS layers.

Device Construction. The device consisted of cell culture and immunoassay layers fabricated from silicon molds made via photolithography and deep reactive ion etching (DRIE) [1]. The cured PDMS structures sandwiched the PMM atop a glass slide via a O_2 plasma-assisted bonding process.

Device Testing / Functional Immunophenotyping. Device testing included capture efficiency of the PMM, quantified with ImageJ. The cultured cells were labeled and captured according to previous protocol [1]. Microbeads and cells were quantified via hemocytometer, then imaged via fluorescence microscopy (see Figure 4). After microfiltration of cells, LPS addition induced cytokine secretion. AlphaLISA signal detection was facilitated by AlphaLISA bead interaction with cytokines [1, 3].

Results and Discussion:

The PMM was successfully fabricated and integrated into the device (see Figures 2 and 3). Some membranes were corrupted during the micromachining process due to separation between photoresist and PDMS layers following exposure. Moderate success rates during PMM fabrication suggest a need for improvement in the micromachining process, including an adjustment in soft-baking or plasma-activation steps to ensure adequate photoresist-PDMS annealing. High capture purities (~95%, whole and lysed) confirm that the PMM successfully filters cells. Percentage of monocytes were at 4% and 6% for whole and lysed blood, respectively, within the range of $CD14^+$ monocyte content for a healthy individual (see Figure 4), confirming that the correct subpopulation was isolated. The multi-component device facilitates multi-step processes with high specificity and reduced time (10-fold reduction), sample volume (5 μL / assay) and effort of processes, confirming it as a superior immunophenotyping device.

Conclusions:

We successfully fabricated a PDMS-based, bioparticle separation membrane that is easily integrated into a microfluidic, immunophenotyping device. Immune cells were isolated and characterized for use in functional immunophenotyping. The testing of microfiltration capabilities revealed that the membrane had a high capture yield and capture purity. The same device yielded successful characterization of immune cells via AlphaLISA biosensing with a vast reduction in process time. With the shortened assay time, heightened sample efficiency, and the ability to determine the functional status of subpopulations of immune cells, the PMM-integrated device is a novel approach to diagnosis and prognosis of immune diseases and disorders.

Acknowledgements:

Research was supported by the National Science Foundation (NSF) and the National Nanotechnology Infrastructure Network Research Experience for Undergraduates (NNIN REU) Program. Further thanks are offered to the Integrated Biosystems and Biomechanics laboratory at the University of Michigan, Ann Arbor, and the Lurie Nanofabrication Institute (LNF).

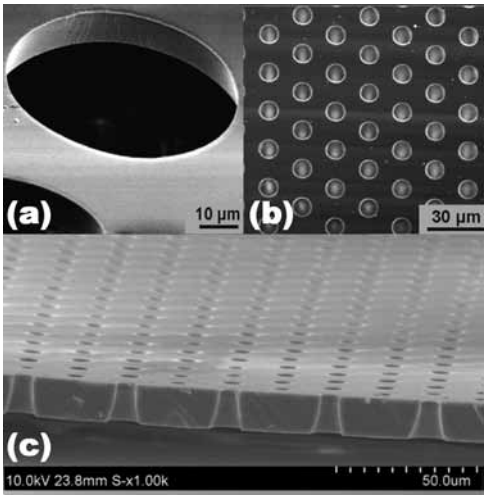

Figure 2: SEM views of the PMM, including above-membrane (a) and (b), and cross-sectional (c).

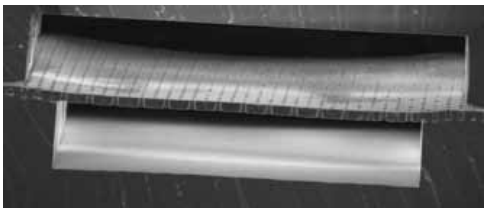

Figure 3: The complete device, with PMM between chamber components.

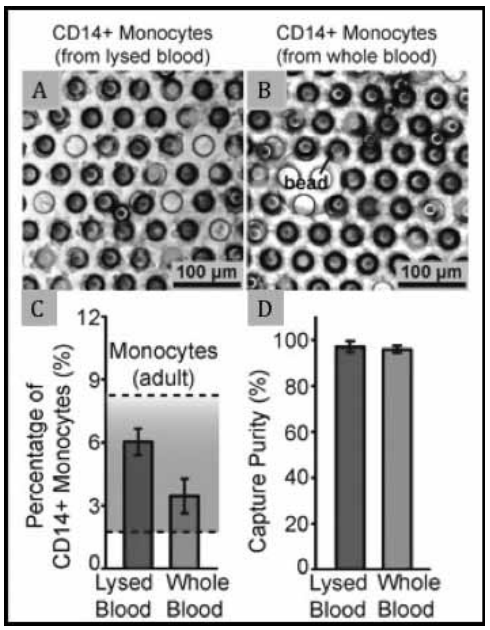

Figure 4: Images of monocyte capture from lysed and whole blood (A and B), monocyte percentages and capture purity for samples (C and D).

References:

[1] Chen, W., et al., Material Views, 1-11, 2013.
[2] Chen, W., et al., Lab Chip, 12, 391-395, 2012.
[3] Bielefeld-Sevigny, M., Assay Drug. Dev. Technol., 7, 90, 2009.

Cell Polarization on Circular Topography with Various Radii of Curvature

Peter Kim
Material Science and Engineering, Northwestern University

NNIN REU Site: NanoTech User Facility, University of Washington, Seattle, WA
NNIN REU Principal Investigator: Professor Deok-Ho Kim, Bioengineering, University of Washington
NNIN REU Mentors: Peter Kim and Kevin Mun, Bioengineering, University of Washington
Contact: peterkim2016@u.northwestern.edu, deokho@uw.edu, pkim40@uw.edu, kmuney@u.washington.edu

Abstract:

Recent studies have shown that cells orient along micro/nano-scale grooves that model the extracellular matrix (ECM) and provide a bidirectional cue for migrating cells [1]. Using ultraviolet (UV)-assisted capillary lithography techniques, sub-cellular sized arrays with varying radii of curvature were fabricated as a model system to probe cellular migration on curved substrata. Chinese hamster ovary (CHO) cells were cultured and plated on substrates with and without the micro-scale circular patterns. From time lapsed live cell imaging, the results demonstrated more explicitly that the cells polarized along the direction of topographic feature, and preliminary data showed that cell elongation was greater on the patterned surface verses cells on the flat surface.

Introduction:

The topographical and mechanical properties of the structure a cell adheres to are key factors in determining cellular response. These features are important for controlling the direction and speed of migration during cellular growth [2]. Better understanding of how cells sense and react to the physical features of their substrata can lead to optimized methods for tissue and muscular regeneration. With advances in fabrication techniques of biomaterials that has enabled stronger control over micromechanical and environmental properties such as local rigidity and curvature of the ECM components, micro-scale circular concentric ring patterns were constricted to model the natural curvatures in the ECM. We hypothesized that Chinese hamster ovary (CHO) cells will react to the micrometer range topographical features of the patterns by sensing the curvature and migrating along the grooves.

Experimental Procedure:

Liquid polyurethane acrylate (PUA, 301 MPa) was drop-dispensed onto treated cover glass (~ 10 μL/cm^2). A mold with the circular concentric patterns was pressed down on the PUA and rolled flat to form a uniform PUA layer on the cover glass. This combination was then exposed to UV light for 20 seconds, after which the mold was carefully peeled off from the cover glass, and an identical circular concentric array remained on the cover glass. The fabricated cover glasses were then placed under a UV lamp overnight to completely cure any remaining liquid PUA. Each cover glass was subsequently attached to the bottom of a cell culture device for cell plating.

Prior to plating the cells, each well of the cell culture device was coated with a 1.0 mL solution of Collagen Type I (50 μg/mL) for six hours. To detach the CHO cells from their culture dishes, 2.0 mL of trypsin base (0.05%) was pipetted into each dish for three minutes. The detached cells were washed down and added to 6.0 mL of Dulbecco's modified eagle medium (10.0% fetal bovine serum, 1.0% penicillin strip). One milliliter of this solution was added to each well of the cell culture device. The CHO cells were given 24 hours to adhere to the surface of the cover glass. Time-lapse image series were acquired from an electronic, inverted microscope (Nikon).

Results and Conclusions:

As seen in Figures 1 and 2, the cells on the flat substrate had random orientation while the cells on the patterned substrate aligned along the direction of the micro-scale grooves. After quantifying our data (Figure 3), the results confirmed that the cells on the flat substrata had a substantial amount of directional deviation from the curvature of a circle, while the cells that migrated on the patterned substrata had a very small average directional deviation from the curvature of a circle. Our protocol allowed us to successfully polarize cells along the grooves of our micro-patterned arrays.

As shown in Figure 4, cell elongation was greater for the cells on the patterned surface compared to the cells on the flat surface. Our preliminary data also suggested that cell elongation slightly increased as distance from the center of the concentric rings increased. This may be due to factors involving focal adhesions to increasing degrees of curvature. Our results confirmed that the topographical features of the micropatterns increased the elongation of the cells that migrated on them, and the elongation of a cell may be dependent upon the degree of curvature of the substrata underneath.

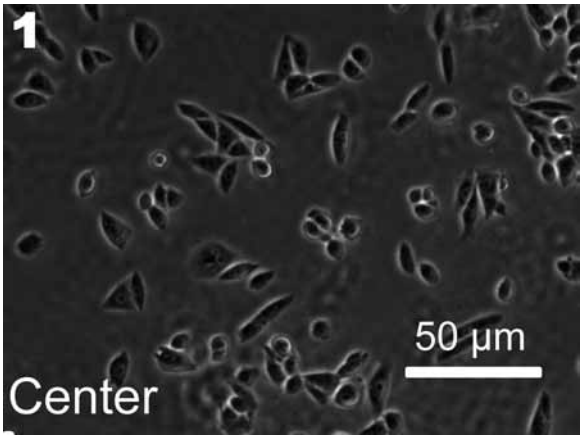

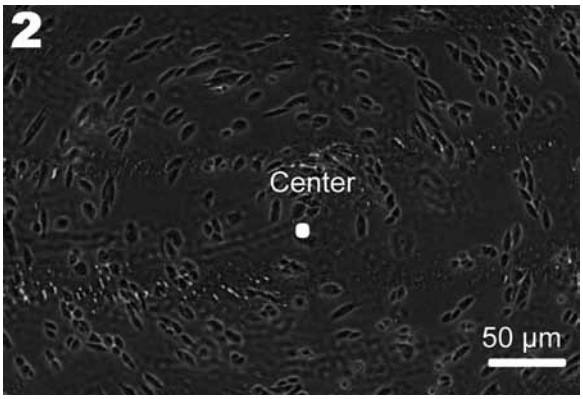

Figure 1, top: Cells on flat substrata after 24 hours of plating.

Figure 2, bottom: An entire micro-patterned array after 24 hours of plating. Cells appear to polarize along the concentric arrays.

Future Steps:

Studying initial adhesion processes, focal adhesions, and the attachment/detachment of cells will allow us to better understand how cells are able to sense the topographical features of the substrata they grow on. Observing cell skeletal fiber alignment and alpha-actin stress fiber distribution will help us better understand the mechanisms behind cellular migration.

Acknowledgements:

This research was supported by the National Nanotechnology Infrastructure Network Research Experience for Undergraduates (NNIN REU) Program and the National Science Foundation. I would like to thank the Kim Lab for their valuable guidance and the NanoTech User Facility at the University of Washington for providing the equipment and training necessary for this project.

References:

[1] D.-H. Kima, E.A. Lipkea, P. Kimc, R. Cheonga, S. Thompsona, M. Delannoyd, K.-Y. Suhc, L. Tunga, and A. Levchenkoa. Proceedings of National Academy of Sciences. J. 2010, 107, 565-570.

[2] D.-H. Kim, Kshitiz, R.R. Smith, P. Kim, E.H. Ahn, H.-N. Kim, E. Marba, K.-Y. Suhf, and A. Levchenko. Integrative Biology. J. 2012, 4, 963-1144.

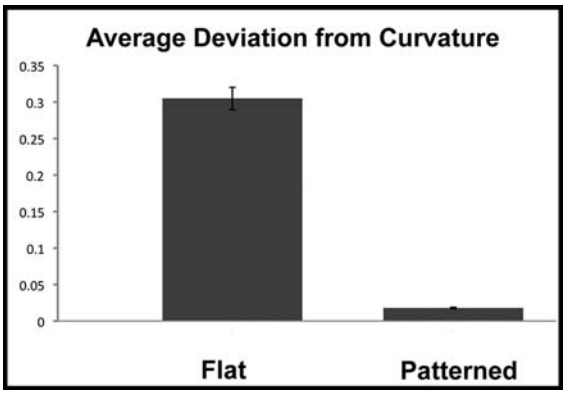

Figure 3: Cells on the concentric arrays showed much less directional deviation from curvature compared to the cells on flat substrata.

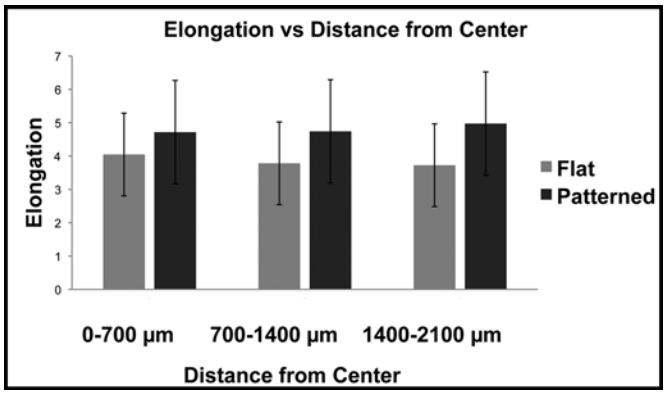

Figure 4: Cells on the concentric arrays had greater elongation than cells on flat substrata. Also, there seems to be a correlation between increasing distance from the center of the concentric arrays and increasing elongation.

Fabrication of "Barcode" Nanowires for Multiplexed Detection in Biological Assays

Seung Yeon Kim
Chemical and Biomolecular Engineering, Georgia Institute of Technology

NNIN REU Site: Minnesota Nano Center, University of Minnesota-Twin Cities, Minneapolis, MN
NNIN REU Principal Investigator: Dr. Bethanie Stadler, Electrical and Computer Engineering, University of Minnesota
NNIN REU Mentor: Anirudh Sharma, Electrical and Computer Engineering, University of Minnesota
Contact: skim639@gatech.edu, stadler@umn.edu, shar0340@umn.edu

Abstract and Introduction:

"Barcode" nanowires, composed of multilayers of gold (Au) and nickel (Ni), suggest a possibility of replacing the fluorophore cell labeling technique used today, which will introduce a "macro" magnetic detection and classification method for multiplexed biological assays. Low cost of fabrication [1] and a huge variety of magnetic signatures give barcode nanowires great advantage over fluorophores, which are costly and limited by the spectrally resolvable wavelengths. The nanowires can be functionalized with antibodies, so that different cell types can be tagged with unique barcode nanowires. The ferromagnetic properties of nickel are employed for nanowire characterization and manipulation, e.g. separation from the supernatant in the experimental procedure. Here, fabrication and characterization of barcode nanowires and their application in biological multiplexing studies were investigated. Two cell lines, A549 (human lung carcinoma) and HFF (human foreskin fibroblast), were incubated with two types of barcode nanowires that were conjugated with antibodies targeting the respective cells. The result demonstrated successful specific targeting of cells by the corresponding barcode nanowires. Together with quantitative magnetic characterization, successful functionalization of our barcode nanowires showed much promise in various cell detection applications.

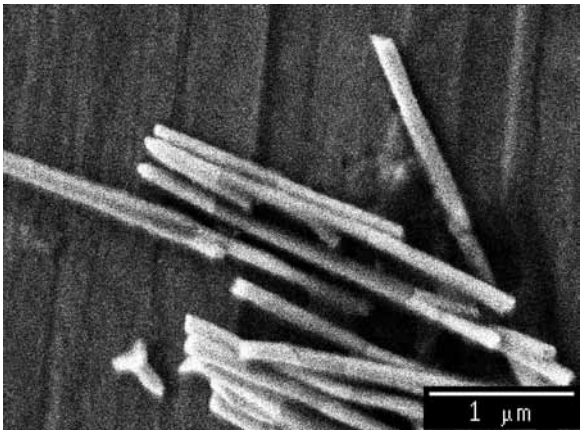

Figure 1: SEM of barcode nanowires (Au-Ni-Au). Minnesota Nano Center.

Experimental Procedure:

Nanowire Fabrication. Nanowires were grown through sequential electrodeposition in gold (HS-434 RTU, Technic, Inc.) and nickel ($NiSO_4$) electroplating solutions. A porous anodized aluminum oxide (AAO) template was sputtered with a copper conductive layer on one side and used as a working electrode. The working electrode, reference electrode, and counter-electrode were all immersed in a plating solution, and electrical charges were applied for metal deposition in the pores. The length of each metal segment was controlled by electrodeposition time. Once the nanowires were grown, the back copper contact was etched by ion-milling process and then freed by dissolving the AAO template in sodium hydroxide. The nanowires were suspended in deionized water until use.

Nanowire Characterization. While still in the template, the nanowires were characterized by vibrating sample magnetometry (VSM) at different angles ranging from 0° to 180°, with 0° being parallel and 90° perpendicular with respect to the magnetic field. Once the nanowires were freed and suspended in an aqueous solution, the nanowires were observed through scanning electron microscopy (SEM) for dimensions (Fig. 1).

Multiplexed Detection. Two types of barcode nanowires, Au-Ni (0.306 μm, 3.104 μm) and Au-Ni-Au (0.126 μm, 1.8 μm, 0.27 μm), were functionalized with primary antibodies, each specifically targeting A549 and HFF cells, respectively. Then, Au-Ni nanowires were conjugated with a green fluorophore, fluorescein isothiocyanate (FITC), to be distinguished from non-fluorescent Au-Ni-Au nanowires. Both A549 and HFF cells were conjugated with blue nuclear stains, Hoechst 33342. Plasma membranes of only HFF cells were tagged with wheat germ agglutinin with green Alexa Fluor 488 conjugate to optically distinguish the two cell types. The nanowires suspended in corresponding cell media solutions were titrated into cell cultures, in which A549 and HFF cells were plated 24 hours in advance, and incubated for six hours at 37°C. The cell media was aspirated, and formalin was added for cell fixation. Finally, formalin was replaced with a phosphate buffered saline (PBS) solution.

Results and Conclusions:

The VSM measurements successfully characterized each nanowire type, providing a specific magnetic signature of coercivity versus angle curves. Coercivity is the magnitude of magnetic field required for any magnetic materials to be demagnetized after reaching the saturation moment, and it can be measured at different angles discussed in the procedure. This way, our characterization methods rely on the nanowires' magnetic properties rather than optical imaging.

Three nanowires with different Ni deposition times, 10, 15, and 20 minutes, gave coercivities of 212.24, 261.17 and 285.37 Oe, respectively, all measured at 0°, and 131.54, 180.09, and 366 Oe, respectively, at 90° (Figure 2).

In multiplexing studies, the fluorescent nanowires, which were coated with antibodies targeting A549 cells, were observed to be tagged onto A549 cells only (Figure 3). Equivalently, the non-fluorescent nanowires, which were conjugated with antibodies targeting HFF cells, were found tagged to only HFF cells that were distinguished from A549 cells with their fluorescent plasma membranes (Figure 4). Through this experiment, specific cell-targeting by barcode nanowires was successfully tested and observed. The applications of barcode nanowires in biological assays seem highly viable with our magnetic characterization and antibody-functionalization techniques.

Future Work:

More experiments with various cell lines need to be conducted to ensure standardization of our nanowire-tagging methods. The possibility of nanowires being internalized after the tagging can also be looked into, in comparison to prior research findings of non-specific internalization of barcode nanowires in osteosarcoma cells [2]. The magnetic characteristics of our barcode nanowires suggest more possibilities of research topics, such as manipulation of cell matrix with influence of magnetic field gradient on the internalized nanowires.

Acknowledgements:

Special thanks to Professor Beth Stadler and Anirudh Sharma for mentorship. Thanks to Professor Allison Hubel for collaboration in biological studies. Thanks to the NSF and NNIN REU for funding and program. Thanks to the University of Minnesota facilities and staff for all the support.

References:

[1] Schwarzacher, W. Interface 15.1 (2006): 32-35.

[2] Sharma, A., et al. Magnetics, IEEE Trans. on 49.1 (2013): 453-456.

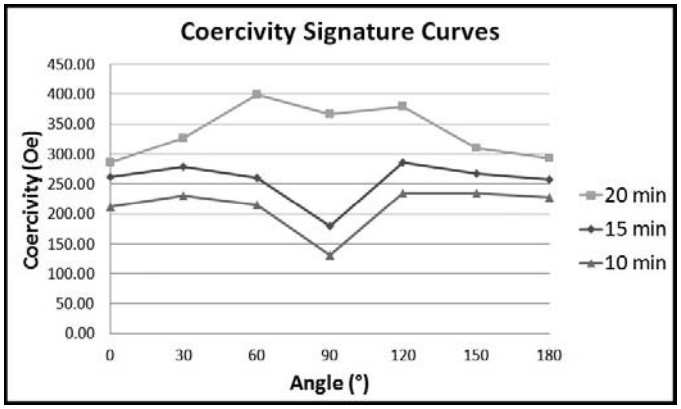

Figure 2: Coercivity vs. Angle curves of nanowires differentiated by deposition time of nickel.

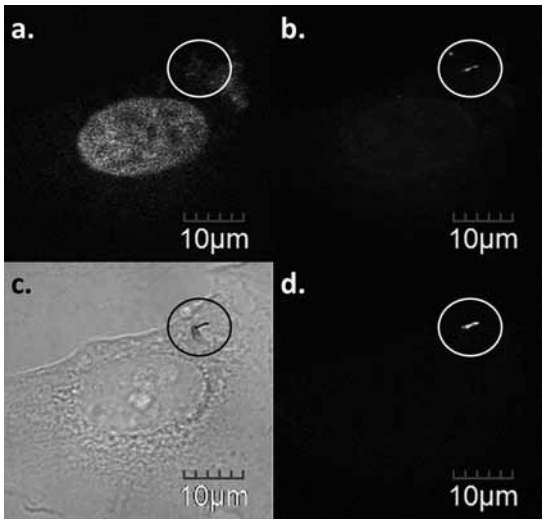

Figure 3: Fluorescence (a. 405 nm excitation laser, b. 488 nm), bright-field (c), and reflectance (d) images of A549 cells tagged with fluorescent nanowires (circled). (a) Fluorescence of nucleus confirming presence of a cell (identified as A549 by non-fluorescent plasma membranes in b); (d) Nanowires are the only metallic objects that can reflect light in the culture, confirming the identity of the dark spot in (c) to be nanowires. University Imaging Center.

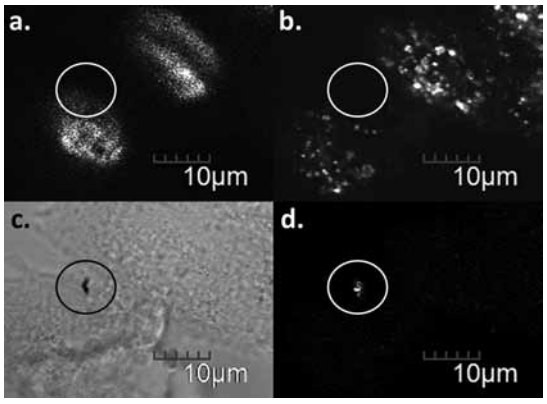

Figure 4: Fluorescence (a. 405 nm, b. 488 nm), bright-field (c), and reflectance (d) images of HFF cells with fluorescent plasma membranes (b) tagged with non-fluorescent nanowires (circled). University Imaging Center.

Effects of Cellular Architecture on MDA-MB-231 Breast Cancer Cell Motility

Ted Kocher
Biological Systems Engineering, University of Nebraska-Lincoln

NNIN REU Site: Minnesota Nano Center, University of Minnesota-Twin Cities, Minneapolis, MN
NNIN REU Principal Investigator: Dr. Patrick Alford, Biomedical Engineering Department, University of Minnesota-Twin Cities
NNIN REU Mentor: Kerianne Steucke, Biomedical Engineering Department, University of Minnesota-Twin Cities
Contact: tedkocher@huskers.unl.edu, pwalford@umn.edu, ksteucke@gmail.com

Abstract:

Over 200,000 women living in the United States will be diagnosed with breast cancer this year. Of those whose cancer metastasizes, wherein the cells migrate away from the initial tumor, only 23% will survive [1]. Cellular mechanics and architecture drive a wide range of cellular behaviors, such as contractility and apoptosis [2, 3]. Here, we assessed the role of cellular architecture in breast cancer motility. MDA-MB-231 breast cancer cells were micropatterned into two sizes of four shapes. We explored cytocellular architecture, measured lamellipodia extension as a function of that architecture, and investigated cellular invasion into a collagen gel. Results suggest that cellular architecture plays a role in determining the likelihood of tumor cell metastasis.

Introduction:

Metastasis of a tumor to vital organs greatly decreases chances of survival [1]. The factors that drive tumor metastasis are poorly understood. Cellular architecture has been shown to dictate certain cellular processes indicative of migration intent [4]. Thus, we hypothesized that cellular architecture plays a role in tumor metastasis.

We studied the correlation between cellular architecture and breast cancer cell motility. MDA-MB-231 breast cancer cells were micropatterned into two sizes of four shapes each. Cells patterned at 100% area were patterned on fibronectin microfeatures, which displayed 100% of the cross-sectional area attributed to a single MDA-MB-231 cancer cell on an unpatterned substrate. Immunofluorescence confocal microscopy was used to examine cytocellular architecture. We also measured lamellipodia extension as a function of cytocellular architecture to determine cell motility with respect to cell shape. Finally, we assessed the effect of cytocellular architecture on cell migration into a collagen gel overlay.

Experimental Procedure:

As per Figure 1, casts for production of polydimethylsiloxane (PDMS) stamps were fabricated from SU-8 photoresist spun on a silicon wafer via standard photolithography technique. Casts were coated with Sylgard 184 polydimethylsiloxane (PDMS) (10:1 base: curing agent), degassed, and baked at 90°C for four hours.

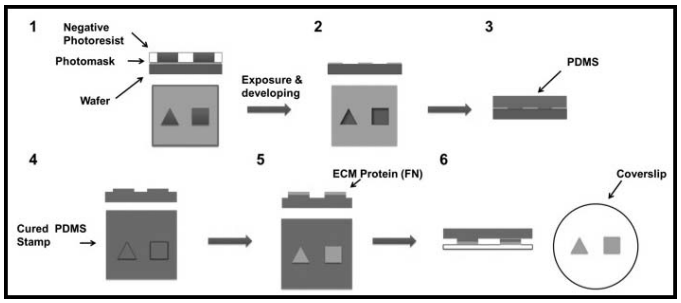

Figure 1: Photolithography and Microcontact Printing Methods.

1. Photomask aligned on SU-8 coated wafer.
2. Microfeatures developed on the wafer via selective exposure and a chemical etching process.
3. PDMS poured onto the wafer and heat-cured.
4. PDMS stamp with microfeatures is peeled off the wafer.
5. PDMS stamp coated with extracellular matrix (ECM) protein, fibronectin (FN).
6. FN coated PDMS stamp is stamped onto a coverslip transferring FN to the coverslip, providing guidance cues for cell shape.

Stamps were coated with fibronectin (50 mg/mL in H20), an extracellular matrix protein, and incubated for one hour. The fibronectin was then stamped onto PDMS-coated glass coverslips. A suspension of MDA-MB-231 human breast cancer cells (75,000 cells/mL) was seeded onto the coverslips. Overnight incubation at 37°C and 5% CO_2 allowed cells to settle and conform to the fibronectin microfeatures.

Micropatterned cells were fixed with 4% paraformaldehyde and permeablilized with 0.05%Triton-100 (in PBS at 37°C). Cells were stained with AlexaFlour 488 Phalloidin and 4′, 6-diamidino 2-phenylindole (DAPI) in PBS, then imaged with an Olympus IX81ZDC inverted confocal microscope.

Results and Discussion:

Microcontact printing reliably produced the confocal images shown in Figure 2.

Time-lapse photography acquisition every five minutes for one hour of micropatterned cells allowed for quantification of cell area change. The lamellipodia protrusion parameter (LPP), which is the standard deviation of the normalized area measurements spanning this hour, was used to quantify lamellipodia extension.

Figure 3 indicates a relatively large LPP for the 100% triangle cell. This was attributed to the high concentration of actin filaments found at the cellular periphery (Figure 1). It was noted that, for all but the triangle, the smaller cell size produced a higher LPP. However, further data acquisition is required to validate the results.

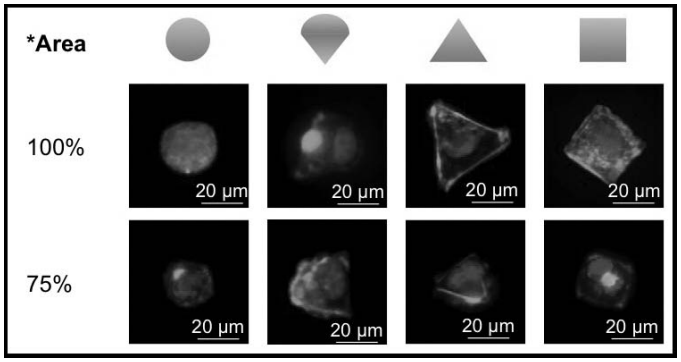

*Figure 2: Fluorescent images of micropatterned MDA-MB-231 cancer cells. Blue: nucleus Green: actin * Percent area is defined as the percentage of the total area of an MDA-MB-231 cell on an unpatterned substrate. Shapes are circle, teardrop, triangle, and square from left to right. The top row of shapes was patterned at 100%; the bottom row was patterned at 75%. Shapes were selected based on number of corner regions to constrain lamellipodia extension as explained in [4].*

Future Work:

Attempts at a collagen invasion assay adapted from previous work by Goswami et al. [5] were made. Methods for the assay can be found in Figure 4. Imaging techniques are yet to be perfected. We aim to solidify a protocol and imaging technique that allows us to quantify degrees of invasion with respect to cellular shape.

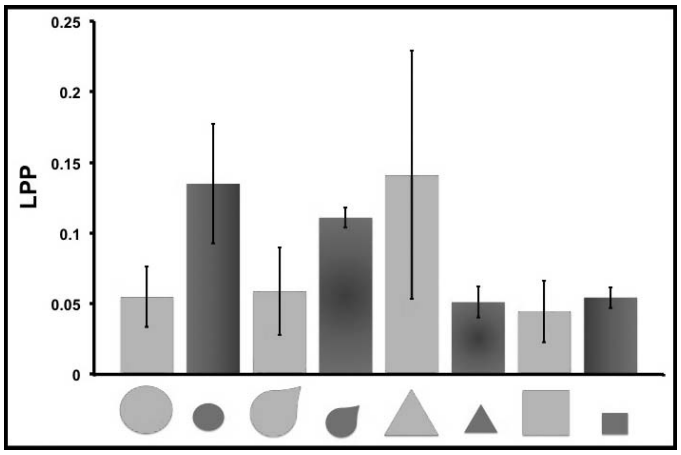

Figure 3: Lamellipodia protrusion parameter (LPP). The LPP is the standard deviation of the normalized area. The mean LPP and standard deviation error bars are given for each shape and size (N = 3, 3, 5, 3, 4, 7, 4, 3 from left to right, respectively).

Acknowledgements:

I wish to thank the National Science Foundation and National Nanotechnology Infrastructure Network Research Experience for Undergraduates (NNIN REU) Program for funding this research. Additionally, thanks to Kerianne Steucke, Patrick Alford, and the University of Minnesota.

References:

[1] American Cancer Society, Breast Cancer Facts and Figures, Atlanta: American Cancer Society, Inc., 3, 2011-2012.

[2] Alford, et al. Vascular smooth muscle contractility depends on cell shape. Integrative Biology 1063-1070. (2011).

[3] Chen, C.S., et al. Geometric Control of Cell Life and Death. Science 276:1425-1428. (1997).

[4] Parker, K.K., et al. Directional control of lamellipodia extension by constraining cell shape and orienting tractional forces. FASEB Journal 16:1195-1204. (2002).

[5] Goswami, et al. Macrophages Promote the Invasion of Breast Carcinoma Cells via Colony-Stimulating Factor-1/Epidermal Growth Factor Paracrine Loop. Cancer Research 65:5278-5283. (2005).

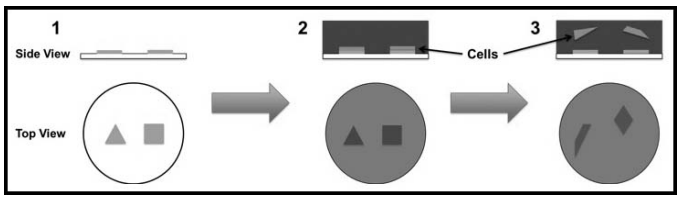

Figure 4: Collagen invasion assay methods. 1. Seed micropatterned coverslip with MDA-MB-231 breast cancer cells. 2. Overlay with 2.5 mg/mL rat tail collagen. Allow to cure at room temperature for 30 minutes. 3. Cells invade matrix for eight hours.

Microfluidics for the Study of Breast Cancer

Lisa Kriegh
Biosystems Engineering, Oklahoma State University

NNIN REU Site: ASU NanoFab, Arizona State University, Tempe, AZ
NNIN REU Principal Investigator: Prof. Jennifer Blain Christen, Electrical Engineering, Arizona State University
NNIN REU Mentor: Tao Luo, Electrical Engineering, Arizona State University
Contact: lisa.kriegh@okstate.edu, jennifer.blainchristen@asu.edu, tluo6@asu.edu

Abstract:

We present a microfluidic system for determining the efficacy of chemotherapy drugs on breast cancer. The volume of the device is approximately 12 μL total, including a control chamber and an experiment chamber. A protocol for fabrication, preparation for cell introduction, culture and introduction of the experimental and control reagents is described. We were able to use the protocol to prepare MCF-7 human breast cancer cells in the device. The cells were able to adhere to the culture surface, proliferate and survive the culture protocols. However, the assessment of the efficacy of the chemotherapy drug tamoxifen was not successful due to the crystallization of the drug as the temperature in the device dropped during the observation periods.

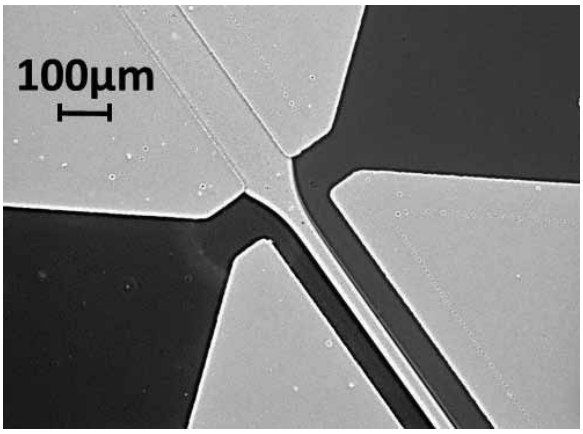

Figure 1: Separation of fluids in the two chambers by flow in the central channel.

Introduction:

Early diagnosis and treatment are a cancer patient's best chance of survival. To that end, microfluidic systems show great promise for developing point of care diagnostic technologies and quick evaluation of treatment options. Microfluidic systems allow precise manipulation of cells in a controlled environment, and can be cheaply and easily fabricated using standard soft lithography techniques. Microscale systems use smaller sample and media volumes, and provide fast results. Testing chemotherapy drugs on a biopsy within a microfluidic system can give patient-specific results so high efficacy treatment can begin as soon as possible.

The objective of this project was to determine the time for a known chemotherapy drug to have an observable effect on cancer cells in a microfluidic device. The cells used were from the MCF-7 cell line, immortalized human breast cancer epithelial cells. The cells were dosed with 20 μM tamoxifen, a chemotherapy drug proven to be effective against MCF-7 cells after a minimum of seven days with traditional methods [1].

Methods:

A microfluidic device was fabricated using standard soft lithography replica molding. A polydimethylsiloxane (PDMS) microfluidic structure was bonded to a glass microscope slide to form a device with two identical 5.95 μL chambers, experiment and control, separated by a central channel. This design allowed mixing between the two chambers initially to establish uniform cell growth in the experimental and control chambers. Diffusion between the chambers could be prevented simply by the flow of fluid through the central channel at a rate ten times higher than the flow into the chambers. The functionality of the design was confirmed by filling the chambers with food coloring and running water through the central channel. This effectively separated the chambers, as shown in Figure 1.

To set up the experiment, each input and output of the microfluidic device was connected to Tygon® Microbore tubing with 20 gauge blunt needles. A three-way stopcock was attached to the end of each tube to facilitate input changes. Three-milliliter syringes were used at the side inputs In1 and In2 to fill the chambers shown in Figure 2. The cell culture chambers were initially filled with gelatin to facilitate cell attachment. Phosphate-buffered saline (PBS) was used to wash out the excess gelatin

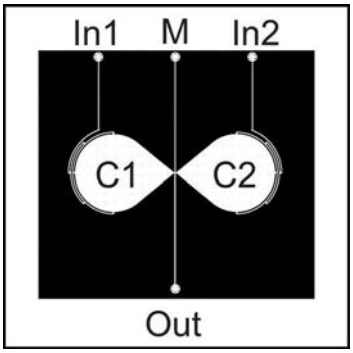

Figure 2: Diagram of the microfluidic device.

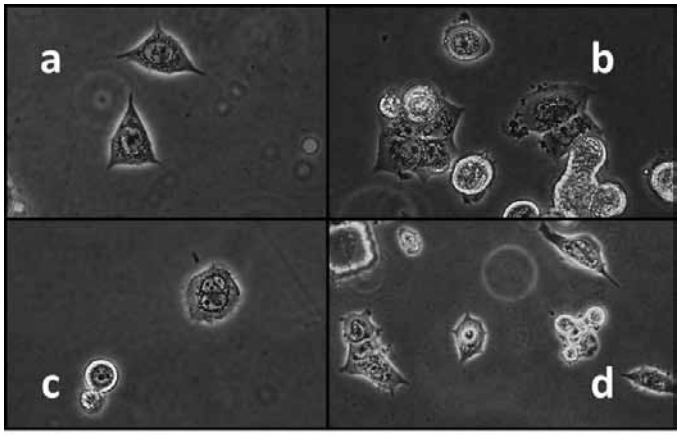

Figure 3: (a) Control group before adding the control solvent, and (b) after 20 hours with the control solvent. (c) Experimental group before adding tamoxifen, and (d) after 20 hours with tamoxifen.

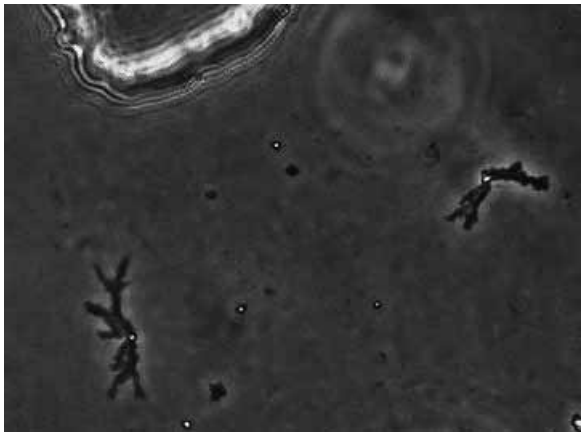

Figure 4: Tamoxifen crystals at 12 hours.

and wet all the surfaces. The PBS was then replaced with cell culture media, Dulbecco's modified eagle medium, plus 5% fetal bovine serum and 1% penicillin-streptomycin. MCF-7 cells were introduced into the chambers, and the microfluidic device was placed in an incubator until the cells adhered to the surface, forming a monolayer.

When healthy cell cultures had been established in each chamber, a syringe pump was used to run media through the middle channel and separate the experimental and control groups. Another syringe pump was then used to introduce 20 μM tamoxifen into the experimental chamber and the same amount of tamoxifen solvent, ethanol, into the control chamber. Cell viability of the two groups was then compared over the next 24-hour period. The flow rates into the chambers were 1 mL/h for 50 min to introduce the tamoxifen, then 2 μL/h complete media to maintain the cells. The corresponding flow rates for the central channel were 10 mL/h and 20 μL/h. These flow rates were shown to maintain the separation of fluids and provide sufficient media for cell growth without introducing harmful levels of shear stress to the cells.

Results and Conclusions:

After 14 hours with tamoxifen outside of the incubator, the MCF-7 cells still appeared to be healthy. The microfluidic device was placed in the incubator. Six hours later both the control and experimental groups showed new cell growth (Figure 3). Tamoxifen crystals were visible in the experimental chamber, indicating conditions were too cool outside the incubator (Figure 4).

The MCF-7 cells failed to exhibit inhibited growth or cell death within 24 hours of tamoxifen introduction. Removing the cells from the incubator for observation cooled the tamoxifen causing crystals to form that the cells couldn't absorb.

Future Work:

Future work includes improving the experimental procedure to prevent crystallization of tamoxifen and broadening the scope to simultaneously test different chemotherapy drugs at varying concentrations.

Acknowledgments:

I would like to thank my PI, Prof. Jennifer Blain Christen, my mentor Tao Luo, and Dixie Kullman for all of their help and guidance. Thanks to the National Nanotechnology Infrastructure Network Research Experience for Undergraduates Program, the National Science Foundation, and the Center for Solid State Electronics Research at Arizona State University for research support and funding. I would also like to thank Prof. Karen Anderson and Eva Amouzougan from the Biodesign Institute Center for Personalized Diagnostics for providing the cells and reagents.

References:

[1] E.R.L. Sutherland, R.E. Hall, and I.W. Taylor, "Cell proliferation kinetics of MCF-7 human mammary carcinoma cells in culture and effects of tamoxifen on exponentially growing and plateau-phase cells", Cancer Research, 43, pp. 3998-4006, 1983.

Design of Synthetic Protein Membranes Using Droplet Microfluidics

Corey Landry
Biological Engineering, Louisiana State University

NNIN REU Site: Center for Nanoscale Systems, Harvard University, Cambridge, MA
NNIN REU Principal Investigator: Professor David A. Weitz, School of Engineering and Applied Sciences, Harvard University
NNIN REU Mentor: Dr. Peter Yunker, School of Engineering and Applied Sciences, Harvard University
Contact: cland83@tigers.lsu.edu, weitz@seas.harvard.edu, pyunker@seas.harvard.edu

Abstract and Introduction:

Protein conjugated beads and particles are often used in biomedical processes [1]. However, these particles suffer a number of limitations. Proteins are chemically attached to fixed locations on the particle surface, and cannot move independently of the particle, even in the presence of external stimulation. This can also lead to partial protein denaturation and loss of activity [2]. The goal of this work was to overcome the limitations of solid particles by studying the behavior of proteins on a liquid-liquid interface. By engineering artificial membrane proteins using the PURExpress *in vitro* protein synthesis platform from New England BioLabs (NEB) and attaching them to droplets using droplet microfluidics, the detrimental effects of denaturation can be greatly mitigated or avoided completely. Preliminary measurements and observations show that protein droplets are uniformly coated with mobile, active proteins. These characteristics distinguish protein droplets from solid particle systems and make them a promising solution to problems in drug delivery, biosensing, as well as the study of protein interactions. Of particular interest is the application of protein droplets to the study of apoptosis.

Experimental Methods:

Using template DNA provided by NEB, protein-transmembrane helix complexes were synthesized as single proteins using their PURExpress synthesis kit [3]. For the purpose of this work, membrane versions of green fluorescent protein and streptavidin were studied.

Droplets were made using PDMS microfluidic devices, as in Guo, et al. [4], and by simple emulsification. Protein membranes were observed on both water-in-oil and oil-in-water droplets. Droplets were incubated at 37°C after formation to allow proteins to be synthesized and coat the droplet interface.

The structure and properties of these protein droplets were studied using confocal microscopy. Engineered transmembrane green fluorescent protein was used as a model system to study protein droplets and membranes. Fluorescent biotin dyes allowed the use of streptavidin protein drops to demonstrate protein activity.

Results and Conclusions:

Protein Density. While protein-conjugated solid particles vary widely in their degrees of coverage, protein droplets show uniform coatings on the entire surface of the drop. Preliminary measurements also show that droplets are covered with a higher density of proteins than are commercially available particles. Commercially available streptavidin particles are coated with approximately 1.5 ng/cm^2, but preliminary data shows that streptavidin drops could have coverage levels above 700 ng/cm^2.

Protein Mobility. Unlike proteins bound to solid particles, proteins attached to droplets were observed to move in small groups along the plane of the membrane. This could lead to engineered proteins that can respond to stimuli and assemble into complex structures, similar to proteins on the cell membrane.

Protein Activity. To determine if attachment to the droplet interface severely damaged the proteins, streptavidin droplets were placed in a solution of biotinylated dye, which only active streptavidin would bind. Fluorescence microscopy demonstrated that the entire surface of the streptavidin drop had the dye molecule bound to it. Further testing is needed to determine the degree of activity and assess the potential of protein droplets as biosensors.

Future Works:

One of the most promising applications of protein droplets is to the study of apoptosis. Malfunctions of apoptosis, the natural process of programmed cell death, play a major role in the development and progression of cancer [5]. However, the study of apoptosis requires costly and specialized cell culture conditions and soluble synthetic substitutes have proven to be inefficient.

Natural apoptosis occurs when a cell presents a complex of transmembrane proteins called the FAS ligand on its surface, which binds to corresponding receptor on the target cell and induces cell death. Droplets coated with the FAS ligand proteins have the potential to act as synthetic cellular analogs, since they are densely coated with active proteins that can move to assemble into the complete ligand complex.

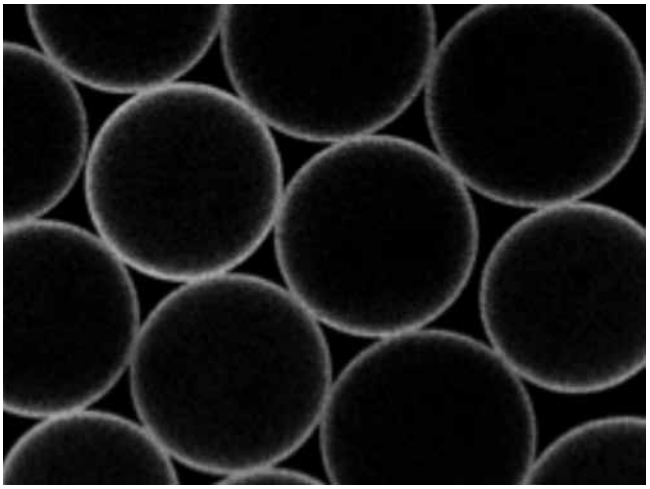

Figure 1: Droplets covered in engineered transmembrane green fluorescent proteins.

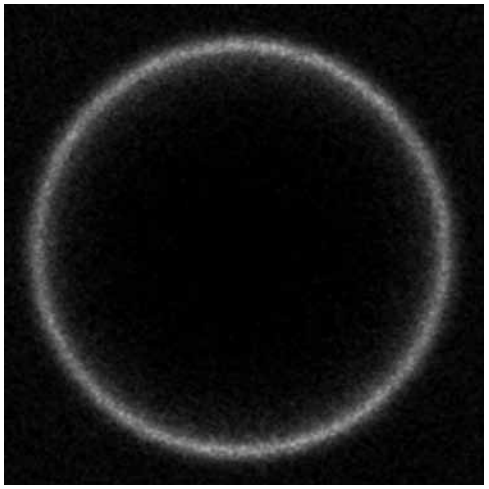

Figure 3: Active streptavidin-coated droplet binds fluorescent biotin dye.

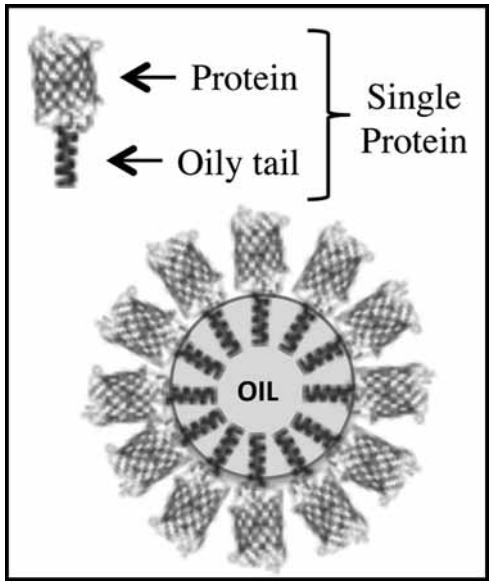

Figure 2: Schematic of engineered membrane proteins (top) with fully coated oil droplet (bottom).

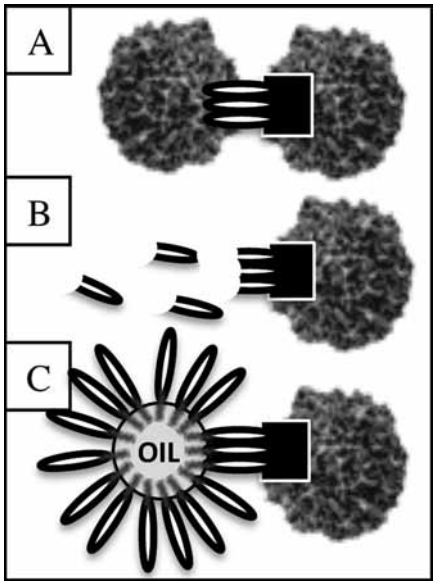

Figure 4: FAS ligand binding to receptor on target cell bound to (A) another cell, (B) soluble FAS ligand fragments, and (C) FAS ligand protein droplet.

Droplet protein technology has the potential to greatly reduce the cost barrier of entry for researchers hoping to study apoptosis for the development of cancer therapies.

Acknowledgements:

This project was a part of the National Nanotechnology Infrastructure Network Research Experience for Undergraduates (REU) Program and was funded by the National Science Foundation. This work was supported by the Harvard School of Engineering and Applied Sciences REU and the Harvard Center for Nanoscale Systems. The author would like to thank Professor David Weitz for the opportunity to work in his laboratory. The author would like to especially thank Peter Yunker and Shaorong (Ron) Chong for their guidance and mentorship throughout this project.

References:

[1] Katz, E., and Willner, I., Angewandte Chemie-International Edition 2004, 43 (45), 6042-6108.

[2] Prosperi, D., et al., Chembiochem 2007, 8 (9), 1021-1028.

[3] Asahara, H., and Chong, S., Nucleic Acids Research 2010, 38 (13).

[4] Guo, M. T., Rotem, A., Heyman, J. A., and Weitz, D. A., Lab on a Chip 2012, 12 (12), 2146-2155.

[5] Kasibhatla, S., and Tseng, B., Molecular Cancer Therapeutics 2003, 2 (6), 573-580.

Curved Functionalized Microfluidic Channels for the Study of Cell Dynamics

Ang Li
Department of Biomedical Engineering, Georgia Institute of Technology

NNIN REU Site: Center for Nanoscale Systems, Harvard University, Cambridge, MA
NNIN REU Principal Investigator: Professor David A. Weitz, School of Engineering and Applied Sciences, Harvard University
NNIN REU Mentors: Dr. Adrian Pegoraro and Thomas Kodger, School of Engineering and Applied Sciences, Harvard University
Contact: ali41@mail.gatech.edu, weitz@seas.harvard.edu, apegoraro@seas.harvard.edu, tkodger@fas.harvard.edu

Abstract:

There have been studies in which physical environments are simulated by growing cells on different stiffness substrates to observe changes in migration speed, cell stiffness, etc [1]. However, these flat, two-dimensional systems do not accurately simulate *in vivo* environments in which cells exist. The vast majority of tissue in the human body exhibits at least some additional parameter, whether it is depth, curvature, etc. The objective of this study was to make observations on how curvature and stiffness affect cell proliferation, growth, and orientation preferences in channel-like structures. Polyacrylamide/bisacrylamide gels with different substrate stiffness were fabricated with cylindrical voids of varying channel diameters. Two-dimensional gels with similar substrate stiffness were also observed as a control for the system. Initial observations indicate curvature prompts fibroblasts to migrate along the lumen (length) of the channel as well as aggregate.

Introduction:

Many groups have simulated wound healing by performing scratch assays on a group of fully confluent cells on a flat surface and observing migration towards the wound. However, these substrates do not accurately simulate *in vivo* environments, as most tissues exhibit some additional parameter, whether it is depth, curvature, etc. Substrate stiffness has also been seen as a factor that influences cell migration velocities [2]. The aim of this study was to see how curvature affects cell migration on different substrate stiffness with the purpose of creating a curved wound-healing environment.

Experimental Procedure:

Substrates were made by polymerizing a mixture of 8 wt% and 4 wt% polyacrylamide with 0.3 wt% bisacrylimide solutions. 8 wt% / 0.3 wt% polyacrylamide/bisacrylamide gels yielded a Young's modulus of 25 kPa (stiff), while 4 wt% / 0.3 wt% polyacrylamide/bisacrylamide gels yielded a Young's modulus of 5 kPa (soft). Channels were made with diameters of 736 μm, 384 μm, and 114 μm. Flat substrates with the same composition served as the control. Gels were embedded with a synthesized GRGDSP acrylamide to promote cell adhesion to the substrate surface. Human foreskin fibroblasts from the BJ line were transfected with green fluorescent protein to observe migration patterns.

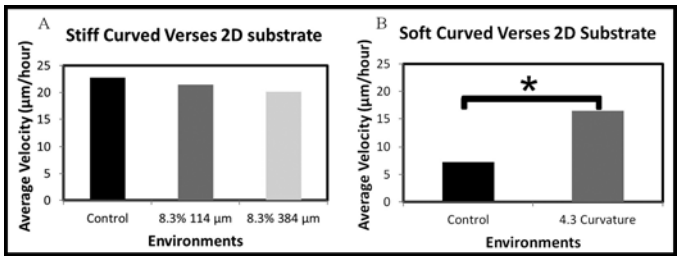

Figure 1: No significance was shown between curved environments verses flat substrates in the stiff gel (Figure 1A, n = 15, 27, p-value of control vs stiff 114 µm = 0.261, control vs. stiff 384 µm = 0.094, 114 µm vs 384 µm = 0319). Curved substrate resulted in cells having a significantly higher total velocity than that of the control (Figure 1B, n = 12, 13 p-value of 0.0019).

Migration was tracked using confocal microscopy with stacks starting and ending where green fluorescent protein detected. Projections were made along the Z axis in order to average the fluorescent signals for two-dimensional tracking. Migration was tracked using an ImageJ plugin, MtrackJ. Total average velocity calculated along with velocities in the X and Y vectors.

Results:

In looking at the migration patterns on the stiffer substrates, there was no statistically significant difference in total velocity between the control verses the curved environments. Additionally, there was no difference in total velocity between the 114 μm diameter channel and the 384 μm channels in the soft gel. However, cells that were seeded within the 768 μm channel in the softer gel exhibited a higher total velocity verses the cells on the two-dimensional substrate.

To better understand how the curvature of the substrate affects the migration patterns of the cells, the velocity along the major axis of the channel and around the curvature of the channel were measured. The total average velocities were broken down into their subsequent X and Y components. From our initial observations, fibroblasts within the 736 μm channel preferred

to move along the channel, having a higher average X velocity than average Y velocity. Fibroblasts within the 384 μm diameter channel did not have a preference for movement along one axis or the other. Within the 114 μm channel, fibroblasts had a higher X velocity, indicating faster movement along the channel.

Cells within curved channels had a tendency to aggregate and stay together, whereas fibroblasts that were seeded on the two-dimensional substrates exhibited little to no aggregation. During the course of the two-dimensional substrate experiment, fibroblasts that did come into contact with each other would instantaneously repel each other, whereas fibroblasts in the curved channel would aggregate together and stay together for the entire duration of the experiment.

Conclusions and Future Works:

There are indications that curvature has a minimal effect on the total velocity of fibroblasts. However, once these velocities have been broken down, there is a clear indication that fibroblasts grown on the curved channels have a preference to move along the major horizontal axis rather than moving around the curvature of the channel. In looking at the X and Y velocities in the stiff 384 μm channel, there was no difference between them. In qualitatively analyzing the migration patterns of the cells, the vast majority tend to also move along the major horizontal axis of the channel. This disparity may simply be attributed to having a small sample size, as there were only 49 samples measured.

Aggregation in the curved environments was quite unexpected, as fibroblasts are contact inhibitive cells. In future studies, we would like to see how the cells pull on their environment through traction force microscopy, as there are obvious differences in movement between both axes. We would also like to observe how cells pull on the substrate as well as each other on curved environments using traction force microscopy [3].

Figure 2: Cells were shown to have no preference migrating along the channel verses around the curvature in stiff 384 μm channels (n = 49, p-value = 0.127). (See full-color version on inside cover.)

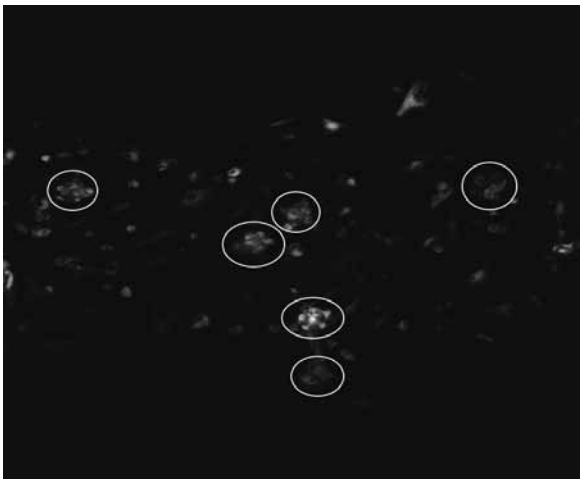

Figure 3: Fibroblasts grown on stiff two-dimensional substrates did not have a tendency to aggregate, whereas those in the curved channels did.

Acknowledgements:

I would like to thank my principal investigator, Professor David Weitz, Dr. Adrian Pegoraro, Thomas Kodger, Dr. Kathryn Hollar, the National Nanotechnology Infrastructure Network Research Experience for Undergraduates (NNIN REU) Program, and the National Science Foundation (NSF).

References:

[1] Legant, W.R., Choi, C.K., Miller, J.S., et al. Proc Natl Acad Sci USA. 2013;110(3):881-6.

[2] Ulrich, T.A., de Juan Pardo, E.M., and Kumar, S. Cancer Res. 2009;69(10):4167-74.

[3] Trepat, X., Wasserman, M.R., Angelini, T.E., Millet, E., Weitz, D.A., Butler, J.P., and Fredberg, J.J. (2009). Nat. Phys. 5, 426-430. doi: 10.1038/nphys1269.

Identifying the Biomechanical Effects of UV Resistant Molecules and Nanoparticles on Human Skin

Sarah Nainar
Biochemistry, Washington & Jefferson College

NNIN REU Site: Stanford Nanofabrication Facility, Stanford University, Stanford, CA
NNIN REU Principal Investigator: Prof. Reinhold Dauskardt, Materials Science and Engineering, Stanford University
NNIN REU Mentor: Krysta Biniek, Materials Science and Engineering, Stanford University
Contact: sarah.nainar@gmail.com, rhd@stanford.edu, kbiniek@stanford.edu

Abstract:

The stratum corneum (SC) is the outermost layer of the epidermis and experiences significant amounts of mechanical stress. A lipid matrix surrounding layers of protein-filled cells forms the stratified SC, which is essential for proper functioning at the nano- and micron-scale. Ultraviolet (UV) radiation due to sun exposure can alter the organization and structural integrity of the SC components. The administration of UV-absorbing chemical compounds and nanoparticles, namely titanium dioxide (TiO_2) and zinc oxide (ZnO), can reduce damage. However, it is not fully understood how these UV-resistant treatments interact with the SC, and their efficacy at protecting biomechanical properties from UV exposure is unclear. In this work, we investigated the ability of various topical sunscreens containing UV-resistant molecules and nanoparticles to protect the biomechanical properties of UV-irradiated human SC. We examined the tissue's resistance to crack propagation, given by the intercellular delamination energy. We also used attenuated total reflectance Fourier transform infrared spectroscopy (ATR-FTIR) to study UV inhibitor diffusion into the SC as well as structural changes that occurred from UV exposure. We found that the UV-resistant treatments successfully protected the biomechanical properties up to relatively large UV dosages.

Introduction:

The stratum corneum is essential for wound healing, infection prevention and equally important, protecting underlying layers of skin from solar radiation. UVB radiation in particular has proven harmful to the skin, not only on a cellular level but also on a biomechanical level. Irradiation damage can produce changes in the lipid matrix and cellular structure, leading to disrupted barrier function. This obstructs the skin's ability to desquamate, or shed, as well as provide mechanical strength. The effects of this include cracking and chapping, as well as other cosmetic defects [1].

Nanoparticles such as TiO_2 and ZnO possess UV-inhibiting qualities, making them ideal components of commercial sunscreens. However, it is unknown how they interact with and protect the stratum corneum from harmful radiation.

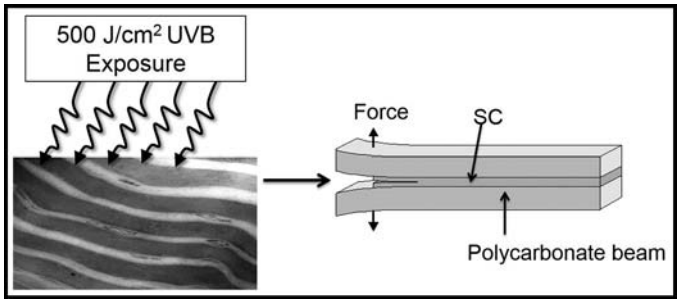

Figure 1: Double cantilever beam testing of stratum corneum exposed to UVB radiation with or without nanoparticle sunscreen treatment yields the extent of cellular cohesion.

Experimental Procedure:

We obtained samples of SC through blunt dissection of human cadaveric tissue from Caucasian female donors. To analyze the mechanical properties of the SC, double cantilever beam (DCB) testing was employed to yield the delamination energy, G_c (J/m^2), which reflects the extent of cellular cohesion within the SC. Figure 1 displays the DCB sample configuration. Nanoparticle sunscreen (SS) was applied to SC samples to obtain an even coating of 2 mg/cm^2 before exposure to 500 J/cm^2 of broadband UVB radiation.

Fractured samples were repeatedly delaminated by attaching a new polycarbonate beam to remove lower layers of cells from the original beam with adhered SC. This yielded second and third delamination energies, which increased with depth due to greater intercellular cohesion in the SC.

We used attenuated total reflectance Fourier transform infrared spectroscopy to characterize fractured samples. Changes in height and location of characteristic C-H lipid peaks further revealed how nanoparticle sunscreen interacted with the SC.

Results and Conclusions:

We employed dynamic light scattering particle sizing to obtain an estimate of the nanoparticle diameter. An average diameter of

135 nm was seen, which was larger than expected. This discrepancy was likely due to agglomerations caused by the sunscreen ingredients.

We obtained the delamination energies of samples with no treatment, 500 J/cm^2 UVB only, sunscreen only, and sunscreen plus 500 J/cm^2 UVB. As seen in Figure 2, samples irradiated without nanoparticle sunscreen have significantly lower delamination energies due to reduced intercellular strength. However, the sunscreen-treated and UVB-irradiated samples possess delamination energies that are not significantly different than that of the unexposed samples. This indicates that the sunscreen is indeed protecting the SC from UV damage.

Figure 3 shows that underlying layers of the SC are protected in the same fashion, as the second and third energies of sunscreen-treated samples were greater than the untreated plus irradiated samples.

ATR-FTIR analysis showed peak shifts, which suggest changes in SC lipid fluidity due to emollient diffusion into lower layers [2]. The lack of ZnO and TiO_2 peaks near 2275/2350 cm^{-1} and 1645/3400 cm^{-1}, respectively, (not shown) suggest there was no nanoparticle diffusion.

Overall, it was determined that nanoparticle sunscreen effectively protects the biomechanical properties of the stratum corneum at relatively high broadband UVB dosages. Diffusion of the emollient was suggested by peak shifts of the second and third delamination lipid C-H stretches. However, nanoparticle diffusion was not observed, in agreement with the unexpectedly large particle size. This is fortunate, as unwanted nanoparticle diffusion is a potential harm of using such sunscreens.

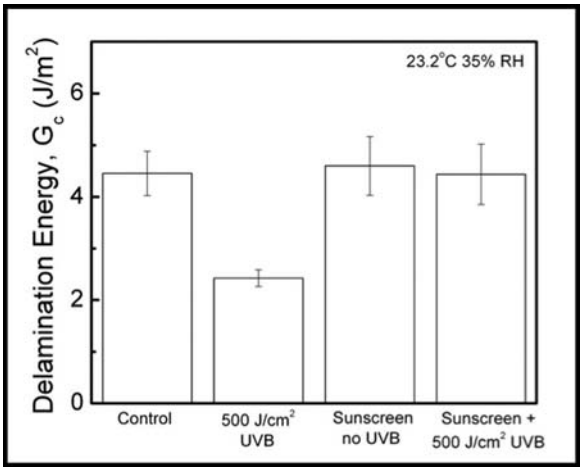

Figure 2: SC delamination energy gives crack length and first delamination energies of various samples.

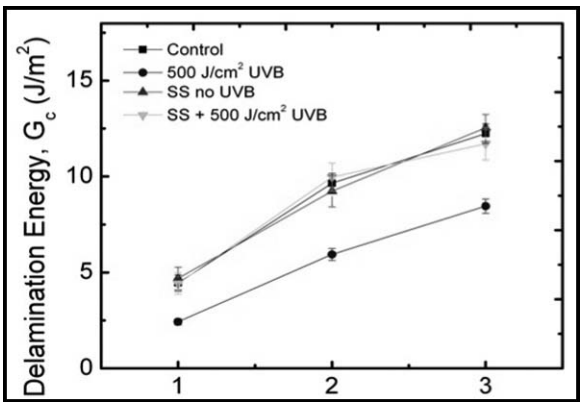

Figure 3: Delamination energy as a function of depth into the stratum corneum.

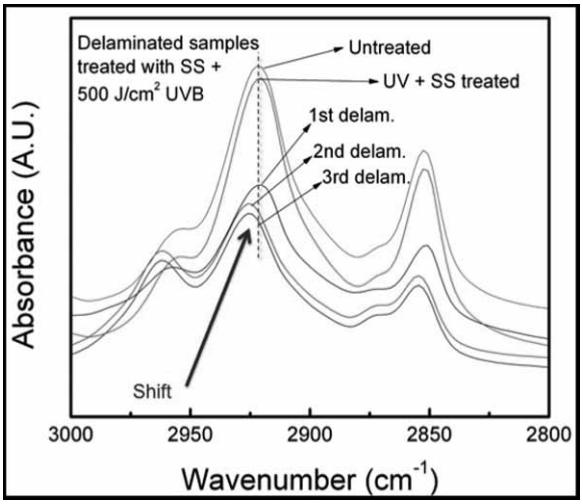

Figure 4: Overlapped ATR-FTIR spectrum shows changes in the characteristic asymmetric and symmetric C-H lipid stretching.

Future Work:

We hope to further this study by exploring how nanoparticle sunscreen can affect previously UV-damaged tissue, wherein the barrier function has already been significantly compromised. ATR-FTIR analysis of sunscreen-treated damaged tissue will also help us understand the way nanoparticles diffuse into lower layers of the SC.

Acknowledgements:

Many thanks to Dr. Michael Deal, Krysta Biniek, Prof. Reinhold Dauskardt, Maureen Baran, SNF, fellow SNF REU students, Melanie-Claire Mallison, NNIN REU, and NSF for all of their help and support.

References:

[1] Biniek K., et al. Solar UV radiation reduces the barrier function of human skin. Proc. Natl. Acad. Sci. U. S. A. 2012, 109:17111-171162.

[2] Levi, K., et al. Emollient molecule effects on the drying stresses in human stratum corneum. Br. J. Dermatol. 2010, 163:695-703.

Fabrication of Nano Ion Pumps for Retinal and Neural Prosthesis

Zachary Pritchard
Chemical and Biomolecular Engineering, Georgia Institute of Technology

NNIN REU Site: UCSB Nanofabrication Facility, University of California, Santa Barbara, CA
NNIN REU Principal Investigator: Prof. Luke Theogarajan, Electrical and Computer Engr., University of California, Santa Barbara
NNIN REU Mentor: Samuel Beach, Electrical and Computer Engineering, University of California, Santa Barbara
Contact: zach.pritchard@gatech.edu, ltheogar@ece.ucsb.edu, beach@umail.ucsb.edu

Abstract:

In some cases, permanent vision loss may be treated using retinal prostheses; however, current methods of neural stimulation pose potential health risks. To overcome these risks, an approach based on ion stimulation rather than electrical stimulation may be more appropriate. To this end, fabrication techniques were investigated for anodized aluminum oxide (AAO) membranes for use in electrically-gated, ion-selective nanoscale pumps. Additionally, track-etched polycarbonate (PC) membranes were functionalized using crown-ether compounds and their ion selectivity was characterized. Fabrication of AAO membranes was successfully completed, and a K^+-selective compound was determined.

Introduction:

Age-related macular degeneration is the leading cause of permanent vision loss in the United States [1]. It and similar conditions may be treated using retinal prostheses [2]; however, current prostheses rely on electrical stimulation, which can be neurotoxic and can lead to tissue-damaging electroplating [3]. To overcome these risks, an approach based on ion stimulation may be used. In this route, neural firing is triggered via injection of sequestered potassium cations (K^+). This method has been shown to be viable, and the activation threshold and response latency in rabbit retinal cells has been investigated [4, 5].

To facilitate implementation of this approach, fabrication techniques for an electrically-gated, ion-selective nanoscale pump were investigated. In order to fire neurons when desired, the pump must be capable of both sequestering and releasing ions as directed; this is accomplished using a gating system in which ions are driven through a membrane by an applied voltage across the device. The membrane must also be ion-selective so only usable K^+ ions are stored and released; this will be accomplished through functionalization of pores in the membrane. An overview of the device is shown in Figure 1.

In this study specifically, fabrication techniques were investigated for anodized aluminum oxide (AAO) membranes, which are used in the pumps due to their biocompatibility, previously investigated preparation, and ability to be functionalized for ion selectivity. Additionally, track-etched polycarbonate (PC) membranes were functionalized with crown-ethers and their ion selectivity was characterized using cyclic voltammetry.

Experimental Procedure:

The general fabrication procedure for a suspended AAO membrane is shown in Figure 2. A dielectric barrier layer was first deposited on one side of a double-side polished silicon wafer using atomic layer deposition (ALD). Next, Al

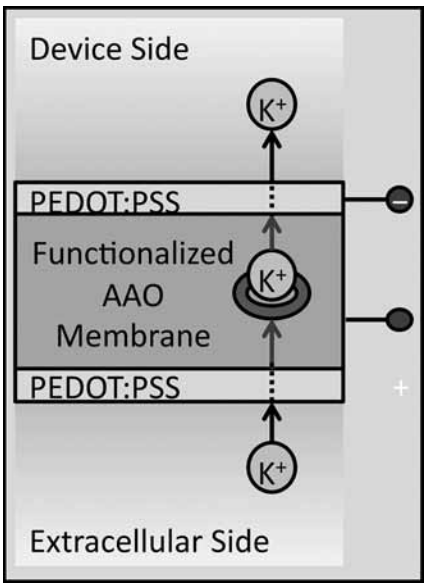

Figure 1: General structure and operation of the device. Ion flow is driven by a potential applied across the membrane. PEDOT:PSS is a conductive polymer. K^+ ions are selectively allowed through the membrane due to functionalization.

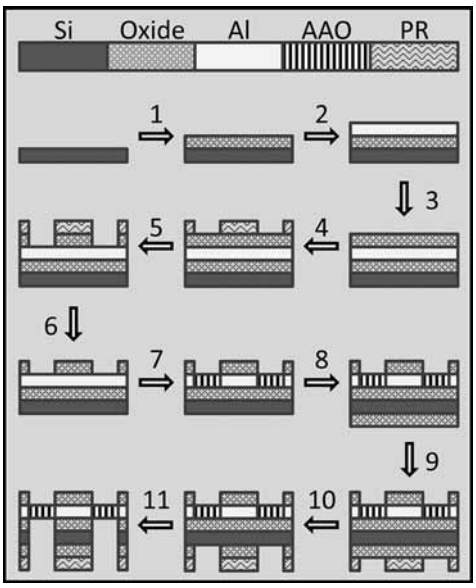

Figure 2: Fabrication Scheme. 1. ALD, 2. E-beam, 3. ALD, 4. Photolithography, 5. ICP-RIE, 6. Clean, 7. Anodization, 8. Photolithography, 9. ICP-RIE, and 10. Bosch etch.

was deposited using electron beam evaporation followed by another ALD dielectric layer. A mask of photoresist (PR) was created and the dielectric was etched in the open windows using inductively coupled plasma reactive-ion etching (ICP-RIE). The exposed aluminum was then anodized in a solution of sulfuric acid. On the backside, dielectric barrier layers were added via ALD, masked, and etched using ICP-RIE to provide windows for the Bosch etch. Finally, the wafer underwent a Bosch etch until AAO membranes were suspended over each window. A phosphoric acid etch was used to open nanopores blocked by barrier layers.

Functionalization studies were completed on track-etched polycarbonate (PC) membranes treated with crown ethers. Membranes were mounted between two polymer gaskets between two reservoirs. Reservoirs were loaded with 0.01 M solutions of NaCl, KCl, and $CaCl_2$ and electrodes were inserted. Applied potentials ranged from -4 V to 4V.

Results and Conclusions:

Using the techniques described above, AAO membranes containing nanopores were successfully fabricated. Figure 3 shows the cross-section of such a membrane imaged on a scanning electron microscope (SEM). From this image, it can be seen that the nanopores extend completely through the membrane and are open on both ends.

Figure 4 shows the result of one functionalization study. The figure compares cyclic voltammetry results for PC membranes that are untreated and treated with a specific crown ether compound. Functionalization with this compound results in selectivity for K^+. Results from the untreated membrane roughly align with expectations based on diffusion coefficients; in the untreated membrane, however, more K^+ is transported than Na^+, and comparatively little Ca^{2+} is transported.

Future Work:

In the near future, functionalization studies will be performed using AAO membranes prepared using the techniques investigated in this project. Beyond this, work will begin on fabricating complete pump devices.

Acknowledgments:

I would first like to thank Prof. Luke Theogarajan and Samuel Beach, my PI and mentor. I would additionally like to extend my thanks to Cara Hale-Hanes (a fellow intern on this project), Samantha Cruz (our site coordinator), and the other UCSB interns. The support of the National Nanotechnology Infrastructure Network Research Experience for Undergraduates (NNIN REU) Program, the National Science Foundation, and the National Institutes of Health is also greatly appreciated.

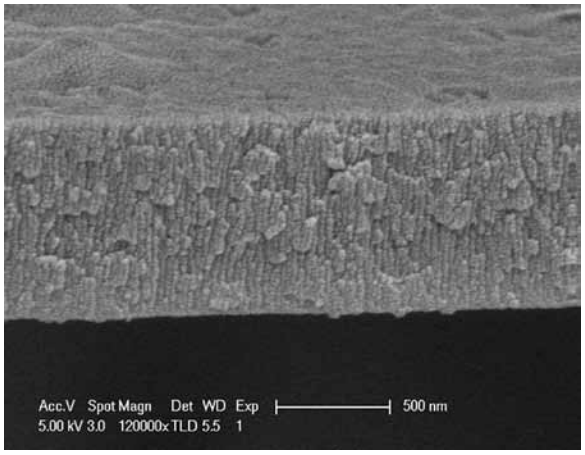

Figure 3: SEM image of AAO membrane cross-section.

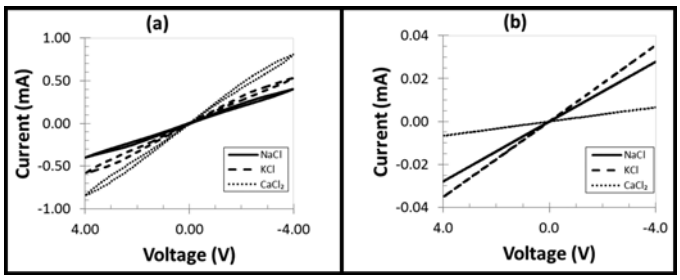

Figure 4: Each plot shows the resulting current as a varying potential is applied across the membrane. (a) untreated PC membrane, (b) 18-crown-6 treated membrane.

References:

[1] Ciulla, T.A.; "Age-Related Macular Degeneration: A Review of Experimental Treatments"; Surv.Ophthalmol, V43, #2, pp 134-46 (1998).

[2] Shire, D.B.; "Development and Implantation of a MinimallyInvasive Wireless Subretinal Neurostimulator"; IEEE Trans. Biomed. Eng., vol. 56, no. 10, pp. 2502-2511 (2009).

[3] Cogan, S.F.; "Over-pulsing degrades activated iridium oxide films used for intracortical neural stimulation," J. Neurosci. Methods, vol. 137, no. 2, pp. 141-150 (2004).

[4] Theogarajan, L.S.; "Stimulation of Rabbit Retinal Ganglion Cells by altering K^+ Ion Gradients: Dose-Response Curve," Arvo Meet. Abstr., vol. 45, no. 5, p. 4215 (2004).

[5] Isaksson, J.; "Electronic control of Ca^{2+} signaling in neuronal cells using an organic electronic ion pump," Nat.Mater., V6, #9, pp. 673-679 (2007).

Differentiation of Human Mesenchymal Stem Cells to Schwann Cells on Electrospun Nanofibers

Shelby Pursley
Biological Engineering, Department of Biological and Agricultural Engineering, Louisiana State University

NNIN REU Site: Nanotechnology Research Center, Georgia Institute of Technology, Atlanta, GA
NNIN REU Principal Investigator: Dr. Younan Xia, The Wallace H. Coulter Department of Biomedical Engineering, School of Chemistry and Biochemistry, School of Chemical and Biomolecular Engineering, Georgia Institute of Technology
NNIN REU Mentor: Wenying Liu, School of Chemical and Biomolecular Engineering, Georgia Institute of Technology
Contact: shelbykpursley@gmail.com, younan.xia@bme.gatech.edu, liuwenying@gatech.edu

Abstract:

Injuries to the peripheral nervous system (PNS) are irreparable even with surgical intervention. Tissue engineering strategies use a combination of cellular therapies and biocompatible scaffolds in an effort to restore full function to damaged nerves. In this study, electrospun nanofibers were used as the substrate for investigating the differentiation of the human mesenchymal stem cells (hMSCs) into Schwann cell lineage for nerve repair. We investigated the effects of fiber diameter and cell seeding density on the differentiation process. Poly-(ε-caprolactone) nanofibers of various diameters were fabricated using the electrospinning technique and their average diameters were assessed via scanning electron microscopy. The hMSC-derived Schwann cells were visualized through immunofluorescence microscopy for S100, a widely recognized Schwann cell marker.

Introduction:

The human body possesses very limited regenerative capabilities. For example, severe damage to the peripheral nervous system is irreparable even with surgical intervention due to the limited availability of Schwann cells (SCs), a type of glial cell that supports the extension of axons and communication between synapses. Therefore, this project aims at supplementing hMSC-derived SCs to facilitate the repair of damaged nerves to their full function in combination with biocompatible scaffolds, constructs that provide an encouraging environment for the regeneration.

The electrospinning technique is a simple technique requiring little equipment, but has the ability to produce fibers from biocompatible materials with diameters in the nanometer range. These nanofibers resemble the structure of the extracellular matrix (ECM) making them an effective scaffold. Electrospun nanofibers are particularly attractive for use with nerves and other anisotropic tissues because the electrospinning technique readily allows for uniaxial alignment of nanofibers, mimicking their anisotropic anatomy. In this study, poly-(ε-caprolactone) (PCL) electrospun nanofibers were used as the substrate for investigating the differentiation of hMSCs into Schwann cell lineage for nerve repair. Bone marrow derived hMSCs were chosen particularly due to their clinical relevancy. We investigate the effects of fiber diameter and cell seeding density on the differentiation process, two parameters chosen due to their correlation to conditions governing the initial development of the PNS.

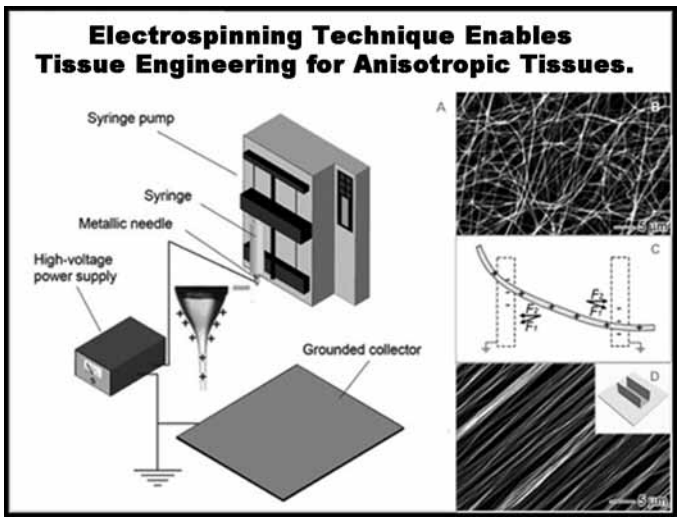

Figure 1: In the (A) electrospinning technique, a high voltage was applied to a syringe containing a polymer dissolved in solution — causing the droplet at the tip to form a Taylor cone. A thin jet stream emerged at the apex of that cone and traveled toward a grounded collector. (B) Fibers randomly oriented, but could be (D) readily aligned using a staple collector, which applied an (C) electrostatic force to the incoming fiber.

Methods:

Uniaxially aligned electrospun nanofibers were constructed using the electrospinning technique outlined in Figure 1 from PCL, a biocompatible polymer, dissolved in various solvent systems and spun at various parameters to achieve three distinct diameter sizes. Samples of each fiber type were assessed for size

and morphology using scanning electron microscopy, which is shown in Figure 2. PCL nanofibers were sterilized with ethanol and coated with collagen for cell seeding.

The hMSCs were cultured up to P5 in Dulbecco's modified eagle medium (DMEM). Once confluent, cells were detached by trypsin and seeded on the PCL nanofibers at 1×10^5 cells/mL for the fiber diameter study, and both 1×10^5 and 1×10^4 cells/mL on the intermediate fiber for the cell density study.

The differentiation of hMSC was carried out over a 2.5 week period using an established technique prescribing neuronal inducing factors including β-mercaptoethanol, retinoic acid, platelet derived growth factor AA, nerve growth factor, and forskolin as supplements in DMEM media. The hMSC-derived Schwann cells were visualized through immunofluorescence microscopy for S100, a cytoplasmic protein widely used as a Schwann cell marker.

Results and Discussion:

Differentiation to Schwann cell lineage was observed on all fiber types (Figure 3), but clear advantage caould be seen in the thick fibers, which provided a larger surface area. We predict this larger surface area would promote myelination in co-culture with neurons. In the case of cell density (Figure 4), advantage was obvious in 1×10^5 cells/mL, but the upper limit of cell density should be tested. Further optimization of the culture system should be investigated, but, even in its current state, this system has great promise. The ability to culture healthy Schwann cells for cellular therapies without introducing donor site morbidity could be highly impactful in achieving full PNS nerve repair.

Future Work:

In the future, we seek to apply this approach to nerve repair in model animals for *in vivo* studies in rats with the eventual goal of successful nerve regeneration in human subjects.

Acknowledgements:

We would like to acknowledge the following institutions involved with or in support of this project: National Nanotechnology Infrastructure Network Research Experience for Undergraduates (NNIN REU) Program, National Science Foundation (NSF), Georgia Institute of Technology, and Institute for Electronics and Nanotechnology (IEN).

References:

[1] Caddick, J., et al. "Phenotypic and functional characteristics of mesenchymal stem cells differentiated along a Schwann cell lineage." Glia 54(8): 840-849. (2006).

[2] Liu, W., et al. "Electrospun nanofibers for regenerative medicine." Adv Healthc Mater 1(1): 10-25. (2012).

[3] Xie, J., et al. "Electrospun nanofibers for neural tissue engineering." Nanoscale 2(1): 35-44. (2010).

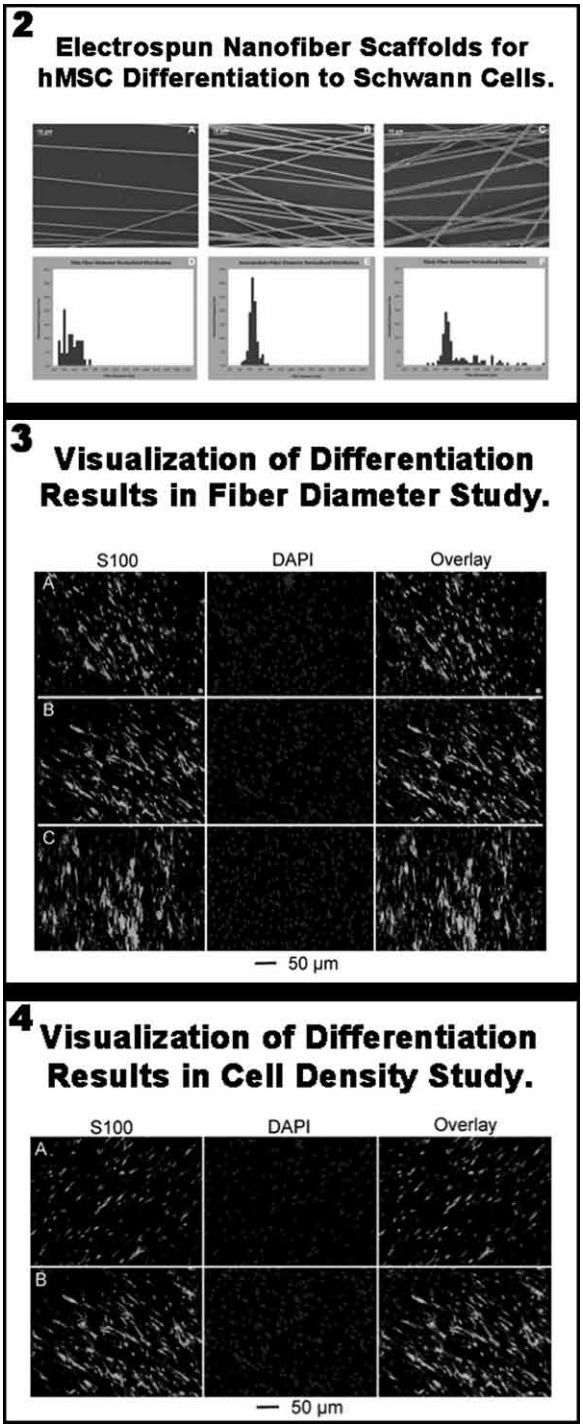

Figure 2, top: (A-C) SEM images taken at 1,000x magnification and (D-F) fiber diameter distribution data for each fiber type. The average diameters of the (L-R) thin, intermediate, and thick fibers were 484.5 ± 31% nm, 617.5 ± 13% nm, and 1.198 ± 35% µm, respectively.

Figure 3, middle: Differentiated hMSCs were imaged using fluorescent microscopy for (L-R) S100 and DAPI stains, and the overlay depicts success of differentiation to Schwann cell lineage on (A-C) thin, intermediate, and thick PCL nanofibers.

Figure 4, bottom: Differentiated hMSCs were imaged using fluorescent microscopy for (L-R) S100 and DAPI stains, and the overlay depicts success of differentiation to Schwann cell lineage for hMSC seeding densities of (A) 1×10^4 and (B) 1×10^5 cells/mL on PCL nanofibers.

Electrohydrodynamic Jet Printing on Hydrogel Substrates for Cell Culturing Applications

Audre Ramey
Mechanical Engineering, University of Portland

NNIN REU Site: Lurie Nanofabrication Facility, University of Michigan, Ann Arbor, MI
NNIN REU Principal Investigator: Prof. Kira Barton, Mechanical Engineering, University of Michigan
NNIN REU Mentor: Leo Tse, Mechanical Engineering, University of Michigan
Contact: ramey14@up.edu, bartonkl@umich.edu, tselaiyu@umich.edu

Abstract:

Patterning cell cultures on a biologically compatible surface has the potential to significantly extend cell biology knowledge. Electrohydrodynamic jet (e-jet) printing has the capability to pattern surfaces with various biological compounds. This project focused on the use of an e-jet printer to pattern a protein complex, fibronectin, used for cell attachment, on the surface of polyacrylamide hydrogels. E-jet has the potential to print fibronectin ink droplets as small as 2 μm. Polyacrylamide gel stiffness can be modified to mimic various biological tissues. This research has the potential to make advancements in cellular biology knowledge, three-dimensional cellular patterns or bio-arrays, and tissue engineering.

Introduction:

Cell cultures are affected by many different factors. Being able to control and manipulate the environment (biocompatible substrates) and location of a cell culture can provide important information to cell biology knowledge [1]. The ability to place a single cell on a substrate in a flexible pattern has the potential to affect many areas of research. Electrohydrodynamic jet (e-jet) printing can be used for high-resolution (< 10 μm) free form patterning of biological materials on a wide range of substrates [2]. A schematic of the e-jet printer can be seen in Figure 1. The main components of the system are a charged nozzle and a grounded substrate that create an electric field. As the electric field is increased, the ink in the nozzle tip is drawn into a conical formation and onto the substrate [3]. The system is computer controlled through LabVIEW [2]. The system can be run on a direct current mode for continuous jetting or a pulsed printing mode for drop-on-demand printing [4].

The e-jet printing system was used to pattern fibronectin on the surface of polyacrylamide hydrogels for cell culturing applications.

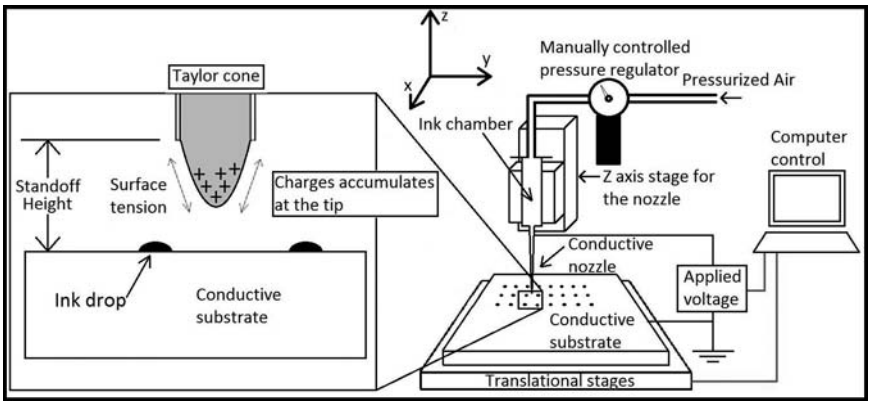

Figure 1: Electrohydrodynamic jet printer schematic [1].

Experimental Procedure:

Fibronectin Production. Fibronectin was made from a 40 μg/mL fibronectin concentrate [1]. The fibronectin was made with filtered 1X phosphate buffered sulfate (PBS) [5].

Polyacrylamide Hydrogel Production and Activation. The hydrogels were made with 8% acrylamide and 0.3% bis-acrylamide solution in double distilled water (ddH_2O) along with 1M HEPES stock solution buffer and 0.2% acrylic acid [1]. To initiate polymerization of the gel, 10% ammonium persulfate and 0.05% tetramethylethylenediamine (TEMED) were added. Then 35 μL of the liquidous (and quickly polymerizing) hydrogel was placed between an indium tin oxide (ITO) microscope slide and a standard glass coverslip. After the gels were fully polymerized, the gels were soaked in an n-hydroxysulfosuccinimide (NHS) and n-(3-dimethylaminopropyl)-n′-ethylcarbodiimide hydrochloride (EDC) bath to activate the surface for printing by reacting with acrylic acid within the gel [1]. The gels were then stored in ddH_2O to keep hydrated before printing.

Printing Protocol. Hydrogels on ITO slides were placed on the vacuum chuck of the e-jet printer. The syringe was filled with 1-3 drops of fibronectin and initialized by pressurized air pushing the fibronectin to the end of the nozzle. The nozzle was positively charged until jetting occurred and parameters were set

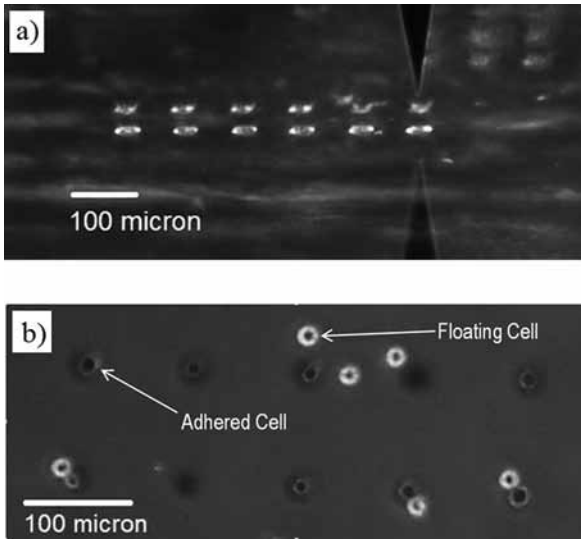

Figure 2: Fibronectin patterning during; a) printing process, and b) cellular seeding.

Figure 3: 'NNIN' pattern.

for printing [2]. Figure 2a shows the printing process underway, while a dot matrix on fibronectin is patterned. All gels were stored in ddH_2O until time of imaging or cellular seeding.

Cellular Seeding Protocol. Gels were cultured with retina pigment epithelial (RPE) cells with 10% fetal bovine serum, 50x 1M HEPES and 200x penicillin-streptomycin. All samples seeded with cells were stored in a 37ºC incubator until imaging was needed [6]. Images of cells seeded on hydrogels patterned with fibronectin can be seen in Figure 2b.

Results and Conclusions:

The fibronectin was successfully patterned on the hydrogel surface and cells were subsequently seeded on those patterns, Figure 3. Various patterns were developed using both electronic and manual techniques. Ink droplet size was characterized using an Olympus BX51 microscope. The droplet size was varied by changing either the stand-off height (the distance between the charged nozzle and the substrate) or the pulse width (the duration of time that the nozzle is charged in one location). The pulse width provided more consistent size variations. Figure 4 shows the relationship between pulse width and droplet size. As the pulse width increased the droplet size increased exponentially. The vertical bars on this graph show the standard deviation from the average droplet size. As can be seen, the standard deviation increased as pulse width increased; mostly likely, a function of increased variation due to the larger number of droplets released in a given period.

Future Work:

The next phase of this project will focus on cell culturing. During this research phase, the cell cultures did not uniformly adhere to the patterned fibronectin. This requires further investigation, including looking into different ink materials like collagen. Printing quality and properties using variations in hydrogel stiffness and water content is another potential research avenue.

Acknowledgements:

I would like to thank my principal investigator, Prof. Kira Barton, as well as my mentor Leo Tse, along with members of the partnering lab, Prof. Allen Liu, Xinyu Tan, and Elizabeth Steel for their extensive help during the duration of this project. I want to also commend the University of Michigan NNIN site coordinators, Sandrine Martin, Brandon Lucas and Trasa Burkhardt for their assistance within the program. I also want to extend a huge thanks to the National Nanotechnology Infrastructure Network Research Experience for Undergraduates Program and the National Science Foundation for providing the opportunity to participate in this program.

References:

[1] M. Poellmann, et al., Macromolecular Bioscience, vol. 11, pp. 1164-1168, 2011.
[2] K. Barton, et al., Elsevier: Mechatronics, vol. 20, pp. 611-616, 2010.
[3] J. U. Park, et al., Nature Materials, vol. 10, pp. 1-8. 2007.
[4] S. Mishra, et al., Journal of Micromechanics and Microengineering, vol. 20, 2010.
[5] Liu's Lab protocol for fibronectin.
[6] Liu's Lab protocol for cell culturing.

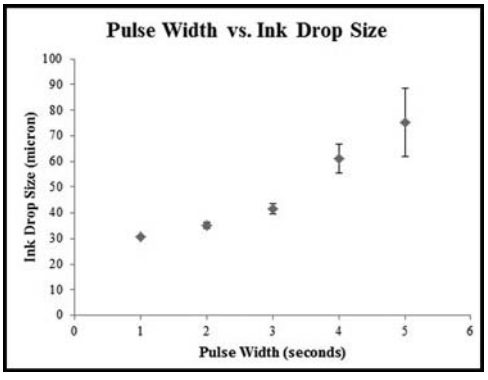

Figure 4: The relationship between pulse width and ink drop size.

Surface Ligand Density Dependence of Collective Cell Migration on Photoactivatable Self Assembled Monolayers

Radu Reit
Biomedical Engineering, Georgia Institute of Technology

NNIN iREU Site: National Institute for Materials Science (NIMS), Tsukuba, Ibaraki, Japan
NNIN iREU Principal Investigators: Jun Nakanishi and Yukio Nagasaki, MANA-WPI, National Institute of Material Science
NNIN iREU Mentors: Yoshihisa Shimizu and Masao Kamimura, MANA-WPI, National Institute of Material Science
Contact: reit.radu@gmail.com, nakanishi.jun@nims.go.jp, nagasaki@nagalabo.jp, shimizu.yoshihisa@nims.go.jp, kamimura.masao@nims.go.jp

Abstract:

Cell migration is an important biological process that can be influenced by many extracellular factors. In this study, the effect of surface density of an extracellular matrix (ECM) ligand on collective migratory characteristics is explored using a tunable, photoactivatable substrate. The substrate exposes cyclic arginine-glycine-aspartic acid (cRGD) ligand at a given surface density upon photoirradiation. HeLa cervical cancer cells and Madin Darby canine kidney (MDCK) cells were photopatterned on circular regions (r = 75 μm) for 5 h and migration was induced by irradiating surrounding regions. Results show an increasing speed for MDCK cells as the cRGD ratio decreases ($p < 0.001$) and a constant migration speed for HeLa cells on all substrates.

Introduction:

Cell migration is an important component of cancer metastasis and the wound healing process, where the collectivity of migration can be influenced by many factors such as the composition of ECM, soluble factor gradients, etc. [1, 2]. Previous studies have also shown the dependence of patterned substrates on various cellular functions during *in vitro* experiments [3]. Here, the effect of cRGD surface density on collective migratory characteristics was explored in HeLa and MDCK cells using a photoactivatable substrate. As MDCK cells expressed a stronger cell-to-cell binding mechanism than HeLa cells (E-cadherin versus N-cadherin), it was expected that with varied concentrations of surface cRGD, a faster migration speed would be observed for HeLa cells in comparison to MDCK cells.

Experimental Procedure:

Polymer Synthesis. Photocleavable poly(ethylene glycol) (PCP) was synthesized through a 2:1 mixing of alpha-methoxy-omega-amino poly(ethylene glycol) (PEG, MW = 12K) and Bis(12-(4-(1-(succinimidyloxycarbonyloxy)ethyl)-2-methoxy-5-nitrophenoxy)disulfide (DSNBD) and reacted overnight at room temperature. Similarly, cyclic cRGD peptides were reacted in a 2:1 ratio with dithiobis (succinimidyl-3,6,9,12,15,18,21-heptaoxo-dotriacotanoate) (DSHODA) and reacted overnight at room temperature. Commercially available bis-1-(11-[2-{2-(2-[2-{2-(2-hydroxy-ethoxy)-ethoxy}-ethoxy]-ethoxy)-ethoxy}-ethoxy]-undecyl) disulfide (EG) was used as the diluting agent for cRGD. All disulfide compounds were dissolved in dimethyl sulfoxide (DMSO) to a final concentration of 50 μM.

Substrate Fabrication. Substrates were fabricated on quartz glass with a 5 nm titanium adhesion layer and 20 nm gold layer. EG was used to dilute cRGD to the studied concentrations and then each mixture of cRGD:EG was diluted in a 4:1 ratio of PCP:[cRGD:EG]. The final mixture of 4:1 PCP:[cRGD:EG] was mixed and 15 μL of the solution was pipetted onto the substrate. After an overnight incubation, the substrates were immersed in a DMSO bath and rinsed of unfunctionalized disulfides. Next, substrates were sterilized in 70% ethanol and prepared for photopatterning.

Cell Culture. HeLa and MDCK cells were seeded on circular photopatterned substrates (r = 75 μm) for 2 h in serum-free Dulbecco's modified eagle medium (DMEM) after which the media was exchanged to DMEM containing 10% fetal bovine serum (FBS). The cells were then incubated for 3 h at 37°C before being exposed to a secondary UV irradiation (Figure 1).

Results and Conclusions:

HeLa cells were cultured on a range of cRGD:EG concentrations (1:10 to 1:100,000,000) to test cell attachment and shape. Attachment was observed on concentrations ranging between 1:10 and 1:10,000 with the number of attached cells decreasing with lower concentrations of cRGD. Additionally, the shape

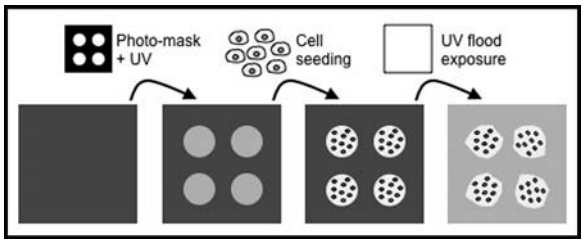

Figure 1: Outline of experimental procedure for culturing cells on circular patterns.

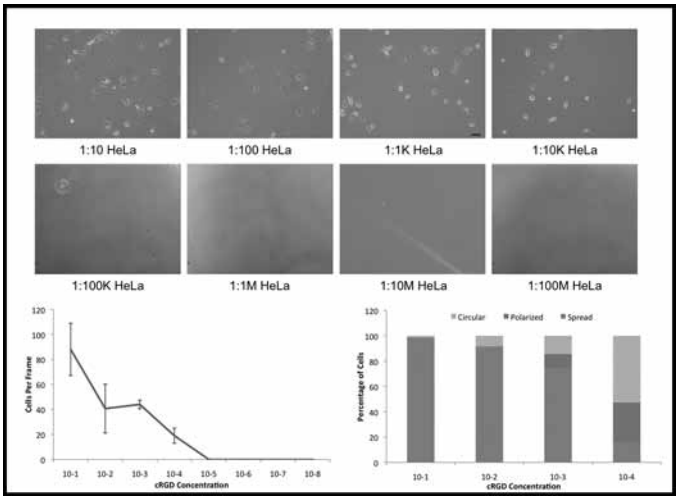

Figure 2: HeLa attachment and morphology on 8 cRGD concentrations.

of attached cells shifted from a spread to a more rounded morphology as cRGD density decreased (Figure 2).

Next, cell migration from the circular cluster was examined. After confinement cells were released via secondary UV irradiation and representative images of migration were collected every fifteen minutes for four hours (representative snap shots shown in Figure 3). MDCK and HeLa migration speeds were evaluated using time profiles of the average cluster radius change after confinement release and compared at each cRGD concentration. While MDCK cells show an inversely proportional relationship between cRGD density and speed ($p < 0.001$), HeLa cells show no significant difference at any cRGD concentration (Figure 4). When compared between cell lines, HeLa cells show a significantly higher migration speed at cRGD densities of 1:100 ($p < 0.001$) and 1:1,000 ($p < 0.05$), with no difference at 1:10,000.

In conclusion, it was found that HeLa cells selectively attach to a certain range of cRGD densities. After testing this range in MDCK and HeLa cells, an inversely proportional relationship between speed and cRGD density was observed in MDCK cells while no relationship was observed in HeLa cells. These results indicate a correlation between receptor type (E- versus

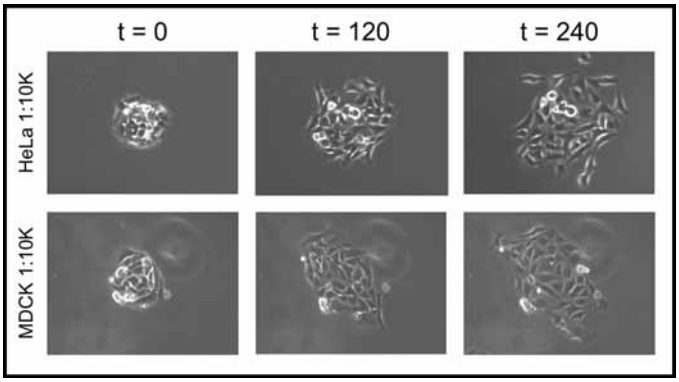

Figure 3: HeLa and MDCK cells seeded on circular (r = 75 μm) patterns at two and four hours after release.

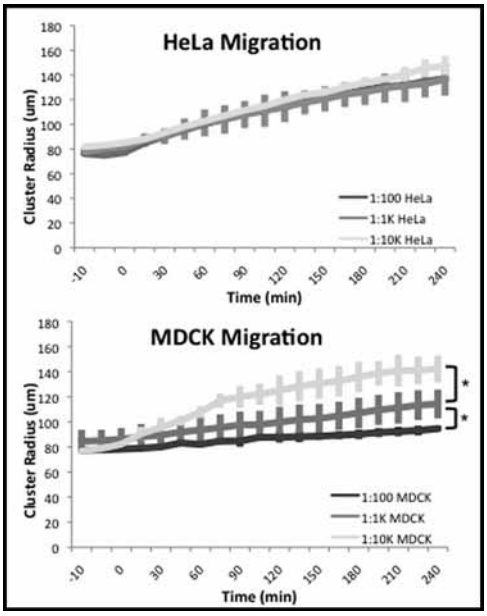

Figure 4: Migration speed profiles for three cRGD densities for the first four hours after release.

N-cadherin) and migration speed at high cRGD densities which could help predict migration characteristics in new cell lines based on cell-to-cell adhesion type.

Future Work:

In this study, a high throughput testing bed for cell migration was fabricated. By using this substrate for testing cell migration, the migratory behavior of cell lines can be determined at specific surface ligand concentrations. For future studies, cells will be fixed three hours after release and stained for E- and N-cadherin junctions. By quantifying cell-to-cell adhesion, the importance of receptor type on migration speed can be determined.

Acknowledgments:

The author would like to thank the National Science Foundation and the National Nanotechnology Infrastructure Network International Research Experience for Undergraduates Program for their financial support as well as the host institution, The National Institute of Material Science.

References:

[1] Rolli, Claudio G., et al. "Switchable adhesive substrates: Revealing geometry dependence in collective cell behavior." Biomaterials 33.8 (2012): 2409-2418.

[2] Roberts, Carmichael, et al. "Using mixed self-assembled monolayers presenting RGD and (EG) 3OH groups to characterize long-term attachment of bovine capillary endothelial cells to surfaces." Journal of the American Chemical Society 120.26 (1998): 6548-6555.

[3] Otsuka, Hidenori, et al. "Two-Dimensional Multiarray Formation of Hepatocyte Spheroids on a Microfabricated PEG-Brush Surface." ChemBioChem 5.6 (2004): 850-855.

Micro-Scale Microbial Fuel Cell: Petroleum Biosensing

Anne Showalter
Biological Chemistry, Culver-Stockton College

NNIN REU Site: ASU NanoFab, Arizona State University, Tempe, AZ
NNIN REU Principal Investigator: Dr. Junseok Chae, Electrical Engineering, Arizona State University
NNIN REU Mentor: Hao Ren, Electrical Engineering, Arizona State University
Contact: aes221@culver.edu, junseok.chae@asu.edu, haoren.ustc@gmail.com

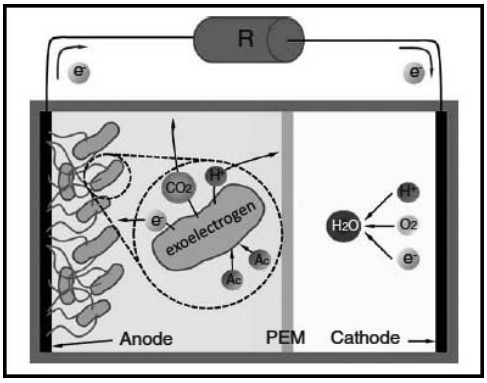

Figure 1: Simplified explanation of an MFC [4].

Introduction:

A microbial fuel cell (MFC) employs a certain type of bacteria categorized as exoelectrogenic, meaning they allow electrons to be transported from the inside to the outside of their cell membranes, via their catabolic reactions [1]. This process produces electricity as the electrons flow over an external load as shown in Figure 1. The anode and cathode chambers must be completely separate and no oxygen can enter the anode chamber, as the bacteria we explore are an anaerobic species. The final electron acceptor in the cathode is generally an inorganic catholyte [1], i.e. potassium ferrocyanide. The most common bacteria used are proteobacteria, especially those from the genus *Shewanella* and *Geobacter* [1]. An MFC has multiple applications such as water sustainability, clean energy, and biosensing. In this research, the MFC will be considered micro-scale, with a 1 cm^2 anode.

The main goal of this study was to test the effectiveness of an MFC as a biosensor in order to sense organic pollutants. The idea behind the sensor relies on a change in current generated by the MFC or series of MFCs. The bacteria in the MFC were able to oxidize organic materials such as acetate in order to produce current depending on the size of the MFC and the thickness of the biofilm [1]. When a pollutant was introduced into the anode, the bacteria were unable to break it down in the same way as the normal organic substance, causing a change in current that was detectable after knowing the previous baseline data [2].

The basis of this research project was to see if the micro-scale MFC had the ability to sense for petroleum without destroying the biofilm of bacteria. Oils spills are a major concern in any aquatic environment and it can impact the water quality for years after the initial spill. Other problems can be economic or socially problematic, such as a reduction in the tourist industry [3].

Experimental Procedure:

The micro-scale microbial fuel cells in this research were set up in a manner consistent with the micro-scale devices described by Ren [4]. The anode and cathode were glass slides with gold thin-film electrodes. Silicone gaskets prevented leakage and a proton exchange membrane (PEM) allowed protons to flow from anode to cathode. Nanoports allowed the anolyte and catholyte to reach the anode and cathode respectively at a controlled flow rate of 2 μL/min. *Geobacter sulfurreducens* enriched inoculum was used to form biofilm on the anode. The MFCs were started and allowed to reach a steady current before any testing began. The concentration of sodium acetate in the anolyte was

25 mM. In order to test the sensitivity of the MFCs to the petroleum, petroleum was diluted into the anolyte solution through a solvent bridge of toluene and ethanol. The final concentrations used were 0.5 mM and 1 mM. The anolyte used was either the 25 mM acetate with the petroleum or a buffer solution with the same ionic characteristics as the anolyte but containing no acetate. This was flowed into the MFCs at the main flow rate for several hours each and data points were taken every minute.

Results and Conclusions:

A transient curve of current density over time was taken from a working MFC in order to see the effects of the buffer solution with 0.5 mM petroleum being added, as shown in Figure 2. The results indicated in each case that the MFCs were sensitive to petroleum. If petroleum was added without other organic substrates, the MFCs could not oxidize the petroleum and the current was drastically reduced as shown in Figure 3. However, if the petroleum was added in addition to the 25 mM acetate, the MFCs were able to oxidize both the acetate and petroleum as shown in Figure 4. Previous research indicates that *Geobacter sulfurreducens* might be able to break down benzene, a large component of petroleum, via the reaction $C_6H_6 + 30Fe(III) + 12H_2O \rightarrow 30Fe(II) + 6CO_2$ [5]. More research would be required to determine if this was a consistent response.

The MFCs were able to recover from a lack of organic substrates after being starved for multiple hours. The experiments show the MFCs can be re-used after a series of spiking petroleum samples.

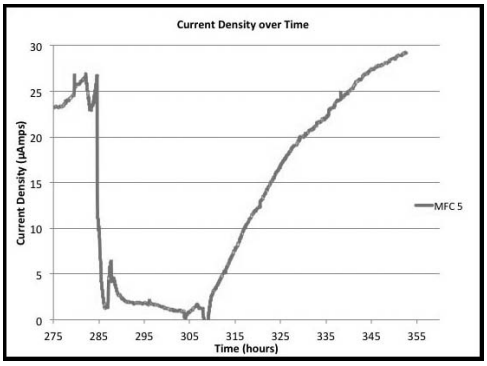

Figure 2: Current density over time with the addition of petroleum after 25 mM acetate as well as the addition of 25 mM acetate to determine recovery.

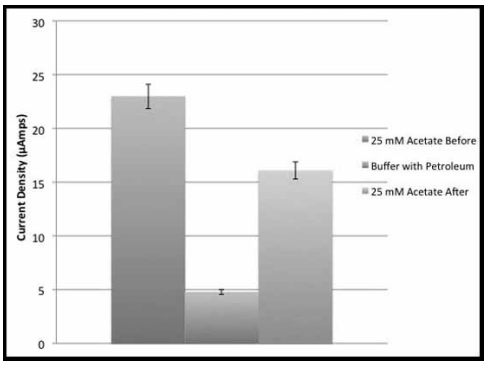

Figure 3: The average current density during each part of the curve before, during, and after the addition of buffer containing petroleum.

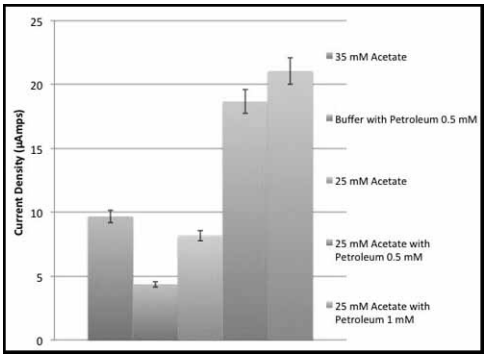

Figure 4: The addition of buffer with petroleum as well as adding different concentrations of petroleum to the 25 mM acetate to see if it could facilitate a different response from the MFC.

Acknowledgments:

I would like to thank Dr. Junseok Chae, Hao Ren, and everyone in my lab for their help with this research, Dr. Trevor Thornton for coordinating my stay at ASU, and the National Nanotechnology Infrastructure Network Research Experience for Undergraduates Program and the National Science Foundation for funding this research.

References:

[1] Logan, B. Microbial Fuel Cells. (1st ed.). Hoboken, New Jersey: John Wiley and Sons, Inc. (2008).

[2] Feng, Y., Kayode, O., and Harper, Jr., W. "Using microbial fuel cell output metrics and nonlinear modeling techniques for smart biosensing." Science of the Total Environment 449, 223-228. (2013).

[3] Garza, M., Prada, A., Varela, M., and Rodriguez, M. "Indirect assessment of economic damages from the prestige oil spill: consequences for liability and risk prevention." 2009 Mar;33(1):95-109. doi: 10.1111/j.1467-7717.2008.01064.x. Epub 2008 May 21. (2008).

[4] Ren, H., Lee, Y., and Chae, J. "Miniaturizing microbial fuel cells for potential portable power sources: promises and challenges." Microfluid Nanofluid 13:353-381. (2012).

[5] Zhang, T., Bain, T., Nevin, K., Barlett, M., and Lovley, D. "Anaerobic benzene oxidation by geobacter species." Applied Environmental Microbiology, 78(23), 8304-8310. (2012).

Dynamics of Bacterial Quorum Sensing in Microfluidic Devices

Peter Youpeng Su
Chemical and Biomolecular Engineering, University of California, Berkeley

NNIN REU Site: Nanotechnology Research Center, Georgia Institute of Technology, Atlanta, GA
NNIN REU Principal Investigator: Dr. Craig Forest, Bioengineering, Georgia Institute of Technology
NNIN REU Mentor: Caitlin Henegar, Bioengineering, Georgia Institute of Technology
Contact: su.peter@berkeley.edu, cforest@gatech.edu, chenegar3@gatech.edu

Introduction:

Quorum sensing is an essential communication mechanism in bacteria. By transmitting small molecules to each other, bacteria can sense their own population and respond accordingly. Coupling such mechanisms with synthetic biology can lead to a wide range of potential applications, including microbial detection of heavy metals [1]. Although many quorum sensing mechanisms have been characterized at the molecular level, variations in population-level responses are not well understood.

We engineered the *luxI*/*luxR* quorum sensing mechanism from *V. fischeri* into *E. coli* cells such that the cells functioned as fluorescent receivers of a signal molecule, an acyl homoserine lactone (AHL) [2]. The cells were studied in a microfluidic device to allow for constant population density and dynamic media variation, to introduce signal molecules. Finally, we created and extended a deterministic mathematical model to characterize the responses of the fluorescent experiments. Utilizing the model's predictions will allow for the use of quorum sensing in practical applications.

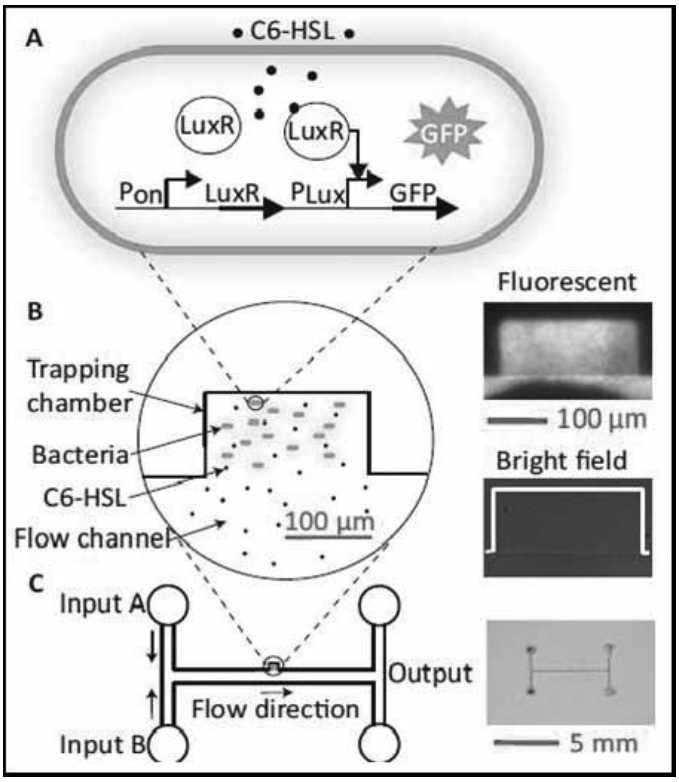

Figure 1: E. coli *cells engineered with the* luxI/luxR *system and the microfluidic device setup in our experiments [4]. C6-HSL is a specific type of AHL.*

Experimental Procedure:

SU-8 master molds were fabricated via a two-step photolithography process in order to produce 10 μm tall channels and 5 μm deep chambers. Wafers were silanized with tridecafluoro-1,1,2,2,-tetrahydrooctyl-1-dimethylchlorosilane in a vacuum dessicator.

The polydimethylsiloxane (PDMS) devices were fabricated by pouring a mix of 10:1 polymer to cross-linking agent (65 g total weight) onto the SU-8 mold then cured for four hours at 50°C, then removed.

COMSOL software was used to create a model of the fluid dynamics and transport processes in the channel and chambers, and a time frame for AHL transport into the chamber from the channel was determined.

Fluorescent microscopy using 2 μM fluorescent bovine serum albumin (Alexa Fluor 488) pumped through the chip using 5 mL syringes and a charge-coupled-device (CCD) camera were utilized to validate the devices. Results were compared against COMSOL simulation, and confirmed the accuracy of the simulation's predictions of mass transfer in an empty chamber, as seen in Figure 2.

The mathematical model was set up to capture the following biochemical interactions: External AHL diffuses into the cells, reversibly binds with *luxR* to form a dimer, which acts as a transcription factor for the *luxI* promoter. Upon binding of this transcription factor, transcription and translation of the *gfp* gene is initiated. The green fluorescent protein (GFP) undergoes chemical maturation before fluorescing. All species degrade over time.

The model was programmed into MATLAB, using generalized mass action to capture the species mentioned above vs. time. Euler's method for 1st order linear differential equations was used, and parameter estimation was coded in order to estimate

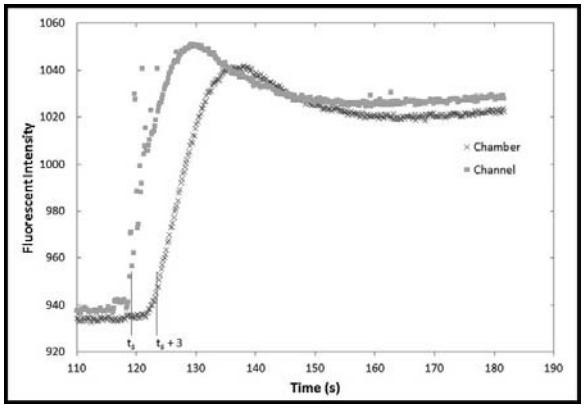

Figure 2: Fluorescent BSA experiment showing the start time of fluorescent increase in the channel (t_0). The 3-second delay between channel and chamber supports COMSOL predictions.

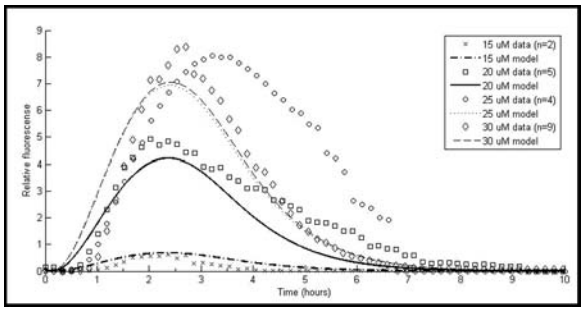

Figure 3: Model fit to experimental data of multiple concentrations, varying only protein production rates.

the rate constants governing each term. The mean-squared-error was minimized to best-fit the model to experimental data.

Results and Discussion:

Figure 3 depicts the model's fit to an AHL pulse length of fifty minutes at varying concentrations, using identical rate constants for all experiments, varying only protein production rates. Our model clearly captured the fluorescent responses for most of our experiments, with some deviations, as the 25 μM curve shows. We believe this is due to the wider peak generated in the 25 μM experiment, for unknown reasons. Finally, Figure 4 applies our model to data taken from literature and directly compares our fit with theirs [3]. Since their experiment setup is different, allowing for unbounded growth, some of the rate constants were adjusted accordingly.

One major improvement that needs to be made includes accounting for the delay in the response in our data. In quorum sensing, transcription levels are basal until a critical concentration of the signal molecule is reached, upon which a burst of transcription occurs [2]. This is likely due to some form of internal feedback control. Still, these fits prove that our model's ability to characterize a variety of experimental setups, and has promising potential to predict future experiments.

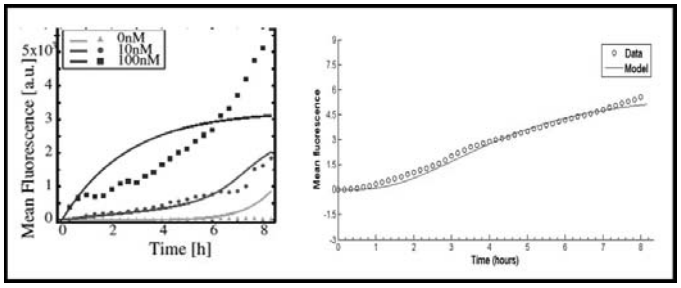

Figure 4: Comparison of literature fit (left) vs. our model fit (right) to the 100 nM concentration data points [4].

Future Work:

Our model will be extended to fit other growth conditions. Once the model has been validated with a sufficiently wide range of experiments, we will begin testing the model by predicting experiments with specific signal pulse profiles and concentrations.

We will use transmitter cells that produce AHL and emit it via diffusion, and run experiments with both transmitters and receivers. These experiments more closely represent quorum sensing in nature. We can then begin moving towards genetically engineering bacteria for practical applications such as the biosensor mentioned earlier for detecting toxic heavy metals in water. Our work will open the door for many applications of quorum sensing in the bioengineering field.

Acknowledgements:

I would like to sincerely thank the following people for giving me this great opportunity: Caitlin Henegar, Prof. Craig Forest, the Forest Lab, Georgia Tech cleanroom staff, Dr. Nancy Healy and Ms. Leslie O'Neill. In addition, my thanks to NNIN REU and NSF for funding.

References:

[1] T. Charrier, et al., "A multi-channel bioluminescent bacterial biosensor for the on-line detection of metals and toxicity. part ii: technical development and proof of concept of the biosensor," Analytical and Bioanalytical Chemistry, vol. 400, pp. 1061-1070, 2011.

[2] Taga, M.E., and Bassler, B.L. "Chemical communication among bacteria." Proc. Natl. Acad. Sci. USA 100: 14549-14554. (2003)

[3] Meyer, A., et al., "Dynamics of AHL mediated quorum sensing under flow and non-flow conditions." Physical Biology, vol. 9, no. 2, p. 026007, 2012.

[4] Krishnaswamy, B., et al., "Time-elapse communication: Augmenting bacterial communication on a chip." Submitted to Journal IEEE Transactions on Communications Aug. 2013.

Fabrication of Flexible, Implantable Probes for *in vivo* Recording of Neural Activity

Brianna Thielen
Engineering, Harvey Mudd College

NNIN iREU Site: Centre Microélectronique de Provence, Ecole Nationale Supérieure des Mines de Saint Etienne, France
NNIN iREU Principal Investigator: Professor George Malliaras, Department of Bioelectronics, Centre Microélectronique de Provence, École Nationale Supérieure des Mines de Saint-Etienne, France
NNIN iREU Mentor: Marc Ferro, Department of Bioelectronics, Centre Microélectronique de Provence, École Nationale Supérieure des Mines de Saint-Etienne, France
Contact: bthielen@hmc.edu, malliaras@emse.fr, ferro@emse.fr

Introduction:

In order to study the brain activity of living organisms, electrode arrays can be implanted into a rat brain and can determine the source of an electrical signal down to the firing of a single neuron. Commercial probes containing these arrays are available; however, most of these probes contain an inflexible silicon backbone. Because of the large discrepancy in flexibility between the silicon probe and the brain tissue, the probe is seen as a foreign object and is encapsulated during the body's immune response.

In order to perform long term neural recordings, flexible materials that better match the Young's modulus of brain tissue (approximately 100 kPa) [1] must be used as the probe backbone. In addition, a conducting polymer coating made of poly(3,4-ethylenedioxythiophene) doped with poly(styrene sulfonate) (PEDOT:PSS) can be coated on top of the electrodes to improve the performance of the probe.

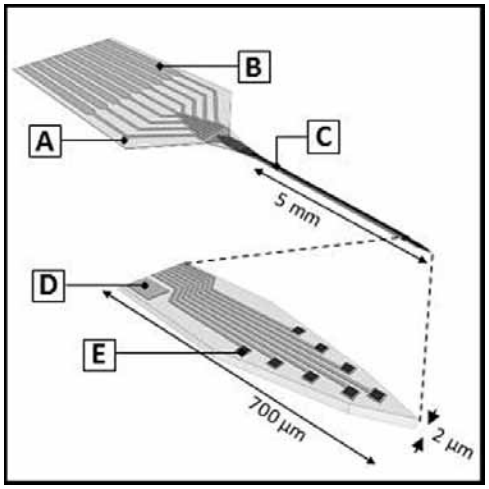

Figure 1: The configuration of the neural probe with PaC probe backbone (A), metal contacts (B), probe shank (C), temperature control pad (D), and the PEDOT:PSS coated electrodes (E).

Probe Configuration:

In this study, flexible neural probes (with the configuration shown in Figure 1) were fabricated. The probe backbone (Figure 1-A) was made of a Parylene-C film. On top of the backbone, metal contacts to interface with a data acquisition device (Figure 1-B), electrodes to collect the neural signals (Figure 1-E), a temperature control pad to adjust for thermal drift (Figure 1-D), and the wires connecting all of the components were patterned. A layer of PEDOT:PSS was coated on top of the electrodes, then a layer of DE1 permanent photoresist (Orthogonal, Inc.) was added on top of the probe to insulate everything except for the electrodes and metal contacts.

Materials and Fabrication:

Probe Backbone: Parylene-C. Parylene-C (PaC) is an FDA approved biocompatible polymer that is electrically insulating, durable, and conformable to most surfaces, while having a relatively simple fabrication process [2]. Using a PDS 2010 Labcoater (Specialty Coating Systems), PaC dimer can be vaporized and deposited as a uniform film onto a surface at room temperature. The film thickness is controlled by the amount of dimer loaded into the instrument. For this project, four grams of dimer were deposited onto silicon wafers, resulting in a film thickness of approximately 2 μm.

Electrodes, Contacts, and Wires: Metal. Metal was patterned by spin-coating photoresist onto the PaC-coated wafers, exposing the pattern using an MJB4 mask aligner (SUSS Microtech), coating the surface of the substrate with metal using an Auto500 metal evaporator (BOC Edwards), then lifting off in an acetone bath. The acetone dissolved the remaining photoresist and removed the metal above it, leaving only the patterned metal (as shown in Figure 2-1).

Electrodes (Conducting Polymer): PEDOT:PSS. Poly(3,4-ethylenedioxythiophene):poly(styrenesulfonate) (PEDOT:PSS) is an electrochemically stable conductive polymer that is able to translate ionic signals into electronic signals by moving holes in the polymer structure. When coated on an electrode, the "fuzzy"

polymer structure increases the surface area, thus decreasing the impedance (due to better contact with the target tissue) and improving the performance of the electrode [1].

Rather than using a traditional PaC lift-off technique to pattern the PEDOT:PSS, a subtractive technique was used in order to prevent damage to portions of the probe fabricated in prior steps while also significantly reducing fabrication time. The fabrication process began by spin-coating a layer of PEDOT:PSS on top of the substrate (a silicon wafer coated in PaC with the metal patterned on top). The electrode pads were then masked using a layer of OSCoR 4000 photoresist (Orthogonal, Inc.) (Figure 2-2). The substrate was then etched in an Oxford Plasmalab 80^+ reactive ion etcher (RIE) to remove the unprotected PEDOT:PSS (this process is shown in Figure 2-3). Finally, the remaining OSCoR 4000 photoresist was stripped off the surface using a fluorinated stripper (Orthogonal, Inc.), leaving only the PEDOT:PSS on the electrode pads (Figure 2-4).

Insulating Coating: DE1 Photoresist (Orthogonal, Inc.). DE1 photoresist from Orthogonal, Inc. is a permanent, biocompatible photoresist. It was used as an insulating layer for the probe (to prevent damage and expose only the electrodes to the brain tissue) and was patterned via standard photolithography (result shown in Figure 2-5).

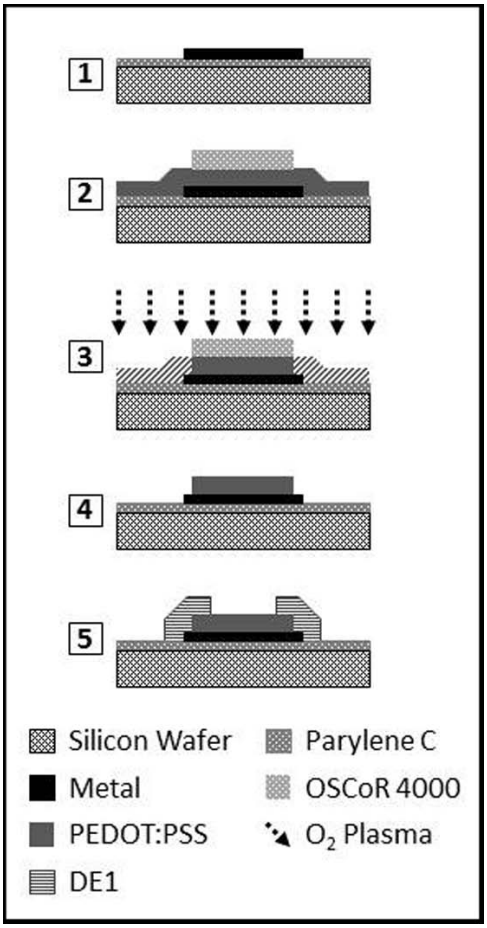

Figure 2: A process flow diagram of the PEDOT:PSS patterning and probe insulation processes, beginning with a silicon wafer coated in PaC and patterned with metal (1), followed by PEDOT:PSS coating and OSCoR 4000 patterning (2), etching in an RIE (3), stripping remaining OSCoR 4000 (4), and insulating the probe using DE1 (5).

Results and Future Work:

Each component of fabrication was tested and optimized; however several steps must be taken prior to the completion of the electrode and probe production process. First, a stiff "shuttle" layer must be added to aid in the insertion of the probe into the rat brain. The shuttle must attach to the probe, minimize insertion damage to the brain, maintain flexibility of the probe, and must allow for accurate insertion (a flexible, removable, or dissolvable shuttle). After the shuttle is completed, the probes must be tested *in vivo* by implanting into a rat brain and recording neural signals over time. A successful probe will not be walled off or otherwise damaged in the immune response and will not wear over time.

Acknowledgements:

This work was sponsored by the National Science Foundation and the NNIN iREU Program. The bioelectronics department, specifically Professor George Malliaras and Marc Ferro, provided the equipment, materials, training, and all other necessary support for this project.

References:

[1] D.H. Kim, et al., Soft, Fuzzy and Bioactive Conducting Polymers in W.M. Reichert, Indwelling Neural Implants: 165-207 (2010).

[2] C. Hassler, et al., Polymers for Neural Implants, Polymer Science Part B: Polymer Physics 49.1, 18-33 (2011).

The Study of Disposable Substrates in Surface Acoustic Wave Devices

Christine Truong
Physics, Polytechnic Institute of New York University

NNIN REU Site: Penn State Nanofabrication Laboratory, The Pennsylvania State University, University Park, PA
NNIN REU Principal Investigator: Prof. Tony Jun Huang, Engineering Science and Mechanics, The Pennsylvania State University
NNIN REU Mentor: Dr. Xiaoyun Ding, Department of Engineering Science and Mechanics, The Pennsylvania State University
Contact: christinehtruong@nyu.edu, junhuang@psu.edu, xding@psu.edu

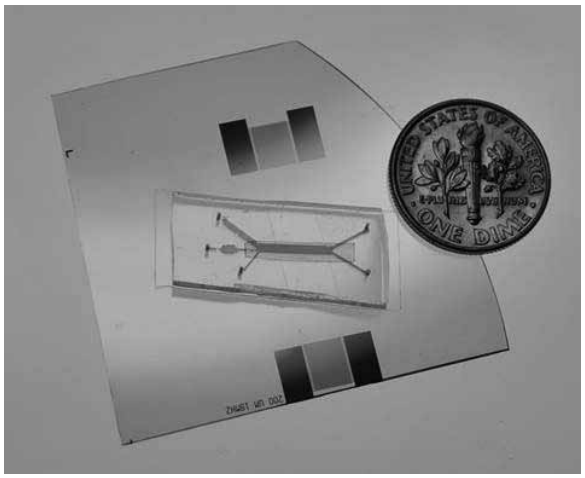

Figure 1: The SAW device, coupled with double-sided tape.

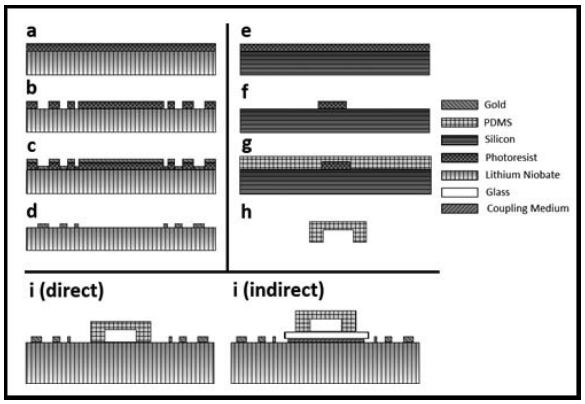

Figure 2: For the SAW device, the fabrication of the (a-d) IDTs (e-h) the channels, and (i) the difference between the traditional setup and the coupled setup.

Abstract:

Surface acoustic wave (SAW) devices have been widely used in microfluidics to manipulate fluids and particles. Applications include single cell manipulation, particle focusing, particle patterning, cell separation and cell sorting. However, in typical SAW devices, if channels are defective or if channels become contaminated after use, the device cannot be reused because the channel component is directly bonded to the SAW device substrate.

Here we show that SAW devices, whose components were coupled through 25 μm double-sided tape or petroleum jelly, can perform the same functions as a typical SAW device. Polydimethylsiloxane (PDMS) channels, which are normally directly bonded to a lithium niobate ($LiNbO_3$) piezoelectric substrate with deposited gold interdigital transducers (IDTs), were instead bonded to glass slips and coupled to gold IDT-deposited $LiNbO_3$. The modified SAW device retained the ability to manipulate particles, given an increase of power. This study shows that coupled SAW devices can be as effective as typical devices, allowing more widespread use.

Introduction:

SAWs are efficient cell and microparticle manipulators [1]. The concept behind particle manipulation is simple: A function generator sends an electrical signal to an IDT pair. The IDTs then convert that signal into SAWs on the surface of a $LiNbO_3$ substrate. The two identical SAWs propagate toward each other and interfere to form a standing SAW within a PDMS channel between these two IDTs. The pressure nodes in the standing SAW apply an acoustic forces on particles, guiding them toward pressure nodes, allowing particles suspended in the PDMS channel to be manipulated [2]. Our approach is similar, except that SAWs will travel from $LiNbO_3$ through a coupling agent and a glass slip before reaching the channel. The advantage is that the bonded channel and glass can easily be removed from $LiNbO_3$, allowing the device to be disposable and re-used.

Experimental Procedure:

Standard lithography procedures were used to deposit IDTs on a $LiNbO_3$ wafer. The wafer was spin-coated with SPR 3012 photoresist at 4000 rpm at 45 seconds (s) and then baked at 65°C, 95°C, and again at 65°C for 60 s each. Wafers were then exposed to ultraviolet light for 18 s and baked using the same parameters. The product was developed using a CD26 developer for approximately 60 s and cleaned using de-ionized water and nitrogen. The wafer was further cleaned using a plasma cleaner, with 1000 sccm O_2, and 50 sccm He after vacuum-down at 600 torr and 200 W for four minutes. After, a 5 nm adhesion layer of chrome and a 50 nm layer of gold were coated on the wafer to produce the IDTs.

The wafer-IDT composite was submerged in PG remover overnight; a sonicator was used with the IDT-wafer composite with isopropyl alcohol to remove excess gold.

The fabrication procedure for the PDMS channel was similar. Silicon wafers were coated with a SU-8-50 photoresist, spun at 2000 rpm for 45 s, and then baked at 65°C and 95°C for 5 min and 20 min, respectively. The wafer was exposed to ultraviolet light for 65 s and baked at the same temperatures for 2 min and 8 min. The product was developed by submerging in SU-8 developer for 3 min, and cleaned using isopropyl alcohol. The wafer was then baked at 150°C for 10 min. The PDMS channel was created by mixing one part elastomer curing agent to ten parts elastomer base, poured over the pattern, and incubated at 65°C for half an hour. Then channels were drilled to create inlets and outlets and bonded (via plasma induced bonding) to 250 μm glass.

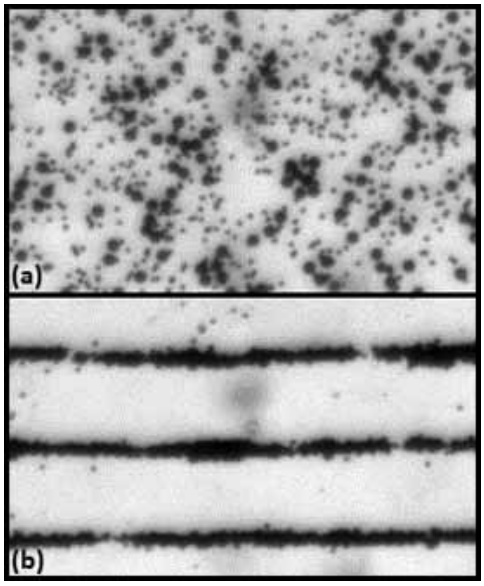

Figure 3: Patterning results using double-sided tape as the coupling agent, (a) before and (b) after toggling the SAW.

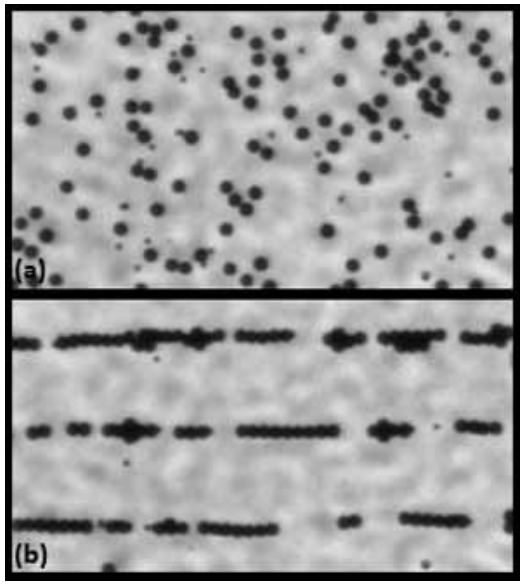

Figure 4: Patterning results using petroleum jelly as the coupling agent, (a) before and (b) after toggling the SAW.

Coupling the wafer-IDT with the channel-glass composite was accomplished using either petroleum jelly or 25 μm thick double-sided tape as a coupling agent. Figure 2 shows a schematic of each major step.

Results:

Coupling results showed that our coupled SAW device retained the ability to pattern stationary particles. Four and ten micron polystyrene beads aligned along pressure nodes after the SAW was toggled, using a frequency of 24 MHz and a power of 17.0 dBm. Figures 3 and 4 show patterning results for each coupling agent. In addition, our device was also able to separate those 4 and 10 μm diameter beads if the power was large enough; for tape coupling, the power (19.5 dBm = 89.1 mW) was nearly twice as large compared to the power needed to separate particles with petroleum jelly coupling (17.0 dBm = 50.1 mW).

Conclusions and Future Work:

We have demonstrated that coupled SAW devices can pattern and separate particles and can be as effective as traditional SAW devices, despite needing a higher input power, and that petroleum jelly is a more efficient coupling agent than 25 μm tape. In the future we hope to quantify the coupling efficiency (i.e. how much power is required to separate beads using coupling agents of varying density), examine different coupling agents, and expand the experiment by manipulating cells instead of beads.

Acknowledgements:

I would like to thank the NSF and NNIN REU for providing the research opportunity, Prof. Huang, and members his research group for their help with the project, and Dr. Xiaoyun Ding for his constructive advice and tremendous assistance in the project.

References:

[1] Ding, X., et al. "On-chip manipulation of single microparticles, cells, and organisms using surface acoustic waves." PNAS, 109 (28), 11105-11109, 2012.

[2] Shi, J., et al. "Acoustic Tweezers: Patterning Cells and Microparticles using Standing Surface Acoustic Waves (SAW)." Lab Chip, 9, 2890-2895, 2009.

The Impact of MEMS-Produced Micro-Electrode Material Coating on Dental Plaque Biofilm Growth

Katherine Warthen
Bioengineering, Montana State University

NNIN REU Site: Lurie Nanofabrication Facility, University of Michigan, Ann Arbor, MI
NNIN REU Principal Investigator: Dr. Carlos Gonzalez-Cabezas, School of Dentistry, University of Michigan
NNIN REU Mentors: Dr. Robert W. Hower, Lurie Nanofabrication Facility, University of Michigan;
Dr. Alexander H. Rickard, Epidemiology, University of Michigan
Contact: kwarthen26@gmail.com, carlosgc@umich.edu, hower@umich.edu, alexhr@umich.edu

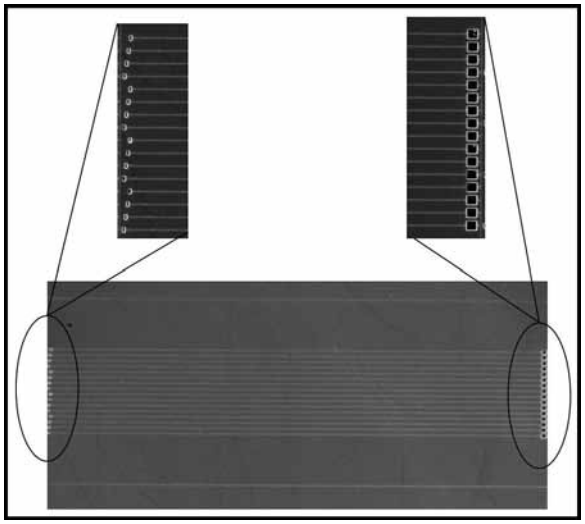

Figure 1: Magnified view of micro pH chip. Close up images are views of the pH sensors (right) and connection terminals for wiring (left).

Abstract:

The development of dental biofilms can create damaging acidic environments due to the production of metabolic byproducts. A micro pH electrode has been created (Figure 1) using microelectromechanical (MEM) fabrication techniques to continuously measure the pH at different distances from saliva-coated surfaces on which biofilms can develop. A coating was needed for this micro pH electrode to prevent the environment of the biofilm and oral cavity from altering the functionality of the pH sensor. Three different material coatings were selected for their known biocompatibility with living cells: parylene, silicon dioxide, and silicon nitride. To determine which coating was best suited for this purpose, the micro electrode was tested in micro flow cells and batch cultures inoculated with fluorescent *Streptococcus gordonii* bacteria. The biofilm was then imaged in three dimensions using a fluorescent microscope.

Medical Relevance:

The oral cavity provides an opportunity for microbes to develop very complex and potentially harmful biofilms. These biofilms can contribute to the formation of dental caries lesions through the production of acidic metabolic byproducts. The longer this biofilm is left undisturbed through substandard dental hygiene, the more likely it is that the caries lesion will worsen [1].

A deeper understanding of the metabolic and acidic conditions in dental biofilms would allow the scientific community to produce better dental hygiene products. Micro-electrode sensors placed within these biofilms could allow for real time data collection of the pH conditions in these micro environments.

Experimental Process:

The micro pH chips were fabricated on silicon wafers. Each chip contained four sets of sensors placed at staggered heights in order to measure pH at different positions within the biofilm. Photolithography techniques such as spinning, evaporation, liftoff, masking, and etching were used to pattern the chips with iridium sensors. The electrochemical sensing sites were then activated by the conversion of iridium to iridium oxide through exposure to an electrically pulsed signal in a sulfuric acid solution (Figure 1).

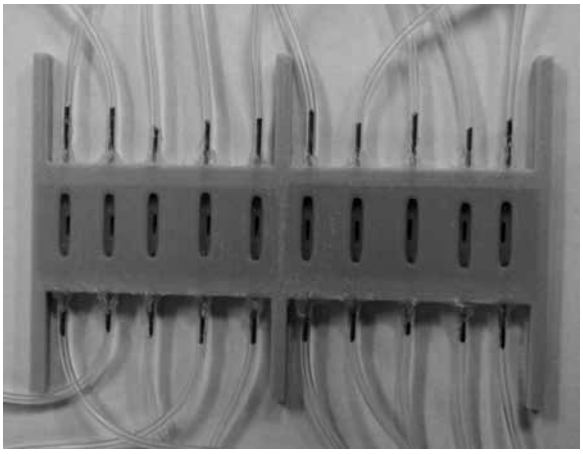

Figure 2: 3-D printed flow cell.

A 3D printer was used to fabricate micro flow cells. A syringe pump modification was also designed to accommodate additional flow channels necessary for efficient testing. The micro flow cells were designed to contain 100 μl of a mixture of human saliva and bacterial growth medium in which the biofilm was cultured (Figure 2).

Discussion:

The micro pH chips produced can successfully signal a change in pH, with an intensity of approximately 20 millivolts per pH unit change (Figure 3). This response can theoretically be improved to between 60 and 80 millivolts per pH unit change following the Nernst Equation and documented iridium oxide electrode responses in the literature [2].

These coatings were then tested in growth media inoculated with *S. gordonii* expressing mcherry, a red protein. Batch experiments conducted on the micro pH chips showed bacterial growth on all materials. Further tests and quantification are needed to determine if there is a significant difference in growth for any material.

Conclusions:

Micro pH sensing chips were produced that can detect a difference in pH conditions in a chemical solution. Three different coatings were tested on these pH micro-electrodes; silicon dioxide, silicon nitride, and parylene. Tests conducted under flow cell conditions showed that *S. gordonii* will grow in the developed flow cell in saliva mixed with growth medium (Figure 4).

Additionally, a new biofilm testing system was developed, consisting of a ten chamber flow cell which could be connected to a syringe pump fitted with a ten syringe expansion attachment. The ten chamber flow cell was custom designed to fit the pH sensing chips into the top of the flow cell. The entire apparatus could then be imaged from below by a confocal microscope to obtain images of biofilm formation on the pH sensing chips in real time (Figure 2).

Future Work:

Future studies will involve improving the accuracy and sensitivity of the sensors, as well as obtaining sufficient biofilm growth for 3D imaging in the flow cell. Eventually the micro pH sensors could be connected to a bluetooth device with an antenna which could be placed into an intraoral retainer to study dental plaque in real time under clinical conditions. The work done during the course of this project serves as preliminary research to produce this type of pH sensor for use in humans.

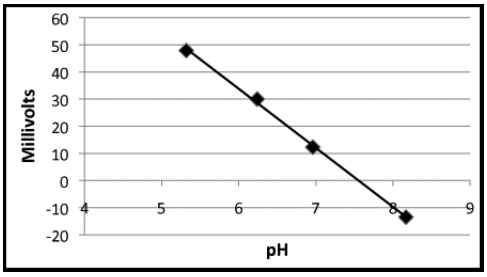

Figure 3: Millivolts emitted by sensor vs. change in pH of solution in which sensor is placed.

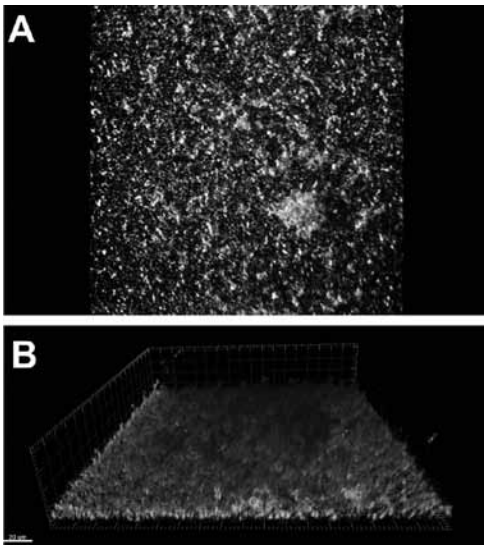

Figure 4: 3-D confocal image of Streptococcus gordonii *biofilm grown in flow cell.*

Acknowledgements:

I would like to thank the labs of Dr. Carlos Gonzalez-Cabezas in the University of Michigan School of Dentistry, Dr. Alexander H. Rickard in the department of Epidemiology, and Dr. Robert W. Hower and Cionca Codrin with the Lurie Nanofabrication Facility at the University of Michigan. In addition, I thank the NNIN REU Program and NSF for funding.

References:

[1] Sachdeo, A., Haffajee, A. D., and Socransky, S. S. Biofilms in the edentulous oral cavity. Journal of Prosthodontics, 5(17), 348-356. Retrieved from http://www.ncbi.nlm.nih.gov/pubmed/18355168 (2008).

[2] Johnson, M. D., Kao, O. E., and Kipke, D. R. Spatiotemporal ph dynamics following insertion of neural microelectrode arrays. Journal of Neuroscience Methods, 160(2), 276-287. (2006).

[3] Bard, A., and Faulkner, L. Electrochemical methods fundamentals and applications. (2nd ed., V1, pp. 1-83). John Wiley and Sons, Inc. (2001).

Fabrication of Microchemical Field-Effect Transistor

Ming-Lun Wu
Biomedical Engineering, University of Florida

NNIN REU Site: Minnesota Nano Center, University of Minnesota-Twin Cities, Minneapolis, MN
NNIN REU Principal Investigator: Dr. Stephen Campbell, Department of Electrical and Computer Engineering, University of Minnesota
NNIN REU Mentor: Jun Young Lim, Department of Electrical and Computer Engineering, University of Minnesota
Contact: minglwu427@gmail.com, campb001@umn.edu, limxx218@umn.edu

Abstract:

The commonly manufactured metal-oxide field-effect transistor (MOSFET) amplifies electrical signals applied to the gate electrode. If one replaces the metal gate of a MOSFET with a selectively permeable membrane, it enables transistors to amplify electrical signals based on the ion concentration of a solution. Such devices are known as chemical field-effect transistors (ChemFETs). A research group at Minnesota envisions these micro-scale ChemFETs could analyze sweat droplets as small as one millimeter in diameter. This will allow noninvasive tests to detect diseases such as cystic fibrosis, osteoporosis, diabetes, and other conditions, as part of a larger program to use the mapping of sweat production to detect loss of neural function due to diabetes, chemotherapy, industrial or defense-related exposure to toxins, alcoholism, HIV, and other conditions. Casting of poly(2-hydroxyethyl methacrylate) and including ionophores, valinocycin and ETH 2120 in the membrane enhances the selectivity and responses of ChemFETs.

Introduction:

The ultimate goal of this project is to find a way to quantify sweat gland function to detect peripheral neuropathy. Peripheral neuropathy is damage of the peripheral nervous system; its symptoms include decrease of sensory sensitivity, random pain, and itching in the damaged region. Although these symptoms are definitive, the severity can be different base on the other parameters like ages and pain tolerance. In order to prevent peripheral neuropathy, precise monitoring of nervous function is required. The Minnesota group is developing a way to electrically measure sweat production. This determines sudomotor neural function, a good replacement for the function of the central nervous system. However, if sweat were to be measured, it would be useful to measure the content of sweat. It is possible to detect many conditions through a simple noninvasive test.

A transistor amplifies electric signals according to the voltage applied to the device. For most transistors, they contain three major regions: the source, the drain, and the gate. Source and drain are where the electric current is being amplified, while the gate is where the external voltage is provided. For a chemical field-effect transistor (ChemFET), a selective membrane replaces the gate oxide. The membrane, with positive charge ionospheres, would work similarly to an external voltage and amplifies the electrical signal according to positive ion concentration in a solution.

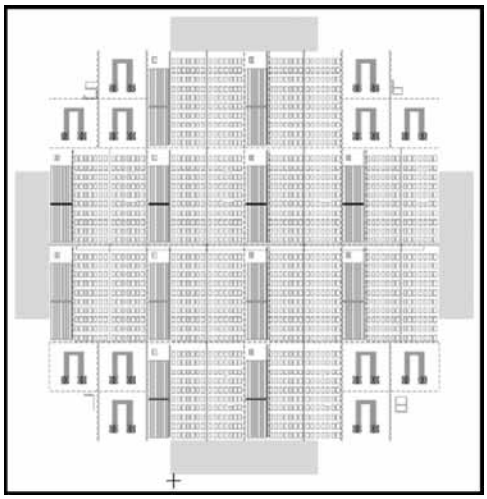

Figure 1: A design of wafer map.

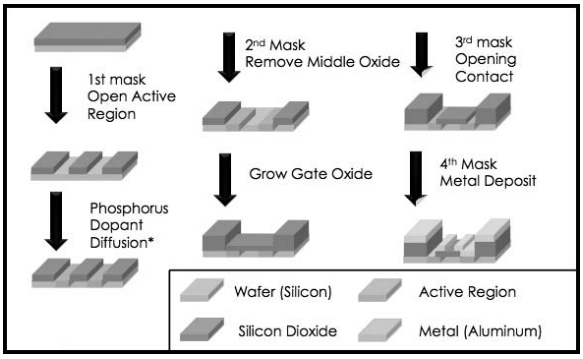

Figure 2: Fabrication overview.

Experimental Procedure:

Prior to the fabrication process, a design of wafer map was completed with L-Edit programs. Every wafer included twelve chips, shown in Figure 1. Each chip included 120 ChemFETS,

120 n-type metal oxide semiconductors (nMOS), and four actives regions. The ChemFET and nMOS channel lengths varied from 5 to 10 μm. One 100 μm capacitor was used as well.

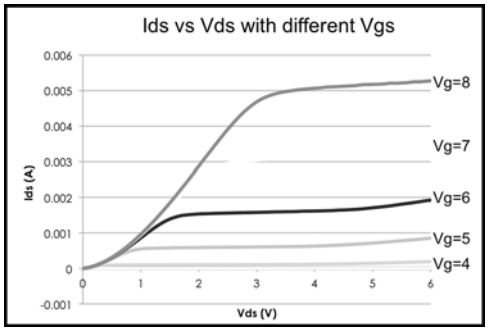

Figure 3: V_{ds} and I_{ds} graph with varying gate voltage, expected response from a functional nMOS.

Figure 4: Deposition of polyHEMA, the hydrogel are visible on the gate.

Thermal oxidation of silicon wafers was performed with steam at 1000°C for 100 minutes. Active regions were opened with the first lithography step and followed by wet etching. Etch completion was determined by the hydrophobic nature of Si compare to SiO_2. Impurities were induced by diffusion; a phosphorous-containing liquid was cast onto the wafer followed by heating at 1000°C for 10 minutes. The presence of the impurity was confirmed using four-point probe. The middle oxide was removed with the second mask. Growth of the gate oxide was achieved by dry thermal oxidation for 15 minutes. The contact region was opened with the third mask. Aluminum was deposited by thermal evaporation or sputtering and patterned with the fourth mask. Finally, annealing was performed at 450°C for five minutes.

An nMOS functionality was used to verify the fabrication procedures. Each transistor was tested by sweeping the drain voltage while keeping the gate at a constant voltage between zero and eight volts (Figure 3). Once fabrication validity was confirmed, silyation was carried out by submerging the wafer in a mixture of 2.5 ml of 3-(trimethoxysilyl) propyl methacrylate and 22.5 ml of toluene at 90°C for four hours. The 40 mg of polyHEMA crystal was dissolved within 2 ml of reagent alcohol overnight. Finally, 71.2 mg 2,2 dimethoxyphenylacetophenone photoinitiator was added to the polyHEMA mixture and cast onto the wafer, followed by UV light exposure for two minutes.

Results and Conclusions:

The validity of fabrication techniques was confirmed. The first successful fabricated chip has 44% of functioning devices, while the latest chip has 100% yields. The increased in yield is believed to be due to changing the dopant diffusion cycle from 950°C for 15 minutes, to 1000°C for 10 minutes. Based on the preliminary result, the higher diffusion temperature increased the doping concentration. The anneal process proven to be essential to the functionality of the device. Without annealing, the yield of successful devices in a chip was zero.

The final dimension of the device is roughly 450 μm in width and 800 μm in length. This is important considering the smallest test droplet produced from a syringe is 1000 μm in diameter. Although the hydrogel was visible under microscope, it is unclear whether the bonding between the gate oxide and hydrogel is covalent or mechanical (Figure 4). More tests are required.

Future Work:

Investigating the bonding mechanism of the hydrogel is essential to the functionality of our device. Hence, testing the mechanism by ethanol washing should be performed. The selective membrane casting should be the following step of fabrication. Once the membrane is attached characterization of ChemFETs can begin.

Acknowledgements:

The author would like to thank National Science Foundation and National Nanotechnology Infrastructure Network Research Experience for Undergraduates (NNIN REU) Program for making this project possible. Also, special thanks to the University of Minnesota, Nanofabrication Center, Dr. Stephen Campbell, and Mr. Jun-Young Lim, a graduate student in Professor Campbell's research group.

Exploring the Effects of Theophylline on Neutrophil Function in Inflammatory Diseases

Ashlyn Young
Biomedical Engineering, University of North Carolina at Chapel Hill

NNIN REU Site: Minnesota Nano Center, University of Minnesota-Twin Cities, Minneapolis, MN
NNIN REU Principal Investigator: Dr. Christy Haynes, Chemistry, University of Minnesota-Twin Cities
NNIN REU Mentor: Xiaojie Wu, Chemistry, University of Minnesota-Twin Cities
Contact: youngat@live.unc.edu, chaynes@umn.edu, wuxx0406@umn.edu

Abstract:

Neutrophils play a key role in the human immune system as the first cells to migrate to sites of inflammation. Several common respiratory diseases, such as chronic obstructive pulmonary disease (COPD) and asthma, are characterized by excessive chemotaxis and damaging apoptosis of neutrophils around infection. Theophylline, one potential therapeutic candidate, was employed to examine drug effects on neutrophil function. The chemotactic behaviors of neutrophils were monitored using a microfluidic platform after incubation with various concentrations of theophylline for different time periods. Theophylline worked to limit the motility of neutrophils in small concentrations and long incubation times; however, there was no influence on the polarization of neutrophils. Meanwhile, theophylline induced a tremendous decrease in neutrophil viability based on colorimetric assay. This work provides new insights on how theophylline affects neutrophil function *in vitro*, potentially guiding drug application for the treatment of neutrophilic inflammation *in vivo*.

Introduction:

Chemotaxis is a dynamic cellular process by which cells migrate to inflammatory areas in the presence of chemical gradients composed of signaling molecules called chemokines [1]. Abnormal excessive chemotaxis and failure in apoptotic pathways are the main contributors for neutrophil accumulation around infection sites. Neutrophilic inflammation is resistant or poorly responsive to some traditional drugs targeted for chronic respiratory diseases, such as corticosteroids. Theophylline has been successfully utilized as a pharmaceutical treatment for neutrophilic inflammation, but the detailed mechanisms are not clear. In this work, the drug effects of theophylline on neutrophil function were studied to explain the mechanism of drug-cell interaction and provide direction for the design of novel anti-inflammatory approaches.

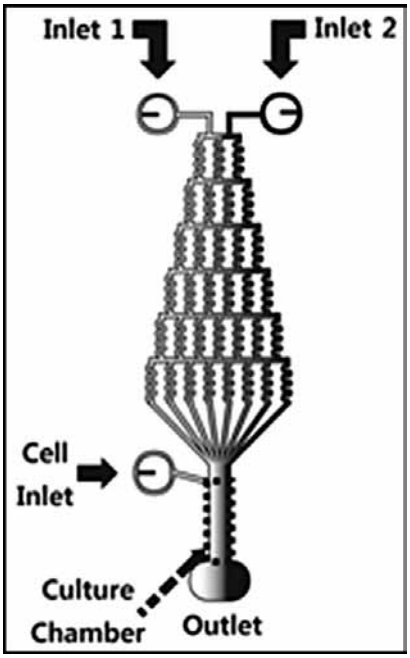

Figure 1: Schematic of the device in this work.

Microfluidic technology is unique in its ability to mimic *in vivo* process *in vitro* by maintaining a flow vital to observing biological processes. More importantly, microfluidic devices are able to provide stable chemokine gradients with high spatiotemporal resolution and quantitative data for describing chemotactic behaviors in different conditions. A gradient microfluidic device containing parallel serpentine channels and a cell culture chamber was employed in this study (Figure 1) [2].

Method:

Microfluidic device molds were fabricated through photolithography methods with SU-8 photoresist spun onto a silicon wafer. Polydimethylsiloxane (PDMS) was poured on the mold and cured overnight, followed by permanently bonding PDMS and glass slides using oxygen plasma.

Human blood samples were layered on separation medium and centrifuged to isolate neutrophils. Cell mixtures were washed with Hank's balanced salt solution (HBSS) buffer and cell lysis buffer, then pure neutrophils were counted and diluted to the appropriate concentration.

Prior to injecting neutrophils into the device, the cell culture chamber was incubated with fibronectin. Next 5-10 μL of neutrophil suspension (3-5 $\times$ 10^6 cells/mL) in HBSS buffer was introduced into the device (Figure 2). Three different

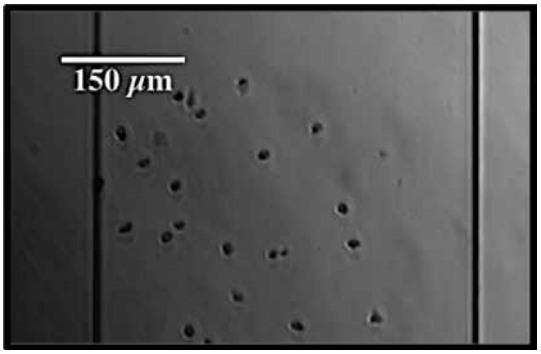

Figure 2: Neutrophils incubated on the bottom of the cell culture chamber.

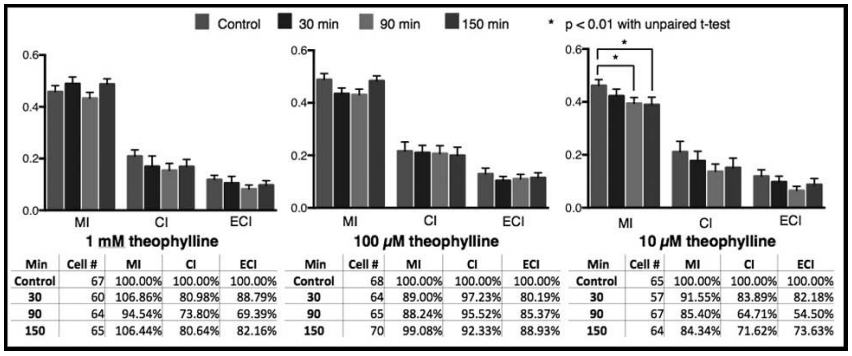

Min	Cell #	MI	CI	ECI
Control	67	100.00%	100.00%	100.00%
30	60	106.86%	80.98%	88.79%
90	64	94.54%	73.80%	69.39%
150	65	106.44%	80.64%	82.16%

Min	Cell #	MI	CI	ECI
Control	68	100.00%	100.00%	100.00%
30	64	89.00%	97.23%	80.19%
90	65	88.24%	95.52%	85.37%
150	70	99.08%	92.33%	88.93%

Min	Cell #	MI	CI	ECI
Control	65	100.00%	100.00%	100.00%
30	57	91.55%	83.89%	82.18%
90	67	85.40%	64.71%	54.50%
150	64	84.34%	71.62%	73.63%

Figure 3: Results summary of neutrophil chemotaxis after incubation with 1 mM, 100 μM and 10 μM theophylline for different lengths of times. Error bars indicate standard deviation.

theophylline concentrations were tested: 1 mM, 100 μM, and 10 μM, for durations of 30 minutes, 90 minutes, or 150 minutes.. A chemokine gradient was created by mixing buffer and 10 mg/mL interleukin-8 (IL-8) solution in the serpentine channels under 100 μL/h flow rate.

Neutrophil activity was assessed for 20 minutes by calculating the motility index (MI), chemotactic index (CI), and effective chemotactic index (ECI) with Metamorph software. MI quantifies the overall movement of the neutrophils, and CI analyzes how much cells moved in the gradient direction. ECI is the product of MI and CI, examining the effectiveness of neutrophil migration.

The cytotoxicity of theophylline was monitored using the MTT (3-(4,5-dimethylthiazol-2-yl)-2,5-diphenyltetrazolium bromide) assay. In the 96-well plate, 100 μL of neutrophil suspension (6×10^5 cells/mL) was incubated with each drug concentration for the various time periods. After incubation, neutrophils were mixed with 100 μL MTT solution (0.5 mg/mL) for two hours to produce precipitation, and 100 μL DMSO was added to dissolve otherwise insoluble crystals. Finally, optical density was measured at 570 nm, with 655 nm as reference, using a microplate reader.

Results and Conclusions:

As shown in Figure 3, 10 μM theophylline and long incubation times (90 and 150 minutes) induced a significant decrease in motility of neutrophils; however, larger concentrations (1 mM and 100 μM) had no impact on MI. There was no influence on the polarization and effectiveness of neutrophil chemotaxis under any of the conditions. Meanwhile, theophylline caused an obvious drop in neutrophil viability based on the MTT assay in a time-dependent manner. Cell viability was reduced to 50% compared to the initial viability after 150 minutes of incubation for all concentrations of theophylline.

These preliminary results displayed that theophylline is not an effective regulator of neutrophil chemotaxis except at the lowest concentration considered, contradicting previous findings that theophylline attenuated neutrophil chemotaxis in the traditional chamber-based assays [3]. A reasonable explanation is that theophylline has slight effects on neutrophil chemotaxis in short term. Instead, high cytotoxicity was observed, implying that theophylline acts as a potent treatment by inducing cell death, which was not taken into account in current literature (Figure 4). This work supplied a better understanding of the relationship between drug effects and neutrophil function relevant in multiple diseases.

Acknowledgements:

Thank you Dr. Christy Haynes, Xiaojie Wu, the Haynes Research Group, Dr. Douglas Ernie, Dr. Jim Marti, and Dr. Ted Higman for your mentorship, assistance, and guidance. This research was supported by the NNIN Research Experience for Undergraduates Program and the National Science Foundation.

References:

[1] Cicchetti, G., Allen, P. G., and Glogauer, M. Crit. Rev. Oral Biol. Med., 13, 220-228, 2002.

[2] Kim, D., and Haynes, C. L. Anal Chem., 84, 6070-6078, 2012.

[3] Culpitt, S., de Matos, C., Russell, R., Rogers, D., and Barnes, P. Am. J. Respir. Crit. Care Med., 165, 1371-1376, 2002.

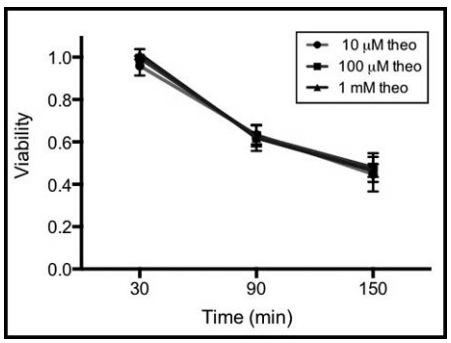

Figure 4: Results of cell viability using MTT assay.

Use of Field-Induced Surface-Organometallic Interactions to Control Selectivity in Rhodium-Catalyzed Organic Reaction

Dylan Barber
Chemistry Major, Williams College

NNIN REU Site: Stanford Nanofabrication Facility, Stanford University, Stanford, CA
NNIN REU Principal Investigator: Professor Matthew Kanan, Chemistry Department, Stanford University
NNIN REU Mentor: Craig Gorin, Chemistry Department, Stanford University
Contact: dylan.m.barber@williams.edu, mkanan@stanford.edu, cgorin@stanford.edu

Abstract:

A major challenge facing chemists is to control the selectivity of chemical reactions. The common response is to focus entirely on catalyst design to improve yields of desired products. Electric fields generated at the interface of an electrode and electrolyte solution have shown promise as an additional method to control chemical reactions. In previous work, our group showed that Lewis acid-catalyzed rearrangements of epoxides favor different products when subjected to interfacial electric fields [1]. It was also established that interfacial electric fields can induce surface-organometallic interactions that can change product ratios in a rhodium-catalyzed carbene reaction more than 100-fold [2]. In this work, we exploited a field-induced TiO_2-rhodium porphyrin interaction to change the site selectivity of a C-H insertion reaction (Figure 1). Depending on the interfacial charge density, the product ratio in the rhodium porphyrin-catalyzed reaction of 1-diazo-3-(3-methoxyphenyl) propan-2-one (1) to 5-methoxy-1*H*-inden-2(3*H*)-one (2) and 4-methoxy-1*H*-inden-2(3*H*)-one (3) changes 16-fold, with a 3.6-fold increase in conversion of the starting material. We also investigated alternative HfO_2 and Ta_2O_5 dielectrics, which showed similar field-induced selectivity effects.

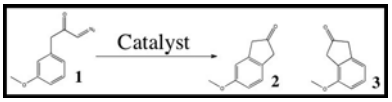

*Figure 1: Reaction scheme for conversion of 1-diazo-3-(3-methoxyphenyl)propan-2-one (1) to 5-methoxy-1*H*-inden-2(3*H*)-one (2) and 4-methoxy-1*H*-inden-2(3*H*)-one (3).*

Introduction:

Chemists can exert substantial control over the selectivity of many reactions by changing the steric and electronic properties of the relevant catalyst, but very little is known about the impact of certain environmental factors on catalytic selectivity. Specifically, the application of an electric field has the potential to affect selectivity in chemical reactions by stabilizing aligned transition-state dipolar species, lowering the activation barrier towards—and altering selectivity in favor of—the associated product. In the model reaction cell outlined in Figure 2, an applied potential induces the formation of an electric field at the interface between a charged dielectric surface and the contiguous electrolyte solution.

Using a catalyst fixed to the dielectric surface by intermolecular forces, previous work by our group has shown two interesting results. First, electric fields can change the selectivity of certain chemical reactions. Second—in the case of a rhodium porphyrin-catalyzed carbene reaction—an electric field can induce an interaction between the catalyst and a titanium dioxide (TiO_2) dielectric. This result is interesting because the selectivity change was in the opposite direction to that shown on an aluminum oxide (Al_2O_3) dielectric under otherwise identical conditions. This and other experiments conducted in the same study indicated an electric field-induced interaction between a TiO_2 dielectric surface and the rhodium porphyrin catalyst that could potentially be used to control selectivity in other reactions [2].

The purpose of this study is to further investigate this electric field-induced catalyst-dielectric interaction by examining a carbene insertion reaction (Figure 1) using a rhodium porphyrin catalyst on aluminum oxide, titanium oxide, and other dielectric surfaces.

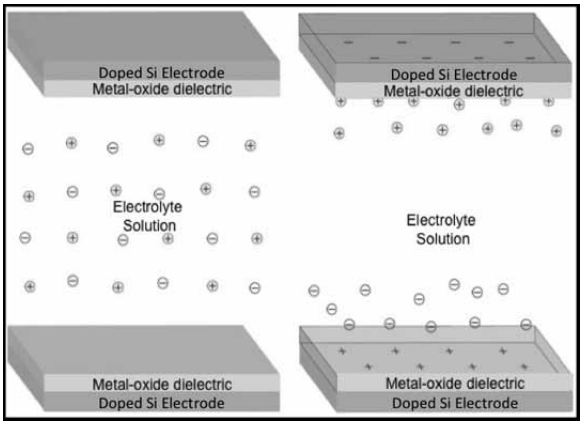

Figure 2: Model of the reaction cell used in this study. Left: a neutral reaction cell. Right: a reaction cell with applied potential, forming a localized electric field at each dielectric surface.

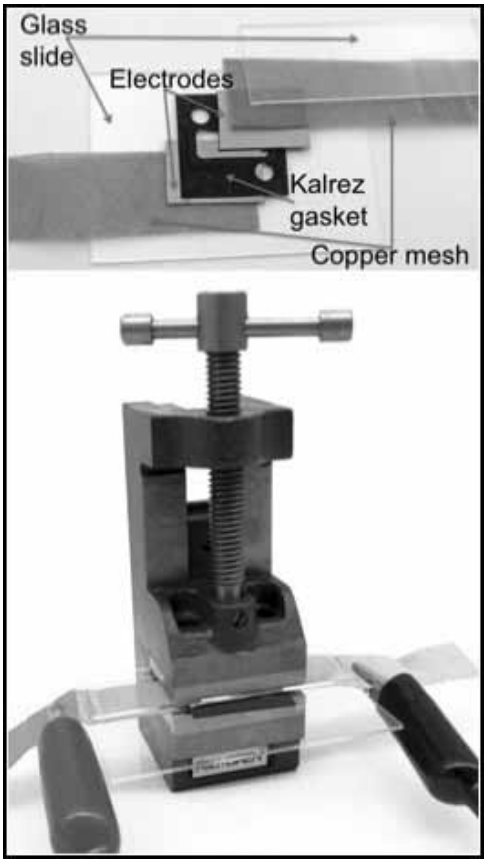

Figure 3: The parallel plate cell.

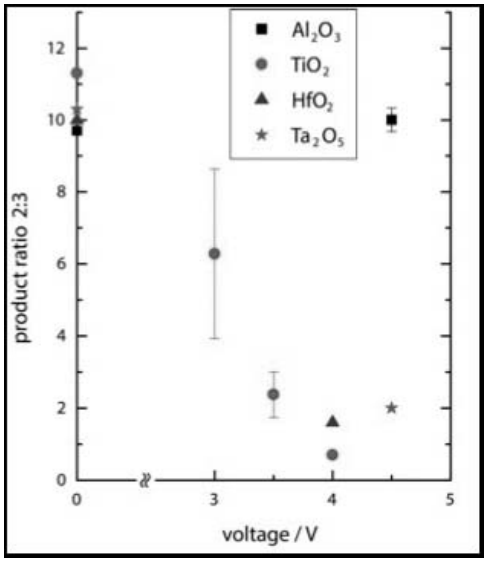

*Figure 4: Product ratio **2:3** as a function of applied voltage on Al_2O_3, TiO_2, HfO_2, and Ta_2O_5 dielectrics.*

Experimental Procedure:

Using atomic layer deposition (ALD), 50Å of metal oxide were deposited on highly doped silicon wafers. The wafers were then sliced into smaller pieces and used to assemble multiple parallel plate cells (Figure 3). A reaction solution consisting of 5 millimolar (mM) substrate **1**, 500 micromolar (μM) tetrabutylammonium hexafluorophosphate (TBA PF_6) electrolyte, and 10 μM rhodium tetraphenylporphyrin iodide (RhTPPI) catalyst in dichloromethane solvent was added to the cell via pipette. The cell was then compressed in a vice and a potential difference applied to the copper mesh contacts. The reaction was allowed to run overnight then stopped. The cell was opened and the reaction solution examined by high pressure liquid chromatography to determine total product conversion and product ratio.

Results and Conclusions:

When using an aluminum oxide dielectric in our parallel plate cell, we found that we could not alter the selectivity in this reaction by applying a potential difference. As can be seen in Figure 4, the product ratio **2:3** remains at about 10:1 for both a 0 volt (V) and a 4.5 V potential. However, when a titanium oxide dielectric was used, we found that the **2:3** ratio was 11.3:1 at 0 V, but fell to 0.7:1 at 4 V. We also observed electric field-induced selectivity changes when using hafnium oxide and tantalum oxide dielectrics. These results are all shown in Figure 4, which displays product ratio **2:3** as a function of voltage applied to the plate cell for each of the four dielectrics used.

These results support our earlier hypothesis that there exists an electric field-induced interaction between a TiO_2 dielectric and rhodium porphyrin catalyst, which can be used to control selectivity in a chemical reaction. This phenomenon is seen with both HfO_2 and Ta_2O_5 dielectrics, but not with an Al_2O_3 dielectric.

Future Work:

This as-yet untapped phenomenon in catalysis has huge potential as a future tool in industrial and academic chemistry, but several challenges remain before it can be effectively exploited. These include elucidating the mechanism of the selectivity change, developing a method to increase the scale of the reaction cell (the experiments in this study were run on a 75 microliter scale), and determining the applicability to industrially relevant chemical syntheses.

Acknowledgements:

Professor Matthew Kanan, Craig Gorin, the Kanan Lab Group, Dr. Michael Deal, the National Nanotechnology Infrastructure Network Research Experience for Undergraduates (NNIN REU) Program.

References:

[1] Gorin, C., Beh, E., Kanan, M.; "An Electric Field-Induced Change In The Selectivity Of A Metal-Oxide-Catalyzed Epoxide Rearrangement"; Journal of the American Chemical Society, 134, p186-189 (2011).

[2] Gorin, C., Beh, E., Kanan, M.; "Interfacial Electric Field Effects on a Carbene Reaction Catalyzed by Rh Porphyrins"; Journal of the American Chemical Society, 135, p 11257-11265 (2013).

Area-Selective Atomic Layer Deposition: New Recipe Development

Tyler Erjavec
Physics, The Ohio State University

NNIN REU Site: Cornell NanoScale Science and Technology Facility, Cornell University, Ithaca, NY
NNIN REU Principal Investigator: Prof. James Engstrom, School of Chemical and Biomolecular Engineering, Cornell University
NNIN REU Mentors: Wenyu Zhang and Rambert Nahm, School of Chemical and Biomolecular Engineering, Cornell University
Contact: tje43@cornell.edu, jre7@cornell.edu, wz89@cornell.edu

Abstract:

Atomic layer deposition (ALD) allows thin films to be deposited layer-by-layer onto a substrate by a sequential flow of gaseous chemical precursors. These precursors interact with the substrate surface via self-limiting reactions and then the cycle can be repeated until the thin film reaches a desired thickness. Area-selective ALD deposits material onto one substrate while leaving another substrate unaffected. This is applicable in device manufacturing. The focus of this project is to develop a recipe to selectively deposit tantalum nitride (TaN_x) on one surface (SiO_2), while limiting the growth on another surface (Cu). We are interested in the thermal TaN_x ALD system, using pentakis(dimethylamino)tantalum (PDMAT) and ammonia (NH_3) as precursors. From previous studies, we know that PDMAT forms strong bonds with the SiO_2 substrate surface in the first half-reaction of the ALD cycle. We decided to add an 'etchant' — dimethylamine, $(CH_3)_2NH$ (DMA) — to the TaN_x ALD recipe to drive the reaction backwards, selectively favoring deposition on SiO_2. We investigated the effect of DMA concentrations, DMA step placement, DMA dose times, and sub-saturation of PDMAT doses.

Introduction:

Tantalum nitride (TaN_x) is used as a diffusion barrier layer [1] in integrated circuits and devices to prevent copper (Cu) diffusion into the surrounding dielectric. It can be deposited via atomic layer deposition (ALD) onto a substrate via sequential flow of gaseous chemical precursors as seen in Figure 1.

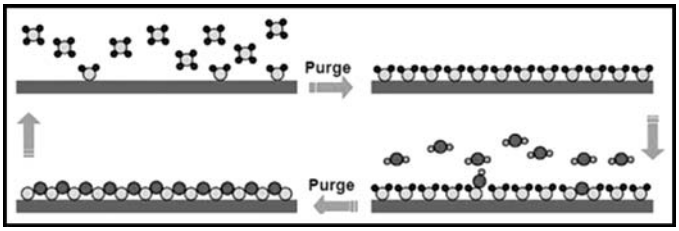

Figure 1: Schematic illustration of the ALD process. Photo Credit: http://gcep.stanford.edu/research/factsheets/atomic_layer_deposition.html

Area-selective ALD deposits material onto one substrate while leaving another substrate unaffected. This has many applications in industrial device manufacturing because it eliminates the need for patterning steps and is potentially more efficient and cost-effective.

Because the Ta precursor used, PDMAT, contains five diethylamido-groups, we have decided to use dimethylamine (DMA) to attempt the reversal of the first half-cycle reaction on Cu.

Experimental Procedure:

In order to develop a selective TaN_x ALD process with the addition of DMA, we decided to test three DMA dose parameters: 1) DMA dose time, 2) DMA dose step-placement, and 3) DMA partial pressure. For each parameter, we deposited 20 cycles of TaN_x on silicon dioxide, SiO_2 (native oxide), and Cu. The nominal sample temperature was 225°C for all depositions. The resulting thin-films were then analyzed using spectroscopic ellipsometry (SE) and wavelength-dispersive x-ray spectroscopy (WDX).

Results and Conclusions:

From spectroscopic ellipsometry (SE), we determined the average growth rate of TaN_x using SiO_2 substrates. SE is model-dependent so results vary depending on which model is used [Ta_2O_5 (because thin films oxidize in air) and Cauchy].

Growth rates of 0.43 Å/cycle (Ta_2O_5 model) and 0.39 Å/cycle (Cauchy model) were obtained, giving an average at approximately 0.4 Å/cycle. This agreed with our expected growth rate of TaN_x on SiO_2. From previous studies, we have found that the Cu substrate is rough and does not form an abrupt interface with the TaN_x layer, preventing reliable SE measurements [2].

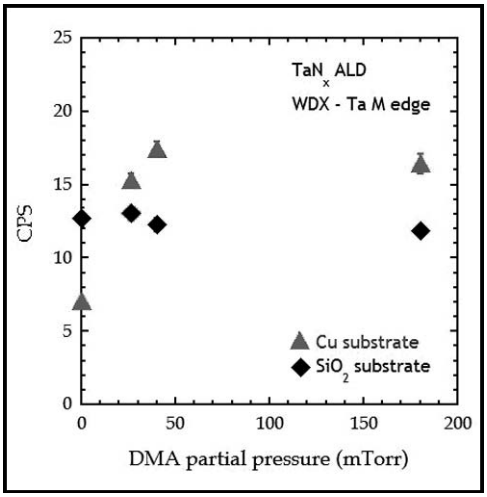

Figure 2: WDX intensities for Ta M edge for TaN_x films deposited on Cu (filled triangles) and SiO_2 (filled diamonds) substrates, plotted against amount of DMA introduced to the system.

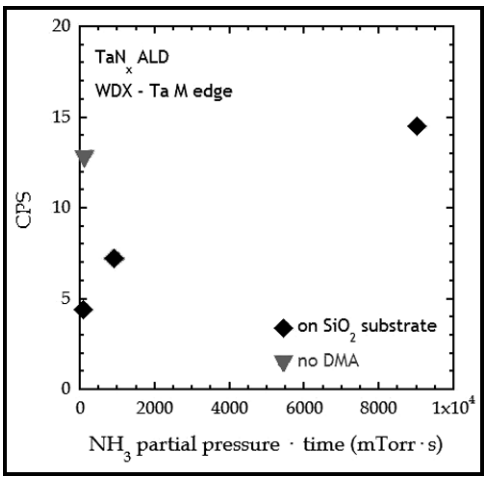

Figure 3: WDX intensities for Ta M edge for TaN_x films deposited on SiO_2 (filled diamonds) substrates, plotted against amount of NH_3 introduced to the system.

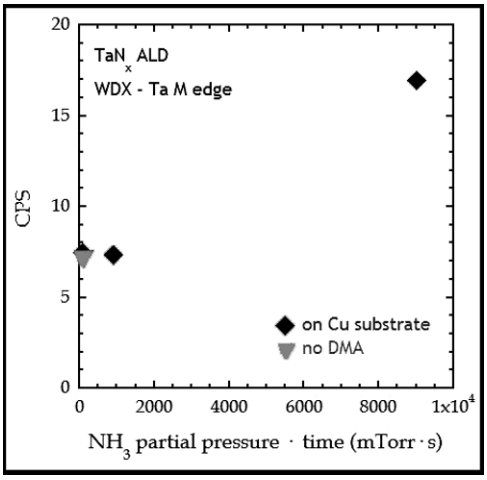

Figure 4: WDX intensities for Ta M edge for TaN_x films deposited on Cu (filled triangles) substrates, plotted against amount of NH_3 introduced to the system.

In Figure 2, we show that DMA partial pressure does not affect TaN_x film growth on SiO_2. On the Cu substrates however, a clear increase in Ta signal is observed with increasing DMA concentration.

We also introduced DMA in the NH_3 dose step (an NH_3|DMA co-exposure) in the hope that the NH_3 would react with the PDMAT on the surface where we wanted it to deposit (SiO_2) while the DMA would act to remove the adsorbed PDMAT from the surface where we did not want TaN_x deposition (Cu). From Figure 3, we see that NH_3|DMA co-exposure exhibited a typical saturation curve as expected. The upside down triangle shows the typical TaN_x recipe, which agrees with the saturated dose of NH_3.

However on the Cu substrates (Figure 4), we see that the TaN_x does not exhibit an expected saturation curve. From this result, we infer that DMA doses do not affect TaN_x on SiO_2 yet increases growth on Cu.

Future Work:

Although manipulating DMA dose placement, step time, and concentration to inhibit TaN_x on Cu — but not SiO_2 — did not affect growth as intended, there are still additional avenues where TaN_x on Cu can be suppressed (ALD temperature, DMA dosage in conjunction with PDMAT sub-saturation doses etc.). Additionally, the stoichiometry of our TaN_x films on SiO_2 and Cu has yet to be determined. We may be depositing more Ta on Cu, but it is likely that many of the ligands from PDMAT were not removed. Future x-ray photoelectron spectroscopy (XPS) measurements will shed some light on this subject.

Acknowledgements:

I would like to thank the National Nanotechnology Infrastructure Network Research Experience for Undergraduates (NNIN REU) Program and the National Science Foundation. I also appreciate guidance, support, and assistance from Wenyu Zhang, James Engstrom, Melanie-Claire Mallison, and the CNF staff. This work made use of the Cornell Center for Materials Research Shared Facilities, which are supported through the NSF MRSEC program (DMR-1120296).

References:

[1] Wang, S. MRS bulletin 19, 30 (1994).

[2] W. Zhang, R.K. Nahm, P.F. Ma, J.R. Engstrom, J. Vac. Sci. Technol. A 31, 061101 (2013).

Poly(3-alkyldithienothiophene): Synthesis, Structure and Optical Properties

Yuki Hamasaki
Applied Chemistry, Kyushu University, Fukuoka, Japan

NNIN iREG Site: NanoTech User Facility, University of Washington, Seattle, WA
NNIN iREG Principal Investigator: Prof. Christine K. Luscombe, Materials Science and Engineering, University of Washington
NNIN iREG Mentor: Dr. Ken Okamoto, Department of Materials Science and Engineering, University of Washington
Contact: y.hamasaki@mail.cstm.kyushu-u.ac.jp, luscombe@uw.edu, keno2@uw.edu

Abstract:

Organic semiconductors that consist of conjugated oligomers or polymers are the subject of considerable current research interest, owing to their fundamental optoelectronic properties and their potential applications for organic photovoltaics. In this context the regioregular alternative copolymer of 3-alkylsulfanylthiophene (AST) and 3-alkylthiophene (AT), *alt*-P3AST-*co*-3AT, has an intriguing structure because the repeating unit can be transformed into 3-alkyldithienothiophen (3ADTT) to serve as a quinoid moiety. The preparation methods of *alt*-P3AST-*co*-3AT are discussed.

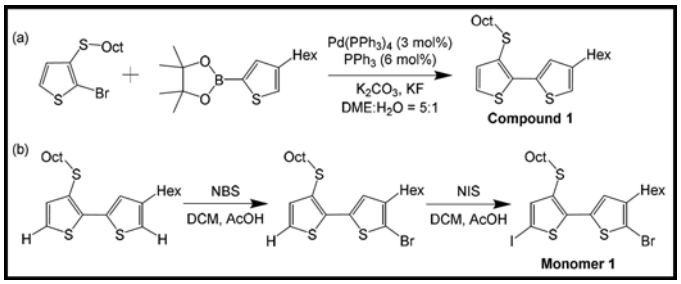

Scheme 1: Monomer synthesis.

Introduction:

Organic electronics is a growing area of research that investigates the properties and applications of conjugated polymers and semiconducting small molecules. Devices made from organic materials have the potential to be flexible, are inexpensive to process, and weigh less than their inorganic counterparts. Organic photovoltaic (OPV) devices are currently under investigation as a low-cost alternative to silicon-based photovoltaic devices. Poly(3-hexylthiophene) (P3HT) is one of the most successful homopolymers due to its semi-crystalline structure, strong light absorption properties, and high charge carrier mobility [1]. However, the short-circuit current density (J_{sc}) and open-circuit voltage (V_{oc}) of P3HT devices are limited due to a wide HOMO-LUMO gap and high HOMO energy level. For these reasons, quinoid polymers are being developed to control the energy levels. Since the quinoid resonance form is lower in energy than the aromatic form, stabilizing the quinoid form will effectively reduce the band gap of related conjugated polymers. According to a theoretical calculation using the Semi-empirical Method, AM1, dehedral angles of regioregular 3-ethylthiophene and 3-thioalkylthiophene, 3-hexyldithienothiophene are 143.8° and 179.5°, 179.7°, respectively.

Here, we report another approach to the design and synthesis of new organic semiconductors for photovoltaics, using the fused thiophene derivative, dithieno[3,2-b:2′,3′-d]thiophene as a building block.

Experimental Procedure:

Synthesis of 5-bromo-4-hexyl-5′-iode-3′-(octylsulfanyl)-2,2′-bithiophene (Monomer 1) via Suzuki coupling method (Scheme 1)

(a) 4-hexyl-3′-(octylsulfanyl)-2,2′-bithiophene (Compound 1). Compound 1 was prepared via Suzuki coupling [2]. In N_2, 2-bromo-3-(octylsulfanyl)thiophene (5 mmol), 4-hexyl-thiophene-2-boronic acid (7 mmol), K_2CO_3 (12.5 mmol, 1.73 g), 10 mL DME and 2 mL distilled water were added to a Schlenk flask. After degas-stirring for 30 minutes, triphenylphosphine (PPh_3) (77.5 mg, 0.3 mmol), $Pd(PPh_3)_4$ (0.173 g, 0.15 mmol) and KF (12.5 mmol, 0.725 g) were added. The mixture was allowed to stir under 90°C (oil bath) overnight. After quenching with NH_4Cl, the reaction mixture was extracted with ethyl acetate. The solvent was evaporated under vacuum. Flash chromatography on silica gel (hexane) gave the Compound 1.

(b) 5-bromo-4-hexyl-5′-iode-3′-(octylsulfanyl)-2,2′-bithiophene (Monomer 1). 4-hexyl-3′-(octylsulfanyl)-2,2′-bithiophene (3.21 mmol, 1.27 g) was added to a flask with 5 mL acetic acid and 5 mL DCM stirring at 0°C. To the flask was added NBS (3.21 mmol, 0.572 g). The solution was brought to room temperature and allowed to stir for one hour before being poured into 50 mL of 10% $Na_2S_2O_3$, and then extracted with diethyl ether. The organic phase was finally dried over anhydrous Na_2SO_4, and evaporated under vacuum to yield a crude oil. Flash chromatography on silica gel (hexanes) gave

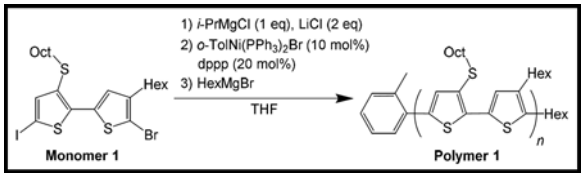

Scheme 2: Polymerization.

the 5-bromo-4-hexyl-3′-(octylsulfanyl)-2,2′-bithiophene. Then, 5-Bromo-4-hexyl-3′-(octylsulfanyl)-2,2′-bithiophene (0.861 mmol, 0.409 g) was added to a flask with 2 mL acetic acid and 2 mL DCM stirring at 0°C. To the flask was added NIS (0.861 mmol, 0.194 g). The solution was brought to room temperature and allowed to stir for 30 minutes before being poured into $Na_2S_2O_3$, and then extracted with diethyl ether. The organic phase was finally dried over anhydrous Na_2SO_4, and evaporated under vacuum to yield a crude oil. Flash chromatography on silica gel (hexanes) gave the Monomer 1.

Initiated Polymerization (Scheme 2). In a procedure adapted from literature [3], Monomer 1 (0.178 g, 0.297 mmol) and 44.5 mg lithium chloride was dissolved in THF (10 mL) and cooled to 0°C with stirring. Then 0.15 mL of a 2.0 M isopropyl magnesium chloride in hexanes was added dropwise over 5 min and stirring continued for 30 minutes. At this point, a solution consisted of 22.3 mg of *cis*-chloro(*o*-tolyl)1,3-bis(diphenylphosphino)propanenickel(II) (10 mol%) and 24.5 mg of diphenylphosphinopropane (dppp) (20 mol%) was added rapidly via syringe. The reaction was allowed to warm to room temperature. The solution was left to polymerize over 10 hours, then quenched with a solution consisted of hexylbromide (0.178 mL, 2 mmol) and magnesium (54.5 mg, 2.2 mmol) in diethyl ether. The reaction mixture was washed by MeOH, acetone, and hexane, in order.

Results and Future Works:

We have succeeded in synthesizing 5-bromo-4-hexyl-5′-iode-3′-(octylsulfanyl)-2,2′-bithiophene, which evaluated by ^{1}H NMR (Figure 1). Polymer 1 showed too complex a NMR spectrum to assign. The next step will be chemical transformation of *ot*-P3OST-*co*-3HT to P3HDTT and measuring the optical properties of synthesized polymer. Moreover, we will fabricate the OPV device consisted of P3HDTT and evaluate their properties.

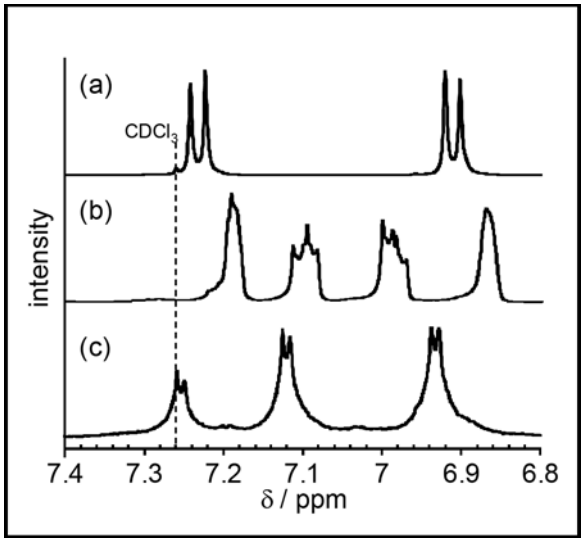

Figure 1: NMR spectra of 2-bromo-3-(octylsulfanyl)thiophene (a), Compound 1 (b), and Monomer 1 (c).

Acknowledgments:

This research was supported by the National Nanotechnology Infrastructure Network (NNIN), the National Science Foundation (NSF) and National Institute for Material Science (NIMS). I would also like to thank the Luscombe Lab for their valuable guidance and assistance, and the NanoTech User Facility (NTUF) at the University of Washington for providing the equipment and training necessary for this project.

References:

[1] Youngkyoo Kim, Jenny Nelson, Donal D. C. Bradley et al., Nature Mater. 2006, 5, 197-203.

[2] Dong, C.-G., T.-P. Liu, and Q.-S. Hu, SYNLETT 2009, 1081-1086.

[3] Hugo A. Bronstein, Christine K. Luscombe, J. Am. Chem. Soc. 2009, 131, 12894-12895.

Synthesis and Characterization of Functional Organic and Supramolecular Nanomaterials

Melinda Jue
Chemical Engineering, University of Texas at Austin

NNIN iREU Site: National Institute for Materials Science (NIMS), Tsukuba, Ibaraki, Japan
NNIN iREU Principal Investigator: Dr. Masayuki Takeuchi, Organic Materials Group, Polymer Materials Unit, NIMS
NNIN iREU Mentor: Dr. Soichiro Ogi, Organic Materials Group, Polymer Materials Unit, National Institute for Materials Science
Contact: melindajue@gmail.com, takeuchi.masayuki@nims.go.jp, ogi.soichiro@nims.go.jp

Abstract:

Artificial photosynthetic systems offer a potential renewable energy source to manage the increasing global energy demand. Organized dye molecules, in particular *J*-type aggregates, exhibit efficient excitation-energy transfer suitable for light-harvesting antennas necessary in artificial photosynthetic systems. We designed and synthesized a porphyrin chromophore (**1S**) so as to self-assemble into a supramolecular polymer with a stable *J*-aggregate mode in solution. Ultraviolet-visible (UV-Vis), infrared (IR), nuclear magnetic resonance (NMR), and circular dichroism (CD) spectroscopic analyses were performed to investigate the aggregation properties.

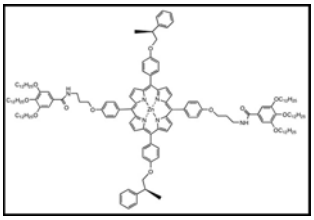

*Figure 1: Chemical structure of **1S**.*

Introduction:

Artificial photosynthesis represents another possibility to harness energy from the sun. In an artificial photosynthetic system, sunlight is absorbed by a light-harvesting antenna before being used to breakdown water into hydrogen and oxygen gas. Ideally a light-harvesting antenna is a chromophore that has a stable *J*-aggregate mode as well useful absorption properties such as broad spectral absorbance and high extinction coefficient [1]. Porphyrin is a conjugated cyclic compound that exhibits self-assembly properties fitting for a potential light-harvesting antenna. It can be synthetically functionalized to form a variety of different chemical structures depending on the application. A natural light-harvesting antenna, chlorophyll, is also a porphyrin derivative [2]. Two aggregation modes, *J*-aggregate and *H*-aggregate, are possible in porphyrin based systems. The *J*-aggregate forms with the porphyrin π systems overlapped partially and the *H*-aggregate is face-to-face stacks of the π systems. Although the H-aggregate is more thermodynamically stable, the *J*-aggregate has desirable light-harvesting properties necessary to transfer energy in artificial photosynthesis. Compound **1S** was designed to form a supramolecular polymer with a stable *J*-aggregate mode in solution.

As seen in Figure 1, **1S** is based on a porphyrin ring with a zinc center. Chiral groups are included to introduce directionality to the aggregate, amide groups to allow for hydrogen bonding, and long alkyl chains to both increase the solubility in nonpolar solvents as well as allow for van der Waals interactions.

Experimental Procedure:

The target molecule was synthesized by a seven step series of reactions starting from pyrrole and ending with **1S**. All compounds were identified with ^{1}H NMR spectroscopy in $CDCl_3$. The aggregation properties of **1S** were characterized with UV-Vis spectroscopy, IR spectroscopy, CD spectroscopy, and atomic force microscopy (AFM). Characterization measurements were taken with solutions of **1S** (10-100 μM) in methylcyclohexane (MCH) at 283-378 K.

Results and Conclusions:

The aggregation properties of **1S** in solution were measured by a combination of spectroscopic techniques. First UV-Vis spectral measurements were conducted to determine the stacking mode of the porphyrin molecules in a MCH solution. At concentration of 50 μM, both Soret and Q bands of the solution were red-shifted in comparison with those of monomeric **1S**, which indicated that the porphyrin molecules overlap in the *J*-aggregate mode. In addition, CD signal was observed with negative maxima at 433 nm, which corresponds to the absorption maximum for Soret band that arises in the UV-Vis spectra upon aggregation. These combined results imply that

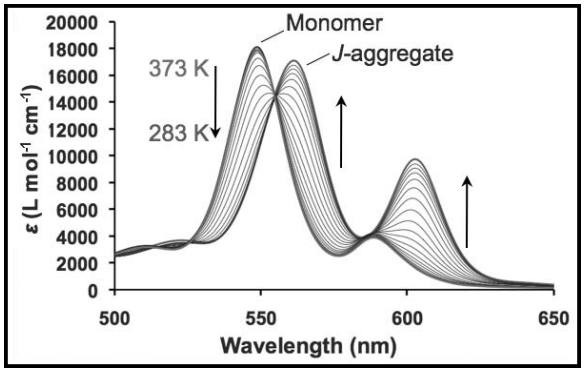

Figure 2: Temperature-dependent UV-Vis spectra of Q band to monitor the formation of J*-aggregate in MCH (*C_T *= 50 μM).*

the chiral groups induce a chiral excitonic coupling between the porphyrin π systems within the *J*-aggregate. IR spectral measurements confirmed both the N-H and C = O stretching vibration peaks were shifted to smaller wavenumbers. These results are indicative of hydrogen bonding between the amide groups of adjacent monomers.

Next the supramolecular polymerization mechanism was investigated with temperature-dependent UV-Vis spectroscopy (Figure 2). As the temperature was decreased from 373 K to 283 K (1 K min^{-1}), a shift of the Q band was induced with a sigmoidal transition that is characteristic of the isodesmic mechanism. This mechanism assumes that each species of aggregation (monomer, dimer, trimer, etc.) are formed with a same equilibrium constant (K_e).

Based on the isodesmic model, the equilibrium constant can be described using Equation 1, where the left side is a fraction of monomeric **1S**, and C_T is an initial concentration of **1S** [3]. The aggregation process was well fitted by an isodesmic analysis, which yielded equilibrium constants at various temperatures. A van't Hoff plot based on these values showed a linear relationship, from which the standard enthalpy change ($\Delta H°$) and entropy change ($\Delta S°$) were determined to be -88 kJ mol^{-1} and -193 J mol-1 K^{-1}, respectively.

$$\frac{M}{C_T} = \frac{2C_TK_e + 1 - \sqrt{4C_TK_e + 1}}{2(C_TK_e)^2}$$

Equation 1: Isodesmic model for determining equilibrium constant.

Furthermore, the aggregation shape was examined with AFM (Figure 3). The average aggregation height is 2 nm while the minimum distance across **1S** varies from 2.5-2.9 nm based on simulations. From this information, the aggregates lay approximately 50° to the surface and not perpendicularly. This stacking height further indicates that *J*-aggregates are formed in solution as well as on the substrate.

In conclusion, we successfully synthesized **1S** and characterdized its aggregation behavior. From the results of various spectroscopic analyses, we revealed that **1S** could form a stable *J*-aggregate with the twisted absorption transition dipoles through π–π stacking and hydrogen bonding in MCH. The aggregation mechanism was well fitted by an isodesmic model so that the equilibrium constant and the thermodynamic properties were determined. Compound **1S** exhibits properties that are beneficial to the synthesis of a light-harvesting antenna.

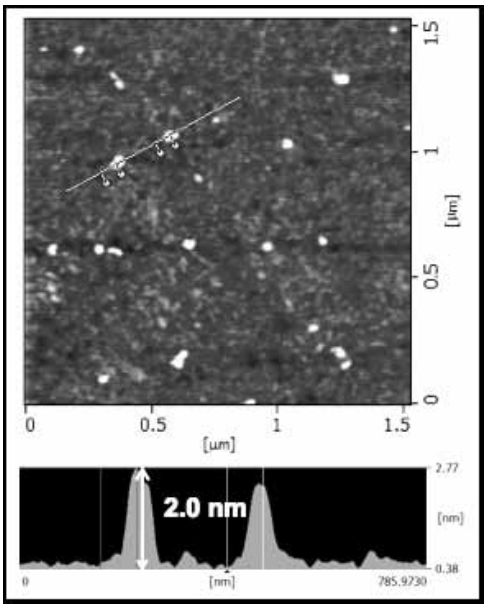

Figure 3: AFM height image of the J*-aggregate spin-coated onto a silicon wafer from a MCH solution.*

Acknowledgments:

Thank you to Dr. Soichiro Ogi, Dr. Kazunori Sugiyasu, Dr. Masayuki Takeuchi, the National Institute for Materials Science, the National Nanotechnology Infrastructure Network International Research Experience for Undergraduates (NNIN iREU) Program, and the National Science Foundation for making this research possible.

References:

[1] Frishmann, P. D., et al., Powering the future of molecular artificial photosynthesis with light-harvesting metallosupramolecular dye assemblies, Chem. Soc. Rev., 2013, 42, 1847-1870.

[2] Wurthner, F., et al., J-aggregates: From serendipitous discovery to supramolecular engineering of functional dye materials, Angew. Chem. Int. Ed., 2011, 50, 3376-3410.

[3] Martin, R. B., Comparisons of indefinite self-association models, Chem. Rev., 1996, 96,3043-3064.

Crumpled Graphene Oxide Nanostructures for Advanced Water Treatment Technologies

Christine Le
Biochemistry, Brown University

NNIN REU Site: Nano Research Facility, Washington University in St. Louis, St. Louis, MO
NNIN REU Principal Investigator: Dr. John Fortner, Energy, Environmental, and Chemical Engr., Washington University in St. Louis
NNIN REU Mentor: Yi Jiang, Energy, Environmental, and Chemical Engineering, Washington University in St. Louis
Contact: christine_le@brown.edu, jfortner@seas.wustl.edu, jiang.y@wustl.edu

Abstract:

The global water crisis calls for water treatment technological advancements, which, based on the state of the art, will be increasingly underpinned by engineering/application of nanoscale materials. Our project aimed to develop an efficient aerosol-based technique to synthesize crumpled graphene oxide (CGO) nanocomposites for enhanced water purification applications. Specifically, we aimed to synthesize and characterize two types of CGO nanocomposites: CGO-TiO_2 (as a high-performance photocatalyst for pollutant degradation) and CGO-magnetite (as a monomeric self-assembling component of a robust and magnetically manipulatable thin-film membrane). We also intended to examine CGO nanocomposites' water-stability under different water chemistries (such as pH). Scanning electron microscopy (SEM) and transmission electron microscopy (TEM) were utilized for size and morphology measurement while electrophoretic light scattering (ELS) and dynamic light scattering (DLS) were used to test zeta potential and nanoparticle size, respectively. Our results indicate an inverse relationship between pH and mean nanoparticle size, and solutions with pH > 3.0 enable CGO stability (zeta potential < -30 mV).

Introduction:

Currently, there are over three million deaths annually, resulting from water-, sanitation-, and hygiene-related diseases [1]. According to the World Water Council, 3.9 billion people are predicted to live with deficient and unsanitary water supply by 2030 [2].

Thus, our project aimed to construct a water treatment membrane using a thin film of CGO-based nanocomposites consisting of both encapsulated photocatalytic materials like TiO_2, which enables enhanced photo-reactive (UVA irradiation) activity for organic pollutant degradation, and adequate amounts of monomeric, nanoscale magnetite components, allowing for magnetic manipulation of nanocomposites in water. CGO provides the membrane with sufficient accessible surface area for water permeability and increased pollutant adsorption.

Two-dimensional graphene oxide has been extensively researched previously because of its unique nanosheet morphology, extreme specific surface area (~ 2650 m^2/g) and broad chemical functionalization possibilities. However, restacking issues caused by van der Waals attraction between the sheets significantly reduces its surface area, thereby limiting its applications. Fortunately, a new field has opened up with the discovery of three-dimensional CGO [3]. Its properties, which include a crumpled ball-like morphology, high free volume, and aqueous stability, make it an ideal candidate for various applications, including water treatment.

Experimental Procedure:

Graphene oxide was synthesized using a modified Hummers method [4]; TiO_2 (Degussa Aerodisp 740X) and magnetite (Fe_3O_4, Sigma Aldrich) were used. A furnace aerosol reactor was used to synthesize CGO through an aerosolization process. First, a Collison nebulizer atomized a GO-TiO_2 precursor into fine droplets; and the droplets were delivered by N_2 into the furnace. Crumpling of GO and encapsulation of TiO_2 was induced by capillary compression caused by rapid evaporation of the aerosol droplets in the furnace (400°C). Finally, CGO nanocomposites were collected at the downstream of the reactor. SEM (NOVA NanoSEM 230) and TEM (Tecnai TM Spirit) were used to determine the size and morphology of the CGO. Zeta potential and aqueous nanoparticle size distribution were measured by ELS and DLS, respectively (Malvern Zetasizer Nano ZS).

Results and Discussion:

GO crumpled and TiO_2 successfully became encapsulated, as evidenced from the SEM (Figure 1) and TEM (Figure 2) images. The SEM images illustrated the nanocomposites' crumpled ball-like morphology, while the TEM images confirm TiO_2 encapsulation and nanoparticles with a size range of 250-350 nm. The CGO nanocomposites had a quasi-spherical morphology resembling a crumpled piece of notebook paper, considerably smooth surfaces, and black color. The color results from GO reduction.

Figure 3 displays ELS results showing the relationship between pH and zeta potential of the aqueous GO-TiO_2 solution. Zeta

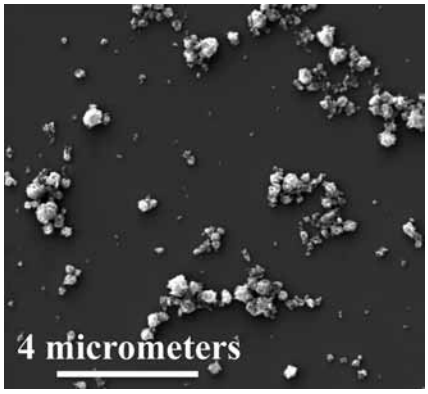

Figure 1: The SEM image demonstrates CGO's crumpled ball morphology.

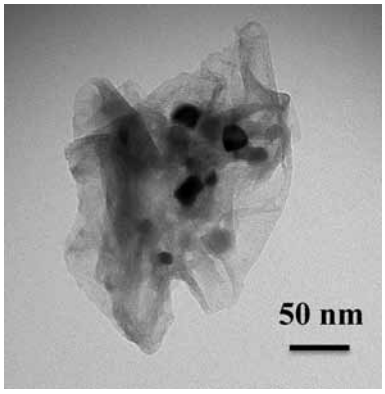

Figure 2: The TEM image denotes TiO_2 encapsulation.

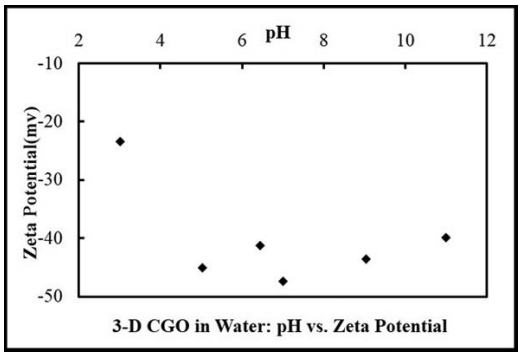

Figure 3: The relationship between pH and zeta-potential of GO-TiO_2 solution.

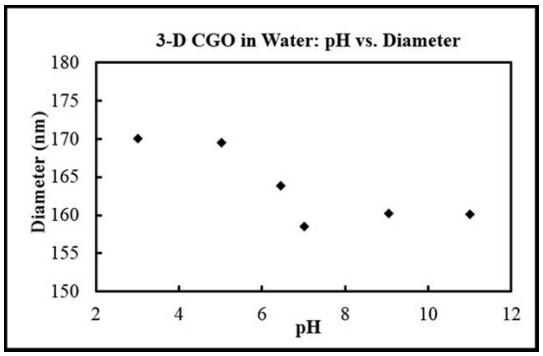

Figure 4: The relationship between pH and nanoparticle size of GO-TiO_2 solution. As pH increases, NP size decreases.

potential, reflecting a nanoparticle's surface charge, indicates the degree of its tendency to resist aggregation and therefore its stability in solution. The data suggested that solutions with pH > 3 yield stable CGO (< -30 mV).

A general inverse relationship was also observed between pH and nanoparticle size (Figure 4). Higher pH values (more basic) imply large OH-concentrations, which enable more negative CGO surface charges. The repulsive electrostatic forces increased between nanoparticles, leading to less aggregation and smaller nanoparticles.

Understanding the interrelationship between pH, nanoparticle size, and zeta potential will facilitate tailoring of CGO behavior according to the acidic conditions of aqueous suspensions for optimized water purification.

Future Work:

Doping TiO_2 has attracted research interest because it narrows TiO_2's band gap, allowing it to activate under sunlight exposure, hence minimizing energy costs. Doping is when impurities are added to semiconductor crystals to tune their conductivity and other characteristics. We will experiment with various dopants/dopant combinations to measure their efficacy in further enhancing TiO_2's photocatalytic properties. A porous, reactive, thin-film membrane will be assembled using the fabricated CGO and a polyvinylidene difluoride support membrane.

Membrane performance will be tested using ultraviolet-visible light spectroscopy and methyl orange will be employed as a model pollutant.

Acknowledgments:

I would like to thank the National Nanotechnology Infrastructure Network Research Experience for Undergraduates Program and National Science Foundation for their generous support, as well as Dr. John Fortner, Yi Jiang, Fortner lab, Dr. Wei-Ning Wang, the Nano Research Facility, Nathan Reed, Dee Stewart, Howard Wynder, Kate Nelson, and Lijie Zhang for their encouragement and guidance.

References:

[1] WHO/UNICEF, Progress on Drinking Water and Sanitation: 2012 Update. 2012, WHO/UNICEF: Geneva/New York.

[2] Urban Urgency, Water Caucus Summary, World Water Council (WWC), Marseille, France, 2007.

[3] Wang, W.-N., Y. Jiang, and P. Biswas, Evaporation-Induced Crumpling of Graphene Oxide Nanosheets in Aerosolized Droplets: Confinement Force Relationship. J. of Physical Chemistry Letts, 2012. 3(21): p. 3228-3233.

[4] W.S. Hummers and R.E. Offeman, Preparation of Graphitic Oxide. Journal of the American Chemical Society, 1958. 80(6):1339-1339.

Direct Nano Patterning of Anisotropic Conjugated Polymer

Azusa Miyagawa
Materials Science, Japan Advanced Institute of Science and Technology, Ishikawa Prefecture, Japan

NNIN iREG Site: Lurie Nanofabrication Facility, University of Michigan, Ann Arbor, MI
NNIN iREG Principal Investigator: Dr. Jinsang Kim, Materials Science and Engineering, University of Michigan
NNIN iREG Mentors: Dr. Pilar Herrera-Fierro, Lurie Nanofabrication Facility, University of Michigan;
Kyeongwoon Chung, Materials Science and Engineering, University of Michigan
Contact: s1340015@jaist.ac.jp, jinsang@umich.edu, pilarhf@umich.edu, kychung@umich.edu

Abstract:

Conjugated polymers with a one-dimensional p-orbital overlap exhibit optoelectronic anisotropy. Their unique anisotropic properties can be fully realized in device applications only when the conjugated chains are aligned. To align chains, we directly drew conjugated polymer lines via dip pen nanolithography (DPN) using a NanoInk DPN 5000. As the first step, poly(3-hexylthiophene) was used as a polymeric material and patterned lines on a gold (Au) surface, changing the solution concentration and writing speed. The line quality was evaluated by fluorescence microscope and atomic force microscope. Our results indicated that solution concentration was not important, but writing speed was critical for writing continuous lines. There are more factors to be considered to write fine lines. However we also revealed that nanoscale lines can be written by DPN technique.

Introduction:

Conjugated polymers (CPs) are active materials for various optoelectronic applications, such as organic solar cells, thin film transistors and light-emitting diodes. Their highly anisotropic optical and electronic properties are owing to the one-dimensional p-orbital overlap along the conjugated polymer backbone. However, these properties of conjugated polymer cannot be fully realized in device applications unless CPs are molecularly and macroscopically assembled and aligned with a well-defined structure. In reality, the directed assembly and particularly macroscopic alignment of CPs is a challenging task, because CPs do not have good self-organization owing to their non-planar structure in solution.

In our previous work, we could obtain well-defined conjugated polymer films by setting of molecular-design rules for improving the directional alignment of CPs under the application of shear stress [1]. In this study, to further improve the CPs alignment, the dip pen nanolithography (DPN) technique was used to make well-aligned CP lines in nanoscale, which is known to be potentially capable of patterning in the nanometer range [2-4]. The DPN process uses a scanning probe tip (the "pen") to directly deposit a material ("ink") with nanoscale onto a substrate. The influence of writing speed and solution concentration on the line continuity was investigated.

Experimental Procedure:

The polymeric material used in this study was poly (3-hexyl-thiophene) (P3HT) purchased from Rieke Metals. P3HT was dissolved in a mixture of o-dichlorobenzene and 1.8-octanedithiol (10:1) and filtered through a 0.45 μm PTFE filter before use. Solution concentrations were 2.5 and 10 g/l. Silicon wafers with a gold (Au) top layer were used. Au substrates were cut into pieces of 1 cm × 1 cm and cleaned by immersion in acetone. The substrates were treated with oxygen plasma.

DPN was carried out using a DPN 5000 (NanoInk, Inc.) in an atmosphere control chamber. Lithography was performed at a temperature of 25°C and 50% relative humidity. The writing speed were 1.0 and 0.001 mm/s. Silicon nitride single pens (Type A, NanoInk, Inc.) were used. The ink was filled in an Inkwell (IWL-0031-01, NanoInk, Inc.). Image analyses were done with the Olympus BX-51 fluorescence microscope (FM) and Nano Man atomic force microscope (AFM).

Results and Conclusions:

Fluorescent Microscopy. Figure 1 shows the FM image of the line written with the ink of 2.5 g/l concentration and the writing speed of 0.001 mm/s. Changing concentrations did not show any noticeable changes in the line continuity. However, continuous lines were not generated via a writing speed of 1.0 mm/s, even though that writing speed was critical for line quality. Furthermore, it was found that lines could be written more than 1000 μm on a one-time ink loading.

Atomic Force Microscopy. The AFM topography image of generated lines with the ink of 10 g/l concentration and the writing speed of 0.001 mm/s is shown in Figure 2. Changing concentration also does not show a difference even in AFM images, indicating that the solution concentration does not affect the line continuity. The AFM image of the cross section reveals that the generated line width and thickness was 0.8 μm and 20 nm, respectively (Figure 3).

Comparing direct writing processes, whereas inkjet printing is limited to feature sizes of some tens of microns [5], generated lines in this study are the nanometer range. However, even written in the same condition, continuous lines are not obtained constantly. This indicates that there are more parameters to be considered to write continuous lines. For instance, ink amount of the probe [3], probe conditions [4], humidity [2], writing force and surface conditions are also important to writing patterns and we have to consider them.

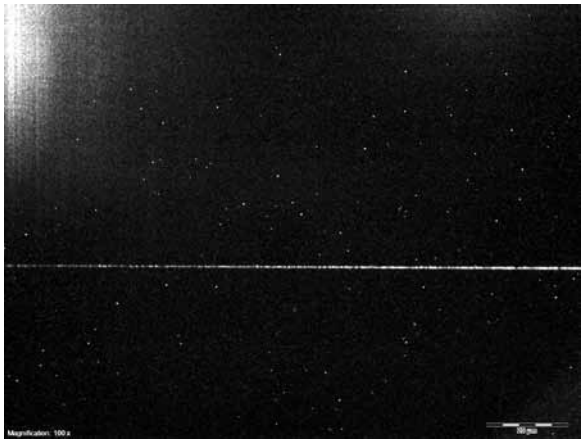

Figure 1: The FM image of P3HT line written with 2.5 g/l concentration ink.

Future Work:

The most important is to write continuous lines constantly. We need to write lines with changing other properties such as ink amount, writing force and humidity.

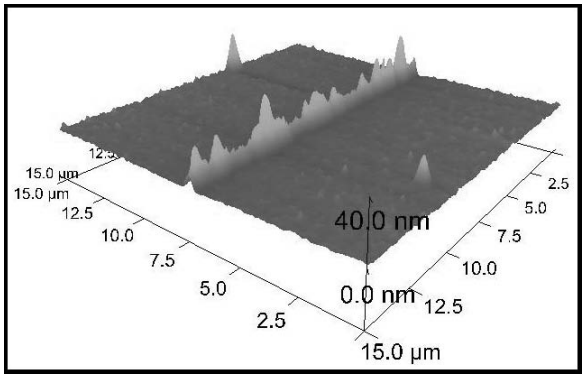

Figure 2: The AFM image of P3HT line written with 10 g/l concentrations ink.

Acknowledgements:

I would like to thank the National Nanotechnology Infrastructure Network International Research Experience for Graduates (NNIN iREG) Program, the National Science Foundation, Nanotechnology Platform, Japan, the Lurie Nanofabrication Facility and staff, Dr. Jingsan Kim, Dr. Pilar Herrera-Fierro, and Mr. Kyeongwoon Chung.

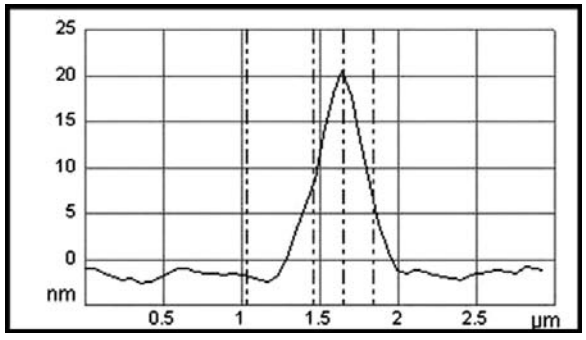

Figure 3: The AFM image of the cross section for Figure 2.

References:

[1] Kim, B., Jeong, E., Chung, J. W., Seo, S., Koo, B., Kim, J. "A molecular design principle of lyotropic liquid-crystalline conjugated polymers with directed alignment capability for plastic electronics." Nature Mater. 12, 659 (2013).

[2] Wang, H. T., Nafday, O. A., Haaheim, J. R., Tecaarwerk, E., Amro, N. A., Sanedrin, R. G., Chang, C. Y., Ren, F., Pearton, S. J. Toward conductive traces: Dip Pen Nanolithography of silver nanoparticle-based inks. Appl. Phys. Lett. 93, 143105 (2008).

[3] Kramer, M. A., Ivanisevic, A. Parallel dip-pen nanolithography using spore- and colloid- terminated cantilevers. Small 8, 3791 (2012).

[4] Lenhert, S., Sun, P., Wang, Y., Fuchs, H., Mirkin, A. Massively parallel dip-pen nanolithography of heterogeneous supported phospholipid multilayer patterns. Small 3, 71 (2007).

[5] Calvert, P. Inkjet printing for materials and devices. Chem. Mater. 13, 3299 (2001).

Synthesis and Covalent Attachment of $\{M_4\}$ Polynuclear Metallic Complexes to Oxidized Carbon Nanotubes

Christopher A. Nakamoto
Chemistry, Beloit College

NNIN iREU Site: Institut Für Bio- Und Nanosysteme (IBN), Forschungszentrum, Jülich, Germany
NNIN iREU Principal Investigator: Dr. Carola Meyer, PGI-6, Jülich Forschungszentrum
NNIN iREU Mentor: Dr. Claire Besson, PGI-6, Jülich Forschungszentrum
Contact: nakamoto.c60@gmail.com, c.meyer@fz-juelich.de, c.besson@fz-juelich.de

Introduction:

Carbon nanotubes (CNTs) are one-dimensional conductors with excellent spin transport properties that can be modified by chemical functionalization. This makes them an extremely interesting material for spintronic applications. For example, grafting single molecule magnets to CNTs through π–π interactions produces magnetoresistance [1]. Such dispersion forces are relatively weak, though, resulting in poor adhesion or orientation.

In contrast, covalent bonding offers stronger, better-oriented functionalization of CNTs and has been demonstrated with tetramaganese(II) $\{Mn_4\}$ complexes and oxidized CNTs; $\{Mn_4\}$ represents the general formula $[Mn_4L_2(CH_3COO)_4]$ (H_2L=2,6-bis(1-(2-hydroxyphenyl)iminoethyl)pyridine) [2]. The $\{Mn_4\}$ consists of a Mn_4O_4 cubane core held in place by rigid ligands and capped by exchangeable acetate ligands [3]. The exchange of these carboxylate ligands has little effect on the overall structure and magnetic behavior of $\{Mn_4\}$. This is ideal for a ligand exchange route of covalent functionalization. In the case of oxidized CNTs, carboxylate functionalities on the CNTs exchange with acetates in $\{Mn_4\}$ to directly bind to the metal nuclei of $\{Mn_4\}$.

In this report the versatility of ligand exchange functionalization is demonstrated with oxidized CNTs and two newly synthesized $\{M_4\}$ (M = Co, Zn) complexes with chemical structures similar to $\{Mn_4\}$. The effects of functionalization on resistivity at room temperature are additionally explored.

Experimental Procedure:

Co_4[2,6-bis(1-(2-hydroxyphenyl)iminoethyl)pyridine]$_2$[acetate]$_4$. A mixture of 2,6-diacetylpyridine (400.3 mg, 2.45 mmol), 2-aminophenol (536.4mg, 4.91 mmol), and $Co(CH_3CO_2)_2 \cdot 4H_2O$ (1,2298 g, 4.94 mmol) in methanol (5 ml) was refluxed for 3.5 hours under argon (Ar) to obtain a dark-orange solution. After cooling, degassed diethyl ether (20 ml) was transferred to the solution by cannulation to produce dark-red crystals and orange microcrystalline powder. Recrystallization from ethanol top-layered with pentane afforded the product as red crystals (180.6 mg, 74.2% yield).

Zn_4[2,6-bis(1-(2-hydroxyphenyl)iminoethyl)pyridine]$_2$[acetate]$_4$. A mixture of 2,6-diacetylpyridine (400.1 mg, 2.45 mmol), 2-aminophenol (536.2mg, 4.91 mmol), and $Zn(CH_3CO_2)_2 \cdot 2H_2O$ (1.0853 g, 4.94 mmol) in methanol (20 ml) was refluxed for two hours in air to obtain a dark-orange solution. After cooling, diethyl ether (100 ml) was transferred to the solution slowly to produce needle-like, orange crystals and light-orange powder. Recrystallization by slow evaporation of chloroform afforded orange crystals.

Mn_4[2,6-bis(1-(2-hydroxyphenyl)iminoethyl)pyridine]$_2$[acetate]$_4$. $\{Mn_4\}$ was synthesized following the procedure outlined by Kampert et al. [3].

$\{M_4\}$ Characterization. The $\{M_4\}$ complexes were characterized by IR, Raman, UV-Vis spectroscopy, single crystal XRD, and cyclic voltammetry. The $\{Zn_4\}$ was further characterized by ^1H and ^{13}C NMR.

Preparation of CNT Networks. A catalyst solution of AEROXIDE® Alumina (24.7 mg, 242 μmol), $Fe(NO_3) \cdot 9H_2O$ (41.4 mg, 171 μmol), and bis(acetylacetonato)-dioxomolybdenum(VI) (8.6 mg, 26 μmol) in methanol (30 ml) was prepared by 10 min of sonication. One by one centimeter square pieces of <100> Si with an insulating layer of SiO_2 were treated with a few drops of catalyst solution and dried under a N_2 stream, followed by heating at 120°C to remove solvent. Samples were placed in a quartz tube furnace and heated under Ar to 850°C. Once at 850°C, Ar flow was stopped and a mixture of 520 sccm CH_4 and 700 sccm H_2 was passed over the samples for 10 min followed by cooling under Ar. Formation of carboxylate functionalities on the CNTs occurred by oxidation in air at 450°C for 8 min.

CNT Network Characterization. CNT networks were characterized by atomic force microscopy (AFM) to ensure adequate coverage and growth density. Electronically, oxidized CNT networks were tested before and after functionalization using a two-terminal setup and e-beam evaporated Pt contacts.

CNT Network Functionalization. Oxidized CNT networks were placed in acetonitrile solutions containing 2.5 mg/ml of $\{Co_4\}$, $\{Zn_4\}$, or $\{Mn_4\}$ and left to sit for one week with a

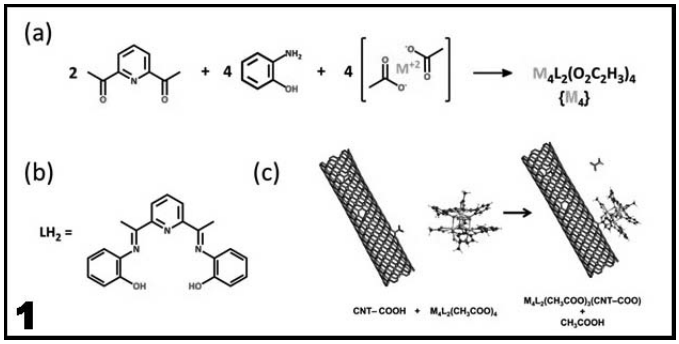

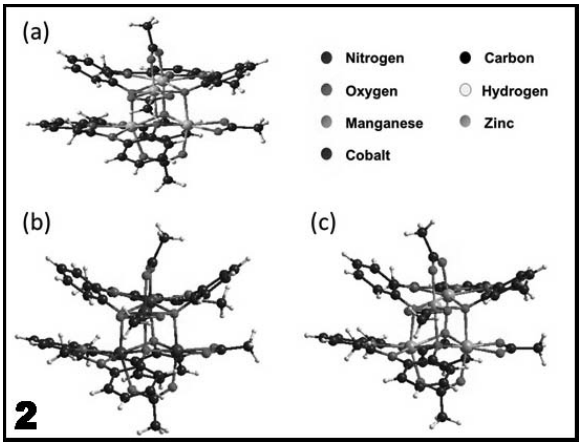

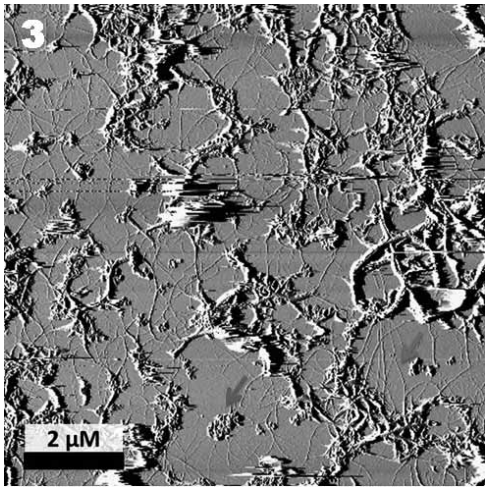

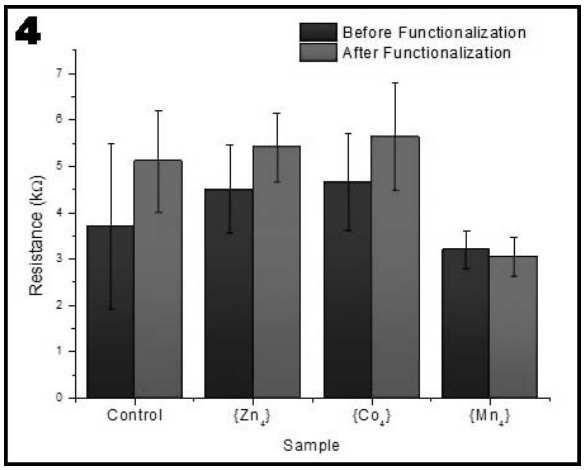

control in pure acetonitrile. To rinse the samples thoroughly, the samples were soaked in acetonitrile for four days followed by three more days in fresh acetonitrile.

Results and Discussion:

$\{Co_4\}$ and $\{Zn_4\}$ Synthesis. Figure 1a shows a reaction scheme for the synthesis of $\{Mn_4\}$, $\{Co_4\}$, and $\{Zn_4\}$. The resulting crystal structures obtained by x-ray crystallography, shown in Figure 2, demonstrate the syntheses were successful despite using metals with different preferred coordination geometries. (See a full-color version of Figure 2 on the inside cover.) The $\{M_4\}$ species are extremely similar in structure consisting of a metal-oxide cubane core held in place by the ligand shown in Figure 1b. Similarities in the positioning of acetate ligands imply ligand exchange with CNTs is possible for all three shown schematically in Figure 1c.

CNT Network Characterization. AFM of the CNT networks showed dense CNT growth and good substrate coverage, shown in Figure 3. Al_2O_3 supported catalyst particles can also be observed. Electrical characterization of the CNT networks before and after functionalization with $\{M_4\}$ indicated no change in resistance within a 95% confidence interval as seen in Figure 4, although there is a trend of increased resistance with functionalization.

Conclusions:

Two new $\{M_4\}$ complexes with a similar structure to $\{Mn_4\}$ were synthesized using Zn^{+2} and Co^{+2}. All three $\{M_4\}$ complexes were reacted with oxidized CNT networks and were found to have a statistically insignificant effect on CNT networks resistances at room temperature.

References:

[1] Urdampilleta, M., Klyatskaya, S., Cleuziou, J.P., Ruben, M., Wernsdorfer, W. Nat. Mater. 2011, 10(7), 502-506.

[2] Meyer, C., Besson, C., Frielinghaus, R., Saelhoff, A.-K., Flötotto, H., Houben, L., Kögerler P., Schneider, C. M. Phys. Status Solidi B. 2012 249(12), 2412-2415.

[3] Kampert, E., Janssen, F.F.B.J., Boukhvalov, D.W., Russcher, J.C., Smits, J.M.M; Gelder, R., Bruin, B., Christianen, P.C.M., Zeitler, U., Katsnelson, M.I., Maan, J.C., Rowan, A.E. Inorg. Chem. 2009, 48, 11903-11908.

Effects of Hydrophilic Membrane Modifications and Natural Organic Matter Fouling on Reverse Osmosis Membrane Performance

Justin Nauman
Chemical Engineering, Purdue University

NNIN REU Site: Nano Research Facility, Washington University in St. Louis, St. Louis, MO
NNIN REU Principal Investigator: Dr. Young-Shin Jun, Energy, Environmental, and Chemical Engr., Washington University in St. Louis
NNIN REU Mentor: Ms. Jessica Ray, Energy, Environmental, and Chemical Engr., Washington University in St. Louis
Contact: nauman@purdue.edu, ysjun@seas.wustl.edu, jessica.ray@go.wustl.edu

Abstract:

Reverse osmosis diffusion processes offer an effective method for filtering brackish and sea waters. Thin-film composite (TFC) membranes function as the filter in these systems. However, the main drawback to using the TFC membranes is their susceptibility to fouling by hydrophobic natural organic matter (NOM) and various inorganic salts commonly found in brackish waters. One proposed method of mitigating this problem is to modify the polyamide active layer of the TFC membrane to be more hydrophilic using polyethylene glycol (PEG). The focus of the project is to determine the effect of hydrophilic PEG grafting on membrane performance in the presence of NOM and model brackish water constituents. Using a tabletop reverse osmosis setup, feed stream conditions containing NOM and/or aqueous salts were tested for both grafted and unmodified membranes. Analysis of the permeate stream indicated that PEG-grafted membranes reduced permeate flux but also increased the ion rejection in most systems.

Introduction:

The desalination of brackish water and seawater is employed to provide fresh water to people around the world. A common method of desalinating water is reverse osmosis (RO), where an applied pressure is used to overcome the osmotic pressure through a semipermeable membrane. A feed stream often containing inorganic salts and NOM (which are generally hydrophobic) is fed to the system, with permeate, or filtered, and concentrate streams leaving the system [1]. However, the TFC membranes, shown in Figure 1, used during the process are often fouled by the deposition and clogging of pores caused by the NOM and salts present in the feed stream. This reduction in efficiency leads to less effective filtration and more frequent membrane cleaning/replacement [2].

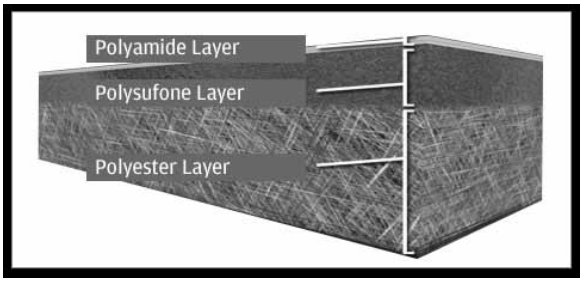

Figure 1: TFC membrane displaying the three layers including the top polyamide active layer [2].

One proposed method of mitigating this problem is to modify the top polyamide layer of the TFC membrane to be more hydrophilic and resistant to fouling. PEG has been determined to be a suitable candidate for this process because it is a flexible, water-soluble polymer with a hydrophilic head [3].

Experimental Procedure:

Membranes were tested using a reverse osmosis benchtop setup to determine their fouling characteristics in different feed solutions. Half of these membranes were grafted with PEG using a cross-linker solution of ethylene glycol dimethacrylate and potassium disulfate and potassium persulfate initiators. The membranes were placed in the system depicted in Figure 2. The various feed solutions were placed in the plastic tub and

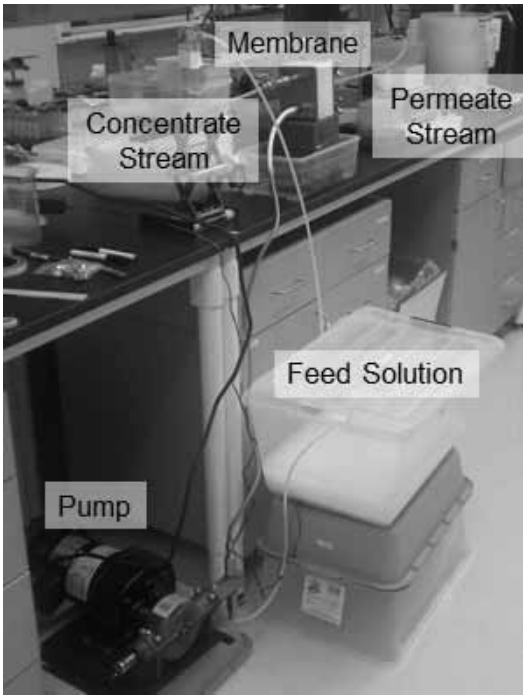

Figure 2: Reverse osmosis benchtop setup used for testing.

each system was left to run for four hours. The feed streams all contained one molar sodium chloride and at least one added potential fouling agent. For our potential foulants we used humic acid as the NOM and calcite ($CaCO_3$) and gypsum ($CaSO_4$) as our salts, two common foulants found in brackish waters. An autosampler collected a sample of the permeate stream every three minutes during the experiment. After each system finished running, we measured the calcium and chlorine ion concentrations in the permeate stream using ion selective electrodes. Permeate flux was also calculated using the collected volume in each test tube. The NOM concentration was measured using a Total Organic Carbon Analyzer. We then took a sample from each used membrane and analyzed the fouling morphology using scanning electron microscopy (SEM).

Results and Conclusions:

From the SEM images gathered, the calcite was found to form a consistent rhombohedra aggregate on the surface of the membrane. The gypsum formed more irregular rod and sheet-like structures. From the ion concentration data, we found that PEG-grafted membranes had an increased ion rejection (calcium and chloride) in calcite forming systems, but a decreased ion rejection in gypsum forming systems, as shown in Figure 3. When systems containing just the calcium salt and systems containing both a calcium salt and humic acid were tested, the PEG-grafted membranes in the gypsum (Ca^{2+} - SO_4^{2-}) systems also showed more overall fouling than the unmodified systems, even at a lower saturation index. In addition, PEG-grafted membranes did also reject more NOM than their unmodified counterparts as you can see in Figure 4. Interestingly, the PEG-grafted gypsum system did not reject the humic acid as well as the PEG-grafted calcite system or the PEG-grafted system with only humic acid, but it did perform better than the unmodified gypsum system. However, PEG-grafted membranes also resulted in a lower permeate flux amounting at about a 65% decrease in systems not containing NOM and roughly a 33% decrease in systems containing NOM. Cost analysis would have to be performed to determine if the PEG modification to the TFC membranes would be economically beneficial because the decrease in flux could potentially outweigh the benefit of increased NOM and ion rejection (except in gypsum systems).

Future Work:

The next step would be to replicate the reverse osmosis test. Ideally, more systems would also be tested using other inorganic salts and NOM commonly found in brackish waters, such as $MgSO_4$ and $MgCO_3$. Another important aspect to further investigate is the driving force of the inverse effects of fouling in Gypsum systems.

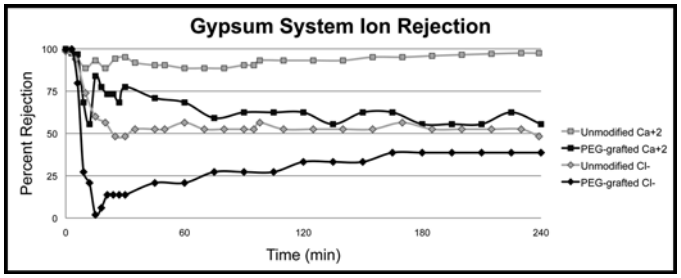

Figure 3: Graph modeling gypsum system ion rejection.

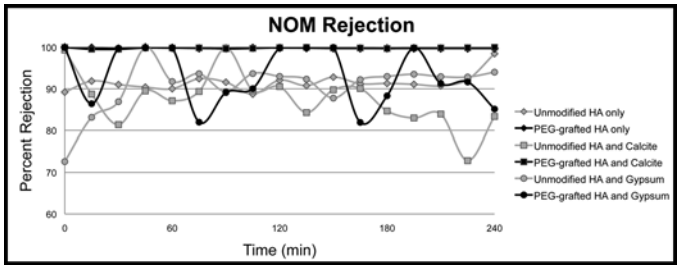

Figure 4: Graph modeling NOM rejection.

Acknowledgments:

I would like to thank Dr. Young-Shin Jun, Ms. Jessica Ray, and everyone at the Environmental Nanochemistry Lab for their guidance and support. I would also like to acknowledge the National Nanotechnology Infrastructure Network Research Experience for Undergraduates Progam and the National Science Foundation for giving me this exceptional opportunity and experience.

References:

[1] Greenlee, et al., Reverse osmosis desalination: Water sources, technology, and today's challenges. Water Research, Volume 43, Issue 9, Pages 2317-2348, May 2009.

[2] Elimelech, M., and Phillip, W. A. The future of seawater desalination: Energy, technology, and the environment. Science, 333 (6043), 712-717, 2011.

[3] Tiraferri, et al., Superhydrophilic Thin-Film Composite Forward Osmosis Membranes for Organic Fouling Control: Fouling Behavior and Antifouling Mechanisms. Environmental Science and Technology, 46 (20), 11135-11144, 2012.

Controlled Self-Assembly of Metallated and Non-Metallated Peptidic Arrays

Geoffrey Vrla
Chemistry, Middlebury College

NNIN iREU Site: National Institute for Materials Science (NIMS), Tsukuba, Ibaraki, Japan
NNIN iREU Principal Investigator and Mentor: Dr. Kentaro Tashiro,
Reticular Materials Group, National Institute for Materials Science
Contact: gvrla@middlebury.edu, tashiro.kentaro@nims.go.jp

Abstract:

Peptide-based compounds are desirable targets for the development of novel nano-materials due to their propensity to form self-assembled, supramolecular architectures. Chemical modification of self-assembling peptides has been investigated as a route for the formation of functional nanostructures designed for specific applications. Here, we have modified the diphenylalanine (FF) peptide, previously shown to spontaneously form fibrous self-assemblies, with two organic chelating groups capable of coordinating various transition metals. We investigated the self-assembling behaviors of this peptide in coordination with several combinations of Pt(II), Re(I), or Rh(III) using Fourier transform infrared (FTIR) spectroscopy, circular dichroism (CD) spectroscopy, and scanning electron microscopy (SEM). SEM analysis indicated that both homo-metallated species of Pt(II) and Re(I) as well as the non-metallated species form fibrous self-assemblies. However, the heterometallic peptide coordinating Pt(II)and Rh(III) did not form distinguishable fibrous structures under identical conditions. We propose that the charge states of the metal centers may affect the self-assembly properties of these peptide compounds. Further investigation into possible self-assembling heterometallic dipeptides could be beneficial for the future development of more complex, metallated nanostructures.

Introduction:

Peptide-based compounds are desirable targets for the development of novel nano-materials due to their propensity to form self-assembled, supramolecular architectures. Short, aromatic peptides such as diphenylalanine (FF) exhibit particularly strong tendencies to self assemble; FF has been previously shown to self-assemble into discrete, robust nanotubes [1]. The biocompatibility of these peptide nanostructures, as well as the ability to modify the peptide backbone with numerous function groups, has given these compounds versatility and usefulness in a wide range of applications [2].

The incorporation of transition metals into the structure of self-assembling peptides may provide a route towards the development of more complex metallic nanostructures with novel properties. Recently, the FF structural motif has been incorporated into a Ru(II) complex, resulting in the first metallo-hydrogellator capable of redox-responsive self-assembly and gelation [$_3$]. The incorporation of multiple chelating functional groups capable of coordinating a broader range of transition metals into a self-assembling peptide could significantly increase the complexity of these nanostructures, and provide potential catalytic or fluorescent properties.

Here, we have developed a method for the incorporation of heterometallic complexes into the backbone structure of a self-assembling peptide. We modified the FF structural motif with two organic chelating groups capable of coordinating either Pt(II), Re(I), Rh(III), or Ru(II). This technique not only allows for the synthesis of heterometallic peptidic arrays, but also allows for the sequential addition of amino acid subunits to achieve peptide chains with more than two metal centers.

Experimental Procedure:

Metallated peptides were synthesized previously using either a conventional solution phase synthesis technique or a modified form of the Merrifield solid-phase synthesis technique [4]. One non-metallated and three metallated peptides studied here are shown in Figure 1.

SEM Analysis. A 0.1 mM sample stock solution was prepared by suspending 0.5 mg (0.3 μmol) of peptide in 3 mL acetonitrile (ACN). The suspension was sonicated for 30 s followed by heating at 50°C for one min; this process was repeated until the solid had fully dissolved. After 24 hr of incubation at 22°C, the solution was spotted onto a silicon substrate and visualized using a Hitachi SU8000 scanning electron microscope.

CD Analysis. Samples were prepared identically to SEM samples, with the addition of a 10-fold dilution to achieve a proper concentration for CD analysis. Their CD spectra were recorded on a JASCO Type J-820 spectropolarimeter at -10°C.

FTIR Analysis. Samples were prepared as pellets in solid KBr and their spectra were recorded using a Thermo Scientific model Nicolet 4700 Fourier transform infrared spectrometer.

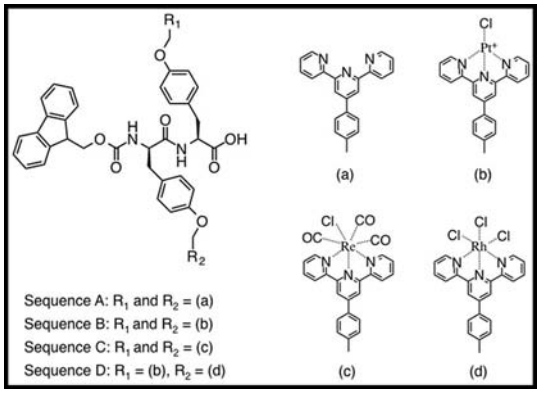

*Figure 1: Series of non-metallated (**A**) and metallated (**B**-**C**) peptides.*

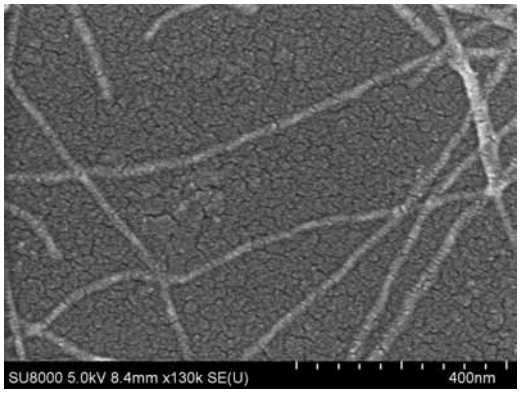

*Figure 2: SEM of non-metallated peptide (**A**) self-assemblies.*

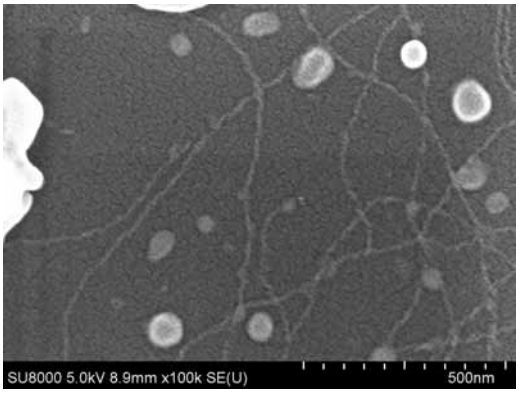

*Figure 3: SEM of Pt^{+}-Pt^{+} peptide (**B**) self-assemblies.*

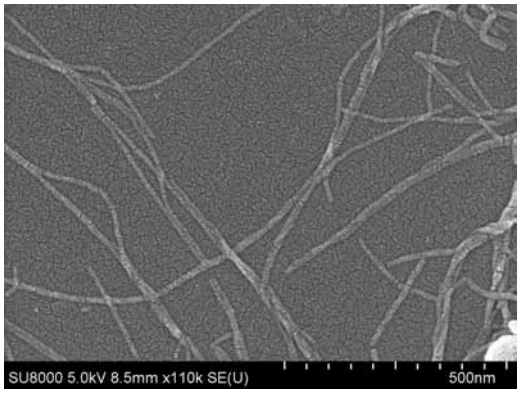

*Figure 4: SEM of Re-Re peptide (**C**) self-assemblies.*

Results and Conclusions:

All four peptide compounds were weakly soluble in ACN. After several hours of incubation at 22°C, the formation of solid aggregates was observed. SEM analysis indicated that sequences **A**, **B**, and **C**, but not **D**, formed fibrous assemblies shown in Figures 2-4. While the charge state of the metal centers was identical (either $^{+}1$ or 0) for **A**, **B**, and **C**, the charge state of the Pt(II) and Rh(III) in **D** were different ($^{+}1$ and 0, respectively). It is possible that the charge symmetry of the metal centers may affect the self-assembling properties of the compound, which may explain the absence of fibrous aggregates in the hetero-metallic species.

The non-metallated sequence (**A**) gave a relatively strong CD signal with a positive peak at 198 nm, while the CD signals of the metallated peptides were too weak to distinguish. Additionally, two strong bands between 1670-1690 cm^{-1} and 1607-1612 cm^{-1} in the infrared spectra of compounds **A**-**D** were observed. Previously studied FF-based nanostructures have characteristic IR stretching frequencies around 1630 cm^{-1}, attributed to peptide amide groups in the β-sheet conformation [1]. The absence of an amide stretch around 1630 cm^{-1} in the metallated peptides suggests that these monomers are not arranged in a β-sheet conformation.

Future Work:

Future work will investigate the conditions most appropriate for the formation of fibrous structures of hetero-metallated species. The ability to develop self-assembling peptides with hetero-metallic centers is useful for the development of more complex metallated architectures. Such compounds have not been reported previously, and may possess interesting catalytic or electronic properties. Additionally, field effect transistor measurements can be performed on homo-metallated dipeptides to measure the potential semi-conductive properties of these compounds.

Acknowledgements:

I would like to thank the Dr. Kentaro Tashiro and Reticular Materials Group for their guidance. I acknowledge the NSF and NNIN iREU Program for financial support, and the National Institute of Materials Science for hosting me.

References:

[1] Reches, M.; Gazit, E. Science 2003, 300, 625.
[2] Gazit, E. Chem. Soc. Rev. 2007, 36, 1263.
[3] Zhang, Y., et al., J. Am. Chem. Soc. 2013, 135, 5008.
[4] Vairaprakash, P., et al., J. Am. Chem. Soc. 2011, 133, 759.

Directed Self Assembly of Mixed Nanowire Populations via Lithographic Microwells

Allison Wustrow
Chemistry, University of California Berkeley

NNIN REU Site: Penn State Nanofabrication Laboratory, The Pennsylvania State University, University Park, PA
NNIN REU Principal Investigator: Christine Keating, Chemistry, The Pennsylvania State University
NNIN REU Mentor: David Kirby, Chemistry, The Pennsylvania State University
Contact: wustrow@berkeley.edu, djk291@psu.edu, keating@chem.psu.edu

Introduction:

Vertical nanowire arrays can be used for both energy harvesting and storage. Using assembly to create such arrays allows two populations to be mixed together, while standard fabrication limits the product to a single material. However in the absence of applied fields [1] or controlled drying conditions [2], nanowires typically assemble parallel to the surface, forming horizontal arrays. The Keating group has worked with anisotropic particles, called partially etched nanowires, which form arrays where up to 70% of wires were vertically oriented on a planar surface when their internal asymmetry was tuned to optimize van der Waals and electrostatic interactions [3]. Array quality was increased to nearly 100% standing when microwells were used to direct assembly [4].

A similar approach was used for this work to generate vertical arrays of single component nanowires that lacked the material anisotropy used previously. Wire-wire interactions, such as van der Waals forces, which depend on the composition of the nanowire, were also studied by mixing wires of two different compositions.

Understanding these assemblies could help with design of reconfigurable materials.

Experimental Fabrication:

Nanowires were made by templated electrodeposition [5] in porous alumina membranes. Silver (Ag, 300 nm) was evaporated on to the membrane (Whatman). Plating solutions of silver cyless R, orotemp 24, and pallaspeed VHS_RTU (Technic inc.) were used to make palladium and gold wires with diameters around 300 μm, as determined using transmission electron microscopy.

The evaporated Ag layer, which served as a working electrode, was dissolved in nitric acid, and the alumina template was dissolved in sodium hydroxide, freeing the wires into suspension.

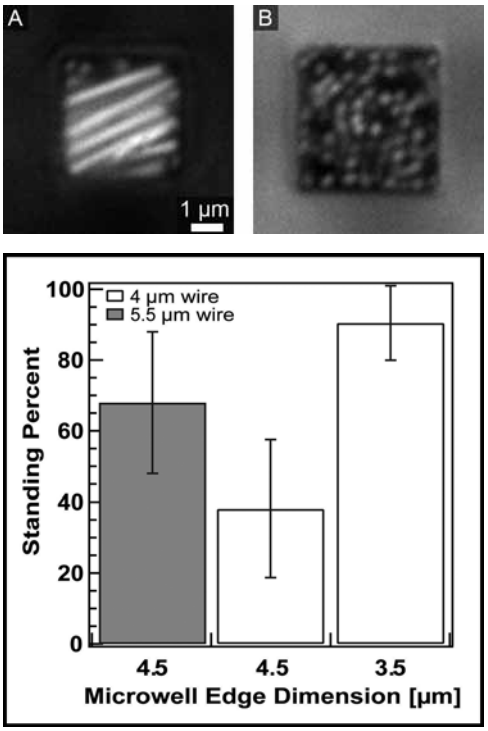

Figure 1, top: Assembled nanowires after one hour. (A) shows 4 µm wires in a 4.5 µm well which have a low standing percentage. (B) shows 5.5 µm wires in a similar well which have a high standing percentage.

Figure 2, bottom: Standing percentage for different particle lengths in different sized wells. At least 480 wells were counted for each data point.

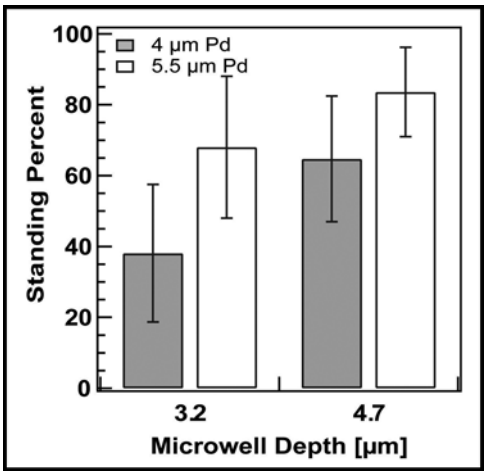

Figure 3, top: Standing percentages for nanowires assembled in microwells of different depths. At least 900 wells were counted for each data point.

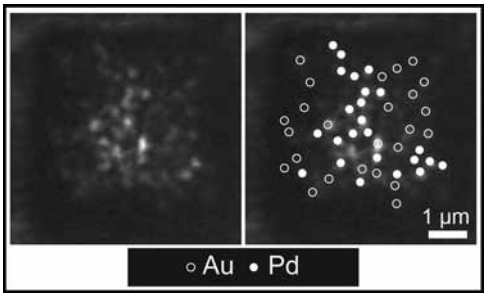

Figure 4, bottom: Optical micrograph of a binary nanowire assembly. Images are an overlay of reflectivity information collected at wavelengths of 488, 514, and 543 nm. A ratio of the intensities was used to determine the assignments as labeled in the right image.

Nanowires were cleaned by repeated centrifugation in sodium hydroxide or ethanol, and were ultimately suspended in deionized water. Particles were coated with a silica shell using a modified Stober process [3]. Wire concentration was determined using a hemocytometer. Microwells were made using SPR 955 photoresist (Microchem).

Assembly:

An assembly chamber was created by isolating a selection of microwells using a polydimethylsiloxane spacer (DOW Corning). Enough particles to form a single monolayer of standing wires were rinsed in deionized water. The suspension was sonicated and added to the assembly chamber, where it was allowed to settle for one hour before imaging. Standing percentage was determined using previously published methods in which image analysis software distinguished standing from laying down wires [3]. In binary mixture experiments, the wire material was determined by comparing the reflected light intensity for 488, 514, and 543 nm light.

Results:

Wire length affected standing percentage when well size was constant for palladium nanowires assembled into microwells. Longer wires in general had higher standing percentages (Figure 1). Palladium wires 4 μm in length assembled in 4.5 μm wells had 20 percentage points lower standing than 5.5 μm wires (Figure 2). Gravity drove the wires into the wells, where the longer wires were unable to fit in the horizontal conformation, and thus form vertical arrays. Microwell size also affected standing percentage. When 4 μm wires were assembled in 4.5 μm wells, standing percentage was higher than when the same wires were assembled in 3.5 μm wells (Figure 2). Deeper wells could support the wires along the entire length of the 4 μm wires, as well as a larger fraction of the 5.5 μm wires. This extra support raises the standing percentage in the wells regardless of nanowire length.

After vertical array quality had been optimized, binary nanowire mixtures were assembled. For these experiments, gold wires 4 μm in length were mixed with 5.5 μm palladium wires. These wires had the potential to exhibit interesting physical behavior due slight differences in their Hamaker constants (i.e. van der Waals interactions). Here we successfully assembled mixtures of these particles into vertical arrays and using optical microscopy we were able to distinguish the two populations via their differing reflectivities. Further study is needed to explore potential phase behavior.

Conclusions and Future Directions:

Nanowires were assembled vertically in microwells by controlling the particle and microwell dimensions. Mixtures of two types of wires were placed in the wells and identified by the differing reflectivities of the metals. As more samples are examined, it will be possible to study the phase behavior caused by the differences in inter-wire interactions, allowing generation of phase diagrams to describe the system. Understanding the mixing and demixing of vertical nanowire arrays will allow for the development of reconfigurable materials.

Acknowledgements:

This work was primarily supported by funding from the NNIN Research Experience for Undergraduates Program and the National Science Foundation. Acknowledgement is also made to the Donors of the American Chemical Society Petroleum Research Fund (ACS PRF 50888-ND10). We appreciate the use of the Huck Institute of Life Sciences Electron Microscopy Facility. This publication was supported by the Pennsylvania State University Materials Research Institute Nanofabrication Lab and the National Science Foundation Cooperative Agreement No. ECS-0335765.

References:

[1] Loaiza, Ó. A., et al. Angew. Chem. Int. Ed, 46, 1508-1511, 2007.
[2] Zhang, X., et al. J. Phys. Chem. C., 113, 5947-5951, 2009.
[3] Smith, B., et al. Small, 6, 781-787, 2011.
[4] Kirby, D., et al. Manuscript submitted to Part. Part. Syst. Charact.
[5] Nicewarner-Peña, S., et al. Science, 294,137-141, 2001.

Azobenzene Functionalized DNA for Light-Induced DNA Stringency

Hannah Zeitler
Physical Chemistry, Whitworth University

NNIN REU Site: NanoTech User Facility, University of Washington, Seattle, WA
NNIN REU Principal Investigator: David Ginger, Chemistry, University of Washington
NNIN REU Mentor: Yunqi Yan, Chemistry, University of Washington
Contact: hzeitler15@my.whitworth.edu, ginger@chem.washington.edu, yanyunqi@uw.edu

Abstract and Introduction:

Azobenzene functionalized deoxyribonucleic acid (DNA) and DNA modified gold nanoparticles (AuNP) are used to study light-induced DNA stringency, a method to distinguish perfectly matched DNA from partially matched DNA using light. To do this, AuNP are functionalized with DNA [1], and azobenzene modified DNA is attached to glass slides to use chip-based assays. The photoisomerization quantum yield of azobenzene, chemically attached with DNA molecules, is also measured in order to study the temperature's effect on azobenzene isomerization efficiency.

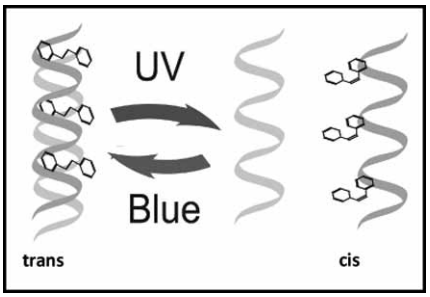

Figure 1: Azobenzene modified DNA switching between dsDNA and ssDNA with light. (See full-color version on inside cover.)

Azobenzene is an organic molecule that can photoisomerize between the *trans*- and *cis*-form. *Trans*-azobenzene can isomerize into the *cis*-form under UV light, and the reverse will happen under blue light. Azobenzene can be chemically attached to DNA [2], which will permit control over whether DNA is a double or single strand using light (Figure 1).

Complementary single-stranded DNA (ssDNA) will form double-stranded DNA (dsDNA) when azobenzene is in the *trans*-form. Under exposure to UV light, a properly formed dsDNA incorporating azobenzene modifications will denature into ssDNA, since the formation of *cis*-azobenzene will induce steric hindrance. Previous research has shown that azobenzene resists photoisomerization into the *cis*-form when it is attached to a perfectly matched dsDNA, as compared with when it is attached to a partially matched dsDNA [3]. This result explains the phenomenon that with the same amount of UV energy, perfectly matched dsDNA stays bound while partially matched dsDNA denatures. This difference in behavior allows light to be used to perform DNA hybridization stringency.

While previous studies have shown photo-controlled DNA stringency in solution, the focus of this summer's research was to attach DNA to a glass substrate and study its photoswitching properties.

Experimental Procedure:

To achieve chip-based DNA stringency, a glass substrate was functionalized with azobenzene modified DNA, 5′-/5Thio MC6-D/AAA AAA AAA TG/ iAzoBenz/ AA/iAzoBenz/ CT/iAzoBenz/ AA/iAzoBenz/ CG-3′. A silanized glass slide was covered with a hybridization chamber that was filled with succinimidyl 4-(p-maleimidophenyl)butyrate, SMPB, overnight. Azobenzene was added for six hours and bonded to the SMPB. Unbound SMPB was pacified with 6-mercapto-hexanol for thirty minutes.

A target strand of DNA was attached to the azobenzene DNA for two hours. The glass was exposed to UV light for two hours. Then DNA modified AuNP were inserted into the chamber for one hour. A silver enhancement solution was added for ten minutes so that the silver ions ionized around the AuNP creating a spot where the AuNP remained.

Quantum yield is a calculation based on how much *trans*-azobenzene has isomerized into *cis*-azobenzene divided by the number of photons [4]. To measure quantum yield, a solution of ssDNA containing azobenzene was prepared. The experimental apparatus for calculations consisted of an Agilent 8453 UV-Vis spectrometer, UV LEDS, a temperature controller, and a stirring plate. A photodiode was used to measure the UV light intensity before photoswitching. The DNA solution was placed in a cuvette and allowed to equilibrate in the apparatus without UV exposure for an hour. After the time elapsed, the solution was exposed to the UV light, and UV-Vis spectra were taken over the next hour at specific times. The data from the spectra was collected focusing on the 330 nm wavelength. This data was then analyzed with a curve-fitting program which created a numerical analysis of the quantum yield as the azobenzene transformed from *trans* to *cis*.

Result and Conclusions:

When looking at the glass slides that had been silver enhanced, a solid grey square was expected when a perfectly matched target strand of DNA was present. However, when it was a partial match, the intensity of the grey was expected to be less. This research focused on perfecting these steps to make the process more effective. To do this, the different steps were analyzed. From this, the importance of attaching the DNA in high quantities to the glass was understood. Otherwise, the AuNP could directly attach to the glass via non-specific interactions. This would create a false positive when the silver enhancer was used.

Another key factor was the age of the DNA attached to the glass (Figure 2 and Figure 3). From the figures, it is shown that the newer DNA allowed for a greater difference for observation of perfectly matched DNA compared to completely mismatched DNA. This shows that the older DNA began to break down and allowed the AuNP to directly attach to the glass.

The quantum yield was studied for A-azo, 5′-AAA AAA AAA /iAzoBenz/ AAA AAA AAA-3′, and T-azo, 5′-TTT TTT TTT/ iAzoBenz/TTT TTT TTT -3′. Research has shown that A-azo is more rigid than T-azo [5]. Because of the differing rigidity, the effect of temperature on the DNA strands was studied. A-azo at 29°C had a quantum yield of 0.044 ± 0.001, while at 37°C the quantum yield was 0.053 ± 0.00005. T-azo at 29°C had a quantum yield of 0.067 ± 0.014, while at 37°C the quantum yield was 0.064 ± 0.016. A-azo had a 19.5% increase in quantum yield at higher temperatures, and T-azo had a 5.1% decrease in quantum yield at higher temperatures.

As a result, it can be concluded that the higher temperatures have a greater effect on the more rigid DNA.

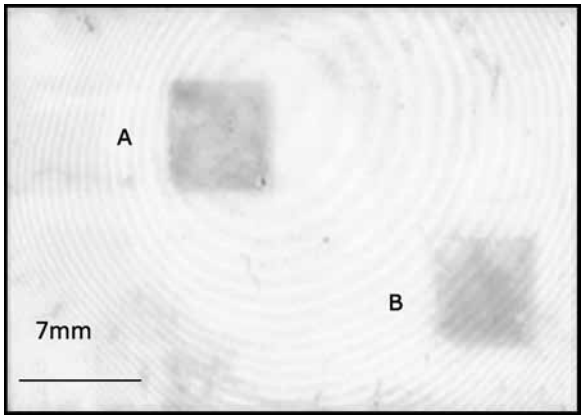

Figure 2: Old DNA; A) Perfectly matched DNA, and B) Mismatched DNA.

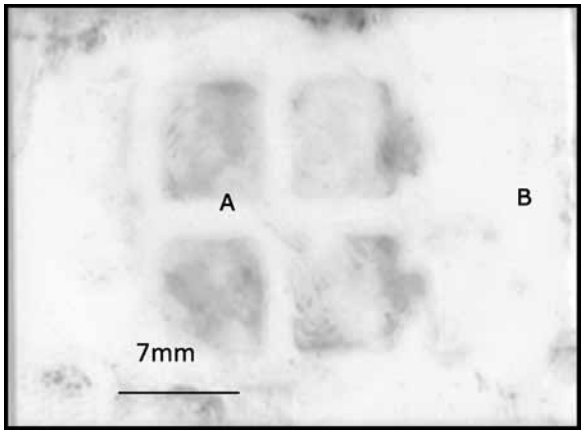

Figure 3: New DNA; A) Perfectly matched DNA, and B) Mismatched DNA.

Acknowledgments:

This researcher would like to acknowledge the NNIN REU Program funded by NSF as well as the Ginger lab, especially Yunqi Yan for her guidance as mentor and David Ginger as the Principal Investigator. Additionally, Mack Carter, as site coordinator, was a valuable resource.

References:

[1] Mirkin, C. et al. Nature, 382, 607, 1996.
[2] Asanuma, H., et al. Nature Protocols, 2, 203, 2007.
[3] Yan, Y.Q., et al. Nano Lett., 12, 2530-2536, 2012.
[4] Yan, Y., et al. Journal of the ACS, 135 (22), 8382-8387, 2013.
[5] Goddard, N. L., et al., Phys. Rev. Lett., 85, 2400-2403, 2000.

Inkjet Printed Interconnects for Multilayer Flexible Electronics

J. Daniel Binion
Electrical Engineering, Grove City College

NNIN REU Site: Microelectronics Research Center, The University of Texas, Austin, TX
NNIN REU Principal Investigator: Prof. Ray T. Chen, Electrical and Computer Engineering, The University of Texas at Austin
NNIN REU Mentor: Dr. Harish Subbaraman, Omega Optics, Austin, TX
Contact: binionjd1@gcc.edu, raychen@uts.cc.utexas.edu, harish.subbaraman@omegaoptics.com

Abstract:

We have developed a method to fabricate fully interconnected flexible multilayer circuits at a high rate using inkjet printing. Ink containing silver nanoparticles was used for the conducting layers, and SU-8 2002 photopolymer was used for the insulating layers. During fabrication, vias with diameters between 65 μm 0and 100 μm were printed consistently, and the measured resistance of the multilayer interconnects differed little from that of single layer circuits. Bend tests revealed a slight increase in resistance, which stabilized with repeated bending.

Introduction:

Inkjet printing is emerging as an efficient and versatile method for the mass production of flexible electronic devices, such as organic light-emitting diode (OLED) displays, phased-array antennae and radio-frequency identification (RFID) tags. Many such devices require complex circuitry, which can take up considerable space. Thus, there is need for a method to create multilayer circuits in order to make the devices more efficiently utilize the available real estate.

The main objective of this project was to develop a method to reliably create multilayer interconnections for printed electronics at a high rate. The aim was to consistently create via holes that had a diameter of 100 μm or less. In addition, the process needed to be completely additive and able to be implemented using a high speed roll-to-roll printer for high throughput manufacturing.

Experimental Procedure:

The printing process involved printing a bottom conducting layer on a flexible Kapton® substrate, followed by a middle insulating layer containing via holes, and finally a top conducting layer, which connected to the bottom layer through the vias. Silver nanoparticle ink was used for the conducting layers and SU-8-2002 photopolymer was used for the insulating layer. These materials were chosen because they were readily available; however, this technique can be implemented using any printable material ink.

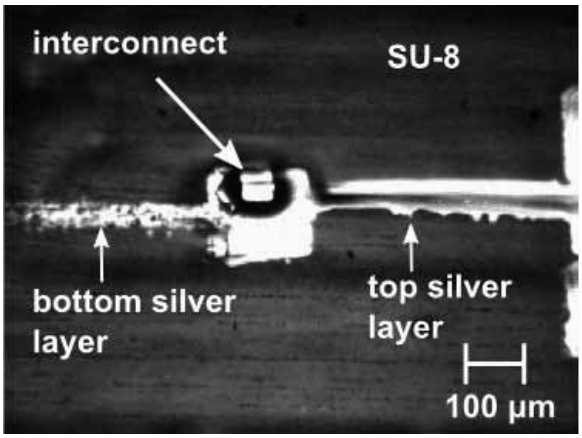

Figure 1: Optical image of multilayer interconnect.

The circuit elements were designed using AutoCAD and printed using a Fujifilm Dimatix Materials Printer, DMP 2800. The layers were aligned using ink-jet printed silver alignment marks on the flexible substrate and the printer's fiducial camera. The bottom silver layer was printed on the substrate and annealed at 150°C for permanency and conductivity. The SU-8 layer containing via holes was then printed on top of the bottom silver layer and cured using heat and ultraviolet radiation. The SU-8 was treated with oxygen plasma to increase its wettability. The entire structure was heated at 150°C to prepare the SU-8 surface for the top silver layer. The top silver layer was printed and annealed on the SU-8 with interconnects to the bottom layer through the vias (Figure 1).

In order to determine the minimum printable via hole size, we printed holes with sizes ranging from 20 μm to 180 μm using SU-8, (100 holes of each size), and determined how many were left open after printing. The minimum printable hole diameter was 120 μm in the design file, but the printed diameter was between 65 μm and 100 μm due to the viscosity of the SU-8. Ninety-nine percent of the holes of this size were open.

A test structure was printed with one via hole in the insulating layer connecting a top conductor to a bottom conductor.

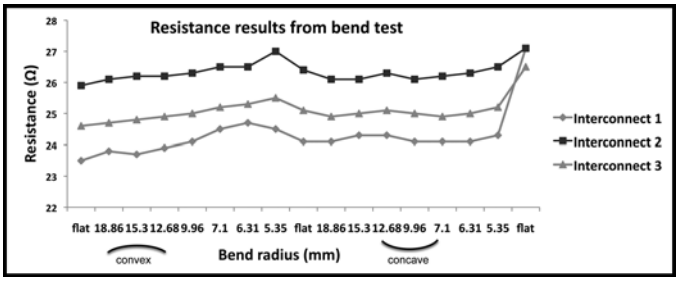

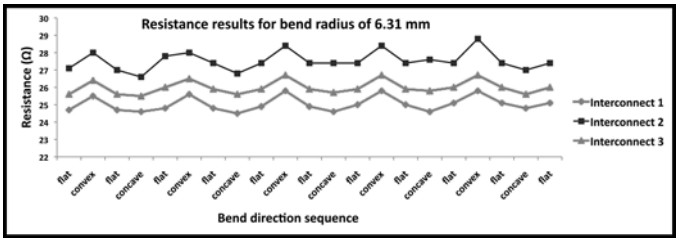

Figure 2, top: Resistance of test structure during first bend test sequence.

Figure 3, bottom: Resistance of test structure during second bend test sequence.

A digital multimeter was used to measure the resistance of the test structure. The structure was then wrapped around cylindrical rods of different radius, and a multimeter was used to measure the resistance at each bend radius.

Finally, a multilayer daisy-chain test structure was constructed to demonstrate continuity through multiple interconnects, and insulation between unconnected conductors.

Results:

The measured resistance of the test structure was 34.33 Ω. Assuming an average thickness of 0.4 μm [1] we calculated the resistivity to be 4.08×10^{-8} Ω.m and the sheet resistance to be 0.10 Ω/square. These values are both well within the range of published specifications for silver ink [1], however, they can be further improved by optimizing the annealing conditions.

Resistance of the test structure increased with decreasing convex bend radius, as expected, with slight decreases for concave bending (Figure 2). A large increase in resistance was observed in the flat state after concave bending. The increases in resistance were due to silver particles in the via being stretched apart, and the decrease in resistance for concave bending was due to the particles being compressed and forming a stronger contact [2].

An additional bend test was performed using a single bend radius of 6.31 mm in order to determine whether resistance would stabilize or continue to increase with repeated bending. Small fluctuations in resistance in the bent positions were observed, but resistance in the flat position stabilized for the last three to five measurements (Figure 3).

The daisy-chain structure successfully demonstrated continuity between interconnected conductors with acceptable resistance, and insulation between unconnected conducting layers.

Conclusions:

Our goal of developing a fully inkjet printed interconnection process for flexible electronics was successfully achieved. The via hole size was small enough to fit our constraints and the resistance of the interconnects proved to be stable with repeated bending. Unlike current interconnection methods, this process is completely additive and no chemicals are needed to remove material. This process can be implemented using a high speed roll-to-roll printer for high throughput manufacturing in the future.

Acknowledgments:

This work was funded by the National Science Foundation and the National Nanotechnology Infrastructure Network Research Experience for Undergraduates Program. The author would also like to thank Ray T. Chen, Harish Subbaraman, and Xiaohui Lin for their guidance and support.

References:

[1] Cabot Conductive Ink CCI-300 Data Sheet, Cabot Printed Electronic Materials. Retrieved July 15, 2013, www.cabot-corp.com/wcm/download/en-us/nb/ATTH4YZ5.doc

[2] Pham, et al., "Self-aligned carbon nanotube thin-film transistors on flexible substrates with novel source-drain contact and multi-layer interconnection," IEEE Trans. Nanotechnol. vol 11, no. 1, pp 44-50, 2012.

Investigation of Molybdenum Disulfide Transistors with Aluminum Oxide Passivation

Marc Castro
Electrical Engineering, University of Texas at San Antonio

NNIN REU / NASCENT Site: Nanomanufacturing Systems for Mobile Computing and Mobile Energy Technologies, The University of Texas at Austin, Austin, TX
NNIN REU / NASCENT Principal Investigator: Dr. Deji Akinwande, Electrical Engineering, University of Texas at Austin
NNIN REU / NASCENT Mentor: Sherry Chang, Electrical Engineering, University of Texas at Austin
Contact: marc.castro@ieee.org, deji@ece.utexas.edu, sherry0501@gmail.com

ELEC

Abstract:

Two methods were investigated as a means of achieving conformal nucleation of aluminum oxide (Al_2O_3) on molybdenum disulfide (MoS_2). The first method consisted of depositing a thin metal layer on MoS_2, and the second method was treating the MoS_2 with oxygen (O_2) plasma. Next, four types of MoS_2 back gate transistors were fabricated and treated with a different metal layer or O_2 plasma. Electrical measurements were then compared.

Introduction:

To further Moore's law, two dimensional (2D) materials are being investigated as a possible replacement for silicon in transistors, because of their ability to achieve a thickness smaller than 1 nm. The 2D material graphene, which has been extensively investigated, does not intrinsically possess a bandgap, preventing it from being used in logic transistors; on the other hand, the 2D material MoS_2 does possess a bandgap. Although logic transistors have been fabricated using MoS_2 [1], there has been difficulty in obtaining a uniform deposition of the dielectric Al_2O_3 on MoS_2, as shown in Figure 1. The difficulty has been attributed to the lack of dangling bonds on MoS_2. Several treatments have been suggested to improve nucleation by intentionally producing nucleation sites on MoS_2 [2, 3]. We examine two of these methods. First is the deposition of a thin layer of metal, referred to as a seed layer. And second is an oxygen plasma treatment.

The purpose of our investigation was to find a method that would enable the production of a high quality top gate dielectric that would not degrade the performance of the device. In this investigation, we fabricated back gate transistors. Once a suitable method is determined, fabrication of top gate MoS_2 transistors with Al_2O_3 passivation will be pursued.

Experiment:

The MoS_2 flakes were obtained using micromechanical exfoliation and transferred to an Si wafer with 280 nm of SiO_2. The wafer was then split into four pieces. Three of the samples each had a different seed layer of aluminum (Al), chromium (Cr), or titanium (Ti); all were deposited by electron beam physical vapor deposition (EBPVD), with an average thickness of 1 nm. For the oxygen plasma treatment, a wafer with MoS_2 was placed in a reactive ion etcher (RIE) for 30 s, at room temperature, with a power of 55 W and a flow rate of 19 sccm. Using atomic layer deposition (ALD), 25 nm of Al_2O_3 was deposited on all four samples at 200°C. Inspection was done using an atomic force microscope (AFM). As shown in the AFM image in Figure 2, all four treatments did achieve conformal nucleation of Al_2O_3 on the MoS_2 flakes.

Figure 1: Al_2O_3 deposition on MoS_2 flakes with no treatment. The black regions are devoid of Al_2O_3.

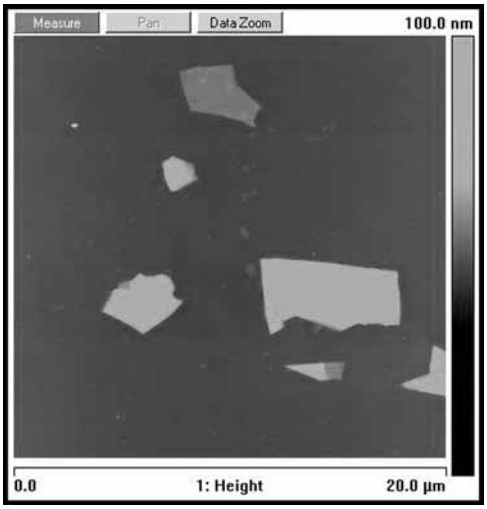

Figure 2: Uniform deposition of Al_2O_3 on MoS_2 flakes with Al seed layer. All treated samples produced similar results.

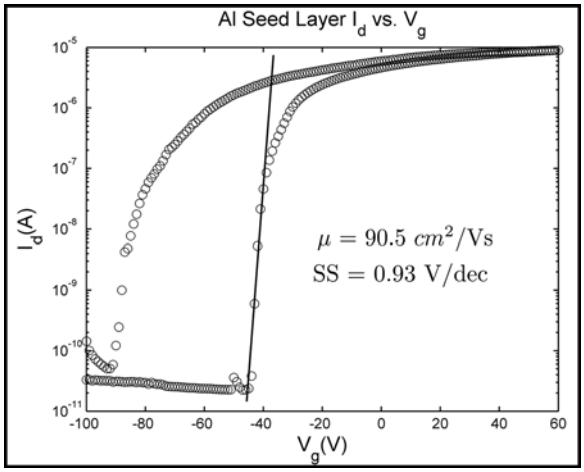

Figure 3: I_d vs. V_g hysteresis of Al seed layer transistor.

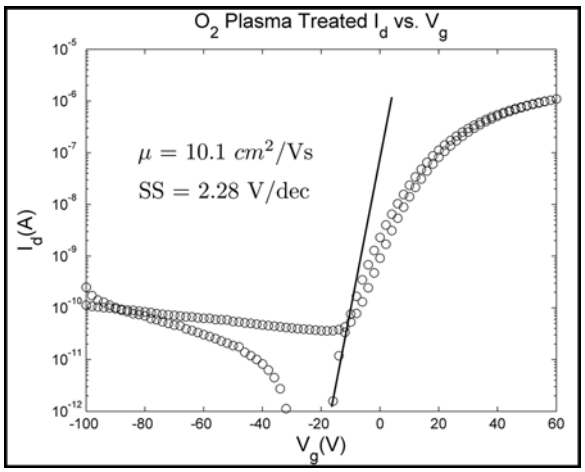

Figure 4: I_d vs. V_g hysteresis of O_2 treated transistor.

For the fabrication of the back gate transistors, four wafer samples with MoS_2 flakes had two layers of resist spin-coated onto the substrate, with MMA on the top and PMMA on the bottom. Next, the metal contacts were fabricated employing electron beam lithography for the pattern, followed by the deposition of 50 nm of gold using EBPVD, and finally lift-off. Then, each of the four samples received a different treatment, just as the four samples mentioned above. Three had a different seed layer; the thicknesses were 8Å for Al and 6Å for both Cr and Ti. The fourth sample was treated with O_2 plasma. Lastly, Al_2O_3 was deposited. The electrical measurements were collected using a two point probe, where the substrate served as the bottom gate.

Results:

The electrical measurements that were collected from the transistors included mobility and the subthreshold slope. From the results, it appeared that, out of the four, the best performance came from the transistor with the Al seed layer, with a mobility of 90.5 cm^2/Vs and a subthreshold slope (SS) of 0.93 V/dec, as shown in Figure 3. The Cr seed layer transistor had a mobility of 47.9 cm^2/Vs and a SS of 3.01 V/dec. And the Ti seed layer transistor had a mobility of 38.1 cm^2/Vs and a SS of 0.99 V/dec. Finally, the oxygen plasma treated transistor had a mobility of 10.1 cm^2/Vs and a SS of 2.28 V/dec.

Although the O_2 plasma treated transistor did not have impressive numbers, its I_d vs. V_g graph was intriguing, as seen in Figure 4. The threshold voltage shifted significantly to the right and the hysteresis curve was narrower than any of that produced by the seed layer transistors. Further analysis showed that the poor measurement numbers were not entirely due to the O_2 treatment and could be mostly attributed to the MoS_2 flakes. This finding is promising for further investigations of the O_2 treated transistors.

Conclusions:

Two methods were investigated as a means of achieving conformal nucleation of Al_2O_3 on MoS_2. The first treatment was the deposition of a seed layer, and the second was an O_2 plasma treatment. From the electrical measurements, it appears that the Al seed layer transistor had the best improvement in mobility, and the O_2 treated transistor showed promise for modifying the threshold voltage and the hysteresis effect. Future work includes an investigation to see if the current results are reproducible, and further analysis will be done to determine the cause of the observed effects.

Acknowledgements:

Thank you, Dr. Akinwande, for welcoming me into your group. Thank you, Sherry, for being my mentor. And thank you to the NNIN REU Program, NASCENT, and NSF for making this opportunity possible.

References:

[1] Radisavljevic, et al., Nature Nanotechnology 6, 147-150 (2011).

[2] Liu, et al., Applied Physics Letters 100, 152115 (2012).

[3] Yang, et al., Applied Materials and Interfaces 5, 4739-4744 (2013).

Fabrication of Accelerometers using Paper MEMS Substrates

Marco De Lira
Mechanical and Energy Engineering, University of North Texas

NNIN REU Site: Howard Nanoscale Science and Engineering Facility, Howard University, Washington, DC
NNIN REU Principal Investigator: Dr. Gary L. Harris, Electrical Engineering, Howard University
NNIN REU Mentor: Dr. William L. Rose, Electrical Engineering, Howard University
Contact: marcodelira@my.unt.edu, gharris@msrce.howard.edu, wbullrose@gmail.com

Abstract:

The purpose of this research project was to make an accelerometer using microelectromechanical systems (MEMS) with paper as the substrate. This method was chosen because it was inexpensive; the fabrication process was fast and did not require specialized tooling or cleanroom time. Piezoresisitive material changes resistance and or capacitance when force is applied. We designed a number of experiments to determine this relationship. Our test design consisted of paper cantilevers on which piezoresisitive carbon ink and conductive silver ink were painted. Our results indicated a linear relationship between the applied force and resistance and capacitances shown by from the respective graphs. Next we designed an accelerometer by arranging a number of cantilevers in a circular configuration with a central seismic mass. We programmed an Arduino Uno to measure the change in capacitance and correlate that to a change in voltage. The measured voltage we then converted to acceleration and the subsequent G-Force.

Introduction:

The applications and uses of microelectromechanical systems (MEMS) have grown significantly over the last decade. MEMS are microelectronic devices that can be used as sensors, actuators, and energy conversion devices and much more [1]. Our goal for the research project was to fabricate an accelerometer using paper and piezoresistive material. We observed and correlated the relationship between the applied force and change in resistance and capacitance on the piezoresistive material [2]. Using this relationship of piezoresisitive material, we designed and implemented an accelerometer for the measurement of concussive forces. By using paper as the substrate for the accelerometer, it will greatly reduce the cost of fabrication without significantly reducing the performance of the device.

Fabrication and Experimental Procedure:

We designed paper MEMS cantilevers to test and correlate the relationship between force and capacitance. We used the software Corel Draw X5 to design our cantilevers and an Epilog Helix Laser to cut out the design of the cantilevers.

Next carbon-based piezoresistive was painted on the fulcrum of the cantilever and a silver-based conductive ink for the contacts.

We used a Wheatstone bridge circuit consisting of two known resistors a potentiometer and our MEMS to measure resistance changes of the paper MEMS cantilever with applied force [3]. A micro-probe holder was used to lower the cantilever end onto the weighing balance, to determine the specific force on the cantilever. By applying a force onto the cantilever, a compressive force was transferred to the piezoresistive material causing a change in resistance. The potentiometer was adjusted until the voltage read zero. The resistance of the potentiometer was then read using a multi meter.

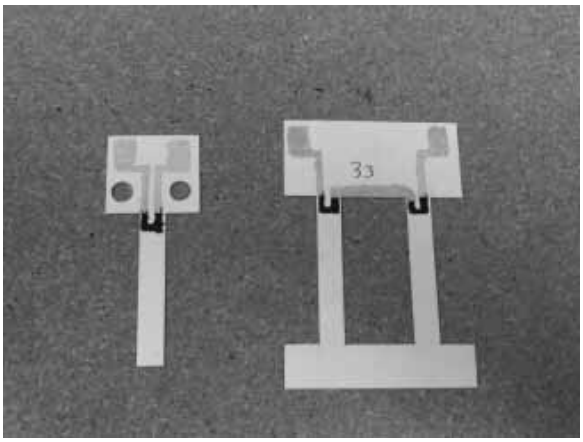

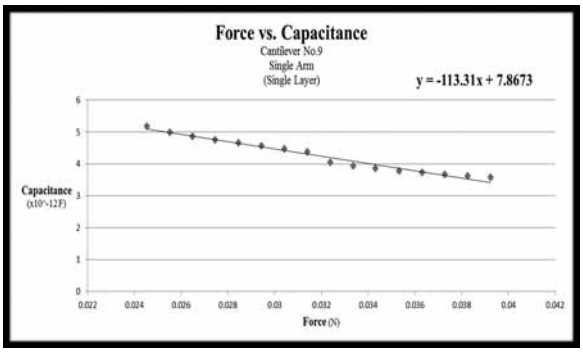

Figure 1, top: Single and double arm cantilever.

Figure 2, bottom: Force vs. capacitance single arm cantilever (single layer).

By applying an equation for the Wheatstone bridge, the unknown resistance of the cantilever was calculated and therefore correlated to the applied force.

Capacitance changes were tested using the micro-probe holder to adjust the force on the balance. A capacitance meter was used to measure the change in capacitance, which could then be converted, to a force. Experiments were made using single arm cantilevers, and double arm cantilevers, as well as single and double layers of each (Figure 1). The sensitivity of each cantilever was determined from the slope of the graphs. From our results we were able to establish a linear relationship between the applied force and the change in resistance and capacitance (Figure 2).

For the next part of our research, we designed and fabricated an accelerometer to measure concussions. The accelerometer was fabricated using four cantilevers, four springs in a circular configuration, with a seismic mass in the center. When there is an applied force the movement of the seismic mass translated the force by the cantilevers to the piezoresistive material causing a change in capacitance of the MEMS. We used an Arduino Uno to convert this capacitance change to a useable voltage from which we were able to calculate the G-Force (Figure 3). We fabricated, tested and optimized several accelerometers to increase the accuracy of the accelerometer.

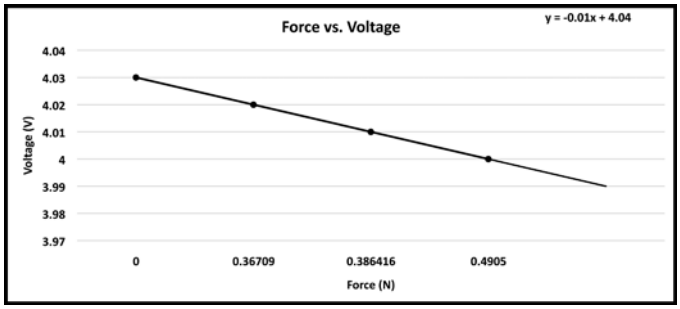

Figure 3: Applied force vs. voltage.

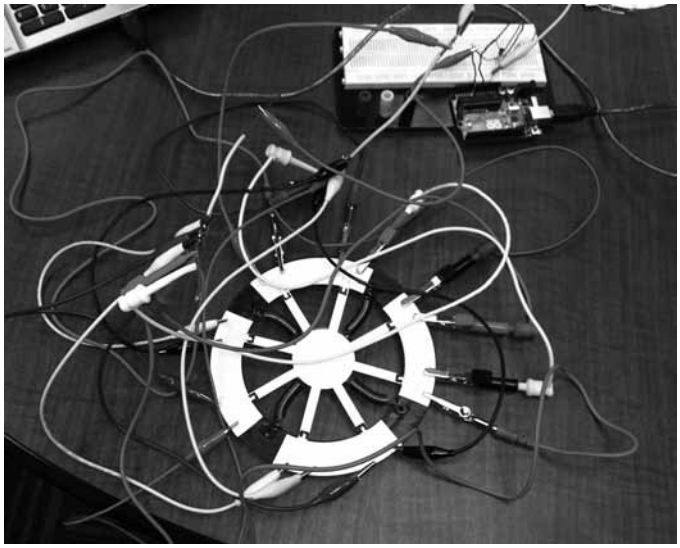
Figure 4: Accelerometer final design.

Results and Conclusions:

We successfully designed and implemented a series of experiments to establish a linear relationship between applied force and the change in resistance and capacitance of the piezoresistive carbon material. Using this relationship we designed and fabricated an accelerometer constructed from paper capable of measuring concussive forces. This fabrication was inexpensive and gave us effective results.

Acknowledgements:

I would like to thank Dr. William L. Rose, Dr. Gary L. Harris, and all the staff at Howard Nanoscale Science and Engineering Facility (HNF). I am thankful to the National Nanotechnology Infrastructure Network Research Experience for Undergraduates (NNIN REU) program, and the National Science Foundation (NSF) for giving me this great internship opportunity.

References:

[1] http://www.memsnet.org/mems/what_is.html
[2] http://www.nanomotion.com/piezoelectric-effect.html
[3] http://www.engineersedge.com/instrumentation/wheat_stone_bridge.htm
[4] http://www.gracey.co.uk/downloads/accelerometers.pdf

Nanoscale High-Speed Transparent Electronics using E-Beam Patterning of Zinc Tin Oxide Thin Film Transistors

Andinet Desalegn
Material Science and Engineering, University of Maryland at College Park

NNIN REU Site: Lurie Nanofabrication Facility, University of Michigan, Ann Arbor, MI
NNIN REU Principal Investigator: Dr. Becky (R.L.) Peterson, Electrical and Computer Engineering, University of Michigan
NNIN REU Mentor: Wenbing Hu, Electrical and Computer Engineering, University of Michigan
Contact: andinetdes23@gmail.com, blpeters@umich.edu, wbhu@umich.edu

Introduction:

Zinc tin oxide semiconductors can be used to produce transparent thin film transistors. These transistors are needed for many new applications in heads up displays and invisible microsystems. The focus of this project was to miniaturize the gate length of zinc oxide-based transistors to below 100 nanometers and characterize the performance of these transistors as a function of their gate length. As the gate length of a transistor is reduced the drive current increases, thus increasing circuit speed and performance [1].

Here, we used electron beam (e-beam) lithography to fabricate narrow gate length zinc tin oxide transistors. A beam of electrons bombards a layer of resist, creating the desired patterns. Since the size of the beam is very narrow we are able to fabricate very small features. However, when using e-beam patterning to create sub 100-nm geometries, we must take into account the proximity effect. The proximity effect involves the back-scattering of electrons once they penetrate the resist and substrate and interact with other atoms. Back-scattering of electrons causes further exposure and enlargement of the desired pattern [2].

Experimental Procedure:

First, we characterized the e-beam exposure and lift off of molybdenum (Mo) and titanium (Ti) electrodes with narrow gaps using poly(methyl methacrylate) — PMMA — resist on glass (Corning Eagle XG). Pairs of electrodes had designed gaps ranging from 10 μm to 40 nm. We exposed these structures with dosages of 600, 700, 800, 900, and 1000 microCoulombs/cm^2 using the JEOL 6300FS Electron Beam Lithography System. Lift off was then performed and the electrodes were inspected by scanning electron microscope (SEM) and electrically tested to determine whether the gap was open (as intended) or electrically shorted (indicating incomplete patterning or lift off).

The detailed process is as follows. We spun a 10 nm thick layer of PMMA A2% and soft baked for three minutes at 180°C. A 200 nm layer of e-spacer was spun on top of the resist and soft baked at 110°C for two minutes. E-spacer is a conductive polymer needed to ground the glass substrate and prevent electron deflection when using the e-beam. After e-beam lithography, the sample was dipped in distilled water for 45 seconds to strip the e-spacer, the PMMA resist was developed in 1:3 methyl isobutyl ketone : isopropyl alcohol for 30 seconds, and the sample was rinsed in isopropyl alcohol for 30 seconds. Finally, 40 nm of source/drain metal was deposited. For liftoff, the samples were left in a room-temperature acetone bath overnight, following which the bath is heated at 60°C for 1.5 hours with moderate sonication.

Once the narrow-gap electrode process was complete, we used photolithography to pattern the larger source/drain structures needed for electrical testing. E-beam lithography is a serial write process and would require a massive amount of time to write these structures. We used SPR 1813 resist and exposed using an MA/BA6 contact aligner tool. We developed the resist in MF 319; 100 nm of the secondary source/drain material was then deposited and lifted off in acetone. The electrodes were characterized using a SEM and current-voltage (I-V) measurements were taken using an Alessi probe station and HP 4155A semiconductor parameter analyzer.

For transistor processing, the samples additionally contained patterned gate metal, insulator, and patterned semiconductor layers which were prepared before the source/drain metal was deposited.

Results and Conclusions:

Figure 1 plots the measured gap between e-beam patterned electrodes as a function of the designed gap width and the e-beam dose. Gaps larger than 100 nm were not significantly affected by the differences in dosage. Using evaporated Ti, we consistently obtained separated electrodes for gaps of 40 nm and above. The electrode separation was verified by electrical testing, which indicated a very high resistance of greater than 5×10^8 Ohms, as seen in Figure 2. Electrodes with gaps down to 20 nm were fabricated using Ti (Figure 3), although their yield was not consistent. In contrast, sputtered Mo had difficulty lifting off for electrode gaps of < 500 nm. We then fabricated working transistors using photolithography to determine the effectiveness of a new separated gate and gate insulator process. Figure 4 shows electrical data for a transistor with a channel width of 100 μm and a channel length of 6 μm. The low off current and gate current, as well as the large on current indicate that the transistor is working properly.

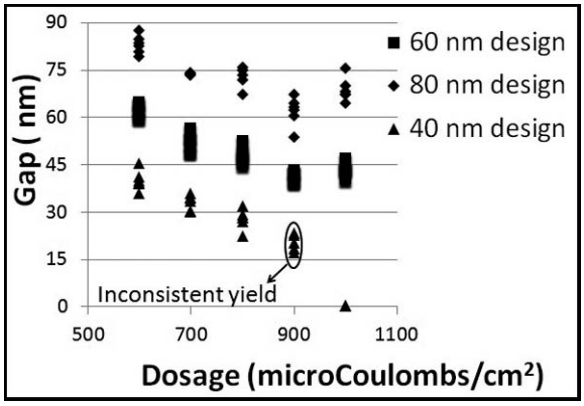

Figure 1: Electrode gap as a function of electron beam dose.

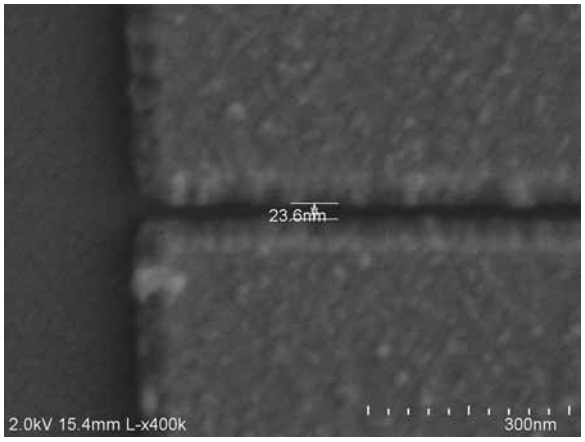

Figure 3: Open gap between 40 nm designed titanium electrodes.

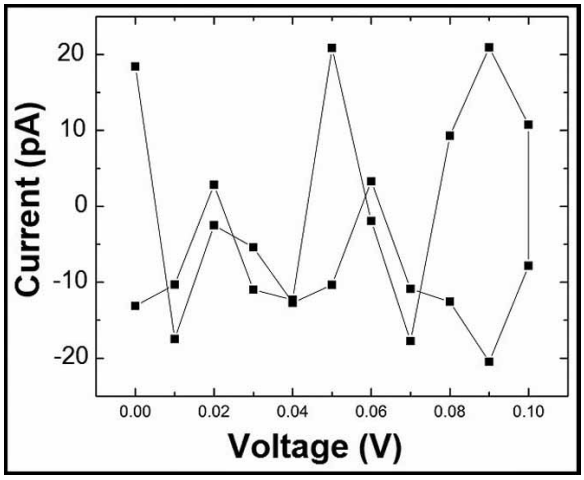

Figure 2: I-V measurement of 40 nm designed titanium electrode, indicating an open gap.

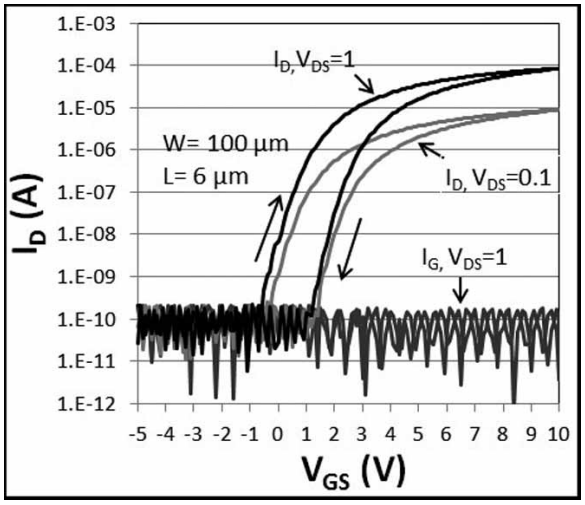

Figure 4: Electrical characteristics of photolithographically-defined transistor.

In conclusion, we were able to use e-beam lithography on transparent glass substrates to fabricate electrodes with sub 100-nm gaps. Since we were using a non-conductive substrate, a conductive polymer layer was needed to disperse charge build up. Evaporated titanium electrodes with gaps of 40 nm and above and sputtered molybdenum electrodes with gaps of 500 nm and above were consistently produced. We believe the conformality of sputtering causes difficulty for molybdenum lift off. We also were able to produce working transistors using a new separated gate and gate insulator process.

Future Work:

With successful transistors produced using photolithography, the next step is to integrate the narrow gap electrodes made using e-beam lithography into the new gate and gate insulator process to form transistors with sub-100 nm gate lengths, and then characterize their performance.

Acknowledgments:

I would like to thank my principal investigator and my mentor for their help throughout my research. I would also like to thank the Lurie Nanofabrication Facility staff, especially Dr. Vishva Ray, for their support. Finally, I would like to acknowledge financial support from the National Science Foundation for NSF BRIGE Award #ECCS1032538 and the National Nanotechnology Infrastructure Network Research Experience for Undergraduates (NNIN REU) Program.

References:

[1] Pierret, Robert F. "Semiconductor Device Fundamentals," 1st edition, Addison Wesley, 1996. Print.

[2] Yang, Xiang. "Electron Beam Lithography - Application." Penn Engineering. University of Pennsylvania, http://www.seas.upenn.edu/~yxiang/courses/Final%20Paper_EBL_Xiang%20Yang_ESE%20574.pdf.

Zinc Oxide Based Ultraviolet Solar Cells for Self-Powered Smart Window Application

Benjamin Helfrecht
Materials Engineering, Purdue University

NNIN REU Site: ASU NanoFab, Arizona State University, Tempe, AZ
NNIN REU Principal Investigator: Dr. Hongbin Yu, Electrical Engineering, Arizona State University
NNIN REU Mentor: Ebraheem Ali Azhar, Electrical Engineering, Arizona State University
Contact: ben.helfrecht@gmail.com, hongbin.yu@asu.edu, eazhar@asu.edu

ELEC

Abstract:

A controlled study was completed in order to determine the best structure for a zinc oxide (ZnO) based solar cell that could be used to drive an electrochromic stack. Gold (Au), aluminum (Al), silver (Ag), and the organic polymer poly(3,4-ethylenedioxythiophene) poly(styrenesulfonate), or PEDOT:PSS, were used as top contacts for the device with the aim of creating a Schottky barrier junction with ZnO. The devices were fabricated on both silicon (Si) and indium tin oxide (ITO) substrates. The most effective solar cell structure showed an open circuit voltage (V_{oc}) of 1.90 V and a short circuit current density (J_{sc}) of 0.180 μA/cm^2. However, the device had an ideality factor of 1.66 and an efficiency of 0.057%, indicating that several loss mechanisms are hindering its performance.

Introduction:

Integrating electrochromic films into existing business and residential windows has been proposed as a way of reducing building power consumption by cooling it in a passive manner. A voltage can be applied to the electrochromic stack, thereby increasing its opacity and blocking the solar infrared and ultraviolet radiation from entering the structure and heating the interior. ZnO based solar cells are promising candidates for supplying such a voltage, as ZnO possesses a wide bandgap, is visibly transparent in thin film microstructures, and forms a large Schottky barrier with a variety of metals and organic compounds, including Au (0.71 eV) [1], Ag (0.69 eV) [2], and PEDOT:PSS (0.9 eV) [3].

In theory, a device containing a ZnO-metal Schottky diode is capable of driving an electrochromic stack.

Experimental Procedure:

The solar cells to be investigated were fabricated using highly-doped Si (20 mΩ/cm) and ITO coated glass substrates that were sputtered with 1 μm of ZnO. All of the devices were then treated with an oxygen plasma for fifteen minutes to clean the surface and to increase its hydrophilic nature. PEDOT:PSS was then dynamically spun onto half of the devices at 5000 rpm for 60 s and then annealed on a hot plate in air at 160°C for five minutes. Gold and aluminum top contacts were evaporated onto all of the devices using a shadow mask. Conductive silver paint was also applied to the devices as an inexpensive alternative to evaporated silver contacts. A device schematic is shown in Figure 1.

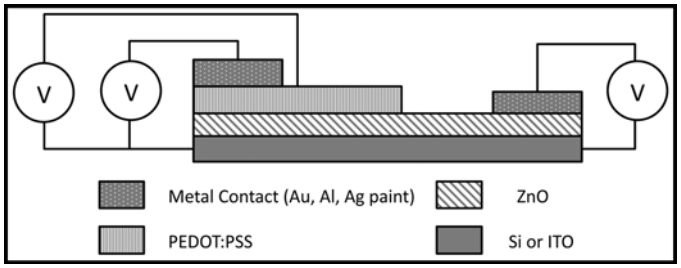

Figure 1: Schematic of a complete solar cell, showing all of the contact configurations that were used.

To characterize the performance of the solar cells, the current-voltage characteristics of each were measured under dark conditions as well as under a halogen white light lamp and a 365 nm ultraviolet lamp.

Results and Conclusions:

The current-voltage (I-V) measurements of the devices proved to be inconsistent, and not all devices exhibited a photovoltaic response. Of the devices that did show a photovoltaic response, the best performance came from one with a Au/PEDOT : PSS/ZnO/Si structure, exhibiting a V_{oc} of 1.90 V and a J_{sc} of 0.180 μA/cm^2. The I-V characteristics and dark current density plot for this device are shown in Figure 2 and Figure 3, respectively. However, the device possessed an ideality factor of 1.66 and an efficiency of just 0.057% and did not exhibit diodic behavior. The devices that did not show a photovoltaic

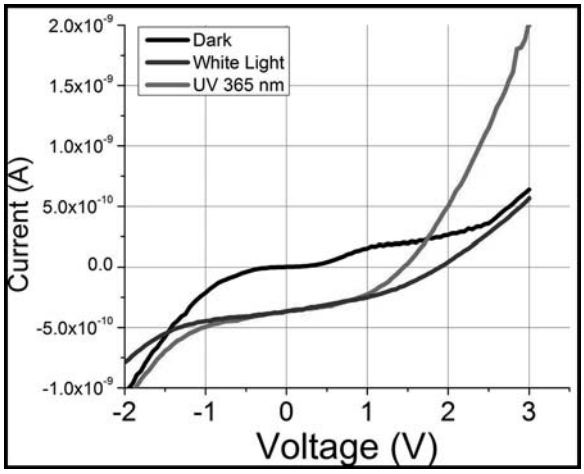

Figure 2: I-V characteristics of the Au/PEDOT:PSS/ZnO/Si device. The offset between the dark and illuminated currents indicates a photovoltaic response. However, the curve does not resemble that of a diode.

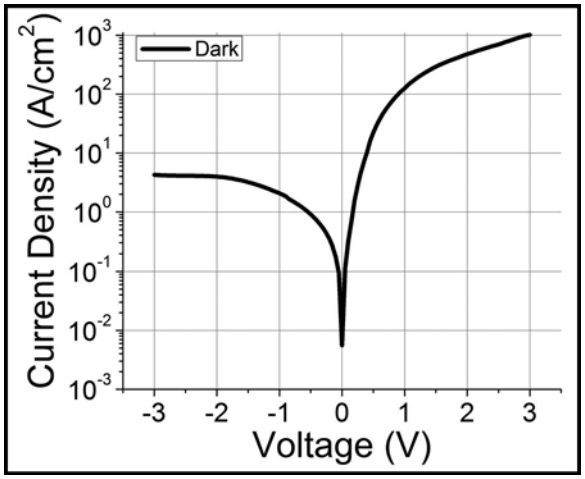

Figure 3: Dark current density plot for the Au/PEDOT:PSS/ZnO/Si device.

response demonstrated consistent rectifying behavior with Au contacts, but the Al and Ag contacts only showed occasional rectifying behavior. None of the PEDOT:PSS contacts showed rectifying behavior.

It is also of note that none of the devices that showed a photovoltaic response also showed rectifying behavior; conversely, the devices that showed rectifying behavior did not show a photovoltaic response. This is likely due to the presence of several loss mechanisms within the devices, including spontaneous polarization, oxygen deficient surfaces, grain boundaries, and recombination at the surface and back contacts. It is believed that recombination is the most significant of these mechanisms.

Future Work:

Deep-level transient spectroscopy must be used to measure the electrical defects so that they can be targeted and mitigated. If recombination is determined to be a major factor in the compromised performance in the solar cells, an electron blocking layer could be introduced to inhibit the process. The V_{oc} and J_{sc}, and efficiency of the devices could also be improved by treating the PEDOT:PSS layer so as to enhance its conductivity. Xia et al. has proposed that dilute sulfuric acid treatments of PEDOT:PSS can enhance its conductivity to ~ 3000 S/cm [4]. P-type doping of the photoactive ZnO layer could also be explored, possibly enabling the use of a p-n junction rather than a Schottky barrier junction.

Acknowledgements:

I would like to thank my Principal Investigator, Dr. Hongbin Yu, and my mentor, Ali Azhar, for all of their help and guidance. I would also like to thank the Center for Solid State Electronics Research and the Leroy Eyring Center for Solid State Science for all of the research support that they provided. Finally, I extend my gratitude to the National Nanotechnology Infrastructure Network and the National Science Foundation for their funding contributions and organization of the Research Experience for Undergraduates program.

References:

[1] B. J. Coppa, C. C. Fulton, S. M. Kiesel, R. F. Davis, C. Pandarinath, J. E. Burnette, R. J. Nemanich, and D. J. Smith, J. Appl. Phys. 97, 103517 (2005).

[2] A. Y. Polyakov, N.B. Smirnov, E. A. Kozhukhova, and V. I. Vdovin, K. Ip, D. P. Norton, and S. J. Pearton, Appl. Phys. Lett. 83, 1575 (2003).

[3] M. Nakano, A. Tsukazaki, R. Y. Gunji, K. Ueno, A. Ohtomo, T. Fukumura, and M. Kawasaki, Appl. Phys. Lett. 91, 142113 (2007).

[4] Y. Xia, K. Sun, and J. Ouyang, Adv. Mater. 24, 2436-2440 (2012).

Researching All-Aluminum n-Type Silicon Solar Cells

Tomoyuki Inoue
Electrical Engineering, the University of Tokyo

NNIN iREG Site: ASU NanoFab, Arizona State University, Tempe, AZ
NNIN iREG Principal Investigator: Professor Meng Tao, Electrical Engineering, Arizona State University
NNIN iREG Mentor: Wen-cheng Sun, Electrical Engineering, Arizona State University
Contact: inoue@hotaka.t.u-tokyo.ac.jp, meng.tao@asu.edu, wen-cheng.sun@asu.edu

Abstract and Introduction:

One of the fundamental bottlenecks for silicon solar cells in reaching terawatt scales is the scarcity of silver (Ag). Furthermore the price of Ag has been rising sharply. We have proposed that Ag should be replaced by other metals. In order to improve these contacts, high doping level layers were fabricated on the both sides of our cells.

Generally, p-type silicon wafers are used in solar cells, but in our research n-type wafers are used. These types of solar cells have enormous potential to be high efficiency solar cells. However they have a few problems due to the surface states on the surface of the p^+-type layer. In order to increase cell performance, an aluminum oxide (Al_2O_3) layer has been chosen for a passivation layer, it is also a dielectric containing a fixed negative-charge density. This effect results in the reduction of surface recombination.

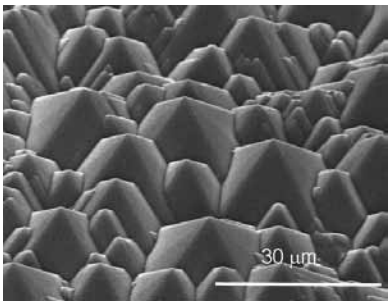

Figure 1: SEM of the surface texturing.

Experiment Procedure:

First the random texturing was fabricated on the both sides of a cell for reducing the reflectance. By using the anisotropic wet etching method, the pyramid shape texturing was fabricated.

Second, the diffusion processes were applied to the samples for fabrication of the cell structure. There were three steps in the diffusion processes. The n^+-type back surface field (BSF) layer was fabricated in the phosphorus diffusion process. This layer worked as a barrier against minority carriers in the n-region. The depth and the donor concentration of n^+-type layer were controlled by firing time and temperature. Boron diffusion was also applied to the cell in order to make a p^+-type layer after the first diffusion. Subsequently the sample was annealed at 1050°C in nitrogen ambient gas. This is called the "drive-in diffusion process." In order to reduce the doping concentration on the each surface of the cell, we applied the drive-in diffusion.

Third, the aluminum was sputter deposited on the both sides. After metallization, the Al_2O_3 was applied on the front surface as a passivation layer. Subsequently the front surface was covered with SiN_x. These SiN_x/Al_2O_3 layers worked as an anti-reflection coating. Finally, the sample was annealed in ambient forming gas ambient at 350°C.

Results:

By using anisotropic wet etching, the pyramid shape texturing was fabricated on the both sides (Figure 1). Reduction of reflectance was observed because of this texturing. Finally, after deposition of SiN_x, the average of reflectance became 4.53% in the range from 300 nm to 1000 nm.

After diffusion processes, depth dependent doping concentrations was measured (Figure 2). From this doping profile, we could observe that the doping concentrations on the both surfaces were still high. It means that the drive-in diffusion did not work.

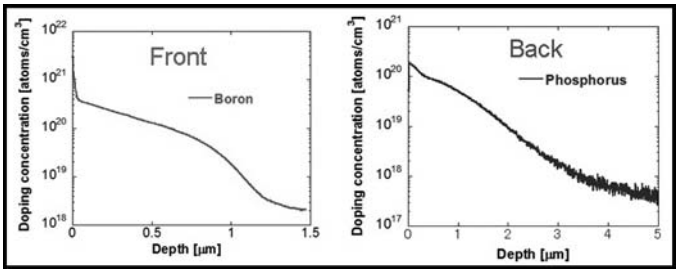

Figure 2: Depth dependent doping concentrations on the both sides.

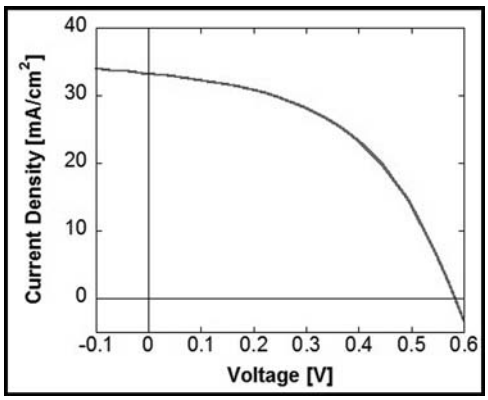

Figure 3: I-V characteristic.

After finishing all processes, all samples showed short-circuited behavior. In order to remove some parts which were short-circuited, the samples were cut into some pieces. After cutting the samples, the I-V characteristic measurement was taken (Figure 3). The surface area was 5 cm^2 and 20% of it was covered with front electrode. From this assumption, each parameter was calculated. The efficiency achieved was 9.3%.

The doping profile indicates the drive-in diffusion did not work. We assume that after the diffusion for fabrication of the p^+-layer, boron silicate glass (BSG) was formed on the surface and then during the drive-in diffusion, the boron diffused into the samples from the BSG. Because of it, the high doping concentrations on the surface were formed and some parts of the samples were short-circuited.

Each parameter was compared with some references [1, 2]. From this comparison and I-V characteristics, low fill factor showed us that there was large leakage current and series resistance (Figure 4). This series resistance included the problems of contacts however we could not investigate them separately. Low open-circuit voltage (V_{oc}) and short-circuit current density (J_{sc}) were mainly because of high recombination rate. From the doping profile, high doping concentrations on the surface and deeper junction helped recombination occur at high rates on the front surface.

Conclusions and Future Works:

In conclusion, an all-aluminum n-type Si solar cell was fabricated. The efficiency achieved was 9.3%. Random texturing was fabricated to reduce the reflectance. From J_{sc} and V_{oc}, high surface recombination was identified for the low efficiency. From the doping profile, the high doping concentrations on the surface reduce diffusion lengths and deeper junction allows recombination near the front surface.

For next steps, we should apply an *in situ* oxidation step in order to remove the BSG after the diffusion process for the p^+-layer. This process is supposed to make it possible to fabricate the samples which have the desired doping profile and do not need to cut into some pieces. Form this effect, the larger surface area of the samples improves the fill factor by reducing the leakage current and series resistance, whereas lower doping concentrations on the front surface help to reduce recombination near the front surface.

Acknowledgments:

I would like to thank my PI, Prof. Meng Tao, and my mentor Wen-cheng Sun for all of their help and guidance. Thanks also to the National Nanotechnology Infrastructure Network International Research Experience for Graduates (NNIN iREG) Program, the National Science Foundation, the Nanotechnology Platform Japan, and the Center for Solid State Electronics Research at Arizona State University for research support and funding.

References:

[1] J. Benick, et al., "High efficiency n-type Si solar cells on Al_2O_3-passivated boron emitter", APL, 92, 253504 (2008).

[2] M. Kesseler, et al., "High-Efficiency Back-Junction Silicon Solar Cell with an In-Line Evaporated Aluminum Front Grid", 37th IEEE Photovoltaic Specialists Conf, 2011.

	J_{sc} [mA/cm^2]	V_{oc} [mV]	FF	η [%]
Our Sample	33	590	0.48	9.3
From Some References	40	700	0.80	23

Figure 4: Comparison each sample parameters with other studies.

Trap Density Analysis of High Dielectric Oxides on III-V Semiconductors

Daniel Loman
Physics, Siena College

NNIN REU Site: UCSB Nanofabrication Facility, University of California, Santa Barbara, CA
NNIN REU Principal Investigator: Dr. Susanne Stemmer, Department of Materials, University of California, Santa Barbara
NNIN REU Mentor: Ms. Varistha Chobpattana, Department of Materials, University of California, Santa Barbara
Contact: dh08loma@siena.edu, varistha@mrl.ucsb.edu, stemmer@mrl.ucsb.edu

Abstract and Introduction:

The prospect of III-V semiconductors offer a higher efficiency alternative to the commonly used silicon, which is currently facing size limitations. One of the major problems surrounding the III-V semiconductors is the high trap density (D_{it}) between the oxide and semiconductor interfaces. In this project, metal-oxide-semiconductor capacitors (MOSCAPs) were fabricated using different annealing processes and time frames. Three experiments were conducted on the MOSCAPS for midgap D_{it} analysis. First, three samples were annealed using forming gas, nitrogen (N), and oxygen (O), respectively. Next, three samples were annealed to 300, 350, and 400°C. Finally, a sample which underwent metal deposition one week after being annealed was compared with a sample with no such time delay. Capacitance-voltage (CV) and conductance-voltage (GV) data was extracted from each sample using the impedance analyzer and manipulated to reveal information about the midgap D_{it}.

Experimental Procedure:

The MOSCAP samples were fabricated in several steps. Initially, an $In_{53}Ga_{47}As$ substrate was doped with silicon and wet cleaned. The sample was put in the atomic layer deposition (ALD) reactor at 300°C, where it was cleaned for nine cycles with N_2 plasma/TMA, followed by oxide deposition of 35 cycles HfO_2 to the top surface. The sample was then annealed to various temperatures in different gasses. Using the thermal evaporator, Ni was deposited to the top of the sample while Cr and Au were deposited to the bottom.

Both the conductance and Terman methods were used for data analysis, and there are several differences between the two. The conductance method uses only raw data, while the Terman method uses raw and ideal data. The conductance method is most useful at low frequencies (1 kHz), while the Terman method is most useful at high frequencies (1 MHz). Finally, the conductance method shows only the midgap D_{it}, which is around 0.3 eV, while the Terman method shows a broader range for the trap density.

In this research, however, the Terman method showed results that were either negligible or contradictory to the conductance method, which was considered more reliable since it uses only the raw data. We think this could either have been because of impurities across the interfaces of the samples or because the non-midgap D_{it} among samples was too close to analyze. For this reason, this paper will only discuss results from the conductance method.

In the first part of the project, we compared samples that were annealed in different gases: forming gas (95% nitrogen, 5% hydrogen), nitrogen and oxygen. Figure 1 shows the raw CV data for the different samples at 1 kHz frequency.

The area of most interest was the midgap bump in the negative bias region. A smaller bump would indicate a lower midgap D_{it}. Figure 1 shows a lower bump for the oxygen-annealed sample, which would indicate that oxygen is a better annealing gas than forming gas and nitrogen.

Another way to interpret this data is with a G_p/w 3D plot. Shown in Figure 2, G_p/w is a function of capacitance, conductance, and the natural properties of the sample at every voltage and frequency point. This is useful because the midgap D_{it} is roughly 2.5 times the peak of this graph. Figure 2 shows the G_p/w data for the oxygen annealed sample.

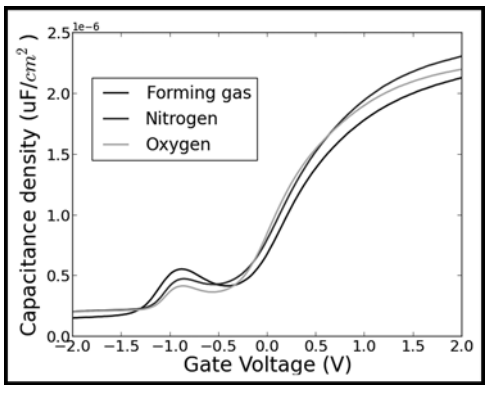

Figure 1: CV curves for samples annealed in different gases.

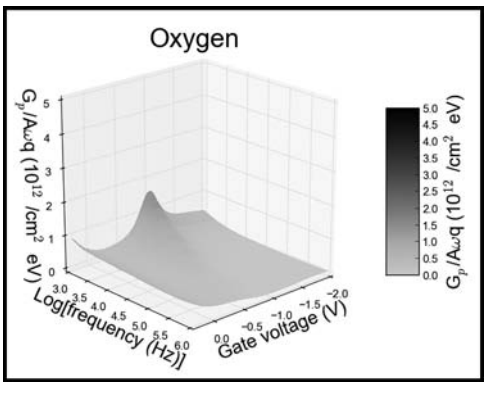

Figure 2: 3D G_p/w plot for samples annealed in different gases.

While the graphs for the other samples are not shown, the peak for the oxygen annealed sample was in fact lower, which shows that oxygen was in fact a better annealing gas.

In the next part of the project, we varied the annealing temperature, while keeping a constant ramp rate. Figure 3 shows the CV data for the three samples, which were annealed to 300, 350, and 400°C. It is apparent from Figure 3 that the optimal annealing temperature was 400°C. We could see, however, that there was a very small difference between 350 and 400°C, while the sample annealed at 300°C was significantly worse. This led us to believe that since the sample was put in the ALD at 300°C, it was important to anneal it to a higher temperature than that.

In the final part of the project, we compared two samples with the same fabrication parameters, but one sample underwent metal deposition a week after it has been annealed, while in the other metal was deposited on the same day. Figure 4 shows the CV curves for these two samples. There was a vast difference between the two, as it was clear that the smaller bump belongs to the sample that was metal-deposited on the same day. This experiment was important to run because if this discovery hadn't been made, it could have tarnished our other comparisons.

In this project, we noticed a lower midgap D_{it} in the samples that were annealed in oxygen at high temperatures with gate metal deposited immediately after annealing. We concluded that these were favorable conditions for lowering the trap density in HfO_2/n-InGaAs MOSCAPS.

There are still many more parameters to test and a great deal more work to be done to achieve a low enough trap density, but our discoveries are a step in the right direction for determining the optimal fabrication process for these devices.

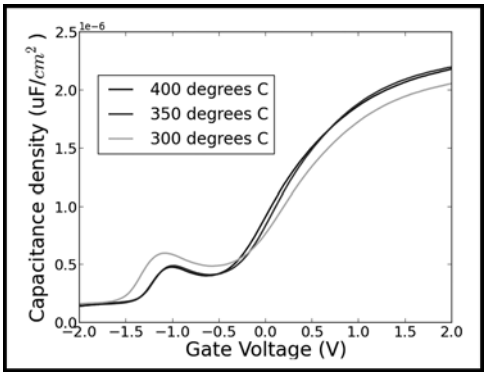

Figure 3: CV curves for samples annealed to different temperatures.

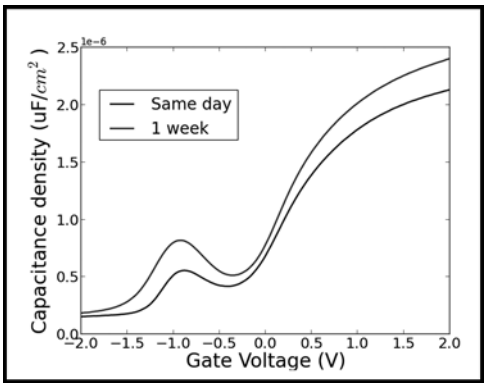

Figure 4: CV curves for samples with different time conditions.

References:

[1] Engel-Herbert, R., Hwang, Y., and Stemmer, S. Comparison of methods to quantify interface trap densities at dielectric/III-V semiconductor interfaces. J. Appl. Phys. 2010;108(12):124101.

[2] Hwang, Y., Engel-Herbert, R., Rudawski, N.G., and Stemmer, S. Analysis of trap state densities at $HfO_2/In_{0.53}Ga_{0.47}As$ interfaces. Appl. Phys. Lett. 2010;96(10):102910.

[3] Engel-Herbert, R., Hwang, Y., and Stemmer, S. Quantification of trap densities at dielectric/III-V semiconductor interfaces. Appl. Phys. Lett. 2010;97(6):062905.

Influence of Planar Organic Electrochemical Transistor Device Geometry in the Characterization of Barrier Tissue

Kaleigh Margita
Chemistry, Newberry College

NNIN iREU Site: Centre Microélectronique de Provence, Ecole Nationale Supérieure des Mines de Saint Etienne, France
NNIN iREU Principal Investigator: Professor George Malliaras, Department of Bioelectronics, Centre Microélectronique de Provence, Ecole Nationale Supérieure des Mines de Saint Etienne
NNIN iREU Mentor: Dr. Marc Ramuz, Department of Bioelectronics, Centre Microélectronique de Provence, Ecole Nationale Supérieure des Mines de Saint Etienne
Contact: kaleigh.margita@newberry.edu, malliaras@emse.fr, ramuz@emse.fr

Introduction:

The interfacing of electronics with biological systems, using novel organic materials that are easily processed, have soft mechanical properties, and the ability to conduct both ions and electrons, has led to endless applications in the field of bioelectronics. Organic electrochemical transistors (OECTs) are one application of this innovative technology [1].

Our aim for this project was to take various geometric aspects of the OECT, diagramed in Figure 1, and evaluate the effects the variable had on the electrical characteristics of the transistor and in the characterization of barrier tissue. Planar OECTs offer the advantages of a simple fabrication process — cells can be seeded directly on top of the transistor and the electrical and optical characterization can be correlated since the device is fully transparent. The p-type semiconductor poly(3,4-ethylened ioxythiophene):poly(styrenesulfonate) (PEDOT:PSS) was used as the active layer for the gate and the channel. The contacts were made of gold [2]. When a positive voltage was applied to the gate, the cations, from the cell media, were pushed into the PEDOT:PSS channel layer. The film was thus dedoped, becoming less conducting.

Madin-Darby canine kidney (MDCK) epithelial cells were grown on top of the transistors imitating barrier tissue, which regulates the passage of ions, nutrients, and pathogens through both transcellular and paracellular transportations. Barrier tissue integrity was electronically measured by the OECT and the optimal device geometry was determined.

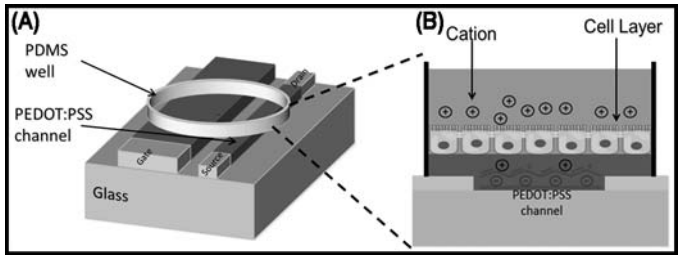

Figure 1: (A) Schematic of the planar OECT with PEDOT:PSS gate and channel on the same plan. (B) Cross section of the OECT sensor with cells grown on it. The presence of this cell layer modulates the flux of ions that can penetrate in the PEDOT:PSS channel.

Device Fabrication:

For the fabrication of planar OECT, shown in Figure 2, glass substrates (75 mm × 25 mm) were obtained, cleaned, spin-coated with S1813 photoresist, and patterned with the desired device geometry using photolithography. The substrates were developed in MF-26 developer. Using the metal evaporator, 10 nm of chromium and 100 nm of gold, was deposited on the surface. Acetone and sonication was used to remove the photoresist and excess gold, leaving patterned substrates. A 2 μm layer of Parylene C was deposited. Then AZ-9260 photoresist was spin-coated. The substrates were again exposed to UV-Light for PEDOT:PSS patterning. With the plasma etcher, areas without photoresist were removed. PEDOT:PSS was deposited on the substrates with the spin coater and the Parylene C layer was then peeled off, removing photoresist and PEDOT:PSS that was not attached to the glass substrate. The substrates were hard baked for 30 minutes at 140°C and PDMS wells where attached to each pixel on the transistor.

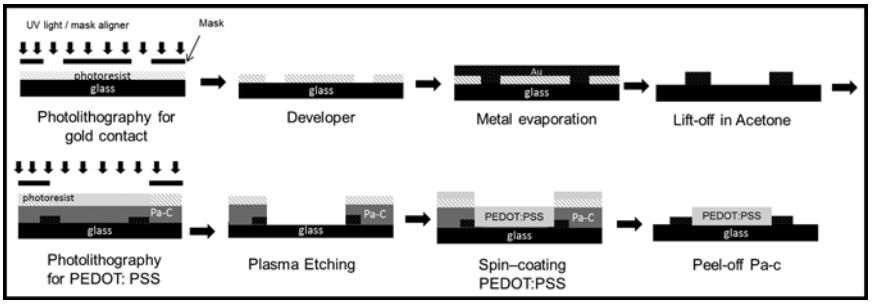

Figure 2: Organic electrochemical transistor fabrication process.

Characterization of OECT:

For the electrical characterization of the OECT, a probe station and a Keithley 2612 Source Meter were used. The channel current modulation under a pulsed gate was measured and the highest modulation was expected.

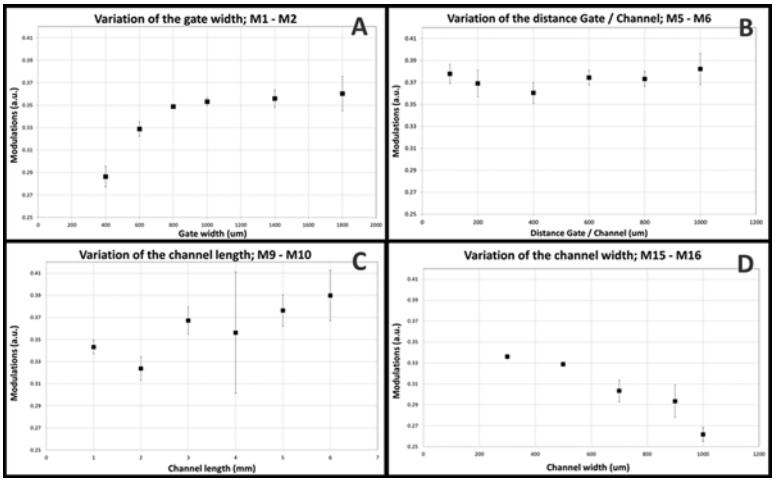

Figure 3: OECT electrical characterization, showing average and standard deviation of the modulation. A) Gate width variance (400-1800 µm), B) Distance between gate and channel variance (100-1000 µm), C) Channel length variance (1-6 mm), and D) Channel width variance (100-1000 µm).

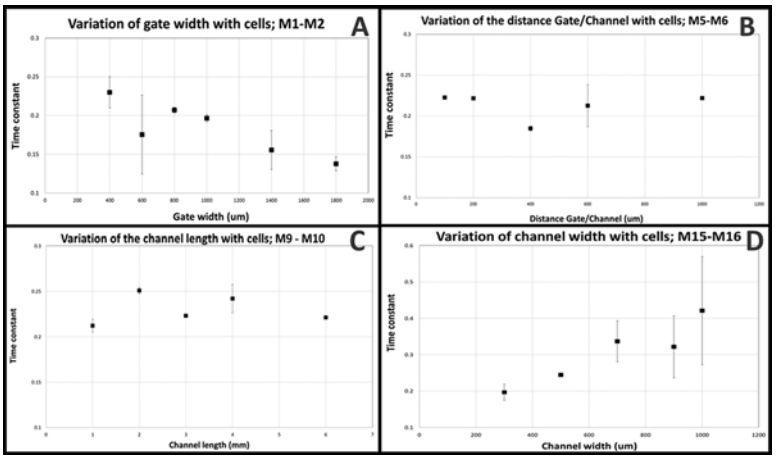

Figure 4: Characterization of barrier tissue. Average and standard deviation of Tau value are shown. A) Gate width variance (400-1800 µm), B) Distance between gate and channel variance (100-1000 µm), C) Channel length variance (1-6 mm), and D) Channel width variance (100-1000 µm).

Data for each varying parameter was obtained, the modulation graphed and standard deviation calculated (Figure 3). The same procedure was used for the characterization of the barrier tissue of MDCK cells at Day 6, according to OECT geometry. With MDCK cells, instead of modulation, the time constant Tau was used as a figure of merit representing the speed of the dedoping / doping of the channel layer. The highest Tau was expected and the data obtained was graphed in Figure 4 along with the standard deviation.

Results and Conclusions:

Varying geometric aspects of the OECT were evaluated, and the effects the variable had on the electrical characteristics of the transistor barrier tissue were observed. It was found that, initially, transistors without the layer of cells required a minimum gate width of 800 μm to dedope the PEDOT:PSS in the channel effectively (Figure 3A). From the graph of modulation versus the varying the distance between the gate and channel, in Figure 3B, it was concluded that this parameter had no effect on the success of the transistor. With an increase in channel length, an increasing trend was observed indicating that more charges were involved (Figure 3C). Increasing the channel width reduced the modulation because the ratio of the gate to channel did not remain consistent and there were not enough ions to fully dedope the channel.

In the presence of a cell layer, increasing gate width reduced the Tau value (Figure 4A) indicating that a larger gate was required in order to push ions through the cell barrier. Variation of the distance between the channel and gate and of the channel length did not have an effect on the Tau value (Figure 4B and 4C). Increasing the channel width improved the Tau value (Figure 4D) leading to the conclusion that with a larger channel covered with cells, it takes longer for the ions to be passed through the cell barrier.

Overall it can be concluded that in both sets of data, channel and gate width have a large and opposite effect on the OECT biosensor illustrating the importance of the (gate / channel) aspect ratio. An aspect ratio (area gate / area channel) of 8 is a good tradeoff between high enough modulation and Tau value, effectively dedoping the PEDOT:PSS while still monitoring small changes in the barrier tissue integrity. The distance between the gate and the channel does not affect the modulation or the time constant. When increasing the channel length, the modulation increases without increasing the Tau value, because there is an increase in the number of charges. The fact that the Tau value stays constant demonstrates the independence of the sensibility (represented by Tau) to the length and by extension to the area of the OECT.

Acknowledgments:

I would like to thank Professors George Malliaras and Roisin Owens, the Bioelectronics Laboratory, and Dr. Marc Ramuz for their guidance. I am grateful to the NNIN iREU Program and NSF for this research opportunity.

References:

[1] Jimison, L.H., et al., Measurement of Barrier Tissue Integrity with an Organic Electrochemical Transistor. Advanced Materials, 2012.

[2] Cicoira, F., et al., Influence of Device Geometry on Sensor Characteristics of Plana Organic Electrochemical Transistors, Advanced Materials, 2010.

Examining Metal/SnS Contact Resistances for the Increase of SnS Solar Cell Efficiency

Shay Goff Wallace
Materials Science and Engineering, University of Minnesota-Twin Cities

NNIN REU Site: Center for Nanoscale Systems, Harvard University, Cambridge, MA
NNIN REU Principal Investigator: Prof. Roy Gordon, Chemistry and Chemical Biology, Harvard University
NNIN REU Mentor: Leizhi Sun, Chemistry and Chemical Biology, Harvard University
Contact: walla403@umn.edu, gordon@chemistry.harvard.edu, leizhis@gmail.com

Abstract:

Many current solar cell technologies use toxic elements (such as cadmium) and rare elements (such as tellurium, indium, and gallium) in their construction. These components add expense and are major impediments to increased usage of solar cell technologies. As a result, research is being done into solar cells that use non-toxic and abundant elements such as tin (II) sulfide solar cells. The focus of this research was the investigation of the contact resistance of the metal back contact of a tin sulphide (SnS) solar cell. SnS solar cells have a record efficiency of only 2.04. This efficiency needs to be increased for these cells to be commercially viable.

Background:

Tin (II) sulfide solar cells utilize SnS deposited onto a metal back contact via atomic layer deposition (ALD). The production and structure of these cells is described by Sinsermsuksakul et al. [1]. A crucial part of a solar cell is the metal back contact (molybdenum in the case of Sinsermsuksakul [1]). This contact between SnS and the metal contributes a resistance to the electrical circuit known as the contact resistance. This contact resistance affects the efficiency and by selecting a contact with a low contact resistance, the overall efficiency of the cell should be increased.

The method used to examine the contact resistance of the metal/SnS contact is known as the transmission line method (TLM). Specifically, the method used was the transmission line method with circular patterns, similar to the method described by Deepak [2]. This method involves measuring the resistance of metal patterns on a substrate and using the physical geometry of the patterns to determine both the contact resistance of the metal and the sheet resistance of the substrate.

This research involved examining patterns of different metals to determine their contact resistances with SnS. The metals examined were aluminum, gold, copper, indium, molybdenum, nickel, and titanium.

Experimental Procedure:

First, samples of SnS were formed by depositing SnS onto thermal oxide on silicon via atomic layer deposition (ALD). All of the samples were as deposited by the ALD reactor and some were then annealed in H_2S. The samples next had the circular metal patterns deposited onto them. The metal patterns were created by using photolithography to create a pattern of exposed substrate and then depositing 300 nm of the metal onto the sample with electron beam evaporation. After this process, the remaining mask pattern was removed, leaving just the circular metal patterns on the surface.

After the metal patterns were created on the SnS substrates, the resistance of each pattern was determined via I-V probe testing. This testing revealed that copper, indium, and aluminum created non-Ohmic contacts and thus did not need to be investigated further as they would not lead to an increase in efficiency. However, nickel (Ni), titanium (Ti), molybdenum (Mo), and gold (Au) did form Ohmic contacts. A plot showing the current-voltage characteristic of nickel on annealed SnS is shown in Figure 1. Each line is a different pattern size. For each metal, the resistance of each pattern size was plotted against a parameter based on the geometry of the pattern. An example of this relationship for Ni on annealed SnS is shown in Figure 2. The equation of the line of best fit of these points allows values for the contact resistance and sheet resistance to be obtained. The slope is the sheet resistance and the intercept is a factor based on both the sheet resistance and contact resistance. The results of the calculations of both sheet and contact resistance for all Ohmic metals are shown in Table 1.

Results and Conclusions:

As can be seen in Table 1, gold has the lowest contact resistance. However, the cost of gold means that it could be uneconomical to use it in a solar cell that is meant to be cheaper than current technologies. Even though the identity of the substrate (either annealed or as-deposited SnS) is in question for the gold contacts, it is clear that it has the lowest contact resistance by

far. The next best choice for back contact is the currently used material, molybdenum. This means that molybdenum is still the best choice for back contact in a SnS solar cell.

As can also be seen, there was great variation in the measurements of sheet resistance for each of the samples. This was likely due to difficulties in the delicate processes involved in both fabrication and characterization. The sheet resistance values should be more consistent as the SnS films were all deposited in the same run and should thus have very similar hole concentrations and resistivities. This consistency in sheet resistance was shown in previous work by this research group. Additionally, the sample of Ni deposited onto as-deposited SnS has a rather high contact resistance in comparison to other values. This could also be due to problems in fabrication and characterization.

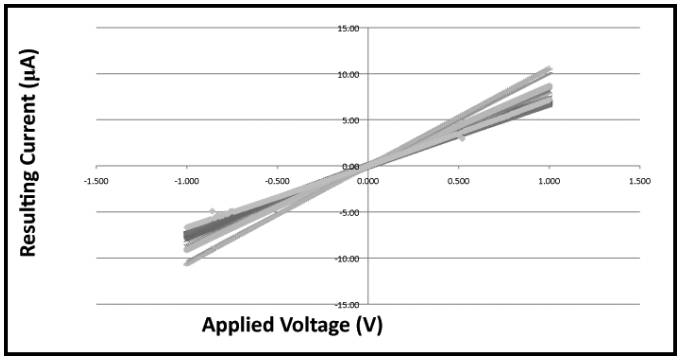

Figure 1: Current vs. voltage measurements for nickel patterns of various sizes on annealed nickel.

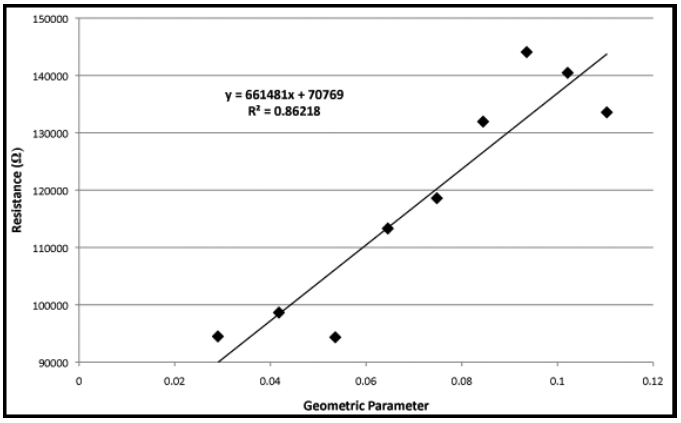

Figure 2: Resistance values of various pattern sizes vs. a geometric parameter of the pattern size. The slope of the line of best fit is the sheet resistance and the intercept is a result of the sheet resistance and the contact resistance.

Acknowledgements:

I would like to thank Professor Roy Gordon, Leizhi Sun, the Harvard Center for Nanoscale Systems, and the other members of the Gordon group for making this research possible. I would also like to thank Dr. Kathryn Hollar, the National Science Foundation, and the National Nanotechnology Infrastructure Network Research Experience for Undergrads Program for making this research opportunity possible.

References:

[1] P. Sinsermsuksakul, K. Hartman, S. B. Kim, J. Heo, L. Sun, H. H. Park, R. Charkraborty, T. Buonassisi, and R. G. Gordon, Appl. Phys. Lett. 102, 053901 (2013).

[2] Deepak and H. Krishna, J. Electron. Mater. 36 (5), pp. 598-605 (2007).

	Sheet Resistance (kΩ/sq)	Error in Sheet Resistance (kΩ)	Contact Resistance (Ω-cm2)	Error in Contact Resistance (Ω-cm2)
Annealed Nickel	661.5	100	1.868	0.496
As-Deposited Nickel	1861.3	907.4	35.588	20.092
Annealed Titanium	1424.7	94	0.662	0.154
As-Deposited Titanium	4461.3	275.2	0.343	0.194
Annealed Molybdenum	1473.5	109.6	0.163	0.085
As-Deposited Molybdenum	7232.8	123.3	0.187	0.046
As-Deposited* Gold	1858.9	70.5	0.000749	0.003582

**Gold could be on annealed SnS*

Table 1: Sheet resistance and contact resistance values for various metal patterns deposited onto both annealed and as-deposited SnS.

Radio Frequency Switches Using Phase Change Materials

Kosuke Wataya
Mechanical Engineering, Tohoku University, Sendai, Japan

NNIN iREG Site: Lurie Nanofabrication Facility, University of Michigan, Ann Arbor, MI
NNIN iREG Principal Investigator: Professor Mina Rais-Zadeh, Electrical Engineering and Computer Science, University of Michigan
NNIN iREG Mentor: Dr. Yonghyun Shim, Electrical Engineering, University of Michigan
Contact: wataya@nme.mech.tohoku.ac.jp, minar@umich.edu, yhshim@umich.edu

Abstract:

Phase change (PC) materials have two separate states: crystalline state and amorphous state. In the crystalline state, the electrical resistance is relatively low, while a high resistance level is observed in the amorphous state. If the two states are properly controlled and resistance level difference is sufficient throughout radio frequency (RF) range, this material can be utilized as an ohmic switch. The main goal of this project was to fabricate RF switches using germanium telluride (GeTe), a PC material. More practical structure was proposed with separate RF and heater electrodes. For better performance and effective phase transition, fabrication process was characterized. First, to improve metal contact resistance, oxidized molybdenum (Mo) electrodes in contact area with GeTe were etched using diluted hydrofluoric acid (HF) solution. Also, additional aluminum nitride (AlN) layer was deposited under the GeTe switch for better heat dissipation into the high resistivity silicon (Si) substrate. An additional oxide layer was also deposited on the bottom heater electrode to get better access to the GeTe area for phase transition and improved crystallization condition.

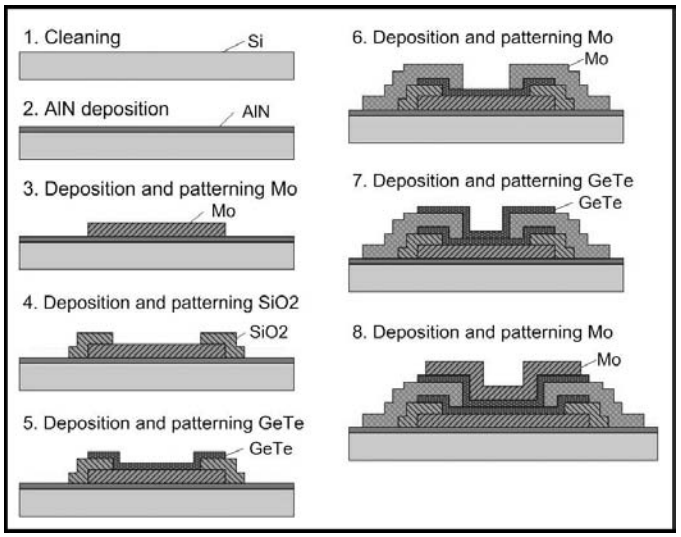

Figure 1: Fabrication flow of RF switches using phase change material.

Introduction:

These days, RF switches are used for switching signals or antennas such as wireless local area network (LAN) in mobiles phones or laptops etc. Using the RF switches, we can enable high speed communications. There are many kinds of RF switches: solid state devices, micro-electro-mechanical system (MEMS) switches and phase change switches. The most conventional ones are solid state devices. In solid state devices, electrical circuits are used for switching. MEMS switches are investigated these days and switch mechanically. Compared to solid state devices, MEMS switches have some advantages: higher linearity and lower power consumption [1, 2]. Phase change switches use PC material for switching. Compared to MEMS switches, PC switches have some advantages; having smaller size, easier integration with CMOS, lower gate voltages, and not having special packaging requirements [3].

PC materials have two separate states; crystalline state and amorphous state. In the crystalline state, the electrical resistance is relatively low, while in the amorphous state, the resistance is high. If the two states are controlled, this material can be an ohmic switch. The main goal of this project was to fabricate practical RF switches using GeTe.

Experimental Procedure:

The RF switches using PC material were fabricated on Si wafers. The fabrication flow was shown in Figure 1. Fabrication process is described below. First of all, an AlN layer was deposited on a prepared Si wafer. AlN has high insulation and high thermal conductivity so heat can easily dissipate. Next,

Mo was deposited on the AlN layer and patterned using liftoff process. This Mo layer would be the bottom heater electrode. Next, a silicon dioxide (SiO_2) layer was deposited and patterned using radical ion etching (RIE). This SiO_2 was used to insulate completely between the bottom heater electrode and the RF electrode, which would be deposited later.

The next step was depositing a GeTe layer and patterning it with liftoff process. After depositing GeTe, Mo layer was deposited and patterned using liftoff process and this layer would be the RF electrodes. Next, a second GeTe layer was deposited and patterned using liftoff process. Finally, a Mo layer was deposited and patterned using liftoff process. This Mo layer would be the top heater electrode. Right before each Mo deposition, oxidized Mo on the surface of Mo was etched using diluted HF solution, so that the electrical resistance would be lower.

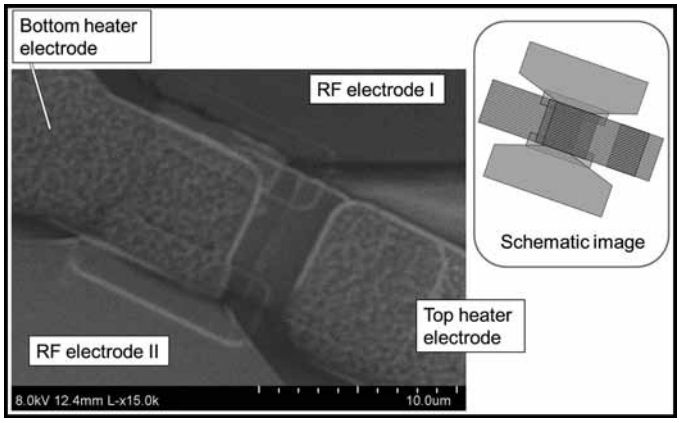

Figure 2: SEM image of structure of a phase change switch.

Results and Conclusions:

With above processes, the structure was fabricated. A scanning electron microscope (SEM) image of this structure is shown in Figure 2. Compared to the schematic image, this structure seemed to be fabricated well. Next, these devices were measured to determine if they worked or not. Voltage pulses were applied between two metals, but the phase change didn't happen. The phase change material GeTe was probably damaged.

There are many possible reasons why the GeTe was damaged: resist remover, ultrasonic cleaning, heating, diluted HF, or ashing.

Future Work:

It is important to determine which process damaged the GeTe. The GeTe should be measured at each step of the process to see if it works.

Acknowledgments:

I really would like to appreciate the following people and institutions: Prof. Mina Rais-Zadeh, Dr. Yonghun Shim, Resonant MEMS Group, Brandon Lucas, and LNF staff for their assistance; the National Nanotechnology Infrastructure Network International Research Program together with Nanotechnology Platform, Japan, and the National Science Foundation for funding.

References:

[1] Infineon, RF CMOS SPDT Switches BGS12xx for Applications up to 3GHz, Application Note No. 175, Rev. 1.1, Feb. 2009.

[2] V. Kaper, et al, "Monolithic AlGaN/GaN HEMT SPDT switch," 12th GAAS Symp., Amsterdam, 2004.

[3] H. Lo, "Probe reconfigurable phase change material switches," Ph.D. Thesis, Carnegie Mellon University.

Fabrication and Characterization of InGaAs Metal-Oxide-Semiconductor Capacitors (MOSCaps) with HfO_2 Dielectrics

Jill Wenderott
Physics, University of Kansas

NNIN REU Site: UCSB Nanofabrication Facility, University of California, Santa Barbara, CA
NNIN REU Principal Investigator: Prof. Mark Rodwell, Electrical and Computer Engineering, University of California Santa Barbara
NNIN REU Mentor: Cheng-Ying Huang, Electrical and Computer Engineering, University of California Santa Barbara
Contact: jillk@ku.edu, rodwell@ece.ucsb.edu, cyhuang@ece.ucsb.edu

Abstract and Introduction:

III-V indium gallium arsenide (InGaAs) metal-oxide-semiconductor field effect transistors (MOSFETs) are promising candidates for next-generation low power logic technology. A major challenge for III-V MOSFETs is the development of suitable gate dielectrics with low interface trap densities (D_{it}). This project focused on the fabrication of InGaAs metal-oxide-semiconductor capacitors (MOSCaps) with hafnium oxide (HfO_2) dielectrics grown by atomic layer deposition (ALD). Several studies were conducted involving *in situ* ALD surface cleaning, HfO_2 growth temperature, and post-deposition forming gas anneal (FGA) parameters. The two types of surface cleaning investigated to reduce interface trap density were hydrogen (H_2) plasma/trimethylaluminum (TMA) and nitrogen (N_2) plasma/TMA. Various HfO_2 deposition temperatures were explored to probe the ALD window of HfO_2 growth. Finally, the post-deposition FGA was optimized by testing different ramp rates and annealing temperatures. The InGaAs MOSCaps were characterized using capacitance-voltage (C-V) measurements, and the interface trap densities were evaluated using the conductance method.

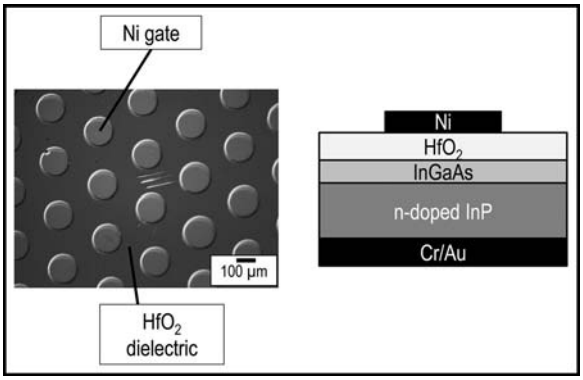

Figure 1: Top-down view of MOSCaps taken with an optical microscope (left); schematic of MOSCap from side view (right).

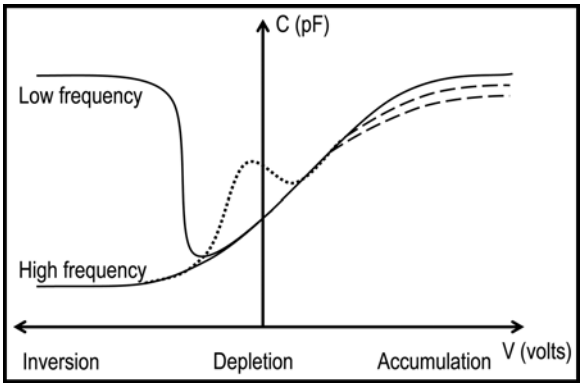

Figure 2: Ideal C-V curves shown with solid lines; mid-gap bump shown with dotted line; frequency dispersion represented with dashed lines.

Methods:

InGaAs MOSCaps were desirable for study in this project because of their short fabrication time. First, the semiconductor bulk and channel (InP/InGaAs) were grown by molecular beam epitaxy (MBE). The sample was then solvent-cleaned with acetone and isopropyl alcohol and dipped in buffered hydrofluoric acid to prepare the semiconductor surface for the oxide layer.

Before HfO_2 was deposited via ALD, the sample was again cleaned *in situ* with either H_2 plasma/TMA or N_2 plasma/TMA. The H_2 plasma/TMA and N_2 plasma/TMA were performed for five and nine cycles, respectively, as these numbers have been shown to be optimal [1]. HfO_2 was grown with a general recipe calling for a one second tetrakis(ethylmethylamino)hafnium (TEMAH) pulse and 0.5 second water pulse at 300°C, though this parameter space was explored. An oxide thickness between 40-50 Å was sought; this was accomplished by using between 35-40 cycles of TEMAH/water pulses and purges.

After ALD, the sample was annealed in forming gas. The standard conditions were 15 minutes at 400°C with a ramp rate of 75°C/min, but these parameters were also altered and studied. Upon removal from the FGA furnace, the nickel (Ni) gate and chromium/gold (Cr/Au) backside metal contacts were thermally evaporated to complete the MOSCap fabrication (see Figure 1).

Characterization of the MOSCap was completed using an impedance analyzer to extract C-V and conductance-voltage (G-V) data. C-V curves were plotted and significant attention

was paid to the size of the mid-gap bump (see Figure 2) as this was indicative of the D_{it}, with a smaller mid-gap bump signifying a smaller D_{it}.

$$G_p = \frac{\omega^2 C_{ox}^2 G_m}{G_m^2 + \omega^2 (C_{ox} - C_m)^2}$$

$$D_{it} \approx \frac{2.5}{Aq} \left(\frac{G_p}{\omega}\right)_{max}$$

Figure 3: Conductance method equations used to find D_{it}.

Frequency dispersion in the positive bias was also noted, because smaller dispersion suggested a smaller number of border traps, another oxide defect.

Furthermore, C-V and G-V data was used to quantify the D_{it} using the conductance method (see Figure 3) and assess MOSCap quality. In the conductance method, G_m and C_m are measured conductance and capacitance values, C_{ox} is oxide capacitance, ω is the frequency, G_p is the parallel conductance, A is the capacitor area and q is the elementary charge.

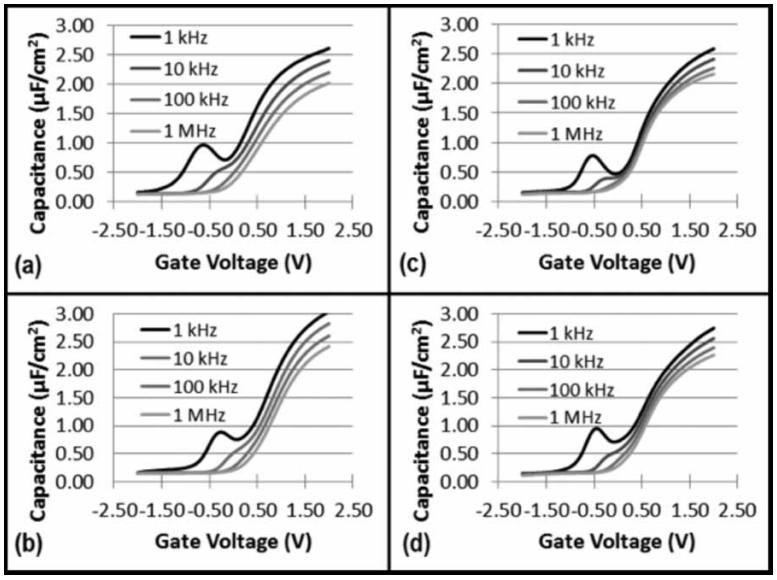

Figure 4: C-V characteristics as a function of frequency. Plots (a), (b) and (c), (d) were from samples pre-treated with H_2 plasma/TMA and N_2 plasma/TMA, respectively. Plots (a), (c) and (b), (d) were from samples subjected to FGA ramp rate of 10°C/min and 75°C/min, respectively.

Results and Conclusions:

The various studies intended to lower D_{it} and achieve good C-V profiles yielded interesting findings. Varying the ALD growth temperature of HfO_2 from 200-300°C did not substantially affect the D_{it}, though the 300°C sample did show a slightly smaller D_{it} than the others. Another study that looked at several FGA temperatures for H_2 plasma/TMA pre-treated samples confirmed, by comparing D_{it}, that 400°C was the optimal for use during annealing.

The differences in the H_2 plasma/TMA and N_2 plasma/TMA *in situ* surface cleanings did not at first appear to be noteworthy with standard growth and FGA conditions applied. Upon more closely studying the FGA parameters, an exciting observation was made. A smaller ramp rate (10°C/min) paired with N_2 plasma/TMA pre-treatment returned MOSCaps with better C-V profiles than those that coupled a higher ramp rate with N_2 plasma/TMA pre-treatment. The exact opposite was true for the MOSCaps pre-treated with H_2 plasma/TMA, which showed higher ramp rates (75°C/min) giving better C-V profiles (see Figure 4).

These results implied that *in situ* ALD surface cleaning and FGA parameters cannot be viewed entirely separately, but rather they should be taken into consideration together when trying to lower D_{it}.

Future Work:

With the discovery that *in situ* ALD surface cleaning and FGA parameters should be examined together in order to lower D_{it} in InGaAs MOSCaps, more studies will be completed that optimize the two pre-treatment methods with their respective FGA conditions. In the same vein, it should be shown why lower ramp rates during annealing reduce the D_{it} in the N_2 plasma/TMA pre-treatment devices, but higher ramp rates reduce the D_{it} in the H_2 plasma/TMA pre-treatment devices. This will be accomplished by probing the interfacial layer that develops during ALD between the oxide and semiconductor and inspecting how this layer is dissimilar depending on the surface cleaning employed.

Acknowledgments:

This project would not have been possible without the support of many parties. Many thanks are owed — the National Nanotechnology Infrastructure Network Research Experience for Undergraduates (NNIN REU) Program and National Science Foundation, for funding; Samantha Cruz, Jamie Pillsbury and UCSB Nanotech staff, for assistance; Rodwell group members, for advising; my Nanofam, for unmatched friendship and kindness. In particular, I would like to thank my mentor, Cheng-Ying Huang, for providing me with the perfect balance of encouragement and freedom for a successful summer.

References:

[1] Chobpattana, V.; "Nitrogen-passivated dielectric/InGaAs interfaces with sub-nm equivalent oxide thickness and low interface trap densities"; Applied Physics Letters 102, 022907 (2013).

Effect of Reactive Ion Etching on Laser-Annealed Low-k SiCOH Materials

Kris Beykirch
Physics, Corning Community College

NNIN REU Site: Cornell NanoScale Science and Technology Facility, Cornell University, Ithaca, NY
NNIN REU Principal Investigator: Dr. Michael Thompson, Associate Professor, Materials Science and Engineering, Cornell University
NNIN REU Mentor: Robert Bell, Materials Science and Engineering, Cornell University
Contact: kmb364@cornell.edu, mot1@cornell.edu, rtb83@cornell.edu

Introduction:

The speed of current microelectronic devices is limited due to parasitic capacitance between wires in the back end. The dielectric constant, or κ value, of the insulator between wires can be reduced to shorten this delay. To reduce the dielectric constant of standard SiO_2, carbon can be added to form bonds that are not as polar, and the material can be made porous, introducing air with its low κ value. These are generally referred to as SiCOH materials. Porosity, however, is achieved at the expense of modulus, meaning that the lower the κ value of a given SiCOH material, the weaker and less useful it is in industry.

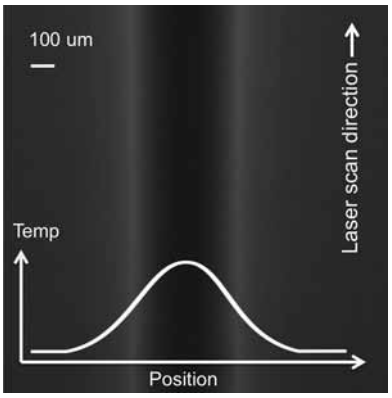

Figure 1: A representative diagram of a laser anneal stripe.

Our group hoped to use millisecond laser spike annealing (LSA) to produce a stronger but still low-κ material. Annealing was performed at higher temperatures than conventional thermal anneals, with the short duration limiting many of the damaging material changes.

LSA involves focusing a high-power laser, and then tracing a line across the sample. By varying the dwell (the amount of time any particular region is heated) and laser power, different maximum anneal temperatures can be achieved. The beam intensity (and therefore, anneal temperature) follows a Gaussian profile. Consequently, temperature varies with position, with the highest temperature in the center of the line, as shown in Figure 1. This project involved characterizing the etch behavior of SiCOH films after laser heating.

Experimental Procedure:

A 2 × 2 cm sample was annealed using a CO_2 laser at dwells ranging from 0.2 to 2 ms, all with a maximum temperature of 1200°C. As the 1 ms and shorter dwell anneals exhibited signs of material failure, only the 2 ms dwell (power 50.2 W) and the 1.5 ms dwell (power 52.6 W) anneals were considered in subsequent steps. (The failure was likely due to heat transfer from previous anneals; had the 0.2 ms anneal been performed first and the 2 ms anneal performed last, the material may not have failed.)

Photoresist was patterned so that only a small area of the sample was exposed to any given etch process. Two reactive ion etches were performed using an Oxford 82 etcher, both typical SiO_2 etches: CF_4 etch (30 sccm CF_4, 40 mTorr, 150 W power) and a CHF_3/O_2 etch (50 sccm CHF_3, 2 sccm O_2, 40 mTorr, 240 W). Both 30 and 60 second etches were performed, each on a new region of the sample. Profilometry measurements were taken laterally across the anneal line, before and after etching, using a P10 profilometer. (During data analysis, the average of every ten values was plotted to reduce noise.)

A film appeared on the sample post resist removal. Following all CF_4 and CHF_3/O_2 etches, the part of the sample containing all of the etched regions was exposed to oxygen plasma (50 sccm O_2, 60 mTorr, 150 W) for two 4-second intervals in the Oxford 82 in an attempt to remove this film. The remainder of the sample was covered in thick (S1827) resist. While the film removal was largely unsuccessful, enough was removed to allow for basic profilometry measurements.

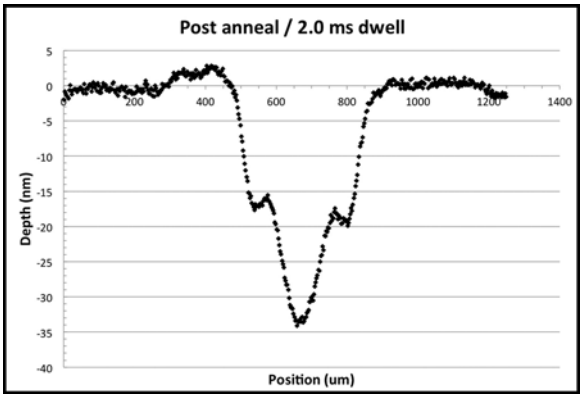

Figure 2: Depth vs. lateral position across the laser line (position as indicated in Figure 1).

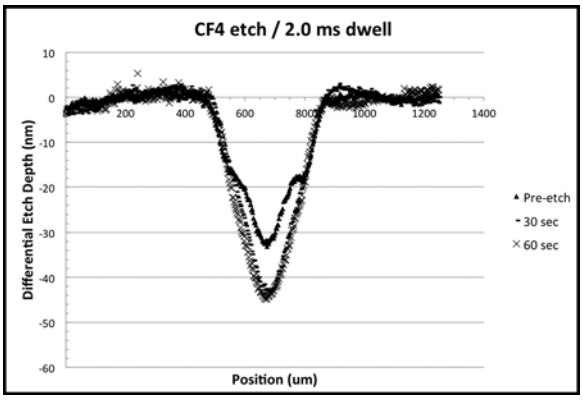

Figure 3: Differential etch depth vs. position for 2.0 ms dwell and CF_4 etch.

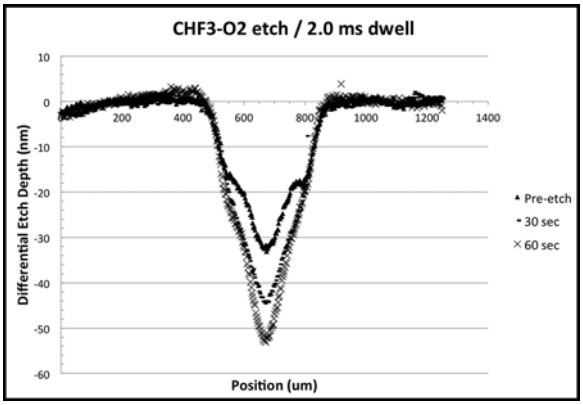

Figure 4: Differential etch depth vs. position for 2.0 ms dwell and CHF_3 / O_2 etch.

Results and Conclusions:

Figure 2 shows the change in depth with respect to position (and therefore temperature) across the laser line after anneal and before etch or oxygen clean. The material densified as it was heated, and the thickness of the film (originally about 200 nm) decreased. Of particular note are the two "shoulder" threshold regions, located at about 525-575 and 750-800 nm, where for a brief interval densification did not continue with increasing temperature.

After 30 and 60 second CF_4 etches, the surface profiles were virtually identical (as seen in Figure 3), indicating that at or some time before or at 30 seconds, the etch rate became uniform for all previous annealing temperatures. The shoulder regions also disappeared, hinting at the presence of a residue in the high temperature region (roughly between and including the shoulders) that etched away very quickly during initial etching, leaving behind only material that etched at a constant rate. The CF_4 etch profiles for 2.0 and 1.5 ms of dwell (not pictured here) were extremely similar, to the point that the etch behavior appeared to be independent of dwell.

The CHF_3/O_2 etch displayed slightly different behavior, with the shoulder regions remaining to an extent and a significant difference in the high temperature annealed region between the 30 and 60 second etch profiles, as seen in Figure 4. The residue appeared to take more than 30 seconds in order to etch, with a continued higher etch rate in the high temperature region after 30 seconds. In addition, the 60 second etch profile for 1.5 ms dwell (not pictured here) had a maximum depth of approximately -48 nm as opposed to approximately -53 nm.

Our hypothesis is that laser annealing leaves behind a residue in the high-temperature regions, possibly decomposed organic material, which is rapidly etched away so that only a material that etches at a uniform rate is left behind.

Acknowledgments:

I would like to thank Professor Thompson and my mentor Robert Bell, as well as the staff of the Cornell NanoScale Facility for their help. I would also like to acknowledge the National Science Foundation and the National Nanotechnology Infrastructure Network Research Experience for Undergraduates (NNIN REU) Program for funding this research.

Characterization of Single Component Molecular Glass Resists

Maike Blakely
Chemistry, Chatham University, Pittsburgh, PA

NNIN REU Site: Cornell NanoScale Science and Technology Facility, Cornell University, Ithaca, NY
NNIN REU Principal Investigator: Prof. Christopher K. Ober, Materials Science and Engineering, Cornell University
NNIN REU Mentor: Katherine Camera, Chemistry, Cornell University
Contact: mblakely@chatham.edu, cko3@cornell.edu, kc737@cornell.edu

Abstract:

Molecular glasses (MGs) are materials that exist in an amorphous state below their glass transition temperature, which allows us to study their glassy properties and behavior as photoresists. This research explored single component MG photoresists designed for future use in physical vapor deposition studies. This study investigated the critical doses, etch resistance rates, and electron beam lithography performance of three MGs. The CM-CR6 MG photoresist was identified as the most suitable candidate due to its relatively high etch resistance and high resolution patterning of 80 nm line and space patterns.

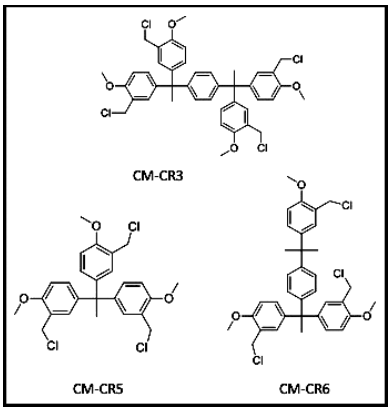

Figure 1: Structures of MG resists.

Introduction:

MG photoresists have specific characteristics like small molecular size, ability to form films, and high glass transition temperatures (Tg), which make them strong candidates for next generation lithography [1]. As polymeric photoresists are reaching their limits in feature size and roughness, attention has turned to small molecule photoresists like MGs [2]. To help optimize MGs in the lithography process, fundamental studies of their glass-forming properties can be explored using physical vapor deposition. For this, new single component molecular glasses must be designed and characterized before deposition studies are conducted. Figure 1 displays the chemical structures of the chloromethylated Cornell resists (CM-CR) that were studied. Using this model resist system, we can characterize their lithographic performance using contrast curves, etch resistance rates, and patterning through electron beam lithography.

Experimental Procedure:

The MG resist was dissolved in 2-butanone, making a 5 weight percent (wt%) solution. If necessary, 5 wt% with respect to resist of photoradical initiator, 2,2- dimethoxy-2-phenyl-acetophenone (DPAP) was added to the solution. The resist was filtered through a 0.2 μm membrane filter onto a HDMS primed silicon wafer and spun at 2000 rpm for one minute. The wafer then underwent a post apply bake for one minute at 100°C.

For the contrast curves, the resist was first flood-exposed using the ABM contact aligner with 254 nm broadband light, and developed for one minute in 1-butanol. The film thickness was then measured as a function of dose using the Woollam spectroscopic ellipsometer. For the etch resistance studies, the resists were flood exposed as mentioned previously, and then plasma etched on the Oxford 80^{+} plasma etcher for varying amounts of time. Film thickness was measured as a function of etch time, and the rate determined in nanometers per minute. To study the patterning capabilities of the photoresists, they were exposed using the JEOL 9500 electron beam (e-beam) lithography system. Their performance was evaluated using scanning electron microscope images, and SuMMIT software was used to calculate the line edge roughness (LER) and line width roughness (LWR).

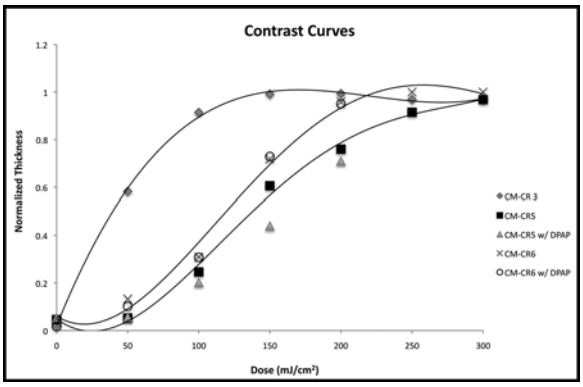

Figure 2: Contrast curves.

Results and Conclusions:

The contrast curves for the three MGs are shown in Figure 2. They did not display a desired steep slope, however the critical doses were identified for CM-CR3, CM-CR5, and CM-CR6 as 150 mJ/cm^2, 300 mJ/cm^2, and 250 mJ/cm^2 respectively. The addition of DPAP did not affect the critical dose of CM-CR5 or CM-CR6, and therefore, the experiment was not carried out with CM-CR3. This deep ultra-violet light behavior is not ideal however; this information is essential for quick testing of other properties.

The etch resistance of each resist were measured and compared to poly(hydroxystyrene) (PHOST), an industry standard (Figure 3). With CHF_3/O_2 etch gas, the etch resistance rates of the three MGs were the slowest and are comparable to PHOST, making CHF_3/O_2 the most favorable etch gas for this system.

The e-beam patterning performance is one of the most important aspects of these MGs. CM-CR6 showed patterns down to 80 nm 1:1 line:space with a low LER of 3.8 nm and LWR of 5.9 nm. The addition of DPAP allowed for comparable results using less than half of the original required dose, as seen in Figure 4. CM-CR3 was also able to pattern down to 80 nm 1:1 line:space, but had higher LER (5.0 nm) and LWR (9.3 nm) compared to CM-CR6. CM-CR5's performance was poor compared to CM- CR3 and CM-CR6, as it was only able to pattern down to 150 nm 1:1 line:space.

From these results, CM-CR6 was recognized as the most suitable resist for future use, due to its e-beam patterning performance and its proficient etch resistance. Future Work In general MG photoresists have shown promise but have not been optimized. Therefore future characterization and further optimization is needed to make MG photoresists a viable option for next generation lithography.

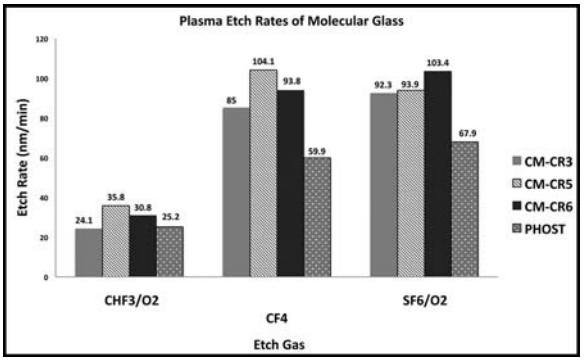

Figure 3: Etch resistance study.

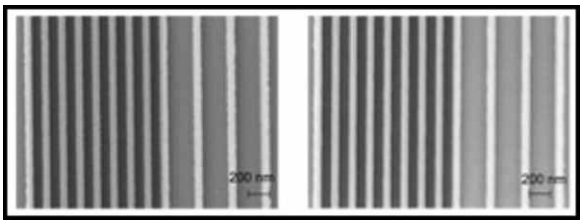

Figure 4: SEMs. Left: CM-CR6 without DPAP with a dose of 1250 mJ/cm^2. Right: CM-CR6 with DPAP with a dose of 500 mJ/cm^2.

Acknowledgements:

I would like to thank the National Science Foundation, National Nanotechnology Infrastructure Network REU Program and the Cornell NanoScale Science and Technology Facility. A special thanks to Rob Iliac, Daron Westly, Melanie-Claire Mallison, and the Ober group especially my mentor, Katherine.

References:

[1] Shirota, Y. J. Mater. Chem. 2005. 15, 75-93.

[2] Dai, J., Chang, W., Hamad, A., Yang, D., Felix, N., Ober, C.K. Chem. Mater. 2006. 18, 3404-3411.

Silver Nanoplates; Structural Stability and Optical Properties

Tyler Burkett
Chemical Engineering, University of Florida

NNIN REU Site: Nanotechnology Research Center, Georgia Institute of Technology, Atlanta, GA
NNIN REU Principal Investigator: Dr. Dong Qin, Materials Science and Engineering Department, Georgia Institute of Technology
NNIN REU Mentor: Graham Parkinson, Materials Science and Engineering Department, Georgia Institute of Technology
Contact: tburkett55@ufl.edu, dong.qin@mse.gatech.edu, grahamdbp@gatech.edu

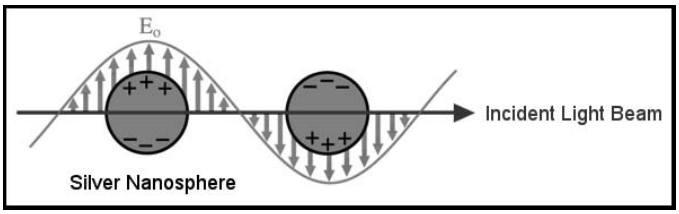

Figure 1: A figure explaining the optical properties of a generic nanoparticle. The example is using a silver nanosphere, with the incident light beam shown as a arrow and the electrical component of the light labeled E_o.

Abstract and Introduction:

Silver nanoplates have attracted significant attention in the nanomaterials community for their numerous possible future uses. These nanoparticles are classified as 'plates' because they have high aspect ratios. Their edge lengths can be made to be between 30 and 500 nm, and they are typically triangular in shape. These plates exhibit interesting optical properties, because they are smaller than the wavelengths of incident light. Because of this, the conduction electrons of the nanoparticles interact and oscillate with the electrical component of light. The oscillation is what allows for these distinct optical properties and it also allows for distinct colors to be shown for different structures. This explanation can be seen clearly in Figure 1.

The material of silver was chosen for several reasons. One is that it is cheaper than other materials, specifically platinum and gold. A sizeable portion of the research of nanoparticles has been done using gold, which is more expensive. Another is that silver is highly electrically conductive. Also the silver nanoplates that are produced in the Qin Lab [1] are ideal for these studies. With the absence of a strong capping agent such as citrate, we can manipulate the shape, size, and local environment of these nanoplates and test optical effects.

It has been seen that any change in structure of these nanoplates creates changes in optical properties. These changes can be seen visually through a color change and can be quantified through UV-vis spectra. Also morphology is verified with scanning electron microscopy (SEM) and transmission electron microscopy (TEM). Understanding this 'building block' of nanoscience is a key step towards utilizing metallic nanomaterials in more intricate applications.

Experimental Procedure:

The first objective involved the synthesis of silver nanoparticles with ~ 50 nm edge-lengths. Chemically, this synthesis involved the reduction of ionic silver to atomic silver. As the process occurred, silver nucleation sites were created, which then grew into plates. The process involved has been honed to have anion-to-solid conversion greater than 99% [1]. The starting materials were silver nitrate ($AgNO_3$), which is the source of silver, and polyvinyl pyrrolidone (PVP), both dissolved in ethanol. PVP is the chemical that acts as the reducer and also is called a capping agent, because it binds to the surface of the nanoplate and allows it to remain relatively stable. The mixture of these ingredients was then placed into a Teflon® liner, which was sealed into a stainless steel vessel. This vessel was then placed into an oven for 4-5 hours.

Results and Conclusions:

Experiments with these as-prepared silver nanoplates included vertical and lateral growth experiments. Vertical growth was created with a very fast injection rate of more ionic silver with the presence of mild reducers, including PVP. This process successfully created bipyramidal nanoparticles. This showed a color change from blue to yellow. Slowing the injection rate

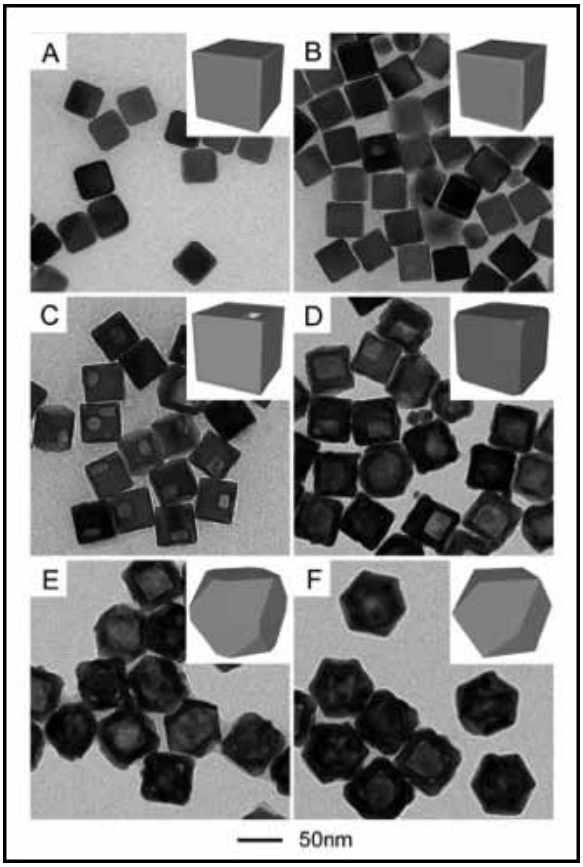

Figure 2: A collection of TEM images and illustrations showing silver nanocubes (A) coated with increasing amounts of gold (B through F). Deposition occurs first around the edges (B) before alloy structures are formed (C and D), eventually resulting in a gold shell (E and F).

allowed for a switch from vertical growth to lateral growth. This process successfully created larger plates with edge-lengths of 300 nm and visually showed a shift of color from blue to green.

Smaller nanoplates were produced in an ethanol system and were relatively stable. However, in water, they were typically unstable and selectively etch at the corners. This etching created truncated corners and hexagonal shapes. Etching occurred at corners because sharp corners have the highest chemical energy. These plates were tested with tap water and salt water. It has been shown that even a very small addition of chlorine ions can create this truncation and a large color change.

Stability is key for other future application. Stabilizing these nanoparticles may be achieved with a thin gold coating; a technique previously achieved with nanocubes, seen in Figure 2. This synthesis involves using nanocubes created by the lab group, ionic gold, and ascorbic acid as the reducing agent.

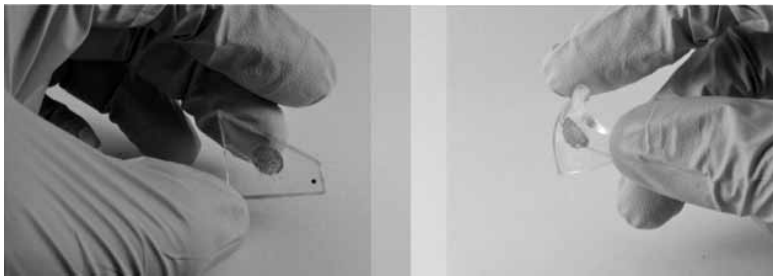

Figure 3: Silver nanoplates deposited onto the surface of PDMS. This is the first step towards flexible electrodes that utilize these plates.

When this knowledge was beginning to be transferred to nanoplates, the goal was to create the thinnest full coating of the plate.

Future Work:

The instability of plates in the water provides promising future applications in sensing and bio-sensing because of the drastic changes in color produced by small additions of ions. Once all knowledge of platecoating is transferred to silver nanoplates, these stable nanoplates can then be applied to several different applications. One notable application that is promising is metallic ink; because of their electric conductivity and the variety of colors that can be produced. Another application that was explored was flexible electronics.

The first steps towards this goal were taken with the deposition of these plates onto PDMS, a flexible substrate, seen in Figure 3. Popular possible types of flexible electronics include, flexible computers, electronics within fabric, and medical implants such as a pacemaker that can mold to the shape of the patient's body.

Acknowledgments:

Thanks to the NNIN REU Program, the NSF and the Institute for Electronics and Nanotechnology (IEN) for their support. Specifically I would like to thank the NNIN REU site coordinator at Georgia Tech, Leslie O'Neill, as well as Dr. Nancy Healy. It has been a privilege to work this summer with Dr. Dong Qin under the mentorship of Graham Parkinson.

References:

[1] Zhang, Q.; Yang, Y.; Li, J.; Iurilli, R.; Xie, S.; Qin, D. ACS Appl. Mater. Interfaces, 2013, 6333-6345.

Low-Temperature Cu Segregation and Oxidation in Microwaved Ag-Cu Alloys

Brandi T. Burton
Physics, Norfolk State University

NNIN REU Site: ASU NanoFab, Arizona State University, Tempe, AZ
NNIN REU Principal Investigator: Dr. T. L. Alford, Department of Chemistry and Biochemistry, and School for Engineering of Matter, Transport and Energy, Arizona State University
NNIN REU Mentors: Mr. Sayantan Das, Department of Chemistry and Biochemistry, Arizona State University; Mr. Benjamin Roos, School of Engineering of Matter, Transport and Energy, Arizona State University; Dr. A. Lanz, Department of Mathematics, Norfolk State University
Contact: b.t.burton@spartans.nsu.edu, ta@asu.edu, sdas30@asu.edu, bravokiloromeo@gmail.com, dr.l.lanz@gmail.com

Abstract:

Samples of a silver-copper (Ag-Cu) alloy of 13% Cu were annealed in a microwave cavity for up to 200 seconds, with a maximum temperature of 80°C. Rutherford backscattering spectrometry (RBS) indicated copper segregation to the surface. Oxygen resonance analysis and x-ray diffraction (XRD) showed that a thin copper oxide layer began forming on the surface at 40 seconds and completed at 80 seconds. Four-point probe measurements showed a decrease in the sheet resistance and XRD suggested that subsequent annealing resulted only in additional Ag grain growth.

MATS

Introduction:

Microwave processing has gained, and is gaining, much attention regarding materials processing due to its ability to process materials at low temperatures, and its efficiency in respect to time and energy savings, which lead to monetary savings [1]. Silver is a great conductor and has a high electromigration resistance [2], however, silver particles tend to cluster at high temperatures and oxidize in certain environments. To control these downsides, it is vital that an encapsulation layer be formed, in a sense, to protect the silver.

In this paper, it is noted that the copper will diffuse out of the alloy and react with ambient oxygen to form a copper oxide layer, which will act as an encapsulation layer protecting the silver from agglomeration and oxidation [3].

Experimental Procedure:

An Ag(Cu) alloy was fabricated by co-sputtering pure, 99.99%, Ag and Cu targets onto a silicon (Si) substrate with a previously deposited 100 nm thick silicon nitride (SiN_x) layer. The SiN_x layer ensured that the silver did not diffuse into, or agglomerate on, the Si substrate. The alloy structures were heated in a 2.45 GHz microwave cavity for up to 200 seconds. The temperatures of the samples were recorded using a Raytek low-temperature pyrometer. The resistivity of the samples, taken before and after the heating, was measured using a four point probe. RBS measurements using the RUMP simulation program determined the thickness and composition of the alloy. Glancing angle x-ray diffraction (XRD) measurements confirmed the phases of the alloy.

Results and Conclusions:

Glancing angle x-ray diffraction, using Cu K• particle radiation, at a wavelength of 1.54Å, rendered the preferential orientation for the alloy. An asymmetrical omega-two-theta scan was performed on the as-deposited and the 200 second annealed samples. JCPDS x-ray card number 04-0783 confirmed the defined Ag <111> and <220> peaks for both samples. Figure 1 shows that the Ag <111> and <220> peaks became narrow after annealing, suggesting that the alloy gained a better crystalline structure. We contributed the narrowing of the peak to be evident of the grain growth of the underlying silver layer.

RBS spectra, portrayed in Figure 2, showed an oxygen peak for the annealed sample only. RBS measurements showed that as the heating continued, the oxygen peak increased, indicating the formation of a thicker oxide layer. Figure 3 shows that as the heating time increased, the copper segregated to the surface of the alloy; also the front edge of the silver layer moved back, providing evidence that copper oxide formed on the surface of the alloy. By simulating the data using the RUMP program, we were able to determine how much copper remained in the alloy after annealing. Initially at 13% in the as-deposited sample, the copper decreased to 3% after 200 seconds of annealing. A more detailed analysis of the percent of residual copper per anneal time is detailed in Table 1.

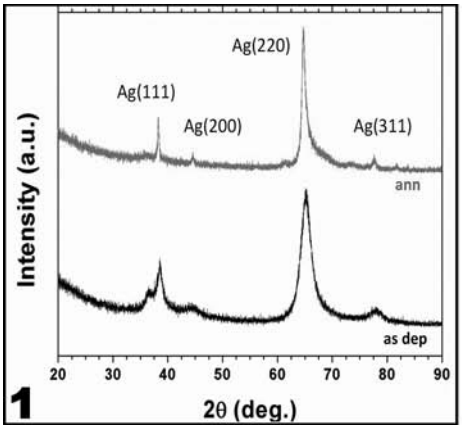

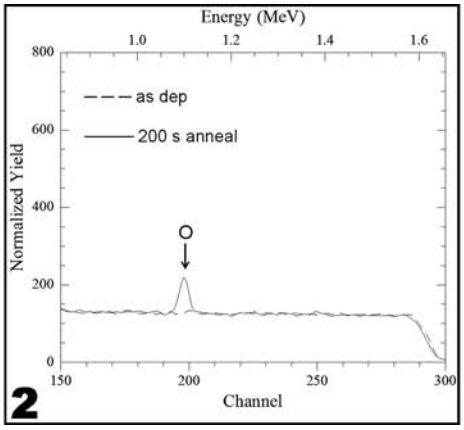

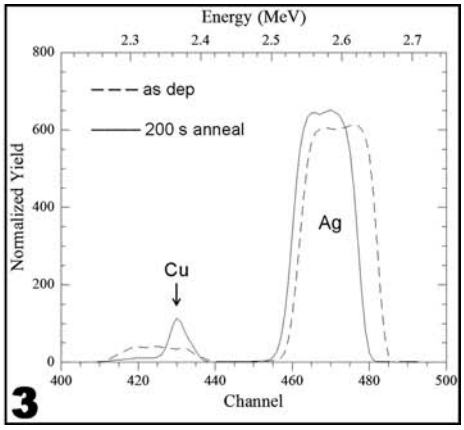

Figure 1, left: Glancing angle XRD measurements suggests the alloy's preferential orientation.

Figure 2, center: The RBS spectra for the as deposited and 200 second annealed samples highlighting the oxygen peak.

Figure 3, right: The RBS spectra for the as deposited and 200 second annealed samples highlighting the copper and silver peaks.

A four-point-probe was employed to measure the sheet resistance of the samples before and after heating. The sheet resistance decreased as the annealing time increased. Combined with the thickness measurements from RBS and RUMP simulations, the resistivity of each sample was approximated. The resistivity measurements, with respect to various anneal times is also described in Table 1. Since the newly formed copper oxide layer was considered to be an insulator, this decrease in resistivity can be attributed to the grain growth of the underlying silver layer. The grain size of both the as-deposited sample and the heated sample for 200 seconds were approximated using the Debye Scherrer Equation. It approximated that the grain size of the silver layer did increase from 39 nm to 111 nm.

Microwave annealing proved to be a sufficient method for annealing thin metal films. It promotes a processing technique that provides short processing times and efficiency. Ag(Cu) alloy structures at 13% percent copper, annealed at temperatures below 80°C for times ranging between zero to two minutes did prove to have enhanced electrical properties.

Future Work:

X-ray photoelectron spectroscopy measurements will determine whether a copper (I) oxide or copper (II) oxide formed on the surface of the alloy.

Acknowledgments:

I would like to thank my PI, Dr. T. L. Alford, and my mentors Mr. Sayantan Das, Mr. Benjamin Roos, and Dr. A. Lanz for their assistance and guidance. I would also like to thank Dr. Trevor Thornton, and the National Nanotechnology Infrastructure Network Research Experience for Undergraduates (NNIN REU) Program, the National Science Foundation, and the Center for Solid State Electronics Research at Arizona State University for research support and funding.

References:

[1] Das, S., Alford, T. L; Materials Letters, 89, 163-165 (2012).

[2] Zeng, Y., Chen, L., Zou, Y., Nguyen, P., Hansen, J., Alford T. L; Materials Chemistry and Physics, 66, 77-82 (2000).

[3] Akepati, S., Cho, H., Lee, K; "Growth of ultrathin Ag films of TaN_x layer and their optical properties." (to be published).

Microwave Processing Time	Resistivity	% of Residual Cu
0 s	5.63 μΩ cm	13%
40 s	3.60 μΩ cm	9%
80 s	3.32 μΩ cm	6%
120 s	3.37 μΩ cm	3%
200 s	3.21 μΩ cm	3%

Table 1: As the heating time increases, the resistivity and the percent of residual copper decreases.

Development of Platinum Embedded in Reduced Graphene Oxide (Pt@rGO) for Fuel Cell Applications

Michelle Chen
Chemical Engineering, Cornell University

NNIN REU Site: UCSB Nanofabrication Facility, University of California, Santa Barbara, CA
NNIN REU Principal Investigator: Prof. Daniel E. Morse, Institute for Collaborative Biotechnologies, Department of Molecular, Cellular, and Developmental Biology, University of California, Santa Barbara
NNIN REU Mentor: Dr. Chang Sun Kong, Center for Energy Efficient Materials, University of California, Santa Barbara
Contact: mc2258@cornell.edu / michelle.chen888@yahoo.com, d_morse@lifesci.ucsb.edu, cskong@icb.ucsb.edu

Introduction:

For the past century, researchers have been searching for an environmentally friendly alternative energy conversion device to replace the antiquated 18th-century internal combustion system. One of the most promising and emerging alternative energy conversion devices is the polymer electrolyte membrane fuel cell (PEMFC). The hydrogen fuel cell essentially converts hydrogen gas and oxygen gas into water while producing electrical energy, rendering this system significantly more environmentally attractive [1]. Some of the reasons that this system is not implemented today include its high cost and relatively low efficiencies from its catalyst layer, compared to its combustion system counterpart. Conventionally, the catalyst layer is composed of a supporting matrix of porous carbon black and platinum (Pt). Platinum serves the pivotal role as the catalyst, converting the incoming hydrogen gas into its hydronium ions and electrons. Once the platinum is embedded within the carbon black, some of carbon black's pores close during synthesis, rendering the platinum nanoparticles inside the pores useless.

Instead of using a porous carbon material, we will be employing reduced graphene oxide (rGO), a planar carbon structure, to maximize the efficiencies of Pt in fuel cell's catalyst layer. The aggregation of Pt particles on the carbon composite is still one of the imminent obstacles for hydrogen fuel cell integration; this conglomeration decreases the catalyst efficiencies in the catalyst layer [2]. Different concentrations of stabilizers, such as Nafion ionomer and polyvinylpyrrolidone (PVP) were employed to prevent aggregation of Pt nanoparticles. Nafion ionomer is a sulfonated tetrafluoroethylene based fluoropolymer with a hydrophobic backbone and with hydrophillic side chains. In solution, Nafion ionomer forms micelles due to its amphiphillic property. PVP is a water soluble polymer with the ability to quickly form thin films. Because of this property, PVP can coat other molecules. These two dispersing agents lower the tendency for Pt nanoparticles to conglomerate. An increase Pt nanoparticle conglomeration would in turn lower the effective surface area of Pt and hence decrease catalytic activity in the hydrogen fuel cell.

Experimental Procedure:

We added 33 wt% PVP, 60 wt% PVP, and 33 wt% PVP and 2.5 vol% Nafion in Sample 1, 2 and 3 respectively. The solutions underwent catalytic vapor diffusion and heat treatment at 500°C. The composites were then observed under the scanning electron microscope (SEM), x-ray diffraction (XRD), and cyclic voltammetry (CV).

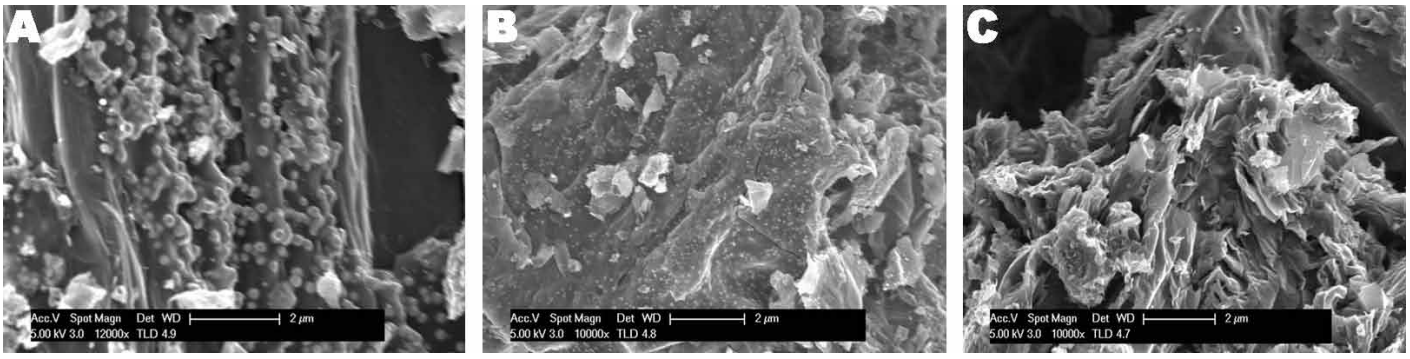

Figure 1: a) Scanning electron microscope (SEM) of Sample 1 containing 33 wt% PVP; b) SEM of Sample 2 containing 60 wt% PVP; c) SEM of Sample 3 containing 33 wt% PVP and 2.5 vol% Nafion ionomer.

Results and Conclusions:

The samples were observed through the SEM to visually understand the Pt behavior in each of the samples. In Figure 1 a), Sample 1 displayed Pt aggregation on rGO surface. With 2 μm as the resolution, the aggregated particles were estimated to be ~ 100 nm average in diameter. In Figure 1 b), the SEM image displayed significantly less Pt aggregation on the rGO surface for an increase of PVP. In Figure 1 c), an inclusion of a low concentration of Nafion depicted no visible Pt nanoparticle aggregation at a 2 μm resolution.

Each aggregated Pt particle was composed of the amalgamation of Pt nanoparticles. The average crystalline size of the aggregated particles can be calculated using the Scherrer equation for XRD data. From the summarized data in Figure 2, the Pt crystal size ranges from 5 nm to 9 nm in diameter of the Pt embedded in rGO (Pt@rGO) composites. The ACS amongst the three samples was relatively similar despite the different concentrations of stabilizing agents.

The efficiencies of the Pt in each sample were also observed with cyclic voltammetry (CV). CV was ramped from potentials of -0.4 V to 1.6 V with sweep rate of 10 mV/s. At negative potentials, the hydrogen oxidation reactions ($H_2 \rightarrow 2H^+ + 2e^-$) were measured. The total charge accumulated (proportional to the area underneath the cathodic peak) was converted into the amount of Pt surface area useful for oxidation purposes. A low concentration of PVP proved to have the lowest performance as it yielded the lowest effective surface area (ESA) of Pt. The inclusion of a low concentration of Nafion and PVP drastically increased Pt ESA. PVP was hypothesized to act as a coating layer over the Pt nanoparticles, sterically stabilized Pt nanoparticles from aggregating. Likewise, the behavior of Nafion ionomer at low concentrations could account for dramatic increase in performance. Nafion was composed of a hydrophobic backbone with hydrophillic side chains. In water-based solutions, Nafion ionomer formed micelles. These structures physically prevented Pt nanoparticles from aggregating. At a 2.5 vol% Nafion concentration, Nafion cluster size was large enough to prevent Pt conglomeration.

Sample	ACS[a] (d.nm)	ESA[b] (m^2/g)
Sample 1 (33 wt% PVP)	8.61	24.14
Sample 2 (60 wt% PVP)	5.45	28.50
Sample 3 (2.5 vol% Nafion + 33 wt% PVP)	6.76	40.85

Figure 2: Summary of results. Average crystal size (ACS) calculated from XRD data. Effective surface area (ESA) of Pt calculated from CV data.

Future Work:

The parameters are not yet optimized as these results are still preliminary results. Carbon black showed better performance than the current results, ranging from 40 m^2/g - 100 m^2/g as the Pt ESA. In the future, we will explore the efficiencies of platinum embedded in different carbon supporting matrix or varying the concentration of multiple dispersing agents to maximize the performance in rGO.

Acknowledgments:

I would like to thank Professor Dan Morse's group and the UCSB NNIN REU internship group for providing me with the necessary support and tools. I would personally like to acknowledge Dr. Chang Sun Kong for his unprecedented guidance during the 10-week internship. Finally, thank you to the National Nanotechnology Infrastructure Network Research Experience for Undergraduates Program for funding.

References:

[1] "Fuel Cells." Fuel Cell Technology Program. U.S. Department of Renewable Energy, Nov. 2010. Web. 25 August 2013.

[2] Nice, Karim; Strickland, Jonathan; "How Fuel Cells Work." How Stuff Works. Web. 25 August 2013.

An Experimental and Theoretical Investigation of Ultrasound Transmission in Bubbly PDMS Phononic Crystals

Caleb Christianson
Engineering Physics, University of Kansas

NNIN REU Site: Cornell NanoScale Science and Technology Facility, Cornell University, Ithaca, NY
NNIN REU Principal Investigator: Dr. Derek Stewart, Cornell NanoScale Science and Technology Facility, Cornell University
NNIN REU Mentor: Dr. Saikat Mukhopadhyay, Cornell NanoScale Science and Technology Facility, Cornell University
Contact: caleb.christianson@gmail.com, derek.stewart@cornell.edu, saikat.mukhopadhyay@cornell.edu

Abstract:

Phononic crystals are two- and three-dimensional structures with a periodic arrangement of two or more materials with different acoustic properties. Depending on the size, structure, and characteristics of the constituent materials, meta-materials with interesting acoustic properties can be formed. These crystals can be used to control the transmission of sound at selected frequencies, focus sound, or serve as waveguides. In this study, we investigated the transmission of ultrasonic waves through polydimethylsiloxane (PDMS) films with entrapped air bubbles. We examined how ultrasonic transmission through PDMS layers can be engineered by varying the dimensions, separation, and arrangement of air bubbles. We reproduced previously published data using two different theoretical models that describe ultrasonic transmission in air-PDMS crystals: (1) a simple scattering model for a series of partially reflective thin films, and (2) the code MULTEL, which calculates the transmission solution using multiple scattering theory. We then used these models to predict the performance of new phononic structures by scanning a large parameter space. To create these structures, we first fabricated arrays of micron-scale pillars on a silicon wafer. PDMS layers were then cast on these pillar templates and stacked to form air bubble arrays with two- and three-dimensional periodicity. A series of processes were developed to stack layers of the crystals with unprecedented alignment. Finally, we measured the ultrasonic transmission through the films using a transducer/receiver setup in a water bath and compared it to the theoretical results.

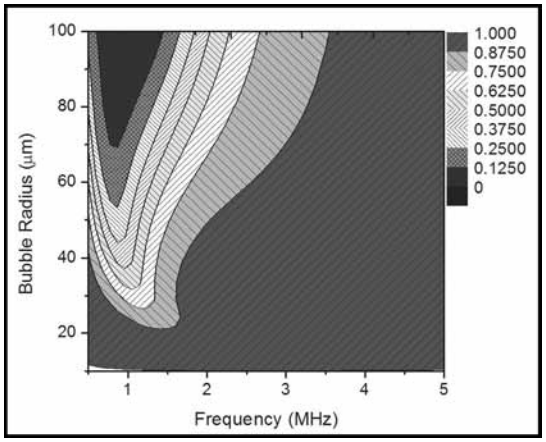

Figure 1: Contour plot of transmission for analytical model as a function of bubble radius and frequency. N = 1, a_x = 300 μm.

Modeling Ultrasound Transmission:

We used two theoretical models to fit published experimental data [1] of a single PDMS layer with a square bubble lattice (a = 300 μm) and a four-layer PDMS stack with a tetragonal bubble lattice (a_x = 300 μm; a_z = 350 μm). The first analytic approach treats each bubble layer as a partially reflective plane and then iteratively calculates the reflection and transmission through all layers [1, 2]. We also used a more rigorous multiple scattering theory (MST) approach [3] where each bubble served as a scattering source for incoming ultrasonic waves. We found excellent agreement with previously measured values and the theoretical approaches gave consistent results for much of the frequency range. We then used these models to explore a broad parameter space to determine the variation of transmission with the key parameters (e.g., number of layers, bubble radius and separation). Figure 1 demonstrates one such investigation, where we fixed the bubble separation and calculated the transmission up to 5 MHz as we varied the bubble radius up to 100 μm. Using a similar approach, we showed that the crystal can be tuned to block certain frequencies. The blocked frequency followed the isolated bubble Minnaert resonance [4]. However, due to the bubble periodicity, we could tune the blocked frequency away from the Minnaert resonance by adjusting the in-plane bubble separation.

Phononic Crystal Fabrication and Measurements:

After establishing our theoretical models, we set out to build the crystals to measure the transmission experimentally. Contact lithography was used to pattern an array of pillars on silicon and we then etched the wafer down 50 μm. We then spun 350 μm of PDMS on the etched wafer, giving a flat, uniform film over the pillar array. PDMS was lifted off and stacked for ultrasonic measurements. Ultrasonic measurements were carried out in a

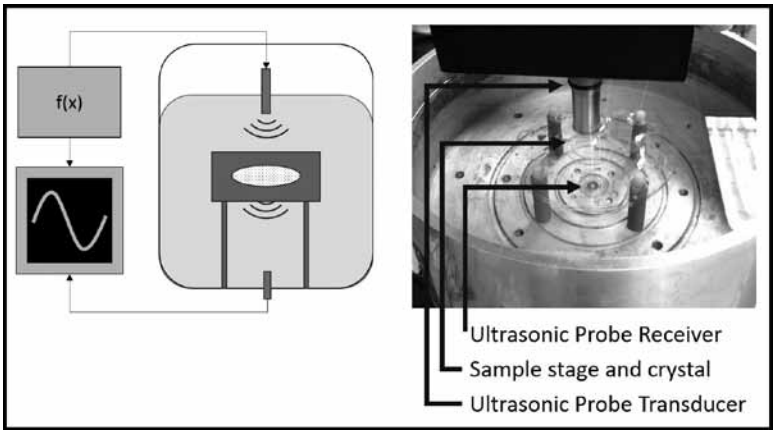

Figure 2: Schematic and image of the ultrasonic transmission experiments.

water chamber using a 10 MHz transducer positioned above the crystal (Figure 2). The ultrasonic waves were transmitted through the crystal, which was suspended on a sample stage, and the signal was then detected by a receiving probe at the bottom of the chamber.

Results and Conclusions:

A key challenge was the proper alignment of the bubble arrays in multi-layer films. Leroy et al. [1] described the alignment of the layers as, "a problematic issue" and their phononic crystal shows an offset between different bubble layers. Challenges include the inherent difficulties caused by the flexibility of the PDMS film, issues with entrapping errant air bubbles, adhering multiple PDMS layers, and perfectly aligning each layer. Figure 3 shows a top-down view of our well-aligned, two-layer film with the published two-layer film from Ref. [1] overlaid for comparison. Through a series of careful alignment procedures with a SUSS MA6/BA6 contact aligner, we were able to produce a two-layer crystal with no visible offset between bubble layers. After aligning two layers, we measured the ultrasonic transmission using the process described previously. Our transmission measurements for single- and two-layer films are plotted with our theoretical models in Figure 4. Overall, the measured transmission matches the trends expected from our theoretical models and from previously published data.

In this work, we have used two theoretical models to match published experimental data and also examine a broad parameter space for phononic crystals. We have fabricated single- and two-layer crystals and demonstrated better layer alignment than previously published work. Ultrasonic transmission measurements through these new crystals are comparable to our models and previous works.

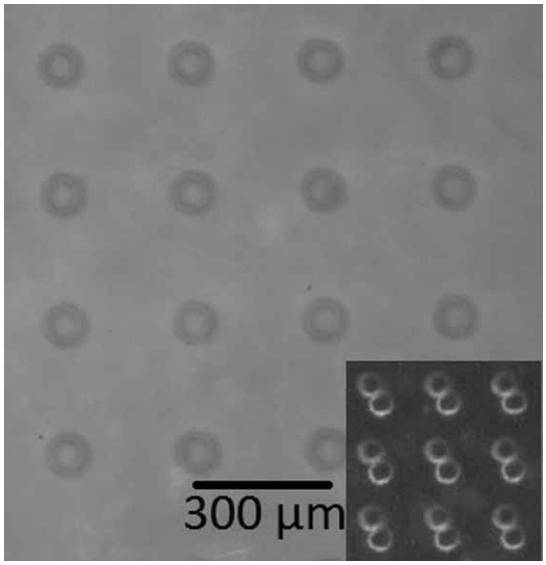

Figure 3: Micrograph of our two-layer film in comparison with previously published two-layer film [1] (inset).

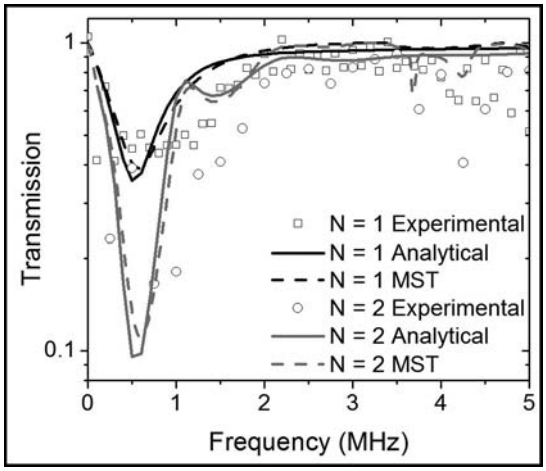

Figure 4: Transmission results for single- and two-layer films. R = 39 µm, a_x = 300 µm, and a_z = 360 µm.

Acknowledgments:

This work was supported by the National Science Foundation and performed at the Cornell NanoScale Facility, as part of the NNIN REU Program. Special thanks to Rob Ilic, Melanie-Claire Mallison, Christopher Alpha, Edward Camacho, Meredith Metzler, Beth Rhoades, Wolfgang Sachse, Michael Skvarla, Daron Westly, and Sam Wright.

References:

[1] V. Leroy, A. Bretagne, M. Fink, H. Willaime, P. Tabeling, and A.Tourin, Appl. Phys. Lett. 95, 171904 (2009).

[2] M. Devaud, et al., Eur. Phys. J. E, 32, 13 (2010).

[3] R. Sainidou, N. Stefanou, I. E. Psarobas, and A. Modinos, Comp. Phys. Comm. 166, 197 (2005).

[4] M. Minnaert, Philos. Mag. 16, 235 (1933).

Growth of Graphene on Various Substrates

Crystal T. Chukwurah
Biomedical Engineering, Duke University

NNIN REU Site: Howard Nanoscale Science and Engineering Facility, Howard University, Washington, DC
NNIN REU Principal Investigator: Dr. Gary L. Harris, Electrical and Computer Engineering, Howard University
NNIN REU Mentor: Mpho Musengua, Materials Science and Electrical Engineering, Howard University
Contact: crystal.chukwurah@duke.edu, gharris@msrce.howard.edu, mmusengua@yahoo.com

Abstract:

Graphene is a single layer of graphite. Its unique properties consist of chemical stability, high tensile strength, flexibility, and high thermal conductivity. These properties make graphene suitable for future applications such as hydrogen storage, lighter prosthetics, and flexible electronics. Past methods of graphene preparation such as exfoliation are efficient for lab purposes, but are not suited for mass production. With applications in mind, suitable substrates and methods for large quality graphene growth are necessary. This project focused on which methods of graphene growth are suitable for different substrates. Graphene was grown by the following methods: simple chemical vapor deposition (CVD), hot filament CVD, and radio-frequency plasma CVD. The methods were selected because they provide the option to use various substrates under unique conditions. From these methods, graphene growth was attempted on the following substrates: copper, 3C-silicon carbide on silicon, nickel, nichrome, and nickel films on 3C-silicon carbide. These substrates were selected for their strength, ductility, and resistance to corrosion and heat. The grown films were characterized using scanning electron microscopy (SEM) and Raman spectroscopy. Raman results have confirmed graphene on nickel films on 3C-silicon carbide, diamond nanoseeded nichrome, nickel foil, and annealed nickel foil by the hot filament CVD method. Ultimately, these results may uniquely contribute to the mass production of graphene on potentially any substrate.

Introduction:

Graphene growth is a fairly new technology and many growth methods are currently being evaluated. Popular techniques to form graphene include exfoliation, sublimation of silicon carbide, and CVD onto metal foils [1-3]. Exfoliation requires physically removing multiple layers of graphene to obtain single layer. The sublimation method is limited to silicon carbide and requires transferring to other substrates. CVD is practiced on metal foils at high temperatures to get quality graphene. Unfortunately, this limits graphene growth to only a select few substrates; of which, have little favorability for graphene applications. Enhanced CVD processes like hot filament CVD (HFCVD) and radio-frequency plasma CVD (RFCVD), which uses hot filaments or a plasma to disassociate hydrocarbon gases, allow graphene to be grown on more substrates over a broader range of temperatures. With help from the filaments or the plasma, graphene growth no longer relies on the substrates to be at high temperatures. Enhanced CVD can grow graphene directly onto various substrates, which eliminates the transfer process and is valuable for mass production of high quality large area graphene.

Experimental Procedure:

In this work, graphene was grown on various substrates by the following methods: simple CVD, RFCVD, and HFCVD. The growth conditions are given in Figure 1. The various substrates (copper, 3C-silicon carbide on silicon, nickel, nichrome, and nickel films evaporated on 3C-silicon carbide) were pretreated through sonication in 1) trichloroethylene, 2) acetone, and 3) methanol for three minutes each. In pretreating the substrates, copper and nickel were annealed *in situ* under H_2 at ~ 1000°C from ~ 0-40 min. Additional trials were completed using other substrate pretreatments conditions namely: non-*in situ* annealed copper, unannealled substrates, and UV radiated substrates. With conventional CVD, graphene growth was attempted on copper and nickel substrates with the following growth conditions: H_2/CH_4 = 3 at ~ 1000°C for 10 min. With RFCVD, graphene growth was attempted on all substrates with the following growth conditions: Ar/CH_4 = 19 at ~ 1000°C for 5-10 min. With HFCVD, graphene growth was attempted on all substrates with

Growth Conditions	Simple CVD	RFCVD	HFCVD
Substrate Temperature	1000°C	1000°C	0-750°C
Filament Temperature	N/A	N/A	2100-2300°C
Gas Flowrates (sccm)	H_2=5 CH_4(5%)=35	N/A	H_2=30; 50 CH_4(5%)=5;10
Gas Ratio H_2/CH_4	3	N/A	5; 60; 125
Gap Distance	N/A	N/A	15-45mm
Plasma Intensity	N/A	250-300 Watts	N/A
Pressure	0.3 Torr	1.3E-4 Torr	20-35 Torr
Anneal Time (min)	45 min	0-30 min	0-40
Growth Time (min)	10 min	5-10 min	5-10min

Figure 1: Graphene growth conditions for simple CVD, radio-frequency plasma CVD, and hot filament CVD.

the following growth conditions: H_2/CH_4 of 5, 60, and 125 from 5-10 min. Additionally, the substrate and filament temperatures for HFCVD were 0-750°C and 2100-2300°C, respectively. Uniquely, HFCVD's substrate temperature range was trialed for lower temperature growth.

Results and Conclusions:

The substrates were characterized using Raman spectroscopy and scanning electron microscopy (SEM). CVD and RFCVD method did not yield any graphene films. Raman results have confirmed graphene by HFCVD on nickel films on 3C-silicon carbide (Figure 2). The results correspond to multi-layer graphene. The SEM image of graphene grown on nickel films on 3C-silicon carbide shows graphene grain sizes on the order of 1-3 μm (Figure 3). Similar Raman results confirmed graphene by HFCVD on the following other substrates: diamond nanoseeded nichrome, nickel foil, and annealed nickel foil. The SEM image of graphene grown on nickel foil shows graphene grain sizes on the order of 30-40 microns (Figure 4).

Improper annealing of the copper substrate may explain the lack of graphene on copper. Lack of graphene by RFCVD may be due to the substrate temperature being significantly lower than the thermocouple reading due to heat loss. Future research will require a more extensive evaluation of the growth conditions for each system and what substrate properties are important in the formation of graphene. Also some effort will be required to increase grain size.

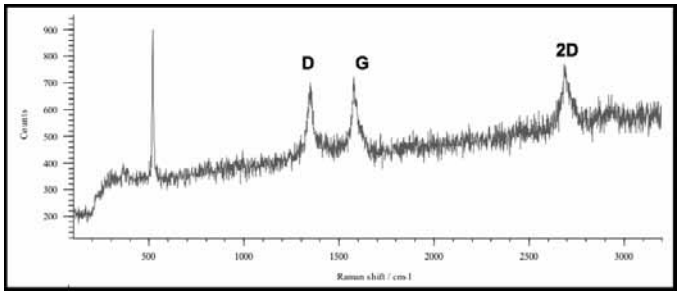

Figure 2: Raman spectroscopy results for 100 nm Ni film evaporated on SiC on Si grown by HFCVD.

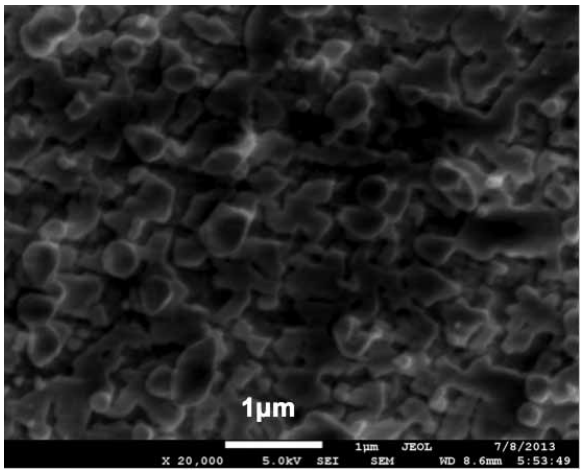

Figure 3: SEM image of graphene grown by HFCVD on 100 nm Ni film on SiC on Si.

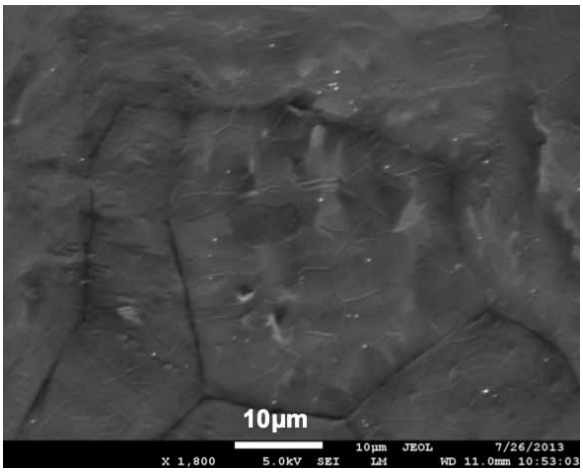

Figure 4: SEM image of graphene grown by HFCVD on Ni substrate.

Acknowledgements:

I would like to thank the following for their support: PI Dr. Gary Harris, Research Mentor Ms. Mpho Musengua, Site Coordinator Mr. James Griffin, the staff at the Howard Nanoscale Science and Engineering Facility, the National Nanotechnology Infrastructure Network Research Experience for Undergraduates (NNIN REU) Program, and the National Science Foundation.

References:

[1] Cai, Minzhen, et al. "Methods of graphite exfoliation." Journal of Materials Chemistry 22.48 (2012): 24992-25002.

[2] de Heer, Walt A., et al. "Large area and structured epitaxial graphene produced by confinement controlled sublimation of silicon carbide." Proceedings of the National Academy of Sciences 108.41 (2011): 16900-16905.

[3] Li, Xuesong, et al. "Graphene films with large domain size by a two-step chemical vapor deposition process." Nano letters 10.11: 4328-4334 (2010).

Investigation of Microfluidic Integration in Magneto-Nanosensor Based Protein Biomarker Detection

Stephanie Cone
Biomedical Engineering, University of Arkansas

NNIN REU Site: Stanford Nanofabrication Facility, Stanford University, Stanford, CA
NNIN REU Principal Investigator: Professor Shan X. Wang, Electrical Engineering and Materials Science, Stanford University
NNIN REU Mentor: Daniel Bechstein, Mechanical Engineering, Stanford University
Contact: scone@uark.edu, sxwang@stanford.edu, bechst@stanford.edu

Abstract:

The use of magnetic nanoparticles in conjunction with a spin-valve type giant magnetoresistive (GMR) sensor provides a method for the detection and quantification of picomolar concentrations of proteins in biological samples. The magnetic nanoparticles act as a magnetic tag for proteins which allow the quantification of targeted proteins. Recent developments in the lab's custom microfluidic integration approach with the spin valve sensor array allow for simultaneous testing for multiple samples on a single chip and a variety of proteins within a given sample. In this work, testing is being conducted to study the distribution of magnetic nanoparticles following the completion of microfluidic assay experimental procedures. Specifically, the final locations and local densities of the magnetic nanoparticles and the presence of washing buffer fluid following the assay are being compared to the geometry of the microfluidic channels. The comparison of these patterns may lead to improvements in the efficiency and reproducibility of the bioassays.

An SEM was used as the primary source of images in this study. Some potential applications for this technology include multiplexing of surface interface sensors within automated point-of-care diagnostic devices.

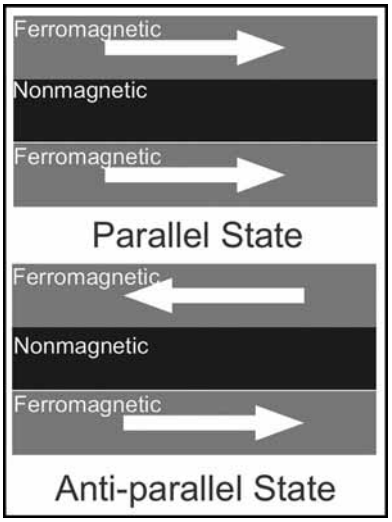

Figure 1: View of the magnetic parallel and antiparallel states.

Experimental Procedures:

Lab-on-a-Chip Devices. Lab-on-a-chip tools are self-contained devices that can run immunoassays on protein samples. These devices are useful for many reasons. One major benefit is their portability, which permits their use in remote locations that would otherwise require the transportation of samples for diagnostic tests. Another major point is that with small devices, very little material is required during a single test, leading to both lower material costs and the generation of less waste. Finally, there is often minimal training required for operators of such tools, as they are primarily self-contained, and highly automated.

Giant Magneto Resistance Sensors (GMR). GMR is a large change in resistance in certain materials and structures upon the application of a magnetic field. With the example of our sensors as pictured in Figure 1, the bottom ferromagnetic layer has a fixed magnetic field, while the field in the top ferromagnetic layer is switched between the parallel and anti-parallel states in order to induce a change in the magnetic field. The observed change in resistance is due to more electrons being scattered when they pass through the material in the anti-parallel state as opposed to the parallel state.

When magnetic nanoparticles, which act as tags for proteins, are added to the top of the GMR, the strength of the magnetic field is affected. This leads to a change in the magnetoresistance which is measured and normalized, resulting in the GMR acting as a sensor to analyze the sample composition.

Bioassays. Bioassays can provide information on the concentration of targeted proteins in samples. In these experiments, BSA was used as a negative control that produced no change in the magnetic resistance, biotin was the positive control that produced a very high signal, and test proteins were applied to sensors in a range of concentrations, resulting in a signal bands located between the controls.

Standard Well Assays. Standard well assays were performed by applying reagents in a preset order to a chip, and adding magnetic nanoparticles while the chip was located in the GMR sensor. These reagents included proteins and matching antibodies, magnetic nanoparticles, biotin, and BSA. Data from bioassays can be plotted in the format of change in

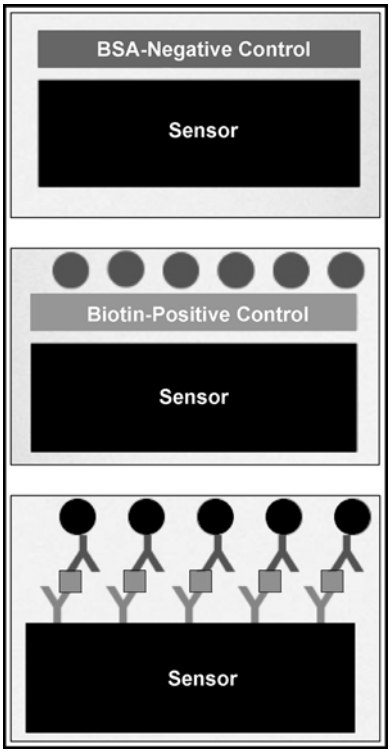

Figure 2: Negative control, positive control, and test biosensors with reagents attached.

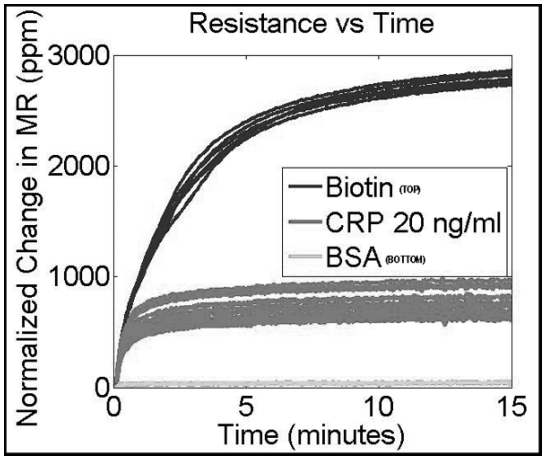

Figure 3: Data plot of corrected resistance versus time from standard well bioassay.

magnetic resistance versus time. In Figure 2, the test protein was C-reactive protein, which is a common protein released as a part of the complement system in the inflammatory response. Throughout the summer, C-reactive protein and FLT3LG were both used as test proteins in various concentrations.

Following the bioassay, the results were recorded in the form of corrected change in magneto-resistance versus time. An example of this data can be seen in Figure 3.

Microfluidic Assays. When used in conjunction with GMR sensors, microfluidics could improve both the reliability and efficiency of bioassays. Some reasons for this are that the use of microfluidics can automate much of the bioassay procedure, it directs reagent material to the sensors, and it can provide separate channels, allowing for concurrent testing of multiple samples. The reliability of microfluidic testing depends on factors including the physical structure of the channels, the surface chemistry of the sensor, and the alignment of the chips.

Conclusions:

Multiple proteins were detected at picomolar concentrations through the use of GMR sensors and magnetic nanoparticles. Microfluidic channels were found to be an effective means of directing reagents along the surface of sensor chips. No cross-contamination was witnessed between the channels, meaning that a variety of tests could be run simultaneously on a single chip.

Future Work:

This research will be continued by the addition of tests involving new proteins, as well as experiments with an expanded range of concentrations, in order to better evaluate the sensitivity of the tool. More research and development will be done to increase the portability of the total diagnostic device, thus increasing its functionality as a Lab-on-a-Chip.

Acknowledgments:

I would like to thank CIS, NNIN REU, NSF, the REU staff at SNF, Daniel Bechstein, Professor Shan X Wang, and the Wang lab group for their assistance in this research.

References:

[1] Gaster, R., et al.; "Matrix-insensitive protein assays push the limits of biosensors in medicine"; Nature Medicine, 15, 1327-1332 (2009).

[2] Gaster, R., et al.; "nanoLAB: An ultraportable, handheld diagnostic laboratory for global health"; Lab Chip, 11, 950-956 (2011).

[3] Osterfield, S., et al.; "Multiplex protein assays based on realtime magnetic nanotag sensing"; PNAS, 105, 20637-20640 (2008).

Ion Transport Through Porous Graphene

Katelyn Conrad
Biomedical Engineering, Arizona State University

NNIN REU Site: Colorado Nanofabrication Laboratory, University of Colorado, Boulder, CO
NNIN REU Principal Investigator: Professor Scott Bunch, Mechanical Engineering, University of Colorado at Boulder
NNIN REU Mentor: Lauren Cantley, Mechanical Engineering, University of Colorado at Boulder
(2010 NNIN REU at the University of Colorado at Boulder)
Contact: kmconra1@asu.edu, scottbunch@gmail.com, laurencantley@gmail.com

Abstract:

Graphene is a two-dimensional carbon material that is only one atom thick with exceptional strength and remarkable gas separation properties [1-3]. Graphene membranes have great potential for applications in DNA sequencing, desalination and water filtration, as well as lab on a chip processes. The focus of this project was to investigate the potential of graphene membranes for liquid separations. A microfluidic device was designed and fabricated to test graphene's separation properties in liquids. Chemical vapor deposition (CVD) graphene was freely suspended over a thin copper foil and attached to a polydimethysiloxane (PDMS) microfluidic substrate. Suspended graphene was fabricated via standard photolithography while a PDMS substrate was fabricated via soft lithography techniques. To observe the permeability of graphene membranes, pressurized deionized water was introduced onto the underside of a graphene membrane through a microfluidic channel and the graphene membrane deflection was measured via atomic force microscopy (AFM) in air. Future work includes electrical testing of water and ionic transport across porous monolayer graphene membranes.

Introduction:

Graphene is a two-dimensional material made of carbon, the same material as the three-dimensional graphite that can be found in pencils. This material is only one atom thick, yet for being so thin, it has exceptional strength. In fact, it is the thinnest and strongest material known [1]. It has been found to have remarkable gas separation properties, and be impermeable to all molecules including helium when in its pristine form [2, 3]. Graphene membranes also have great potential for applications involving liquid separations such as DNA sequencing, desalination, and water filtration, as well as lab on a chip processes [4]. The focus of this project was to investigate the potential of graphene membranes for liquid separations.

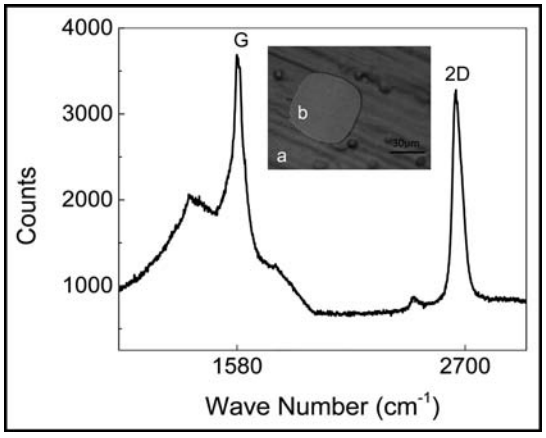

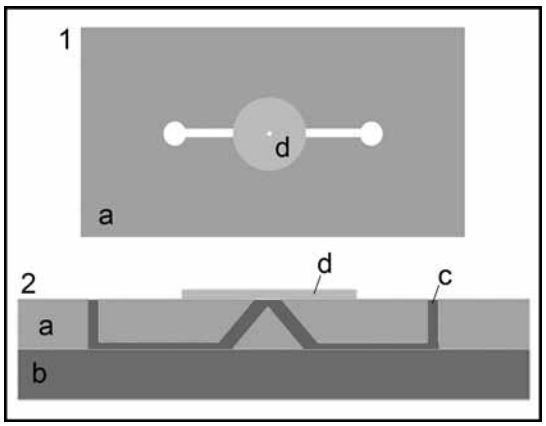

Figure 1, top: Optical image of the copper foil (a) containing suspended CVD graphene (b); Raman spectrum of the suspended CVD graphene.

Figure 2, bottom: (1) Top view of final device. (2) Side view of final device. Key: (a) PDMS (b) glass slide (c) DI water (d) copper.

Experimental Procedure:

In order to investigate the potential of graphene membranes for liquid separations, first the suspended graphene membrane was fabricated. Graphene was grown on a thin copper foil via CVD. The copper was then patterned using standard photolithography techniques and etched by floating the copper in a 0.1M solution of ammonium persulfate. After floating in the etchant for three hours, the copper was inspected every half hour for the next one to nine hours until the copper with graphene on it became a

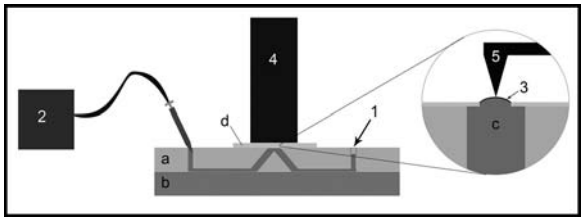

Figure 3: Experimental setup: One end of the channel was plugged with a piece of PDMS (1) and a pump was inserted in the other side of the channel (2). The deflection of the graphene membrane (3) was monitored using the AFM (4) by having the AFM tip (5) move across the surface of the membrane. Key: (a) PDMS (b) glass slide (c) DI water (d) copper.

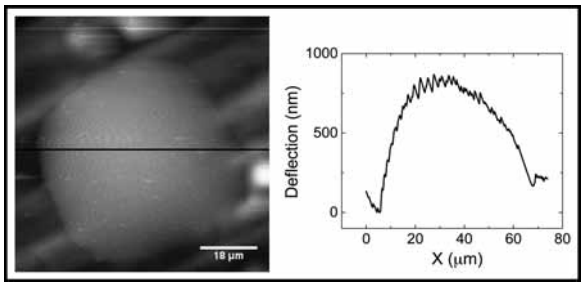

Figure 4: AFM data.

copper disc approximately 7 mm in diameter with a hole in the center approximately 15 μm in diameter, over which graphene was suspended. This copper disc was then critical point dried to avoid damaging the graphene membrane. Raman spectroscopy was used to confirm that graphene was suspended, as indicated by the G peak at approximately 1580 cm^{-1} and the 2D peak at approximately 2700 cm^{-1}, as shown in Figure 1.

The copper disc containing suspended graphene was then adhered to a microfluidic channel made from PDMS. The microfluidic channel was fabricated via standard soft lithography techniques and measured 50 μm deep and 500 μm wide with through holes 1.5 mm in diameter. The final device is shown in Figure 2.

Next, the graphene membrane was pressurized from below by pumping deionized water into the microfluidic channel. To do so, one end of the channel was plugged with a piece of PDMS and a syringe pump introduced deionized water to the other end of the channel, as shown in Figure 3. The effects of this pressurization were monitored using both optical and atomic force microscopy, as shown in Figure 4.

Results and Conclusions:

Initial tests were observed using only an optical microscope and revealed that when the underside of the membrane was pressurized to large values, the graphene quickly burst due to the large pressure difference. To decrease the pressure differential across the membrane, subsequent tests were carried out by pressurizing the graphene membranes at a slower rate. For the duration of these tests, the top surface of the graphene was monitored using AFM, as shown in Figure 3. AFM data revealed that when pressurized from below, the graphene membrane bulged up in response to the increased pressure difference, as shown in Figure 4. Changes in pressure were reflected in the deflection of the membrane. The ability to image the pressurized graphene membranes without the obvious penetration of water across the membrane is an indication that the CVD graphene membranes fabricated via the method described above are indeed impermeable to the transport of water.

Future Work:

The next step in this project will be to etch pores in the CVD graphene membrane using UV-ozone etching. The introduction of pores will allow for exploration into how water moves across porous graphene membrane as well as exploration into ion transport and molecular separation.

Acknowledgments:

I would like to thank the National Nanotechnology Infrastructure Network Research Experience for Undergraduates Program and the National Science Foundation for their support of this project. I would also like to thank Professor Scott Bunch, Lauren Cantley, the Bunch Research Group, and the Colorado Nanofabrication Laboratory for their guidance in this research.

References:

[1] Geim, A. K. and Novoselov, K. S.; "The Rise of Graphene"; Nature Materials, 6, 183-191 (2007).

[2] Bunch, J. Scott, et al.; "Impermeable Atomic Membranes from Graphene Sheets"; Nano Letters, 8.8, 2458-2462 (2008).

[3] Koenig, Steven P., et al.; "Selective molecular sieving through porous graphene"; Nature Nanotechnology, 7, 728-732 (2012).

[4] Garaj, S., et al.; "Graphene as a sub-nanometer trans-electrode membrane"; Nature, 467, 190-193 (2010).

Nanocharacterization of Wood Fibers in Cement

Christopher Florencio-Aleman
Materials Science and Engineering, Columbia University

NNIN REU Site: Nanotechnology Research Center, Georgia Institute of Technology, Atlanta, GA
NNIN REU Principal Investigator: Dr. Kimberly E. Kurtis, Civil and Environmental Engineering, Georgia Institute of Technology
NNIN REU Mentor: Passarin Jongvisuttisun, Civil and Environmental Engineering, Georgia Institute of Technology
Contact: cf2480@columbia.edu, kimberly.kurtis@ce.gatech.edu, p.jongvisuttisun@gatech.edu

Abstract:

Early-age cracking resulting from the absence of water is a major problem in high-performance concrete in which the low water-to-cement ratio is used. This is solved through internal curing methods where absorptive materials, such as saturated lightweight aggregates (LWAs) and super absorbent polymers (SAPs), are added to the cement mix to aid the hydration process. Because of its hygroscopic properties, natural fibers are a novel material in internal curing methods and have often been thought of as an inert material in cementitious composites. However, these fibers are not inert and the nanocharacterization of the cement-fiber system grants insight to the interactions between these fibers and the cement. Through this nanocharacterization, it has been determined that fiber is acting as both a nucleation site and as a semi-permeable membrane which interacts with the cement system and ultimately changes the kinetics of the hydration process.

Introduction:

In terms of worldwide resource consumption, only water is used in greater quantities as compared to concrete each year [1]. Early age cracking is one of the main problems high performance concrete faces due to the low water to cement ratio that is required to achieve high performance. High performance concrete is typically very dense and traditional methods of supplying water through external curing methods, where water is ponded on top of the concrete, are not very effective. A novel method to provide water to high performance concrete is internal curing. These methods aid the cement hydration process by uniformly distributing a hygroscopic material throughout the concrete mix.

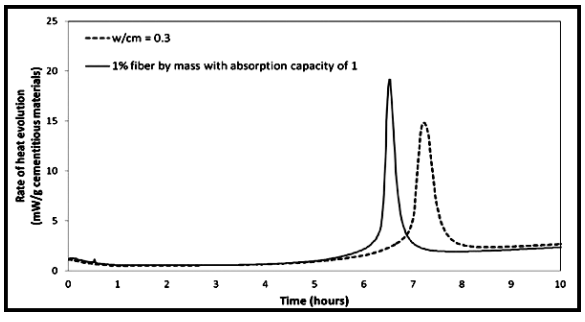

Figure 1: Heat released from the white cement paste compared with that of the fiber-white cement paste.

A novel material used to internally cure concrete is natural fiber. When evaluating the effect of fiber in ordinary Portland cement and white Portland cement, the calorimetry curves in Figure 1 have shown that fiber alters the systems in such a way that it not only aids cement hydration reactions, it also accelerates them to occur earlier in white cement. This suggests that the interactions between fiber and white cement at early ages mainly depends on the chemical composition of the cement.

There are two possibly ways in which the fiber may be interacting with the fiber; 1. The fiber's surface is acting as a nucleation site onto which cement hydration products are forming, and 2. The fiber could be acting as a semi-permeable membrane which changes the ion concentrations and therefore alter the kinetics of the reactions.

Experimental Procedure:

In order to determine certain aspects between these interactions, nanocharacterization techniques were applied in the form of inductive coupled plasma spectroscopy (ICP), scanning electron microscopy (SEM) images, atomic force microscopy (AFM), and x-ray photoelectron spectroscopy (XPS). ICP was used to determine the ion concentrations of both cements used to determine if chemical composition was a factor in these changes, SEM images were taken in order to determine if the fibers were acting as nucleation sites that facilitated the formation of cement hydration products, AFM imaging was used to survey the fiber surface and better understand the surface morphology, and XPS was used to determine ion concentrations at different depths to determine if the fiber was acting as a semi-permeable membrane which ultimately affected the kinetics of the system.

Results and Conclusions:

From the ICP ion analysis, different concentrations were determined for the gray and white cements. Gray cement pore solution was found to contain 60% potassium, 29% sulfur,

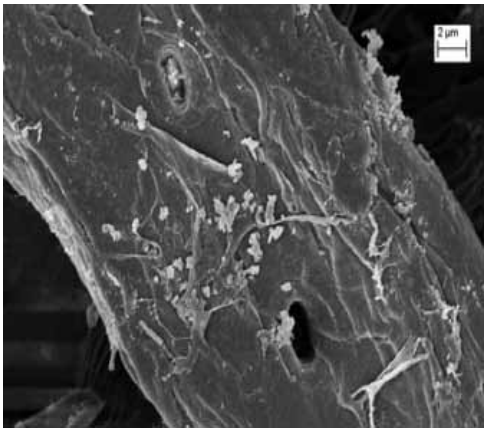

Figure 2: SEM image of fiber exhibits hydration product formation at 24 hour in cement pore solution.

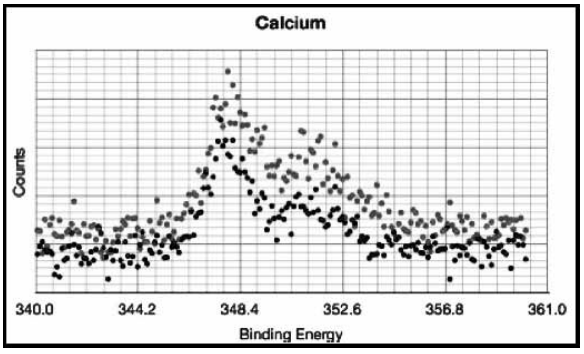

Figure 4: High-resolution XPS spectra of fiber sample in Ca 2p energy region.

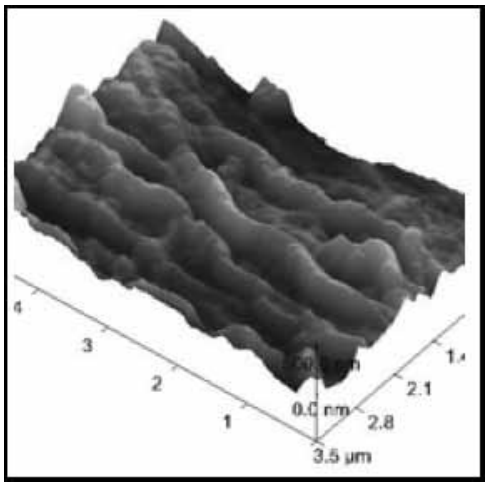

Figure 3: AFM 3D image of a detail of the fiber surface. Fiber features are about 500 nanometers in height.

8% sodium, and 3% calcium. In contrast, white cement pore solution contained 40% calcium, 23% sulfur, 19% potassium, and 18% sodium. Since the chemical composition of the cement pore solution was one of the factors which was hypothesized to be a primary factor of the acceleration in the cement, the calcium difference between the two cements should be noted as the primary difference.

From the SEM and AFM images, the fiber's rough surface could be observed. Further SEM images showed cement products forming onto the rough areas of the fiber. AFM imaging showed the rough features found on the fiber surface were about 1000 nanometers. There was no observable difference between the white cement and grey cement.

From XPS analysis, the main thing that should be noted is the difference in calcium ion concentrations at different depths. Again, there were no notable differences in our analysis between the gray and white cement. The importance of this was factored in when the membrane-like properties of the fiber were considered. The XPS data also showed that the calcium ions were favored due to the selectivity of the fiber membrane.

Since the main difference in the cement chemical composition was the difference of calcium where gray cement had almost no calcium present (3%) and the white cement had an abundance (40%), the selectivity of the fiber for this calcium is what causes this acceleration in the hydration reactions in the white cement as shown in the calorimetry curves.

Future Work:

Additional research into investigating the effect of altering the surface morphology of the fiber could provide additional insight into the physical effects that fiber plays in cement hydration. Experiments that alter the fiber's surface through chemical manipulation to become more rough and therefore accelerate the nucleation properties of the fiber could provide additional insight into the cement hydration phase. Also, further insight into the role of the fiber's cell wall and the effects it has on the kinetics of the hydration reactions could be beneficial.

Acknowledgments:

I would like to thank my principal investigator, Dr. Kimberly E. Kurtis; my mentor, Passarin Jongvisuttisun; Dr. Nancy Healy, and Leslie O'Neill; the National Nanotechnology Infrastructure Network Research Experience for Undergraduate (NNIN REU) Program and the National Science Foundation for funding and making this research possible.

References:

[1] Ashby, M. F., "Materials and the Environment", Butterworth-Heinemann Publisher, 2nd edition (April 11, 2012).

[2] Weiss, J.W., Bentz, D.P., Schindler, A.K., and Lura, P., "Internal curing construction more robust concrete", Structure, January 2012:10-14.

Determination of Strength Degradation Mechanisms of Native Oxide on Silicon Nanostructures

Rafael Jesus Haro
Mechanical Engineering, University of Arizona

NNIN REU Site: Cornell NanoScale Science and Technology Facility, Cornell University, Ithaca, NY
NNIN REU Principal Investigator: Prof. Alan Zehnder, Mechanical and Aerospace Engineering, Cornell University
NNIN REU Mentor: Scott Grutzik, Field of Theoretical and Applied Mechanics, Cornell University
Contact: rharo06@email.arizona.edu, atz2@cornell.edu, sjg242@cornell.edu

Abstract:

Understanding what affects the strength of micro- and nanoelectromechanical systems (MEMS and NEMS) is essential to effectively designing load bearing MEMS / NEMS. Research by Alan, et al. [1], suggests that oxide growth on silicon nanostructures leads to a decrease in strength, therefore increasing the likelihood of failure [1]. To interpret how silicon strength is affected as native oxide grows on the beams, the beams were failure tested weekly for five weeks allowing continuous growth of oxide, after which strength had decreased to 81% of the original strength. After the oxide was removed, strength recovered to 96% of the original strength. Silicon beam failure tests were performed using an atomic force microscope (AFM), which recorded the deflection of the AFM cantilever and the displacement of the piezo. A reference cantilever was used to find the stiffness of the AFM cantilevers used for failure tests. The beam's failure stress was calculated from the beams' failure force using the finite element method.

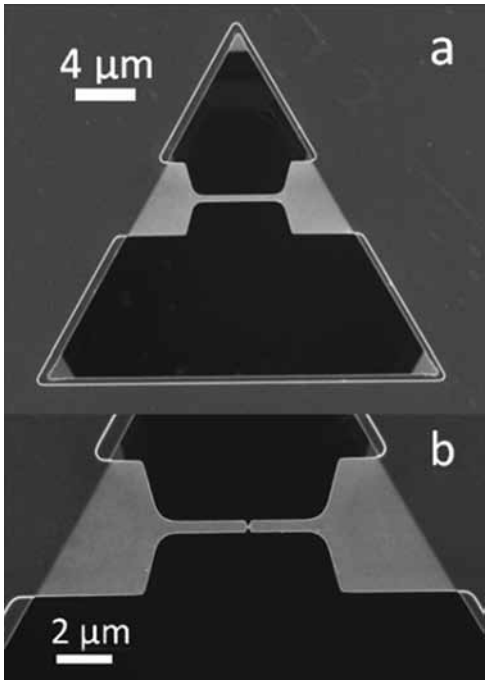

Figure 1: a) Top view scanning electron microscope image of beam and triangular trench. b) Beam with fracture at center.

Introduction:

Due to factors such as large surface to volume ratio and low defect density, nanoscale strength cannot be determined using macroscale experiments. Silicon is a brittle material that fails stochastically, which is why many beams must be tested to obtain accurate strength data. Research suggests that uneven oxide layer growth may form a rough surface on silicon beams, thus causing the AFM cantilever forces to concentrate at one of these stress points [1]. If roughness occurs, the beams' strength before and after oxide removal would be similar. Furthermore, if the strength is changed due to chemical interaction between oxide and silicon, the strength should increase after removal. To find how the mechanisms of native oxide growth correlate to silicon strength, nanoscale fracture specimens were fabricated and allowed to oxidize while tracking the reduction in strength. At the end, the oxide was removed and a final measurement of strength was made. The fabrication and strength analysis of the beams using an AFM was performed as described in Alan, et al. [2], and Namazu, et al. [3].

Methods:

Silicon <111> orientated wafers were used to fabricate the single crystal silicon beams. A photolithography step outlined the shape, and the beam thickness was etched using reactive ion etching (RIE). An oxide coat was grown on the wafer, and a second photolithography and RIE step defined the depth of the beam trenches. An anisotropic potassium hydroxide/ tetramethylammonium hydroxide etch released the beams by etching horizontally beneath them and terminating on their <111> orientation bottom surface. The beams were immersed into a buffer oxide etch removes the oxide to start performing the failure strength tests. The final beam sample is shown in Figure 1. To control the effect of humidity on rate of oxidation, the beams were stored at 100% relative humidity between strength tests.

The failure strength was measured using the deflection of the AFM cantilever and displacement of the piezo. The interaction between the piezo, AFM cantilever, and the beam were taken as springs in series (Figure 2); the piezo displacement equals the sum of the beam and AFM cantilever deflection [4]. A reference cantilever with a known stiffness was used to calculate the force applied on the beams. Finite element analysis was used to calculate the failure stress from the failure force (Figure 3). The failure stresses for each week fit a Weibull distribution as a group, which was used to measure average strength and plot as a function of time.

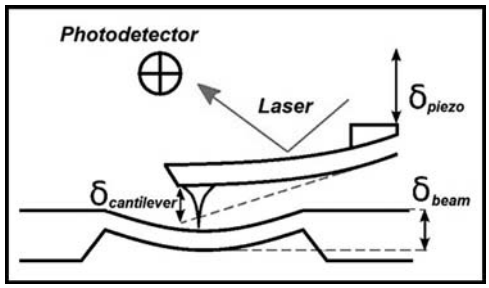

Figure 2: Side view schematic of the AFM cantilever and beam deflections.

Results and Conclusions:

Testing in weeks two and three did not reflect the strength decrease as shown in Alan, et al. The beam strength, however, did increase surprisingly after oxide removal and resembled the strength prior to oxidation. Previous tests show that oxide reduces silicon beam's strength, which is not reflected from weeks two, three, and four (Figure 4). Our hypothesis about the cause of this discrepancy is the repetitive use of the same AFM cantilever. Since the same AFM cantilever was used for weeks one through four, debris from numerous beam fractures may have accumulated and caused this error in the data.

If only the data taken with new AFM cantilevers (weeks one, five, and six) are considered, then the results would fully reflect the degradation and restoration of beam strength. Techniques to protect silicon nanostructures from oxidizing and prevent strength reduction must be developed. Further analysis on the repetitive use of the AFM cantilever is needed to understand if this caused the error in the first few weeks.

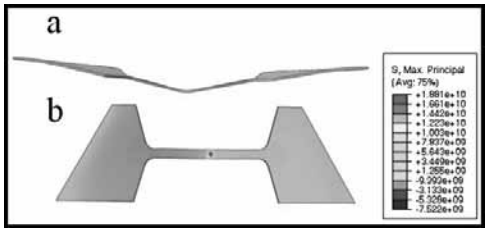

Figure 3: a) Side view finite element model of deflected beam. b) Top view of stress simulation. (See full-color version on inside cover.)

Acknowledgments:

This project was performed using facilities at the Cornell NanoScale Facility (CNF), supported by NSF Grant ECS-0335765, with the collaboration of the National Nanotechnology Infrastructure Network Research Experience for Undergraduates (NNIN REU) Program — as well as the facilities at the Cornell Center for Materials Research (CCMR), supported by NSF grant DMR-1120296. Assistance provided by Scott Grutzik was greatly valued, and my sincere appreciation to Professor Alan Zehnder and future research.

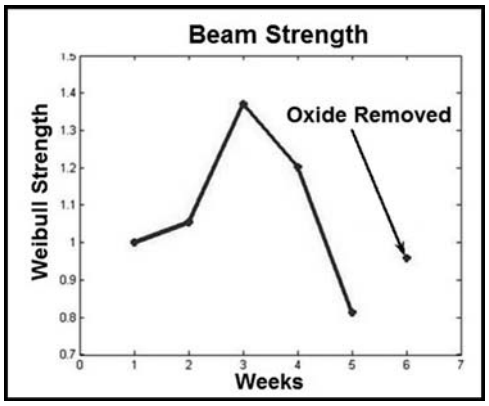

Figure 4: Normalized beam strength and weeks.

References:

[1] T. Alan, A. T. Zehnder, D. Sengupta, and M. A. Hines. Methyl monolayers improve the fracture strength and durability of silicon nanobeams. App.Phys.Letters, 89:231905, 2006.

[2] T. Alan, M. A. Hines, and A. T. Zehnder. Effect of surface morphology on the fracture strength of silicon nanobeams. Applied Physics Letters, 89:091901, 2006.

[3] T. Namazu, Y. Isono, and T. Tanaka. Evaluation of Size Effect on Mechanical Properties of Single Crystal Silicon by Nanoscale Bending Test Using AFM. Journal of Microelectromechanical Systems, 9(4):450-459, 2000.

[4] S. Sundararajan and B. Bhushan. Development of AFM-Based Techniques to Measure Mechanical Properties of Nanoscale Structures. Sensors and Actuators, 101:338-351, 2002.

The Effects of Lanthanum-Doping on Strontium-Titanate Thin Films Grown on Si <001> Substrates

Christine Karako
Chemistry, University of Dallas

NNIN REU / NASCENT Site: Nanomanufacturing Systems for Mobile Computing and Mobile Energy Technologies, The University of Texas at Austin, Austin, TX
NNIN REU / NASCENT Principal Investigator: Dr. John Ekerdt, McKetta Department of Chemical Engineering, University of Texas at Austin
NNIN REU / NASCENT Mentor: Martin D. McDaniel, McKetta Department of Chemical Engineering, University of Texas at Austin
Contact: cmkarako@gmail.com, ekerdt@utexas.edu, mcdanimd@che.utexas.edu

Abstract:

Lanthanum-doped strontium titanate (La:STO) films were grown on silicon <001> substrates at a thickness range of 6-25 nm. Atomic layer deposition was used to grow the films after buffering the substrate with four unit cells of STO deposited via molecular beam epitaxy. La:STO films were successfully grown on silicon (Si) while maintaining a single-crystal structure and achieving good conductivity, in comparison to the insulating properties of undoped STO. The charge density of the La:STO film was calculated to be 2.18×10^{21} cm^{-3}. Charge densities obtained for varying La concentrations ranged from 6.72×10^{20} to 3.86×10^{21}. Only 6% La-doping would be required to obtain the IBM specification of 1×10^{21} charges/cm^3 for use in a transistor [1]. When tested electrically, a 15% La-doped thin film had a resistivity of about 1.6×10^{-3} Ω-cm; however, this is still more resistive than bulk La:STO at the same La-doping concentration (~ 1×10^{-4} Ω-cm) [2].

Introduction:

In the fast-paced, ever-developing silicon industry, research is being done to grow crystalline oxides on silicon. Strontium titanate (STO) is one of the few oxides that is chemically stable when deposited on silicon and would be useful in a variety of applications when integrated with other oxides such as the ferroelectric barium titanate [1]. Although research has been successful in such integration, there is a need to find better and more efficient deposition methods. The commonly used molecular beam epitaxy (MBE) process is costly and impractical for large-scale production. This research focuses on using a chemical deposition method, known as atomic layer deposition (ALD), to deposit La:STO thin films.

Experimental Procedure:

Silicon wafers were obtained and diced into 20×20 mm^2 pieces. They were solvent cleaned and exposed to ozone radiation to remove carbon contamination, according to the procedure outlined by McDaniel et al. [3]. Using MBE growth methods, four unit cells of crystalline STO were grown on the Si interface to provide a crystalline template for the La:STO. The samples were transported *in vacuo* to the ALD chamber, where La:STO films were grown at thicknesses of 6-20 nm. Before removal from the vacuum system, these films were analyzed by x-ray photoelectron spectroscopy (XPS) to determine if the ALD was successful in depositing the correct stoichiometric amounts of the elements. After removal, the crystalline structure and film thicknesses were analyzed by x-ray diffraction (XRD) and x-ray reflectivity (XRR) methods. Contacts for electrical testing were made by gold sputter deposition and liquid gallium-indium metal. Electrical measurements were performed using a four-point probe station.

Results and Conclusions:

The XPS data revealed that the ALD growth method was successful in growing perovskite-structured La:STO. It also showed that increased lanthanum activation occurred after annealing at a substrate temperature greater than 600°C; this further corresponded to a decreased resistivity of the film when tested electrically. High doping concentrations (~30%) distorted the crystal, as was discovered in analysis of the XRD data. The rocking curve was an XRD analysis performed at a set angle to show the degree of crystallinity; it revealed that increasing film thickness as well as high doping concentrations

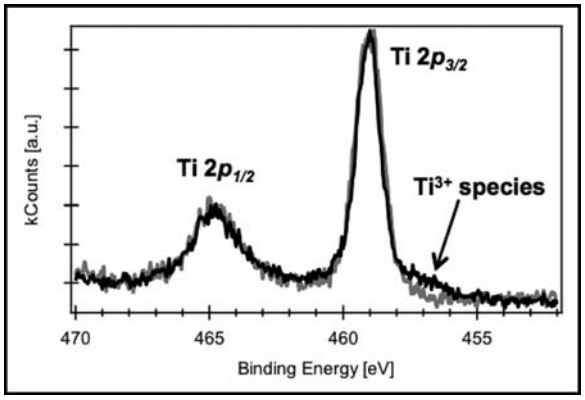

Figure 1: XPS Ti scans, before and after 600°C anneal, showing increased Ti^{3+} concentration from greater La activation.

(>30%) contributed to crystalline defects. Because the STO was compressively strained to match the lattice structure of Si, increasing film thickness would require greater energy to keep the crystals strained. Therefore, thicker films were unable to maintain this higher energy order and the STO relaxed back to its original lattice constant.

XRR analysis was used to determine the thicknesses of the films according to the relationship between the x-ray reflectivity and the film thickness given by Bragg's law: $\lambda = 2d\sin\theta$. It was estimated that the film thickness grown by ALD was the total thickness determined minus ~ 1.5 nm from the MBE template growth.

Future Work:

Future work would be required to study the electrical properties of thin film La:STO. Because a proposed transistor model by IBM would use a thin La:STO film of only 3 nm, it would be important to understand the impact of such a small scale on the mobility of the films [1].

Furthermore, it was hypothesized that uniform, perovskite crystallinity played an important role in the conductivity of these films since thicker, polycrystalline films had a higher measured resistance. Further research would need to be done to validate this supposition. In order to further the purpose of this research to eliminate the need for MBE growth methods, growth on a different substrate such as germanium may be necessary.

Acknowledgments:

This work is based upon work supported primarily by the National Science Foundation under Cooperative Agreements No. EEC-1160494 and No. DMR-1207342. Any opinions, findings and conclusions or recommendations expressed in this material are those of the author(s) and do not necessarily reflect the views of the National Science Foundation.

This research was performed through the support of the National Nanotechnology Infrastructure Network Research Experience for Undergraduates (NNIN REU) Program with funding provided by Nanomanufacturing Systems for Mobile Computing and Mobile Energy Technologies (NASCENT).

Much appreciation goes to Martin McDaniel and Dr. John Ekerdt for their guidance with this project.

References:

[1] Dubourdieu, Catherine A., et al., "Ferroelectric Semiconductor Transistor Devices having gate modulated conductive layer," Patent publication number: 0292677, Nov. 22, 2012.

[2] Marina, Olga A., et al., "Thermal, electrical, and electrocatalytical properties of lanthanum-doped strontium titanate," Solid State Ionics, Vol. 149, Issues 1-2, pp. 21-28, (2002).

[3] McDaniel, Martin D., et al., "Epitaxial strontium titanate films grown by atomic layer deposition on SrTiO3-buffered Si<001> substrates," Journal of Vacuum Science and Technology A, Vol. 31, Issue 1, 01A136-(1-9) (2012). http://dx.doi.org/10.1116/1.4770291

Developing Bioinspired Slippery Coating on Industrial Steels

Keiko Kato
Materials Science and Engineering, University of Illinois at Urbana-Champaign

NNIN REU Site: Penn State Nanofabrication Laboratory, The Pennsylvania State University, University Park, PA
NNIN REU Principal Investigator: Dr. Tak-Sing Wong, Mechanical and Nuclear Engineering, The Pennsylvania State University
NNIN REU Mentor: Jing Wang, Mechanical and Nuclear Engineering, The Pennsylvania State University
Contact: kato2@illinois.edu, tswong@engr.psu.edu, juw246@psu.edu

Introduction:

Creating an omniphobic coating on industrial metals that can repel various liquids and solids would have numerous industrial and medical applications, yet the development of such a coating has been very challenging. Conventional approaches utilizes the lotus effect to create liquid-repellent coating, which capitalizes the idea of trapped air pockets within micro/nanotextures to create low-friction and low-adhesion surfaces As these surfaces cannot sustain its property under extreme conditions such as high temperatures and pressures, another lesson was learned from nature to develop novel liquid/solid repellant mechanism. Inspired by the insect trapping mechanism of a pitcher plant, a novel repelling surface was developed, which was termed as "Slippery Liquid-Infused Porous Surfaces" (SLIPS) [1]. SLIPS is consisted of chemically functionalized micro/nanostructured substrate and infused with a lubricating liquid. In this project, the protocol to apply SLIPS to industrial steels was explored.

Fabrication:

First micro/nanotextures were created on steel surface through chemical etching. Then the surface was chemically functionalized through oxygen plasma cleaning and silanization processes. At last, lubrication was applied to the functionalized micro/nanotextured surface.

Results and Discussion:

The resulting SLIPS-treated metal showed excellent liquid repellent properties against a broad range of fluids, including both water and oils, as well as complex fluids, such as blood. Figure 1 shows the change in surface repellency to octane after the SLIPS treatment.

First, the etched surface was investigated through field emission scanning electron microscope (FESEM) to ensure the existence of micro/nanoscale textures, as shown in Figure 2. Second, the repellent property of the surface was studied by measuring sliding angles with a goniometer. A droplet of 10 μL and a CSS camera were used to capture pictures of droplet's movement at each second. Those pictures were used to determine the sliding angle. Significant decrease of sliding angle was observed for various liquids in Figure 3 as a result of SLIPS treatment. The sliding angle of 90° was decreased to below 3° after the SLIPS coating.

Since the micro/nanoscale textures are mono-lithographically integrated with the metal surfaces, our SLIPS coatings demonstrate excellent robustness against multiple physical damages. The physical damage was demonstrated by applying adhesive tape on the etched metal surface with 500 gram of weight to add an extra force to the tape. The tape was removed and the sliding angle was measured to observe the change in surface repellant properties after the physical damages. Additionally, the application of SLIPS on metals of any geometries was succeeded including a flat surface, sphere, and pipe tube as shown in Figure 4.

The ability to apply omniphobic slippery coatings on industrial steels would enable a broad range of industrial and medical applications including multi-functional coatings for anti-icing, anti-corrosion, anti-scaling, friction reduction, and anti-fouling purposes [2, 3].

Future Work:

SLIPS will be applied to different metals to explore various industrial and medical applications of SLIPS.

Acknowledgements:

I would like to show my appreciation to my principal investigator, Dr. Tak-Sing Wong, and my mentor Jing Wang for the assistance to guide me through the research. I would also like to thank my colleagues, Alexandre P. Blois, and Nanofab and Material Characterization Laboratory staff for their support to prepare the data. I would also like to thank the National Nanotechnology Infrastructure Network Research Experience for Undergraduates (NNIN REU) Program and National Science Foundation for the financial support and the opportunity.

References:

[1] Wong, T.-S., et al. "Bioinspired self-repairing slippery surfaces with pressure-stable omniphobicity", Nature 477, 443-447 (2011).
[2] Kim, P., et al. "Liquid-Infused Nanostructured Surfaces with Extreme Anti-Ice and Anti-Frost Performance", ACS Nano 6, 6569-6577 (2012).
[3] Epstein, A. K., et al." Liquid-infused structured surfaces with exceptional anti-biofouling performance", PNAS, 109, 13182-13187 (2012).

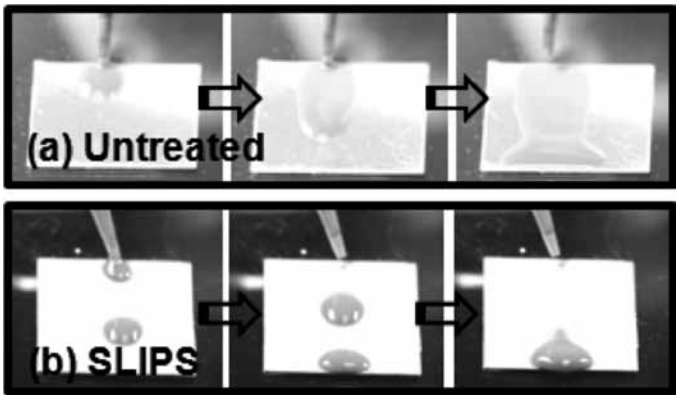

Figure 1: The surface repellency of stainless steel 304 to octane; (a) Untreated steel, (b) SLIPS-coated steel. (See full-color version on inside cover.)

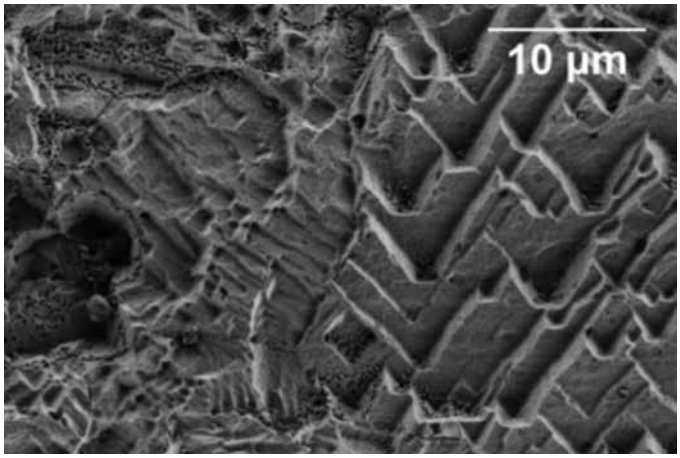

Figure 2: FESEM image of etched stainless steel 304 surface.

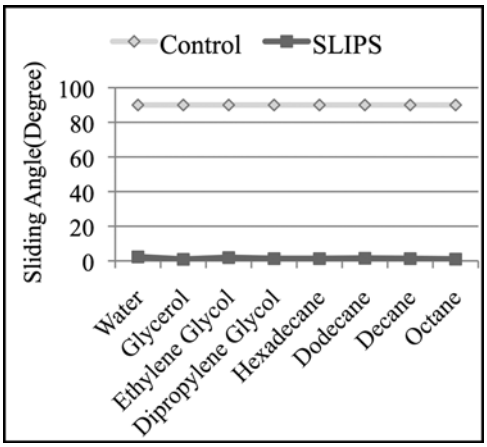

Figure 3: Sliding angles of various fluid droplets on untreated and SLIPS-coated stainless steel 304. The sliding angle before SLIPS treatment resulted in 90°, which decreased to less than 3° after SLIPS treatment against broad range of liquids.

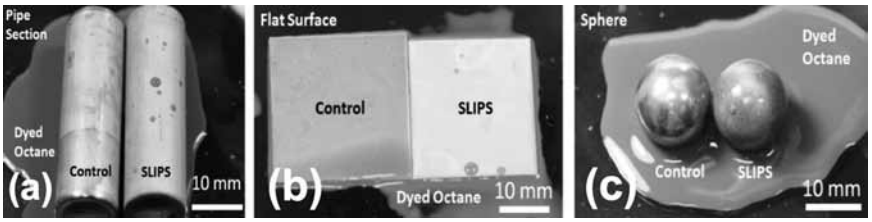

Figure 4: SLIPS was applied on different geometries of stainless steel 304 and the surface repelled octane (dyed in yellow-orange color). In each picture, the left sample is untreated steel and the right sample was SLIPS-treated steel. (a) pipe tube, (b) flat surface, and (c) sphere. (See full-color version on inside cover.)

The Effect of Surface Roughness on Chemical Vapor Deposition of Hexagonal Boron Nitride

Daniel David Kuddes
Physics, University of Texas at Dallas

NNIN REU / NASCENT Site: Nanomanufacturing Systems for Mobile Computing and Mobile Energy Technologies, The University of Texas at Austin, Austin, TX
NNIN REU / NASCENT Principal Investigator: Prof. Rodney Ruoff, The Department of Mechanical Engineering and the Materials Science and Engineering Program, The University of Texas at Austin
NNIN REU / NASCENT Mentor: Dr. Ariel Ismach, Department of Mechanical Engineering, The University of Texas at Austin
Contact: ddk091020@utdallas.edu, r.ruoff@mail.utexas.edu, aismach@austin.utexas.edu

Abstract:

Hexagonal boron nitrite (h-BN) is a favorable substrate for graphene and other two-dimensional molecules due to its lack of inter-planar covalent bonds, smooth topology, insulating properties, and a near epitaxial lattice to graphene. Additionally because of its wide band gap, h-BN has potential applications in electronics as an insulator, in transistors, and in electroluminescent devices [1]. Our strategic goal for h-BN was to find a means to synthesize a large scale homogenous h-BN mono-layer with few gaps, breaks, or lattice defects. The focus of our project was to better understand the role of surface roughness when using chemical vapor deposition to grow h-BN on a catalytic metal and apply that knowledge to create high quality h-BN films. Our experiments showed flatter Ni surfaces lead to considerably more homogenous h-BN with fewer ad-layers and more uniform coverage than h-BN grown on rougher Ni surfaces.

Purpose and Introduction:

The purpose of our experiment was to determine the effect, if any, of catalytic metal's surface roughness on low pressure vapor chemical deposition (LPCVD) of hexagonal boron nitride (h-BN) [2]. H-BN was grown on two samples using the same growth conditions in the same system. Preliminary results show the smoothed sample exhibits a more continuous mono-layer of h-BN containing fewer ad-layers (h-BN layers on top of other h-BN layers).

The experiment took place in two steps. The first step was to determine if a smooth Ni surface would remain smooth despite being heated to 1050°C. After determining that the Ni film remained smooth despite the high heat, the second experiment compared the deposition of h-BN on smooth and rough Ni foils.

Experimental Procedure:

A. Polishing. Mechanical polishing was used to smooth the surface of a 25 μm thick 1-inch by 1-inch Ni film. To polish,

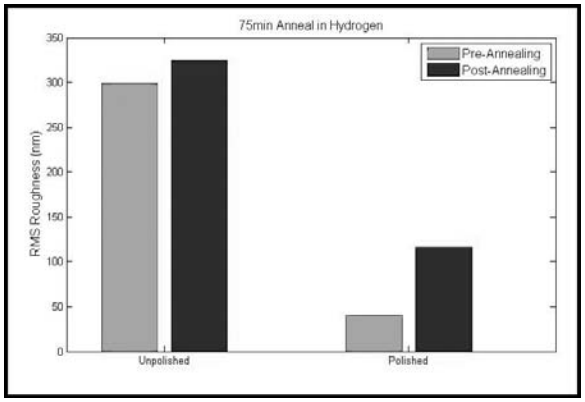

Figure 1: The roughness of the polished Ni sample more than doubled after annealing, but it remained at least three times smoother than the as received sample.

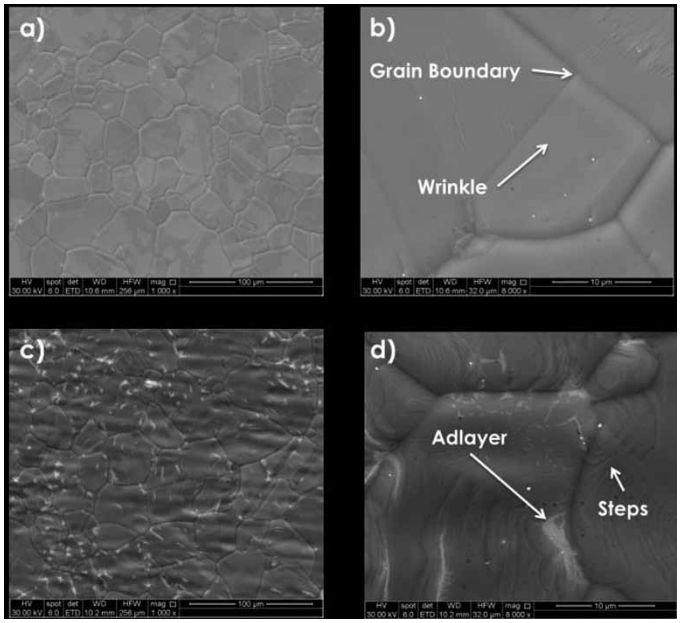

Figure 2: SEM images of h-BN on Ni Taken at 1,000x and 8,000x magnification. Images a) and b) show polished Ni. Images c) and d) show unpolished Ni.

a hand dremel and 1.0 μm grit alumina-based polish were used. The film was polished five minutes per inch, resulting in a surface roughness of 29 nm RMS from an as-received roughness of 300 nm.

B. Low Pressure Chemical Vapor Deposition. Our method of using LPCVD to deposit h-BN on Ni films involved heating the samples to 1050°C — the melting point of Ni is 1455°C. By bringing the temperature of the metal close to the melting point, the metal surface becomes semi-molten. Therefore, it was unclear if any smoothing done to the surface before annealing would have an effect on the surface after annealing.

After determining that the polished Ni film remained substantially smoother than the as-received Ni film, the next experiment involved the growth of h-BN on a polished Ni surface. LPCVD was used to grow h-BN. Our gas flow furnace, where the growth occurred, had a base pressure of 5 mTorr. An amonia boran vial was heated such that the resulting gas, along with methane, was flowed over the samples — resulting in h-BN being deposited on the Ni films.

Results and Conclusions:

It was shown, using an optical profilometer, that the smoothed Ni film remained substantially smoother than the rough nickel film after annealing (see Figure 1).

SEM images were used to compare the smooth and rough samples (see Figure 2). The h-BN on the polished sample showed a number of favorable attributes. The polished film seemed to have more uniform coverage of h-BN. There were fewer steps in the polished film — indicating a smoother surface and fewer ad-layers in the polished film.

While not verified, polishing a Ni surface prior to h-BN growth seemed to lead to fewer ad-layers and a larger continuous area of h-BN. Polishing not only smoothed the surface, but also lefts alumina particles, eliminated as received features, and cleaned the surface of contaminates. While it seemed that more favorable films resulted from polishing, it is not entirely clear that this was a result of a change in surface smoothness and not some other effect of the polishing.

Future Work:

Polishing leaves residual contaminants on the film — identified as Al_2O_3 by energy dispersive x-ray spectroscopy. Eliminating this extra variable could lead to more decisive evidence that a change in surface smoothness is responsible for the changes in h-BN growth and not some other product of the smoothing procedure. Using a smoothing technique that doesn't use a polishing compound, such as pressure induced surface deformation that does not leave contaminates on the Ni surface, would be illuminating [3].

Shifting grain boundaries and other effects resulted in changes in smoothness post-annealing. The effects of theses shifts might be reduced by annealing at or above the growth temperature and then applying a smoothing procedure followed by growth of h-BN. Furthermore, the use of glassy metal may allow for a smoother surface.

Acknowledgments:

I wish to thank Prof. Rodney Ruoff, Dr. Ariel Ismach, Harry Chou, Ruderesh Ghosh, Marylene Pallard, the NASCENT Research Undergraduate Experience coordinators, the National Nanotechnology Infrastructure Network Research Experience for Undergraduates (NNIN REU) Program, and the National Science Foundation for their help in making this work possible.

References:

[1] Colombo, L., R.M. Wallace, and R.S. Ruoff. "Graphene Growth and Device Integration." Proceedings of the IEEE, 101 (7), 1536-1556 (2013).

[2] Pakdel, A., C. Zhi, Y. Bando, and D. Golberg, "Low-dimensional boron nitride nanomaterials." Materials Today, V15, Issue 6, June 2012, Pages 256-265, ISSN 1369-7021, http://dx.doi.org/10.1016/S1369-7021(12)70116-5.

[3] Logeeswaran, V.J., M.-L. Chan, Y. Bayam, M. Saif Islam, D.A. Horsley, X. Li, W. Wu, S.Y. Wang, and R.S. Williams, "Ultra-smooth metal surfaces generated by pressure-induced surface deformation of thin metal films." Applied Physics A. 2007.

Thermodynamic Control of Lead Content in the Piezoelectric Thin Film

Fumiya Kurokawa
Mechanical Engineering, Kobe University, Hyogo Prefecture, Japan

NNIN iREG Site: Penn State Nanofabrication Laboratory, The Pennsylvania State University, University Park, PA
NNIN iREG Principal Investigator: Susan Trolier-McKinstry, Materials Science and Engineering, The Pennsylvania State University
NNIN iREG Mentor: Daniel Marincel, Materials Science and Engineering, The Pennsylvania State University
Contact: fumiya.kurokawa.kobe.ma2@gmail.com, stmckinstry@psu.edu

Abstract:

Recently, piezoelectric thin films have become attractive as a component for low voltage MEMS applications. Lead-based perovskite materials are used because of their excellent ferroelectric and piezoelectric properties. However, the volatility of lead creates difficulties in the deposition process, because high temperature annealing process is required for prerovskite phase development. Conventionally, excess lead is added to thin films in order to control lead content during high temperature processing. However, it is still difficult to precisely control the stoichiometry of lead-based piezoelectric thin film, since the proper amount of excess lead depends on deposition process or conditions.

In this study, lead composition control is being pursued in the piezoelectric thin film via thermodynamic, rather than kinetic control. Post annealing is being conducted for lead deficient piezoelectric thin films in a PbO furnace. Theoretical calculation suggests that it should be possible to control lead content via thermodynamics. Experimentally, we found PbO thin films can be deposited using this system. These results suggest that we could also deposit PbO thin film on Pb-deficient PZT thin film and crystalize stoichiometric PZT thin film.

Introduction:

Recently, piezoelectric thin film has become attractive for low voltage microelectronicmechanical system (MEMS) applications. Among various piezoelectric materials, lead-based materials, especially lead zirconate titanate [$Pb(Zr,Ti)O_3$, PZT], are used because of their excellent piezoelectric properties [1]. However, the volatility of lead creates difficulties in the deposition process, because high temperature annealing is required for prerovskite phase development. Conventionally, excess lead is added to thin films in order to control lead content during high temperature processing. However, it is still difficult to precisely control the stoichiometry of the piezoelectric thin film, since the proper amount of excess lead depends on deposition process or conditions.

We focused on thermodynamic method to control the lead content in the piezoelectric thin film in a PbO metalorganic chemical vapor deposition system using tetra-ethyl lead [TEL] as a lead source. The vapor pressure of PbO was calculated from the thermodynamic reaction:

$$PbO\ (solid) = PbO\ (gas)$$

$$log\ P_{PbO} = -\frac{15030}{T} + 9.51 \quad [atm]$$

$$PbZrO_3 = PbO\ (gas) + ZrO_2$$

$$log\ P_{PbO} = -\frac{13660}{T} + 7.15 \quad [atm]$$

where P and T are the pressure and temperature [2]. These equations suggest that lead content can be controlled by PbO pressure and temperature.

In this study, we suggest a new method to control lead content in the piezoelectric thin film via thermodynamic method. We conducted post-annealing process in the furnace with controlled PbO pressure and annealing temperature.

Experimental Procedure:

Figure 1 shows an optical image and schematic diagram of PbO furnace to deposit PbO thin film and control lead content in a PZT thin film. Tetra-ethyl lead [TEL] is used as a source of PbO. It was supplied by Gelest packaged in bubbler. In this system, we have three important parameters; TEL flow rate, bubbler temperature, and chamber temperature.

At first, we conducted theoretical calculation to estimate the conditions to control lead content. Theoretical values of PbO pressure in the chamber are calculated from the following equation:

$$P_{TEL,Chamber} = \frac{10^{9.361-\frac{2910}{T_{Bubbler}}} \times f_{TEL} \times T_{Chamber}}{\left(f_N + f_O + f_{TEL}\right) \times T_{Bubbler}}$$

where f_N, f_O, f_{TEL}, $T_{Bubbler}$ and $T_{Chamber}$ are the nitrogen flow rate, oxygen flow rate, TEL flow rate, bubbler temperature and annealing temperature, respectively. Then f_N and f_O were fixed at maximum flow rates of 3448 sccm and 1000 sccm, respectively. Figure 2 shows the PbO pressure in the chamber as a function of TEL flow rate at a bubbler temperature of 45°C and an annealing temperature of 750°C. The (▲) and (●) lines indicate boundary pressure for the chemical reaction from PbO gas to PbO solid and from $PbZrO_3$ to PbO gas and ZrO_2,

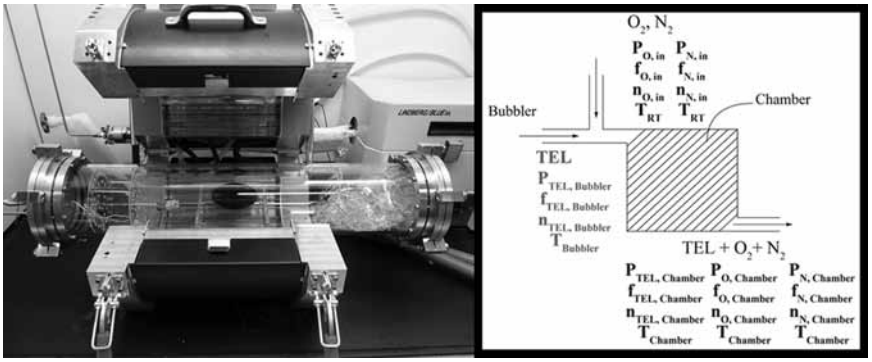

Figure 1: PbO furnace; (a) Optical image, (b) Schematic diagram.

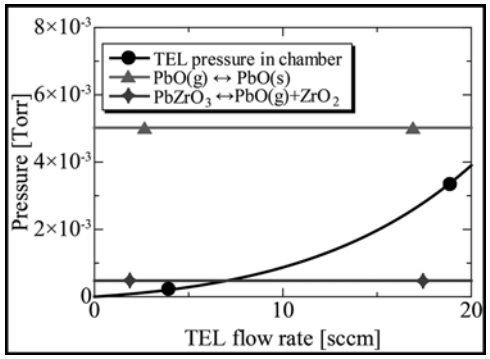

Figure 2: PbO pressure in the chamber as a function of TEL flow rate.

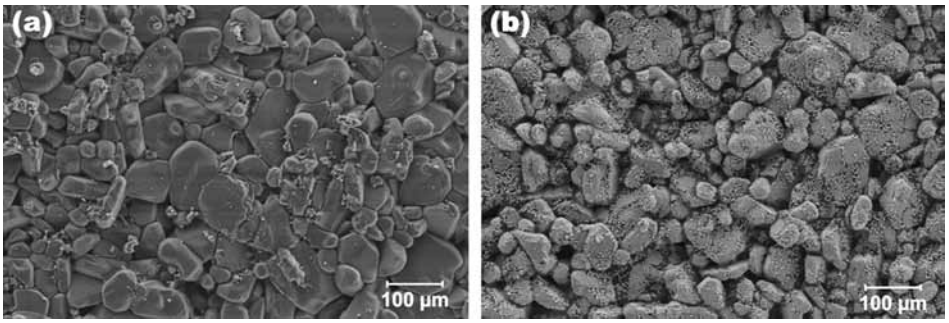

Figure 3: Surface SEM images of Al_2O_3 substrate (a) before (b) after PbO thin film deposition.

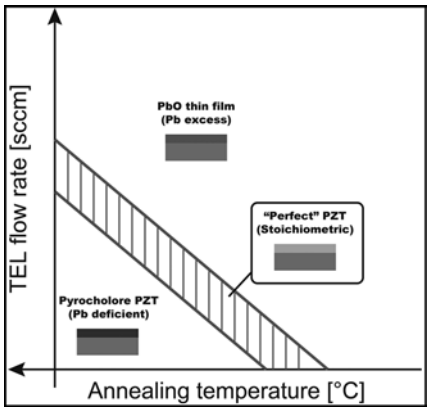

Figure 4: Phase diagram of PZT thin film as a function of annealing temp and TEL flow rate.

respectively. This figure suggests we could compensate lead content with TEL flow rate from 8 to 20 sccm under a bubbler temperature of 45°C and an annealing temperature of 750°C.

Results and Conclusions:

As an initial experiment, we tried to deposit PbO thin film on an aluminum oxide (Al_2O_3) substrate, which doesn't react with lead chemically, to confirm whether this system is useful or not. We conducted annealing at a TEL flow rate 20 sccm, a bubbler temperature of 45°C, and an annealing temperature 500°C. Figure 3 shows surface SEM images before and after PbO deposition. We found PbO thin film can be deposited on Al_2O_3 substrate using this system. Additional experiments need to be conducted to evaluate the growth rate.

We suggest a new approach to control lead content in piezoelectric thin films. Theoretical calculation suggests that we could control lead content via thermodynamic method. Furthermore, we found PbO thin film can be deposited using this system. These results suggest that we could also deposit PbO thin film on Pb-deficient PZT thin film and crystalize stoichiometric PZT thin film.

Future Work:

Figure 4 shows phase diagram of PZT thin film as a function of TEL flow rate and annealing temperature. This diagram is the final objective of this research. To find the boundary of this phase diagram, we should conduct post-annealing for Pb-deficient PZT thin film.

Acknowledgements:

This work was made possible under the NNIN iREG Program, together with Nanotechnology Platform, Japan. I also appreciate my principal investigator Dr. Susan Trolier-MacKinstry, mentor Mr. Dan Marincel, and all group members.

References:

[1] P. Muralt, R. G. Polcawich, and S. Trolier-McKinstry, "Piezoelectric Thin Films for Sensors, Actuators, and Energy Harvesting", MRS. Bull., vol. 34, no. 9, pp. 658-664, 2009.

[2] K. H. Hardtl, and H. Rau, "PbO vapour pressure in the Pb(Ti1-x,Zrx)O3 system", Solid. State, Commun., vol. 7, pp. 41-45, 1969.

Improvement of Lithium Ion Batteries with Selected Dopants

Deanna Lanigan
Materials Science and Engineering, University of Wisconsin-Madison

NNIN REU Site: Nano Research Facility, Washington University in St. Louis (WUSTL), St. Louis, MO
NNIN REU Principal Investigator: Professor Richard Axelbaum, Energy, Environmental, and Chemical Engr., WUSTL
NNIN REU Mentor: Miklos Lengyel, Energy, Environmental, and Chemical Engineering, Washington University in St. Louis
Contact: dlanigan@wisc.edu, axelbaum@wustl.edu, mlengyel@wustl.edu

Introduction:

For electric vehicles to be a feasible option for the general public, batteries need to deliver higher capacities, higher rate capabilities, and longer cycle life at a fraction of the current cost. Nanostructured lithium-ion battery cathode material formed through spray pyrolysis is promising because of its beneficial morphology along with the scalability of the process for mass production. We focused on the layered $Li_{1.2}Mn_{0.53}Ni_{0.13}Co_{0.13}O_2$ composition due to its excellent capacity of over 250 $mAhg^{-1}$. However, this specific structure suffers from voltage fade upon cycling. The purpose of our investigation was to determine the effects of dopant substitution on the voltage fade characteristics of the batteries. Through this study, we hoped to achieve a better understanding of the voltage fade phenomena to aid in the commercial implementation of these materials in electric vehicles.

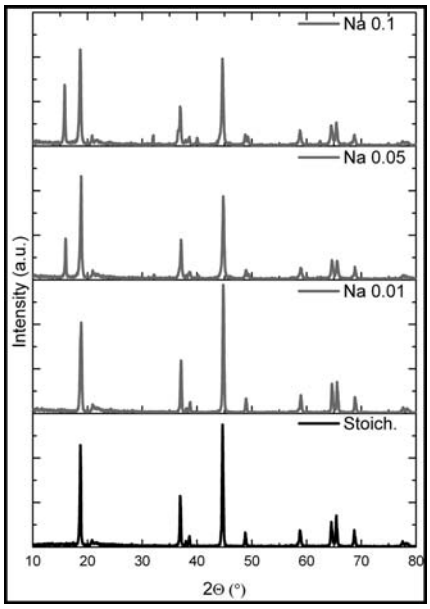

Figure 1: XRD.

Experimental Procedure:

The precursor solutions were made of nitrate solutions dissolved in deionized water for use in spray pyrolysis. The precursor solution was placed in a nebulizer, which created a fine mist. The aqueous droplets were carried into a preheater using air as the carrier gas. There, they underwent rapid drying and then were conveyed into a hot furnace reactor heated to 575°C, where they decomposed, forming oxide particles. The particles were collected downstream of the reactor on porous polycarbonate filters. After each hour, the material was collected and weighed. The as-synthesized particles were then annealed at 900°C for two hours in a box furnace. The powders were converted into a thin film using the doctor blade method. The binder solution contained 10% carbon black, 10% PVDF (poly-vinyledene-fluoride) and 1-methyl-2-pyrrolidinone. The cathodes were then tested in 2032 type coin cells using 1M $LiPF_6$ in ethylene-carbonate:diethyl-carbonate:dimethyl-carbonate (EC:DEC:DMC, 1:1:1).

Battery tests included rate capability tests, cycling tests, and voltage fade tests. All electrochemical testing was performed at room temperature. Rate capability tests demonstrated how well the structure responded to different charge and discharge rates. The rates chosen were C/10, C5, C2, C1, and then C/10 again (where 1C = 200 mA/g). Cycle tests demonstrated the cell's ability to maintain capacity over extended cycling. The entire test spanned over 100 cycles. The cycle test was used for seven different doped batteries, along with an undoped battery cell for comparison. The rates used for this test were C/10 and C/3. The activation cycle was between 2.0-4.8V at C/10 and subsequent cycles were between 2.0-4.6V for cycle and rate tests. Voltage fade tests were performed for 30 cycles, but have not yet been completed. After an initial activation cycle between 2.0-4.8V at C/20, the remaining cycles were performed at C/10.

The powders were characterized using both powder x-ray diffraction (XRD) and scanning electron microscopy (SEM). XRD, as seen in Figure 1, was used to verify the crystal structure of the powders. At low dopant levels, the crystal structure should not have strayed far from the undoped material. However, when the dopant level was too high for the structure to accommodate the dopants, it formed a separate phase, indicated by additional peaks in the diffraction spectrum. Figure 1 shows four different particle compositions, where part of the lithium was substituted for different Na levels.

It is clear that when the 0.05 Li atoms are replaced by Na atoms additional peaks start to occur in the XRD spectra, which become more pronounced as the concentration increases.

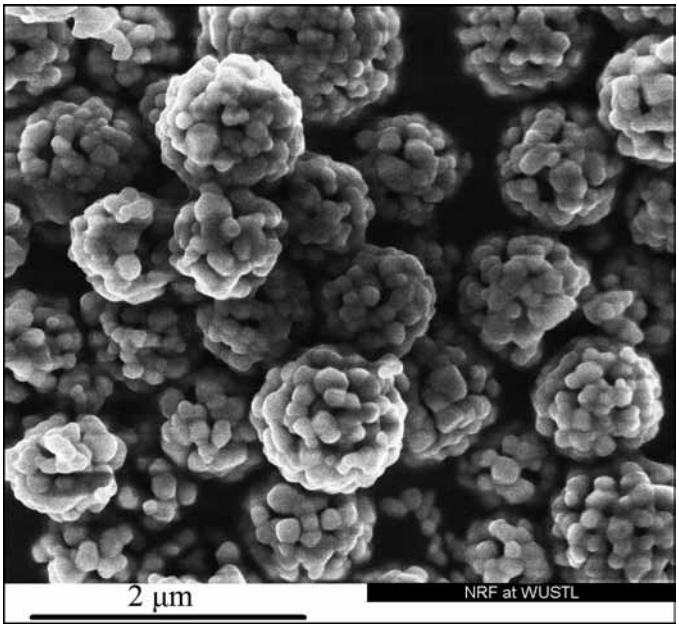

Figure 2: SEM.

Figure 2 shows an SEM image of chromium-doped particles. The particles are primarily spherical in shapes and have 200-400 nm size primary grains, while forming loosely aggregated secondary particles, which range between 0.5-5.0 μm.

Results:

Figure 3 shows the results of the rate test of selected materials compared to the undoped composition. Although there were not significant differences, the battery with the strontium-doped cathode material seemed to outperform the undoped battery in the final C/10 segment by maintaining a high capacity.

Cycle test results are displayed in Figure 4. From these initial results, no significant difference could be observed in the capacity fade behavior of the various dopants. However, the battery with the aluminum-doped cathode material maintained a higher capacity than the undoped sample after 100 cycles. As it can be seen from Figure 4, some of the dopants, most notably magnesium, may have reduced the capacity of the cell. This could be the consequence of exchanging transitional metal ions, which have multiple oxidation states by metal ions, which only have a single oxidation state. This way the host structure may become electrochemically inactive. However these results may indicate that the capacity and stability can be tuned to optimal performance for specific battery applications.

The voltage fade studies that are underway will help determine the dependence of this relationship to dopant levels.

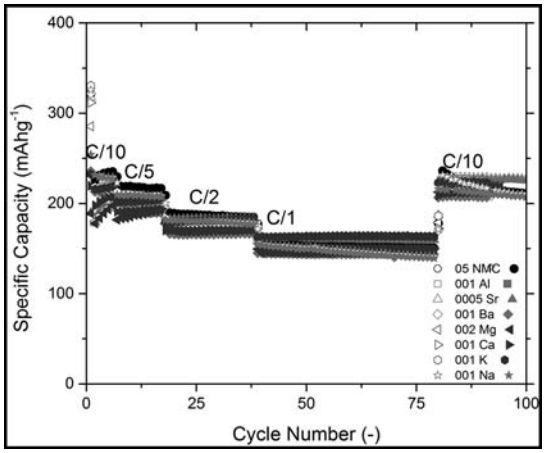

Figure 3: Rate test.

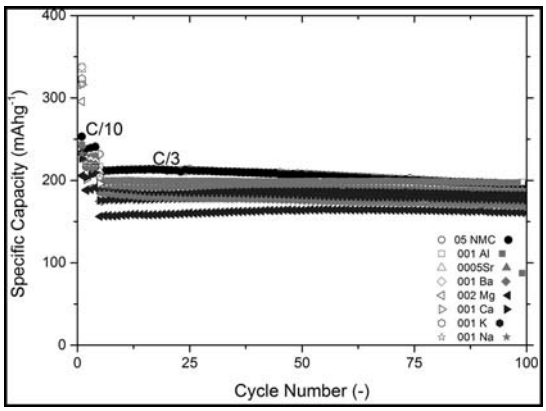

Figure 4: Cycle test.

Future Work:

Future work will focus on evaluating results from the voltage fade study. These results will be used in conjunction with impedance spectroscopy to determine more detailed data about diffusion mechanisms within the material and optimize the composition to reduce and hopefully eliminate the voltage fade of these materials. Studies focusing on two or more dopants will be performed based upon the results of the current study.

Acknowledgements:

I would like to thank my Mentor, Miklós Lengyel, and my Principal Investigator, Dr. Richard Axelbaum. I would also like to thank Dee Stewart, Nathan Reed, and all of the Nano Research Facility staff at Washington University in St. Louis. Finally, I would like to thank the NNIN REU Program and the National Science Foundation for making this research opportunity possible.

Preparation of Transparent Conducting Copper Aluminum Oxide Films

Jeremy Leshin
Chemical Engineering, University of Florida

NNIN REU Site: Nano Research Facility, Washington University in St. Louis, St. Louis, MO
NNIN REU Principal Investigator: Dr. Parag Banerjee, Mechanical Engr. and Materials Science, Washington University in St. Louis
NNIN REU Mentor: Fei Wu, Department of Mechanical Engineering and Materials Science, Washington University in St. Louis
Contact: jleshin@ufl.edu, parag.banerjee@wustl.edu, wufei5433@gmail.com

Introduction:

Most optically transparent materials are electrical insulators. Transparent conducting oxides (TCOs) are exceptions and are used in optoelectronics such as photovoltaics and flat panel displays which need transparent electrodes. Currently, all mass produced TCOs are n-type, such as Sn-doped In_2O_3 and Al-doped ZnO. However, p-type TCOs are also necessary for electronic devices that require the entire p-n junction to be transparent, which would allow for devices that both generate electricity and transmit visible light (e.g. functional windows). P-type TCOs have been under study in recent years after the discovery of p-type conducting $CuAlO_2$ thin films by Kawazoe et al. with light transmittance of up to 70% [1].

However, most known ways of producing $CuAlO_2$ involve high temperature sintering of binary oxides for extended periods of time. In this project, $CuAlO_2$ synthesis was attempted using a DC-sputtering process employing elemental copper and aluminum targets. In this study, films were attempted by depositing Cu/Al bilayer films as well as co-sputtered films formed in the presence of oxygen. Only the co-sputtering process shows promise as a method of $CuAlO_2$ preparation, as the bilayer structure proved an ineffective route for production of such films.

Experimental Procedure:

Films were deposited using direct current (DC)-sputtering physical vapor deposition with a Kurt J. Lesker PVD 75 system, creating both bilayer and co-sputtered structures. To deposit the bilayer structure, a 50 nm layer of silicon dioxide (SiO_2) was grown on 2-inch silicon wafers to act as a diffusion barrier between the metallic film and substrate. Aluminum (Al) was deposited for 250 seconds at 300W for a 39 nm layer. Copper (Cu) was deposited for 43 seconds at 300W to form a 26 nm layer. These thicknesses were chosen to have a one-to-one stoichiometric equivalence of Cu and Al atoms in the bilayer structure. Samples were then annealed in an oxidation furnace for four to 12 hours at temperatures ranging from 400°C-900°C.

Reactive co-sputtering was employed to produce a single layer structure on glass substrate. Cu and Al were deposited simultaneously for 1000 seconds with Cu at 30W and Al at 60W. Deposition was performed in an argon/oxygen (Ar/O) atmosphere with oxygen content ranging from 2-10%. During the deposition process, the glass was heated to temperatures ranging from 100°C-300°C. Bilayer samples were characterized using x-ray diffraction crystallography (XRD) to determine composition. Co-sputtered samples were characterized using energy dispersive x-ray spectroscopy (EDX) to determine atomic composition, as well as UV-Vis spectrophotometry to characterize optical properties of the films at wavelengths between 300 nm and 1100 nm.

Results:

Films produced in the bilayer structure were shown by XRD to be composed primarily of Cu and Al oxides. $CuAlO_2$ reached a maximum purity of approximately 10% at 900°C annealed for 8h. Lower temperatures formed the binary oxides and CuAl alloy. Shorter annealing times also formed a large amount of unoxidized metal (Figure 1). At longer annealing durations, the SiO_2 barrier failed and metal diffused into the wafer forming silicides. Reactive co-sputtered films could not be characterized by XRD (Figure 2); this is an indicator that the films formed through this process were amorphous in nature [3].

UV-Vis showed the transparency of the co-sputtered films to decrease on average with increasing substrate temperature (Figure 3), and increase with the oxygen content present during deposition. Films formed at 100°C showed the highest level of transmittance, while those formed at 300°C and 2% O_2 showed the lowest. The higher oxygen content likely allowed for increased oxidation of the metals in the film to form the transparent $CuAlO_2$ phase. All films except those formed at 300°C and 10% O_2 displayed a peak at about 550 nm, caused by the Cu content in the films.

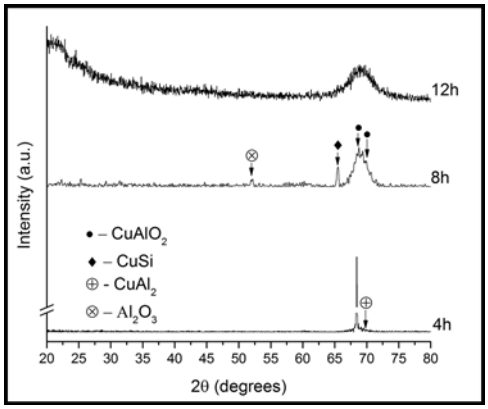

Figure 1: XRD of bilayer films at 900°C.

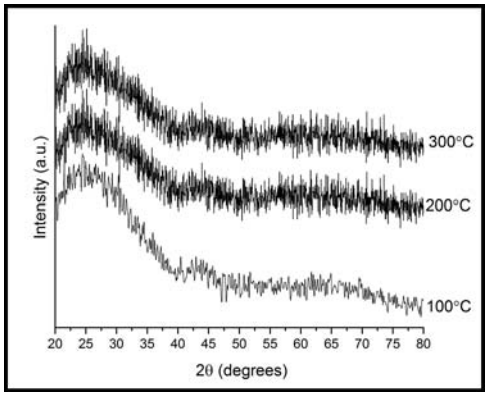

Figure 2: XRD of co-sputtered films in 5% O_2.

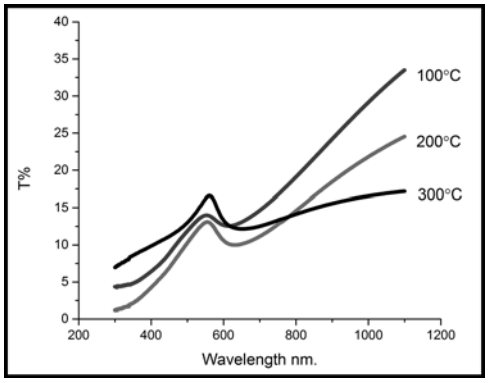

Figure 3: UV-Vis transmittance of Co-sputtered films in 5% O_2.

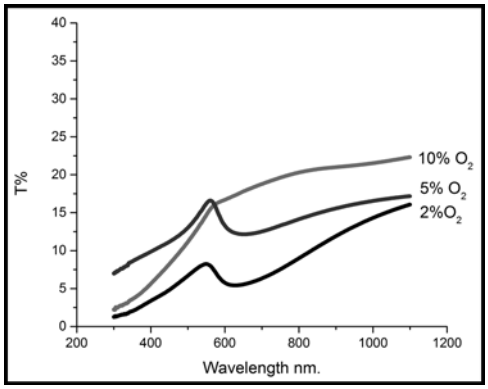

Figure 4: UV-Vis transmittance of Co-sputtered films at 300°C.

EDX was performed on films prepared via co-sputtering at 100-300°C and 5% O_2. Films formed at 100°C and 200°C were shown to have nearly the same relative amounts of Cu and Al. At 300°C, Al content of the film decreased significantly when compared to the Cu content. However, none of the films had the 1:1 Cu:Al ratio necessary for the formation of pure phase $CuAlO_2$.

Conclusions and Future Work:

Ultimately, use of the Cu-Al bilayer structure was proven to be an unviable method of $CuAlO_2$ thin film preparation. Reactive co-sputtering formed films with up to 30% transparency, short of pure phase $CuAlO_2$, but proper characterization of the films would require a crystalline structure. Literature and our preliminary results suggest that $CuAlO_2$ can be formed using this process. Better characterization of the deposition process at various oxygen levels and substrate temperatures will be needed to maintain proper stoichiometric ratios of Cu and Al in order to prepare the $CuAlO_2$ phase.

Possible inclusion of post-deposition annealing will also be tested as a method of ensuring crystalline structure of the films.

Acknowledgements:

I would like to thank Dr. Parag Banerjee, Fei Wu, and the Laboratory for Emerging and Applied Nanomaterials for all of their help and guidance. I would also like to thank the Nano Research Facility, National Nanotechnology Infrastructure Network Research Experience for Undergraduates Program, and the National Science Foundation for this opportunity.

References:

[1] H. Kawazoe, M.Yasukawa, H. Hyodo, M. Kurita, H. Yanagi, and H. Hosono, Nature 389, 939-942 (30 October 1997).

[2] Nandy, S., Maiti, U.N., Ghosh, C.K., and Chattopadhyay, K.K., "Optical and electrical properties of amorphous $CuAlO_2$ thin film deposited by RF magnetron sputtering," IWPSD 2007. pp.443,445, 16-20 Dec. 2007.

Challenges for Diamond Integrated Circuits

Clay T. Long
Physics, The Pennsylvania State University

NNIN iREU Site: National Institute for Materials Science (NIMS), Tsukuba, Ibaraki, Japan
NNIN iREU Principal Investigator: Dr. Yasuo Koide, National Institute for Materials Science
NNIN iREU Mentors: Dr. Eiichiro Watanabe, Dr. Masataka Imura, and Dr. Tsuya Daijyu, National Institute for Materials Science
Contact: clayl@andrew.cmu.edu, koide.yasuo@nims.go.jp, watanabe.eiichiro@nims.go.jp, daijyu.tsuya@nims.go.jp

Abstract:

Diamond is a nontraditional material for use in the transistor industry. It poses many challenges for consistent fabrication over semiconductors such as silicon or gallium arsenide. However, diamond has several desired material characteristics for integrated circuits (ICs). We therefore explored the properties of several simple devices on diamond — namely, transistors, inverters, and ring oscillators.

MATS

Introduction:

Integrated circuits developed using silicon technology in the last several decades have radically changed our way of life. However for some applications such as high power or frequency equipment, silicon is not ideal. Diamond with its large band gap and thermal conductivity and bulk insulating properties could be used. In this experiment, we investigated hydrogen terminated diamond [1]. In this case, the last carbon atoms of the diamond were bonded to hydrogen (H). The difference in electronegativity between the carbon and hydrogen atoms yielded a very thin two-dimensional layer of holes that can be used for a transistor channel.

To illustrate the possibilities of ICs on diamond, we attempted to fabricate several simple electronic devices, namely, transistors, logic inverters, and ring oscillators. A transistor is the fundamental building block of ICs that only allows current flow if a voltage is applied to the gate. An important property for device fabrication is that transistors be normally off, or have no current flowing when no voltage is applied to the gate. Inverters simply flip logic high (1) into a logic low (0) and vice versa. Ring oscillators are more complex device made of an odd number inverters connected in a ring. An input signal is then continually flipped from high to low, ideally yielded an output sine wave. To fabricate these devices, we used a process called microlithography, which uses light to 'draw' on an optically sensitive material covering the sample.

Experimental Procedure:

The electronic devices were fabricated using a standard sequence of nanofabrication steps.

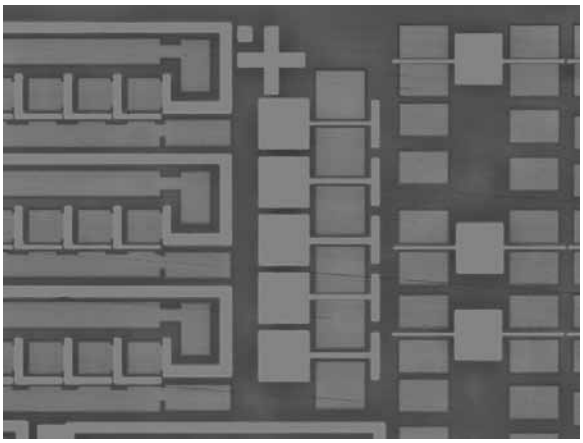

Figure 1: The sample just before the gold source-drain layer was deposited.

First, a square 5 mm H-terminated diamond sample was chosen as the substrate. We used the software Vectorworks to create a layout, measuring 3.5 mm × 4 mm, that was eventually patterned onto the substrate. The patterning process built the devices in a series of layers. The general sequence of steps was spin coat the resist, apply laser lithography, develop, deposit material, and finally liftoff. Once one layer was completed, we systematically moved onto the next.

Photolithography was conducted on a maskless system. Unfortunately our samples were not perfectly flat so the auto-aligning system could not be used. The material deposition step varied based on the layer. For example, the mesa layer consisted of ozone cleaning to strip the hydrogen terminated ends and remove conductivity from the uncovered regions. All other layers deposited a palladium (5nm)/titanium (10nm)/gold (150nm) onto the surface. For the gate region, 30 nm of aluminum oxide was deposited first by atomic layer deposition.

See Figure 1 for a visual representation of the sample, late in the process. Here, lithography and development have already happened for the final layer, so the bare substrate is visible.

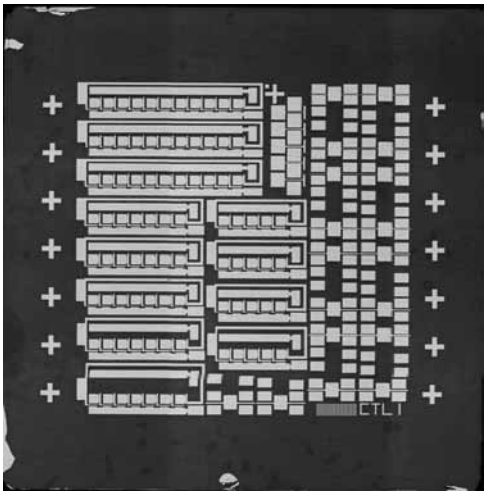

Figure 2: The completed chip with ring oscillators on the left and inverters on the right.

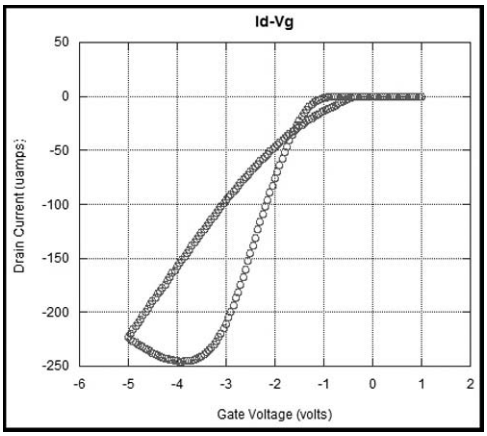

Figure 3: Plot of drain current (I_d) versus gate voltage (V_g), sweeping the voltage in both directions to observe hysteresis.

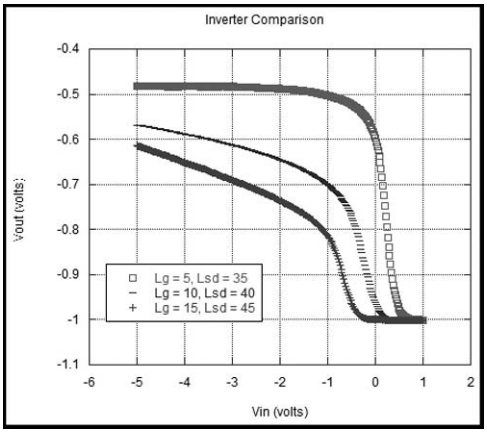

Figure 4: Illustration that inverter operation is more successful for smaller values of gate length.

Results and Conclusions:

We successfully fabricated functioning transistors and inverters on a hydrogen terminated diamond substrate. During the experiment, we fabricated devices in two different orders. In the first batch, they were source-drain first and the second gate first. In theory, the order should not have a large effect on the final functionality of the device. In practice, the normally on/off characteristics were dependent on this order. Depositing the gate first yielded a much higher percentage of normally off devices. This satisfied one of our goals to consistently fabricate normally off devices.

Figure 3 illustrates this using an I_d-V_g graph. Here it is clear that the no current is flowing when zero voltage is applied to the gate. In these transistors, the average drain current achieved was on the order of a milliamp.

A second interesting conclusion can be drawn from Figure 3; there was a major difference in the transistor properties depending on if we swept the gate voltage in forward or reverse. This is known as hysteresis. A possible explanation for this comes from the two-dimensional nature of the charges in the channel, and capture and emission phenomena between holes and defect trap. This may have contributed to the ring oscillators not functioning.

Finally, Figure 4 shows successful inverter operation. Ideal inverters would very sharply transition from high to low voltage. Greater separation between the high and low voltage is also desired. Therefore we observe that inverters with narrower gate lengths perform better. In the same way (graph not pictured), smaller source drain distances perform better. These results were expected because transistors generally perform better at smaller scales.

Future Work:

Possible directions that this research could take in the future include theoretical explanations of the normally off and hysteresis behavior. The causes of these effects are still only loosely understood. There is also a chance that a good model for the hysteresis could facilitate ring oscillator construction.

Acknowledgements:

I would like to thank the National Nanotechnology Infrastructure Network International Research Experience for Undergraduates and the National Science Foundation for funding this research. Additionally, the welcoming and friendly environment that the National Institute for Materials Science provided was appreciated. Finally I would like to thank my research group for guiding and helping me through the project: Dr. Koide, Dr. Watanabe, Dr. Imura, Dr. Liu, and Dr. Tsuya.

References:

[1] H. Kawarada, et al., Appl. Phys. Lett. 65, 1563-1565 (1994).

Mobility of the Two-Dimensional-Electron-Gas in Lattice-Matched InAlN/GaN Grown by Ammonia Molecular Beam Epitaxy

Frank John Luciano, IV
Material Science and Engineering / Physics / Mathematics, University of Florida

NNIN REU Site: UCSB Nanofabrication Facility, University of California, Santa Barbara, CA
NNIN REU Principal Investigator: Dr. James S. Speck, Materials Department, University of California, Santa Barbara
NNIN REU Mentor: Erin C.H. Kyle, Materials Department, UCSB
Contact: fluciano4@ufl.edu, speck@mrl.ucsb.edu, kylee5042@gmail.com

MATS

Introduction:

Transistors are components on electronic boards that amplify signals and power and relay these to the rest of the electronics board. A novel model of a transistor is the high electron mobility transistors (HEMTs), which has several advantages over other transistors: high power per unit width, high frequency, high voltage operation, and low noise [1]. HEMTs operation occurs from the modulation of a two-dimensional-electron-gas (2DEG). The 2DEG channel is created at the interface of two different materials where the conduction band bends below the Fermi-level. In this channel, the material acts like a metal, hence a high mobility. The $In_{0.18}Al_{0.82}N$/GaN material, abbreviated InAlN/GaN, has great potential as a HEMT. One reason is that the material is lattice matched — meaning there is no internal strain [2]. Despite this, growing the bi-material system is difficult because InAlN must be grown at lower temperatures than GaN for In incorporation, typically resulting in poor material quality [3].

A method of growing InAlN/GaN is using molecular beam epitaxy (MBE); conventionally, plasma-assisted MBE using pure nitrogen is used, whereas using ammonia as the nitrogen source is less thoroughly studied. However, ammonia-MBE has potential due to higher achievable growth temperatures and a nitrogen-rich environment. This project studied the effects of the growth-temperature-interrupt-depth and InAlN-layer thickness on electrical properties.

Experimental Procedure:

Samples were grown using molecular-beam-epitaxy (MBE) which uses high temperatures and low pressures to sublime gallium (Ga), aluminum (Al), and indium (In) metal targets onto a substrate and simultaneously flowing ammonia (NH_3) to grow the InAlN/GaN layers. Two series were grown: the first to optimize the growth-temperature-interrupt-depth (GTID), and a second series was grown to optimize the InAlN-layer thickness (See Figure 1). All samples had a very thin 1 nm layer of AlN at the InAlN/GaN interface to improve the mobility [3]. All samples from Series-1 had an arbitrary InAlN thickness of 10 nm, and the samples from Series-2 (dependent on electrical results from Series-1) had a GTID of 2.5 nm. The Series-2 sample with an InAlN thickness of 10 nm was the same sample from Series-1 with a GTID of 2.5 nm. A photolithography procedure was used to pattern parts of the sample for electrical measurements (See Figure 2).

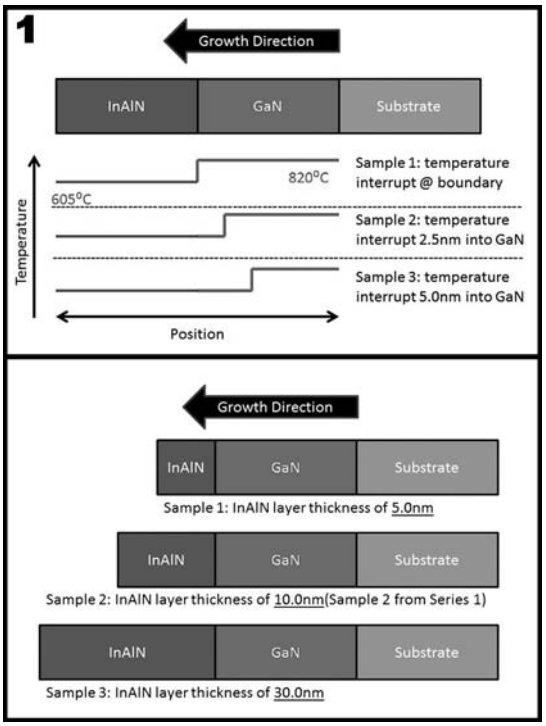

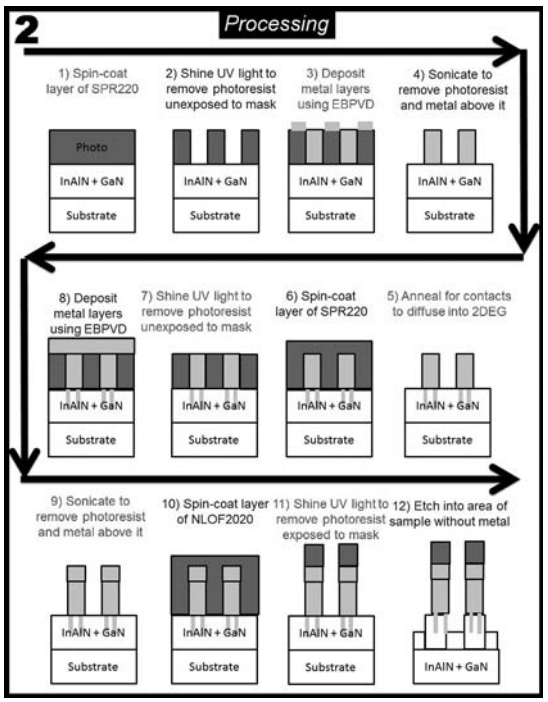

Figure 1, top: (a) Series-1 variation of growth-temperature-interrupt-depth. (b) Series-2 variation of InAlN thickness.

Figure 2, bottom: Overview of photolithography procedure, including before and after images, process flow chart, and Hall/TLM patterns.

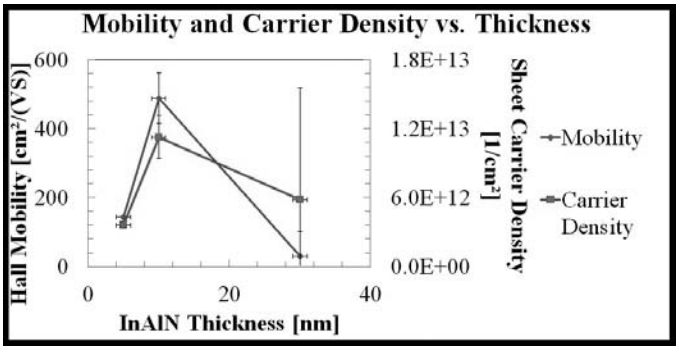

Figure 3: Series-2 mobility (blue) and carrier density (red) dependence on InAlN thickness.

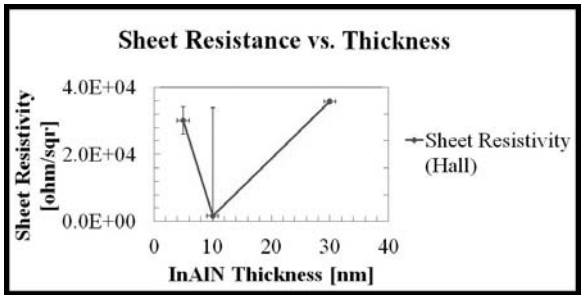

Figure 4: Series-2 sheet resistance dependence on InAlN thickness.

Results and Conclusions:

High-resolution-x-ray-diffraction (HRXRD) was performed on the MRD PRO Thin Film Diffractometer instrument to determine the crystallographic structure and to validate the atomic ratio of In:Al. The <002> peak was analyzed; using Bragg's law, known lattice constants of $In_xAl_{1-x}N$ materials, and the spacing between peaks, the In:Al ratio were calculated in all samples to be $0.15 < x < 0.20$, near-desired $x \sim 0.18$.

Atomic force microscopy (AFM), performed using the Asylum MFP3D instrument, was used to characterize surface topography and roughness, which is defined to be the root-mean-square (RMS) height of a scanned region of the sample. An inversely proportional relationship between roughness and InAlN thickness would be expected, which was not observed in Series-2. For this series, the 10.0 nm InAlN-layer thickness had a RMS roughness of 1.82 nm, much lower than the other two samples grown.

Electrical results (see Figure 3 and 4), done using the Hall patterns from photolithography, were measured using the Lake Shore Hall measurement system; parameters investigated include mobility, carrier density, and sheet resistance.

The average hall mobility of the 2.5 nm GTID sample of Series-1 was a factor five higher than the other two samples, at a value of 488 cm^2/Vs. Additionally, its carrier density was the highest at a value of $1.13*10^{13}$ cm^{-2}, and it had the lowest sheet resistance of 1570 Ω/□. When the Series-2 samples were grown to optimize InAlN-layer thickness, the 10.0 nm InAlN-layer thick sample had the highest mobility, carrier density, and lowest sheet resistance.

At a deeper GTID, the portion of the GaN layer grown at the lower temperature would be much rougher, causing the 2DEG and the InAlN-layers to also be rough and the material quality would be poor. A GTID at the interface will add a high unintentional dopant concentration near the 2DEG, scattering carriers. These arguments could explain why optimum electronic properties were observed at the 2.5 nm GTID. For the InAlN-layer thickness, a thinner layer will cause a loss of charge in the 2DEG from the Schottky barrier height but a thicker layer will decrease transconductance for HEMT devices.

Despite the observations of this work, there are several further steps to be made on the project before the material can be commercialized. The first includes confirming these reported trends to confirm the optimization of these growth parameters. Beyond this, there are other growth conditions that can be worked on, such as growing the precise stoichiometric $In_{0.18}Al_{0.82}N$.

Acknowledgments:

This work was supported by the U.S. Defense Threat Reduction Agency (Dr. James Reed), and the National Science Foundation (MRSEC) to the University of California: Santa Barbara. F. Luciano acknowledges the NSF National Nanotechnology Infrastructure Network Research Experience for Undergraduates Program for the financial support, and the UCSB Nanofabrication Facility.

References:

[1] Mishra, U. K., Parikh, P., and Wu, Y. F AlGaN/GaN HEMTs; an overview of device operation and applications. Proceedings of the IEEE, 90(6), 1022-1031 (2002).

[2] Hoi Wong, M., Wu, F., Hurni, C. A., Choi, S., Speck, J. S., and Mishra, U. K. Molecular beam epitaxy of InAlN lattice-matched to GaN with homogeneous composition using ammonia as nitrogen source. Applied Physics Letters, 100(7), 072107-072107 (2012).

[3] Jeganathan, K., Shimizu, M., Okumura, H., Yano, Y., and Akutsu, N. Lattice-matched InAlN/GaN two-dimensional electron gas with high mobility and sheet carrier density by plasma-assisted molecular beam epitaxy. Journal of crystal growth, 304(2), 342-345 (2007).

Electro-Mechanical Characterization of Gold Nanowire Meshes

Connor G. McMahan
Mechanical Engineering, Massachusetts Institute of Technology

NNIN REU Site: Colorado Nanofabrication Laboratory, University of Colorado, Boulder, CO
NNIN REU Principal Investigator: Dr. Mark P. Stoykovich, Chemical and Biological Engineering, University of Colorado at Boulder
NNIN REU Mentor: Ian P. Campbell, Department of Chemical and Biological Engineering, University of Colorado at Boulder
Contact: cmcmahan@mit.edu, mark.stoykovich@colorado.edu, ian.p.campbell@colorado.edu

Abstract:

The fabrication of stretchable interconnects is imperative for producing stretchable and flexible microelectronic devices, but current patterning approaches are limited to micron-scale features. Successful fabrication of smaller stretchable devices requires the use of new patterning methods, and block copolymer lithography is an emerging technique capable of patterning feature sizes below 10 nm. Upon self-assembly, lamellar-forming block copolymers generate a pattern colloquially known as the "fingerprint" morphology, due to the loops, whorls, and curved interfaces. The lamellar pattern shares many structural features with stretchable interconnects for macroelectronics, and successful translation of the pattern into functional materials may enable the production of stretchable electronic devices at sizes magnitudes smaller than state-of-the-art.

In this work, lamellar-forming polystyrene-block-poly(methyl methacrylate) (PS-*b*-PMMA) was used as a template to fabricate continuous gold nanowire networks (nanomeshes). The sheet resistance of these nanomeshes was below 1000 Ω/□ and the nanomeshes were nearly transparent, with transmittances greater than 85% across the visible spectrum. Successful transfer of the nanomeshes to stretchable substrates showed that nanomesh continuity was maintained during strain — because the path length between network nodes was much greater than the distance between nodes, allowing individual nanowires to elongate and straighten in the direction of strain while maintaining continuous pathways for charge transport.

Introduction:

The motivation of our research is the miniaturization of stretchable and flexible electronic devices. The fabrication of stretchable and flexible microelectronics depends on the fabrication of stretchable and flexible interconnects that present nanoscale features, but current interconnects, known as microribbons, are several microns wide. The nanoscale morphological analogues of microribbons are nanowire networks that assume patterns created by the random self-assembly of lamellar block copolymer structures.

The block copolymer template we use is polystyrene-block-poly(methyl methacrylate) (PS-*b*-PMMA). Since we want continuous nanowire networks, it is important to adjust the composition of PS-*b*-PMMA so that there is a continuous PMMA domain over the wafer. The curvy domains of the block copolymer ensure that the nanowire network will be stretchable once fabricated because the path length between two points is significantly larger than the distance between them. When submitted to a strain, wires will straighten and align themselves in the direction of the force, ensuring that network continuity is maintained.

Fabrication Process:

Block copolymer self-assembly was the first step in the fabrication process of the nanowire networks. A polymer brush was applied to a silicon oxide wafer. This allowed the lamellar structures of PS-*b*-PMMA to orient themselves perpendicularly to the wafer, assuming a two dimensional structure. To achieve lamellar PS-*b*-PMMA structures with a PMMA domain that was continuous throughout the wafer area, the block copolymer's volume fraction had to be adjusted so that there was slightly more PMMA than PS. The end result of this process was a block copolymer that presents a "fingerprint" morphology.

The next step in the process was to remove the continuous PMMA domain from the wafer by exposing the sample to UV light and submerging it in acetic acid. This was followed by a descum step with an oxygen plasma reactive ion etch (RIE), completing a template for continuous nanowire networks. A 2 nm chrome adhesion layer was evaporated, followed by evaporating the desired thickness of gold. PS was then removed by sonicating the sample in toluene, and the nanowire network was all that remained on the silicon oxide, as seen in Figure 1.

Finally, the nanowires were undercut by an SF_6 plasma RIE and transferred to a stretchable or flexible substrate.

Results and Conclusions:

The nanomesh sheet resistance was measured using a two-point probe. We used manually-placed silver epoxy dots as electrodes, verifying under an optical microscope that the electrodes were not short-circuiting the probe measurement, and found areas that were conductive over distances of a few hundred microns.

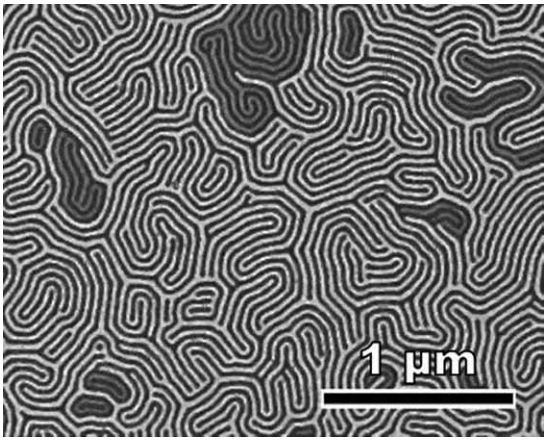

Figure 1: Gold nanomesh. The brighter nanowires are part of a continuous network.

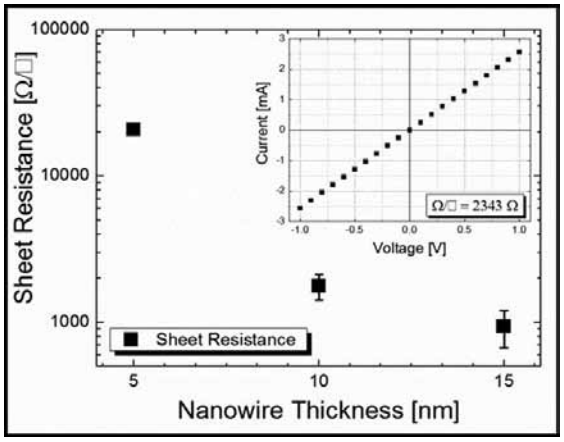

Figure 3: Sheet resistance of nanomeshes of various thicknesses.

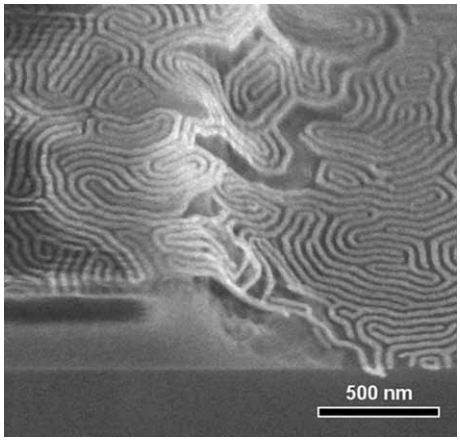

Figure 2: Nanowires stretching to accommodate different step heights.

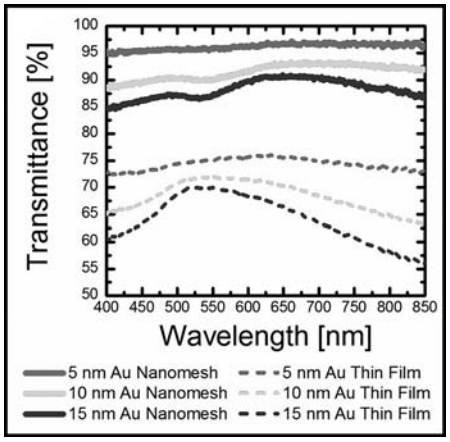

Figure 4: Optical transmittance of nanomeshes throughout the visible spectrum.

Prior to transferring the nanowires to a flexible or stretchable substrate, sheet resistances for nanomeshes of different thicknesses were measured. Nanomeshes that were 15 nm thick had sheet resistances of under 1000 Ω/□. As the nanomesh thickness decreased to 10 nm, the sheet resistances increased to 2000 Ω/□. Transmittances of over 85% were achieved throughout the visible spectrum for 15 nm thick nanowires, a very significant improvement over gold films of the same thickness.

After transferring a different 15 nm nanomesh to a flexible substrate, we achieved a sheet resistance of 3200 Ω/□, showing that the continuity of the network was preserved during the process of transferring the nanowires to a stretchable or flexible substrate.

Our fabrication process was not exclusive to gold nanomeshes. We have also fabricated chrome, zinc oxide, aluminum, silver, copper, and amorphous silicon networks. As a side project, we used nanowire networks composed of these different materials as etch masks for high aspect-ratio anisotropic etching, achieving etches that were several hundred nanometers deep with mask structures that were 25 nm wide. This significantly increased the light absorption of silicon, and could potentially be used to increase the efficiency of solar cells.

Future Work:

The focus of the project was to characterize the electrical and optical properties of gold nanowire networks, as we strived to achieve low sheet resistance and high optical transmittance over the visible light spectrum. We reached these goals and determined that the next step that should be taken in future research is to fabricate devices that are connected by stretchable nanomeshes, as the end goal is to enable the fabrication of stretchable or flexible microelectronics.

Acknowledgements:

I would like to thank Ian P. Campbell, Prof. Mark Stoykovich, and his group, my fellow REU interns, the Colorado Nanofabrication Laboratory and the Nanomaterials Characterization Facility at the University of Colorado at Boulder, the NNIN REU Program and the National Science Foundation.

Growth of Molybdenum Disulfide Atomic Layers

Brendan McMurtray
Chemical Engineering, University of Maryland, Baltimore County

NNIN REU Site: Howard Nanoscale Science and Engineering Facility, Howard University, Washington, DC
NNIN REU Principal Investigator: Dr. Jason Matthews, Department of Chemistry, Howard University
NNIN REU Mentor: Mr. Crawford Taylor, Department of Electrical and Computer Engineering, Howard University
Contact: bmcmurt1@umbc.edu, jsmatthews@howard.edu, crawford@msrce.howard.edu

Abstract:

The deposition of atomic layers of molybdenum disulfide (MoS_2) using a single-source precursor has been investigated. The single-source precursor tetrakis (diethylaminodithiocarbomato) molybdate(IV) ($Mo(Et_2NCS_2)_4$) was synthesized via two routes: a) Molybdenum hexacarbonyl $Mo(CO)_6$ was reacted with tetraethylthiuram disulfide ($Et_2NC(S)SSC(S)NEt_2$), and b) Potassium diethylaminodithiocarbamate ($KS_2CN(C_2H_5)_2$) was reacted with $Mo(CO)_6$. The precursor was purified by annealing at 150°C in a tube furnace, and utilized in the metal-organic chemical vapor deposition (MOCVD) growth of MoS_2 on SiO_2. The resulting atomic layers of MoS_2 were analyzed via scanning electron microscopy (SEM) and accompanying energy-dispersive x-ray spectroscopy (EDS).

Introduction:

Atomically-thin MoS_2 is a direct band gap semiconductor that exhibits interesting optical and electric properties [1, 2]. MoS_2 has been used to fabricate invertors, Negated AND (NAND) gates, and ring oscillators [2]. There are only a few single-source precursors that have been investigated for use in the deposition of thin films of MoS_2 via MOCVD. Factors affecting implementation of CVD precursors include volatility, thermal stability, and the ability to deposit the desired material in high purity. Our current study examined several synthetic routes towards producing an air and moisture stable precursor, tetrakis (diethylaminodithiocarbomato) molybdate(IV) ($Mo(Et_2NCS_2)_4$) [3, 4].

Experimental Procedure:

Tetraethylthiuram disulfide (2.25g, 7.6 mmol) and acetone (25 mL) were added to a 100 mL Schlenk flask. In an inert atmosphere glove box, molybdenum hexacarbonyl (1.00g, 3.8 mmol) was added to a separate 100 mL Schlenk flask. The $Mo(CO)_6$ was removed from the glove box, and the acetone solution of tetraethylthiuram disulfide was added via cannula. The mixture was stirred at reflux for two hours, and the formation of a purple precipitate was observed. The reaction mixture was allowed to cool, and the solvent was removed under vacuum allowing for the isolation of the solid purple precipitate.

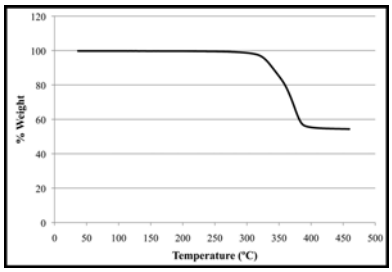

Figure 1: Mass % of sample as a function of temperature.

The resulting product was vacuum filtered and washed with pentane, dried, and annealed at 150°C in a tube furnace to remove unreacted starting material. The formation of the desired precursor was confirmed using Thermogravitmetric Analysis (TGA), with a single weight-loss step at 320°C that can be clearly identified in Figure 1 [4].

The second synthetic route made use of a two-step approach. A solution of potassium hydroxide (KOH) and diethylamine in ethanol was stirred for 15 minutes; a slight molar excess

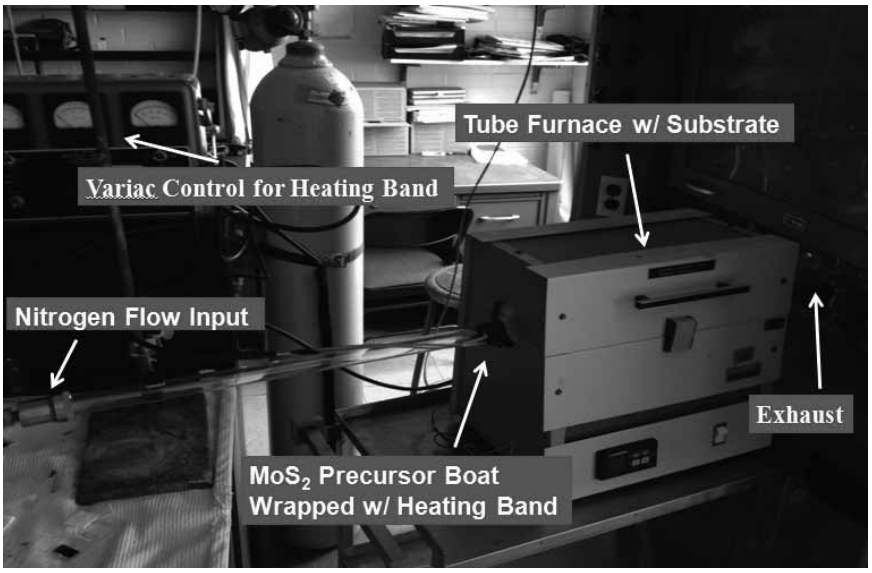

Figure 2: Horizontal hot-wall CVD reactor for growing MoS_2 thin films.

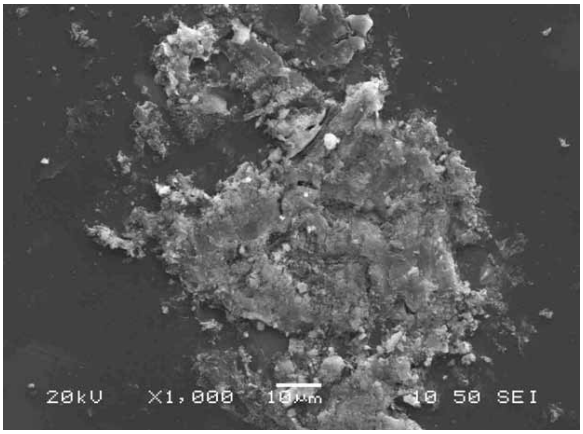

Figure 3: Patch of MoS_2 on SiO_2 substrate.

Element	Atomic%
S	57.11
Ca	0.42
Zr	2.71
Mo	39.76
Totals	100.0

Table 1: Atomic percent by element.

of carbon disulfide (CS_2) was added. The resulting mixture was allowed to stir for two hours, after which the solvent was removed via a rotary evaporator. Using a three-step trituration process, the dried precipitate ($KS_2CN(C_2H_5)_2$) was purified. The yellow powder was dried overnight, and the potassium salt was confirmed via ^1H nuclear magnetic resonance analysis. The potassium diethylaminodithiocarbamate was refluxed in a 4:1 molar ratio with $Mo(CO)_6$ using the same synthetic procedure as was used with tetraethylthiuram disulfide. Unfortunately, this synthetic route did not yield significant amounts of the desired precursor.

Once the desired precursor was synthesized, the horizontal hot-wall CVD reactor was designed as shown in Figure 2. Several different substrates were tested, including silicon (Si), silicon dioxide (SiO_2), gold-plated Si, nickel-plated Si, gold-plated SiO_2, and nickel-plated SiO_2. The substrate was placed vertically in a boron nitride boat in the CVD reactor and held at temperatures of 425°C, 550°C, and 675°C for three different experiments. The precursor was sitting in a boron nitride boat approximately three inches from the substrate at a temperature of 320°C or 365°C. We carried out all trials with a nitrogen flow rate of 7 cm^3/min, 10 cm^3/min, 15 cm^3/min, or 25 cm^3/min. All specific treatment combinations were tested in the CVD reactor in order to elicit the most effective means of producing pure thin films of MoS_2.

Results and Conclusions:

After examining all combinations of independent variable levels, it was determined that the prime conditions for obtaining MoS_2 were a substrate temperature of 675°C, a precursor temperature of 365°C, and a nitrogen flow rate of 15 cm^3/min. The precursor boat was refilled twice for a total of three runs, and each run lasted for 15 minutes. Unfortunately, no combination of parameter values achieved an even coating of the substrate, but we were able to obtain patches of MoS_2, one of which can be seen in Figure 3.

MoS_2 patches were accurately identified via EDS; Table 1 displays the EDS results from the patch seen in Figure 3. As we can see, the atomic percentage of the deposited MoS_2 sample is 57.11:39.76 or ~ 1.44:1, which is approximately a 28% error from the 2:1 atomic ratio of sulfur and molybdenum in MoS_2. Therefore, MoS_2 was successfully deposited; however, a more suitable precursor needs to be identified.

Moving forward, further analysis is needed on the deposited material to confirm the presence of MoS_2. In addition, the second synthetic method involving the potassium salt needs to be refined in order to promote the production of the desired precursor. TGA results in Figure 1 indicate the synthesized precursor is thermally unstable; that is, the first synthetic method leaves residual impurities. This coupled with the fact that large-area MoS_2 deposition was not obtained, means that there is a need for further study of this single-source precursor platform in the form of a structure activity relationship.

Acknowledgements:

I would like to thank Mr. Crawford Taylor, Dr. Jason Matthews, and all the staff at the Howard Nanoscale Science and Engineering Facility (HNF) and Howard Chemistry Department. I also would like to express my gratitude towards the National Nanotechnology Infrastructure Network Research Experience for Undergraduates (NNIN REU) program and the National Science Foundation (NSF) for making this awesome internship opportunity possible.

References:

[1] K.F. Mak, et al., Phys. Rev. Lett. 2010, 105.13605, 1-4.
[2] H. Wang, et al., Nano Lett. 2012, 12.9, 4674-80.
[3] T. Ouyang, et al., The Journal of Phys. Chem. B. 2004, 108.45,17537-45.
[4] R. Lozano, et al., An. Quim. 1983, B79, 41.

Growth and Characterization of Synthetic Diamond

Veronica Medrano
Electrical Engineering, Texas A&M University

NNIN REU Site: Howard Nanoscale Science and Engineering Facility, Howard University, Washington, DC
NNIN REU Principal Investigator: Dr. Gary Harris, Electrical Engineering, Howard University
NNIN REU Mentor: James Griffin, Electrical Engineering, Howard University
Contact: ronnienm08@neo.tamu.edu, gharris@msrce.howard.edu, jagriffin@howard.edu

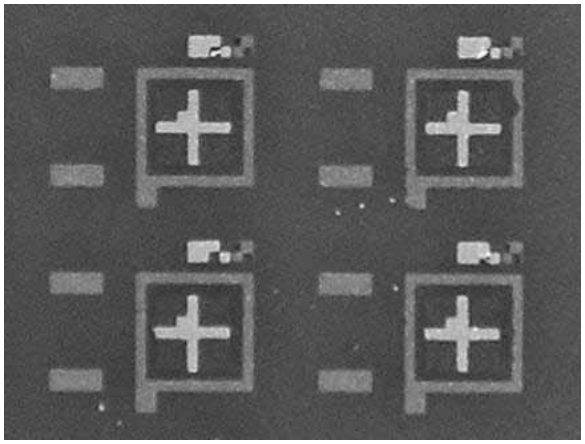

Figure 1: Top view of fabricated diamond device (crosses are Schottky contacts and outer squares are ohmic contacts).

Abstract:

Diamond exhibits superior material properties such as high breakdown field, high saturation velocity, high carrier mobilities, optical transparency over a wide transmission range, and the highest thermal conductivity of all materials [1]. These properties make it desirable to deliver future high quality electronic devices and detectors. Hot filament chemical vapor deposition (HFCVD) was used to grow polycrystalline diamond on various substrates. Atomic force microscopy (AFM) and scanning electron microscopy (SEM) confirmed diamond growth due to the resulting diamond facets on the substrate surfaces. Diamond grown on diamond yielded the highest grain size. A Raman shift value of 1332 cm^{-1} confirmed the presence of high quality polycrystalline diamond. Titanium-gold (Ti-Au) ohmic contacts were fabricated and annealed at 950°C for ten minutes in an H_2/Ar ambient environment. Linear-IV curves confirmed ohmic behavior. Nickel (Ni) was used as a Schottky contact and its IV curve was nonlinear as expected. Electrical properties of selected diamond films were also analyzed using the Hall effect. Diamond grown on 3C-SiC yielded a mobility of 221 cm^2/v-s and carrier concentration of 7.2E16 cm^{-3}.

Introduction:

The first "manmade diamond" was created by General Electric in 1956, using a process called high pressure high temperature (HPHT). This method imitates natural diamond formation, but with carefully selected input materials to catalyze crystal growth [2]. In recent years, chemical vapor deposition (CVD) has been used to produce diamond from a heated mixture of hydrocarbon gas and hydrogen in a vacuum chamber at very low pressures. The method is less expensive and more suitable for diamond growth in the semiconductor industry. This project employed a hot filament CVD system to grow synthetic diamond on various substrates.

Experimental Procedure:

Silicon dioxide (SiO_2)-coated Si, 3C-SiC coated Si, and 6H-SiC were seeded with nanodiamond slurry solution in an ultrasonic bath for ten minutes. This was done in order to create nucleation centers for diamond growth. The samples were then loaded in the HFCVD reactor. Also, the backside of a nanocrystalline diamond layer removed from silicon was loaded. The filament-to-sample gap was set to 20 mm, and hydrogen (H), methane (CH_4), and argon (Ar) gases were introduced. The H_2 flow rate was set to 60 sccm and the CH_4 flow rate was set to 1 sccm.

When the process pressure (20 torr) and the sample temperature (750°C) were reached, the filament temperature was raised to 2300°C. Growth of diamond was then initiated. After growth, the samples were removed and characterized. Titanium (Ti, 20 nm) and gold (Au, 150 nm) were deposited by electron-beam evaporation to fabricate ohmic contacts while Ni (100 nm) was deposited to make the Schottky contacts. The ohmic contacts were annealed at 950°C for ten minutes in an H_2/Ar ambient environment using a tube furnace.

Figures 1 shows the top view of the created device. A Hall effect setup was used to measure mobility, resistivity, and carrier concentration.

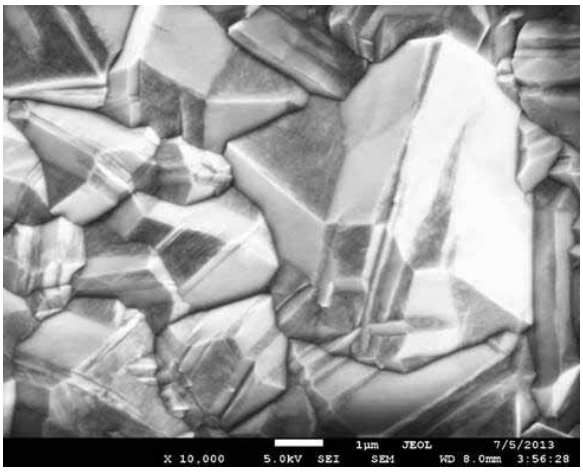

Figure 2: SEM image of diamond grown on diamond.

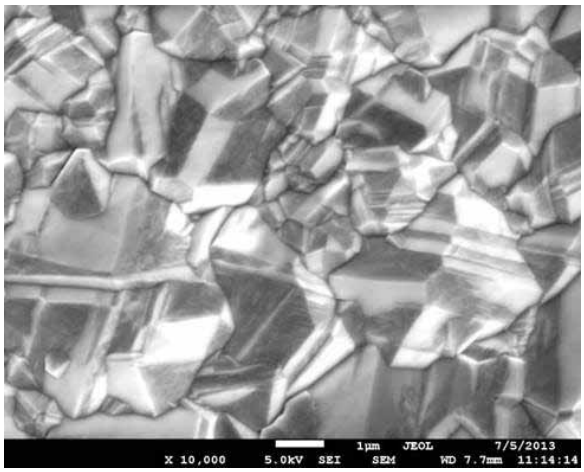

Figure 3: SEM image of diamond grown on 3C-SiC.

Results and Conclusions:

Diamond growth using HFCVD was conducted successfully, as seen in the resulting polycrystalline facets shown on SEM and AFM images. Diamond grown on diamond yielded the largest grain size (~ 7 μm), compared to sizes of 5 μm (Si) and 4 μm (6H-SiC and 3C-SiC) as shown in Figures 2 and 3. Larger grain sizes should translate into improved carrier transport.

Diamond grown on all substrates had a thickness of 12.3 μm. Roughness did not play a huge role in the results since the AFM revealed similar roughness (210-254 nm) for diamond on the various substrates. A Raman spectroscopy graph confirmed the presence of high quality polycrystalline diamond growth due to the diamond peak value of 1332 cm^{-1} (Figure 4). The full-width half-maximum value was measured to be 15 cm^{-1}, close to diamond's true value. Ti-Au ohmic and Ni Schottky contacts were successfully fabricated with linear and nonlinear curves, respectively, although the Schottky behavior was not ideal. Hall effect measured a mobility of 221 cm^2/v-s, resistivity of 0.39 Ω-cm, and carrier concentration of 7.2E16 cm^{-3}. These measurements are similar to previously published data.

Successful diamond growth and electrical fabrication indicates the potential use of these materials in engineering applications. This project is significant for promoting further research of diamond growth and characterization, especially since this novel material has been complex to study over the years.

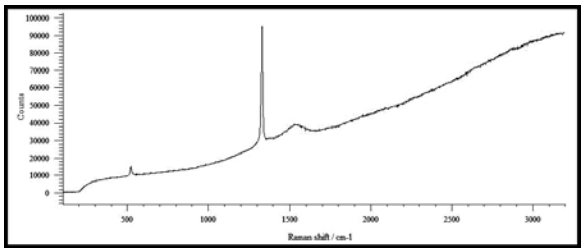

Figure 4: Raman curve of polycrystalline diamond film grown by HFCVD.

Future Work:

The barrier heights of various metals on diamond by internal photoemission will need to take place in the future in order to further analyze metal-diamond interfaces in fabricated diamond devices. The doping of diamond needs to be investigated as well. In addition, research must be done on finding ways to grow single crystal diamond in order to generate more advanced electronics. It may also be necessary to see how different metal contacts play a role in the quality of electrical devices.

Acknowledgements:

I wish to thank my Principal Investigator Dr. Gary Harris, Ph.D., P.E, the National Nanotechnology Infrastructure Network Research Experience for Undergraduates (NNIN REU) Program, Howard Nanoscale Facility, and the National Science Foundation (NSF) for making this project possible and giving me the opportunity to be a part of it. In addition, the mentorship of James Griffin and assistance of Laila Carter and Bokani Mtengi was invaluable over the summer.

References:

[1] Gabrysch, M. (2008). Electronic Properties of Diamond. Uppsala, Sweden: Division for Electricity Dept of Engineering Sciences. Retrieved from http://www.el.angstrom.uu.se/Seminar/MGabrysch_Lic.pdf.

[2] http://www.e6cvd.com/cvd/page.jsp?pageid=405. Accessed 7/20/2013.

High Strain Low Voltage Induced Densified Vertically Aligned Carbon Nanotube Ionic Actuators

Joshua Michalenko
Electrical Engineering, New Mexico State University

NNIN REU Site: Penn State Nanofabrication Laboratory, The Pennsylvania State University (PSU), University Park, PA
NNIN REU Principal Investigator: Professor Qiming Zhang, Electrical Engineering and Materials Science, PSU
NNIN REU Mentor: Mehdi Ghaffari, Materials Science, The Pennsylvania State University
Contact: joshm44@nmsu.edu, qxz1@psu.edu, mxg1019@psu.edu

Abstract:

Electroactuation materials that can generate high strain under low voltages are crucial components in artificial muscles, robotics applications, and micro- and nano- electromechanical (MEMs and NEMs) devices. This project developed ultra-high volume density carbon nanotube (CNT)-based ionic actuators that would increase the actuation strain from a current < 1% to 20% under low voltages (< 4 volts). Using a biaxial mechanical densification (BMD) process increased the volume fraction (V_f) of the vertically aligned carbon nanotubes (VA-CNT) from 1% to 40% [1]. The densification process maintained the vertically aligned morphology of the CNTs, providing non-tortuous pathways for ion transportation. This characteristic is crucial to creating fast, efficient, and high strain actuation devices. One percent V_fCNT forests were densified to 40%V_f, infiltrated with 40%wt Nafion polymer, and immersed in two separate ionic liquids, 1-ethyl-3-methylimidazolium trifluoromethanesulfonate ($[EMI^+][Tf^-]$) and 1-butyl-3-methylimidazolium tetrafluoroborate ($[BMI^+][BF_4^-]$), for strain testing. Experimentation revealed $[BMI^+][BF_4^-]$ showed largest strains of 13% under 0-3V triangular wave signals, while using $[EMI^+][Tf^-]$ showed ~ 5% strains under the same conditions. These results indicated that the size difference between the cations and anions in the ionic liquid was one critical factor that drove the actuation of the device.

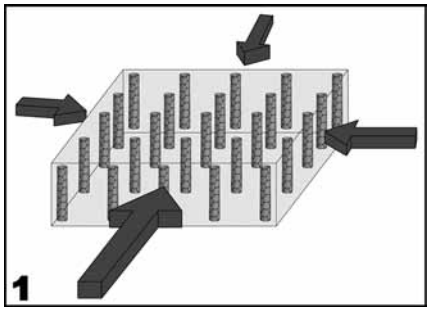

Figure 1, top: Biaxial densification process of CNT forest.

Introduction:

Electroactuation materials are simple devices that perform energy conversion between electrical and mechanical forms. Creating electroactuation devices that can generate large movement under low voltages is one key component to advancing the prominence of actuators in everyday life. VA-CNT based ionic actuators are a proven concept with the potential to produce high strain under low voltages [2]. By densifing the VA-CNTs, it has been theoreticized that the actuation efficiency can be significantly increased.

Fabrication and Experimental Procedure:

One percent V_f VA-CNTs were grown, 500 μm thick, on a silicon substrate using a modified chemical vapor deposition process with a Fe-on-alumina catalyst system [3]. After removal from the substrate, samples were put through a BMD process (Figure 1) to decrease the spacing between the CNTs and increase the density from 1% V_f (10 mm^2) to 40% V_f (1.6 mm^2). CNT samples were then placed in 3D metal cages with a metal mesh on the top side and were infiltrated with a 2.5% Nafion (NR-211) dispersion in DMF to contain 40% wt of NR-211. Samples were placed under vacuum at 5 mmHg for 5-7 days or until the solvent had completely dissolved. The samples were then annealed at 110°C for one hour and immersed in ionic liquid under vacuum at 5 mmHg for one day.

Various waveforms were applied to the CNT actuators in an actuation testing station and their actuation (Figure 2) was characterized with a fiber optic displacement sensor. Both ionic liquids, $[EMI^+][Tf^-]$ and $[BMI^+][BF_4^-]$, were utilized separately in the testing process and triangular waveforms ranging from -3-3V were tested under a 5 mv sec^{-1} scan rate.

Results, Discussion, and Conclusions:

A graph from a test showing the applied voltage as a -3-3V triangular wave and the response of the actuator is shown in

Figure 3. As voltage increased/decreased, the conductive, porous, CNT forests acted as electrodes that attracted/repelled ions of the opposite charge that filled the CNTs, causing expansion/contraction and therefore strain.

Strain is defined as the thickness difference between the initial and final states of the actuator after applying voltage. Figure 4 shows the maximum percent strain recorded from six different testing scenarios of different waveforms and ionic liquids. Phase separation in the applied voltage and response of the actuator were noted and more investigation on this topic is needed.

It was also observed that for the first 10-20 cycles of applied voltage, the actuators mostly expanded during a conditioning phase. After the conditioning phase, the actuators entered into a steady state in which the difference in sizes between the cations and anions in the ionic liquid drove the actuation process [1]. Using three different waveforms and two ionic liquids for each waveform showed that $[BMI^+][BF_4^-]$ was a more effective ionic liquid than $[EMI^+][Tf^-]$. This observation is due to the size difference between the cations and anions of the $[BMI^+][BF_4^-]$, which was greater than the difference in $[EMI^+][Tf^-]$ [4].

As higher voltage was applied, more actuation was observed. Maximum strain of 13.2% occurred under a 0-3V waveform using $[BMI^+][BF_4^-]$. These results are quite significant due to the fact that previous researchers, using undensified samples have achieved < 1% strain [5]; concluding that the densification of VA-CNTs create ionic actuators with the capability of creating higher strain than undensified samples.

Future Work:

Atomic force microscopy (AFM) measurements to obtain the elastic modulus of the CNTs will be used to calculate columbic and electromechanical efficiencies of the devices. Subsequently, a mathematic representation of the system will be formed in the sense of an electrical circuit for simulation purposes. By altering the %wt of N-211 to be added to the samples, the strain on the actuators can also be optimized.

Acknowledgments:

Thank you to my PI, Dr. Qiming Zhang, my mentor, Mehdi Ghaffari, and all of the members of the Zhang group for their guidance and support on the project. Thank you to the REU Site Coordinator Kathy Gehoski, all the members of the Nanofabrication staff, as well as our collaborators at MIT. Lastly, thanks to the National Science Foundation and the National Nanotechnology Infrastructure Network Research Experience for Undergraduates (NNIN REU) Program for funding and organizing the project.

References:

[1] Zhou, Y., and Ghaffari, M., revision submitted to Advanced Energy Materials.
[2] Liu, S., and Yang, Y., Advanced Functional Materials, vol. 20, pp. 3266-3271 (2010).
[3] Wardle, B., and Saito, D., Advanced Materials, vol. 9999, pp. 1-8 (2008).
[4] Liu, S., and Wenjuan, W., Society of Chemical Industry, vol.59, pp. 321-328 (2010).
[5] Liu, S., PhD. thesis, The Pennsylvania State University, (2010).

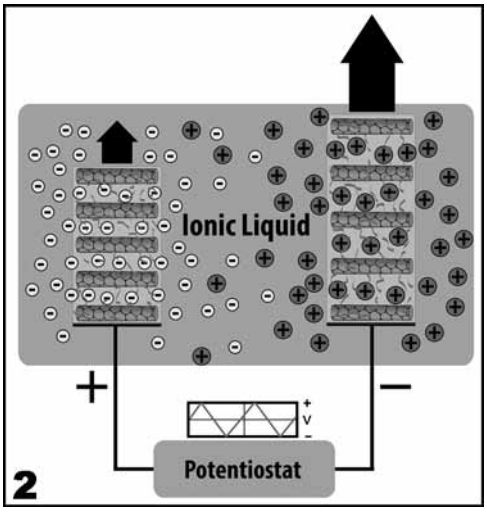

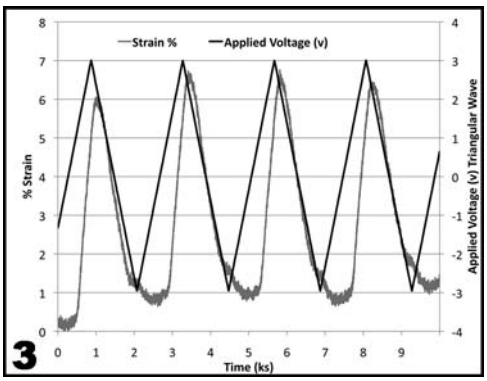

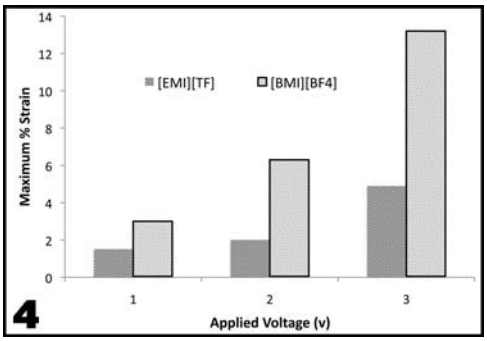

Figure 2, top: Applied voltage to CNT ionic actuators showing expansion of actuators.

Figure 3, middle: Line graph of -3-3v triangular wave being applied to actuators and response of the actuators.

Figure 4, bottom: Maximum strain percent as a function of applied voltage and ionic liquid.

Carbon Coated Tin-Seeded Silicon Nanowires for Lithium-Ion Battery Anodes

Daichi Oka
Department of Chemistry, School of Science, The University of Tokyo, Tokyo, Japan

NNIN iREG Site: Microelectronics Research Center, The University of Texas, Austin, TX
NNIN iREG Principal Investigator: Prof. Brian A. Korgel, Department of Chemical Engineering, The University of Texas at Austin
NNIN iREG Mentor: Timothy D. Bogart, Department of Chemical Engineering, The University of Texas at Austin
Contact: oka@chem.s.u-tokyo.ac.jp, korgel@che.utexas.edu, tbogart@utexas.edu

Introduction:

Lithium-ion batteries (LIBs) are widely used in many applications, such as mobile phones, laptops, and electric vehicles due to their high power density compared to other battery types. However, improvements are needed to meet the upcoming demands of new technology. Silicon (Si) has the potential to increase the power density of LIBs by replacing commercial carbon-based anodes because it has a high lithium-ion insertion capacity (Si: 3579 mA h g^{-1} vs. C: 372 mA h g^{-1} [1]). To accommodate the lithium (Li), the Si lattice must expand by up to 280%. While bulk Si pulverizes under these conditions, Si nanowires (SiNWs) can tolerate this volume expansion (and contraction upon delithiation [2]). However, there are challenges that must be overcome before Si can be used commercially.

Si is a poor electrical conductor, and anodes require the addition of some conductive carbon to improve anode conductivity. Additionally, gold, the typical seed metal to grow SiNWs, is known to have a negative impact on conductivity of SiNWs as gold impurities create deep electron traps in Si. Also, gold catalyzes electrolyte decomposition resulting in continuous growth of a solid electrolyte interphase (SEI) layer, reducing anode stability [3]. Tin-seeding [4] and coating with conductive graphitic carbon [5] are promising ways to overcome these difficulties. In this report we demonstrate the synthesis of carbon coated tin-seeded SiNWs via the supercritical-fluid-liquid-solid (SFLS) growth and their performances as LIB anodes.

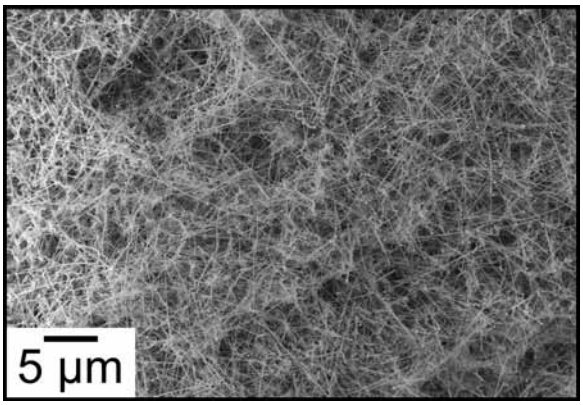

Figure 1, top: SEM of polyphenylsilane-coated tin-seeded SiNWs.

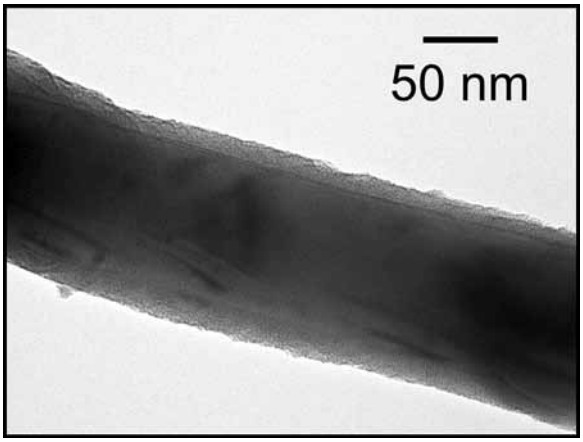

Figure 2, bottom: TEM of polyphenylsilane-coated tin-seeded SiNWs.

Growth of SiNWs:

A reactant solution of 0.5 mL of monophenylsilane and 24 μL of bis(bis(trimethylsilyl)amino)tin ($Sn(HMDS)_2$) in 25 mL of toluene was injected to supercritical-fluid of toluene in a titanum reactor that was heated to 490°C and pressurized to 10.8 MPa at a rate of 0.5 mL/min for 40 minutes. The amount of $Sn(HMDS)_2$ was changed from 24 μL to 48, 72, or 96 μL, corresponding to Si:Sn ratios of 65:1, 32:1, 22:1, and 16:1, respectively, in order to optimize the morphology of the SiNWs. The obtained SiNWs were characterized by scanning electron microscopy (SEM) and transmission electron microscopy (TEM).

When the Si:Sn ratio was as high as 65:1 or 32:1, SiNWs were tortuous and highly kinked with particulate reaction byproduct. TEM also showed that there was a thick carbonaceous shell surrounding the nanowires. At a Si:Sn ratio of 22:1, the SiNWs were predominantly straight and long, 10's to 100's of microns, with no significant particulate inclusions. Figure 1 shows an SEM image of a typical nanowire sample. Figure 2 shows a TEM image of a Si nanowire with a crystalline Si core and polyphenylsilane shell.

Although the Si:Sn ratio of 16:1 also provided with straight and long SiNWs, there was almost no phenylsilane shell on these nanowires. The Si nanowires made with Si:Sn ratio of 22:1 were studied for LIB applications by electrochemically cycling against Li metal in a coin cell.

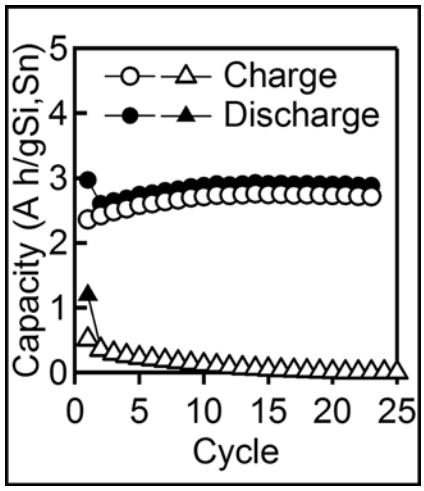

Figure 3: Charge and discharge capacities of the lithium-ion battries with the pyrolyzed/unpyrolized carbon coated tin-seeded SiNWs anodes at the cycle rate of C/10.

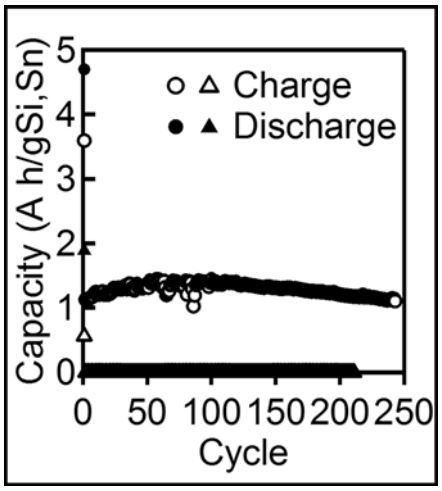

Figure 4: Charge and discharge capacities of the lithium-ion battries with the pyrolyzed/unpyrolized carbon coated tin-seeded SiNWs anodes at the cycle rate of 1C.

Battery Assembly and Testing:

The polyphenylsilane shell was converted to conductive graphitic carbon by annealing the nanowires under forming gas (7% H_2 in N_2) at 900°C for one hour (pyrolysis). Nanowires were tested in LIB coin cells with and without this heat treatment.

For testing in LIB coin cells, SiNWs were combined with poly(acrylic acid) binder with a 4:1 weight ratio. No conductive carbon particles were added. The mixture was dispersed in 1-methyl 2-pyrrolidinone to obtain a viscous slurry. The slurry was doctor-bladed (150 μm gap) onto copper (Cu) foil and vacuum-dried. Individual 11 mm diameter circular electrodes are hole-punched from the coated Cu foil and combined in coin cells. The assembly and testing procedures are detailed in Ref. 4.

Charge and discharge capacities were measured at rates of one cycle per ten hours (C/10) and one cycle per one hour (1C) (Figures 3, 4). At both rates, the charge capacities of the unpyrolyzed SiNWs were very low (< 1000 mA h g^{-1}) in the first cycle and decayed to 0 mA h g^{-1} after a few cycles. On the other hand, the pyrolyzed SiNWs showed high capacities over 2500 mA h g^{-1}. Even at the higher rate of 1C, the capacities of the pyrolyzed SiNWs were over 1000 mA h g^{-1} and stable for more than 200 cycles.

These results revealed that the carbon-coated Si nanowires have sufficient electrical conductivity for good battery performance without the need for additional carbon in the formulation, thus increasing the total battery anode gravimetric charge storage capacity.

Conclusions:

Long and straight SiNWs with nanometers-thick poly-phenylsilane coatings were synthesized by SFLS growth with tin seeds. Pyrolysis of the polyphenylsilane shell to carbon led to SiNWs with high and stable lithium insertion capacities, eliminating the need to use gold seeds for nanowire growth and the need for additional conductive carbon in the Si-based battery anode.

Acknowledgments:

I would like to thank Prof. Brian A. Korgel, Timothy D. Bogart, and all the other members of Korgel group, for their support in the research. Dr. Marylene Palard and Christine Wood helped me as the site coordinators. This work was funded by the National Nanotechnology Infrastructure Network International Research Experience for Graduates (NNIN iREG) Program/ National institute for Material Science Graduate Exchange Program Fellowship, and the National Science Foundation.

References:

[1] X. H. Liu, et al. Nano Letters 11, 2251-2258 (2011).

[2] H. Wu, et al. Nano Today 7, 414-429, (2012).

[3] A. M. Chockla, et al. The Journal of Physical Chemistry C 116, 18079-18086 (2012).

[4] A. M. Chockla, et al. Chemistry of Materials 24, 3738-3745 (2012).

[5] A. M. Chockla, et al. Journal of the American Chemical Society 133, 20914-20921 (2011).

Advanced Synthesis and Nano-Characterization of Graphene on Platinum <III> Substrates

Stephen A.O. Olson
Applied Physics, Bethel University; Electrical Engineering, University of Minnesota

NNIN iREU Site: National Institute for Materials Science (NIMS), Tsukuba, Ibaraki, Japan
NNIN iREU Principal Investigator: Dr. Daisuke Fujita, Division Director, Advanced Key Technologies Division, NIMS
NNIN iREU Mentors: Dr. Nobuyuki Ishida and Dr. Hongxuan Guo, NIMS Postdoctoral Researchers, Nano Interface Characterization Group, NIMS; Dr. Jian-hua Gao, International Center of Young Scientists, NIMS
Contact: olso5576@umn.edu, fujita.daisuke@nims.go.jp, ishida.nobuyuki@nims.go.jp, guo.hongxuan@nims.go.jp, gao.jianhua@nims.go.jp

Abstract:

Transition metal substrates enable growth of high-quality graphene in large sheets. We investigated graphene grown by surface precipitation and chemical vapor deposition (CVD) on platinum <111> substrates. Surface chemical composition and estimated film thickness were determined using Auger electron spectroscopy (AES). Platinum-graphene work function differences were measured with Kelvin probe force microscopy (KPFM) and shown to be correlated with fabrication methodology. Likewise, x-ray photoelectron spectroscopy (XPS) indicated that platinum-graphene charge transfer and interlayer interaction was affected by growth technique. Inverted surface topographies were observed by atomic force probe microscopy (AFM); the possibility of selective adsorption of water molecules on the substrate surface is proposed. Surface defect states were analyzed with scanning tunneling spectroscopy (STS). Supplemental topographical analysis was conducted using helium ion microscopy (HIM).

Introduction:

Graphene's many unique properties make it ideally suited for application in future technologies. An obstacle facing the commercialization of graphene-based technologies is the efficient production of large-area, defect-free graphene sheets. Transition metal substrates enable the growth of large high-quality graphene sheets; they may be well suited for the large-scale manufacturing of graphene. Platinum (Pt) <111> is one of the weakest interacting graphene-metal systems [1]; there will be less interference from the substrate affecting structural and electronic states of graphene. We wish to characterize graphene films grown on Pt <111> substrates by two methods: chemical vapor deposition (CVD) and the precipitation and segregation of carbon doped substrates (SEG). We consider the two growth methods by measuring monolayer graphene's interaction with the platinum substrate and analyzing unique surface features.

Experimental Procedure:

We began by growing the graphene films.

Segregation. Using carbon-doped platinum substrate, we initiated an 800-1000°C anneal at high vacuum. Carbon precipitated out of the substrate forming a graphene monolayer on the surface.

Chemical Vapor Deposition. At high temperature and vacuum, ethylene gas was introduced in the sample chamber. The carbon bonded to the substrate, forming a graphene monolayer on the surface.

Graphene Monolayer Existence Confirmation. Using AES, we confirmed the existence of graphene on both substrates and were able to estimate the film thickness using a simple model [2].

$$I_{sub} = I_{sub,pure} \exp\left(\frac{-d}{\lambda(E)\sin(\theta)}\right)$$

Film thickness is represented by d, θ is the Auger electron take-off angle (system dependant), λ is the electron inelastic mean free path (energy dependent), I_{sub} is the intensity of the attenuated substrate peak, and $I_{sub.pure}$ is the intensity of the pure substrate peak. This estimation does not take diffractive effects or the number of contributing platinum layers into account. It assumes AES peak intensity attenuation is caused solely by the presence of graphene. Therefore, we estimate 20-30% error using this method. However, even with this error margin, we were able to confirm that the graphene was indeed one monolayer thick.

Surface Potential Measurements. KPFM surface potential mapping revealed statistically significant relative differences in surface potentials between SEG and CVD graphene films. This voltage difference is proportional to a work function difference. We observed an average potential difference of 78 mV for SEG graphene and 103 mV for CVD graphene. We conclude that the two samples have different electronic state compositions.

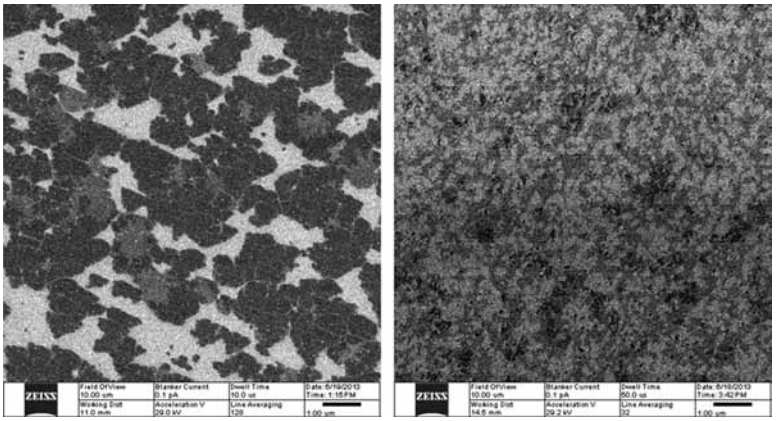

Figure 1: Helium ion microscopy images of SEG (a) and CVD (b) graphene surfaces.

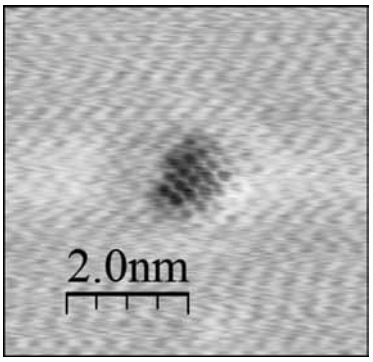

Figure 2: Atomically resolved STM image of suspended graphene.

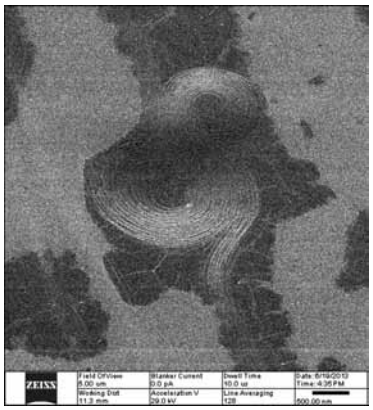

Figure 3: Unexplained graphene defect observed on surface.

XPS Measurements. X-ray photoelectric spectroscopy (XPS) measurements indicated that the binding energy of CVD graphene is lower than binding energy of SEG graphene. The binding energy of CVD graphene was measured to be 284.0 eV, while SEG graphene was at 284.2 and 284.3 eV. This indicates that CVD graphene has less interlayer interaction than SEG graphene. In contrast, segregation graphene on nickel has a binding energy of 284.9 eV, indicating stronger interlayer interaction [3].

AFM Measurements. During atomic force probe microscopy (AFM) measurements, we found the graphene-platinum height relationship inverted. Platinum was measured to be 1.2-1.4 nm higher than graphene. We believe there is a possibility that water was being adsorbed on the hydrophilic Pt <111> surface. If this was the case, it would mark the first instance of such an observation on this scale. Under vacuum, using scanning tunneling microscopy (STM), the graphene and Pt surfaces were observed to be nearly equivalent in height. Because the surfaces were both conductive, we know that the STM tip was in close proximity to the surface, and a difference of 1.2-1.4 nm would certainly have been observed if material was present.

Finally, we observed a suspended graphene defect while performing scanning tunneling microscopy measurements. We found that the dA/dV doubled at the center of the defect, telling us that the localized density of states (proportional to dA/dV) also doubled.

Results and Conclusions:

We observed a statistically significant difference of 25 mV in average surface voltage potential between SEG and CVD graphene. This is proportional to a difference in surface work function for these two growth methods, which is correlated to the composition of electronic states in the material. We also observed a shift of 0.2-0.3 eV in binding energy when comparing SEG and CVD samples. This indicates that CVD graphene has less chemical interaction with platinum. STM analysis of the defects indicates an increased density of electronic states in SEG graphene suspended over a 10-20 Å diameter pit.

Acknowledgments:

The author thanks Daisuke Fujita, Nobuyuki Ishida, Hongxuan Guo, JianHua Gao, and NIMS technical staff. Support was provided by the National Science Foundation and the National Nanotechnology Infrastructure Network's International Research Experience for Undergraduates (NNIN iREU) Program.

References:

[1] Ugeda, M. M., et al. "Point Defects on Graphene on Metals"; Phys. Rev. Let., 10, 116803 (2011).

[2] Xu, M., et al. "Production of Extended Single-Layer Graphene"; ACS Nano, 5, 2, 1522-1528, (2011).

[3] Fugita, D., Yoshihara, K. "Surface precipitation process of epitaxially grown graphite (0001) layers on carbon-doped nickel(111) surface"; J. Vac. Sci. Technol. A 12, 2134 (1994).

Study of the Electron Blocking Layer in Gallium Nitride Devices

Eric Reichwein
Physics, University of California Santa Cruz

NNIN REU Site: UCSB Nanofabrication Facility, University of California, Santa Barbara, CA
NNIN REU Principal Investigator: Dr. Shuji Nakamura, Material Science and Engineering, University of California, Santa Barbara
NNIN REU Mentor: Stacy Kowsz, Material Science and Engineering, University of California, Santa Barbara
Contact: ereichwe@ucsc.edu, shuji@engineering.ucsb.edu, stacy.kowsz@gmail.com

Abstract:

The electron blocking layer (EBL) is thought to increase efficiency in gallium nitride (GaN) light emitting diodes (LEDs) and laser diodes. In the LED, electrons pass through the active region, which is the region where electrons transition to a lower energy level and emit a photon. An EBL will rebound electrons that escape the quantum well back into the active region and produce light. For our project, we looked at how two different substrate growth planes, m-plane and c-plane, affect the potency of the EBL. The LED m-plane and c-plane samples were grown using metal organic chemical vapor deposition (MOCVD) on sapphire substrate and bulk GaN substrates, respectively. After processing the samples, we looked at external quantum efficiency (EQE), which is the percentage of electrons that produce photons, and its dependence on temperature and current. For the c-plane LEDs without an EBL there was a decrease in EQE by up to 15% as compared to the samples with an EBL. The m-plane samples, however, showed that there is possibly a slight efficiency gain for samples with an EBL as compared to those without and EBL for the currents considered in this study. This shows that growth plane has a significant effect on the necessity of the EBL.

Introduction:

With lots of energy waste being created by inefficient lighting, LED research is important to combat the energy crisis. LEDs significantly reduce heat output, last longer, have faster response times, and are safer than traditional light sources.

LEDs work by taking advantage of quantized electronic transitions. During a transition from higher energy to lower, the energy released is in the form of a photon. This happens billions of times a second, which produces the beautiful bright light of LEDs. For every electron that enters the LED on the negative electrode there is an electron vacancy, called a hole, flowing toward the electron. The electron and hole meet at the active region and recombine. This recombination produces light and the electron travelling in its original direction but of lower energy. LEDs are more efficient than incandescent bulbs because LEDs do not rely on current heating up a filament to produce light, rather just by reducing an electron's energy.

Experimental Procedure:

We grew the LEDs using metal organic chemical vapor deposition (MOCVD) and used two different growth planes, c-plane and m-plane, for our substrates. The c-plane LEDs were grown using a sapphire substrates, while the m-plane LEDs used bulk GaN substrate. After growing the LED using MOCVD, we processed them in the UCSB Nanofabrication Facility.

The first step was removing surface oxide with hydrofluoric acid, and then laying down an indium-tin-oxide (ITO) current-spreading layer for the positive electrode, using photolithography and electron beam deposition. After that, we etched down to the negatively doped material. Finally, we applied an electrode so we could pass current from the positive electrode through the active region and into the negative electrode. After fabrication, we used Nakamura's Packaging Lab to test the LEDs.

After testing multiple wavelength LEDs for c-plane, we concluded that the c-plane samples all needed EBLs. This was due to the polarization of the c-plane quantum well (QW), the region where the electrons make an energy transition, because we had to decrease the width of the QW to correct for the fact that the electrons and holes are separated spatially. The spatial separation of electrons and holes allowed electrons to accumulate on the p-side of the QW and this made it easier for electron escape. The EBL rebound most escaped electrons from leaving into the QW, where they recombine to produce light.

Results and Conclusions:

It is difficult to draw conclusions from our m-plane data because of our lack of devices without an EBL. But there may be improvements in efficiency from having an EBL, though efficiency gains are lesser than those seen for the c-plane devices. However, we found that for every other wavelength from 415 nm to 490 nm there was a slight difference in efficiency between LEDs with an EBL and LEDs without an EBL. But once again, there was a larger difference in efficiencies for longer wavelengths.

We also did temperature dependence measurements on both m-plane and c-plane samples, but could not determine conclusively if the EBL affected the thermal droop.

Energy Efficiency & Energy Costs	Light Emitting Diodes	Incandescent Light Bulbs	Compact Fluorescent
Life Span	50,000+ hours	1200 hours	8000 hours
Watts of electricity used	6-8 Watts	60 Watts	13-15 Watts
Kilowatts used	329kW/yr	3285kW/yr	767kW/yr
Annual operating cost	$32.85/yr	$328.60/yr	$76.70/yr

Figure 1: This table is based on each type of light bulb producing 800 lumens of light.

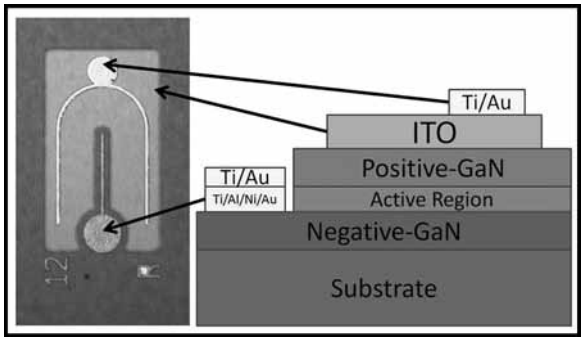

Figure 2: A diagrammatic schematic of our LED.

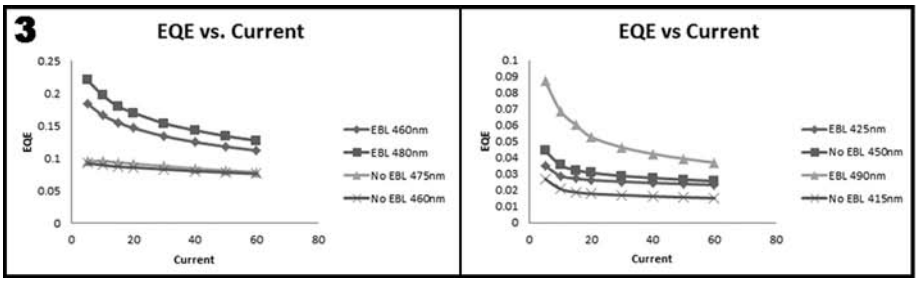

Figure 3: The EQEs of c-plane LEDs on the right are higher due to apparatus change. However, the overall trend is that the EBL increases the EQE of the c-plane LED.

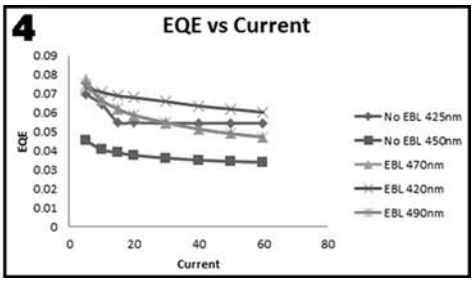

Figure 4: From the graph we see, for m-plane samples, that longer wavelength devices might benefit from an EBL more than shorter wavelength devices.

Future Work:

This study only investigated the wavelengths of 415 nm to 490 nm and only two growth planes. This research was performed as a follow up project of a paper published in Japan Applied Physics in April 2013. Kawaguchi, et al., concluded that, for non-polar and certain semi-polar growth planes, above a certain critical wavelength there is no increase in efficiency resulting from including an EBL. There are still more semi-polar growth planes on which to explore the impact of EBLs.

Acknowledgements:

I would like to thank my mentor, Stacy Kowsz, and the principal investigator of the project, Dr. Shuji Nakamura, and the NNIN UCSB coordinator, Samantha Cruz. I would also like to thank the NNIN REU Program, the National Science Foundation, and the Solid State Lighting and Energy Center (SSLEC). Finally, I would like to thank the Mitsubishi Chemical Corporation for supplying free standing GaN substrates.

Hydrogen as a Potential Cause for Native n-type Conductivity in Tin Dioxide

Emily M. Ross
Engineering, Harvey Mudd College

NNIN iREU Site: National Institute for Materials Science (NIMS), Tsukuba, Ibaraki, Japan
NNIN iREU Principal Investigator: Professor Naoki Ohashi, Optoelectronic Materials Group, NIMS
NNIN iREU Mentor: Dr. Ken Watanabe, Rechargeable Battery Materials Group, NIMS
Contact: emross@hmc.edu, ohashi.naoki@nims.go.jp, watanabe.ken@nims.go.jp

Abstract:

Tin dioxide (SnO_2) has been widely used for chemical sensors and transparent conductive films because of its wide band gap energy of 3.6 eV and n-type conductivity. The exact cause of this native n-type conductivity is not well-known, but density functional theory (DFT) calculations suggest that hydrogen (H) act as "hidden" shallow donors in SnO_2 [1]. To overcome the difficulty of analyzing hydrogen-related phenomena, this analytical study was performed using ^2H as an isotopic tracer. Pure and In-doped SnO_2 ceramics were annealed in humid O_2 gas enriched with ^2H_2O to introduce ^2H into the SnO_2 lattice. Characterization was performed with thermal desorption spectroscopy (TDS) and secondary ion mass spectroscopy (SIMS), as well as Raman, photoluminescence (PL) and Fourier transform infrared (FTIR) spectroscopies. Results indicate that the hydrogen that compensates the acceptor states created by indium, thus preventing p-type conductivity, mostly sit in defect sites that are more stable than those of the hydrogen that was introduced through the humid annealing process. The more stable defect sites are thought to be substitutional sites, while the less stable defects are thought to be interstitial sites.

Introduction:

The native n-type conductivity of SnO_2 is often explained by assuming that oxygen vacancies act as shallow donors, but recent density functional theory calculations claim that oxygen vacancies are too deep to act as shallow donors and instead point to hydrogen as acting as "hidden" shallow donors in SnO_2 [1]. These calculations also indicate that indium and gallium could create shallow acceptor states in SnO_2 that would cause p-type conductivity [1]. However, p-type tin dioxide has never been obtained experimentally. DFT claims this is because the acceptor states created by gallium and indium are compensated by hydrogen [1].

The technique of using isotopic tracers allows characterization based on the mass difference between isotopes. Ideally, a common isotope is exchanged for a less common isotope — ^2H for ^1H in this case. The ^2H is introduced to the system via ^2H_2O. This ^2H_2O then becomes $^2H^1HO$ through an exchange process that allows ^1H to be replaced by ^2H. The ^1H that was previously in the lattice is then carried off by $^2H^1HO$, while the ^2H diffuses further into the lattice.

Experimental Procedure:

Pure and In-doped SnO_2 bulk ceramics were used in this study. Before beginning the humid annealing process, they were polished and sintered to smooth the surface and repair mechanical damage. To introduce ^2H into the SnO_2 lattice as an isotopic tracer, samples were annealed in humid O_2 gas enriched with ^2H_2O for one hour at 200°C, 300°C or 400°C. The ^2H_2O contained 98 atomic% ^2H and had a dew point of 60°C, resulting in an absolute humidity concentration of about 19.6 volume%.

Samples were characterized before and after annealing, mainly using methods that took advantage of the difference in mass between ^1H and ^2H. These methods include TDS, in which the samples are heated from room temperature to 1000°C to create a desorption profile for reactivity analysis; and SIMS, in which the material surface is sputtered to create a composition depth profile for diffusivity analysis. Other characterization techniques used include PL, Raman and FTIR spectroscopes.

Results and Conclusions:

TDS was used to analyze defect stability because it gives information about how much energy is needed to desorb a certain species. Thus, the higher the desorption temperature, the greater the stability of the species. This can be translated to the stability of a species in a particular defect when the species are isotopes, so the main difference between the two is their

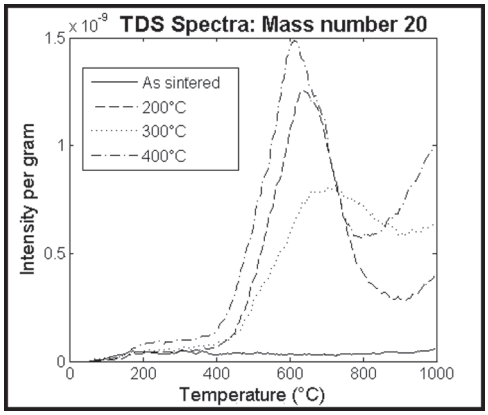

Figure 1: TDS spectra of In-doped SnO_2 for mass number 20, which corresponds to ^2H_2O.

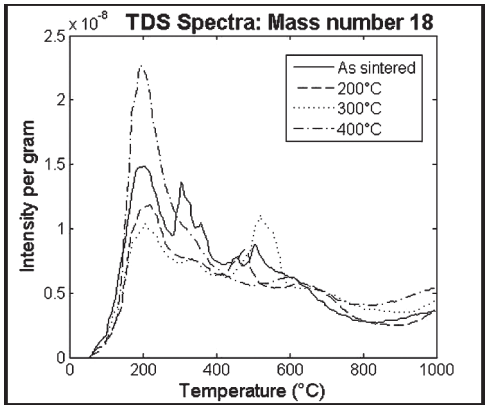

Figure 2: TDS spectra of In-doped SnO_2 for mass number 18, which corresponds to ^1H_2O.

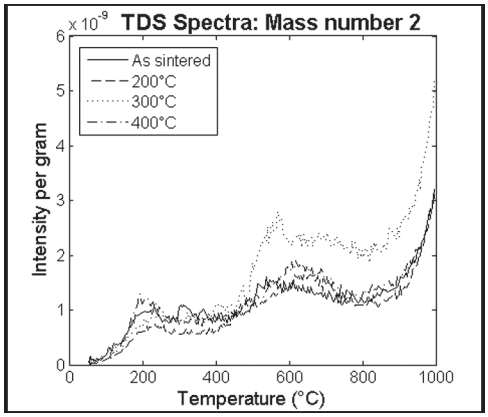

Figure 3: TDS spectra of In-doped SnO_2 for mass number 2, which corresponds to $^1H_2$.

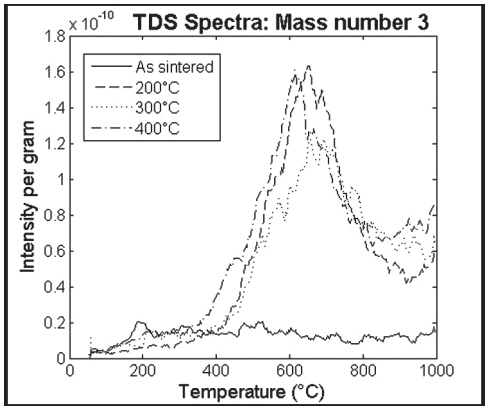

Figure 4: TDS spectra of In-doped SnO_2 for mass number 3, which corresponds to $^1H^2H$.

surroundings. Peaks at 610-690°C and around 1000°C were deemed to be the most important for understanding hydrogen behavior. In the ranges of interest, mass number 2 corresponds to $^1H_2$, mass number 3 to ^1H_2H, mass number 18 to ^1H_2O, and mass number 20 to ^2H_2O.

For mass number 20 (Figure 1), there was a strong peak at 610-690°C for the annealed samples, but no peak for the sample that had not been annealed, as expected. However, there was no peak in that same range for mass number 18 (Figure 2), which indicates that hydrogen was likely being added to SnO_2 lattice instead of being exchanged. This was supported with SIMS data that showed the concentration of ^2H in the In-doped ceramics was approximately an order of magnitude higher than that of the pure ceramics.

For mass number 2 (Figure 3), the dominant hydrogen peak was around 1000°C, while the dominant hydrogen peak for mass number 3 (Figure 4) was at 610-690°C for the annealed samples. This indicates that the ^1H that was initially in the In-doped ceramics and compensated the acceptor states created by In mostly sat in stable defect sites. The ^2H that was added to the material sat in less stable defect sites. These sites are believed to be substitution and interstitial sites, respectively, because of their relative stabilities.

Acknowledgments:

I would like to thank all of the people and organizations that made my summer research possible: Professor Naoki Ohashi and Dr. Ken Watanabe for guiding me and my work; Dr. Minako Hashiguchi, Dr. Noriko Saito and Dr. Takeo Ohsawa for their help; the National Institute for Materials Science for hosting me; and the National Nanotechnology Infrastructure Network International Research Experience for Undergraduates (NNIN iREU) Program and National Science Foundation for providing funding.

References:

[1] Singh, A., et al.; "Sources of Electrical Conductivity in SnO_2"; Physical Review Letters, 101.5, 055502 (2008).

Solid-State NMR of $(CdSe)_{13}(Propylamine)_{13}$

Michael E.H. West
Chemical Engineering and Physics, University of Arkansas

NNIN REU Site: Nano Research Facility, Washington University in St. Louis, St. Louis, MO
NNIN REU Principal Investigator: Dr. Sophia Hayes, Department of Chemistry, Washington University in St. Louis
NNIN REU Mentor: Dr. Zayd Ma, Department of Chemistry, Washington University in St. Louis
Contact: mew016@email.uark.edu, hayes@wustl.edu, zaydma@wuchem.wustl.edu

MATS

Abstract and Introduction:

Cadmium selenide (CdSe) nanoparticles exhibit unique electrical properties due to quantum confinement of electrons, showing potential for wide-ranging nanomaterial applications [1]. A constituent of these nanoparticles are so-called "magic number clusters" of CdSe, which are stable molecular units that can be synthesized with high purity. It is not known what makes these specifically numbered clusters stable and what the actual structure is. Samples of $(CdSe)_{13}$(*n*-propylamine)$_{13}$, one of these magic number clusters capped with *n*-propylamine ligands, were synthesized in near-purity and in quantities suitable for NMR spectroscopy by the Buhro lab at Washington University [2]. All NMR studies were performed in Sophia Hayes's lab.

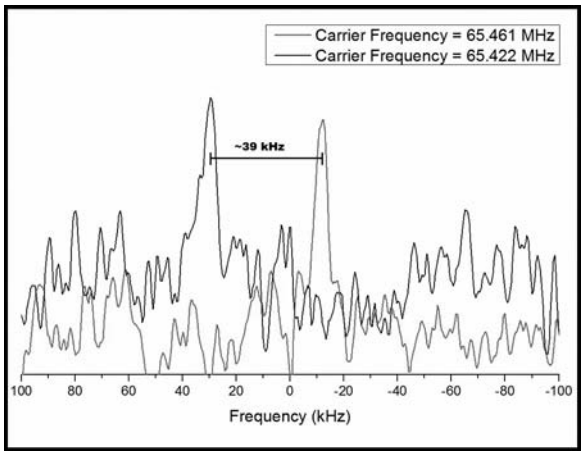

Figure 1: ^{113}Cd DEFT NMR of $(CdSe)_{13}$(propylamine)$_{13}$ at differing carrier frequencies.

Experimental Background:

For this project we focused on the NMR active nuclei ^{113}Cd. ^{113}Cd is a very difficult nucleus to find and acquire signal due to a relatively slow precession frequency (9.4 MHz/Tesla), low isotopic abundance (12.26%), a very large chemical shift range (> 3000 ppm), and exceptionally long longitudinal relaxation times (T_1 values over three hours are not uncommon). The other NMR active nuclei in the cluster are ^{111}Cd and ^{77}Se, which are both less sensitive than ^{113}Cd. On average, only one of each NMR active nuclei will be in the nanocluster, which leaves 23 atoms with spin zero. The absence of spin-zero nuclei has the effect of nullifying any strong dipolar interaction within the cluster and lengthening the relaxation time. Further elongating the relaxation time is the lack of a repeating crystal structure with strong phonon modes to mediate spin flips. The lack of repeating crystal orientation is due to each cluster being encapsulated in propylamine ligands. Even with these experimental realities, we were able to acquire high quality ^{113}Cd NMR data on the $(CdSe)_{13}$(*n*-propylamine)$_{13}$ nanoclusters.

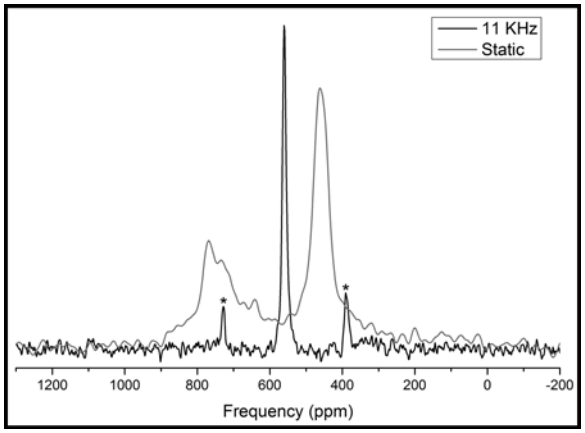

Figure 2: Static CP and 11 kHz CPMAS ^{113}Cd NMR of $(CdSe)_{13}$(propylamine)$_{13}$.

Experimental Procedure:

All solid-state NMR experiments were performed at room temperature on a 7T (300 MHz) superconducting magnet using a 4 mm MAS Chemagnetics probe tuned to 65.45 and 294.97 MHz for ^{113}Cd and ^{1}H, respectively. A 4 mm zirconium rotor, Tecmag Apollo spectrometer, and 1 kW amplifiers on ^{1}H and ^{113}Cd channels were used universally.

Three types of NMR pulse sequences were used to excite and observe the ^{113}Cd spins: "90-acquire," "Driven Equilibrium Fourier Transform" (DEFT), and "Cross-Polarization Magic Angle Spinning" (CPMAS).

The 90-acquire pulse sequences were used to acquire reference spectra and to optimize equipment. DEFT is a pulse sequence that can reduce the effects of long T_1 relaxation times by realigning nuclear spins back along the main magnetic field after observing the NMR signal. CPMAS is a technique developed by a researcher from Washington University [3] that cross-polarizes the ^{113}Cd with the ^{1}H, which allows the use of the ^{1}H relaxation time (typically much faster than ^{113}Cd) and results in a large signal enhancement of the ^{113}Cd. "Magic angle spinning" refers to rapid rotation (> 10 kHz) of the sample about 54.7° relative to the applied magnetic field.

Previous work would indicate that (CdSe) would have a chemical shift that is roughly similar to previous CdSe NMR spectroscopy, such as in the case with Berrettini et al. [1] working with 2 nm CdSe nanoparticles and having a chemical shift of roughly 600 ppm referenced to 0.5M $Cd(NO_3)_2$ solution, so initial signal hunting focused largely on the region from 300-800 ppm from our reference, 0.1M $Cd(ClO_4)_2$.

After pulse optimization and all reference spectra acquisition, our efforts were focused on finding direct ^{113}Cd signal using DEFT. Figure 1 shows results from two DEFT experiments with different excitation frequencies which proved the validity of the signal at 458 ppm. This result ensured we had found the ^{113}Cd signal and told us the frequency range to focus our CPMAS experiments.

Results and Discussion:

DEFT experiments proved to be too long to acquire acceptable signal to noise and we turned to CPMAS. Our goal was to use the ^{1}H magnetization on the propylamine ligands to polarize the ^{113}Cd and then observe the ^{113}Cd signal. This worked exceptionally well and the results of this experiment are shown in Figure 2.

As ^{113}Cd is a spin ½ nuclei, each unique chemical site should result in only one peak. The CPMAS results while spinning indeed indicate only a single site. It is known that different parts of a powder pattern line CP differently depending on their orientation with respect to the applied magnetic field [4] and this is why the static CPMAS result has two peaks. Longer contact times result in the expected static lineshape of an axially symmetric site.

If the $(CdSe)_{13}$ cluster has a central Cd, we would expect it to have a different chemical shift than the outer cadmiums. However, the ability for magnetization to transfer from a ^{1}H to a central Cd would be severely hampered by distance from surface protons to the center, and spin diffusion through the virtually spin-free nanocluster results in a very weak CPMAS signal. Thus, our conclusion at this juncture in the research is we have, for the first time, successfully observed at least one unique cadmium site and further work, such as 77Se NMR, needs to be done to complete the NMR study of this material.

Acknowledgements:

I would like to thank the NNIN REU Program and the NSF for supporting this project. Thank you to Nathan Reed and Dee Stewart for locally coordinating the program. Thank you to the Buhro and Hayes lab, specifically Dr. Sophia Hayes, Dr. Zayd Ma, Yuanyuan Wang, Katie Wentz, and Andrew Surface for their direct contributions.

References:

[1] Berrettini, Mia G., et al.; J. Am. Chem. Soc., 126, 7063-7070 (2004).

[2] Wang, Yuanyuan, et al.; Inorganic Chemistry 52, 2933-2938 (2013).

[3] Schaefer, J., and Stejskal, E.O.; J.Am.Chem.Soc., 98, 1031-1032 (1976).

[4] Pines, A., M. G. Gibby, and J. S. Waugh. The Journal of Chemical Physics 59.2: 582 (1973).

Synthesis of Metal Supported Catalysts for the Hydrogenolysis of Lignin

Jeanne Xu
Chemistry, Wellesley College

NNIN REU Site: Nano Research Facility, Washington University in St. Louis, St. Louis, MO
NNIN REU Principal Investigator: Dr. Marcus Foston, Energy, Environmental, and Chemical Engr., Washington University in St. Louis
NNIN REU Mentor: Yu Gao, Department of Energy, Environmental, and Chemical Engineering, Washington University in St. Louis
Contact: jxu3@wellesley.edu, mfoston@seas.wustl.edu, gaoyu@wustl.edu

Abstract:

Transition-metal (nickel, cobalt, copper, and iron) containing metal-oxide material (silica, alumina, and titania) were screened in an effort to develop heterogeneous catalysts for the hydrogenolysis of lignin that selectively cleave aryl ether linkages. Different combinations of active transition-metal precursors with metal-oxide supports were synthesized by sol-gel processes, and the synthetic conditions for silica-, alumina-, and titania-supported catalysts were optimized. To minimize contamination and avoid oxidation, multiple washes with deionized water followed by sonication, centrifugation, Soxhlet extraction, and calcination under flowing inert nitrogen (N) atmosphere were investigated and an optimal protocol determined. Future characterization studies and investigations on catalytic activity and selectivity for aryl ether hydrogenolysis will determine the optimal transition-metal and metal-oxide support combination for selective hydrogenolysis of lignin.

Introduction:

Plant biomass, a renewable resource rich in carbon and chemical potential energy, is a promising feedstock to displace non-renewable petroleum [1]. In particular, lignin, one of the three main components of the plant cell wall, is an under-utilized feedstock that is currently considered as waste [1].

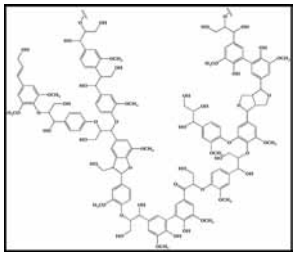

Figure 1: Representation of the molecular structure of lignin.

The highly heterogeneous structure of lignin (Figure 1) makes it difficult to deconstruct and therefore utilize; however, its rich aromatic composition is an ideal precursor for a variety of fuels and value-added reactive intermediates [1]. While many thermochemical processes can exploit lignin's potential, large energy inputs and harsh reaction conditions are required, often leading to a wide distribution of products [1].

Our research goal focused on synthesizing transition-metal containing metal-oxide catalysts that will be utilized in the production of a narrow distribution of phenolic-like products from lignin with minimal energy and material inputs. Sol-gel processes were employed due to better control on catalyst structure and chemical properties, higher thermal stability, and its low-cost [2].

Experimental Procedure:

All catalysts were prepared by co-precipitation methods adapted from literature and had a transition-metal to metal-oxide ratio of 0.6 [2]. Active component metal precursor solutions included: either 30 mL of a 0.86 M transition-metal ($Ni(NO_3)_2 \cdot 6H_2O$, $Co(NO_3)_2 \cdot 6H_2O$, $FeCl_2 \cdot 4H_2O$) or 53 mL of a 0.49 M $Cu(NO_3)_2 \cdot 3H_2O$ solution in 100% ethanol. Mesoporous variants were synthesized to control porosity using various surfactants. In each case, mesoporous variants were generated by adding hexadecyltrimethylammonium bromide (CTAB) prior to the addition of metal-oxide precursor. Figure 2 illustrates the chemistry that occurred in the synthesis of the catalysts. Figure 3 outlines the synthesis of the catalysts.

Silica-Supported Catalyst. An initial solution of tetraethyl orthosilicate and ethanol was added to 1.5 mL of 0.3 M hydrochloric acid (HCl). The solution was stirred at 50°C for 90 minutes. At 25°C, the appropriate active component metal precursor solution was added to the reaction mixture. A firm gel formed upon the slow addition of 35 mL 30% aqueous ammonium hydroxide in 65 mL ethanol.

Alumina-Supported Catalyst. A solution of 10.0 g hexylene glycol in the appropriate active component metal precursor solution was stirred at 95°C for 30 minutes. Aluminum isopropoxide (8.6 g) was then introduced to the solution and stirred at 120°C for four hours. At 95°C, a saturated solution of sodium hydroxide in ethanol (~ 0.5 mL) was added every 30 minutes for a span of 90 minutes. At 25°C, the pH of the solution was adjusted to 9.0 with sodium hydroxide.

Titania-Supported Catalyst: A solution containing 12.2 g titanium isopropoxide, 22 mL ethanol, and the appropriate active component metal precursor solution was mixed under inert (argon) atmosphere. A second solution consisting of 3 mL of 1.8 M nitric acid in 3 mL 100% ethanol was slowly added to the first solution, resulting in the formation of a firm gel.

For all catalysts, the gelled suspension solution was stirred at 25°C for 30 min, sonicated for 1 h, and aged at 25°C for 85 h.

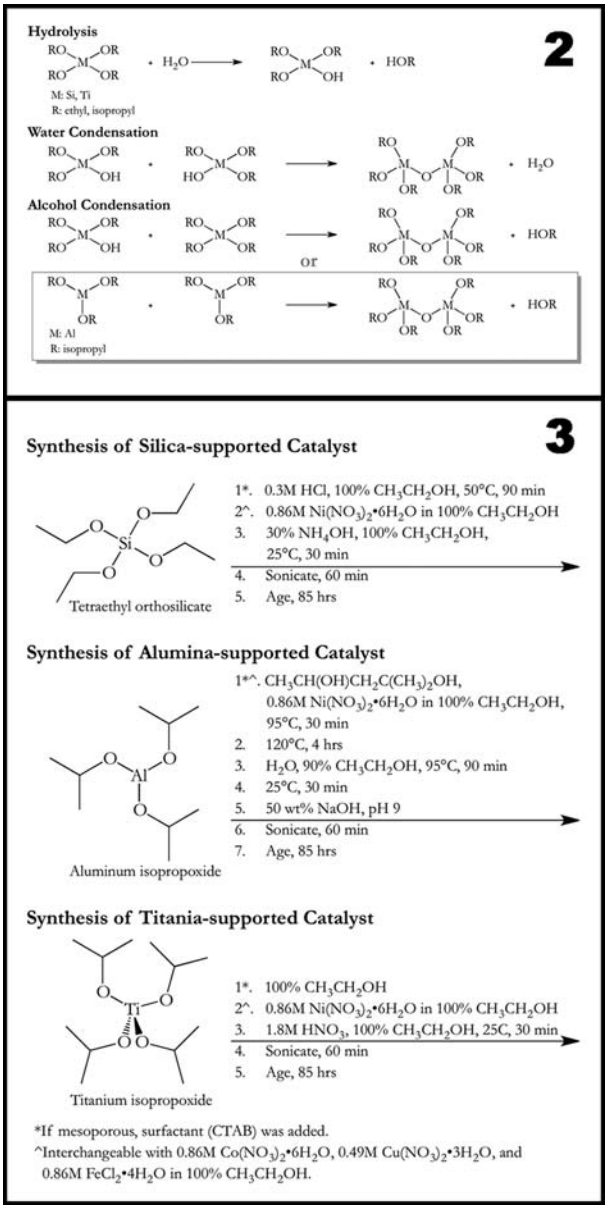

Figure 2, top: Three primary reactions in silica, titania, and alumina gel formation.

Figure 3, bottom: Adapted synthesis protocol for metal supported catalysts.

Purification of Catalysts. Catalysts were washed with deionized water, collected by centrifugation, and underwent Soxhlet extraction with deionized water overnight and then with ethanol overnight or 48 hours for mesoporous variants. Catalysts were dried overnight at 105°C under vacuum and calcincated under flowing inert N atmosphere at 550°C for 5 h.

Conclusions and Future Work:

Metal supported catalysts were successfully synthesized after modifications to the synthesis and purification protocols. Sol-gel condensation reactions in alumina-supported catalysts were optimized at 25°C at a pH of 9.0. To prevent premature gelling and the formation of heterogeneous products, titania-supported catalysts required lower reaction concentrations. Furthermore, the incorporation of the transition-metals in the titania-supported catalysts appeared to be low due to their appearance. Ultimately, future work with titania will use an alternative procedure.

To minimize contamination by unincorporated metal precursors, multiple washes with deionized water followed by sonication, centrifugation, and Soxhlet extraction were determined to be optimal. In addition, calcination can cause significant oxidation and charring, and therefore must be performed under flowing inert nitrogen atmosphere rather than in air.

Future work includes characterizing the chemical and physical properties of the catalysts by several methods (Table 1). To determine the effect catalyst structure has on the activity and selectivity for arylether hydrogenolysis, catalysts will be screened against model compounds and lignin. Various preparation methods will be explored to investigate the effect preparation method has on catalyst structure. Ultimately, the goal is to determine the optimal transition-metal and metal-oxide support combination foraryl ether hydrogenolysis.

Acknowledgments:

My sincerest gratitude to Dr. Marcus Foston, Yu Gao, and Jake Meyer for their guidance and support. I would also like to thank Dee Stewart and Nathan Reed from the NRF, the NNIN REU Program, and the NSF. My grateful thanks are extended to Mindy Prado, Siqin He, Michelle Liberton, and Dr. Wei-ning Wang.

References:

[1] Pandey, M. P., et al.; Chem Eng Technol, 34(1), 29-41 (2011).

[2] Goncalves, G., et al.; Journal of Non-Crystalline Solids, 352(32), 3697-3704 (2006).

Method or Instrument	Purpose
Brunauer-Emmett-Teller (BET) method	Specific surface area
Barrett-Joyner-Halenda (BJH) method	Pore diameter
Fourier transform infrared spectroscopy (FTIR)	Carbon contamination
Inductively coupled plasma mass spectrometry (ICP-MS)	Metal composition
Hammett acidity function	Acidity of catalyst
Esterification	Acidity of catalyst
Transmission electron microscopy (TEM)	Particle size and shape

Table 1: Characterization methods for determining the chemical and physical properties of the catalysts.

Fabrication of Smart Gels with Tunable Stiffness

Carolyn Zhang
Biochemistry and Cell Biology, University of California San Diego

NNIN REU Site: Center for Nanoscale Systems, Harvard University, Cambridge, MA
NNIN REU Principal Investigator: Professor David A. Weitz, Harvard School of Engineering and Applied Sciences, Harvard University
NNIN REU Mentors: Dr. Adrian Pegoraro, Tom Kodger, amd Ming Guo, Harvard School of Engr. and Applied Sciences, Harvard University
Contact: cmzhang@ucsd.edu, weitz@seas.harvard.edu, apegoraro@seas.harvard.edu, tkodger@fas.harvard.edu, mingguo@fas.harvard.edu

Abstract:

The differentiation of stem cells was influenced by many factors, one of which was the stiffness of the cellular microenvironment: soft substrates led to neuronal cells, intermediate stiffness substrates led to myogenic cells, and very rigid scaffolds lead to osteogenic cells [1]. To further understand the kinetics of stem cell differentiation, we designed degradable polyacrylamide hydrogels, which allowed us to change substrate stiffness during differentiation, and observe the effect of this change on the lineage specification of stem cells. With this purpose in mind, 8 wt% polyacrylamide gels composed of permanent *N*,*N*′-methylenebisacrylamide (BIS) and degradable *N*,*N*′-bis-(acryloyl)cystamine (BAC) cross-linkers were constructed. The shear modulus of these gels can be changed from ~ 10 kPa to ~ 400 Pa. Under normal conditions, these gels would lead to osteogenic and neuronal differentiation, respectively. This hydrogel was found to be degraded in a time span that maintained continuous cell proliferation with the biocompatible chemical tris(2-carboxyethyl)phosphine hydrochloride (TCEP) in Dulbecco's modified eagle's medium (DMEM). Since stem cells are known to commit to their final cell type within a week, using these gels will allow us to test whether the time point at which the scaffold is degraded effects the final lineage specification of the cells.

Experimental Procedure:

For our experiments, we made polyacrylamide gels and varied the amount of degradable and permanent crosslinkers. We used an 8 wt% polyacrylamide, 0.46 wt% BAC, 0.03 wt% Bis solution; this ratio was chosen to mimic a stiff, Bis only, gel (8 wt% acrylamide, 0.3 wt% Bis) predegradation and a soft gel (8 wt% acrylamide, 0.03 wt% Bis) after being degraded. By laying a 12 mm diameter coverslip on the solution and polymerizing the gel at 65°C, we fabricated degradable gels that were about 100 μm thick. The gels were then treated with a Sulfo-SANPAH solution followed by a 0.1 mg/ml collagen solution. The addition of collagen to the surface allowed the cells to adhere to the gel.

For initial tests of the degradable gels, HF fibroblasts of the BJ line are cultured on the gels and after about five hours, imaged as the gels degraded in a 10 mM TCEP (pH 7) solution over a period of ten hours. The Young's modulus of the degradable gel was measured on a Squisher device, or modified atomic force microscope (AFM), while the shear modulus was measured on a rheometer.

Results and Conclusions:

We tested several compounds to degrade the gel for both biocompatibility and effective degradation. We defined a compound as being biocompatible if cells continued to proliferate after exposure. To measure degradation, we simply allowed the gel to swell and degrade, and measured the time it took to complete the process. A 10 mM TCEP at a pH of 7 that was diluted in DMEM was determined to be the reducing agent that was biocompatible and able to degrade the gel on a desirable timescale.

Tested Chemicals for Degradation	Degrades gel	Biocompatible: in media	in DMEM
Dithiothreitol = DTT	✓	✗	
Glutathione = GSH	✗	✓	
GSH in HEPES buffer	✗	✗	
L-Cystine	✗	✗	
Hydrazine	✓	✗	
L–Ascorbic acid (Vitamin C)	✓	✗	
2-Phospho-L-ascorbic acid	✗	✗	
Bisulfite	✗	✗	
Tris(2-carboxyethyl) phosphine hydrochloride = TCEP (ph 7)	✓	✗	✓
Tris(2-carboxyethyl) phosphine hydrochloride = TCEP (ph 3)	✓	✗	✗

Figure 1: The chemicals that were tested to degrade the hydrogels composed of 8% polyacrylamide, 0.46% BAC, 0.03% Bis solution.

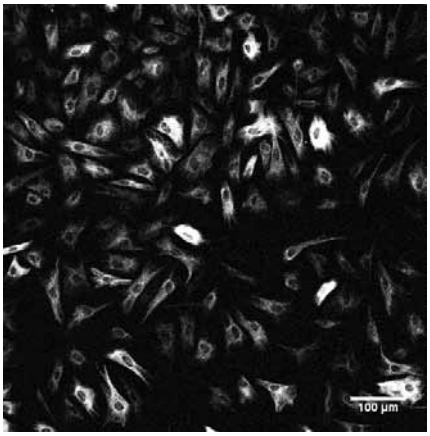

Figure 2: Fibroblasts cultured on the degradable gel before the degradation process.

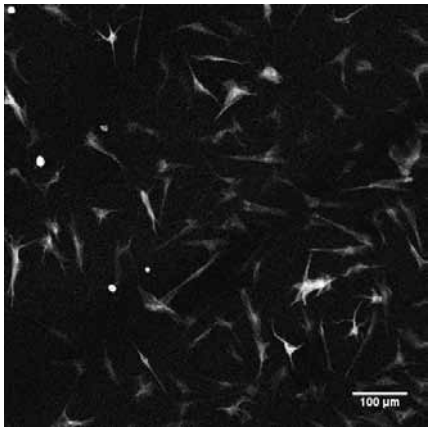

Figure 3: Fibroblasts after a 12 hour 10 mM TCEP treatment to degrade the gel.

Using a rheometer, we measured the change in the gel stiffness during polymerization as the temperature increased to 65°C. Our degradable gels had a shear modulus of the same order as a 0.3% Bis gel (stiff gel) and a degraded gel was estimated to have a shear modulus similar to a 0.03% Bis gel (soft gel) and should favor osteogenic and neurogenic differentiation, respectively.

To confirm these measurements, we used a "Squisher" device. By compressing an indenter into the gel by a known distance, we were able to measure the Young's modulus of the gel and determined that 100 mM and 10 mM TCEP conditions had the same degradation rate during a 12.5 hour degradation process. The kinetics of the degradation process for the degradable gel between 100 mM and 10 mM TCEP remained the same despite changes in the pH of the TCEP conditions.

To measure the effect of degradation on cells, we observed the effect of an ~ ten-fold decrease in the stiffness of our degradable gel on fibroblasts and found that the cell area decreased after the gel is degraded. A morphology change between cells that were cultured on our degradable gel before the degradation process and those cultured on our gels after the degradation process was also noted. Those cultured on the initially stiff gels were spread out and after the TCEP treatment; they remained spread out, while cells cultured on pre-degraded, soft gels had a rounder morphology.

In conclusion, 8% polyacrylamide 0.46% BAC 0.03% Bis gels can be made to have a ten-fold decrease in shear modulus after degradation. A 10 mM TCEP in DMEM was determined to be a biocompatible reducing agent that is able to degrade the gels on a desired timescale. Preliminary results showed that TCEP was biocompatible with and didn't interfere with the differentiation of stem cells, however, further experiments are required to indicate statistical significance.

Future Work:

With applications in tissue engineering, future works for this project include culturing Mesenchymal stem cells on degradable gels to study the differentiation on different stiffness scaffolds as well as finding a biocompatible chemical that reversibly degrades the gels.

Acknowledgements:

I would like to thank my mentors Dr. Adrian Pegararo, Tom Kodger, Ming Guo, my principal investigator Professor David A. Weitz, and my site coordinator Dr. Katherine Hollar for their assistance. I would also like to thank the National Science Foundation and the National Nanotechnology Infrastructure Network Research Experience for Undergraduates Program for providing funding for my research.

References:

[1] Discher, D.E., Janmey, P., and Wang, Y.L. Tissue cells feel and respond to the stiffness of their substrate. Science. 310(5751):1139-43;2005.

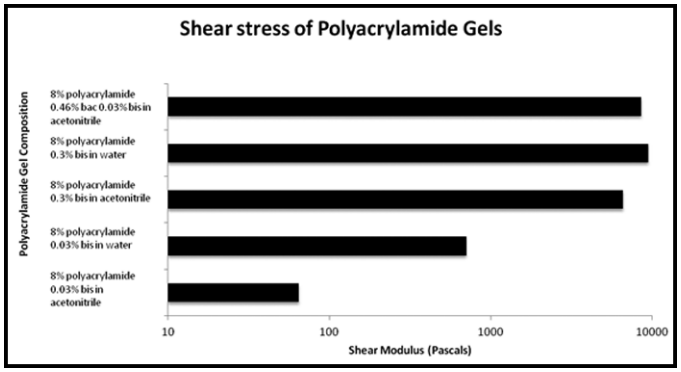

Figure 4: Comparison of the shear modulus of polyacrylamide gels of different cross-linker compositions with the degradable gel being the 8% polyacrylamide 0.46% BAC 0.03% Bis gel.

Design of a Microfluidic Device to Measure the Deformability of Cancer Cells

Gabriel R. López Marcial
Mechanical Engineering, University of Puerto Rico at Mayaguez

NNIN REU Site: Cornell NanoScale Science and Technology Facility, Cornell University, Ithaca, NY
NNIN REU Principal Investigator: Jan Lammerding, Biomedical Engineering, Cornell University
NNIN REU Mentor: Patricia Davidson, Weill Institute for Biomolecular Engineering, Cornell University
Contact: gabriel.lopez3@upr.edu, jan.lammerding@cornell.edu, patricia.davidson@cornell.edu

Abstract and Background:

Metastasis is defined as a "tumor growth or deposit that has spread via lymph or blood to a body area remote from the primary tumor in a cancer patient" [1]. To spread in this manner, cancer cells must deform and pass through dense tissues or blood vessels with constrictions as small as a few microns. Understanding how these metastatic cells deform may give researchers valuable information to diagnose or treat cancerous patients.

The project goal was to create a polydimethylsiloxane (PDMS) microfluidic device that enables the perfusion of cancer cells through narrow constrictions while imaging the cells on a microscope. The well-defined constrictions would force the cell to deform its usually stiff and large nucleus and permit its mechanical characterization. We expect metastatic cells to be more deformable and to transit through the constrictions faster than non-metastatic cells.

The device design was generated using AutoCAD software and transferred to a wafer by photolithography with spin-coated SU-8 photoresist. The wafer was then used as a mold for the final PDMS channels. The cells entered the device through an inlet and were perfused through multiple 5 × 10 μm constrictions. The efficiency of the device is currently being evaluated using images acquired by high-speed video microscopy.

Microfluidic devices for studying nuclear mechanics are not new. However, previous perfusion devices presented problems that greatly impeded their success. In these predecessors, clustering of cells, accumulation of debris and other large particles frequently clogged the main channels of the microfluidic device containing the constrictions.

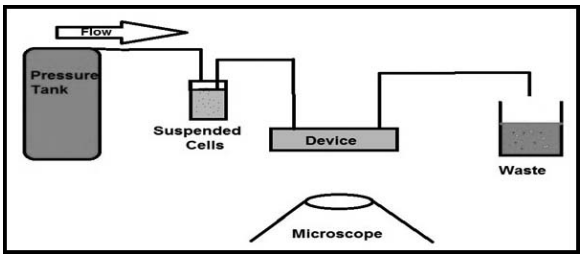

Figure 1: Schematic of perfusion experiments. A gas cylinder pressurizes the air in a tube with the cell suspension, pushing cells through the device at a constant pressure. The device is imaged using a microscope equipped with a high speed camera.

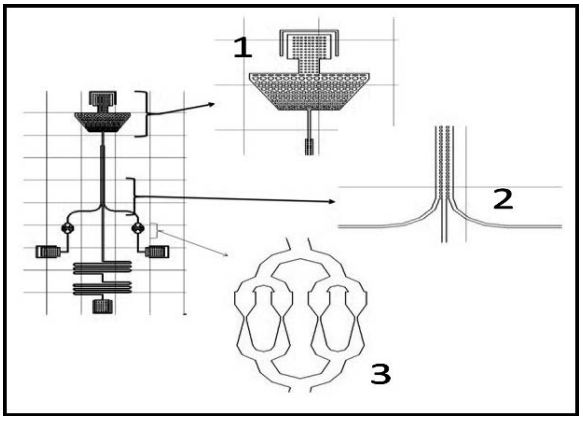

Figure 2: Innovations to the perfusion device design. Seventeen different devices were created with variations in cross-flow filter length, size of constrictions or shape of pillars in cross-flow channel.

Methods:

Devices were designed using AutoCAD software. These patterns were then transferred to a silicon wafer spin coated with SU-8 photoresist using photolithography. The PDMS was poured over the wafer, cured, peeled off, and bound to a glass slide to create the actual experimental device [2]. Perfusion experiments were performed to test the functionality of the devices. Cells in suspension were pushed through the device by a constant pressure of 10 psi. A schematic of the perfusion experiment is shown in Figure 1.

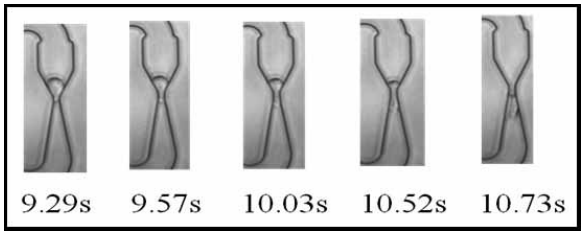

Figure 3: Cell passing through a single constriction in the perfusion device. Below each frame is the time stamp from the video, in seconds. As seen in this example, most cells pass through the 5 x 10 µm constrictions very quickly, making the high speed imaging a necessity for data analysis.

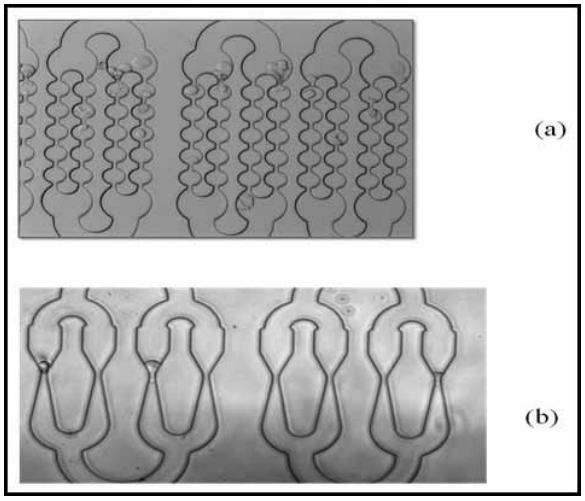

Figure 4: Device comparison. (a) The previous perfusion device, where larger particles and accumulation of cells block the main channels. (b) The new device, which only shows clogging in the far left channel, but is otherwise better suited for perfusion experiments.

Results:

Our new device design (Figure 2) features; (1) an improved coarse filter to hold back debris and larger cells, (2) a cross-flow filter [3] whose purpose is to sort the cells and keep them in a single file to prevent clustering of multiple cells, and (3) redesigned funnel shaped constrictions, through which the cells must deform. A wafer with 17 different variations of this new device was made. The devices varied in small details such as length and width of the cross-flow filter, round or square pillars, and the type of constrictions (single funnel, multiple funnels, or bubbles).

Using the same experimental setup as in previous experiments, we observed significantly reduced clogging of the revised microfluidic device. While devices based on the previous design typically became clogged within a minute or two of the start of the experiment, the new devices performed for periods of 30 to 60 minutes without the constriction channels becoming blocked, allowing for more time to collect experimental data.

After perfusion experiments, an average of 53% of cells were routed into the side constriction channels. Out of these channels, less than 20% of the channels became clogged at any given time. This is a significant improvement over previous designs that exhibited clogging in more than 50% of the channels. Based on preliminary observations, the different variations in length or shape of cross-flow filter had no discernible effect on cell sorting or prevention of blocked channels.

Conclusions:

The new device exhibits reduced clogging and more sustained throughput during the perfusion experiments. Future work will analyze the deformation of the cell nucleus when passing through the constrictions of these perfusion devices in metastatic and non-metastatic cancer cells.

Acknowledgements:

I thank the Cornell NanoScale Facility at Cornell University for giving me the opportunity to be an REU intern this summer, and Jan Lammerding for the great dynamic in his laboratory. I would also like to thank everyone in the Lammerding Lab, especially Patricia Davidson and Celine Denais, for always being there to teach me and help me. Thanks also go out to the National Nanotechnology Infrastructure Network Research Experience for Undergraduates (NNIN REU) Program, the National Science Foundation, and the Department of Defense Breast Cancer Idea Award [BC102152] for providing funds for our work, as well as to Melanie-Claire Mallison and Rob Ilic, the program coordinators at CNF. Everyone played a huge role in my work and is uniquely appreciated.

References:

[1] Dorland, William. 2007. Dorland's Medical Dictionary for Health Consumers. Saunders, an imprint of Elsiever, Inc.

[2] Isermann, P., Davidson, P.M., Sliz, J.D., and Lammerding, J. Assays to measure nuclear mechanics in interphase cells. Curr Protoc Cell Biol. 2012 Sep; Chapter 22: Unit22.16. 2012.

[3] Ji, H., Samper, V., Chen, Y., Heng, C., Lim, T., and Yobas, L. Silicon based microfilters for cell separation. Biomed devices, Springer, 2007.

Designing Directional Micro-Machined Microphones

Alexandro Rocha, Jr.
Applied Science in Nanotechnology, Northwest Vista College in San Antonio, Texas

NNIN REU Site: Microelectronics Research Center, The University of Texas, Austin, TX
NNIN REU Principal Investigator: Dr. Neal A. Hall, Electrical and Computer Engineering, University of Texas at Austin
NNIN REU Mentor: Michael Kuntzman, Electrical Engineering, University of Texas at Austin
Contact: ajrocha2009@gmail.com, nahall@mail.utexas.edu, mlkuntzman@gmail.com

Abstract:

The newest smart phone designs, using noise rejection algorithms, rely strongly on high signal-to-noise ratio (SNR) audio capture. Techniques currently used, involve measuring the difference signal between two "standard" omnidirectional microphones physically separated in space. However, the ability to resolve small difference signals is limited by poor matching or high noise microphones. We designed a pivoting micro-machined microphones that measure spatial pressure differences directly, therefore two microphones are no longer required, reducing cost, power consumption, size, and eliminating microphone matching issues. We found that the rocking structure of the device, anchored by pivots, naturally senses pressure gradients, making it potentially more sensitive than the standard two-omnidirectional-microphone techniques being used. When designing and simulating devices using AutoCAD and ANSYS, we obtained a figure of merit of the first modal resonance showing optimization near the center of the audio band, between (1-3 kHz) to ensure the highest sensitivity and good directivity over the desired range of operation. We discovered that designs that are more flexible will move more in response to an excitation force and have a higher voltage output per input acoustic pressure. During the designing process, we saw that devices with a thinner epitaxial layer and/or thinner and longer pivots produce better figures of merit allowing for lower minimal detectable signal.

Introduction:

The purpose of this project was to design a new directional micro-machined microphone based on a previous design that would provide a lower minimal detectable signal (MDS). The MDS is one of the most important measures of fidelity of a microphone. It is the lowest possible signal that a device can read at the noise floor of the sensor and low MDS is critical for good audio quality and modern noise cancellation features. Figure 1 shows the original design of the in-plane directional microphone with a micrograph inset on the anchored pivot region [1]. It shows the spring component on the outside edge of the device. This was removed in the new device to enhance flexibility.

Experimental Procedure:

We first looked at Hooke's law, $F = kx$, where "k" is the stiffness coefficient. From this formula, we determined that designs that are less stiff will move more in response to a given excitation force and will produce higher voltage output per Pascal of acoustic pressure, and therefore will be more sensitive. We want this in order to produce a low MDS. We used Microsoft Excel to calculate the MDS along with two other figures of merit: 1st modal resonance frequency and capacitance. The 1st modal resonance is proportional to the square root of k so devices with lower 1st modal resonance will have lower stiffness and higher sensitivity. With all other factors being equal, higher capacitances will relax the design requirements on the readout electronics. We tested independent variables that consisted of the thickness of the epitaxial layer between (4-200 μm), and the length between (50-600 μm) and width between (25-200 μm) of the beam pivots. Figure 2 shows a graph comparing the MDS and the pivot width, which shows to be proportional to each other; therefore we are able to conclude that devices with thinner pivots will produce a smaller MDS.

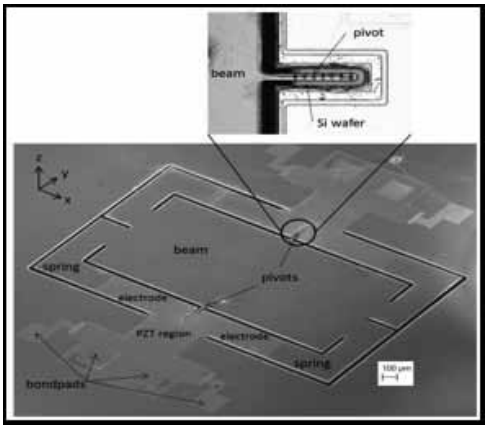

Figure 1: SEM of Generation 1 in-plane microphone with a micrograph inset on the anchored pivot region.

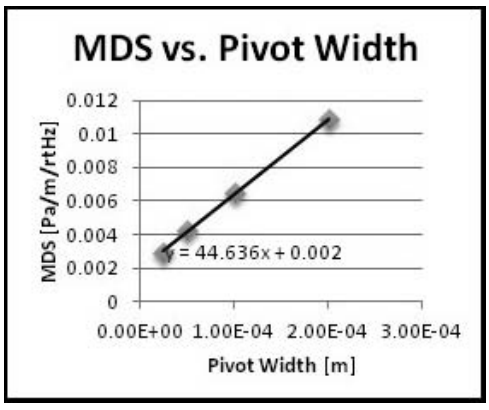

Figure 2: Minimal detectable signal is proportional to pivot width.

We used ANSYS simulation software to find the dependent variables consisting of the 1st and 2nd modal resonance frequencies. Figure 3 shows the ANSYS simulation of the 1st modal resonance frequency of Device A.

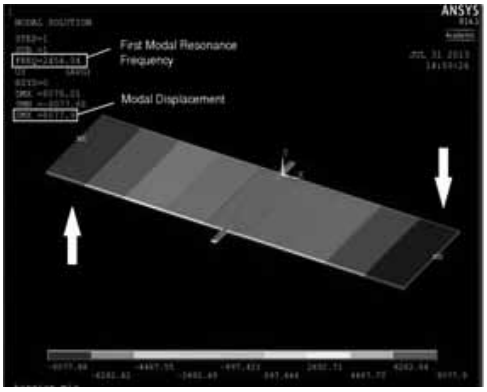

Figure 3: First mode of directional microphone excites from opposite forces pushing from opposite directions.

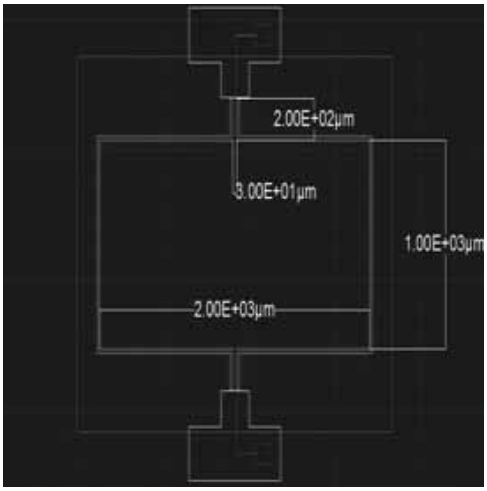

Figure 4: AutoCAD layout of Design B.

Results and Conclusions:

The final steps in the designing process were to decide on four devices that could be fabricated with high quality. We then used AutoCAD, which is a drafting software used to create mask files for fabrication. We decided on using a standard epitaxial layer thickness of 10 μm with all four designs, however alterations were made in the following designs:

Design A; a 50 μm pivot width and a 200 μm pivot length.

Design B; a 30 μm pivot width and a 200 μm pivot length.

Design C; a 25 μm pivot width and a 100 μm pivot length.

Design D; a 50 μm pivot width and a 300 μm pivot length.

We designed the masks in five layers: Top electrodes, bottom electrodes, backside etching, device layer, and lead zirconate titanate (PZT) layer, which is the piezoelectric material being used in the device. Figure 4 shows the AutoCAD mask layout of Design B with all five layers included. The final masks were successfully designed and are awaiting delivery for fabrication.

Future Work:

There is still much to accomplish in order to complete the project with fabrication and characterization of the final devices being the main finishing points. Given the high sensitivity of our mechanical structure combined with the low dielectric loss of our piezoelectric material, the device can result in much more efficient MDS than the current state of the art microphone with regard to pressure gradient measurements. The designs could have an immediate impact on the noise rejection capabilities of next generation smart phones.

Acknowledgements:

I would like to give my sincere gratitude to the National Nanotechnology Infrastructure Network Research Experience for Undergraduates (NNIN REU) Program and National Science Foundation for the opportunity to gain experience in the nanotechnology research field. Also, thank you to my principal investigator Dr. Neal Hall, mentor Michael Kuntzman, site coordinator Dr. Marylene Palard, the University of Texas at Austin, and all of the faculty and staff that provided an extravagant working environment for the ten week program. Finally, I thank Dr. Qiaoying Zhou from Northwest Vista College for always encouraging me to pursue my goals.

References:

[1] M.L. Kuntzman, J. Glorial Lee, N.N. Hewa-Kasakarage, D. Kim, N.A. Hall, Micro-machined piezoelectric microphones with in-plane directivity, Applied Physics Letters (2013) 054109.

Studying the Interfacial Dynamics of Miscible Systems with Microfluidics

John Schwalbe
Chemical and Biomolecular Engineering, Cornell University

NNIN REU Site: NanoTech User Facility, University of Washington, Seattle, WA
NNIN REU Principal Investigator: Dr. Amy Q. Shen, Mechanical Engineering, University of Washington
NNIN REU Mentor: Shilpa Beesabathuni, Mechanical Engineering, University of Washington
Contact: jas699@cornell.edu, amyshen@uw.edu, shilpanb@uw.edu

Abstract:

Various microfluidic features are considered for the study of the interfacial dynamics of miscible systems. We take advantage of upper critical solubility temperature (UCST) behavior of a given miscible system. Fully realizing the potential of our experimental plan will require integrating multiple features in one microdevice. The challenges that arise include varying length scales between features, temperature control, and complex control systems.

Introduction:

We are interested in the dynamics of interfaces between two miscible phases. While interfaces between equilibrated phases are thermodynamically stable, interfaces between miscible phases are inherently transient. These interfaces exhibit interesting mass transfer properties and effective interfacial tension [1]. Understanding these dynamics is important to modeling various industrial and biological processes. Enhanced oil extraction and mucus spreading in the lungs are two examples. Droplet microfluidics is an ideal platform to study interfaces because the small length scales allow for very controlled velocity profiles.

The devices were fabricated using soft lithography [2], so they could be prototyped quickly.

To observe the dynamics of miscible interfaces, it was important that we have a known initial condition. To do this, we took advantage of the temperature dependence of solubility. Below a critical temperature, the UCST, two immiscible phases form. Above it, the two components are miscible in all proportions. To exploit this experimentally, droplets were formed below the UCST, denoted as phases I and II in Figure 1. Next, a single droplet was trapped above a heater. The droplet was then heated above the UCST, shown with dot-dash lines in Figure 1. Finally, thermodynamics took over and the droplet began to dissolve, shown with dashed lines in Figure 1. Isobutyric acid (IBA) and water have a reasonable UCST, for example. But, there are other interesting systems that could be explored with this technique including ionic liquids and thermoresponsive polymers. Implementing this plan was difficult. Droplet formation, trapping, and heating on a single chip were all challenging.

Experimental Procedure:

We considered a variety of device features. For droplet formation, we used T-junctions and flow-focusers [3]. In a T-junction, a channel carrying the dispersed phase entered a channel carrying the continuous phase at 90°. Depending on the relative sizes of the channels and the flow rates, T-junctions

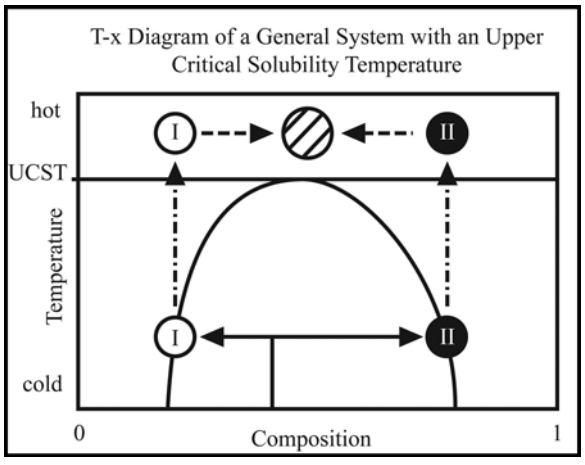

Figure 1: Process schematic.

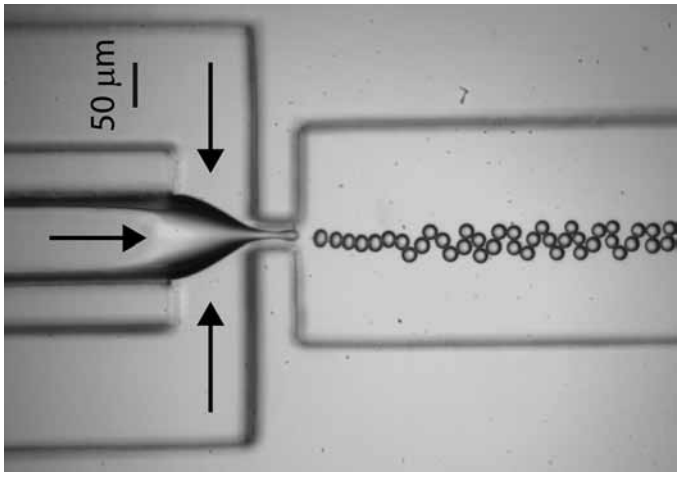

Figure 2: A flow focuser producing droplets of water in oil.

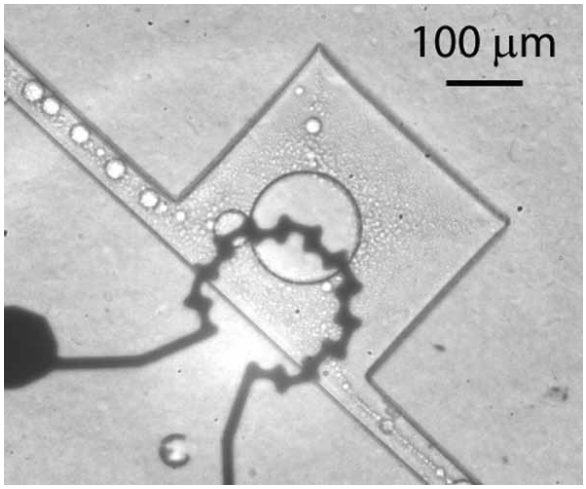

Figure 3: An IBA/water emulsion in a vortex trap.

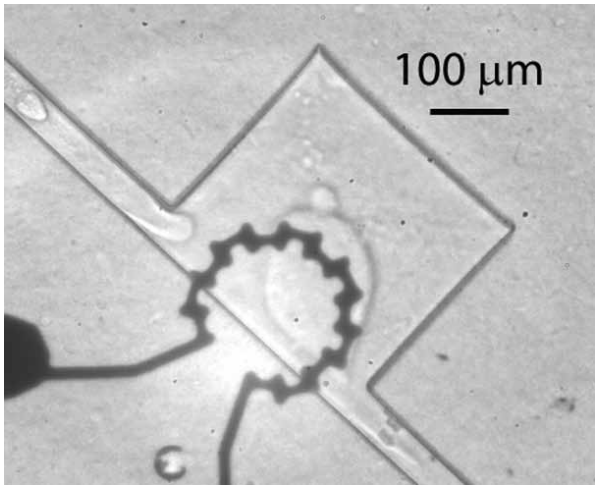

Figure 4: An IBA/water mixture shortly after it was heated above the UCST.

could generate droplets of varying sizes in either a dripping or a jetting mode. In a flow-focuser, the dispersed phase was introduced into the middle of the carrier phase. The resulting two-phase flow was then forced through a constriction. The resulting viscous and capillary forces caused the dispersed phase to break into droplets, as seen in Figure 2 [3].

Trapping the droplet was the next challenge. Cross-slot chambers were a powerful option. They consisted of two channels crossing at 90°. In use, the channels acted as two inlets and two outlets. This created a stagnation point in the middle of the chamber where a droplet could be trapped. When used in conjunction with a feedback control system, droplets could be trapped indefinitely [4]. Another attractive feature was that the droplet deformed in the velocity field, and the effective surface tension could be deduced from the shape of the droplet [5].

A hydrodynamically simpler option was a vortex trap. An emulsion in a vortex trap can be seen in Figure 3. At high enough flow rates, a vortex will form in the expansion. Vortex traps have been used to trap cells [6]. But, it is an open question whether or not they can also be used to trap droplets.

Finally, temperature control was vital to this experiment. Traditional thermal stages cannot ramp the temperature fast enough. We chose resistance heaters made with a lift-off procedure instead. The geometry of the heater could be tweaked to get the desired performance. But, electrolytic gas production was observed in some designs above a threshold voltage. So, it is a constrained optimization problem.

Results and Discussion:

A fully integrated device remains elusive. The most successful feature was the heater. Figure 4 shows the result of heating an emulsion above the UCST of the system, in this case IBA and water. The blurring of the interface clearly shows the dissolution process and the shape of the droplet reflects the effective interfacial tension. However, the variations along the circumference of the droplet show the need for a more homogenous temperature increase. This image also highlights the need for an integrated device. The small droplets surrounding the central droplet are undesirable. They are there because an emulsion was pumped into the trap rather than the uniform droplets that a flow-focuser or T-junction would create.

But, as Figure 3 shows, the vortex traps have potential. Their simplicity is an inherent advantage. They require no complicated feedback control. However, viscous droplets cannot cross streamlines in the sense that particles can. So far vortex traps have worked with emulsions, but this may pose a problem with the orderly, monodisperse droplets produced by a T-Junction or a flow-focuser.

Acknowledgements:

I would like to thank Professor Boris Stoeber and Vahid Bazargan from the University of British Columbia for the fabrication of certain devices. I would also like to thank the UW MFF staff for their invaluable assistance and training. I would like to thank the entire Shen lab for helping me at every opportunity, and the National Nanotechnology Infrastructure Network Research Experience for Undergraduates (NNIN REU) Program for funding.

References:

[1] Lacaze, Laurent, et al. Physical Review E 82, 041606, 1-8. 2010.

[2] Xia, Y., and Whitesides, G. Annu. Rev. Mater. Sci. 28:153-84. 1998.

[3] Christopher, G, and Anna, S. J., Phys. D: Appl. Phys. 40, R319-R336 (2007).

[4] Melikhan Tanyeri, et al., Lab Chip, 11, 1786-1794, 2011.

[5] Cabral, Joao, and Hudson, Steven. Lab Chip, 6, 427-436, 2006.

[6] Soojung Claire Hur, et al., Biomicrofluidics 5, 022206 1-10. (2011).

Full-Body Silicon Medical Tweezers for Cancerous Tissue Detection and Characterization

Connie Wu
Electrical Engineering and Finance, University of Pennsylvania

NNIN REU Site: Cornell NanoScale Science and Technology Facility, Cornell University, Ithaca, NY
NNIN REU Principal Investigator: Prof. Amit Lal, Electrical and Computer Engineering, Cornell University
NNIN REU Mentor: Po-Cheng Chen, Electrical and Computer Engineering, Cornell University
Contact: wuconnie@seas.upenn.edu, amit.lal@cornell.edu, pc445@cornell.edu

Abstract:

We designed and created the first prototype of a full-body silicon surgical tool for detecting and characterizing cancerous tissue. From literature, it had been shown that tissue elasticity and electrical permittivity have been promising non-optical markers for identifying cancerous tissue [1]. Because of the advantages of micro-fabrication technology, a full body silicon device in a tweezer structure was designed and employed with numerous sensors. Strain gauges were used for tissue elasticity by monitoring the insertion force, and the platinum wires were designed for tissue permittivity measurements. Additionally, the platinum electrodes have the capability of electrical physiology signal measurements. Strain gauge resistivity measurements were performed to verify the performance of the tweezers and feasibility for future medical applications.

Introduction:

If a surgeon were to staple bad tissue into the affected site during a colon anastomosis, there is a high chance of intestinal leakage and subsequent high risk for the patient. Our goal is to design a medical tool that can help surgeons distinguish abnormal tissue from normal tissue. The full body silicon tweezer with several different sensors on it can provide assistance for the doctor during operation. The tweezer structure is easily accessible to surgeons, and since the body is constructed from a continuous piece of silicon, it allows for flexibility in integrating sensors and CMOS circuitry for more function, such as wireless transmission of measured signal.

Experimental Procedure and Process:

The device structure was designed using L-Edit and Matlab code that can automatically generate Caltech Intermediate Format (CIF) files with parameter alteration capability. The structural parameters included the hinge radius, hinge thickness, leg length, leg thickness, hinge beginning angle, hinge ending angle, and inter-probe distance.

The first prototype design had a hinge radius of 8000 μm, leg length of 4 cm, thickness at the hinge of 400 μm, and leg thickness of 1000 μm. The tweezers were laser cut for structural testing, during which it was verified the tweezers inter-probe distance could deform at least 5000 μm.

In a COMSOL simulation, it was found that the point of maximum stress at 80.7 MPa was at the apex of the hinge, while the normal stress fracture of silicon was around 1-3 GPa. Four probes were placed on each leg of the tweezers and finger holders were placed along the mid-section of the legs. Each probe had a Wheatstone bridge strain gauge at the cantilever junction. In the eight probes, the strain gauges resistors were realized with LPCVD polysilicon implanted with boron at a dose of 2×10^{15} ions/cm^2 at 100 keV. The sheet resistance of polysilicon was ~ 185 ohms/$\square$. The resistors were electrically contacted with aluminum alloy (Al + 1% silicon) metal lines. Insulating PECVD nitride was deposited, followed by platinum evaporation to define electrical recording sites and permittivity sensors. The device layers are depicted in Figure 1.

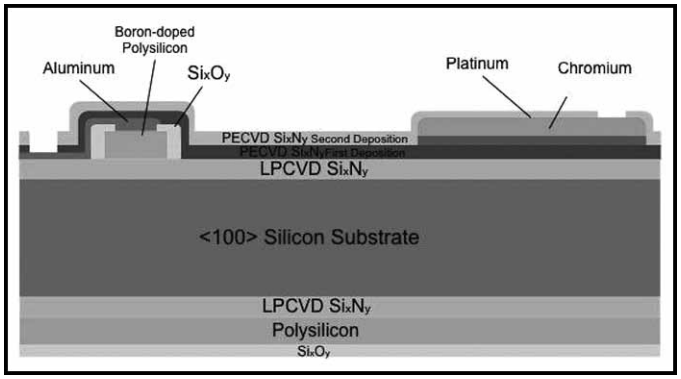

Figure 1: Fabrication layers of the tweezers.

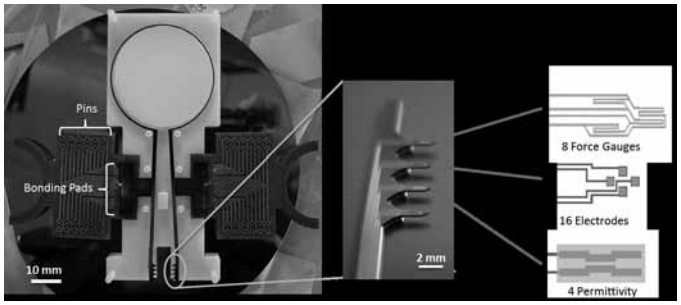

Figure 2: Assembled tweezer device with holder.

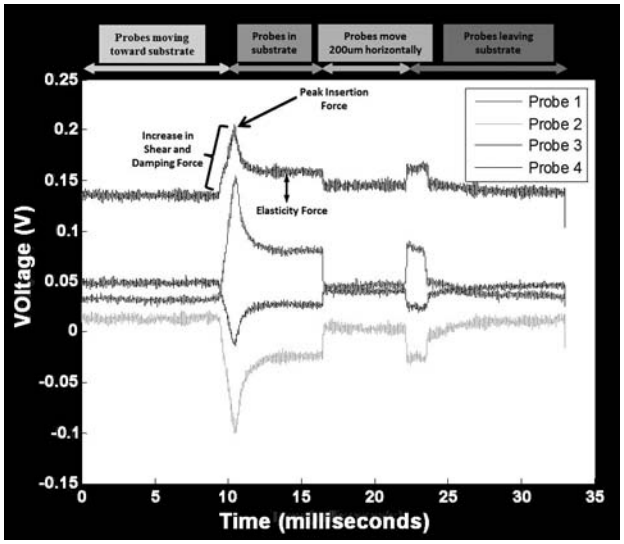

Figure 3: Probe force gauge output at 3000 µm/s insertion speed with horizontal movement of 200 µm.

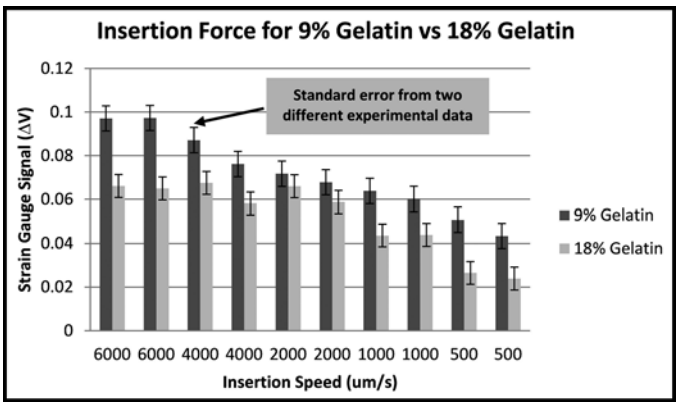

Figure 4: Probe signal from gelatin concentration change.

All of the sensors were connected to the 56 bonding pads located in the finger holders (Figure 2). These bonding pads were wired to a PCB board with pins for testing. The strain gauge pins were connected to a differential amplifier with a gain of 200 that transmitted probe voltage signals to LabView.

Results and Conclusions:

The full body silicon medical tweezers included eight strain gauges, four sets of platinum wires and sixteen platinum electrodes (Figure 2). To test the spring constant of the tweezers, one leg of the tweezers was fixed while the other was displaced horizontally. COMSOL estimated that the spring constant would be around 2 N/m while the empirical result yielded a spring constant was 9 N/m. To test the strain gauge signals, four probes were positioned 8608 μm vertically above 6% gelatin mixture and preset to a 6000 μm/s insertion speed for the control experiment. To get the insertion force signal, we calculated the difference between the signal levels from before the probe is inserted into the gelatin and after it penetrates the sample surface (Figure 3).

Four parameters were altered: insertion speed, insertion height, insertion direction, and gelatin concentration. The results from the experiments indicated that insertion force increased with insertion speed by ~ 15% for every 1000 μm/s increase in speed. Insertion height was found to be negligible when insertion speed was controlled. Whereas the insertion direction in which the substrate was normal to the force gauge had a larger signal change than when the probe tip was normal to the substrate.

An increase of gelatin concentration from 9% to 18% decreased the insertion force by an average of 28% (Figure 4). The strain gauge data profile showed some promising indicators for tissue properties such as a peak for initial insertion force, a second level of height for the tissue elasticity force, and a low reading for when the probe had left the tissue.

Future Work:

Next, we will create a case for the tweezers so that the structure can be durable during surgical usage. Furthermore, more tests will be conducted on healthy tissue versus cancerous tissue to better characterize the force gauge readings. Also, to more comprehensively characterize the tissue samples, the electrodes and capacitors will also be tested and calibrated for usage.

Acknowledgments:

I would like to thank my principal investigator, Amit Lal, and my mentor, Po-Cheng Chen, for providing the inspiration for this project. I am also thankful to the NNIN REU Progam and NSF. Lastly, I would like to thank the CNF staff for fabrication assistance.

References:

[1] K. Yan. "A real-time prostate cancer detection technique using needle insertion force and patient-specific criteria during percutaneous intervention." Medical Physics v. 36, Issue 9 (2009).

[2] P.-C. Chen. "Ultrasonic Neural Probe for Real Time Electromechanical Histology of Neural Interfaces," (Hilton Head 2012).

Fabricating Dual-Sided Micro Lenses and High Frequency Talbot Diffraction Gratings Using Binary Masks

Bradlee Kyle Beauchamp
Engineering Physics, Rose-Hulman Institute of Technology

NNIN REU Site: Colorado Nanofabrication Laboratory, University of Colorado, Boulder, CO
NNIN REU Principal Investigator: Dr. Rafael Piestun, Electrical, Computer and Energy Engineering, University of Colorado Boulder
NNIN REU Mentor: Anurag Agrawal, Electrical, Computer and Energy Engineering, University of Colorado Boulder
Contact: beauchbk@rose-hulman.edu, rafael.piestun@colorado.edu, anurag.agrawal@colorado.edu

Abstract and Introduction:

Binary photomasks are a way of approximating 3D structures when using photolithography. Multiple masks are used and the surface of a substrate is etched into a number of distinct heights.

A Fresnel lens was made employing this method, and was etched into both sides of a quartz substrate; the advantage of using a phase mask on both sides of a lens is that the diffraction effects that take place inside of the medium can be taken advantage of. This idea eventually was carried over to make a diffraction grating that used what is called the "Talbot Effect." This effect describes the phenomenon where light that passes through a periodic grating repeats the grating pattern in the near field at certain distances termed the Talbot length (Z_T). The frequency of the pattern doubles at a quarter of Z_T. By creating relatively shifted diffraction gratings on either side of the substrate, we effectively created a higher frequency grating.

Experimental Procedure:

The Fresnel lens was simulated in MATLAB by first simulating the phase of a conventional lens [1] with a focal length of 50 cm; then the mod function was used on this phase to turn the lens into a Fresnel lens. Masks transferred into Clewin software would approximate the three dimensional surface in eight distinct heights. These binary masks were made on a single chromium photomask in the Heidelberg DWL 66FS and were used to expose our substrate in the SUSS MJB3 Maskaligner. Our substrate consisted of a fused silica slide with a 40 nm coating of chromium (Cr) on one side, which aided in alignment. Negative resist (NR9) was used in the photolithographic process to create the first Fresnel lens. First an aperture was created in Cr by etching it with a chemical known as CR-7S. The fused silica was etched in the Plasma-Therm reactive ion etch II (RIE II), which etched the surface using a plasma. A 3:1 mixture of tetrafluoromethane and trifluoromethane gases was used at a temperature of 25°C giving an etch rate of 12 nm per minute.

For a material of refractive index $n(\lambda)$, the etch depth for a phase difference of 2π is given by $h_{2\pi} = \lambda/(n(\lambda)-1)$. The etch time for the i^{th} photomask is given by $t_{2\pi}/2^i$, where $t_{2\pi}$ is the etching time for $h_{2\pi}$. This lens was made again on the other side of the substrate, opposite of the Cr coated side effectively creating a lens of focal length of 25 cm when using HeNe laser light.

Our Talbot grating was also simulated using MATLAB software. Our substrate for these gratings was a 1 mm thick quartz substrate, which also had a 40 nm coating of Cr on one side. We used the equation provided by Lord Rayleigh [2] in Figure 1 to determine our grating period so that the Z_T would be four times the substrate thickness; this meant that at 1 mm, the intensity pattern of the grating would have twice the frequency as the original grating. The photolithographic process for making the Talbot grating was the same as earlier, except we only needed one etch into the quartz on each side to make the phase grating. The same grating was made four times on the Cr side of the one-inch square substrate in a 2×2 array. On the opposite side, two gratings were made; one grating was shifted by one fourth of a period, and the other was shifted by one half. This was so the effect on the diffraction pattern of the two could be compared against the grating etched on a single side.

$$Z_T = \frac{\lambda}{1 - \sqrt{1 - \frac{\lambda^2}{a^2}}}$$

Figure 1: Equation to determine Z_T. The letter a represents the grating period.

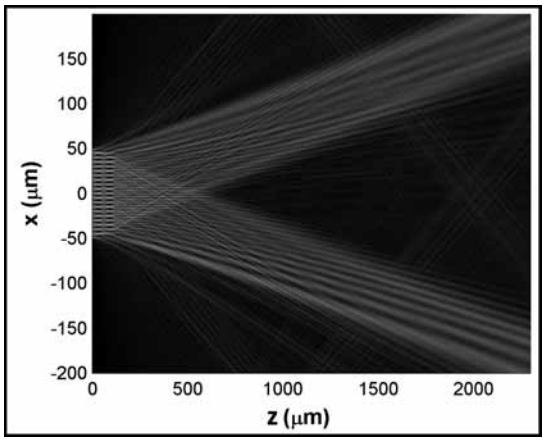

Figure 2: Top view of the MATLAB simulation of the Talbot grating.

OPTS

Results and Conclusions:

To test the Fresnel lens made with NR9, we sent collimated HeNe light through the lens and measured the diameter of the central spot at several distances away; it should have been the smallest at the focal length. The diameter was converted from the number of pixels in the picture with one pixel corresponding to 3.7 μm. We found the focal length to be about ~ 25 cm, at which the central spot diameter matched the theoretical value (from Rayleigh's Criterion). Moreover, the spot did not suffer from higher order aberrations such as astigmatism or coma showing that the alignment between the two sides of the mask was good. Thus, we had our successful proof of concept for aligning and etching a phase mask on both sides of a substrate. The Talbot gratings were tested with the same HeNe laser. The diffraction pattern we expected for both the single and double grating is shown by Figure 2. What we observed, however, is shown in Figures 3 and 4. The main difference observed in these patterns is that in the experiment, light shows up on the 0^{th} order of light, which was not expected. It is hypothesized that this difference could be due to either an error in the simulation, inaccurate etch depths, or misalignment of the photomasks.

Figure 3: Pattern from a single grating.

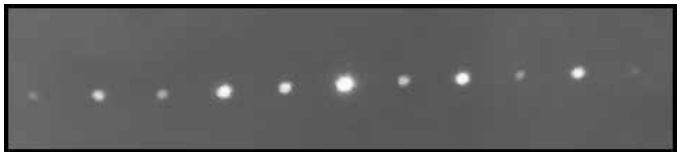

Figure 4: Pattern from a double grating shifted by one half of a period.

Future Work:

Future work would involve investigating the incongruences between simulation and experiment for the Talbot gratings that were tested. The accuracy of our alignment would also be measured. We would also explore using the Talbot effect for improving the resolution of photolithography.

Acknowledgments:

I would like to thank my principal investigator and mentor for their help and guidance in this research as well as Ryan Brow for his help in the cleanroom. I would also like to thank the National Nanotechnology Infrastructure Network Research Experience for Undergraduates (NNIN REU) Program for making this experience possible.

References:

[1] Goodman, J; "Introduction to Fourier Optics"; Second Edition, Pages 102-105 (1996).

[2] Strutt, J; "On copying Diffraction Gratings and On Some Phenomenon Connected Therewith"; Philosophical Magazine, Fifth Series (1881).

Infrared Filtering via Sub-Wavelength Gratings for Hyperspectral Imaging

Arthur Bowman, III
Physics, Wayne State University

NNIN REU Site: Lurie Nanofabrication Facility, University of Michigan, Ann Arbor, MI
NNIN REU Principal Investigator: Jamie Phillips, Electrical Engineering and Computer Science, University of Michigan
NNIN REU Mentor: Justin Foley, Applied Physics, Electrical Engineering and Computer Science, University of Michigan
(2008 NNIN REU at the University of Minnesota)
Contact: abowmaniii@wayne.edu, jphilli@umich.edu, foleyjm@umich.edu

Abstract:

Fabry-Perot cavities are an attractive method of infrared filtering, provided they are made of broadband, lossless reflectors. A long wavelength infrared region (LWIR, 8-12 μm) broadband reflector is demonstrated using a high-index contrast sub-wavelength grating (HC-SWG) based on a suspended silicon system. The expected grating field response was simulated using COMSOL Multiphysics to exhibit greater than 90% reflectance in the LWIR, for transverse magnetic polarization. An un-switched C_4F_8/SF_6 reactive ion etch (RIE) was characterized, and showed improved sidewall profile compared to previously used etch chemistry. Fabricated gratings demonstrate greater than 85% reflectance between 8 μm and 14 μm, with the response agreeing well with simulations incorporating as-built dimensions.

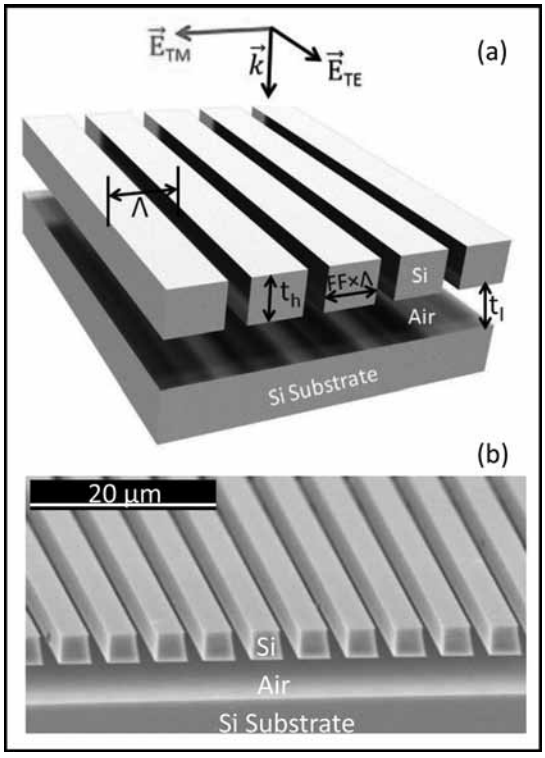

Figure 1: a) A suspended silicon grating schematic, and b) A representative fabricated suspended silicon grating.

Introduction:

Hyperspectral techniques are needed to advance to the next generation of thermal imaging systems. A hyperspectral image contains the electromagnetic spectrum for every point in an imaging plane, providing a "fingerprint" for different objects. These fingerprints improve object discrimination, which is useful in a wide array of applications including satellite analysis of climate change, military surveillance, and biological and chemical sensing. Hyperspectral images are formed from intensity acquired at each wavelength, which requires narrowband filters such as interference-based Fabry-Perot cavity filters. A Fabry-Perot cavity is composed of two parallel reflectors separated by a set distance, and transmits light when a standing wave can be established between the two mirrors. To ensure highly efficient and selective filters, the reflectors must exhibit very high reflectance and be non-absorbing. In this work we designed, fabricated and characterized a low loss reflector using a high-contrast grating.

It was first shown by Mateus [1] using a system of poly-Si gratings (n = 3.48) on top of SiO_2 (n = 1.4) that high-contrast-gratings could function as broadband and lossless reflectors. "High-index-contrast" refers to the large difference between the refractive indices of the grating and surrounding media. Figure 1 shows a schematic of a high-contrast-grating with dimensions and polarization defined as well as a corresponding fabricated grating. The parameters necessary to optimize the response are the grating period (Λ), fill factor (FF), which is the ratio of a grating's width to the period, and thicknesses of the high and low index layers, (t_h and t_l).

Experimental Procedure:

We optimized the design of a silicon (n = 3.4) grating suspended in air (n = 1) using commercial finite element analysis software for transverse magnetic (TM, electric field directed along the grating periodicity) polarized light. A single grating period was used as the computational domain assuming periodic boundary conditions and material optical properties from Palik [2]. Iterative optimization showed an expected reflectance greater than 90% between 8 μm and 12 μm, an important spectral range for thermal imaging.

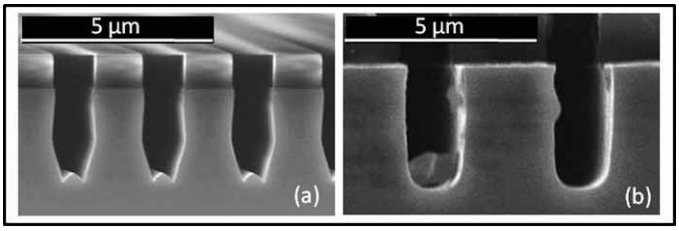

Figure 2: Grating cross-sectional profiles after a) H_2/HBr, and b) C_4F_8/SF_6 reactive ion etches.

We used a commercial silicon-on-insulator wafer as the platform for fabricating our suspended grating using photolithography and reactive ion etching (RIE). Subsequent wet etching of the sacrificial SiO_2 layer with hydrofluoric acid suspended the gratings as shown in Figure 1b. We characterized the grating response using polarization dependent Fourier transform infrared spectroscopy (FTIR) in transmission mode using an aperture to constrain the focused light.

Results:

We compared the sidewall profiles of a fluorine-based RIE chemistry (C_4F_8/SF_6) to a previously used bromide-based etch chemistry (H_2/HBr) using scanning electron microscopy (SEM). The fluorine-based plasma etching improved sidewall profiles over the bromide-based chemistry, as shown in the micrographs of Figure 2. The sidewalls produced by the C_4F_8/SF_6 RIE are more vertical and have minimal bowing compared to the H_2/HBr profiles, both of which are expected to improve the structure response. We further characterized the etch rate dependence on open area of the C_4F_8/SF_6 RIE as shown in Figure 3, which shows larger periods, with larger open areas, exhibit higher etch rates. These results were used to optimize the grating fabrication process.

FTIR characterization of our gratings indicated less than 15% of incident light was transmitted in the spectral range of 8-14 μm. The expected transmittance, obtained from simulation with the as-built dimensions of the structure (Λ = 5.3 μm, FF = 0.7, t_h = 3.3 μm, and t_l = 4.3 μm) agreed well with the experimental transmittance, indicating the reflectance may be approximated as R+Loss = 1-T, where the Loss term is small.

Figure 4 shows the derived reflectance and simulated response of the gratings as well as the reflectance of a control silicon wafer. The derived reflectance agrees well with the simulation further suggesting loss in the materials does not significantly affect the response. The agreement between the expected reflectance and experimental data indicate the grating acts as a broadband reflector, with greater than 85% reflectance between 8 μm and 14 μm.

Conclusions and Future Work:

We fabricated and characterized a high-contrast grating reflector that exhibits greater than 85% reflectance between 8 μm and 14 μm. We improved the fabrication procedure using a C_4F_8/SF_6 etch chemistry, which improved sidewall profiles over a previously used H_2/HBr etch. Future work includes design and fabrication of a polarization independent high-contrast-grating consisting of a two-dimensional layout. Initial design optimization shows a response with greater than 80% reflectance between 9 and 12 μm.

Acknowledgements:

I would like to thank my mentor Justin Foley, Principal Investigator Professor Jamie Phillips, the staff of the Lurie Nanofabrication Facility, especially Shawn Wright, Greg Allion, Kevin Owen, and Vishva Ray, the National Nanotechnology Infrastructure Network REU Program, especially Brandon Lucas and Trasa Burkhardt for their help, and the National Science Foundation for making this research possible.

References:

[1] C.F.R. Mateus, M.C.Y. Huang, L. Chen, C.J. Chang-Hasnain, and Y. Suzuki. "Ultrabroadband Mirror Using Low-Index Cladded Subwavelength Grating," IEEE Photonics Technol. Lett. 16, (2004).

[2] Palik, E. D., "Handbook of optical-constants," J. Opt. Soc. Am. 1, 1297-1297 (1984).

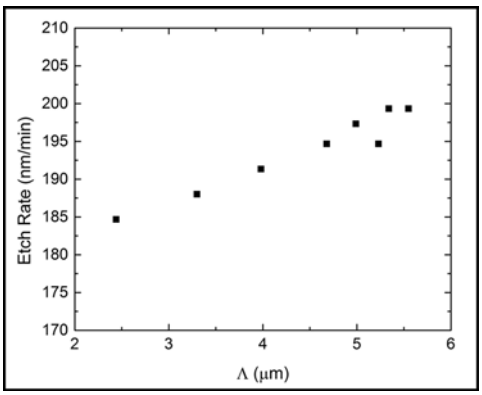

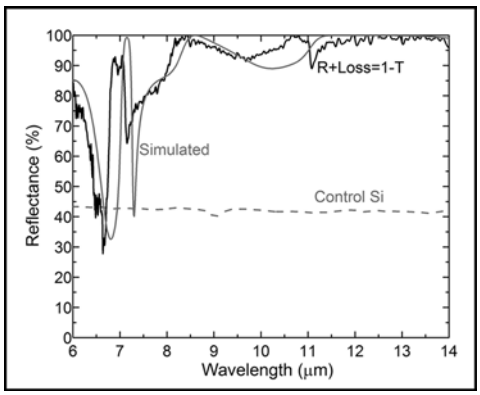

Figure 3, left: Etch-rate dependence on period for C_4F_8/SF_6 reactive ion etching.

Figure 4, right: Derived experimental reflectance spectra, simulated reflectance of as-built structure, and the experimental reflectance of a control silicon wafer.

Silicon Nanophotonic Add-Drop Filter Based on High-*Q* Square Resonant Cavities

Emily Donahue
Engineering Physics, Cornell University

NNIN REU Site: Colorado Nanofabrication Laboratory, University of Colorado, Boulder, CO
NNIN REU Principal Investigator: Dr. Miloš Popović, Electrical, Computer, and Energy Engineering, University of Colorado at Boulder
NNIN REU Mentor: Yangyang Liu, Department of Electrical, Computer, and Energy Engineering, University of Colorado at Boulder
Contact: ed353@cornell.edu, milos.popovic@colorado.edu, yangyang.Liu@colorado.edu

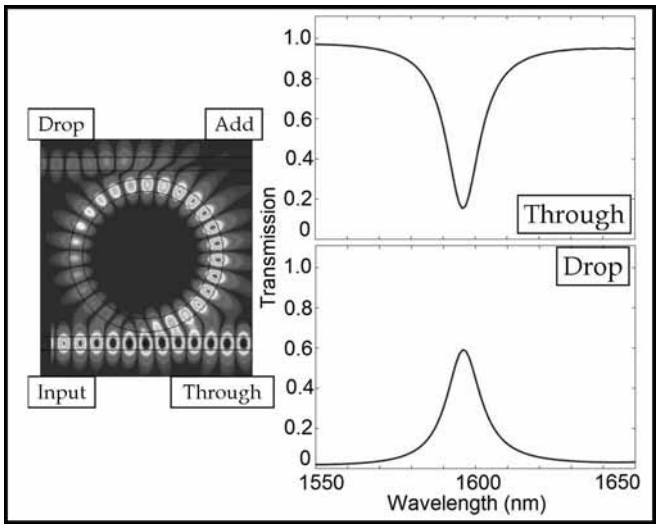

Figure 1: FDTD simulation field plot and modal power transmission for a microring resonator add-drop filter. (See full-color version on inside cover.)

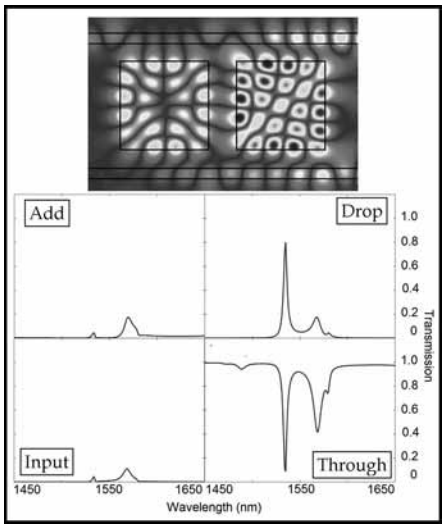

Figure 2: FDTD simulation field for a square cavity add-drop filter. (See full-color version on inside cover.)

Abstract and Introduction:

Silicon nanophotonic devices can process optical signals analogously to the way in which electronic devices process electrical signals. They have applications in telecommunications and the potential to be integrated within computer chips. One key device in photonic circuits is the add-drop filter, which can be used for wavelength-division multiplexing. This filter is commonly implemented with a microring resonator placed in between two parallel waveguides. When light passes through the transmitting bus, the ring resonates at a certain wavelength, based on its geometry. This mode propagates around the ring and into the receiving waveguide. The modal power fraction of light transmitted from the input "port" to each of the output ports, i.e. waveguides' cross-sections, is of interest. Figure 1 shows the through and drop port responses of a microring add-drop filter. A similar response can be achieved with a two-square cavity geometry [1]. In this design, the optical excitation alternates back and forth between the two square cavities in time. This "push pull" behavior means that these standing-wave cavities channel light as does a traveling-wave ring resonator. The goal of this project was to fabricate a two-square cavity add-drop filter.

Procedure:

A silicon-on-insulator wafer was used to fabricate the photonic structures. The wafer consisted of 220 nm of silicon atop 3 μm of silicon dioxide. A 190 nm layer of hydrogen silsesquioxane (HSQ), a negative tone resist, was spun onto the wafer at 1000 RPM for one minute. The wafer was dried in a vacuum oven for five minutes to remove the HSQ's solvent. Electron-beam lithography (EBL) was performed using a JEOL 5910 LV scanning electron microscope (SEM) that interfaces with a computer program to write the desired pattern in a single writing field. The design was created in DesignCAD based on the results of two-dimensional finite-difference time-domain (FDTD) simulations.

Various electron-beam dosages were given for the different structures in the design. The sample was then developed in tetramethyl ammonium hydroxide (TMAH) heated in a 40°C water bath and then in a solution of 1:9 TMAH:water, also heated to 40°C in a water bath.

Process Development:

The HSQ development procedure was changed during this project to fabricate high-contrast structures. Previously, the HSQ was pre-baked at 90°C before EBL to dry the solvent from the solution. After EBL, the sample was developed in the two solutions of TMAH at room temperature. However, polymer chains within the HSQ cross-link when it is exposed to elevated temperatures [2], producing areas of partially developed HSQ near exposed areas. The procedure was improved by drying the solvent at room temperature and development at 40°C. Heating during development removed partially developed HSQ caused by electron beam backscattering.

Another challenge in fabrication were proximity effects from EBL, which are caused by backscattering of secondary electrons that bombard the sample. The proximity effects were mitigated by varying exposure dosages and by adding sidewalls near the gratings to create approximately "even loading" (average dosage) across structures. However, the equipment seemed to give inconsistent exposures, and exact numbers were not calibrated for the electron-beam dosage.

Results:

A grating-to-grating connection via a waveguide was fabricated to obtain a baseline test for the optical fiber-to-fiber power loss. The device's gratings were designed to couple 1550 nm wavelength light into the waveguide. The laser's wavelength was swept from 1495-1640 nm, and the power transmission along this range is shown in Figure 3. Transmission of about -50 dB was achieved, but high coupling loss remains. The response shows a deep modulation with a 21 nm wavelength period, which corresponds to a free spectral range (FSR) of 2.6THz. This could be the result of coupling between the fundamental and third modes within the taper, coupling from a transverse electric (TE) to a transverse magnetic (TM) mode, or mode conversion from TE to TM in the waveguide bends. There is also a secondary ripple with a 0.5 nm period, which could be caused by a reflection between the input and output terminals, with sufficient resonant delay in reflection by the grating couplers.

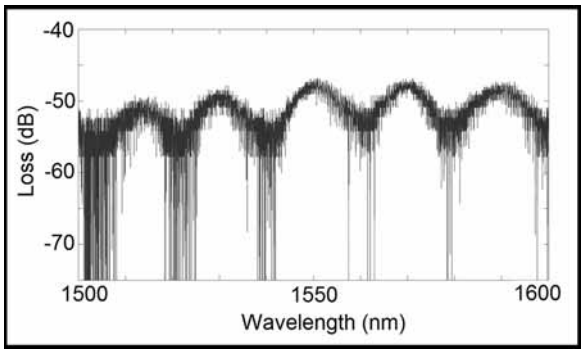

Figure 3: Optical response of the grating-to-grating connection.

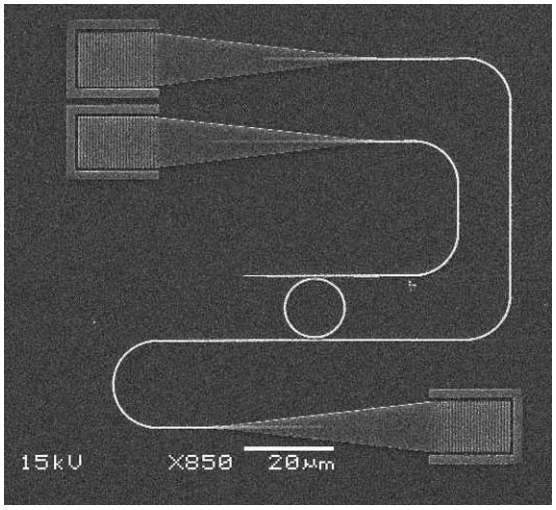

Figure 4: SEM of fabrication including a microring resonator.

A microring resonator was fabricated for testing, because its response is well known [3] (see Figure 4). This device gave no meaningful optical response. SEM images showed inconsistent structure heights, which would have caused high power loss if light had been coupled into the device.

Conclusions:

A photonic fiber-to-fiber connection, comprising two fiber-to-chip grating couplers and a silicon waveguide connection on a silicon chip was demonstrated.

To complete the sought goal, the next step would be to fine tune the fabrication process until a circuit with a working microring resonator add-drop filter is produced. Then, a three-dimensional mode solver software would be used to find the square resonant cavities' dimensions with a high quality factor at a decided wavelength of light. The two-square add-drop filter would be tested optically, and these measurements would be compared with the theoretical response produced by FDTD simulation.

Acknowledgements:

I would like to thank Miloš Popović and Yangyang Liu for their invaluable teaching and help, as well as the staff at the Colorado Nanofabrication Laboratory for their support, the NSF for funding this research project, and the NNIN for this wonderful REU Program.

References:

[1] Manolatou, C., et al. "Coupling of Modes Analysis of Resonant Channel Add-Drop Filters." IEEE Journal of Quantum Electronics, Vol. 35, No. 9, September 1999: 1322-1332.

[2] Häffner, M., et al. "Influence of Temperature on HSQ Electron-Beam Lithography." Journal of Vacuum Science and Technology B, Vol. 25, No. 6, Nov/Dec 2007: 2045-2048.

[3] Little, B. E., et al. "Microring Resonator Channel Dropping Filters." Journal of Lightwave Technology, Vol. 15, No. 6, June 1997: 998-1005.

Voltage-Tunable Plasmonic Metamaterials Based on Stark Tunable Intersubband Polaritons

Priyanka Gaur
Brain and Cognitive Sciences, Massachusetts Institute of Technology

NNIN REU Site: Microelectronics Research Center, The University of Texas, Austin, TX
NNIN REU Principal Investigator: Dr. Mikhail Belkin, Electrical Engineering and Computer Science, The University of Texas at Austin
NNIN REU Mentor: Jongwon Lee, Department of Electrical Engineering and Computer Science, The University of Texas at Austin
Contact: pgaur@mit.edu, mbelkin@ece.utexas.edu, jongwonlee@utexas.edu

Abstract:

This paper explores ways of producing voltage-tunable plasmonic metamaterials. By combining plasmonic metamaterials with intersubband transitions in $In_{0.53}Ga_{0.47}As/Al_{0.48}In_{0.52}As$ coupled quantum well heterostructures, we fabricated and tested devices with optical response sensitive to applied bias voltage. The metamaterials consisted of an array of sub-wavelength plasmonic elements resonant in the mid-infrared. The plasmonic structures were fabricated using electron-beam lithography. The devices were characterized using Fourier transform infrared spectrometer (FTIR)-based reflection measurement. Resonance matching between intersubband transition and plasmonic resonances was confirmed by observing polaritonic splitting of absorption peaks in reflection spectrum. Experimentally, applying 5.5 volts of DC bias achieved 71 nm of wavelength tuning at 7 μm wavelength.

Introduction:

Plasmonic metamaterials are artificial materials constructed on the sub-wavelength scale to provide electromagnetic properties that cannot be obtained by naturally occurring materials. Our goal was to produce voltage-tunable plasmonic metamaterials by combining plasmonic metamaterials with artificial semiconductors designed for electro-optic effect. The tunability was based on the integration of intersubband transitions, which occurred from excitation of an electron between quantized energy levels within a multi-quantum-well (MQW) [1], and plasmonic absorption from surface plasmon polaritons (SPP's), which occurred when infrared waves struck a metal and caused electron oscillations [2]. Intersubband transitions were designed to have diagonal transitions in real space in which sharp absorption allowed for changes in permittivity in the direction normal to the surface based on the Kramers-Kronig relation for transverse-magnetic (TM) polarization; see Figure 1(c). Bias voltage tunes the position of intersubband absorption lines; see Figure 1(a), (b). With proper planar configuration, we could apply bias through the MQW layer and utilize ε_z for tuning. The bias voltage led to significant tuning of absorption peak position in the plasmonic absorption spectrum.

Our device confirmed the potential for spectral tuning in the mid-infrared range with bias voltages, known as the Stark Shift. We modeled a unit cell of our structure with Computer Simulation Technology (CST) Microwave Studio; see Figure 2(a). The structure consisted of a MQW layer positioned between bottom and top metal layers. The plasmonic resonance wavelength was based on the geometry of the elements and dimensions of the resonator. Band structure engineering determined the transition energies and operating wavelengths. Since the refractive index of the surrounding environment of the plasmonic metamaterial changed, there was a resultant shift in the resonance frequency; see Figure 2(b). The resonance frequency of the plasmonic metamaterial and multi-quantum-well structure must coincidently align to achieve maximal tuning of the plasmonic resonance.

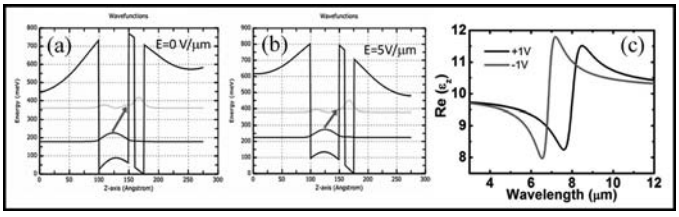

Figure 1: Intersubband transition simulation when the device is biased at (a) 0V and (b) 1V. (c) Calculated real part of dielectric constant at different bias voltage.

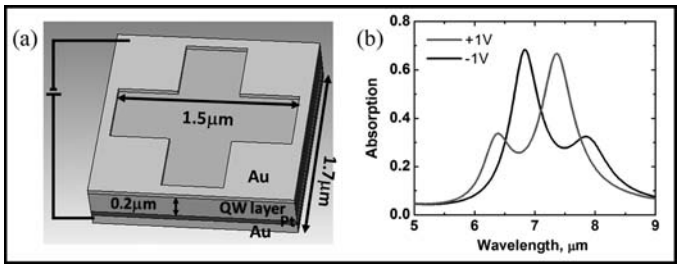

Figure 2: (a) Device structure designed in CST Microwave Studio composed of complementary cross resonators. (b) Simulated plasmonic absorption tuning at different bias voltages.

OPTS

Experimental Procedure:

We fabricated a 400 μm by 400 μm array of complementary cross-shaped resonators on a 200 nm-thick MQW layer. The MQW structure was grown by molecular beam epitaxy (MBE) on an n-doped InP substrate. After wafer bonding, polishing, and wet etching, electron beam lithography (EBL) was used to fabricate the plasmonic structures. The minimum feature was 214 nm, and the maximum was 1.544 μm. Titanium and gold were deposited onto the sample's surface, and lift-off was performed.

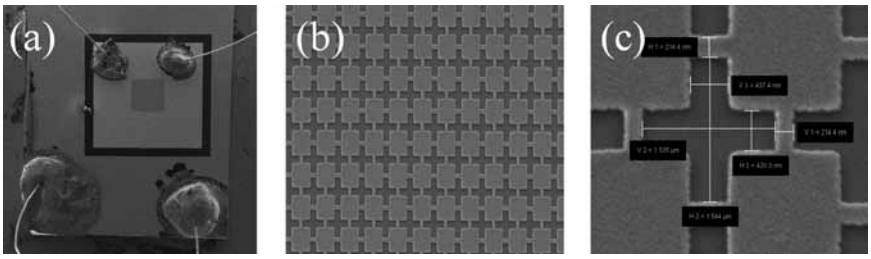

Figure 3: SEM images of (a) a finished device with bonded wires, (b) array of crosses, and (c) one period of cross.

Figure 2 (a-c) show scanning electron microscope (SEM) images of the cross-shaped pattern and finalized device.

A mesa-structure was necessary to prevent current spreading away from the plasmonic metamaterial. The samples were cleaved and mounted to a copper carrier block. Using a manual tool, we created multiple wire connections to bottom and top metal contacts for current flow. We performed several tests to obtain a close approximation to the designed structure, including adjusting the dose factor of the electron beam and changing the dimension of the pattern file during e-beam writing.

The FTIR characterized the finished device with spectral measurements. A broadband mid-infrared light from a globar lamp inside the FTIR was focused onto the plasmonic array via objective lens, and the reflected signal was measured through a beam splitter and ZnSe lens with a liquid nitrogen cooled mercury cadmium telluride (MCT) photo-detector.

Results and Conclusions:

Resonance matching between intersubband transitions in the MQW and plasmonic resonances was confirmed by observing polaritonic splitting of absorption peaks, which occurs when two new energy states are effectively constructed as shown in Figure 4(a). The evident trend proved that as the period of the unit cell increased, the resonance wavelength increased. We were able to see that the polaritonic splitting of the absorption occurred with a period around 1.8 μm. We applied tuning to the structure with matched resonance of period 1.75 μm. We achieved 71 nm of wavelength tuning at 7 μm wavelength with 5.5 volts of DC bias. We observed plasmonic absorption tuning through a quantum-confined Stark Shift by applying bias through the MQW; as the voltage increased, the absorption peak spectrum shifted to longer wavelengths as shown in Figure 4(b).

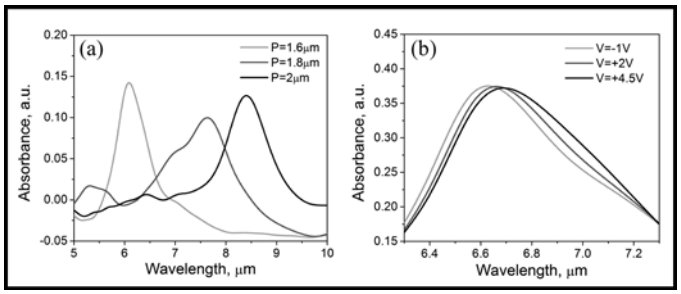

Figure 4: (a) Experimental absorption spectrum of devices with different periods of cross resonator. (b) Experimental absorption spectrum tuning by applied bias voltages.

Future Work:

Adjusting the structure to have a plasmonic absorption line closer to the intersubband absorption line of the MQW may broaden the tuning range. Technologies including spectrometry, photo-detectors, and quantum cascade lasers immensely benefit from such insights.

Acknowledgements:

This research was supported by a grant from the National Science Foundation as part of the National Nanotechnology Infrastructure Network Research Experience for Undergraduates Program. Thank you, Dr. Mikhail Belkin and Jongwon Lee.

References:

[1] Delacourt, Dominique, et al. "Mid-Infrared Phase Modulation via Stark Effect on Intersubband Transitions in GaAs/GaAlAs Quantum Wells." IEEE Journal of Quantum Electronics, 29, 8, 1-4 (1993).

[2] Liu, X., et al. "Infrared Spatial Frequency Selective Metamaterial with Near-Unit Absorbance." Phys. Rev. Lett. 104, 20, 2313-2318 (2010).

Silicon Nanowires for Optical Light Trapping in Solar Cells

Christopher Green
Applied Physics, Lock Haven University

NNIN REU Site: ASU NanoFab, Arizona State University, Tempe, AZ
NNIN REU Principal Investigators: Dr. Stephen Goodnick and Dr. Christiana Honsberg, Electrical Engineering, Arizona State University
NNIN REU Mentors: Dr. Clarence Tracy and Jongwon Lee, Electrical Engineering, Arizona State University
Contact: christopher.green1091@gmail.com, stephen.goodnick@asu.edu, christiana.honsberg@asu.edu, clarence.tracy@asu.edu, jlee159@asu.edu

Introduction:

The advanced development of the semiconductor industry has placed crystalline silicon solar cells at the forefront of solar cell research. Currently, crystalline silicon solar cells (c:Si SCs) average around 20% efficiency in the conversion of sunlight into electricity [1]. Control of the surface morphology of solar cells is key to boosting the conversion efficiency beyond the current average through the reduction of reflectance and the enhancement of electrical performance. Inexpensive surface texturing is commonly used to minimize reflection losses; however, this method is dependent on the refractive index of the semiconductor and quickly reaches a maximum. Nanowires with sub-wavelength dimensions (~ 100 nm) offer great potential for decreasing reflectance beyond the bulk limit. These attributes are shared with other sub-wavelength scaled features, but nanowires offer the unique ability for the separation of light absorption and carrier transport through the confinement of electrons in two dimensions [2].

The approach used in this experiment to fabricate nanowires on silicon devices allowed for well-controlled nanowire structures. Using electron beam lithography (EBL) and deep reactive ion etching (DRIE), highly ordered nanowire patterns were produced on doped c:Si wafers. With additional processing, the resulting silicon nanowire solar cells were characterized optically and electrically. A schematic diagram of the finalized device structure is shown in Figure 1.

Experimental Procedure:

Nanowires were fabricated on back-side junction c:Si SCs with amorphous silicon (a:Si) passivation and aluminum contacts. To begin the fabrication process, a backside junction was formed on p-type c:Si wafers. This was done using backside diffusion of phosphorus at 1000°C for one hour. A drive in stage was performed after diffusion for seven hours at 1000°C. The front side of the wafers was coated with PMMA photoresist and patterned using EBL, forming exposed circular areas of 70 nm and 100 nm diameter after development. To form a hard mask for etching, 30 nm of silicon dioxide (SiO_2) was deposited with electron-beam evaporation, leaving a grid pattern of SiO_2 islands with 700 nm spacing.

DRIE etching was done using a Surface Technology Systems inductively coupled plasma (STS ICP) system. Highly anisotropic nanowires of diameters 70 nm and 100 nm, and a height of around 600 nm, were formed using the Bosch process (shown in Figure 2), which consists of alternating cycles of etchant sulfur hexafluoride (SF_6) and deposition polymer octaflourocyclobutane (C_4F_8). This method inherently creates scalloping on the sides of the nanowires.

A passivation layer was deposited using PECVD, consisting of a 10 nm intrinsic layer of a:Si, followed by 30 nm of p^+ a:Si. This increased the diameters of the nanowires to 150 nm and 180 nm. Electron-beam evaporation was used to deposit 200 nm of aluminum (Al) on the front and back sides of the wafer. A shadow mask was aligned on

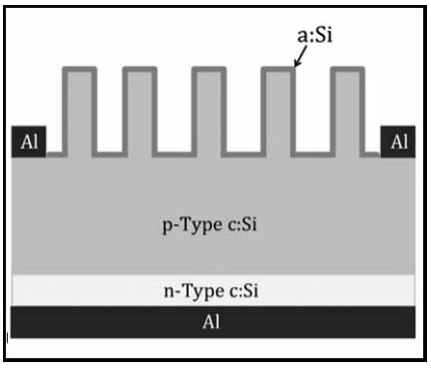

Figure 1, above: Schematic representation of finalized device (not to scale).

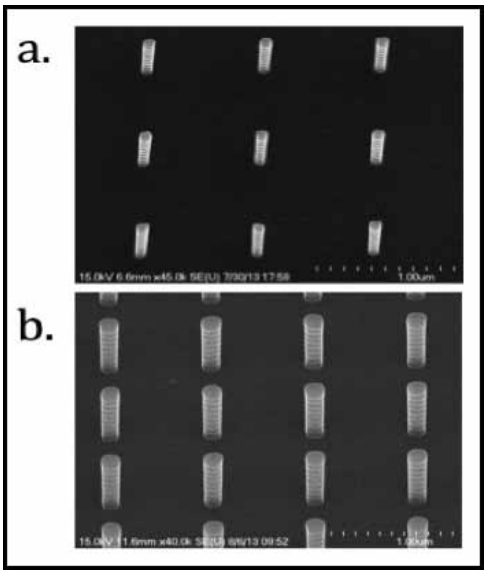

Figure 2, right: SEM images of nanowire (a) after etching and (b) after a:Si deposition.

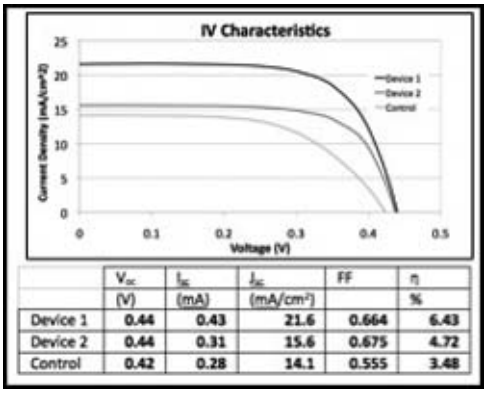

	V_{oc} (V)	I_{sc} (mA)	J_{sc} (mA/cm²)	FF	η %
Device 1	0.44	0.43	21.6	0.664	6.43
Device 2	0.44	0.31	15.6	0.675	4.72
Control	0.42	0.28	14.1	0.555	3.48

Figure 3: (a) IV characteristics of nanowire and control devices and (b) tabulated data from IV characteristics.

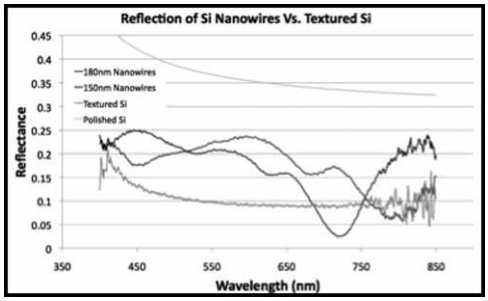

Figure 4: Reflectance measurements of 180 nm and 150 nm devices along with planar and textured Si.

150 nm diameter nanowires and at 800 nm wavelength for 180 nm diameter nanowires. The nanowire structures showed higher absorption at the observed peaks than textured Si. A red shift in absorption peaks with increased diameter shows tunability of the absorption peak through the diameter of the nanowires. Similar results were observed in indium arsenide and indium phosphide nanowires by Kupec [3].

the front side of the wafer during deposition to avoid contact with the nanowires. Finally the wafers were placed in an oven at 300°C for 20 minutes to allow the Al to diffuse through the passivation layer without compromising the amorphous nature of the layer.

Results and Conclusions:

Figure 3 shows the current-voltage (IV) characteristics of the nanowire devices under AM1.5 illumination. Under these conditions, the best device showed an open circuit voltage (V_{oc}) of 0.44 V, a short circuit current density (J_{sc}) of 21.6 mA/cm^2, a fill factor (FF) of 0.664, and an efficiency (η) of 6.43%. The control device used was a planar c:Si device located on the same wafer as the nanowire devices. The control device showed a V_{oc} of 0.42 V, J_{sc} of 14.1 mA/cm^2, FF of 0.555, and η of 3.48%. Light trapping in the nanowire structures increased the absorption of incident photons over the planar device.

Reflectance measurements were taken of 150 nm and 180 nm diameter nanowire patterns, and textured Si using a Filmetrics F40 microscope attachment, and a reference was used for planar Si. The results are shown in Figure 4. Nanowire devices showed higher absorption than planar Si, but textured Si showed a higher total absorption than the nanowire devices. Absorption peaks were observed at 700 nm wavelength for

Future Work:

Further research is needed to optimize the fabrication process so that control devices perform at a higher efficiency. Studies on the effects of nanowire diameter, spacing, and structure on absorbance must be performed to allow for optimization of nanowire structures. Eventual applications may focus on radial p-n junction nanowires and nanowire thin film devices using similar fabrication methods.

Acknowledgements:

I would like to thank my PIs, Dr. Stephen Goodnick and Dr. Christiana Honsberg, along with my mentors, Jongwon Lee and Dr. Clarence Tracy. I would also like to thank the National Nanotechnology Infrastructure Network Research Experience for Undergraduates and the National Science Foundation for funding.

References:

[1] Garnett, Erik, and Peidong Yang. "Light Trapping in Silicon Nanowire Solar Cells." NanoLetters 10 (2010): 1082. 28 Jan. 2010.

[2] Yan, Ruoxue, Daniel Gargas, and Peidong Yang. "Nanowire Photonics." Nature Photonics 3 (2009): 569. 30 Sept. 2009.

[3] Kupec, J., and B. Witzigmann. "Dispersion, Wave Propagation and Efficiency Analysis of Nanowire Solar Cells." Optics Express 17.12 (2009): 10399-10410. 8 June 2009.

Optical and Electrical Studies of Metal:Semiconductor Nanocomposites for Nanophotonics

Stephen D. March
Electrical Engineering, Iowa State University

NNIN REU Site: Microelectronics Research Center, The University of Texas, Austin, TX
NNIN REU Principal Investigator: Professor Seth Bank, Electrical and Computer Engineering, The University of Texas at Austin
NNIN REU Mentors: Erica Krivoy and Rodolfo Salas, Electrical and Computer Engineering, The University of Texas at Austin
Contact: sdmarch@iastate.edu, sbank@ece.utexas.edu, erica.krivoy@utexas.edu, rodolfo.salas@utexas.edu

Abstract and Introduction:

We explored the tunable optical properties of III-V compound semiconductor films grown by molecular beam epitaxy (MBE) for infrared optoelectronics and integrated plasmonics. This project has been twofold. (1) Investigate the optical tunability of MBE-grown rare-earth monopnictide (RE-V) nanoparticle superlattices by adjusting superlattice period and composition to demonstrate intermediate energy states that enable sub-bandgap tunability of gallium arsenide (GaAs). (2) Study the absorption blueshift in highly-doped indium arsenide (InAs) to demonstrate an approximately three-fold increase in the effective bandgap range and the divergence from existing non-parabolic InAs electronic band structure models. Both systems studied demonstrate two separate methods to tune III-V materials to provide greater material flexibility for optical engineering applications.

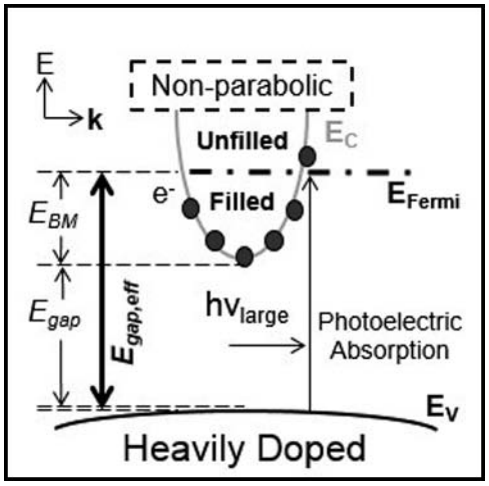

Figure 1: Burstein-Moss (E_{BM}) blueshift caused by heavy doping.

Material Systems Studied:

RE-V/III-V superlattice structures consist of periodically repeating layers with a 5 to 20 nm thick GaAs layer and a 0.25 to one monolayer (ML) deposition of RE-V, where the fractional volume of RE-V is equivalent in each structure. We investigated erbium arsenide (ErAs), lanthanum lutetium arsenide (LaLuAs), and lutetium arsenide (LuAs) RE-V nanocomposites. Work by Hanson et al. [1] on similar RE-V/III-V superlattice structures demonstrated strong sub-bandgap absorption in gallium antimonide (GaSb). We sought similar absorption changes in GaAs as our first method to optically engineer III-V materials.

InAs is a direct, narrow-bandgap semiconductor with a room temperature bandgap of 0.33 eV. We studied 500 nm thick films doped with silicon (n-type) and beryllium (p-type) with high active carrier concentrations of 6×10^{18} cm^{-3} to 9×10^{19} cm^{-3}. High n-type carrier concentrations, n, resulted in a strong absorption blueshift, which is attributable to band-filling, as described by Burstein [2] and Moss [3]. As n increases, the Fermi energy increases and more states in the conduction band, Ec, become filled with electrons. Since photoelectric absorption from the valence band, Ev, requires an unfilled state in the conduction band, the effective bandgap, $E_{gap,eff}$, increases with the Fermi energy, as shown in Figure 1. This study investigates unexplored high n values to tune $E_{gap,eff}$ in InAs as our second method to optically engineer III-V materials.

Experimental Procedure:

Near- and mid-infrared reflection and transmission spectra were collected with a 0.5 m grating spectrometer, using an InGaAs detector and a tungsten-filament source for the near-infrared, and an indium antimonide detector and carbon-rod source for the mid-infrared. Overlapping wavelength spectra were collected using LabVIEW and spliced using MATLAB, resulting in single spectra spanning wavelengths from 800 to 5000 nm (photon energies from 0.2 to 1.4 eV). The $E_{gap,eff}$ for different materials was found by using a linear extrapolation of the square of the absorption coefficient for a thin-film material, as suggested by Wu et al. [4].

Results and Conclusions:

RE-V/III-V Nanoparticle Superlattices. An aggregate transmission spectrum of several representative RE-V/III-V samples is shown in Figure 2. From 0.2 to 1.4 eV, GaAs exhibited a constant reflection value, thus any change in the transmission spectrum produced an opposite change in the absorption spectrum (e.g. decreased transmission produces increased absorption). Nanocomposites with Er and LaLu, small nanoparticles (small ML), and a small number of periods showed a small dip in transmission for incident photonic energy greater than 0.75 eV. Nanocomposites with Lu, large ML, and many periods showed a more pronounced transmission spectrum dip near 0.8 eV, which is far below 1.4 eV bandgap for intrinsic GaAs. RE-V nanoparticles create sub-bandgap energy states (Figure 3) that allow for sub-bandgap photoelectric absorption [1]. By adjusting the composition and structure of superlattices we can engineer GaAs for absorption near 0.8 eV. This value is critical for fiber optic systems, because 0.8 eV (1550 nm) is used by the existing fiber optic infrastructure for optimal signal relay and acquisition; III-V-based detectors using RE-V nanocomposites may be quickly adopted to work with existing technology. Future work will explore other RE materials and adjusted MBE growth techniques to refine the tunable properties of RE-V/III-V nanocomposites.

Heavily-Doped InAs. A plot of $E_{gap,eff}$ versus n is given in Figure 4. We observed a tunable $E_{gap,eff}$ range of 0.64 to 1.16 eV, which is several times larger than the intrinsic bandgap of InAs of 0.33 eV and indicates InAs absorption may be engineered by controlling n. The data agreed well with previously published results at lower carrier concentrations and diverged noticeably from the best fit non-parabolic band model available [5, 6]. Although non-parabolic behavior is expected for large n, modeling such behavior is limited by low n values previously explored. Our larger-n trend describes non-parabolic behavior more completely and can be used to study and optically engineer narrow-bandgap materials. Future work will concentrate on quantifying a new non-parabolic model and exploring even higher n.

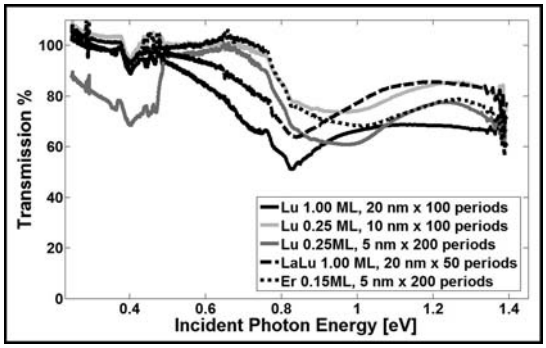

Figure 2: Transmission spectrum for RE-V/III-V nanoparticle superlattices.

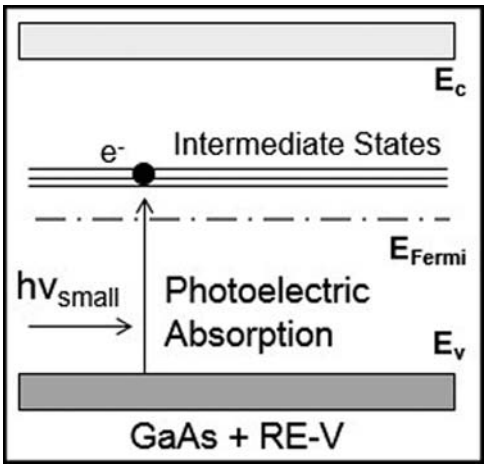

Figure 3: Sub-bandgap photoelectric absorption caused by RE-V nanoparticles.

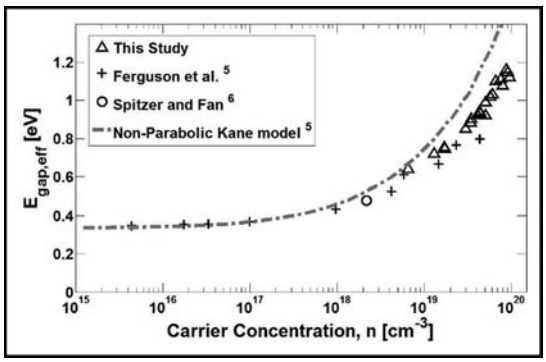

Figure 4: $E_{gap,eff}$ *versus* n *with literature values and a non-parabolic band model.*

Acknowledgments:

I want to thank Professor Seth Bank, Erica Krivoy, Rodolfo Salas, Scott Maddox, and the LASE group for their direction and creating a terrific work environment. I also want to thank the National Nanotechnology Infrastructure Network Research Experience for Undergraduates Program and the National Science Foundation for funding.

References:

[1] Hanson M., et al.; "Strong sub-bandgap absorption in GaSb/ErSb nanocomposites attribues to plasma resonances of semimetallic ErSb"; AIP Conf Proc, 772 (2004).

[2] Burstein, E.; "Anomalous Optical Absorption Limit in InSb"; Phys Rev, 93 (1954).

[3] Moss, T.; "The Interpretation of the Properties of Indium Antimonide"; Proc Phys Soc B, 67 (1954).

[4] Wu, J., et al; "Effects of the narrow band gap on the properties of InN"; Phys Rev B, 66 (2002).

[5] Ferguson, I., et al.; "Infrared reflection and transmission of undoped and Si-doped InAs grown on GaAs by molecular beam epitaxy"; Semicond Sci Technol, 8 (1993).

[6] Spitzer, G., and Fan, H.; "Determination of Optical Constants and Carrier Effective Mass of semiconductors"; Phys Rev, 106 (1957).

Stabilizing Fiber Optic Pressure Sensor Measurements by Fabricating an Enclosed Photonic Crystal Cavity

Jacqueline Ong
General Engineering, Harvey Mudd College

NNIN REU Site: Stanford Nanofabrication Facility, Stanford University, Stanford, CA
NNIN REU Principal Investigator: Professor Olav Solgaard, Department of Electrical Engineering, Stanford University
NNIN REU Mentors: Cathy Jan and Insun Park, Department of Electrical Engineering, Stanford University
Contact: jong@hmc.edu, solgaard@stanford.edu, cathyjan@stanford.edu, insun@stanford.edu

Abstract:

Fiber optic pressure sensors are optical microelectromechanical systems (MEMS) devices used in a variety of industrial applications. Current sensors are assembled by affixing a silicon photonic crystal (PC) chip near an optical fiber-tip with a glass ferrule, which forms a Fabry-Perot (FP) cavity. However, environmental factors beyond human control decrease the sensor's overall measurement stability by inducing fluctuations in the cavity length. A potential method to reduce this variability is to incorporate the FP cavity construction into the fabrication stage of the PC itself. To accomplish this, a silicon wafer was patterned and etched downward to form PCs, which were etched radially outward to create overlapping spherical cavities. Silicon oxide was deposited by low pressure chemical vapor deposition (LPCVD) to seal off the air cavities, after which their reflectivity was measured. Many PCs were fabricated with different diameters to determine the optimal parameters that will yield the highest PC reflectivity. Based on our measurements, PCs with higher photolithographic exposure (larger diameters) are optimal. By successfully implementing this design into the fabrication process, this compact pressure sensor's measurement reproducibility will significantly improve for its industrial applications.

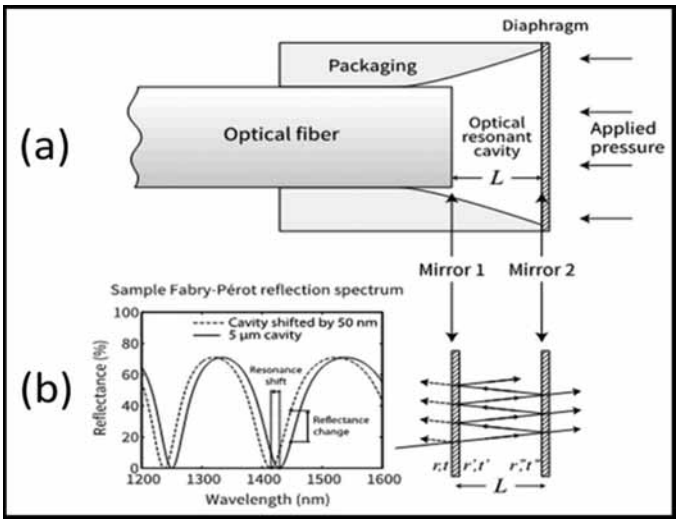

Figure 1: (a) Structure of fiber optic pressure sensor. (b) Applied pressure varies cavity length (L), and thus, shifts the reflection spectrum.

Introduction:

Fiber optic pressure sensors are used for their compactness and measurement sensitivity. Current sensors are comprised of a silicon PC chip near an optical fiber-tip, which forms the FP cavity, a cavity between two highly reflective mirrors (see Figure 1(a)). These sensors function by propagating light through the fiber, which is partially reflected from both mirrors. These reflections interfere to create the total optical reflected power as a function of wavelength (see Figure 1(b)).

However, because the FP cavity is usually assembled after fabrication, environmental factors decrease the sensor's overall measurement stability by fluctuating the cavity length during periods of constant applied pressure. To reduce measurement variability and increase measurement stability, a procedural modification was developed and implemented where an external FP cavity is constructed and sealed during the fabrication stage of the PC itself, which is confirmed by the scanning electron microscope (SEM) and PC characterization.

Photonic Crystal Fabrication Process:

To investigate the parameters that affect the reflectance performance of the FP cavity, three initial silicon wafers were prepared by undergoing oxidation. They went through photolithography, which involved patterning and developing the mask design of 2D PCs. For each PC, a square lattice of circular holes spans over 500 μm by 500 μm. The three wafers were uniformly exposed to 180 mJ/cm^2, 210 mJ/cm^2 and 240 mJ/cm^2, respectively. Once patterned and developed, they were anisotropically and isotropically etched to form overlapping spherical cavities that form the PC cavity. To seal off the finished cavity, silicon oxide is deposited via LPCVD (see Figure 2).

Results and Discussion:

In Figure 3(a), the oxide deposition mostly sealed the 240 mJ/cm^2 PC holes from the 710 nm pre-deposition diameter to the 95 nm remaining hole, but is capable of completely sealing the holes given a longer deposition. The low exposure post-

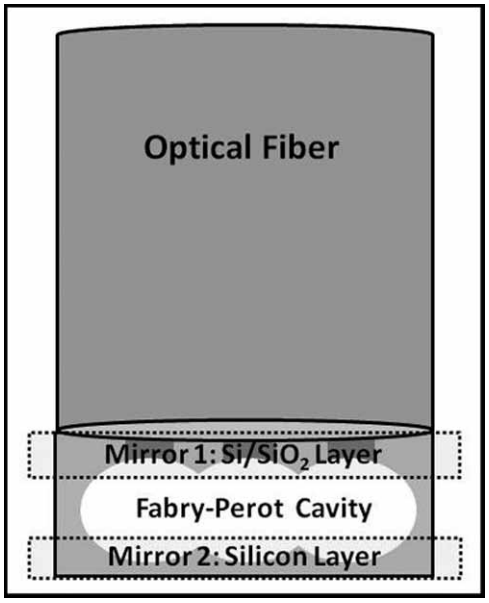

Figure 2: Cross-section of the pressure sensor. For mirror 1, grey is Si and white is SiO_2.

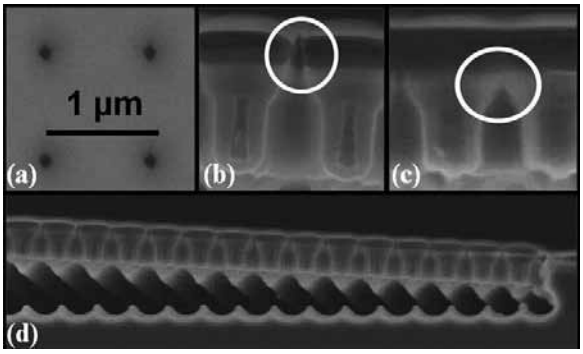

Figure 3: Post-deposition SEM images. (a) 240 mJ/cm² PC's top view. (b) 240 mJ/cm² and (c) 180 mJ/cm² cross-sectional view of PC. (d) Zoomed-out image of FP cavity from (b).

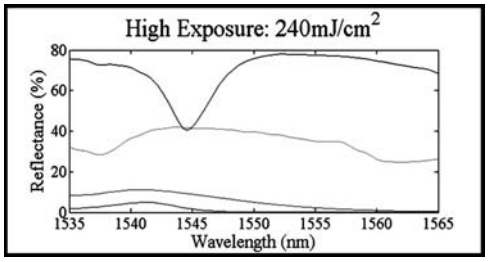

Figure 4: A single 240 mJ/cm² photonic crystal characterization, a representative reflectance spectrum for the three exposure levels of inconsistent reflectances.

deposition image (not displayed) had a remaining blur, suggesting that those holes were successfully sealed with a substantial oxide layer on top. This is confirmed in the circled portion of Figure 3(c) that indicates the 180 mJ/cm² holes closed as opposed to the 240 mJ/cm² holes. The stress that the silicon PC chip endured from oxide deposition caused the evident "buckling" (i.e. bending) effect in Figure 3(d) because of the compressive stress that the silicon oxide imparts on the silicon. The formed FP cavity has varying lengths across the entire cavity, which made the light behavior and ultimately the reflectance power spectrum inconsistent.

The freespace reflectances were measured by focusing a laser onto the PC chips and coupling the reflection into an optical spectrum analyzer. In Figure 4, each of the four curves is the reflectance recorded from four different locations on a single photonic crystal, which illustrates the inconsistent reflectance measurements observed for any PC at any of the given exposure levels by the evident dissimilar curves and reflectance values across each curve. Even though there is high measurement variability amongst the reflectances for a given photonic crystal, the higher exposure PCs have better reflectances.

Comparing the lowest and highest exposure photonic crystals (180 mJ/cm² and 240 mJ/cm²), their reflectances reached up to 21% and 80%, respectively. The higher photolithographic exposure produced a better photonic crystal reflectance most likely due to the larger holes.

Conclusions:

A fabrication method was developed that successfully seals the FP cavity, as indicated by SEM imaging. We found there is a direct relationship between the PC's reflectance and the photolithographic exposure, despite the "buckling" effect. While the low exposure PCs exhibit higher sealing capability, the high exposure PCs exhibit higher reflectance, which allows for sensors with higher sensitivity. For future work, we recommend performing pressure sensing measurements and finding methods to handle the silicon oxide "buckling."

Acknowledgments:

Thank you to Professor Olav Solgaard, Cathy Jan, and Insun Park, SNF, NNIN REU Program, NSF, and CIS for providing this opportunity to do cutting edge research.

References:

[1] Wu, et al. "Short-cavity multimode fiber-tip Fabry-Perot sensors," Optics Express, Vol. 21, Issue 12, p.14487-14499.

[2] Akkaya, et al. "Modeling and Demonstration of Thermally Stable High-Sensitivity Reproducible Acoustic Sensors," J. MEMS, V.21, No. 6, Dec.2012.

[3] Kilic, et al. "External fibre Fabry-Perot acoustic sensor based on a photonic-crystal mirror," J. IOP Science Meas. Sci. Technol., Vol. 18, 2007.

Surface Scatterers on Slab-Wave Guides for Uniform Bacteria Growth

Brandon Thomas Pereyra
Mechanical Engineering, Binghamton University

NNIN REU Site: Cornell NanoScale Science and Technology Facility, Cornell University, Ithaca, NY
NNIN REU Principal Investigator: Professor David Erickson, Sibley School of Mechanical and Aerospace Engineering, Cornell University
NNIN REU Mentor: Syed Saad Ahsan, Applied Physics, Cornell University (2007 NNIN REU at UT Austin)
Contact: bpereyr1@binghamton.edu, de54@cornell.edu, ssa27@cornell.edu

Abstract:

Stacked bioreactors are built using slab-waveguides. Light is directed into the side of the waveguide and inside the light totally-internally reflects. Using photolithography, pillars of SU-8 photoresist, with a higher index than glass, were patterned on a waveguide. SU-8 pillars acted as a mechanism to scatter light into the reactor [1]. Experiments using florescent dyes, simulating a thin biofilm, were conducted to determine the rate at which the light intensity decreases at maximum SU-8 patterning density. The decrease was fit to an exponential and used to generate a gradient of coverage along the length of the reactor required for uniform scattering light distribution. To achieve uniform light distribution, the final gradient was generated by calculating the required percentage of coverage required at every mm along the reactor. The waveguide was fabricated and tested for uniform light distribution. Finally, single-stack reactors for algal growth were assembled to test the efficacy of different scattering schemes.

Introduction:

Cultures of algae, such as the cyanobacteria *Synechococcus elongates*, grown in bioreactors are a promising source of renewable energy [2]. However, algae growth is highly dependent on light intensity and standard bioreactors do a poor job at distributing light uniformly for algae utilization due to shading [3]. The goal of a stacked bioreactor is to uniformly distribute the optimum amount of light to all of the algae growing inside the reactor.

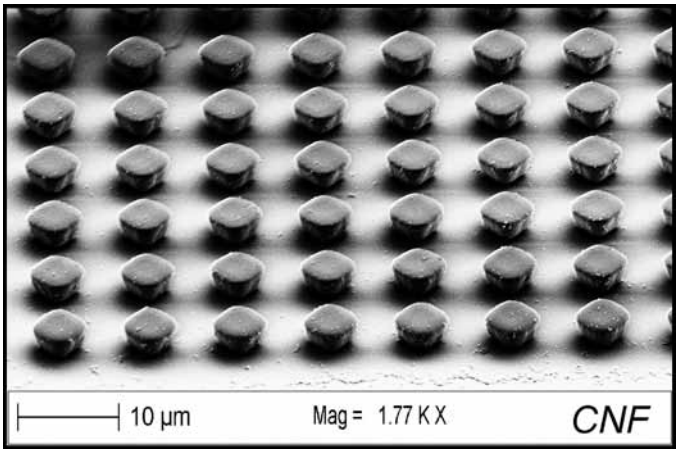

Figure 1: SEM of 25% coverage of SU-8 2002 pillars on glass surface.

Experimental Procedure:

Waveguides were made by applying SU-8 2002 photoresist (Microchem) on the surface of borosilicate glass slides with dimensions of 75 mm × 50 mm × 1 mm or 60 mm × 24 mm × 0.15 mm. The 25% uniform coverage waveguides were made by patterning an array of 5 μm by 5 μm pillars spaced 5.0 μm apart on the glass (Figure 1). Gradients of different percent coverage at each mm along the glass were constructed by changing the spacing between the pillars.

To fabricate the pillars, a 2.8 μm thick layer of SU-8 was exposed for seven seconds using hard contact exposure on the SUSS MA6-BA6 contact aligner and developed in SU-8 developer for 1 min. Chambers designed to hold florescent dye, with dimensions of 40 mm × 60 mm or 10 mm × 40 mm, were constructed using the waveguide for the top of the chamber. A mixture of 1:100 carbon black to polydimethylsiloxane (PDMS) was poured over a mold the dimensions of the SU-8 coverage, and placed in a 90°C oven for 30 min. The molded PDMS formed the base of the chamber and was bonded to the waveguide. The chambers were filled with Alexa Fluor 680 dye, by Life Technologies. The short edge of the chamber was placed 10 mm away from the center of a 10 × 10 array of LEDs, emission wavelength ~ 630 nm, spaced 2 mm apart.

The dye was imaged, at 10X magnification, with a Sony XCD-X710 Firewire Camera attached to a microscope. An image was taken over the length of the chamber every 1 mm. The average pixel intensity of each image was extracted and plotted on a graph. This data was fit to an exponential curve to determine the exponential decrease coefficient, k. The decrease coefficient for 25 percent coverage was doubled to obtain a maximum k value, at 50 percent coverage. The percentages of coverage required for the gradient design were calculated

$$k_{max} = k * \frac{SC_{max}}{SC}$$

K_{max}=maximum decrease coefficient

$$k_0 = \frac{|k_{max}|}{1 + (L * |k_{max}|)}$$

L= desired length of reactor

$$k(x) = \frac{1}{(\frac{1}{k_0} - x)}$$

SC= SU-8 surface coverage

$$SC(x) = k(x) * \frac{SC_{max}}{k_{max}}$$

The maximum surface coverage (SC_{max}) used was 50%.

Figure 2: Calculations that generate the required percent coverage of SU-8 necessary for uniform light distribution.

using k (Figure 2). The gradients for the 0.15 mm and 1 mm thick waveguides started at 6.9 and 17.8 percent coverage, respectively, and increased exponentially every 1 mm, reaching a maximum of 50% coverage at the end. The highest percent coverage used was 50%; spacing the pillars less than 2.1 μm apart resulted in pillars overlapping and forming a film.

Results and Conclusions:

With 50% uniform coverage of SU-8, the maximum decrease coefficient (k_{max}) was -0.156 for a 0.15 mm thick waveguide (Figure 3) and -0.028 for a 1 mm thick waveguide. These negative k_{max} values indicate a large exponential decrease in intensity. Our gradient of SU-8 coverage for the 0.15 mm thick waveguide improved the decrease coefficient k_{max} from -0.156 to 0.001. This low absolute value of k indicates no substantial change in light intensity along length of chamber. The gradient for the 1 mm thick waveguide was also successful, improving the decrease coefficient from -0.028 to -0.0001 (Figure 4). We have demonstrated a successful design for uniformly distributing light into a bioreactor.

Future Work:

Algae have been grown inside these waveguide chambers to measure growth. Florescent pictures of algae growing inside the reactor have been taken and will be analyzed to confirm uniform growth. The next step in our process will be to find a way to upscale our waveguide to the reactor scale. These manufacturing methods should allow for the waveguide to be mass produced. Once a manufacturing process has been selected, combining waveguide technology with nutrient delivery technology would result in a high efficiency bioreactor.

Acknowledgements:

I thank the National Science Foundation, the National Nanotechnology Infrastructure Network Research Experience for Undergraduates Program, the Cornell NanoScale Science and Technology Facility (CNF), Syed Saad Ahsan, David Erickson, Melanie-Claire Mallison, Rob Ilic, and all of the CNF Staff.

References:

[1] Garcia De Abajo, F. J.; "Colloquium: Light scattering by particle and hole arrays"; Rev. of Modern Physics, vol. 79(4), pp. 1267-1290 (2007).

[2] Ooms, M. D., et al.; "Evanescent photosynthesis"; Physical Chemistry Chemical Physics, vol. 14(14), pp. 4817-4823 (2012).

[3] Chisti, Y.; "Biodiesel from microalgae"; Biotechnology Advances, vol. 25(3), pp. 294-306 (2007).

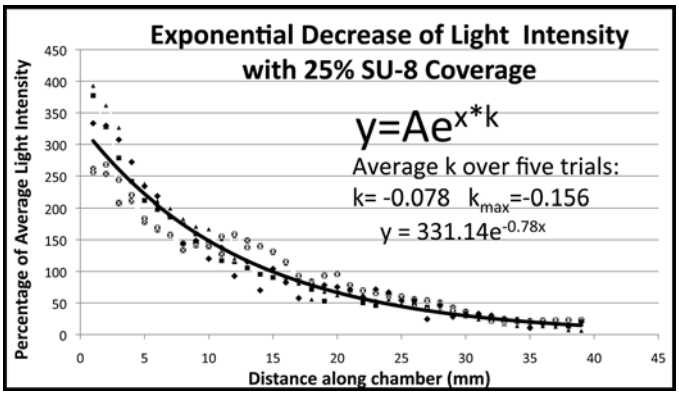

Figure 3: A graph of the exponential decrease of light intensity with 25% coverage.

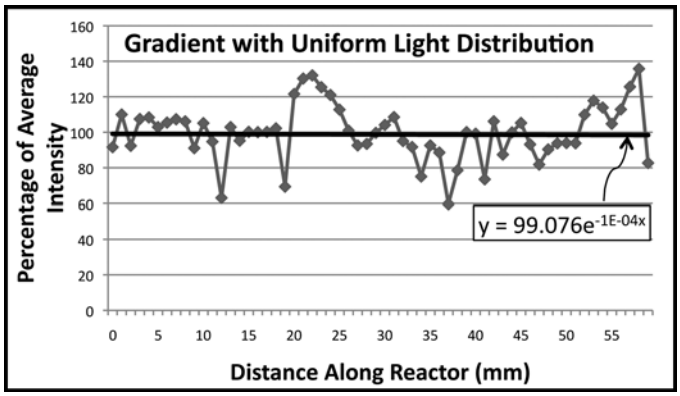

Figure 4: A graph of the light intensity over the length of a 60 mm chamber.

XPS Analysis of Sulfide and Aluminum Nitride Based Buffer Layers for Epitaxial Zinc Oxide Growth

Jacob M. Rothenberg
Physics, University of Rochester

NNIN iREU Site: National Institute for Materials Science (NIMS), Tsukuba, Ibaraki, Japan
NNIN iREU Principal Investigator: Dr. Toyohiro Chikyow, International Center for Materials Nanoarchitectonics (MANA), NIMS
NNIN iREU Mentor: Dr. Nam Nguyen, International Center for Materials Nanoarchitectonics (MANA), NIMS
Contact: jr3360@columbia.edu, chikyo.toyohiro@nims.go.jp, nguyen.nam@nims.go.jp

Abstract:

Thin films of non-polar MnS and AlN/MnS were grown on Si <100> by PLD. The chemical compositions of the samples were investigated by angle-resolved XPS. It was found that AlN serves as a barrier to preserve MnS films from oxidation. It was also found that Mn-Si bonds existed on the surface of Si, while Si-S bonding was not observed. Finally, a native SiO_x layer was observed to diffuse to the surface of the sample, residing on top of epitaxial AlN. It is also likely that a thin Al_2O_3 layer existed alongside SiO_x.

Introduction:

Group III-V nitrides have become vital in the advancement of short wavelength opto-electronic devices. Using these materials, devices like the blue-green light-emitting diode (LED) have seen rapid development in recent years. For these devices to function at their maximum potential, epitaxial gallium nitride (GaN) films are necessary. More specifically, epitaxial growth of GaN on silicon (Si) <100> is necessary for integration of these devices in widespread technology. Unfortunately, there has been some difficulty in growing polar GaN <0001> on Si <100> substrates. In addition, the polar nature of GaN <0001> reduces the quantum efficiency through spontaneous and piezoelectric polarizations. Electrostatic fields that arise from these effects located at the interfaces of the heterostructure lead to band bending and separation of electron-hole pairs, as shown in Figure 1.

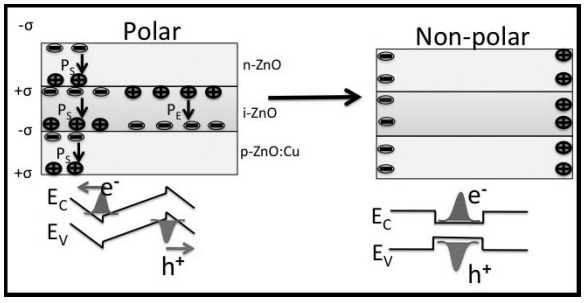

Figure 1: Electrostatic fields reduced in non-polar structure, resulting in reduction of bend bending and higher quantum efficiency [2].

In order to minimize these effects, work has been done to grow epitaxial non-polar <11-20> GaN on Si substrates. This goal was realized using manganese sulfide (MnS) <100> and aluminum nitride (AlN) <11-20> as buffer layers [1]. Work was done in this study to examine the chemical states that exist in these buffer layers.

Experimental Procedure:

Si <100> substrates were first cleaned by hydrogen fluoride (HF) etching to remove the native silicon dioxide (SiO_2) layer. MnS was deposited using pulsed laser deposition (PLD) using a substrate temperature of 700°C and pressure (P) of 3×10^{-7} torr to ensure clean MnS films. The film was then post-annealed for 30 minutes at 700°C and $P = 2 \times 10^{-7}$ torr to further improve the film quality. AlN was then deposited using PLD at a temperature of 700°C and $P(N_2) = 1 \times 10^{-4}$ torr, with a post anneal time of five minutes at 700°C. Analysis of the films was performed using angle-resolved x-ray photoelectron spectroscopy (XPS). Due to the shallow penetration depth of XPS, the thickness of MnS and AlN films were kept between 2.5-5.0 nm.

Results:

Figure 2 shows XPS results of the Sulfur 2p peak. Comparison of the left graph (2.5 nm MnS / Si) to the right graph (2.5 nm AlN / 2.5 nm MnS / Si) demonstrates that AlN acts as a protective layer for MnS against oxidation and allows for epitaxial MnS growth. Figure 3 shows XPS results of the Manganese 2p peak. The shoulder in the right graph is strongly indicative of Mn-Si bonding. In XPS larger angles correspond to information about deeper in the sample, so the sharp 90-degree peak and absence of a 30-degree peak means that Mn-Si bonding is located against the substrate.

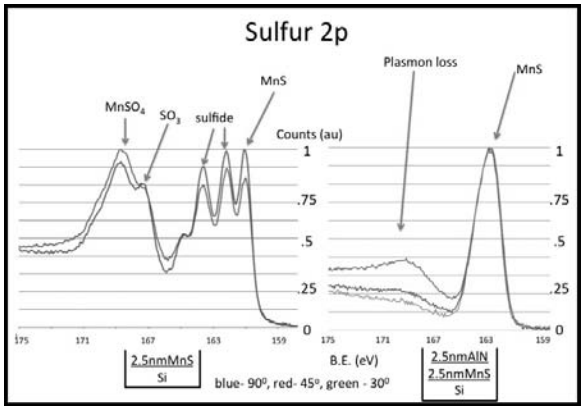

Figure 2: AlN acting as a protective layer for MnS, preventing other oxide states from forming.

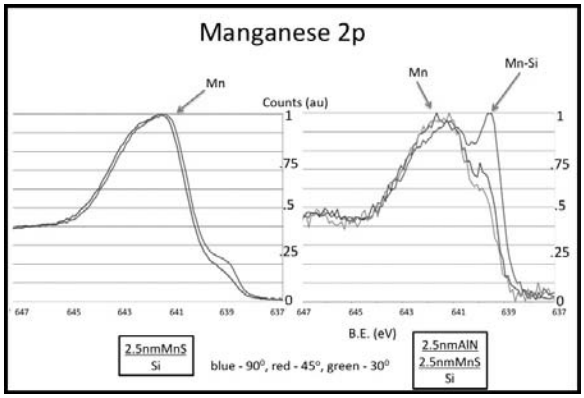

Figure 3: Formation of Mn-Si bonding observed in AlN/MnS/Si sample.

This result demonstrates that only Mn interacts with the Si substrate, while sulfur does not. While it is unclear whether there is a MnSi layer or if Si is simply bonding to Mn at the Mn/Si interface, Mn-Si bonding was clearly shown.

In addition, XPS analysis of the Silicon 2p peak (not shown) provided evidence that SiO_x is present in the structure. The angular resolution of the measurements showed that SiO_x diffuses to the surface of the thin-film structure, along with a probable monolayer of Al_2O_3. Examination of the aluminum and nitrogen peaks showed that AlN was epitaxial. These findings led us to model the buffer layer structure as shown in Figure 4.

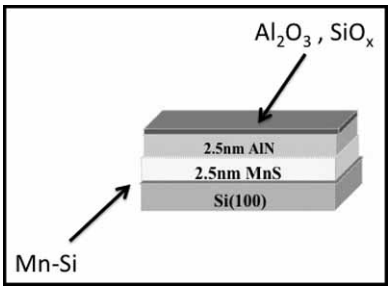

Figure 4: Model of buffer layer structure chemical composition.

Conclusions:

It was found that AlN serves as protective barrier for MnS against oxidation and that a thin layer of AlN allows for epitaxial MnS growth. From the Manganese 2p spectra, it was found that Mn-Si bonding is formed at Si/MnS interface while no S-Si bonding was formed. Lastly, SiO_x and Al_2O_3 (likely) exist at surface of structure. It was found that SiO_x diffuses to the surface of AlN regardless of the thickness of AlN.

Acknowledgements:

I would like to thank Dr. Toyohiro Chikyow, Dr. Nam Nguyen, Dr. Akihiro Tanaka, NIMS, NNIN iREU Program, and the NSF for providing me with a memorable and rewarding experience this summer.

References:

[1] Song, J.-H., Y.-Z. Yoo, T. Sekiguchi, K. Nakajima, P. Ahmet, T. Chikyow, K. Okuno, M. Sumiya, and H. Koinuma. "Growth of Non-polar a-plane III-nitride Thin Films on Si(100) Using Non-polar Plane Buffer Layer." Physica Status Solidi (C) 2524 (7) (December): 2520-2524. doi:10.1002/pssc.200303444. http://doi.wiley.com/10.1002/pssc.200303444. 2003.

[2] Jeong-Hwan Song,"Epitaxial Growth of Nitride on Si with Sulfide Buffer Layer", Ph.D Dissertation, Department of Innovative and Engineered Materials, Tokyo Institute of Technology, 2002.

Influence of the Type of Wetting Layer on the Contact Resistance in Metal-Graphene Ohmic Contacts

Yuki Sunayama
Graduate School of Engineering, University of Shiga Prefecture, Japan

NNIN iREG Site: Colorado Nanofabrication Laboratory, University of Colorado, Boulder, CO
NNIN iREG Principal Investigator: Professor Thomas R. Schibli, Physics, University of Colorado
NNIN iREG Mentor: Chien-Chung Lee, Physics, University of Colorado
Contact: zn21ysunayama@ec.usp.ac.jp, trs@colorado.edu, chienchung.lee@colorado.edu

Abstract:

In recent years, graphene has received a lot of attention because of its unique features, such as its high mechanical strength, its unique optical properties and the ultrahigh electron mobility. These unique properties promise a wealth of novel applications and devices. For example, graphene-based ultrathin and ultra-broadband electro-optic modulators, which employ the electrostatic-doping-induced transparency of graphene to create a voltage-controlled optical absorption, have enabled a variety of new applications. The ultra-high carrier mobility also promises transistors with switching speeds well in the terahertz range. However, we must take the evil with the good, as fabricating devices that rely on a single molecular organic layer can be very challenging. One of the main challenges is to fabricate ohmic metal contacts on graphene, as the density of states near the Dirac point is low. High contact resistance in such thin devices can severely degrade the performance. In this study, we focused on the influences of wetting metal layers and doping of graphene on the metal-graphene contact resistance.

Introduction:

Electronic and optoelectronic devices exhibit parasitic capacitance, which, if paired with a series resistance, limits the useful bandwidth of a device. To fabricate ohmic contact on semiconducting materials, it is necessary to avoid a Schottky potential barrier by choosing metal that allows the majority carriers to flow freely in and out of the semiconductor. For graphene, which is typically hole-doped in ambient conditions, this implies that the work function of metal should be higher than the energy gap between vacuum and graphene's Fermi level. In this work we investigated the influence of the contacting metal on the series resistance in graphene devices.

Experimental Procedure:

As shown in Figure 1, silicon wafers were used as both the substrate and the back-gate electrode. A 260-nm-thick aluminum oxide (Al_2O_3) layer was deposited on the wafer by DC reactive sputtering (Target: Al metal, Pressure: 3 mTorr, Argon flow: 32 sccm, Oxygen flow: 1.6 sccm, Deposition rate: 9 nm/min). The breakdown voltage of the Al_2O_3 was measured to determine the allowable range of gating voltages. Monolayer graphene — synthesized by chemical vapor deposition on copper — was then transferred onto the dielectric and patterned by a reactive ion etch. To investigate the effects of adhesion layer on the contact resistance, three metals (10 nm Cr, Ni, and Ti) were used in combination with Al (100 nm). These metal electrodes were thermally evaporated and patterned by a lift-off process.

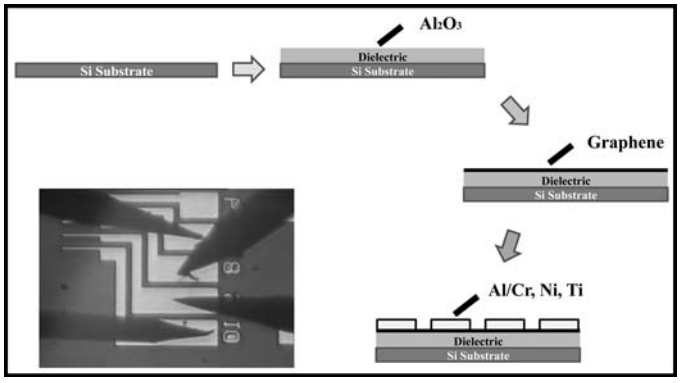

Figure 1: Schematic diagram of the fabrication.

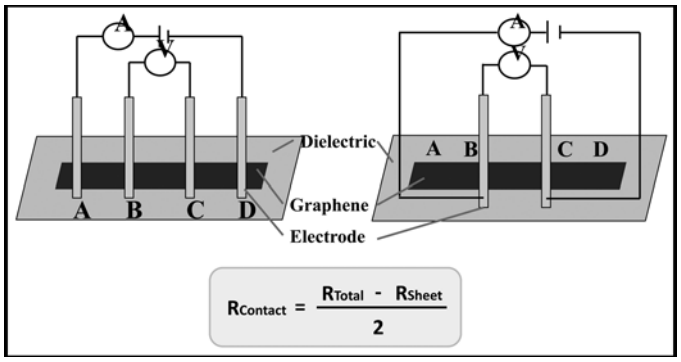

Figure 2: Breakdown voltage measurement.

To measure the contact resistance, a four-point probe method was employed: four electrodes were used to measure the sheet

OPTS

resistance of the graphene between the inner electrodes (see Figure 2, B and C). Then the two probes were moved from A and D to the inner two contacts (B and C), to measure the total resistance between the metal and the graphene at the contacts. B and C was then given by the difference between these two measured values. Compared to a transmission line method, our method was much less subject to cracks in graphene, and individual pairs of contact resistance could be measured instead of an averaged value.

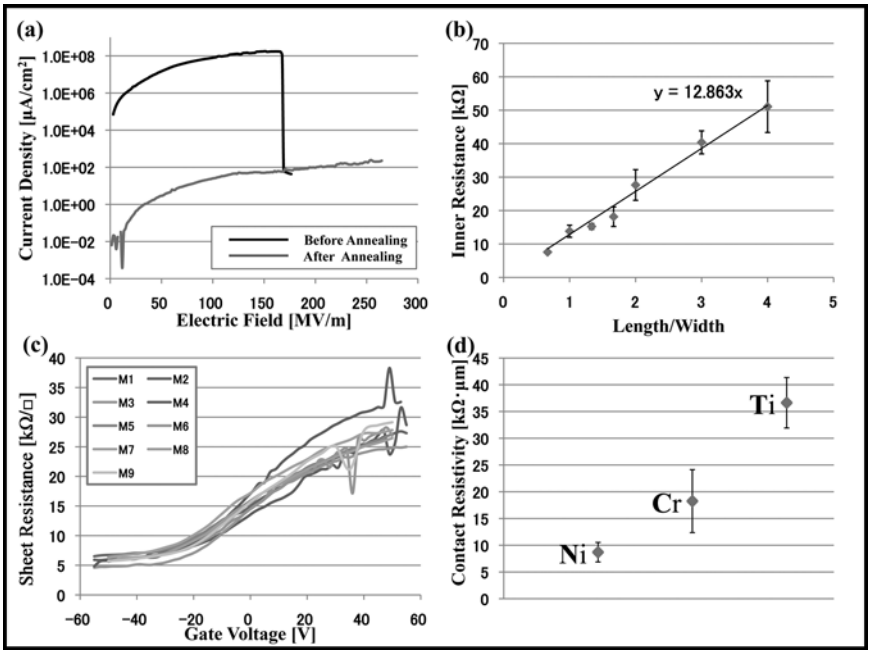

Figure 3: (a) Breakdown voltage of Al_2O_3 before and after annealing the sample at 500°C. (b) The dependence of the resistance of the graphene-bridge vs. the length/width ratio of the graphene between the two center contacts. (c) Influence of the field-gating on the sheet resistance of the graphene. (d) The dependence of contact resistance on types of adhesion layer metals.

Results and Discussion:

Without annealing, the DC sputtered Al_2O_3 layer showed very high leakage currents (see Figure 3a). After annealing the oxide layer at 500°C in H_2 and N_2 atmosphere, the leakage current was significantly reduced and the break-down voltage was measured to be ~280 MV/m.

Figure 3b shows the dependence of the sheet resistance on the length/width ratio of the graphene. From the slope of the line-fit to the data one can infer that the sheet resistance of the un-gated graphene is 12.8 ± 0.5 kΩ/□.

Figure 3(c) shows the dependence of the sheet resistance on the gating voltage. Field doping effectively changes the sheet resistance between 5 and 28 kΩ/□, for gate voltages of the order of ± 50 V, respectively. The carrier density was calculated to be 9.03×10^{12} cm^2, assuming that the Dirac point is near 55 V.

Figure 3(d) shows the influence of the choice of the metal adhesion layer on the contact resistance. Nickel showed the lowest contact resistance (8.7 ± 1.8 kΩ•μm) of the three, while titanium lead to the highest resistance of 36.6 ± 4.7 kΩ•μm.

Conclusions:

We have shown that aluminum oxide can be deposited by reactive sputtering and, when annealed, can serve as a good dielectric for electric field strength up to 280 MV/m. There was a clear influence of the wetting metal on the contact resistance in the fabricated devices. In particular we found that nickel (ϕ ~ 5.2 eV) provides the lowest contact resistance (~ 8.7 ± 1.8 kΩ•μm) and titanium (ϕ ~ 3.8 eV) led to the highest contact resistance (~ 36.6 ± 4.7 kΩ•μm). Our result is in agreement with the result reported by Giovannetti et al. [1].

Acknowledgements:

I would like to offer my special thanks to my principal investigator Prof. Thomas R. Schibli and my mentor Chien-Chung Lee for their support and encouragement. And also special thanks go to the Colorado Nanofabrication Laboratory (CNL) staffs. I would also like to express my gratitude to the National Institute for Materials Science in Japan and the NNIN iREG Program for their financial support.

References:

[1] G. Giovannetti, et al., "Doping graphene with metal contacts." Phys. Rev. Lett 101 (2008) 026803

Graphene-Based Electro-Optic Modulator Fabrication

Michael Sunyak
Electrical Engineering, Ohio Northern University

NNIN REU Site: Colorado Nanofabrication Laboratory, University of Colorado, Boulder, CO
NNIN REU Principal Investigator: Prof. Thomas R. Schibli, Physics, University of Colorado
NNIN REU Mentor: Chien-Chung Lee, Physics, University of Colorado
Contact: m-sunyak@onu.edu, trs@colorado.edu, chienchunglee@colorado.edu

Abstract:

Graphene exhibits many useful properties including high carrier mobility, fast relaxation of photo-excited carriers, and carrier-density-dependent optical absorption. Because of graphene's unique band structure, an external electric field can be used to change its carrier density and thus its optical absorption. Graphene modulators fabricated based on this principle have been employed as fast actuators to stabilize unwanted noise in lasers, paving the way to a new generation of ultra-low-noise optical frequency synthesizers. Although graphene modulators provide the above-mentioned benefits, during their fabrication it remains challenging to prevent defects introduced by chemicals, such as photoresists and developers, or processes such as sputtering and UV light exposure. In this work, we established a wet-etch fabrication procedure for patterning the metallic contact on graphene in graphene-based electro-optic modulators. Different approaches of wet-etching were investigated, which included the use of different metals.

Introduction:

Graphene exhibits strong interband absorption (~2.3%) for visible and near-infrared light. The interband transition is highly sensitive to the density of charge carriers, due to graphene's cone-like band structure. It is possible to prohibit the interband transition at low photon energies by increasing the carrier density through electrostatic doping. To achieve this, we employed a gated graphene structure with a dielectric. By applying a voltage between the gates, we induced an electric field in the dielectric.

The thickness of such a dielectric layer was selected to have an optical thickness that was a quarter wavelength for light at 1550 nm. This maximized the interaction between incident light and the graphene on the dielectric. Modulators with a ring shape were chosen to provide a more uniform modulation over the active area. The backgate served a second function as a mirror, in our modulators.

Previously, a liftoff method was used to produce metal contacts on graphene. In this new procedure, metal covering the whole graphene surface was wet-etched. As Figure 1 shows, by using this wet-etch fabrication procedure, sources of doping and defects could be better controlled, and UV and photoresist contamination was completely eliminated. Exposing graphene to etchants, rather than photoresists and developers offered more control over potential sources of chemical contamination.

Etchants offer a wide variety of options, whereas photoresists and developers are limited to a few suitable products.

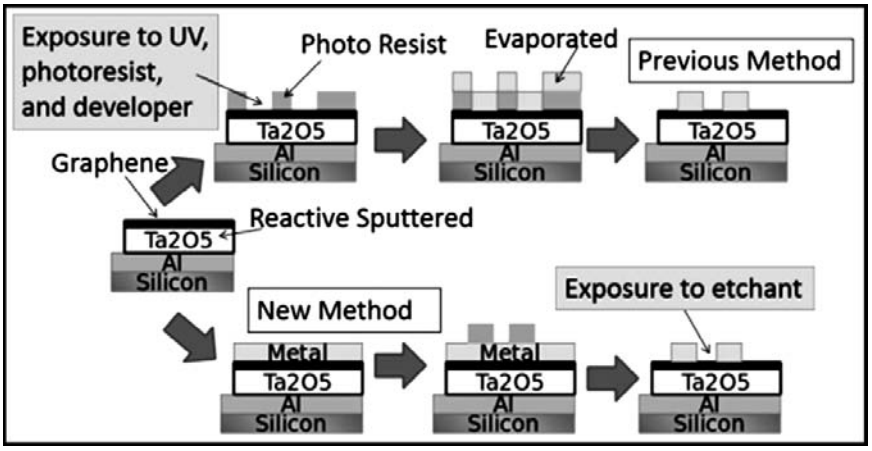

Figure 1: Differences between the previous and new fabrication process.

Experimental Procedure:

A 100 nm layer of aluminum (Al) was evaporated onto a silicon substrate, and subsequently patterned via wet-etch. Tantalum pentoxide (Ta_2O_5, 185 nm) was deposited via DC reactive sputtering. Ta_2O_5 features a high permittivity, transparency, and breakdown voltage. Monolayer graphene sheets were prepared via chemical vapor deposition (CVD) and transferred onto the Ta_2O_5 layer. Several different metals, of varying thicknesses, were evaporated onto the graphene, and subsequently patterned via wet-etch.

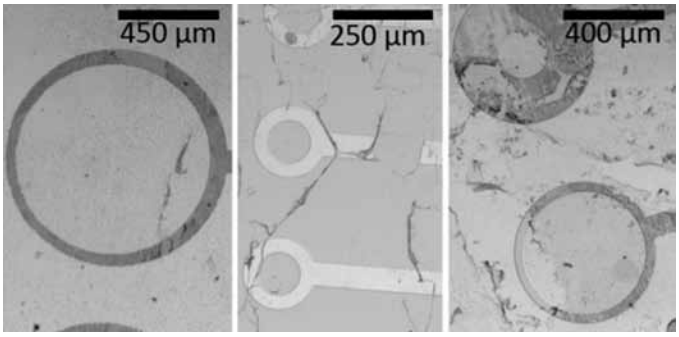

Figure 2: Modulators with 35 nm Ni (Left), 10 nm Ni and 100 nm Al (Middle), and 10 nm Ni and 85 nm Au (Right).

Results and Discussion:

There were also drawbacks to using wet-etch fabrication procedures. Photoresist adhesion to metal was a large issue. Certain etchants lifted off resist around the edge of metal structures. This effectively caused a lateral etching in excess of 30 μm in the worst cases. Adhesion to graphene was another issue; some chemical etchants caused the metal to lift off of the graphene or the graphene off of the Ta_2O_5. Backgate liftoff also occurred, as the porosity of the sputtered Ta_2O_5 layer allowed the etchant to penetrate and lift the Al backgate off of the substrate. Careful selection of metals and metal etchants, as well as annealing of the Ta_2O_5 effectively improved the quality of the devices.

Figure 2 shows functioning devices that were fabricated using this new method. The three top gates consisted of 35 nm nickel (Ni), a 10 nm Ni adhesion layer with 100 nm Al on top, and a 10 nm Ni adhesion layer with 85 nm gold (Au). The addition of the Ni layer improved the adhesion of the top gate to the graphene layer. Ni was etched with low concentration nitric acid (HNO_3), Al with Transene Al Etchant Type A, and Au with Gold Etchant Type TFA.

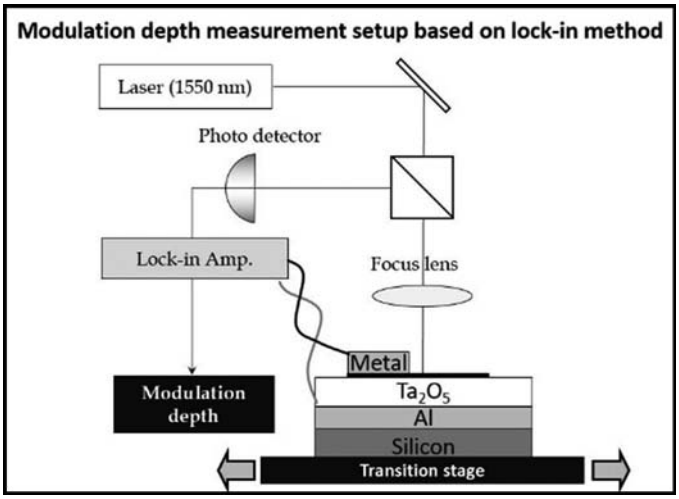

Figure 3: Modulation depth measurement setup.

We examined the performance of the modulators using the setup shown in Figure 3. A continuous wave laser illuminated the modulator, while a sinusoidal voltage applied between the graphene and the metal mirror provoked the optical modulation. A computer-controlled x-y stage was employed to raster scan and produce a modulation heat map of the devices.

Figure 4 shows that although there were some breaks in the graphene, we were able to achieve a measurable modulation depth across a large area of nearly 1 mm in diameter. Outside of the contacting ring, no modulation was observed as the graphene was removed to reduce device capacitance.

Conclusions and Future Work:

We were able to establish a wet-etch fabrication procedure for electric contacts on graphene without deteriorating the electronic properties of graphene. With this new procedure we fabricated functioning graphene-based electro-optic modulators. Further studies are needed to show if this wet-etch fabrication procedure really offers improvements in the electrical and optical performance of the modulators. Raman spectroscopy performed on both sets of graphene, would for instance allow one to quantify the defects created in graphene by either process. The results of such a study may be significant for any graphene-based electronic devices. These initial results, however, already show a lot of promise.

Acknowledgements:

I would like to thank the National Science Foundation and National Nanotechnology Infrastructure Network for funding this REU project and program. I would also like to thank the University of Colorado for their support. Special thanks go to Chien-Chung Lee and Thomas R. Schibli for their guidance. I would like to thank Bart Van Zeghbroeck, Tomoko Borsa, Tzu-Min Ou, Ryan Brow, and Zefram Marks.

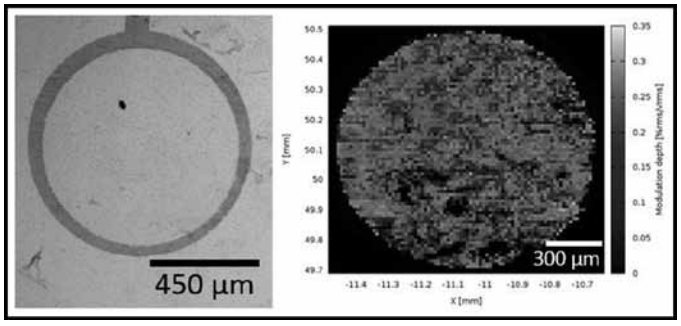

Figure 4: Optical microscope image (Left) and modulation depth measurement (Right) of a completed ring modulator.

Resistive Switching in Tantalum Oxide with Varying Oxygen Content

Adam Zachary Blonsky
Physics, University of Wisconsin - Madison

NNIN iREU Site: Institut Für Bio- Und Nanosysteme (IBN), Forschungszentrum, Jülich, Germany
NNIN iREU Principal Investigator: Dr. Regina Dittmann, PGI-7, Jülich Forschungszentrum
NNIN iREU Mentor: Katharina Skaja, PGI-7, Jülich Forschungszentrum
Contact: azblonsky@gmail.com r.dittmann@fz-juelich.de k.skaja@fz-juelich.de

Abstract:

Silicon based non-volatile memory is nearing its practical limit and several other possibilities are being examined more closely as potential replacements. One of these possible replacements is resistive switching. Resistive switching is a phenomenon in which a metal-insulator-metal (MIM) structure can change to a low resistance state (LRS) at the application of a set voltage and then be switched back to a high resistance state (HRS) by the application of a reset voltage [1]. Much about resistive switching is still unknown in regards to which materials switch and why. Our group examined how the various set and reset voltages of tantalum oxide (TaO_x) changed when prepared with different oxygen to argon ratios during sputtering. By performing electrical characterization of the samples with a basic probe station, we were able to determine the set and reset voltages of each sample, each with differing oxygen contents during formation. Ultimately it was found that the oxygen content during sample preparation changed the initial resistance as expected but did not change the set or reset voltages.

Introduction:

Resistive switching is an interesting phenomenon of certain metal-insulator-metal (MIM) devices where, when a threshold voltage, called the forming voltage, is applied to them, the resistance changes by orders of magnitude. This switching may then be undone by the application of another voltage, called the reset voltage, in the opposite direction, or it may be redone by applying a slightly lower threshold voltage in the original direction and is called the set voltage. This set-reset action can then be cycled. It is thought that the mechanism behind resistive switching is filamentary switching in which a controlled breakdown of the MIM device, caused by the forming voltage, allows for the creation of a conductive filament through the insulator [2]. This filament is then partially destroyed when the reset voltage is applied and is repaired when the set voltage is applied as shown in Figure 1.

Methodology:

In this project, we examined TaO_x, which is a very stable resistive switching material [2]. More specifically we aimed to discover how the switching characteristics of TaO_x (forming, set, and reset voltages) changed when the ratio of argon to oxygen was changed during the initial preparation of the samples. This oxygen to argon ratio was manipulated during the reactive sputtering of the TaO_x and was done in steps of 5% oxygen starting from 10% oxygen to argon all the way to 25% oxygen to argon. The full process of sputtering and device fabrication is outlined in Figure 2.

After the devices were fabricated, characterization was done with an automatic IV probe station. The probe station characterized the 1.5 μm pad size probe and

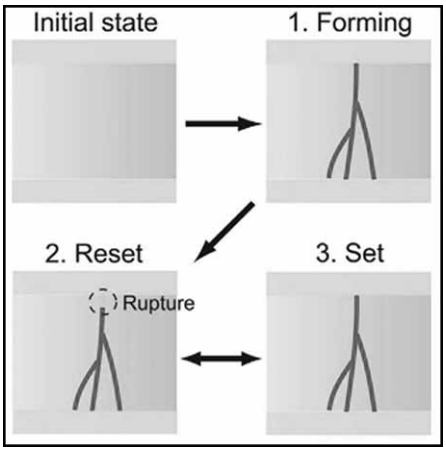

Figure 1: Simple model of the filamentary mechanism [3]. A conductive path is created that provides a low resistance path and then is reset to the original resistance.

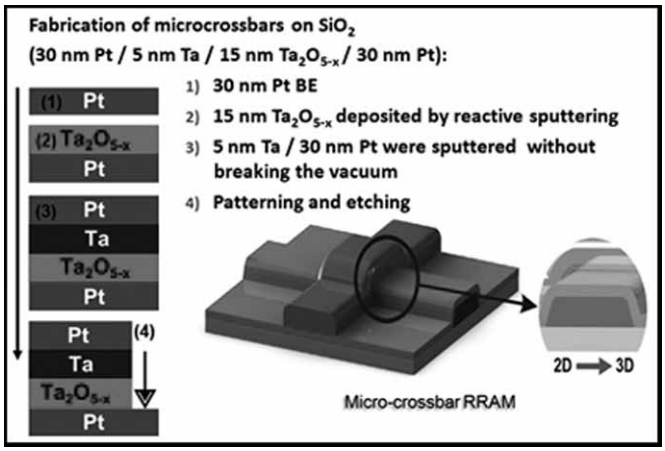

Figure 2: Outline of the device fabrication process for TaO_x devices.

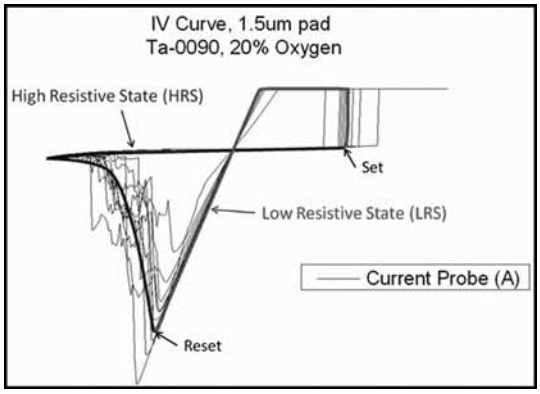

Figure 3: Quasistatic IV curve of a specific trial. Note the two resistive states as well as the set and reset voltage for this stable switching. The plateau arises from the current compliance of the system.

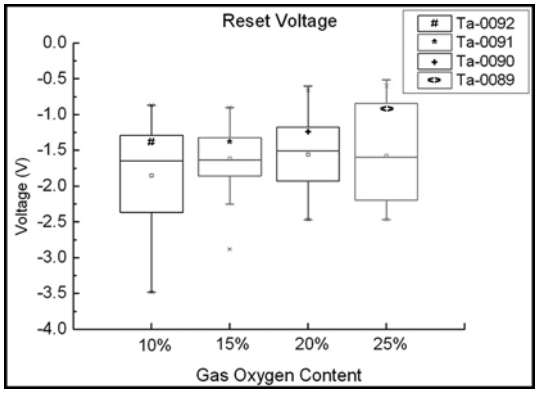

Figure 4: Reset voltage versus oxygen content during sputtering. No apparent relationship between the two.

ran one forming cycle from 0 to 4 volts with a step size of 30 mV, a hold time of 30 ms and a current compliance of 0.2 mA. Then ten set-reset cycles were run with a max voltage of 3.5V, a minimum voltage of -2V, a step size of 30 mV, hold time of 30 ms and a 0.2 mA current compliance up and 20 mA current compliance down. This process was then done on each possible device on the sample totaling about 100 devices per sample depending on availability of the autoprobe.

Results:

Overall there was stable switching of the TaO_x devices. One device example is shown in Figure 3. This allowed for median set, reset and forming voltages to be gathered from the data sets. Ultimately there was no overall trend with set, reset or forming voltages and the changing oxygen contents of the devices as shown in Figure 4. The median set voltage was about 2V, the median reset voltage was about -1.75V and the median forming voltage was about 2.5V with only minor changes with different oxygen content.

Discussion and Future Work:

In the end, the oxygen content during sputtering and sample preparation had no effect on the switching characteristics, which shows that the filamentary mechanism is fully independent of different oxygen content during deposition. In the future, examination of other materials may be worthwhile such as TiO_x in order to see if this oxygen independence during sample deposition is specific to TaO_x or is due to the filamentary mechanism.

Acknowledgements:

I would like to acknowledge the National Nanotechnology Infrastructure Network and their International Research Experience for Undergraduates (iREU) Program, the National Science Foundation and the Jülich Forschungszentrum for allowing me this great opportunity. I would also like to thank my principal investigator, Regina Dittmann, my mentor, Katharina Skaja, and my colleague, Benedikt Arndt. Each of them both helped me in my research and aided me in feeling welcome during my stay in Germany. I would also like to thank my entire lab group for their fantastic suggestions about where I should travel and what to do while there.

References:

[1] R. Waser, et al. Nanoelectronics and Information Technology, Chapter 30, Wiley-VCH, 2012. Print.

[2] C. Lee, et al. IEEE Elec. Dev. Lett, 32 399-401 (2011).

[3] A. Sawa, Materials Today, 11 28-36 (2008).

Understanding Magnetic Plasmon Mode Mixing Using Electron Energy Loss Spectroscopy

Harrison J. Goldwyn
Physics, University of California Santa Barbara

NNIN REU Site: NanoTech User Facility, University of Washington, Seattle, WA
NNIN REU Principal Investigator: David J. Masiello, Chemistry, University of Washington
NNIN REU Mentor: Nicholas W. Bigelow, Chemistry, University of Washington
Contact: harrisongoldwyn@gmail.com, masiello@u.washington.edu, nicholas.bigelow@gmail.com

Abstract:

Circular clusters of gold nanoparticles (Au NPs) support collective magnetically characterized plasmons. Because of their low energy loss and phase dependent bonding characteristics, magnetic plasmons show potential for use in sub-wavelength optical circuitry [1] as well as artificial conjugated molecules [2]. In order to utilize magnetic plasmons in application, a detailed understanding of the mode mixing involved must be developed. Because nanoparticle clusters that support magnetic plasmons are composite, their mode structures are inevitably complex. This project began as a pursuit to describe the fundamental oscillatory modes of some magnetic plasmon supporting systems using electron energy loss spectroscopy (EELS). Over time, the project evolved and focus shifted to a specific structure with interesting magnetic modes capable of being described using the language of hybridized molecular orbital theory.

Computational Method:

All simulations were accomplished using an in-house modified version of Bruce T. Draine's Discrete Dipole Approximation code (DDSCAT) [3]. The DDA approximates a scatterer as a Cartesian grid of polarizable points. The polarization at grid location j is determined by the incident field and the induced fields of all grid points ≠ j. Polarizations of all grid points form a coupled system of equations that can be solved iteratively to convergence. Our version of the DDA incorporates the electron beam as a field source (eDDA) [4]. The eDDA expands our observation of scattering objects because it is an experimentally viable local field source.

Magnetic Plasmon and EELS:

The magnetic plasmon referenced is actually a coherent excitation of circularly polarized electric dipole plasmons. The oscillating electric dipoles form oscillating currents in the structures that support this plasmon (see Figures 1 and 2). These oscillating currents give rise to oscillating magnetic dipoles that characterize the oscillatory mode of interest.

While stimulating the magnetic plasmon mode with an electron-beam (e-beam) requires careful consideration of symmetry, it also allows access to modes not accessible by plane-wave light. In order to stimulate the circular polarizations necessary to mediate alternating currents, the system of particle cluster and beam must posses the proper symmetry.

For the Decamer structure shown in Figure 1, a pair of alternating currents can be stimulated by position of the e-beam very close the outer edge of one of the center particles. The passing electron polarizes the close

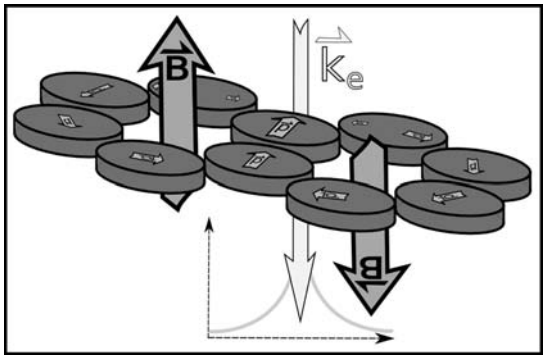

Figure 1: Correct stimulation of magnetic plasmon in decamer using the e-beam. Individual cylinder electric dipole plasmons are shown using polarization arrows (defined negative to positive).

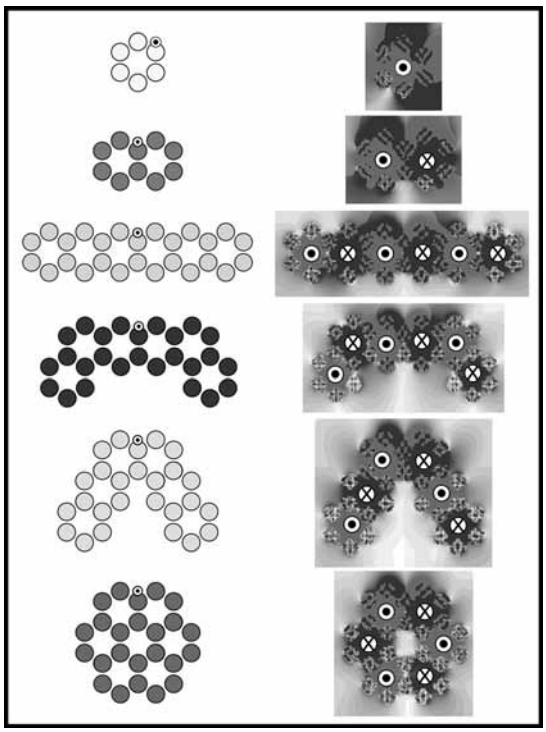

Figure 2: In case of greyscale printing, the magnetic field direction will be marked qualitatively. Beam location is marked per structure. (See full-color version on inside cover.)

PHYS

center particle more than its pair of symmetric neighbors; thus, alternating currents propagate around the two hexamers and two opposing magnetic dipoles begin to oscillate.

Magnetic Plasmon in Various Structures:

Using the simulation methods described above, we confirmed the existence of the magnetic plasmon in six conjugated hexamer structures (relatively normalized field plots seen in Figure 2). For all structures, the hexamer subunit consists of six gold cylinders (260 nm diameter, 80 nm height) — each pair separated by 30 nm. Although the e-beam excitation was local, the magnetic plasmon propagated though neighboring hexamer sub-units, making the magnetic plasmon useful for sub-wavelength optical circuitry.

The EELS for all six structures is shown in Figure 3. Although all six structures supported the same scattered magnetic field in the same spectral range, their EEL spectra were very different. Instead of seeing a spectral peak normally characteristic of a resonance, we saw steep Fano-like line shapes. At that point we could only assume that these obscure shapes were caused by Fano-like interference of the normal oscillatory modes. If this was the case, the spectra imply extremely complicated mode interference.

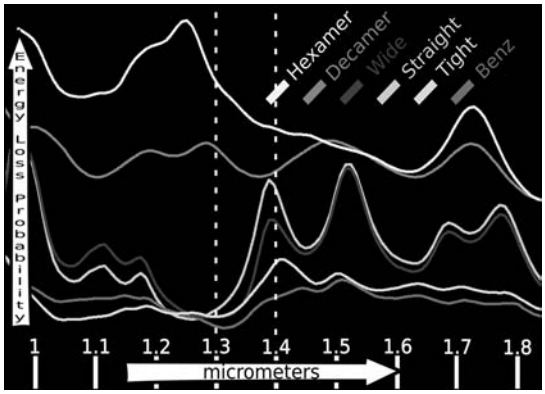

Figure 3: EELS for all six structures.

Artificial Conjugated Molecules:

Now that we understood when and where magnetic plasmons would arise, we began to describe the fundamental mode mixing that was occurring below the surface. In order to avoid the reality of our extremely complicated system of coupled oscillators (the billions of electrons), we decided to model the system as only interactions between neighboring magnetic dipoles. This simplified system is already well understood using molecular Huckel Theory. The task was complicated by the fact that our benzene equivalent structure had less symmetry than molecular benzene.

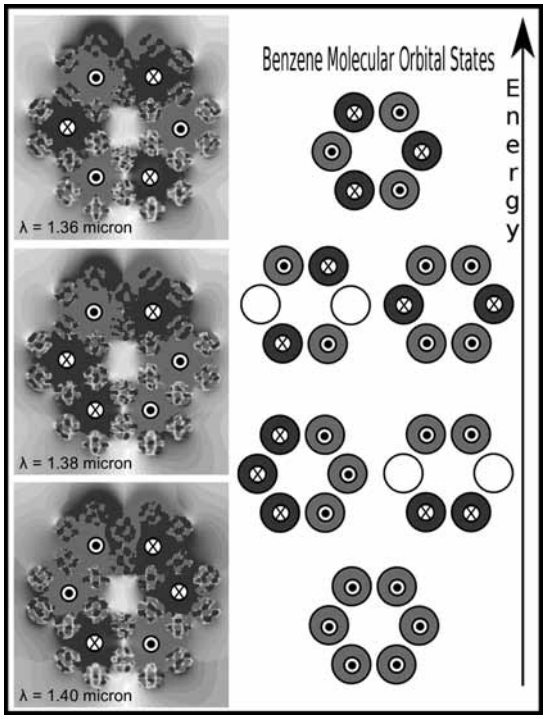

Figure 4: The two lower energy magnetic modes that appear in our benzene analog.

Future Work:

So far, our model describes the two lower energy magnetic modes that appear in our benzene analog (shown in Figure 4) as combinations of three benzene molecular states. We will continue to access our structures for use as molecular models by showing existence of the remaining benzene modes.

Acknowledgements:

David Masiello, Nicholas Bigelow, Mack Carter, the NNIN REU Program, and NSF.

References:

[1] N. Liu, et al. Manipulating Magnetic Plasmon Propagation in Metallic Nanocluster Networks. ACS Nano 6, 5482 (2012).

[2] N. Liu, et al. Magnetic Plasmon Formation and Propagation in Artificial Aromatic Molecules. Nano Lett. 12, 364 (2012).

[3] B. T. Draine. The Discrete-Dipole Approximation and Its Application to Interstellar Graphite Grains. The Astrophysical Journal, 333:848-872, 1988 October 15.

[4] N.W. Bigelow, et al. Signatures of Fano Interferences in the EELS and Cathodo-luminescence of Symmetry-Broken Nanorod Dimers. ACS Nano 2013 7 (5), 4511-19.

Mobile Targeted Objects Steered by Chemical Micropumps

Kyle Marshall
Chemical Engineering, The University of Arizona

NNIN REU Site: Penn State Nanofabrication Laboratory, The Pennsylvania State University, University Park, PA
NNIN REU Principal Investigator: Dr. Darrell Velegol, Chemical Engineering, The Pennsylvania State University
NNIN REU Mentor: Abhishek Kar, Chemical Engineering, The Pennsylvania State University
Contact: kpm1@email.arizona.edu, velegol@engr.psu.edu, ayk5241@.psu.edu

Abstract:

Catalytic nanomotors are bimetallic nanorods that move spontaneously in a solution of hydrogen peroxide (H_2O_2). However, these nanomotors move in random pathways. This research aimed to steer these nanomotors using chemical micropumps, such as calcium carbonate ($CaCO_3$) microparticles, which generate radial diffusioosmotic flows. Here we have shown a nanorod moving with directionality using three $CaCO_3$ micropumps. We also investigated the fabrication of a large, tunable array of micropumps by growing $CaCO_3$ in microwells on a lithographed, PDMS surface. Currently the method of growing $CaCO_3$ in this array of microwells is being refined and we hope to eventually use this method to steer nanorods in strategically-patterned arrays.

Introduction:

In our lab, we study micron-sized particles, such as gold platinum (AuPt) nanorods, that spontaneously move in a solution of H_2O_2, as shown in Figure 1. The movement of these nanorods in H_2O_2 occurs due to a phenomenon known as autoelectrophoresis. The catalytic reaction of H_2O_2 around the bimetallic nanorods creates a self-generated electric field, which then propels the nanorods forward [1]. Recently it has been found that chemical micropumps operate under a similar phenomenon known as autodiffusiophoresis. The dissolution of salt microparticles, such as $CaCO_3$, in an aqueous solution generates radial electric fields due to differences in the diffusion rates of the dissolved ions. Depending on the direction of the electric field and the charge of the mobile objects in solution, objects can be pulled toward these micropumps. Once the mobile objects are near the micropumps, radial diffusioosmotic flows sweep these objects along the charged surface of the substrate on which the micropumps rest, as shown in Figure 2 [2].

The spatiotemporal nature of the micropumps creates exclusion regions around the pumps where we predict the movement of catalytic nanomotors will be restricted. We envision that a strategically-patterned surface of $CaCO_3$ micropumps could direct nanomotors by making them move orthogonal to the radial flows of the micropumps.

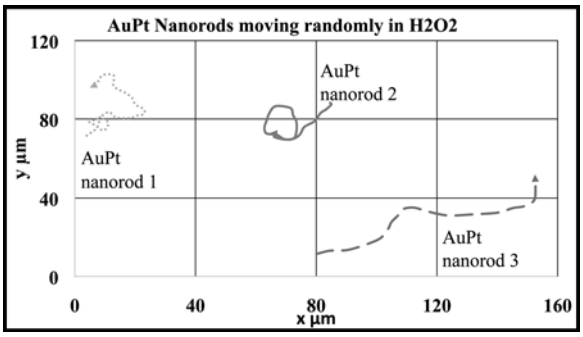

Figure 1: Graph showing the simultaneous, spontaneous movement of AuPt nanorods in a H_2O_2 solution.

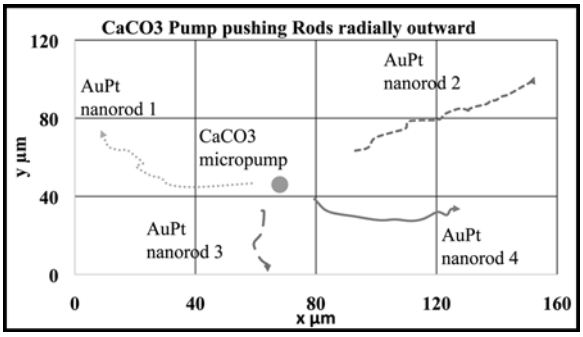

Figure 2: Graph showing AuPt nanorods moving radially away from a $CaCO_3$ micropump.

Therefore, our research question was: can we start with the random pathways of the catalytic nanomotors and get more directionality by strategically placing an array of micropumps around these nanomotors?

Experimental Procedure:

AuPt nanorods were obtained from the Chemistry Department at Penn State. $CaCO_3$ microparticles of roughly 7-10 μm were made through a precipitation synthesis. A solution of 0.33 M calcium chloride ($CaCl_2$) was added to a 0.33 M solution of sodium carbonate (Na_2CO_3), and after minutes of vigorous

stirring, the solution was washed with deionized water. Diluted $CaCO_3$ microparticles and AuPt nanorods in deionized water were added on top of a borosilicate glass slide. A standard microscope was used to capture images and videos at 10×-50× magnification.

An array of microwells in a polydimethylsiloxane (PDMS) surface was made by using standard photo- and soft-lithography on a Karl Suss MA/BA6 contact aligner [3]. $CaCO_3$ was grown in the microwells by first passing a $CaCl_2$ solution horizontally over the microwells. Then after evaporation of this first solution, a solution of Na_2CO_3 was passed horizontally over the microwells and removed after about ten minutes.

Results and Conclusions:

The random pathway of the catalytic nanomotors and the radial pumping of the $CaCO_3$ can be observed in Figure 1 and Figure 2, respectively. When adding a second $CaCO_3$ microparticle and H_2O_2, the movement of the nanomotors was still largely haphazard. However, the spacing of the micropumps in this system may need to be further fine-tuned in order to obtain more directionality by limiting the degree of freedom in the movement of the nanorods.

When adding a third $CaCO_3$ and taking away H_2O_2, a single AuPt nanorod not only moved without H_2O_2, but also moved in a linear path away from the chemical micropumps, as shown in Figure 3. This is the key result of this research and shows that AuPt nanorods can be steered at a local level by chemical micropumps. This system is also important because it may allow for other charged objects to be steered, not just nanomotors.

Figure 4 shows a dark formation, which is believed to be $CaCO_3$, in one 15 μm well of an array of microwells on a PDMS surface. Growing $CaCO_3$ in an array of microwells on a PDMS surface is a promising method to make large, tunable arrays of chemical micropumps.

Future Work:

We hope to further refine the growing method in order to produce large, tunable arrays of micropumps to study long-range, directed motion as well as directed motion with strategic patterns. In the future, comparison of the experimental data to mathematical models of the flows could also give insight to the specific mechanisms by which the chemical micropumps move and steer the nanorods.

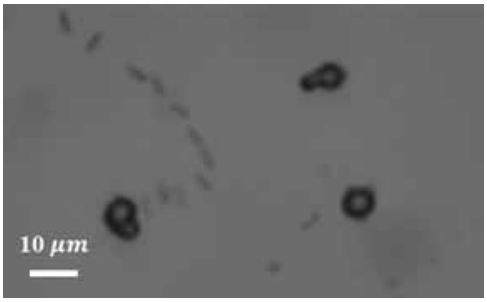

Figure 3: Time lapse image showing a single AuPt nanorod moving with directionality by the radial pumping of three $CaCO_3$ micropumps.

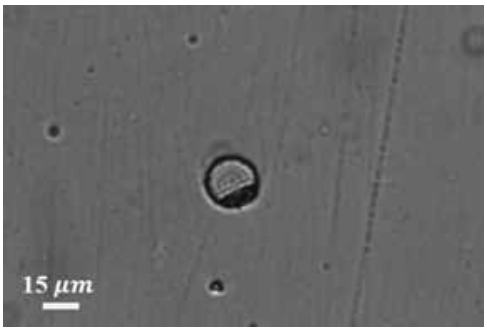

Figure 4: An image of a dark formation, which is believed to be $CaCO_3$, in a 15 μm well on a PDMS surface.

Acknowledgements:

I would like to thank Dr. Darrell Velegol and Abhishek Kar for having me in their lab this summer, Antonio Romero, Flory Wong, and Dr. Ayusman Sen in the Chemistry Department at Penn State for their collaboration on this project, Kathleen Gehoski and the Penn State Nanofabrication Laboratory staff for their support and help, the NNIN REU Program for organizing this undergraduate research experience, and the National Science Foundation for funding.

References:

[1] W. F. Paxton, P. T. Baker, T. Kline, Y. Wang, T. E. Mallouk, and A. Sen. Journal of the American Chemical Society, 128, 14881-14888 (2008).

[2] J. J. McDermott, A. Kar, M. Daher, S. Klara, G. Wang, A. Sen, and D. Velegol. Langmuir, 28, 15491-15497 (2012).

[3] D. Qin, et al. Nature Protocols, 5.3, 491-502 (2010).

Fabricating Nanostructures to Modulate Local Potential in Graphene

Kenton McFaul
Applied Physics, Grove City College

NNIN REU Site: Penn State Nanofabrication Laboratory, The Pennsylvania State University, University Park, PA
NNIN REU Principal Investigator: Dr. Jun Zhu, Department of Physics, The Pennsylvania State University
NNIN REU Mentor: Jing Li, Department of Physics, The Pennsylvania State University
Contact: mcfaulkj1@gcc.edu, jzhu@phys.psu.edu, jil5369@psu.edu

Abstract and Introduction:

Graphene is an atomically thin allotrope of carbon with unique electrical properties. Its high carrier mobility at room temperature and ultra-high thermal conductivity make it a promising material for nanoscale circuit applications. One way to study the nanoscale transport properties of ballistic graphene p-n junctions is to modulate the local potential with lithographic gates that are several tens of nanometers in scale. Lithography can also be used to build graphene nanoribbon (GNR) arrays, which lead to a method to build radio frequency amplifiers.

Our efforts were directed at fabricating GNR arrays and gold split-gates with length scales less than 100 nm. After performing electron-beam lithography, we developed our patterns at low temperatures using an ice bath. Oxygen reactive ion etching (RIE) was employed to etch the graphene into nanoribbon arrays, and electron gun evaporation was used to deposit the gold split-gate electrodes, followed by a lift-off process. In order to optimize the recipe, variables such as resist type, electron beam dose, developer type, and development time were systematically tested. We successfully fabricated nanoribbon arrays with a period of 100-180 nm using poly(methyl methacrylate) (PMMA) as the e-beam resist, and arrays with a period of 60-80 nm using ZEP. We successfully fabricated split-gates separated by 50-90 nm using PMMA/MMA bilayer resist.

Procedure and Results:

We fabricated our nanoribbon arrays with a layer of graphene grown using chemical vapor deposition (CVD). The CVD graphene was transferred onto a silicon wafer with a thin layer of thermally grown silicon oxide. Our first batch of samples was made with PMMA 950K A3 as resist. Electron-beam lithography was used to pattern arrays of nanoribbons using doses ranging from 300-400 μC/cm^2. The nanoribbons we patterned were 20-90 nm wide, separated by a distance equal to their width.

Both MIBK: IPA 1:1 and MIBK: IPA 1:3 were used as developers to test the influence of concentration on feature resolution. Developer with a higher concentration of IPA requires a longer time to develop, but provides finer control. We developed our samples at temperatures below 10°C by immersing our developer in an ice bath. Cold development is known to increase the resolution of nanostructures [1]. Finally, oxygen RIE was employed to etch the graphene into nanoribbons.

With PMMA as a resist, we successfully formed GNR arrays with periods from 100-180 nm at a dose of 400 μC/cm^2. However, arrays with periods from 40-80 nm were either over-etched or completely gone, revealing a fundamental limit of our process using PMMA. We also found that a higher concentration of IPA did not increase the resolution of our nanoribbons; it only slowed down the process, and our samples were underdeveloped.

Electron scattering during e-beam lithography produced exposed stripes that were wider than the intended size, resulting in the overetching of graphene. Reducing this effect was critical at scales less than 100 nm. In order to obtain nanoribbons narrower than 50 nm, we chose ZEP 520a as our resist for the second batch of GNR arrays because of its high contrast and resolution [2]. We also wrote our features smaller than the intended size to compensate for the scattering effect. Doses from 270-390 μC/cm^2 were tested. We developed the arrays in cold n-amyl acetate. With ZEP as the resist, we successfully formed GNR arrays with periods from 60-80 nm at doses of 270-350 μC/cm^2.

We fabricated our gold split-gates on a silicon wafer, and used electron beam lithography to pattern gates that were separated by 50-200 nm. ZEP 520a, which is known to have an inherent undercut [3], and conventional PMMA/MMA bilayer resist were tested.

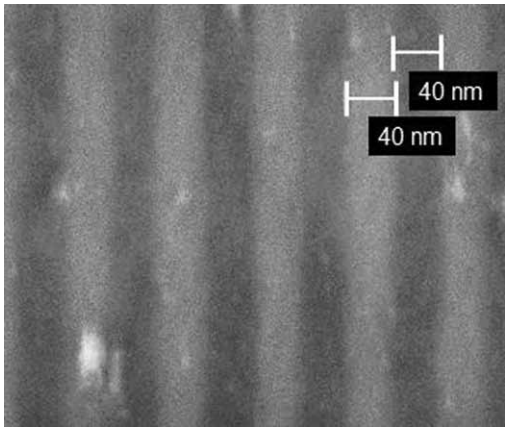

Figure 1: 80 nm period nanoribbon array made with ZEP.

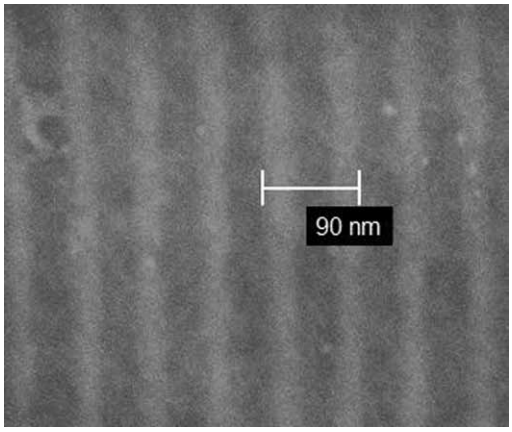

Figure 2: 60 nm period nanoribbon array made with ZEP.

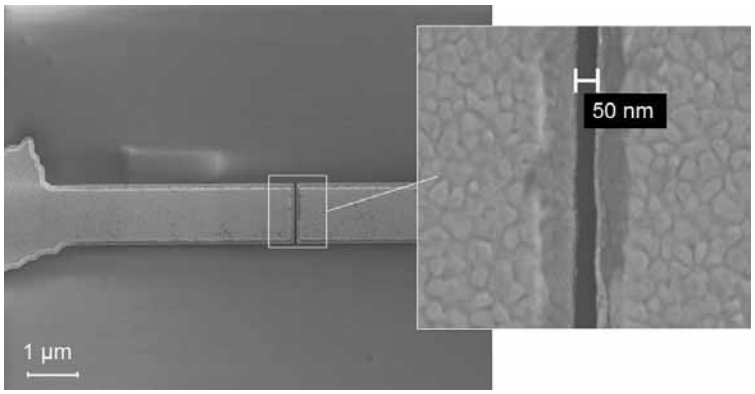

Figure 3: 50 nm split-gate made with a PMMA/MMA bilayer.

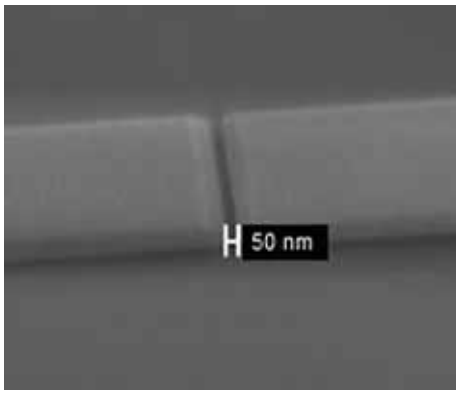

Figure 4: 50 nm split-gate made with a PMMA/MMA bilayer.

The split-gates fabricated using ZEP were written with doses from 250-390 μC/cm^2, and developed in n-amyl acetate below 10°C. We deposited 50 nm of gold with e-gun evaporation, and performed metal lift-off in a heated bath of Remover PG (75-85°C). Scanning electron microscope images and resistance measurements revealed that split-gates 90 nm wide and above were successful, but smaller gates either shorted or had very rough edges.

PMMA/MMA bilayer resist yielded much cleaner results. We wrote the patterns with doses from 300-450 μC/cm^2, and developed in cold MIBK: IPA 1:1. Metal lift-off was performed using acetone. Because of electron scattering, the split-gates were much thinner than the pattern size. This was the desired effect, and split-gates written at 70-90 nm had a final size less than 50 nm.

Conclusions:

It is possible to fabricate nanoscale GNR arrays and local gate structures using our processes. We achieved 30 nm ribbons using ZEP, correcting for electron scattering, and developing in an ice bath. Split-gates with a separation of 50 nm were achieved by writing 70-90 nm gate structures in PMMA/MMA bilayer resist. With these structures and techniques, researches can further study the transport properties of graphene by locally modulating the potential.

Acknowledgments:

I would like to thank Professor Jun Zhu for her advice and the use of her lab. I would also like to thank Jing Li for putting in many hours to teach me and help me with this project. I also greatly appreciate the Zhu Group and the Penn State Nanofab Staff for all the advice, and the National Nanotechnology Infrastructure Network REU Program, along with the National Science Foundation, for providing funding.

References:

[1] Cord, B., et al., "Optimal temperature for development of poly(methylmethacrylate)." Journal of Vacuum Science and Technology B, 25, 2013-2016 (2007).

[2] Chapin, C., et al., "Optimization Studies of ZEP520." Georgia Institute of Technology, Nanotechnology Research Center, 2010. PowerPoint.

[3] Conway, J., "E-beam Process for ZEP-520A to be used for Metal Liftoff and RIE." Stanford University, SNF, 2005. Web.

Tungsten Silicide Films for Superconducting Resonators

Kiwamu Nishimoto
Solid State Physics, Tohoku University, Sendai, Japan

NNIN iREG Site: UCSB Nanofabrication Facility, University of California, Santa Barbara, CA
NNIN iREG Principal Investigator: Professor Benjamin Mazin, Department of Physics, University of California, Santa Barbara
NNIN iREG Mentor: Dr. Gerhard Ulbricht, Department of Physics, University of California, Santa Barbara
Contact: a8tb1191@mail.tagen.tohoku.ac.jp, bmazin@physics.ucsb.edu, ulbricht@physics.ucsb.edu

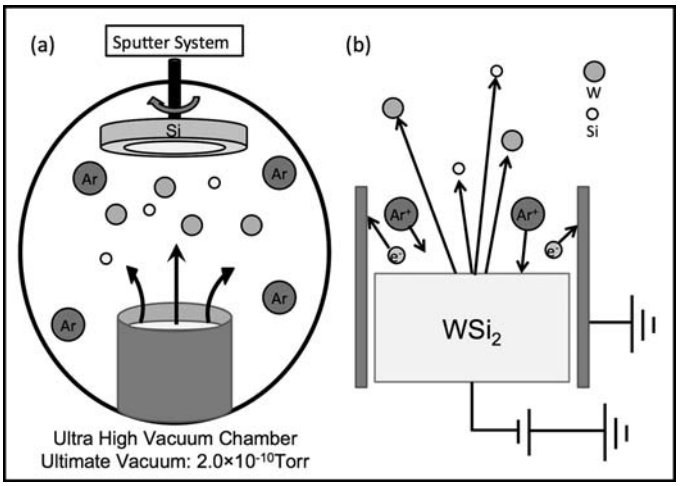

Figure 1: Schematic illustration of (a) the way to deposit WSi_2, and (b) the way to sputter WSi_2.

Abstract:

We have started to examine tungsten silicide (WSi_2) as a possible candidate for microwave kinetic inductance detectors (MKIDs). WSi_2 for MKIDs has to have a suitable critical temperature (T_c) that is uniform over the wafer and very low (about 1-2K), and the films should have low stress. We explored the parameter space of the WSi_2 sputter deposition to find the ideal condition. We used the sputter system located in the cleanroom in order to deposit WSi_2 on silicon (Si) wafers in ultra-high vacuum. We deposited WSi_2 at base pressures below 1.0×10^{-8} Torr on rotating Si wafer (30 rpm) by creating an argon (Ar) plasma above the WSi_2 target. We measured the thickness by using scanning electron microscopy (SEM), and the T_c and the room temperature resistivity of our deposited WSi_2 films.

Introduction:

MKIDs are promising for astronomy because these detectors provide highly multiplexed arrays of detectors that can be configured to operate from the sub-millimeter to the x-ray regime [1]. These detectors allow us to determine the energy and arrival time of individual photons. The applications of this technology ranges from detecting earth-like planets around nearby stars to untangling the emission mechanisms of pulsars.

In its simplest form, a MKID consists of a thin film superconductor patterned into a resonator [1]. When a photon is absorbed in the superconductor, it breaks Cooper pairs, creating an excess of non-equilibrium quasiparticles [1]. This excess of quasiparticles alters the complex surface impedance of the superconductor, raising the kinetic inductance and surface resistance, which causes the resonance feature to shift to a lower frequency and broaden [1]. MKIDs are generally operated at temperatures well below the superconducting transition in order to minimize the thermal population of quasiparticles. To achieve good sensitivity, the T_c of MKID resonator metal (WSi_2) needs to be around 1-2K. In this instance, the target value of T_c is 1-2K. It is known that T_c is different depending on the Si content of WSi_2. Therefore the T_c of sputtered thin film WSi_2 can be controlled by deposition conditions.

Experimental Procedure:

The experiment was conducted in an ultra high vacuum chamber. We sputtered a high purity WSi_2 target by creating DC plasma above the WSi_2 in Ar atmosphere. Si wafer was rotated during experiment so that we could deposit homogeneous WSi_2 over a 3-inch wafer. Varying the parameter space of the WSi_2 sputter deposition (power, Ar pressure, Ar flow, coat time) allowed to control the W:Si ratio. We measured the thickness by using SEM, and the T_c and the room temperature resistivity of our deposited WSi_2 films.

Results and Conclusions:

First, we prepared three pieces from different locations of a 3-inch wafer after deposition to measure the film thickness and T_c, so that we could verify that there are not any morphological differences of WSi_2 over a 3-inch wafer; shown in Figure 2. Position means the distance from center of the wafer. From this data, we could show that T_c did not change depending on the position of the wafer. So, we do not have to worry about the homogeneity of WSi_2.

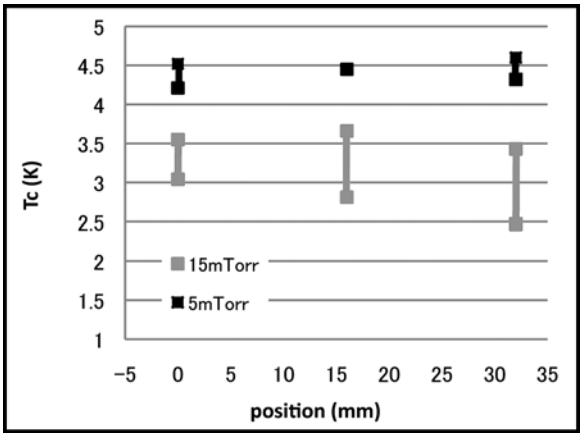

Figure 2: T_c depending on position of the wafer. (Ar flow: 20 sccm, power: 120W).

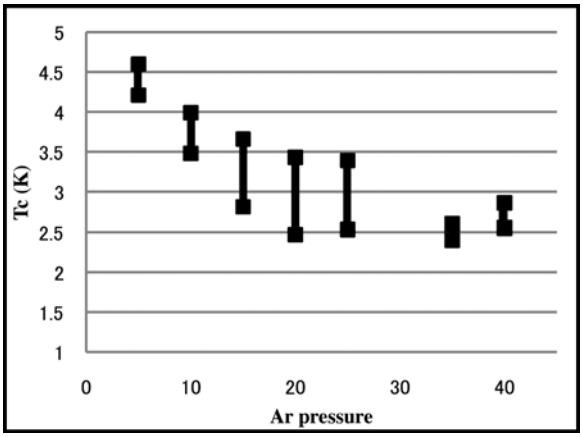

Figure 3: T_c depending on Ar pressure. (Ar flow: 20 sccm, power: 120W).

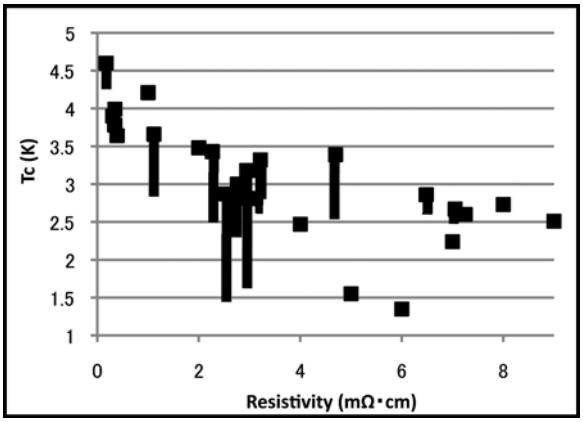

Figure 4: T_c relationship with resistivity. Resistivity was calculated with surface resistivity and thickness.

Figure 3 shows that by varying the Ar pressure T_c of WSi_2 can be minimized. It is guessed that high Ar pressure results in a low Si content in WSi_2, because Si is lighter than W and, therefore, tends to be scattered by Ar atom and ion more than W. T_c of WSi_2 depends on stoichiometry and was mapped by Kondo [2] for transition temperatures above 1.9K. For both very small and large Si concentrations, the T_c falls below 1.9K, but for Si atomic percentages ranging from ~ 7% up to ~ 60%, the T_c rapidly rises up to 5K, with a maximum T_c for Si atomic percentages between 20 and 40%. We guess that higher the Ar pressure becomes, the lower the Si content becomes, but there is a limit a parameter of Ar pressure to minimize Si content. We also got several data of T_c depending on Ar flow, power and coat time but those are not sufficient to discuss.

By measuring resistivity at room temperature, we intended to predict T_c. We wanted to do that because it takes many hours to measure T_c. From previous research, it is known that high resistivity implies low T_c. Figure 4 shows the relationship between T_c and the room temperature resistivity. From the graph, the sample has high resistivity tends to get low T_c. We guessed it is possible to predict if T_c is high or low by room temperature resistivity.

Acknowledgments:

I would like to thank Professor Ben Mazin, Gerhard Ulbricht, Mazin laboratory members for their exceptional guidance, Peter Duda, Lizzie Slaughter for their expertise, and Samantha Cruz for her advice as program coordinator. Finally, I would like to acknowledge and thank the National Nanotechnology Infrastructure Network International Research Experience for Graduates (NNIN iREG) Program and the National Institute for Material Science for funding this project.

References:

[1] T. Cecil, A. Miceli, O. Quaranta, C. Liu, D. Rosenmann, S. McHugh, and B. Mazin, Appl. Phys. Lett. 101, 032601 (2012).

[2] S. Kondo, J. Mater. Res. 7, 853-860 (1991).

Electrical Characterization of GaAs/InAs Core/Shell Nanowires and InAs Nanotubes

Jordan Occeña
Engineering Physics, University of Tulsa

NNIN iREU Site: Institut Für Bio- Und Nanosysteme (IBN), Forschungszentrum, Jülich, Germany
NNIN iREU Principal Investigator: Dr. Mihail Ion Lepsa, Peter Grünberg Institute 9, Forschungszentrum Jülich
NNIN iREU Mentor: Torsten Rieger, Peter Grünberg Institute 9, Forschungszentrum Jülich
Contact: jordan-occena@utulsa.edu, m.lepsa@fz-juelich.de, t.rieger@fz-juelich.de

Introduction:

Semiconductor nanowires (NWs) show promise for a variety of nanoelectronic applications due to their high surface area to volume ratio and two-dimensional confinement of charge carriers. The properties of these NWs can be further manipulated through the formation of radial heterostructures. In particular, the use of a gallium arsenide (GaAs) NW core to support an indium arsenide (InAs) shell can potentially result in a tubular conductor suitable for high performance field effect transistors (FETs). The GaAs core can later be removed by selective etching, resulting in an InAs nanotube. Due to its additional surface area and the relaxation of dislocations associated with the GaAs/InAs interface, it is expected that the mobility (μ_{FE}) of this InAs nanotube would exceed that of the core/shell NW. Here, we investigate and compare the resistivity (ρ), electron concentration (n_e), and μ_{FE} of GaAs/InAs core/shell NWs and InAs nanotubes.

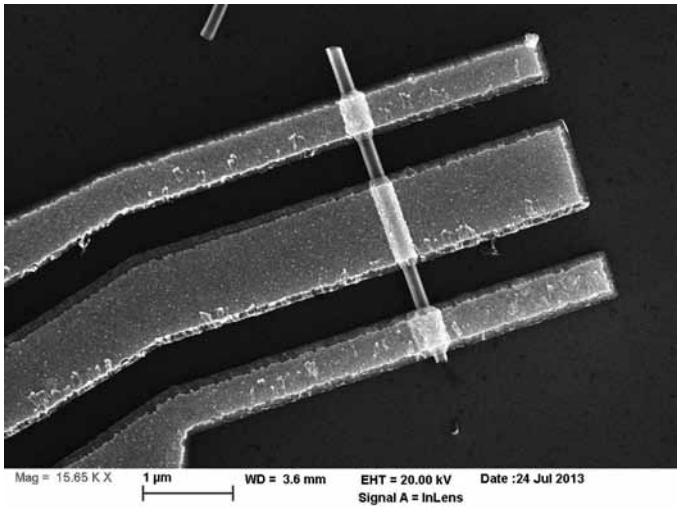

Figure 1: Top-view SEM image of an InAs nanotube FET.

Experimental Procedure:

The core/shell NWs studied were grown by molecular beam epitaxy as described by Rieger, et al. [1]. NWs were grown with three different core diameters/shell thicknesses: 110 nm/15 nm, 110 nm/22 nm, 150 nm/18 nm.

In order to extract ρ, n_e, and μ_{FE}, top-gate NW FETs were fabricated with hafnium oxide (HfO_2) as the gate dielectric and GaAs/InAs core/shell NWs as the channel. Core/shell NWs were first coated with 10 nm of HfO_2 by atomic layer deposition. The NWs were then mechanically transferred to a substrate consisting of 200 nm of silicon oxide on degenerately doped silicon.

Optical microscope images of the distribution of the transferred NWs were used to design source, drain, and top-gate contacts for selected NWs. Electron-beam lithography was used to define 1 μm long Ti/Au top-gates, which were deposited by electron beam evaporation. After gate deposition, the HfO_2 dielectric was removed from the source and drain regions of the NW using a three minute wet etch in 0.05% hydrofluoric acid. Source and drain contacts were then patterned and deposited in the same way as the top-gate contacts. The spacing between adjacent contacts was 500 nm. The electrical properties of the NWs were characterized by two-, three-, and four-probe current-voltage (I-V) measurements on the NW FETs.

After characterization of the core/shell NWs was complete, the GaAs core was selectively etched with a 1:1:40 mixture of NH_4OH:H_2O_2:H_2O for five minutes to obtain InAs nanotubes, while leaving the FETs intact. Electrical measurements were then repeated for the nanotube FETs. Scanning electron microscope (SEM) images of the nanotube FETs were taken after electrical characterization (Figure 1).

Equation 1: $\rho = \frac{RA}{L}$

Equation 2: $C = \frac{2\pi\epsilon_0\epsilon_r L}{ln\left[\frac{t_{ox}}{r}+1+\sqrt{\left(\frac{t_{ox}}{r}\right)^2+2\frac{t_{ox}}{r}}\right]}$

Equation 3: $n_{el} = -\frac{CV_{th}}{eLA}$

Equation 4: $\mu_{FE} = \frac{g_m L^2}{V_{SD}C}$

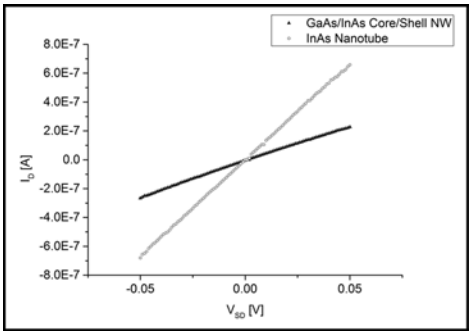

Figure 2: Exemplary two-probe I-V characteristics of a core/shell NW vs. nanotube.

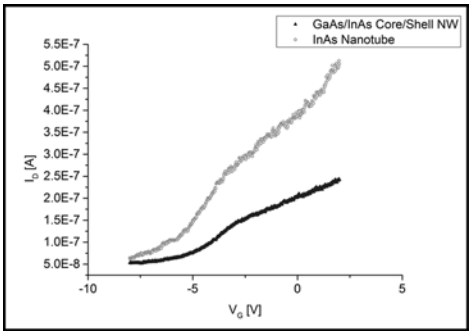

Figure 3: Exemplary three-probe ID-VG characteristics of a core/shell NW vs. nanotube.

The resistivity of each NW and nanotube was determined by two-probe measurements using Equation 1, where L is the length of the NW between source and drain, R is the resistance of the NW taken from the I-V curve, and A is the portion of the cross-sectional area of the NW that conducts, which is limited to the InAs shell in core/shell NWs due to the band alignment of GaAs and InAs [2]. A small number of four-terminal devices were fabricated to measure the contact resistance, which was found to be negligible in comparison to the resistance of the NWs and was not included in calculations of ρ.

Values for n_e and μ_{FE} were extracted from three-probe measurements according to Equations 3 and 4, where C is the gate capacitance, V_{th} is the threshold voltage from the I_D-V_G curve, e is the electron charge, g_m is the transconductance from the I_D-V_G curve, and V_{SD} is the voltage between the source and drain, which was held constant at 0.02 V for all three-probe measurements. The gate capacitance, C, was approximated using Equation 2, which is the general form of the gate capacitance for a back-gate NW FET, where ε_0 is the vacuum permittivity, ε_r is the relative permittivity of the gate oxide, t_{ox} is the gate oxide thickness, and r is the NW radius. To account for the use of a top-gate instead of a back-gate, the capacitance values calculated by Equation 2 were increased by 14%, as suggested in Dayeh et al. [3].

Results and Discussion:

For forty-one GaAs/InAs core/shell NWs tested, an average ρ of 0.14 Ω•cm was found. After etching of the NW cores to obtain InAs nanotubes, the average ρ decreased to 0.05 Ω•cm. An example of two-probe I-V curves for one device before and after etching of the core is shown in Figure 2.

For twenty-nine core/shell NW FETs on which three-probe measurements were conducted, an average n_e of 1.33×10^{19} cm^{-3} and average μ_{FE} of 19.2 $cm^2(V•s)^{-1}$ were found. The same devices, after etching of the GaAs core, exhibited an average n_e of 1.41×10^{19} cm^{-3} and an average μ_{FE} of 32.0 cm^2 $(V•s)^{-1}$. Sample three-probe I_D-V_G curves are shown in Figure 3. For all the parameters, the data showed a large spread most likely related to the device processing.

It was expected that the removal of the GaAs core would allow for the formation of donor-type surface states on the inner surface of the InAs nanotubes in addition to those already present on the outer surface, thus increasing n_e and decreasing ρ. The lack of a significant increase in n_e found experimentally suggests the possible formation of InGaAs at the GaAs/InAs interface. Meanwhile, the small increase in μ_{FE} and decrease in ρ found might still be attributed to relaxation of dislocations associated with the GaAs/InAs interface.

Acknowledgements:

A special thanks to Dr. Mihail Ion Lepsa and Torsten Rieger for their guidance and support, as well as to my colleagues at the Forschungszentrum Jülich and the coordinators of the NNIN iREU Program. Thanks also to the NSF for funding this work.

References:

[1] Rieger, T., et al. Nano Letters, 12(11), 5559-64.

[2] Blömers, C., et al. Nanotechnology, 24(3), 035203.

[3] Dayeh, S., et al. Small, 3(2), 326-32.

PHYS

Current-Voltage Characterization and Two-Step Photocurrent Generation in Lattice-Matched Quantum Dot Solar Cells

Adam Christopher Overvig
Engineering Physics, Cornell University

NNIN iREU Site: National Institute for Materials Science (NIMS), Tsukuba, Ibaraki, Japan
NNIN iREU Principal Investigators: Dr. Takeshi Noda, High Efficiency Solar Cell Group, National Institute for Materials Science, Ibaraki, Japan; Dr. Hiroyuki Sakaki, Toyota Technological Institute, Nagoya, Japan
NNIN iREU Mentor: Dr. Martin Elborg, High Efficiency Solar Cell Group, National Institute for Materials Science
Contact: aco2124@columbia.edu, noda.takeshi@nims.go.jp, sakaki.hiroyuki@nims.go.jp, elborg.martin@nims.go.jp

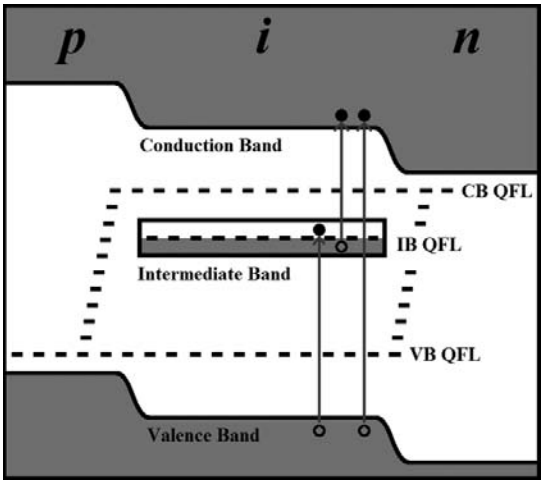

Figure 1: Ideal band diagram of the IBSC, with three distinct quasi-Fermi-levels (QFLs). Adapted from Luque [1].

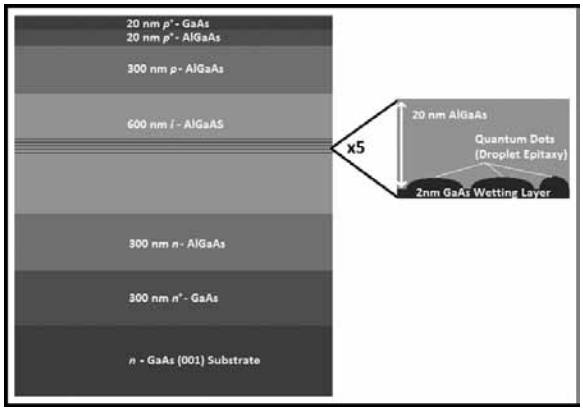

Figure 2: Fabricated QD-IBSC sample structure, grown by MBE.

Introduction and Motivation:

This research focused on studying the intermediate band solar cell (IBSC), which promises a great increase in photovoltaic conversion efficiency by extending the absorption range into the infrared while maintaining a high open circuit voltage. This is achieved by an intermediate band (IB) between the valence band (VB) and conduction band (CB), allowing the so called two-step photocurrent generation, wherein sub-bandgap photons produce a photocurrent by exciting the VB to IB, and IB to CB transitions in series (see Figure 1). The theoretical efficiency is 63% at maximum solar concentration, overcoming the Shockley-Queisser limit [1].

A widely used method of researching IBSCs employs embedded quantum dot (QD) layers. Many such efforts use lattice-mismatched materials because of the simplicity of dot formation. However, the resulting accumulated strain of many dot layers (which are necessary to absorb an appreciable amount of light) degrades the material quality, limiting the efficiency and masking intrinsic characteristics of the solar cell.

Here, we employed strain-free QDs fabricated in a lattice-matched system to eliminate strain related issues. To explore the viability of such a material system for realizing an IBSC, we studied fundamental properties of GaAs/AlGaAs QD solar cells with a focus on the two-step photocurrent generation process, a fundamental operating principle of the IBSC.

Fabrication of Quantum Dot Solar Cells:

A QD solar cell device was grown on n-type gallium arsenide (GaAs) <100> substrate by molecular beam epitaxy (MBE). As illustrated in Figure 2, the device was an aluminum gallium arsenide (AlGaAs) p-i-n structure with five layers of quantum dots embedded within the *i* layer. Each QD layer was separated by a 20 nm thick AlGaAs buffer layer, so adjacent electronic states were decoupled. The GaAs QDs (Figure 3) were fabricated by using droplet epitaxy, wherein metallic Ga droplets were formed on a GaAs wetting layer by supplying Ga in an As-depleted environment, and then As was supplied to crystalize the Ga droplets into GaAs QDs.

In contrast to widely used InAs/GaAs QDs grown by the Stranski-Krastanov growth, these QDs were strain-free (GaAs

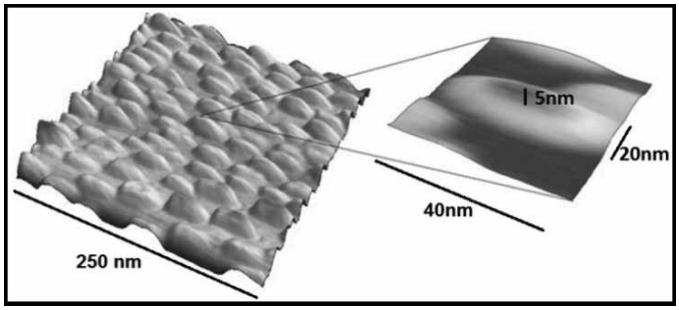

Figure 3: Visualization of QDs (inset to scale).

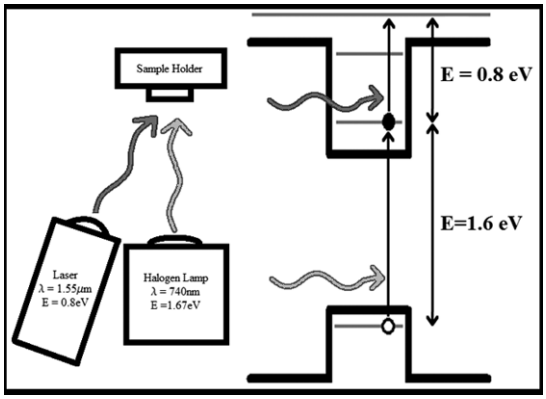

Figure 4: Experimental setup for two-step photocurrent measurements using 740 nm Halogen light.

and AlGaAs have nearly identical lattice constants), and the two-dimensional GaAs quantum well (QW) layer embedded underneath the QDs was controllable during growth. Here, the 2 nm thick QW layer was introduced to increase the confinement energy, aiming for suppression of thermal escape of carriers from the QDs and improved homogeneity of the QDs. The QW layer was doped n-type with Si, and the supplied electrons relax into the QDs.

Device Characterization:

As determined by atomic force microscopy (AFM), the resulting QD heights were 4.8 ± 0.8 nm, and each layer had an area density of 6.7×10^{10} /cm^2. Photoluminescence measurements at 20 K revealed nanostructure transitions with peaks at 1.6 eV and 1.67 eV, corresponding to the QDs and the wetting layer. This indicated that the barrier heights for electrons and holes are on the order of 100 meV, which is sufficiently high (compared to thermal energy, 26 meV, at room temperature) to limit thermal escape.

Photocurrent measurements at room temperature (using a Halogen lamp and a monochromator) demonstrated the absorption of photons with energies below the bandgap (1.8 eV) of AlGaAs. A reduction in photocurrent was observed, starting from negative bias and strengthening at higher biases (up to the open-circuit voltage). These current-voltage characteristics depended on the wavelength (λ) of light, and were explained in terms of the wavelength dependence of the absorption coefficient and the bias dependence of trapping efficiencies of electrons and holes by QDs.

To observe two-step absorption of sub-bandgap photons, we used the Halogen lamp and a 1.55 μm (0.8 eV) laser (see Figure 4). The λ of the Halogen lamp was set at 740 nm (1.68 eV), generating carriers only in the QDs. Upon illumination of the sample with the laser, we observed an increase in photocurrent (ΔI), i.e., two-step photocurrent generation, and found that it depended largely on V. The increase in photocurrent was also observed for shorter wavelengths (450 and 600 nm), where carriers were generated mostly in AlGaAs and then became trapped in the QDs. ΔI was at its maximum at -0.5-0.0 V, followed by a gradual reduction. This dependence of ΔI on V was qualitatively explained by the number of trapped carriers in QDs, and re-trapping of photoexcited carriers by the QDs.

Conclusions and Future Work:

We successfully fabricated lattice-matched GaAs/AlGaAs QD solar cells with five QD layers. A 2 nm thick GaAs wetting layer was embedded underneath each QD layer to suppress thermal escape of carriers generated in the QDs. Current-voltage characteristics were analyzed by comparison to the bias dependence of carrier trapping and absorption coefficients. We observed two-step photocurrent generation due to absorption of sub-bandgap photons, which is necessary for the operation of IBSCs. These results demonstrate the potential of GaAs/AlGaAs QD SCs.

Future work is needed to fully understand the dependences of the two-step process on voltage and incident energy, and will focus on identifying and tuning the necessary parameters to optimize the IB to CB transition.

Acknowledgements:

I would like thank Drs. Noda, Elborg, and Sakaki for their help, patience, and useful discussions; and the National Science Foundation and the National Nanotechnology Infrastructure Network International Research Experience for Undergraduates Program for funding this opportunity.

References:

[1] A. Luque, et al. Nature Photonics 6, 146-152 (2012).

Spin Manipulation of Antiferromagnetic Devices

Alice Perrin
Physics, The College of William and Mary

NNIN REU Site: Cornell NanoScale Science and Technology Facility, Cornell University, Ithaca, NY
NNIN REU Principal Investigator: Dr. Daniel Ralph, Physics, Cornell University
NNIN REU Mentor: Gregory Stiehl, Physics, Cornell University
Contact: aeperrin@email.wm.edu, dcr14@cornell.edu, gms263@cornell.edu

Abstract:

Antiferromagnets (AF), the most common type of magnetically ordered material, exhibit a zero net magnetic moment below a specific temperature, called the Néel temperature, which renders them unresponsive to manipulation by magnetic fields [1]. Previous works have manipulated AF moments indirectly by way of the exchange spring effect, where a magnetic field is used to manipulate a ferromagnet exchange coupled to an AF [2]. Our recent work focused on reproducing this method of AF manipulation through observing tunneling anisotropic magnetoresistance (TAMR) in antiferromagnetic devices in which the antiferromagnet is interfaced with a tunnel junction. The TAMR effect is a change in the resistance through the AF/tunnel junction barrier due to the rotation of the AF moments. Our finished devices exhibited TAMR, thus demonstrating the successful manipulation of the AF magnetic moments through exchange coupling. Future work will introduce magnetocrystalline strain on the devices as another means with which to manipulate the moments.

Introduction:

A better understanding of the dynamics of AF magnetic moments could lead to antiferromagnetic components in magnetic memory storage and a broader range of materials available for use in electronics [1]. Antiferromagnets used as spin torque driven resonators would also allow for further study in the terahertz frequency range. However, because antiferromagnets cannot be manipulated by magnetic fields, other methods must be explored in order to study them. One means of manipulating the AF moments is to interface the antiferromagnet with a ferromagnet. Below the blocking temperature there is an exchange coupling effect, and each AF moment is pinned to a corresponding ferromagnetic moment. In a magnetic field, the AF moments resist the rotation of the ferromagnetic moments until it becomes energetically advantageous for the coupled moments to rotate. However, the AF moments rotate non-uniformly, experiencing a winding effect, seen in Figure 1.

We observed the tunneling anisotropic magnetoresistance effect (TAMR) in order to confirm the success of the exchange coupling. TAMR is an effect in which we see a change in the resistance of a device comprising a tunnel junction interfaced with an antiferromagnet, where the antiferromagnet acts as a single magnetic electrode [3]. This change in resistance occurs because the density of states at the interface changes as the AF moments rotate. As the density of states decreases, less electrons will be able to tunnel through the junction, and there will therefore be a higher resistance through the device.

Fabrication:

We began fabrication of our devices by sputtering a stack of materials onto a 200 micron silicon wafer in a magnetic field. From the substrate upward, the stack was made up of: Ta(5)/Ru(10)/Ta(5)/NiFe(0-10)/IrMn(3)/MgO(2-3)/Ta(3)/Ru(10) where the number after each layer is its thickness in nanometers. The bottom layers of Ta/Ru/Ta made up the bottom electrode of our devices. The next layers contained a NiFe ferromagnetic layer, antiferromagnetic IrMn, a MgO tunnel junction, and a top electrode of Ta/Ru. The finished devices allowed us to pass a current through a pillar containing the ferromagnet, antiferromagnet, and tunnel junction in order to measure the resistance of the stack. These

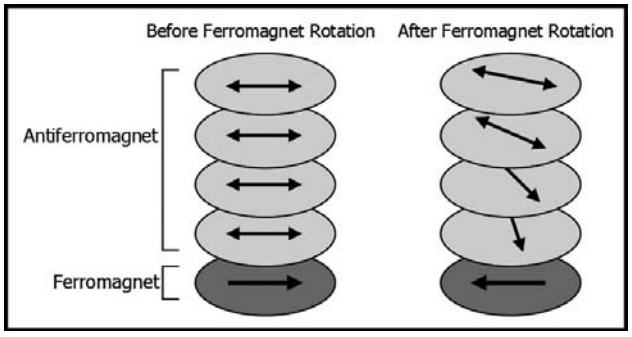

Figure 1: When exchange-coupled, the rotation of the antiferromagnetic moments is non-uniform.

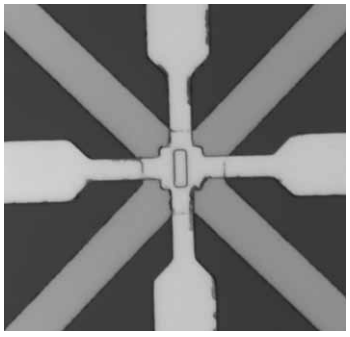

Figure 2: A top view of a finished device with a 3 by 9 μm pillar.

pillars ranged in surface area (as seen from the top) from 1 × ½ μm to 10 × 5 μm to allow us to examine the role of the area on the TAMR effect.

Results and Conclusions:

We gathered data from devices with layers NiFe(10)/IrMn(3)/MgO(2.5) nm, cooling them to temperatures ranging from 2.2K to 50K. We measured the resistance of the devices versus the magnetic field, which swept over a range large enough to induce moment rotation in the coupled ferromagnet and antiferromagnet. In Figure 3, we can see two clear steady resistance states where the slope of the data is near zero. The device switched between these states at ± 500 Oe depending on whether the field was sweeping negatively or positively, due to the drag caused by the antiferromagnet moments resisting rotation. This, along with the two resistance states, provides qualitative evidence of TAMR in our devices and therefore demonstrates successful manipulation of the AF moments through exchange coupling.

Future Work:

Future work on this project will incorporate the use of strain as an addition means of manipulating the AF moments by altering the magnetocrystalline anisotropy of the antiferromagnet. This will redefine the rotation angles at which the energy of the moments are at a minima, allowing for a method of manipulating the moments directly. Our method of inducing strain on the devices can be seen in Figure 4. Strain will be explored as both a supplement to and a replacement for exchange coupling as a means to manipulate the AF moments.

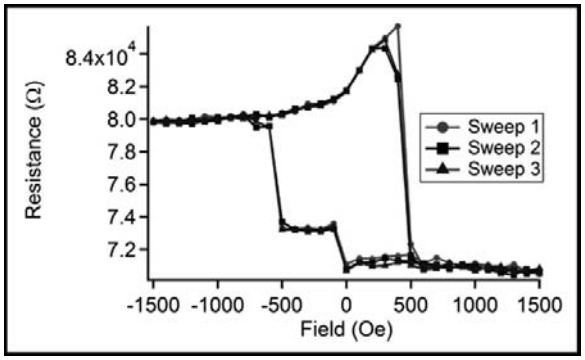

Figure 3: A hysteresis curve demonstrating stable resistance states around 70 kΩ and 80 kΩ, indicative that AF moment rotation has occurred.

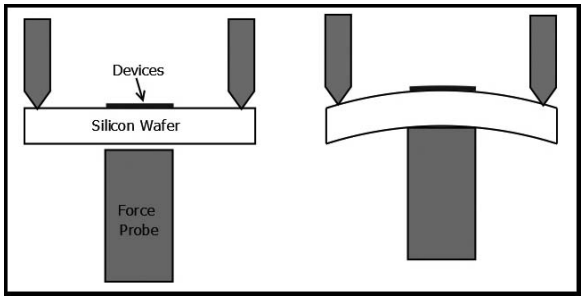

Figure 4: The wafers can be laterally manipulated by a three point strain induction system.

Acknowledgments:

Thank you to the National Science Foundation, National Nanotechnology Infrastructure Network Research Experience for Undergraduates Program, Cornell NanoScale Facility, and Cornell Center of Materials Research for providing all the funds and facilities for this project. A special thanks to Dan Ralph, Greg Stiehl, the Ralph group, the CNF Staff, and Rob Ilic and Melanie-Claire Mallison.

References:

[1] Shick, A.B., et al.; "Spin-orbit Coupling Induced Anisotropy Effects in Bimetallic Antiferromagnets: A Route Towards Antiferromagnetic Spintronics"; Physical Review B, 81, 1-4 (2010).

[2] Marti, X.; "Electrical Measurements of Antiferromagnetic Moments in Exchange-Coupled IrMn/NiFe Stacks"; Phys.Rev.Let., 108, 1-4 (2012).

[3] Park, B.G., et al.; "A Spin-valve-like Magnetoresistance of an Anti-ferromagnet-based Tunnel Junction"; Nature Mats, 10, 347-51, 2011.

Nano-Structuring Diamond for Quantum Sensing

Kevin Tkacz
Physics, Carnegie Mellon University

NNIN REU Site: UCSB Nanofabrication Facility, University of California, Santa Barbara, CA
NNIN REU Principal Investigator: Prof. Ania Bleszynski Jayich, Physics, University of California, Santa Barbara
NNIN REU Mentor: Preeti Ovartchaiyapong, Physics, University of California, Santa Barbara
Contact: ktkacz@andrew.cmu.edu, ania@physics.ucsb.edu, pov@physics.ucsb.edu

Abstract and Introduction:

The ability to structure diamond on the nanoscale is crucial for realizing diamond's potential as nano electro-mechanical material. In particular diamond plays host to the nitrogen-vacancy center, an atom-like defect that is promising for quantum sensing applications. Processing of diamond, however, is difficult and not well established as diamond is the hardest known material and is chemically inert.

In this work, we have pursued two techniques to achieve efficient and controlled diamond structuring. First, we used chemical mechanical polishing (CMP) to planarize and smooth diamond samples. Using 6 μm diameter diamond powder in an ethane-diol suspension, polishing rates were less than 10 μm per hour. Scratching of the diamond surface by the nanodiamond powder was observed. Second, we explored an $Ar/CF_4/O_2$ inductively coupled plasma (ICP) etch and found the diamond etch rate to be 16.7 μm per hour. The surface quality depends heavily on the smoothness of the starting surface, with any irregularities in the starting surface becoming more pronounced after etching. Achieving a fast and smooth diamond thinning process will enable the production of high-quality diamond nanostructures for enhanced sensing.

Experimental Procedure:

The CMP functions similarly to sandpaper. A sample surface is brought into contact with a rotating polishing pad with slurry applied between them. The surface is polished as it contacts the pad through the slurry. We used a 6 μm diameter diamond powder in ethane-diol polishing fluid as our slurry. The samples we worked with were 2 mm by 2 mm, and therefore needed an increase in back pressure while polishing to make adequate contact with the polishing pad. The increased back pressure made the sample carrier convex, which pushed the small sample downward into the pad. Parameters which were considered when using the CMP were the table speed and carrier speed (the speeds of rotation of each body), slurry type and flow rate, and down force or the amount of force applied when pushing the sample into the pad.

The ICP etcher bombards a sample in a vacuum chamber with reactive plasma ions to etch through the bombarded surface. There are many parameters to manipulate when using the ICP including the ICP power, bias power, vacuum pressure, gas composition, and gas flow rate. We used an ICP power of 1000 W, vacuum pressure of 2 Pa and a gas composed of O_2, Ar, and CF_4. Before and after etching, scanning electron microscopy (SEM) was used to examine the quality of the surface, and step profilometry was used to determine etch depths from which etch rates were extracted. Etches were performed on two types of diamond surfaces, which varied in initial quality.

Results and Conclusions:

The polishing rate of diamond is very slow. It has been determined to be less than 10 μms per hour based on the resolution of our height measurements and could be considerable slower than this. The change between Figure 1, the diamond surface before polishing, and Figure 2, the diamond surface after polishing for 40 minutes, is minimal. It remains to be seen whether this process is simply slow and additional polishing time would help or if significant modification to the polishing technique is needed.

We have achieved etching that is both fast and yields areas of minimal pitting as seen in Figure 3. This etch was achieved at a rate of 16.7 μm per hour which is much faster than other etches that yield such quality surfaces. While this etch did yield areas of the sample that had minimal pitting, there are areas that had much more severe deformations. This is likely due to surface defects prior to etching, but should be investigated further.

One very clear result was that the starting diamond surface is important. A smooth starting surface will yield smoother results while a rougher starting surface will become more pitted and its defects will become more pronounced through etching. This is evident when comparing Figure 3 to Figure 4, which shows the same etch on a rougher starting surface.

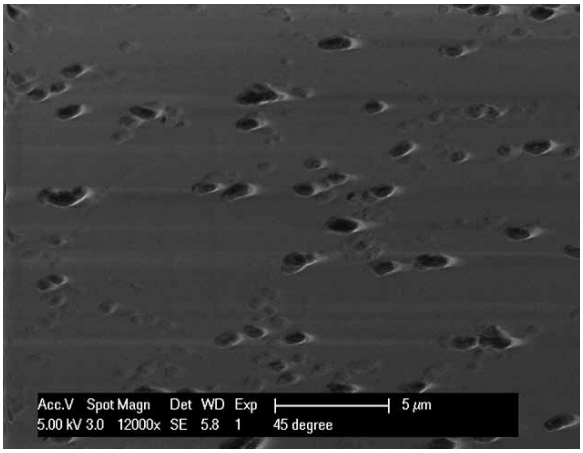

Figure 1: SEM image of diamond surface before polishing.

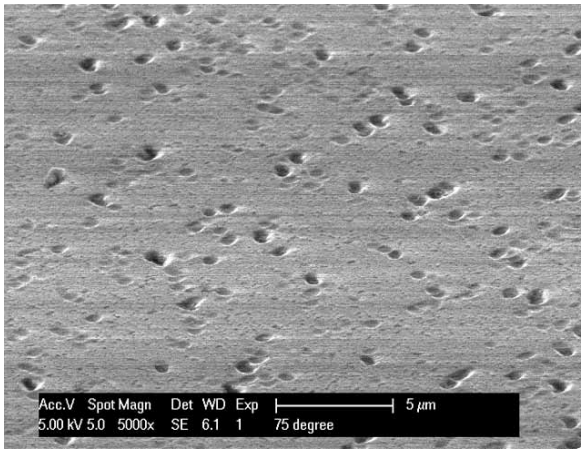

Figure 2: SEM of diamond surface after polishing for 40 min.

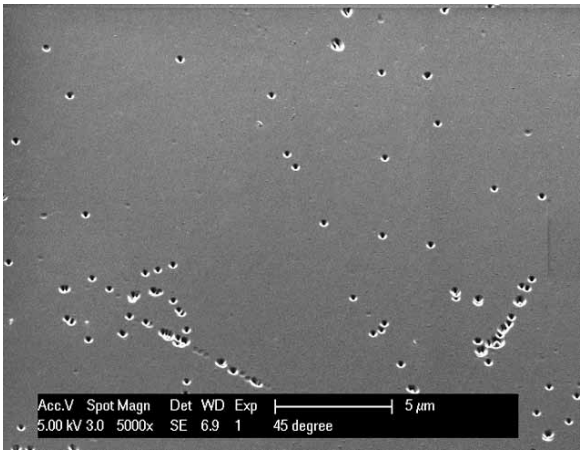

Figure 3: SEM image of etched surface with minor pitting.

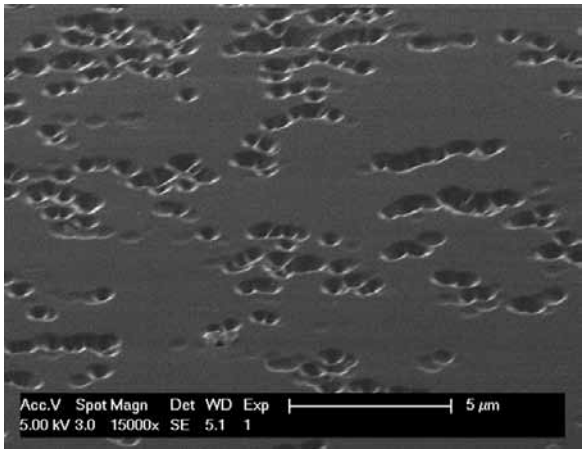

Figure 4: SEM image of etched surface with a great deal of pitting.

We also repeated this same etch on the same type of surface, but reduced the bias to one half of the original value. This etch was significantly slower (closer to 3 μms per hour) and resulted in a highly pitted surface.

Future Work:

More precise determination of the diamond polish rate is required. While we have achieved a useful etch, the parameter space is not entirely understood. Further investigation into this is needed to optimize the etching process. Making adjustments to the bias power or the ICP power should be the first variables to be considered when exploring this parameter space further.

Finally, the effects of these modeling techniques on nitrogen-vacancy centers need to be investigated.

Acknowledgments:

I would like to thank Preeti Ovartchaiyapong, Professor Ania Bleszynski Jayich, and the Jayich group for their help this summer. I would also like to thank the University of California, Santa Barbara clean room engineers who helped me along the way and my fellow University of California, Santa Barbara National Nanotechnology Infrastructure Network interns who made my summer truly enjoyable. I would also like to thank the National Nanotechnology Infrastructure Network Research Experience for Undergraduates Program, the Air Force Office of Scientific Research, the University of California, Santa Barbara, and the National Science Foundation for funding me and providing me with the resources to work this summer.

Fabrication of Graphene Field Effect Transistors on Boron Nitride Substrates

Christopher Addiego
Physics, Carnegie Mellon University

NNIN REU Site: NanoTech User Facility, University of Washington, Seattle, WA
NNIN REU Principal Investigator: Prof. Xiaodong Xu, Physics, University of Washington
NNIN REU Mentor: Grant Aivazian, Physics, University of Washington
chris.addiego@comcast.net, xuxd@uw.edu, aivazian@uw.edu

Abstract:

Graphene is a two dimensional crystal of carbon atoms that has applications to new electronics and optoelectronics when fabricated as a field effect transistor (FET) [1]. The quality of these FETs is quantified partly by the carrier mobility of the device. The goal of this project is to determine a procedure for fabricating graphene FETs on hexagonal boron nitride (h-BN) substrates based on Dean et al. [2] in order to create devices with improved carrier mobility. A combination of chemical solvents and annealing procedures were used to clean the devices during fabrication. We found that only applying the chemical solvents yielded the devices with the highest carrier mobility (~ 500 cm^2/Vs). However, this value is much less than that of typical graphene FETs, indicating our procedure can still be improved.

Introduction:

Graphene is a monolayer of graphite composed of a single layer of carbon atoms arranged in a honeycomb lattice. Graphene has many remarkable mechanical, electronic, and optoelectronic properties stemming from its structure including its high carrier mobility and optical transparency in the visible to infrared wavelength range [1]. These properties make it an attractive material for use in high frequency electronics and devices requiring transparent conductive films [1].

A general measure for the quality of graphene FETs fabricated in the lab is the carrier mobility of the device. Despite graphene's high intrinsic carrier mobility, the carrier mobility of the devices fabricated on silicon dioxide (SiO_2) substrates is limited by scattering caused by the surface roughness, charged impurities, and interactions with phonons of the SiO_2 substrate [2]. Residues deposited during the fabrication process also limit carrier mobility [3]. Our goal was to improve the carrier mobility of our grapheme FETs by fabricating them on h-BN substrates. Previous work by Dean et al. indicates that h-BN can act as a much better substrate for graphene devices than SiO_2 because it has comparable dielectric properties to SiO_2 while also having a smoother surface which should reduce carrier scattering within graphene.

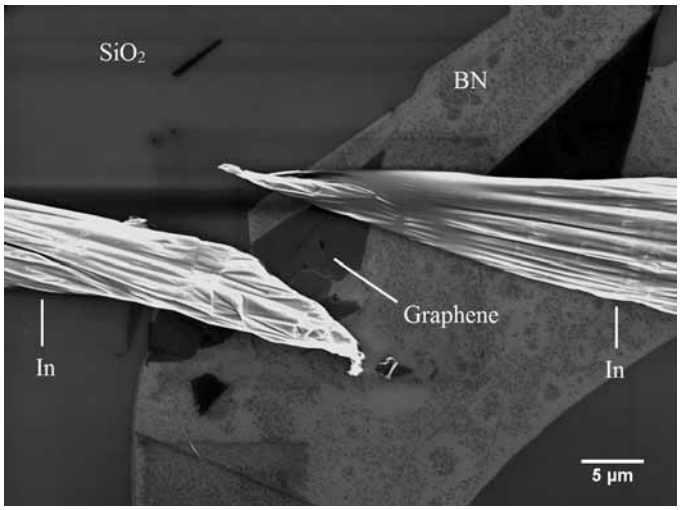

Figure 1: SEM of a graphene device on an h-BN substrate.

Device Fabrication:

Standard graphene FETs are fabricated by first exfoliating graphene onto 300 nm of SiO_2 on a doped silicon wafer, which acts as a back gate, and then writing gold electrical contacts with electron beam lithography (EBL) onto the graphene. The fabrication process we used for our h-BN devices was slightly more complex; graphene was first exfoliated onto a polymer stack and BN flakes were exfoliated onto 300 nm of SiO_2 on doped silicon. Graphene was identified first based on contrast and then later confirmed with Raman spectroscopy. The h-BN flakes were selected using an atomic force microscope (AFM) to have a thickness of 10-30 nm and minimal changes in thickness over the surface. Using the procedure outlined by Dean et al. [2], the graphene was transferred onto the h-BN flake and the polymer stack was dissolved. We decided not to use EBL to write our contacts because it would deposit additional residue onto the device. Instead, we used a micromanipulator to write indium contacts onto the device. A scanning electron microscope (SEM) image of a device can be seen in Figure 1.

To remove residues deposited during the fabrication procedure, we used a combination of chemical solvents and annealing in argon gas (Ar) and molecular hydrogen gas (H_2). Acetone (ACE) and isopropanol (IPA) were the primary solvents, and distilled water as used on select occasions. Annealing was done in a one-inch tube furnace at 350°C for 120 minutes. An AFM was used to identify the residues deposited during the fabrication process.

Results:

Once the devices had been fabricated, the conductance (G) of each device was measured, using a sensitive preamplifier, by maintaining a constant source-drain voltage while sweeping the gate voltage. The carrier mobility (μ) was calculated according to the formula shown in Figure 2 [3]. In the formula, $C = 115 \times 10^{-10}$ F/cm^2, L is the length of the device parallel to the current path, W is the width of the device perpendicular to the current path, and the derivative of G with respect to gate voltage is taken to be the slope of the highlighted region in Figure 3. In searching for the optimal fabrication procedure, we fabricated devices using different permutations on the basic fabrication procedure, altering the anneal parameters and the order in which we performed the annealing and graphene transfer.

$$\mu = \frac{1}{C}\frac{L}{W}\frac{\partial G}{\partial V_{gate}}$$

Figure 2: Equation defining carrier mobility.

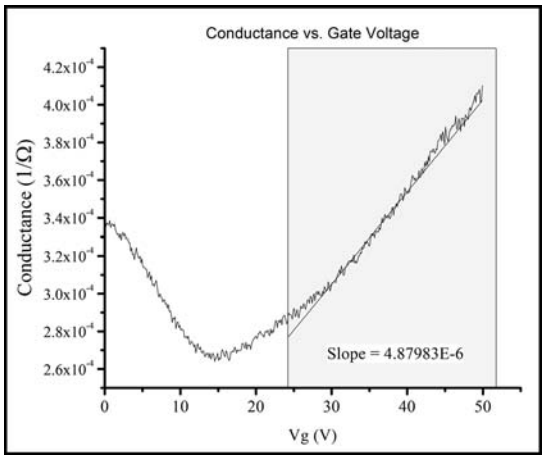

Figure 3: Example of conductance data from a device.

Conclusions:

As shown in Figure 3, we found that washing the h-BN flake in ACE and IPA prior to performing the transfer and then soaking in distilled water and rinsing with ACE and IPA after the graphene transfer and dissolving the polymer stack yields the highest carrier mobility (~ 500 cm^2/Vs). Although other variations of the procedure were tried, the processes described in Figure 4 were the only ones that produced useable devices. In addition, the highest carrier mobility attained by the devices fabricated using our procedure was significantly smaller than that of devices fabricated using the standard process. This suggests that further research is required to develop our fabrication procedure.

Acknowledgements:

I would like to thank Prof. Xu and Grant Aivazian, along with the other members of the Xu Lab and Mack Carter, for their guidance this summer. This project was funded by the National Nanotechnology Infrastructure Network Research Experience for Undergraduates (NNIN REU) Program and the National Science Foundation.

References:

[1] F. Bonaccorso, Z. Sun, T. Hasan, and A. C. Ferrari; "Graphene photonics and optoelectronics." Nature Photonics 4 (2010).

[2] C. R. Dean, et al. "Boron nitride substrates for high-quality graphene electronics." Nature Nanotechnology 5 (2010).

[3] K. I. Bolotin, et al. "Ultrahigh electron mobility in suspended graphene." Solid State Communications 146, pp 351-355, (2008).

Cleaning Processes Before Graphene Transfer	Cleaning Processes After Graphene Transfer and Polymer Dissolution	Carrier Mobility (cm^2/Vs)
Soak/rinse in ACE and IPA	Soak in distilled water, rinse in ACE and IPA	497.4
Soak/rinse in ACE and IPA	Anneal in Ar /H_2	322.2

Figure 4: A summary of the fabrication procedures that yielded useable devices.

PROC

TiO2-Based Core/Shell Nanowires for Adding Gas Sensing Capabilities to Silicon CMOS Circuitry

Satoshi Anada
Materials and Manufacturing Science, Osaka University, Osaka Prefecture, Japan

NNIN iREG Site: Penn State Nanofabrication Laboratory, The Pennsylvania State University (PSU), University Park, PA
NNIN iREG Principal Investigator: Theresa S. Mayer, Electrical Engineering and Materials Science and Engineering, PSU
NNIN iREG Mentor: Xiahua Zhong, Electrical Engineering, The Pennsylvania State University
Contact: anada@uhvem.osaka-u.ac.jp, tsm2@psu.edu, xxz138@psu.edu

Abstract:

Silicon/titanium dioxide (Si/TiO_2) core/shell nanowires were prepared by atomic layer deposition (ALD) of a TiO_2 shell on the surface of high-aspect-ratio Si nanowires that were obtained by deep reactive ion etching (DRIE) of a high resistivity Si substrate patterned using colloidal lithography. The microstructure of the TiO_2 was determined by transmission electron microscopy (TEM) technique. In the as-deposited sample, the shell of the nanowire was found to be amorphous TiO_2. After annealing in O_2 gas at 873 K for two hours, the amorphous phase transformed into a crystalline phase, identified as anatase TiO_2. As a result, it was found that the amorphous shell transformed into anatase TiO_2 by the annealing.

Introduction:

Electronic devices such as microprocessors, microcontrollers, static random-access memories, and other digital logic circuits are based on the complementary metal oxide semiconductor (CMOS) technology because of its low static power consumption and noise immunity. New functionalities obtained by integrating unconventional materials and devices with the Si circuitry will dramatically expand its capabilities and performance. For example, metal oxide materials designed to produce a large electronic response to chemical vapors offer sensing capabilities. However, the high temperatures required to fabricate high-sensitivity metal oxide nanowire sensors would damage the CMOS circuitry, which has made it difficult to effectively couple them in a single integrated circuit (IC) platform. Bottom-up synthesis of nanowires, composed of a diverse range of elemental or compound materials, offers a promising way to add sensing functions CMOS circuits. We have focused on using electric-field directed self-assembly to position arrays of individual nanowires synthesized using bottom-up methods at predefined locations on a CMOS substrate [1, 2].

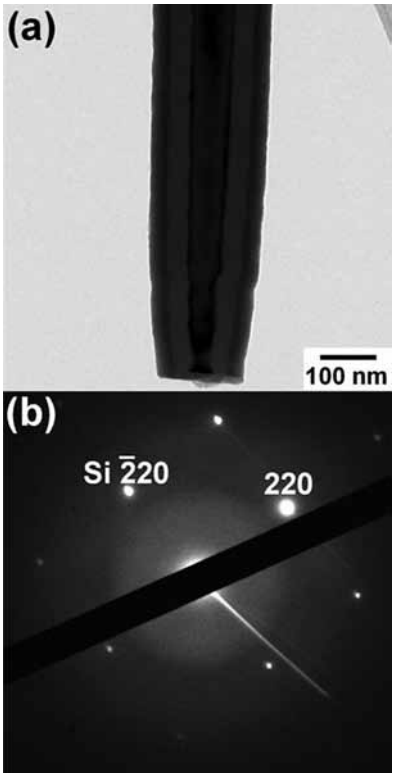

Figure 1: TEM observation of the nanowire before annealing.

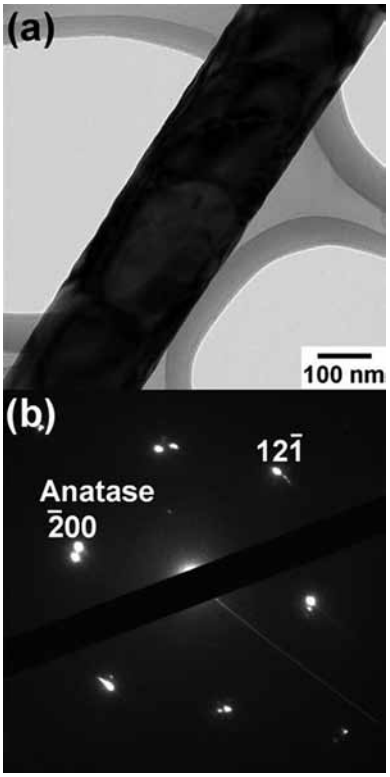

Figure 2: TEM observation of the nanowire after annealing at 873 K.

In this project, Si nanowires coated by TiO_2 (Si/TiO_2 core/shell) were fabricated for gas sensor arrays on Si CMOS. The gas sensor performance of the wires is strongly dependent on the TiO_2 microstructural properties, including uniformity, thickness, composition, and atomic configuration [3]. The goal of this project was to clarify the relationship between the gas sensitivity and the TiO_2 microstructure. In the present study, the microstructure of different types of TiO_2-coated Si nanowires was investigated by TEM to understand the effect of thermal annealing on TiO_2 microstructure.

PROC

Experimental Procedure:

The nanowires were prepared by ALD of a TiO_2 shell on the surface of high-aspect-ratio Si nanowires that were obtained by deep reactive ion etching (DRIE) of a high resistivity Si substrate patterned using colloidal lithography. Thermal annealing was carried out at 873 K in O_2 gas for 7.2×10^3 s with a heating rate of 8.3×10^{-3} K s^{-1}. Then the substrate was allowed to cool to room temperature. The nanowires before and after the annealing were observed by TEM, capturing bright-field (BF) images and selected area diffraction (SAD) patterns.

Results:

Figure 1 shows the microstructure of the nanowire before annealing. In the BF image (a), it was found that the core of nanowire was surrounded by two shells whose contrasts are featureless. The length of the nanowire, diameter of the core and thickness of the inner and outer shells were about 5 μm, 80 nm, 40 nm and 30 nm, respectively. In the SAD pattern (b), a spot pattern and diffuse scattering disk pattern were detected. This spot pattern corresponds to that of crystalline Si <001>. The disk pattern can be attributed to the overlapping halo rings and background of the transmitted wave. These results indicate that the core was single-crystal Si and the shells were amorphous phases of the constituent materials. Further investigation is necessary to identify the exact composition of the amorphous shells; however, based on the nanowire fabrication process, the inner and outer amorphous shells are expected to be SiO_2 and TiO_2, respectively.

Figure 2 shows the microstructure of the nanowire after annealing at 873 K in O_2 gas. In the BF image (a), some grain-boundary and bend-contour contrast were observed, indicating the outer shell consists of coarse crystalline grains. All diffraction spots in the SAD pattern (b) could be indexed by anatase TiO_2 <012> diffraction spots. As a result, it was found that the outer amorphous shell transformed into coarse grains of anatase TiO_2 by annealing at 873 K. It should be noted that no significant changes in the core and the inner shell were detected following thermal annealing.

Conclusions and Future Work:

In this project, Si/TiO_2 core/shell nanowires were fabricated for gas sensor arrays. The nanowires were investigated by TEM focusing on the effect of annealing on the TiO_2 microstructure. As a result, the following conclusions were obtained:

(1) The fabricated nanowires before annealing consisted of three parts, namely, single-crystal silicon core, inner and outer amorphous shells.

(2) The outer amorphous shell transformed into coarse grains of anatase TiO_2 by annealing at 873 K.

In the future, these fabricated nanowires will be integrated onto lithographically patterned Si substrates using electric-field directed self-assembly and their gas sensitivity will be measured to clarify influence of TiO_2 microstructure.

Acknowledgements:

This work was supported by the National Nanotechnology Infrastructure Network International Research Experience for Graduates (NNIN iREG) Program, together with Nanotechnology Platform, Japan. I would like to thank Prof. Mayer, her research group, Kathleen Gehoski, Ke Wang, Nanofabrication Lab Staff, and the Material Research Institute.

References:

[1] T.J. Morrow, M. Li, J. Kim, T.S. Mayer, and C.D. Keating, "Programmed Assembly of DNA-coated Nanowire Devices," Science, 323, 352 (2009).

[2] M. Li, R.B. Bhiladvala, T. Morrow, J. Sioss, K.-K. Lew, J.M. Redwing, C.D. Keating, and T.S. Mayer, "Bottom-up Assembly of Large-area Nanowire Resonator Arrays," Nature Nanotechnology, 3, 88 (2008).

[3] G.F. Fine, L.M. Cavanagh, A. Afonja, and Russell Binions, "Metal Oxide Semi-Conductor Gas Sensors in Environmental Monitoring," Sensors, 10, 5469 (2010).

One-Step Synthesis of Nanostructured Graphene Nanocomposites for CO_2 Capture and Photoreduction

Hannah Bailey
Engineering Physics, Rose-Hulman Institute of Technology

NNIN REU Site: Nano Research Facility, Washington University in St. Louis, St. Louis, MO
NNIN REU Principal Investigator: Dr. Pratim Biswas, Energy, Environmental and Chemical Engr., Washington University in St. Louis
NNIN REU Mentor: Dr. Wei-Ning Wang, Energy, Environmental and Chemical Engineering, Washington University in St. Louis
Contact: baileyh@rose-hulman.edu, pbiswas@wustl.edu, wangwn@seas.wustl.edu

Introduction:

As knowledge of the effect that carbon emissions have on the ecosystem increases, greater attention is being drawn to decreasing carbon dioxide (CO_2) production [1]. Carbon capture and sequestration (CCS) is one method of reducing carbon emissions, often realized with amine adsorption [2], and followed by CO_2 underground storage [1]. CCS is energy intensive and has unknown associated risks [1]. An alternative process, carbon capture and conversion (CCC), can improve CCS using solar energy to reduce CO_2 to useable products, eliminating CO_2 storage risks while meeting energy needs with an available source [1]. CCC can be realized using semiconductor photocatalysis to absorb solar energy and produce electron-hole pairs supporting reduction and oxidation mechanisms [1].

We sought to improve the CCC catalyst by synthesizing a ternary-structured nanoball consisting of ethylenediamine functionalized reduced graphene oxide-titanium dioxide (EDA/rGO-TiO_2) using a one-step furnace aerosol reactor (FuAR) method. TiO_2 was used to provide a suitable semiconductor [1]; rGO provided a conductive support with high surface area and morphology to increase charge transfer and reduce agglomeration [3]; EDA functionalization provided surface groups to increase CO_2 adsorption [2]; FuAR synthesis allowed for fast, relatively inexpensive production that supports bulk implementation [3]. EDA/rGO-TiO_2 was tested as a CCC photocatalyst to determine its effectiveness.

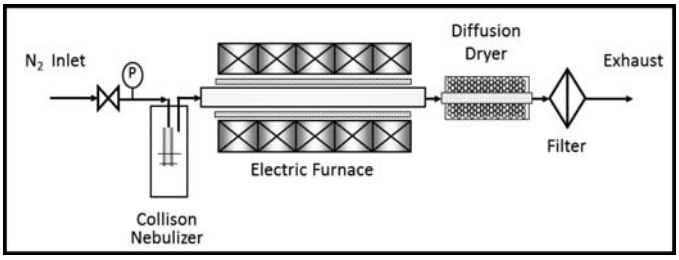

Figure 1: Furnace aerosol reactor.

Experimental:

EDA/rGO-TiO_2 was synthesized employing the FuAR system shown in Figure 1. We prepared a precursor solution by mixing 37.6 μL TiO_2 suspension (40 wt%), 10 mL EDA solution (≥ 99.5%), 50 mL GO suspension (1.4 wt%), and 140 mL deionized water in a covered beaker stirring magnetically at 4000 rpm for 24 hours. The solution was loaded into a Collison Nebulizer and the furnace was set to 200°C. Compressed nitrogen gas entered through a valve at a pressure of 14 psi, traveled into the Collison Nebulizer and atomized the solution into micrometer-sized droplets. The droplets flowed through the furnace wherein the droplet water evaporated, particles formed and passed through a diffusion dryer absorbing excess water before collection on a filter.

We repeated the procedure varying the furnace synthesis temperature to 150, 300, 400, 500, 600 and 800°C, and at 200°C furnace synthesis temperature varying the volumetric ratio of EDA to GO in solution from 10/50 to 15/50, 20/50, 25/50 and 30/50 EDA/GO. The rGO and rGO-TiO_2 particles were synthesized similarly at furnace temperatures of 200°C, 400°C and 600°C from solutions of 50 mL GO (1.4 wt%) and 150 mL deionized water, the latter incorporating 37.6 μL TiO_2 (40 wt%). TiO_2 particles were obtained by drop-casting 10 mg TiO_2 onto a filter. EDA/rGO-TiO_2 was characterized using scanning electron microscopy (SEM), transmission electron microscopy (TEM), Fourier transform infrared (FTIR) spectroscopy and Raman spectroscopy.

We tested EDA/rGO-TiO_2 as a catalyst in CO_2 photoreduction employing the reactor depicted in Figure 2. EDA/rGO-TiO_2 was placed on deionized water-dampened glass wool inside the reaction chamber. Compressed CO_2 was set to maximum flow (> 42 mL/min) into a water bubbler using a mass flow controller to generate a mixture and flow into the chamber to purge the system. After one hour, the ultraviolet lamp was turned on illuminating EDA/rGO-TiO_2. The CO_2 flow rate was lowered to 3 mL/min. The reaction duration was 12 hours during which gas concentrations were recorded after passing through the chamber using gas chromatography (GC).

Results and Discussion:

TEM, given in Figure 3, and SEM showed the GO sheets crumpled into nanoballs without agglomeration and dispersed with TiO_2, which indicates EDA/rGO-TiO_2 maintained high surface area for CO_2 adsorption, amine functionalization and charge transfer with TiO_2 intercalation. FTIR and Raman spectra in Figure 4 allowed for surface functional group characterization of EDA/rGO-TiO_2. EDA/rGO-TiO_2 FTIR and Raman spectra contained characteristic TiO_2 peaks indicating successful TiO_2 incorporation. EDA/rGO-TiO_2 FTIR spectra displayed a C = C graphene peak indicating that GO was reduced; characteristic C-N, N-H and CH_2 peaks evidenced successful EDA functionalization. EDA/rGO-TiO_2 Raman spectra showed characteristic D and G bands of rGO. The greater D/G band intensity ratio indicates a greater number of surface functional groups and defects in the nanoballs and provided evidence of EDA incorporation and remaining GO oxide groups. Spectral analysis of varying parameters showed that synthesis temperature and solution composition effected particle composition. EDA and reduction evidence became more intense and showed consistency at temperatures greater than 200°C and as the EDA/GO ratio increased, which indicated better EDA functionalization and GO reduction with greater temperature and EDA concentration.

Spectra comparison over periods of time showed EDA/rGO-TiO_2 maintained similar surface functional groups over 10 days and exhibited numerous variations after 40 days. This indicated EDA/rGO-TiO_2 has relatively stable surface composition over short periods of time, but significantly alters over extended periods of time. GC measurements using EDA/rGO-TiO_2 synthesized at 200°C with a 10/50 EDA/GO ratio showed carbon monoxide production indicating that the particles are functional catalysts for CO_2 reduction. Repeating the experiment with the same particles showed positive CO_2 reduction results indicating that the particles can be regenerated for reuse.

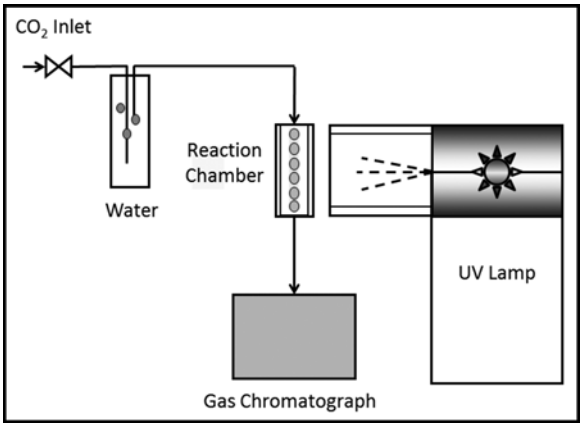

Figure 2: CO_2 photoreduction reactor.

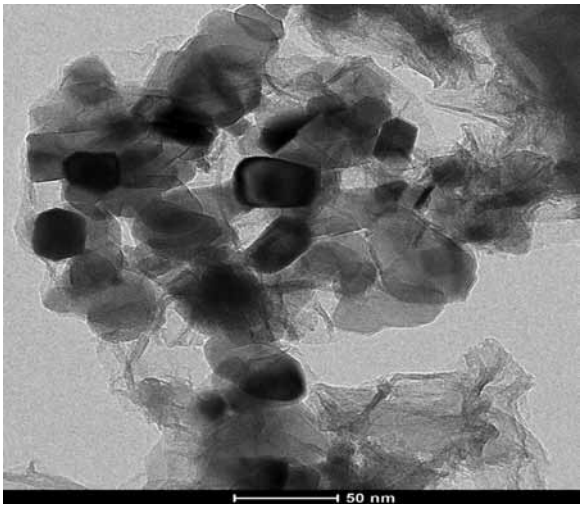

Figure 3: TEM image of EDA/rGO-TiO_2.

Acknowledgments:

I would like to thank Dr. Wei-Ning Wang, Dr. Pratim Biswas and Amruta Joshi from the Aerosol and Air Quality Research Lab for their guidance and expertise. I would also like to thank Dee Stewart, Nathan Reed, Kate Nelson, Howard Wynder and Sanmathi Chavalmane from the Nano Research Facility, the National Nanotechnology Infrastructure Network Research Experience for Undergraduates (NNIN REU) Program and National Science Foundation.

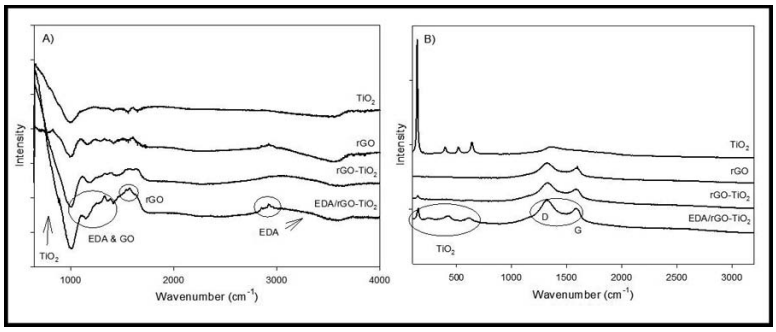

Figure 4: a) FTIR and b) Raman spectra varying particle composition.

References:

[1] W.-N. Wang, J. Park, and P. Biswas, "Rapid Synthesis of Nanostructured Cu-TiO_2-SiO_2 Composites for CO_2 Photoreduction by Evaporation Driven Self-assembly," Catalysis Science and Technology, 1 (4): 593-600 (2011).

[2] Y. Zhao, H. Ding, Q. Zhong, "Preparation and characterization of aminated graphite oxide for CO_2 capture," App.Surface Sci., 258 (10): 4301-4307 (2012).

[3] W.-N.Wang, Y. Jiang, and P. Biswas, "Evaporation-Induced Crumpling of Graphene Oxide Nanosheets in Aerosolized Droplets: Confinement Force Relationship," Journal of Physical Chemistry Letters, 3 (21): 3228-3233 (2012).

MOSFET: Fabrication Process and Performance Analysis

Kristofer Chow
Electrical Engineering, American River College

NNIN REU Site: UCSB Nanofabrication Facility, University of California, Santa Barbara, CA
NNIN REU Principal Investigator: Prof. Mark Rodwell, Electrical and Computer Engineering, University of California, Santa Barbara
NNIN REU Mentor: Dr. Doron Cohen-Elias, Electrical and Computer Engineering, University of California, Santa Barbara
Contact: krischow3@gmail.com, rodwell@ece.ucsb.edu, doroncohenelias@ece.ucsb.edu

Abstract:

The focus of this project was to determine the optimal gate region wet etch time, using the trench method, for the metal-oxide semiconductor field-effect transistor (MOSFET) fabrication process. The gate region, or trench, etching was time-dependent because too little time resulted in short-circuiting devices, while too much time resulted in lower-performing devices. The semiconductor parameter analyzer (SPA) examined the transistors' efficiency by generating current-voltage (I-V) graphs. No devices were successfully produced, but the optimal etching time range was found to exist between 15 and 25 seconds for this project's sample composition.

Introduction:

Scaled MOSFETs enable electronics to be made smaller and consume less power. Nanotechnology researchers solve problems that arise during the attempt to scale down the transistors, decreasing transistors' threshold voltages V_{TH}. With lower V_{TH}, devices have the capability to consume lower amounts of power, resulting in greater device efficiency. The most significant problem associated with this project was the etch stop thickness. Effective etch stops are at least 5 nm thick, preventing etchants from penetrating through the surface. Since the samples' layer was 2 nm thick, the mordant etched through the indium gallium arsenide (InGaAs) and the indium phosphide (InP) of the gate region. Caution was taken to ensure that the etching removed the etch stop, without penetrating into the channel region. By alternating the trench etch time with multiple samples, an optimal gate region etch time was attempted to be found and employed for future processes.

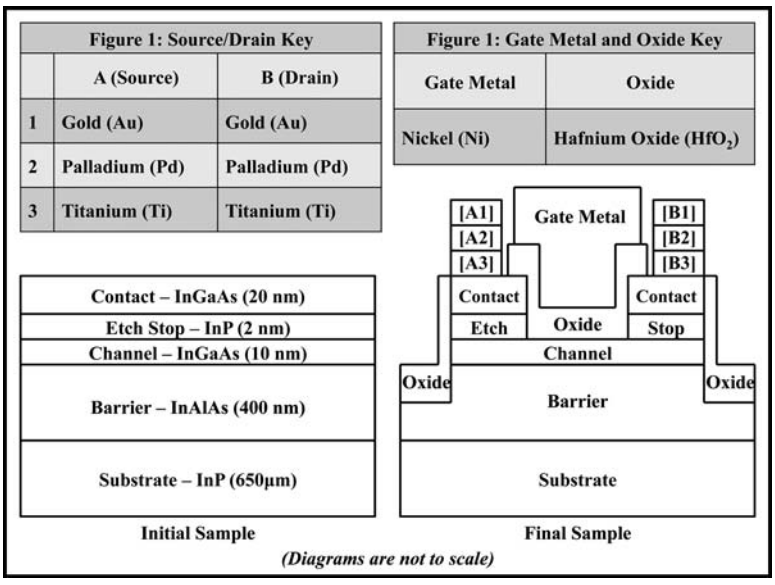

Figure 1: Initial and final stages of the MOSFET fabrication process.

Experimental Procedure:

The trench method consisted of four photolithography stages: isolation, gate region definition, gate metal deposition, and source/drain metal deposition. During each photolithography step, masks containing prints for a set of devices were used to expose the same print multiple times on the samples. Each print was designed for approximately 100 devices, and the total transistor count for each sample varied depending on the wafer size. The isolation process involved dry etching into the hard mask and wet etching the sample, using substance ratios of one part phosphoric acid (H_3PO_4): one part hydrogen peroxide (H_2O_2): 25 parts water (H_2O), until the etch level was in the barrier. This defined the active area of each device and varied the channel widths (5-25 μm). The gate region definition stage consisted of dry etching into the hard mask, and wet etching, using the same mordant from isolation, into the contact and etch stop layers of the exposed devices. This etching phase determined the channel lengths (0.3-1.0 μm); the etching was controlled by time, due to the thin etch stop layer.

The third photolithography step occurred after the hard mask removal, approximately 4 nm hafnium oxide (HfO_2) deposition, and 15 minute annealing at 400°C with forming gas purging. Following the oxide annealing, gate metal — nickel (Ni) — was deposited above the trench region, including the sides along the device for functioning and measurement purposes. The excess Ni was lifted-off and the last photolithography step protected areas where the source/drain metals were not supposed to cover. Hydrofluoric acid (HF) was used to remove some oxide in order to establish contact sites for the source/drain metals.

Etch Time and Deposition Summary					
	Gate Region Etch Time	Oxide Deposition	Gate Metal Deposition	Source/Drain Metal Deposition	Measured by SPA?
Sample 1	10 seconds	3.5 nm HfO_2	64 nm Ni	25 nm Ti/ 30 nm Pd/ 50 nm Au	Yes
Sample 2	15 seconds	3.5 nm HfO_2	64 nm Ni	25 nm Ti/ 30 nm Pd/ 50 nm Au	Yes
Sample 3	25 seconds	3.5 nm HfO_2	75 nm Ni	N/A	No
Sample 4	25 seconds	4.5 nm HfO_2	95 nm Ni/ 75 nm Au	N/A	No

Figure 2: Summary of the samples' etching times and deposition thicknesses.

The source/drain metals — titanium (Ti), palladium (Pd), and gold (Au) — were deposited onto the sample, and the final lift-off removed the excess metal. Ti was deposited for its n^+ contact properties, Pd for its ability to prevent gold diffusion into the semiconductor [1], and Au for its non-oxidizing properties (Figure 2).

Results:

A total of four samples were fabricated during this research project. The first process consisted of two samples that experienced gate region etch times of 10 and 15 seconds. These wafers were tested with no gate voltage and their I-V graphs suggested resistor-like behaviors (see Figure 3). These results led to another process, consisting of a sample with 25 seconds of trench etching. Following gate metal deposition, the sample was examined under the scanning electron microscope (SEM): the gate metal along the sides of the devices did not connect to the Ni above the channel (see Figure 4); voltage could not be applied to the gate without potentially damaging the metal. The last sample also underwent 25 seconds of trench etching, but the gate metal and source/drain photoresist was lifted off during the oxide etching with HF. This unexpected result may have been due to poor photoresist development.

Conclusions:

Although no working transistors were produced, the experimental results obtained will help future researchers. The optimal gate region wet etch time was found to exist between 15 and 25 seconds after attempting to fabricate four samples. The maximum time was observed because the 15-second sample underwent another procedure: the HfO_2 was removed and the devices were wet etched for 10 additional seconds. No current was conducted through the devices when no gate voltage was applied.

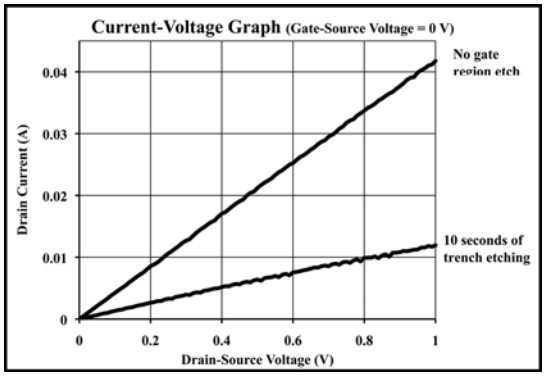

Figure 3: Performance comparison between a trenchless device and a 10-second etched device.

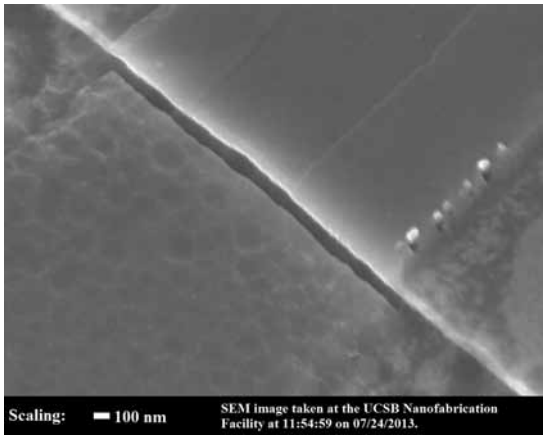

Figure 4: SEM of the third sample's gate metal discontinuity.

Scientific investigators can continue to construct MOSFETs, knowing they can achieve functioning devices with 25 seconds of etching, or they can alter the etch time parameter to define the most optimal trench etch time. Despite the knowledge this research provides, these results do not guarantee perfect-working devices; rather, this information improves the chances of fabricating more efficient MOSFETs.

Acknowledgements:

This project would not have been possible without the generous support from the National Nanotechnology Infrastructure Network Research for Undergraduates (NNIN REU) Program and the National Science Foundation (NSF). Professor Mark Rodwell and Dr. Doron Cohen-Elias deserve significant credit, as principal investigator and mentor, for their guidance and assistance throughout the course of this project. Melanie-Claire Mallison and Samantha Cruz are worthy of recognition for their excellent organization and program coordination.

References:

[1] Brown, D.. "Pd Plating (electroplating) - Palladium per Mil-P-45209." Palladium Plating. Professional Plating, 2008. Web. 19 Aug. 2013.

Deposition of the Immobilization Layer 3-Aminopropyltriethoxysilane on Gallium Nitride for Extremophile-Based Biosensors

Tiffany Huang
Electrical and Computer Engineering, Baylor University

NNIN REU Site: Stanford Nanofabrication Facility, Stanford University, Stanford, CA
NNIN REU Principal Investigator: Prof. Debbie G. Senesky, Aeronautics and Astronautics, Stanford University
NNIN REU Mentor: Ateeq Suria, Mechanical Engineering, Stanford University
Contact: tiffany_huang@baylor.edu, dsenesky@stanford.edu, asuria@stanford.edu

Abstract:

Biosensors composed of biomolecules and electromechanical components have enabled new sensing modalities for chemical sensing, pathogen detection and disease therapy. Traditional biosensors are silicon-based, but silicon has a known limited radiation lifetime. Gallium nitride (GaN), however, is radiation-hard and shows potential for use in biosensors to detect radiation. To support the development of a biosensor based on GaN and the radiation-tolerant extremophile bacteria *Deinococcus radiodurans* (*D. radiodurans*), we studied the attachment of an interfacial organosilane immobilization layer to GaN. More specifically, we attached 3-aminopropyltriethoxysilane (APTES) to GaN using molecular layer deposition. We defined the shape of the layer using die-level photolithography and lift-off, and we used goniometry, ellipsometry, and fluorescence microscopy to characterize the attachment properties of this layer. Optimization of this attachment will allow for long-lasting radiation detectors for applications such as medical radiation therapy and deep space exploration.

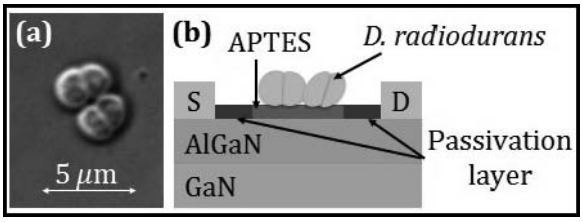

Figure 1: GaN biosensor HEMT device depiction.

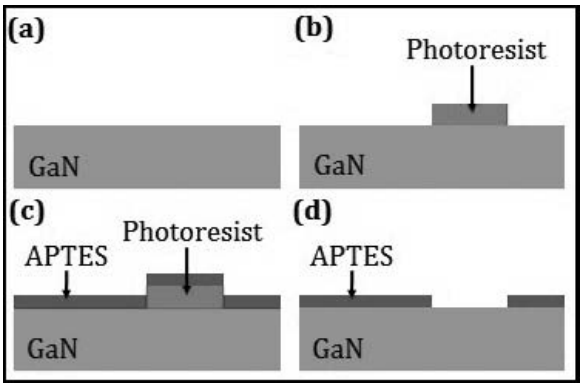

Figure 2: Process flow: (a) hydroxylation, (b) patterning of photoresist by photolithography, (c) deposition of APTES, and (d) patterning of APTES by liftoff.

Introduction:

Biosensors are biomedical or biological microelectromechanical systems (BioMEMS), systems that combine microelectronic materials such as semiconductors with biological components such as bacteria. These systems are largely used for biomedical or biological purposes such as diagnosing DNA and protein arrays [1]. By utilizing biological components composed of radiation-resistant extremophiles, biosensors may also be used in radiation-intense environments to detect radiation.

While traditional biosensors are silicon based and have a limited radiation lifetime [2, 3], gallium nitride (GaN) has a high radiation lifetime due to its large band-gap [4], making GaN ideal for radiation detection. The extremophile bacteria *Deinococcus radiodurans* (*D. radiodurans*) is also radiation-resistant [5, 6] and responds to radiation by generating ions [6]. We intend to combine *D. radiodurans* with GaN to build a biosensor that operates as a high-electron mobility transistor (HEMT), which has a high sensitivity to ions [4]. The biocompatibility of GaN has been shown [4], but no information exists on functionalizing GaN for D. radiodurans. We intend to interface GaN to *D. radiodurans* with the immobilization layer 3-aminopropyltriethoxysilane (APTES) commonly used to functionalize surfaces for bacteria attachment. Figure 1 depicts this APTES layer in the context of the HEMT device. Deposition and characterization of APTES will contribute to understanding the functionalization of GaN and may allow for construction of a HEMT radiation detector.

PROC

Fabrication Procedure:

We performed the following fabrication procedure on GaN samples and on silicon samples, using the silicon samples as references. Figure 2 depicts the fabrication procedure, which began with exposing the samples to 3:1 piranha solution (3:1 sulfuric acid: hydrogen peroxide) for two ten-minute sessions to clean the surface of organic molecules and activate hydroxyl groups on the surface. These hydroxyl groups add to the native oxide of the surface and ensure chemical functionalization of this surface for APTES [7].

Next, we used photolithography to pattern the surface to optimize for the gate size and shape of the HEMT device concept. This photolithography step consisted of depositing hexamethyldisilazane, depositing 1 μm of photoresist (Shipley 3612), exposing the samples to UV light, and developing in MF-26A. We then deposited APTES by molecular layer deposition to promote a conformal monolayer of APTES, and we performed liftoff in acetone. This left a surface patterned with APTES.

Characterization and Results:

To confirm deposition of this immobilization layer, the samples were characterized before and after the deposition step using goniometry and ellipsometry. Goniometry, a commonly used method for detecting changes in surface morphology, measures the wettability of the surface by surface water contact angle (SWCA) measurements. Table 1 shows a significant change in contact angle, indicating deposition of APTES. We used ellipsometry to further confirm the deposition of APTES. Ellipsometry calculates film thicknesses by measuring the change in light polarization and then fitting this experimental data to a model based on refractive index. APTES has a similar refractive index as oxide and therefore can be modeled as an oxide [8]. Table 1 shows a significant change in oxide thickness, indicating deposition of APTES.

	Pre-APTES	Post-APTES	Difference
Goniometry data			
Patterned GaN:	53°	43°	-10°
Patterned Si:	52°	29°	-23°
Bare GaN:	< 5°	27°	+27°
Bare Si:	< 5°	15°	+15°
Ellipsometry data			
Bare GaN:	7.1 Å	8.7 Å	1.6 Å
Bare Si:	17.1 Å	23.4 Å	6.3 Å

Table 1: Goniometry and ellipsometry characterization. Patterned samples underwent hydroxylation and photolithography before deposition. Bare samples only underwent hydroxylation before deposition and were used as reference samples.

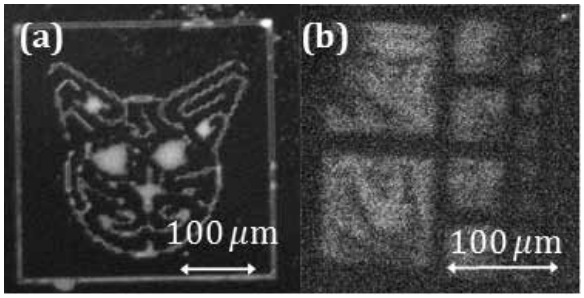

Figure 3: Fluorescence microscopy images of (a) cat and (b) square family on silicon. (See full-color version on inside cover.)

To verify patterning of the samples with APTES, the samples were characterized by fluorescence microscopy after liftoff. The samples were dyed with fluorescein isothiocyanate, which covalently binds with APTES and fluoresces at 510 nm (green light) when excited by 488 nm light (blue light). Figure 3 shows the fluorescently labeled samples, confirming patterning of the APTES.

Conclusions and Future Work:

Deposition and patterning of APTES on GaN were performed and characterized to support the development of a HEMT radiation detector. Future work includes investigating the attachment of *D. radiodurans* to APTES, and investigating the effectiveness of a *D. radiodurans* and GaN-based HEMT device for radiation detection.

Acknowledgments:

Many thanks to the following people and groups for their support: Ateeq Suria, Prof. Debbie G. Senesky, the XLab, Dr. Michael Deal, Maureen Baran, the NNIN SNF REU group, SNF staff and lab members, Cui Group, NNIN REU Program, and NSF.

References:

[1] R. Bashir, Adv. Drug Deliv. Rev., vol. 56, pp. 1565-1586, 2004.
[2] J. Howgate, Ph. D. dissertation, Dept. Physics, Walter Shottky Institut, Munich, Germany, 2012.
[3] G. Steinhoff, et al., Adv. Funct. Mater., vol. 13, pp. 841-846, 2003.
[4] M. Stutzmann, et al., Diamond Relat. Mater., vol. 11, pp. 886-891, 2002.
[5] G. GuanJun, et al., Chi. Sci. Bull., vol. 53, pp. 1675-1681, 2008.
[6] M. J. Daly, Nat. Rev. Microbiol., vol. 7, pp. 16-18, 2009.
[7] B. Baur, et al., Appl. Phys. Lett., vol. 87, pp. 263901, 2005.
[8] F. Zhang, et al., Amer. Chem. Soc., vol. 26, pp. 14648-14654, 2010.

PROC

Electrokinetic Characterization of Nanoscale Metal Oxide Films

Moath Othman
Materials Science and Engineering, San Jose State University

NNIN REU Site: Cornell NanoScale Science and Technology Facility, Cornell University, Ithaca, NY
NNIN REU Principal Investigator: Brian J. Kirby, Sibley School of Mechanical and Aerospace Engineering, Cornell University
NNIN REU Mentor: Alexander C. Barbati, Sibley School of Mechanical and Aerospace Engineering, Cornell University
Contact: moath.othman@gmail.com, bk88@cornell.edu, acb238@cornell.edu

Abstract:

In this work, we constructed a device to characterize the zeta potential of metal oxide films using electrokinetic forcing. In preparation, we characterized aluminum oxide tracer particles in a Malvern Zetasizer over a range of pH and salt concentrations. Then, we prepared oxide films of controlled thickness and chemistry, which were used to define a parallel-plate electrokinetic cell. With the particles suspended in fluids of varying salt concentrations and pH, we applied a voltage to generate an electroosmotic flow in the channel. Through measurements of the particle motion with particle image velocimetry (PIV) we could determine the zeta potential of the solid surface.

Introduction:

In micro- and nano-scale systems, electrokinetics plays an important role in determining the physical and chemical attributes of a system. Many solid surfaces become charged in the presence of a liquid due to (a) ionization of surface groups, and (b) adsorption of ions in solution onto a surface [1]. The charge of a surface will change as the salt concentration and pH of a solution are varied. The electrical potential, or zeta potential, is a measure of the electrokinetic properties of the surface.

Determination of the zeta potential of a surface in solutions of defined pH and salt concentration enables better understanding of the interactions between particles and surfaces. Knowledge of surface zeta potential is relevant to a wide variety of applications which involve a chemical interaction between particles and solutions.

$$u = \frac{-\varepsilon_0 \varepsilon}{\eta}(\zeta_p + \zeta_w)\nabla\phi$$

u: particle velocity
ζ_p: particle zeta potential
ζ_w: wall zeta potential
ϕ: external electric field
η: viscosity of solution
ε: electrical permittivity of solution

Figure 1: By measuring the velocity of particles under an electric field, we could characterize the zeta potential of the surface if the zeta potential of the particles was known.

In this work, we combined electroosmotic forcing and particle electrophoresis to determine the zeta potential of metal oxide surfaces in a custom built electrokinetic device. Using PIV, we could determine the velocity of a particle undergoing electrophoresis in an electroosmotic flow. The particle velocity can be used to determine the zeta potential of the wall, if the particle zeta potential is known, as shown in the equation in Figure 1 [2].

Particle Preparation and Characterization:

We first prepared solutions over a range of salt concentrations and pH; using sodium chloride (NaCl), we prepared 0.1 mM, 1 mM, and 10 mM solutions between pH 1 and 5, using HCl. We then cleaned the 700 nanometer alumina particles by mixing 0.03 grams of alumina particles in a 50 mL solution of deionized water, sonicating the particles to ensure proper dissolution, and centrifuging the particles for 20 minutes at 2500xg. The alumina particles would sediment to the bottom of the flask, and we exchanged the fluid in the flask for another 50 mL of deionized water. The process was repeated a total of three times, after which the particles were removed and dried in an oven for two hours. The particles were then mixed with solutions of known pH and salt concentration, and sonicated.

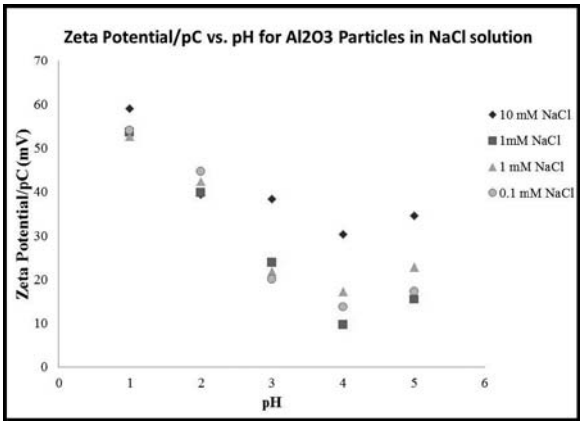

Figure 2: The zeta potential normalized by the counter ion concentration of the alumina particles showed a strong dependence on pH, but minimal variation with respect to salt concentration.

To characterize the zeta potential of the alumina particles, we used a Malvern Zetasizer Nano, which measures properties of suspended particles using dynamic light scattering. We characterized the particle zeta potential in the various solutions described above, as shown in Figure 2. Measured alumina particle zeta potentials were consistent with literature values [3].

Device Fabrication and Experimental Setup:

To fabricate the device, we deposited 300 nm of hafnium oxide (the material of interest) onto two 25 mm × 75 mm glass slides. One glass slide had two thru holes located 40 mm apart along the slide centerline. The two Hafnia substrates were assembled to sandwich a 127 μm Teflon® shim with a center removed, forming a 127 μm tall channel between the Hafnia surfaces. We sealed the edges with epoxy to prevent leaks. We fabricated large reservoirs above the thru holes to minimize surface tension effects and pressure gradients. A cross-section of the device is presented in Figure 3.

To run an experiment, we used a function generator, an amplifier, a voltmeter, two platinum electrodes, a camera, and a Nikon Eclipse TE2000-u inverted microscope. Initially, we filled the channel of our fabricated device with alumina particles suspended in solution. We then generated a square wave, amplifying the signal to our desired voltage, and used this field to actuate fluid in the device via platinum electrodes inserted in the reservoirs. The alumina particles suspended in salt solution could be tracked by taking a sequence of images using a camera, and the particle velocity could be measured via PIV. The experimental setup is shown in Figure 4.

Conclusions and Future Work:

In this work, we were able to successfully construct an electrokinetic device that can be used to determine the zeta potential of metal oxide films deposited on glass substrates. Our future work will be to calculate the zeta potential of hafnium oxide over a new range of pH using particle image velocimetry, fabricate similar devices for other metal oxide films, and improve the overall design of our device.

Acknowledgements:

I would like to particularly thank Dr. Brian Kirby and Alexander Barbati, as well as the Kirby research group and the Cornell NanoScale Facility staff at Cornell University. I'd also like to thank the National Nanotechnology Infrastructure Network Research Experience for Undergraduates (NNIN REU) Program and the National Science Foundation for making this experience possible.

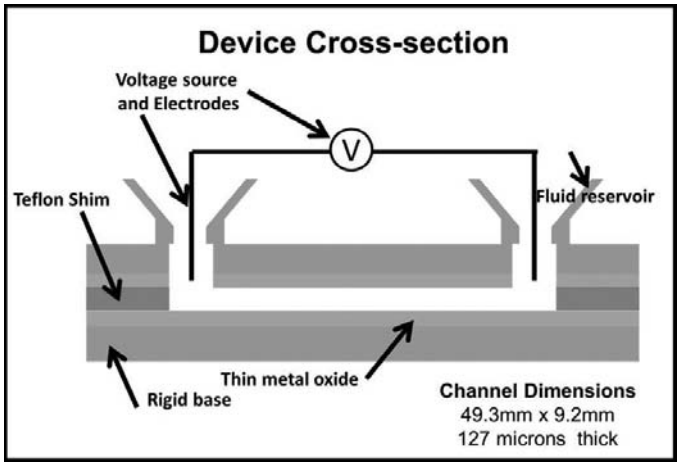

Figure 3: The relatively small channel thickness allowed us to assume 2D motion of alumina particles across the channel.

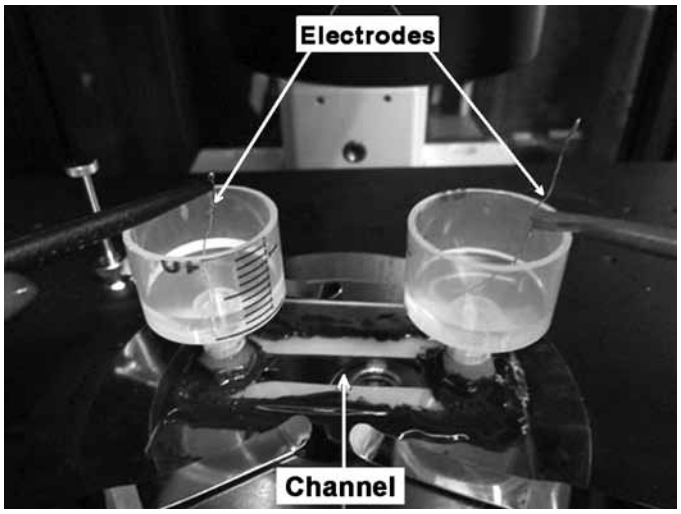

Figure 4: Using an inverted microscope and camera, we tracked alumina particles as they moved through the channel under an electric field.

References:

[1] Tandon, V., et al.; "Zeta potential and electroosmotic mobility in microfluidic devices fabricated from hydrophobic polymers: 1. the origins of charge"; Electrophoresis 29(5):1092-1101, 2008.

[2] Kirby, B.J.; "Micro- and Nanoscale Fluid Mechanics: Transport in Microfluidic Devices," Cambridge University Press, 2010.

[3] Bimal, P., et al.; J. of Colloid and Interface Science, pgs. 181-186 (2011).

Influence of Al_2O_3 Coating on the Annealing Behavior of Si Nanowires

Jaelin Quinn
Chemistry, Elizabeth City State University

NNIN REU Site: Nanotechnology Research Center, Georgia Institute of Technology, Atlanta, GA
NNIN REU Principal Investigator: Dr. Michael Filler, Chemical and Bimolecular Engineering, Georgia Institute of Technology
NNIN REU Mentors: Ildar Musin, Ho-Yee Hui, and Dr. Li-Wei Cho, Chemical and Biomolecular Engineering, Georgia Tech
Contact: quinn704@yahoo.com, michael.filler@chbe.gatech.edu, ildarm@gatech.edu, hhui3@gatech.edu, li-wei.chou@chbe.gatech.edu

Abstract:

Doped semiconductor nanowires have been utilized in many prototype energy harvesting, molecular detection, and plasmonic devices. The use of these materials, which are synthesized via the vapor-liquid-solid (VLS) technique, is dependent on the robust control of carrier concentration. To enable the electrical activation of previously incorporated dopant atoms, rapid thermal annealing (RTP) is generally required. However, due to rapid surface diffusion, silicon nanowires deform at temperatures (~1000°C) far lower than that expected from their bulk melting point (1414°C). To this end, we investigated conformal aluminum oxide (Al_2O_3) coatings as a route to suppress silicon (Si) atom surface diffusion and preserve nanowire structure. Al_2O_3 has a melting point around 2072°C. We studied how nanowire morphology was impacted under annealing in a nitrogen ambient for no more than one second at 900°C, 1000°C, and 1100°C, and used scanning electron microscopy (SEM) to analyze our data. We observed that none of the coated and non-coated nanowires melted, even at the highest temperature, which contradicts previous data collected under vacuum conditions in our laboratory. We then annealed the nanowires at the highest temperature (1100°C) for ten seconds and observed that the non-coated nanowires melted. We suspect the observed differences are due to the ambient chemistry and plan to test different gases, including Ar and H_2, in the future. Shorter annealing times will also be explored in attempt to fully map the process window.

Introduction:

The main goal of this research project was to suppress the Si atom surface diffusion with an Al_2O_3 coating. Al_2O_3 coats conformally, is very cost efficient, and forms a strong bond with Si nanowires, which makes it an ideal system to use in this experiment. Si is ubiquitous, which causes it to have an extensive knowledge base and many well-established methodologies. Dopants make Si conducive, however not all dopants may be active by taking up interstitial sites instead of substitutional in the diamond cubic crystal lattice. Thermal energy can activate dopants by allowing a dopant to take place of a silicon atom and become substitutional. In this experiment, phosphorus was our dopant, and in order for our dopant to be activated, annealing was necessary. Doped Si nanowires could be used for many applications such as plasmonic devices, which are devices that convert light into energy, energy harvesting such as solar cells, and molecular detection.

Experimental Procedure:

Researchers in this study performed atomic layer deposition (ALD), rapid thermal processing (RTP), and a scanning electron microscope (SEM) was used. Nanowires were grown using the vapor-liquid-sold technique. After the wires were complete, the gold was removed using an aqua regia solution. Researchers used two samples, one with Al_2O_3 coating and one without. Using ALD, we first coated the gold-removed Si nanowires with 30 nm of Al_2O_3 at 250°C. We then used RTP to spike-like anneal both samples of our nanowires at ~ 900°C, ~ 1000°C, and ~ 1100°C for less than one second. We also annealed our wires at the highest temperature (~1100°C) for ten seconds. During the annealing process, we used a continuous flow of nitrogen throughout the chamber. SEM was used to analyze our data.

Results and Conclusions:

In conclusion, we observed that the coated and non-coated nanowires that were annealed for less than one second did not melt. We believe that the non-coated nanowires remained in tact longer than expected may have occurred due to the continuous flow of the ambient gas, nitrogen, during the annealing process, which cooled down the nanowires. We also observed that when we annealed the nanowires for ten seconds at 1100°C, the alumina coating protected the wires from melting, and the non-coated wires were completely melted.

Future Work:

In the future, shorter annealing times could be applied to see if that affects the morphology of the nanowires. Also, we could test to see if different ambient gasses such as argon or hydrogen would have a major effect on the preservation of nanowires while being annealed.

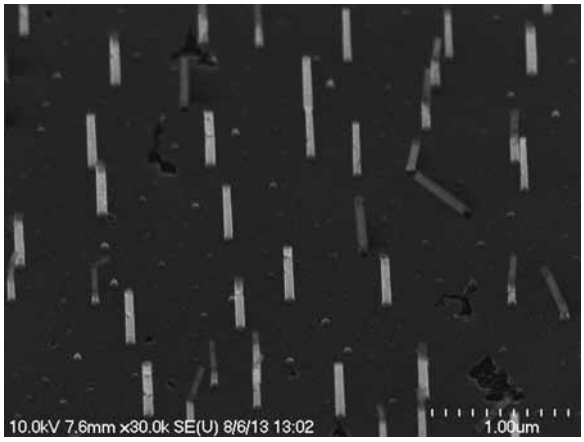

Figure 1: Nanowires coated with Al_2O_3, annealed at the highest temperature (1100°C) for one second.

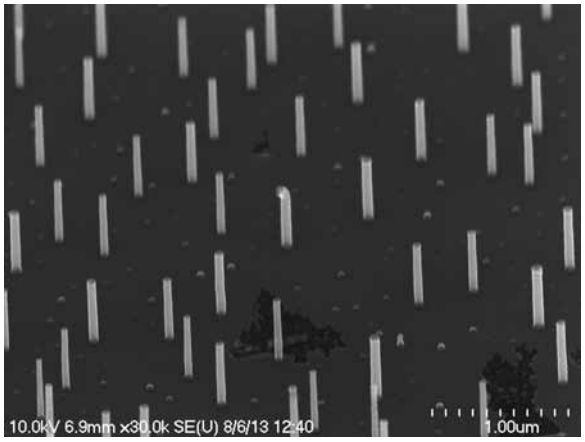

Figure 2: Nanowires with no coating, annealed at the highest temperature (1100°C) for one second.

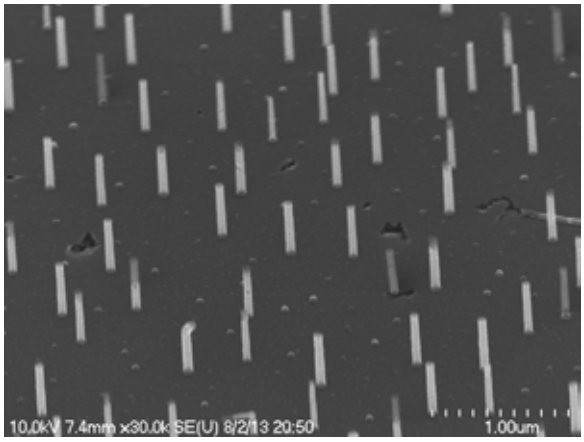

Figure 3: Nanowires coated with Al_2O_3, annealed at the highest temperature (1100°C) for ten seconds.

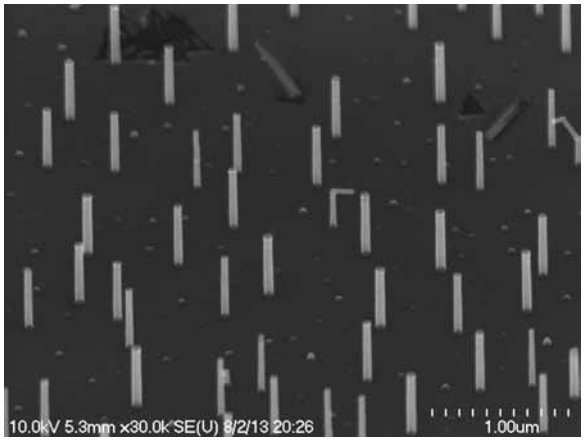

Figure 4: Nanowires with no coating, annealed at the highest temperature (1100°C) for ten seconds.

Acknowledgements:

I would like to thank Dr. Michael Filler, Ildar Musin, Ho-Yee Hui, Dr. Li-Wei Chou, and the entire Filler research group for there support and guidance throughout my internship. I would also like to thank Mrs. Leslie O'Neil, Dr. Nancy Healy, and Ms. Melanie-Claire Mallison for being such great program coordinators and showing strong commitment to the NNIN REU Program at Georgia Tech. Furthermore, I would like to thank the cleanroom staff at Georgia Tech for their great training, especially John Pham for taking time out to assist me during procedures when needed. Also, I would like to thank the E-Spare Program of Elizabeth City State University and Quachel Bazile (2012 NNIN REU), ECSU Alumni for helping me throughout my journey. Finally, I would like to thank the National Nanotechnology Infrastructure Network Research Experience for Undergraduate Program and the National Science Foundation for their support and funding.

References:

[1] Chou, Li-Wei, Dr., and Michael A. Filler, Prof. "Engineering Multimodal Localized Surface Plasmon Resonances in Silicon Nanowires." Wiley College. Onlinelibrary.wiley.com. DOI: 10.1002/anie.201301468, 13 June 2013.

[2] Chou, L.-W., Dr., N. Shin, S.V. Sivaram, and Prof. M.A. Filler, "Tunable Mid-Infrared Localized Surface Plasmon Resonances in Silicon Nanowires." J. Am. Chem. Soc., 134 (39), pp 16155-16158, DOI: 10.1021/ja3075902, September 2012.

[3] Min, B., J.S. Lee, K. Cho, J.W. Hwang, H. Kim, M.Y. Sung, S. Kim, J. Park, H.W. Seo, S.Y. Bae, M.-S. Lee, S.O. Park, and J.-T. Moon. "Semiconductor Nanowires Surrounded by Cylindrical Al_2O_3 Shells. Journal of Electronic Materials, 32.11, 1344-348 (2003).

Deposition and Characterization of Magnetic Permalloy for Future Endomicroscope Actuators

Joseph Rivas
Mechanical Engineering, Binghamton University

NNIN REU Site: Lurie Nanofabrication Facility, University of Michigan, Ann Arbor, MI
NNIN REU Principal Investigator: Kenn Oldham, Mechanical Engineering, University of Michigan
NNIN REU Mentor: Pilar Herrera-Fierro, Solid-State Electronics, and Electrical Engineering, University of Michigan
Contact: jrivas2@binghamton.edu, oldham@umich.edu, pilarhf@umich.edu

Introduction:

When nickel and iron are combined in an 80% to 20% ratio, respectively, the resulting material is called permalloy. Permalloy expresses strong magnetic properties and as such, is a prime candidate for future actuator applications. The biomedical community has taken recent interest in the development of permalloy structures. One potential application in that field is as an alternative to comparatively large piezoelectric actuators currently used in novel prototype endomicroscopes. The use of permalloy will be attempted in order to produce smaller actuators that will instead apply a magnetic field to control lens movement. This project aimed to characterize the different permalloy films that were plated when variables such as current density, plating duration, and pulse timing were varied in the electroplating process.

Oxide-coated wafers were deposited with a chrome-gold seed layer and a secondary oxide coating on the back provided insulation. Photoresist was developed on wafers after electroplating, and was removed in order to begin etching. Ferric chloride, gold etch, and CR-14 etchants were used to etch to the oxide; plasma etch machines etched the oxide and the silicon in order to create cantilevers. A magnetic field was finally applied to test the magnetic properties of these permalloy cantilevers.

Experimental Procedures:

A typical electroplating process requires that a wafer be coated with a conductive seed layer and patterned with photoresist prior to the plating. A seed layer consisting of 500Å of gold and 300Å of chrome was deposited onto the oxide wafers with an EnerJet Evaporator tool. Subsequently, KMPR photoresist was spun at 3000 rpm in order to produce a film 9-10 μm thick. Various different masks were initially used in order to characterize the plating rate and experiment with the current density. Wafers were inserted into a nickel-iron electroplating solution. A dummy was plated for ten minutes at a current density of 20 mA/cm^2 in order to prepare the ion flow in the solution. Wafers were then plated at several different current densities for varying amounts of time. The plating program for the electroplating process consisted of a forward current pulse 90 ms on and 10 ms off for a total pulse duration of 100 ms. After a primary energy dispersive x-ray spectroscopy (EDX) analysis with a scanning electron microscope, it was concluded that a lower current density provided a higher concentration of nickel. Once the permalloy was plated, the photoresist was stripped with acetone and Remover PG.

The permalloy structures were inspected with the Olympus BX-51 microscope and the LEXT Interferometer in order to measure surface roughness and determine if there was any remaining photoresist. A wet etch procedure was conducted with gold etch and CR-14 chrome etch in order to strip the seed layer; a 40 second gold etch produced a substantial undercut in the permalloy features, causing them to fall off.

A different approach was attempted in order to reduce the undercut and produce useful permalloy structures. Thus, permalloy was then plated directly onto the seed layer. Furthermore, the seed layer thickness was reduced to 75Å of chrome and 250Å of gold. Since the permalloy was being plated onto a bare surface, the resulting films were extremely stressed and were peeling at the edges of the wafer.

The plating program was gradually modified to include a reverse current and adjusted pulse timing, as seen in Figure 1. The reverse current allowed the ions to ease off the wafer before being plated, thus reducing the film stress and providing a smoother film.

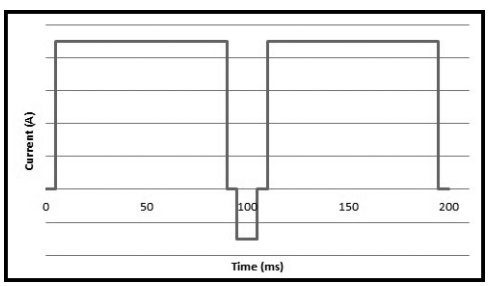

Figure 1: Final pulse timing.

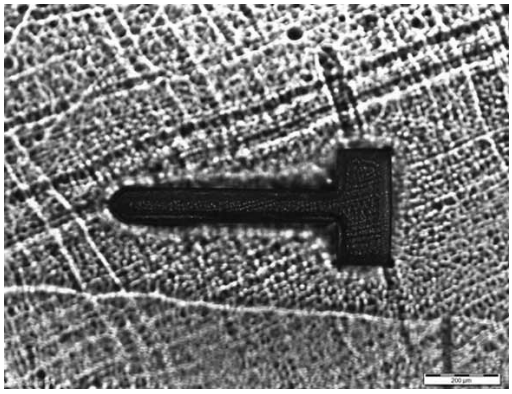

Figure 2: Completed cantilever.

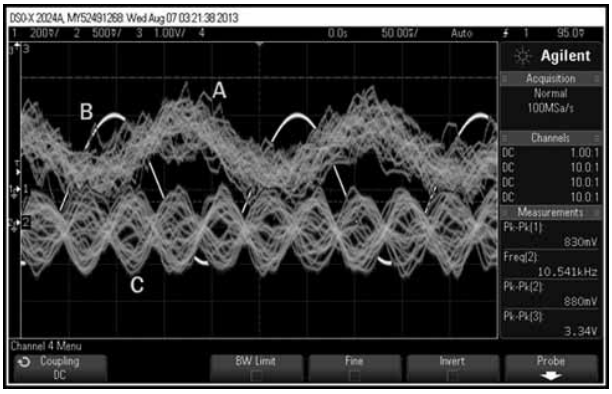

Figure 3: Oscilloscope readings.

The permalloy wafers were then spun with AZ-9260 photoresist. Exposure times for a permalloy base are not given, so we used the same exposure time as one would use for a gold base, in this case 90 seconds (s). The wet etch was attempted again, though this time the excess permalloy was etched with ferric chloride, an etchant typically used for copper. The permalloy structures still suffered from severe undercut, compromising the structural integrity of the cantilevers and rendering them unusable. The etching was characterized and it was determined that 43 seconds of ferric chloride, 18 s of gold etch and 7 s of CR-14 produced stable permalloy features.

Once the seed layer was stripped, the wafers went through a 30 minute plasma etch on the Plasmatherm 790 tool in order to remove the 8000Å oxide layer. The wafers were then subjected to an anisotropic xenon difluoride (XeF_2) etch in order to undercut the cantilever structures and release them from the wafer base. This process ran for a total of 230 cycles at 30 seconds each. Figure 2 shows a cantilever after all the etching has been completed.

Results and Future Work:

After the cantilevers were created, they were tested by applying a magnetic field generated from running a current through a coil. A Laser Doppler vibrometer was placed over the cantilevers in order to measure the vibration of the cantilevers. Frequency sweeps were conducted in an attempt to find the resonant frequency, but most of the input frequencies produced no noticeable patterns from the cantilevers. As seen in Figure 3, wave C shows that a certain frequency did produce some kind of pattern on the cantilevers. Though the LDV did measure a pattern, this was enough to prove the strength of the permalloy films. It is also possible that the LDV was picking up a different motion. More accurate testing must be done in order to confirm that permalloy is indeed a viable alternative to the lead zirconate titanate (PZT) material that is currently used in endomicroscope actuators.

Acknowledgements:

This work would not have been possible without the generosity and guidance of my PI Kenn Oldham and mentor Pilar Herrera-Fierro. I would also like to thank the entire Wet Chemistry Laboratory team for their help and insight. I am indebted to the National Science Foundation and the NNIN REU Program for this opportunity.

PROC

Infrared Photodetectors with Two Dimensional Materials

Andrew Stephan
Physics Department, Bethel University

NNIN REU Site: Minnesota Nano Center, University of Minnesota-Twin Cities, Minneapolis, MN
NNIN REU Principal Investigator: Dr. Steven J. Koester, Electrical and Computer Engineering Department, University of Minnesota
NNIN REU Mentor: Yoska Anugrah, Electrical and Computer Engineering Department, University of Minnesota
Contact: aws33656@bethel.edu, anugr002@umn.edu, skoester@umn.edu

Abstract:

In this work, a new heterostructure photodetector has been designed using monolayer graphene and varying thicknesses of molybdenum disulfide. This device could provide sensitivity in the infrared (IR) region optimal for optical communication, 1550 nanometers (nm), while maintaining low dark current. Monolayer graphene grown by chemical vapor deposition (CVD) has been patterned onto mechanically exfoliated molybdenum disulfide (MoS_2) and titanium-gold (Ti-Au) contacts made to both materials. Initial electrical characterization of the devices has been performed. The resulting resistance and linearity of the contacts agree with predictions. Infrared probing of the device at 1550 nm indicates either more surface area or a different wavelength is required.

Introduction:

As computer processor speed rises exponentially, the bandwidth required for inter-processor communication grows as well. Integrated optoelectronics may solve the interconnect bandwidth bottleneck. The three necessary components are infrared transmitters, modulators and detectors. The field of infrared transmission is already a mature science, and some progress has been achieved with experimental infrared modulators with signs of future success. The remaining piece of the puzzle is suitable infrared photodetectors. The unique properties of two dimensional (2D) materials could be the key to their construction, helping to realize the next generation of high-speed optical communications.

Device Concept:

Previous attempts to construct an IR photodetector with 2D materials focused on graphene, which absorbs radiation over a wide wavelength range spanning from the far infrared to the visible. However, graphene is problematic because of its high conductivity. Any voltage applied to collect charge carriers freed by radiation will also cause non-photoinduced current, or dark current. This dark current is on the same order as the photocurrent from an ordinary source, resulting in a low signal-to-noise ratio. To circumvent this issue, MoS_2 was incorporated

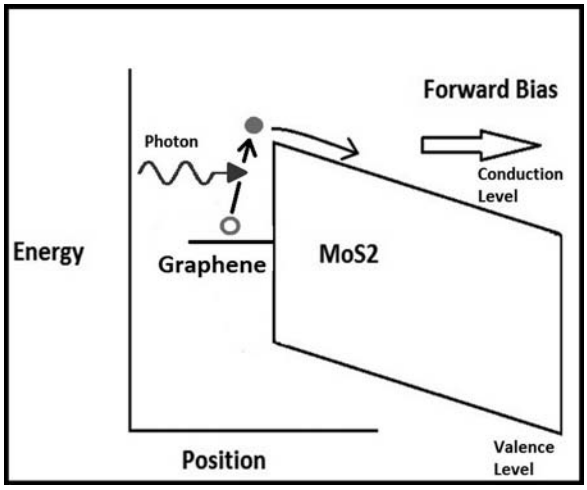

Figure 1: Envisioned operation in the new device. An infrared photon induces a graphene carrier to make the leap into the MoS_2's conduction band, where it is carried away by the applied bias, thus producing a signal. The photon must carry at least enough energy to overcome the graphene-MoS_2 barrier.

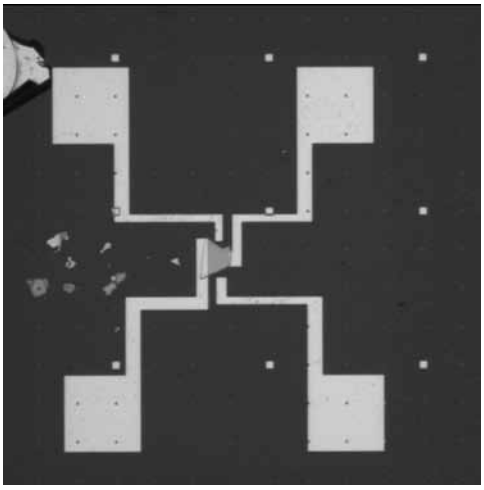

Figure 2: A completed device. The central piece is a flake of MoS_2 of approximately 50 µm by 50 µm. Atop this is a nearly-transparent piece of graphene. A pair of Ti-Au contacts overlaps the edge of each material.

into the device to introduce a band-gap, which minimizes dark current, thus improving the signal. It is believed that the Fermi level in graphene is between the conduction and valence bands of bulk MoS_2. Since the gap exceeds the energy contained in a 1550 nm photon, it should be possible to gate the device so as to induce an energy barrier between the graphene and MoS_2 which corresponds to 1550 nm. This is both the device's absorption and noise-reduction mechanism.

Fabrication Sequence:

A sequence of fabrication steps was developed to produce these devices. The first step was using electron-beam lithography (EBL) and electron beam evaporation (EBE) to attach an alignment grid onto the chosen substrate — in this case, a silicon dioxide and silicon wafer. The second step was mechanical exfoliation of MoS_2 onto the wafer and location of suitable flakes. After their locations were mapped out, a large sheet of monolayer graphene was removed from its copper foil and placed over the substrate. Then EBL was used to pattern a resist polymer onto the flakes to protect certain areas of the graphene sheet. A light oxygen plasma removed the uncoated areas of graphene. Finally EBL and EBE were applied once more to lay down metallic contact pads on the graphene and MoS_2.

Characterization:

After some devices were completed, they were tested by measuring the current induced by applying voltages between the graphene-graphene, graphene-MoS_2, and MoS_2-MoS_2 contact combinations. The resulting I/V characteristics showed that the electrical contacts were alive and behaved as expected. The graphene-graphene characteristic was linear, indicating an Ohmic contact with a resistance of approximately 27 kΩ. The MoS_2-MoS_2 and graphene-MoS_2 tests, on the other hand, exhibited behavior reminiscent of a Schottky barrier, producing asymmetric I/V characteristics whose linear approximations give resistances of approximately 67 MΩ and 33 MΩ. These preliminary results suggest photodetector should be detectable with this device.

However when the same characterizations were performed with an IR laser incident on the sample, no significant change was recorded. There are several possible explanations for this. First, the testing stage used required that the fiber carrying the IR signal be several millimeters over the sample, causing the beam to diverge drastically. Another possibility is that the junction region will not absorb 1550 nm light. This could be rectified by gating the junctions appropriately to shift the Schottky barrier. Another possibility is that the device's small surface area did not allow enough absorption for an appreciable photocurrent, but this seems less likely as other detectors of a similar size have been fashioned from graphene alone.

Future Work:

There is a vast amount of progress left to be made. The very first step, as mentioned above, is to achieve photodetection in the ideal region near 1550 nm. Subsequently various optimizations must be performed to determine the ideal size, thickness and possibly shape of the MoS_2 flakes that should be used. Monolayer, or 2D, MoS_2 should be an area of special interest due to its unique band structure. If these devices can be made as effective as is hoped, then a more efficient exfoliation process must also be found so as to make mass production a more realistic goal.

Conclusions:

A new heterostructure photodetector using 2D materials has been proposed, a fabrication sequence developed and prototypes constructed. Initial characterizations show promise but much work remains before actual photodetection is measured. If the potential of these devices is realized they could replace current electronic communications systems, greatly enhancing computational data transfer bandwidth.

Acknowledgements:

I would like to thank Dr. Steven Koester and my mentor Yoska Anugrah for helping me at every step of the way, and the National Science Foundation, the National Nanotechnology Infrastructure Network Research Experience for Undergraduates (NNIN REU) Program, and the University of Minnesota for making this research possible.

Electron Transfer Dynamics in Polymer Solar Cells Studied by Femtosecond Transient Absorption Measurements

Andrew Tam
Electrical Engineering, Rice University

NNIN iREU Site: National Institute for Materials Science (NIMS), Tsukuba, Ibaraki, Japan
NNIN iREU Principal Investigator: Dr. Kohei Uosaki, Director General of Global Research Center for Environment and Energy based on Nanomaterials Science (GREEN), National Institute for Materials Science (NIMS)
NNIN iREU Mentors: Dr. Hidenori Noguchi, Nano Interface Group, National Institute for Materials Science (NIMS); Dr. Mikio Ito, Global Research Center for Environment and Energy based on Nanomaterials Science (GREEN), National Institute for Materials Science (NIMS)
Contact: andrew.m.tam11@gmail.com, uosaki.kohei@nims.go.jp, noguchi.hidenori@nims.go.jp, ito.mikio@nims.go.jp

Abstract and Introduction:

Organic molecules offer a cheaper alternative to traditional bulk crystalline materials for solar cells. Unfortunately, none have yet shown efficiencies as high as those in silicon devices. Efficient solar cell materials must have an electronic band gap suitable for absorbing most of the radiation emitted by the sun, optimally 1.1-1.4 eV. So far, the band gaps of all organic polymers created for this purpose have been much higher or the molecules have been insoluble, preventing cheap production of efficient polymer solar cells. To improve the cost-efficiency of polymer solar cells, new soluble molecules are needed with smaller band gaps. PDTNT-DPPOD is a new such organic molecule synthesized by Dr. Yasuhiro Shirai of the Japanese National Institute for Materials Science (NIMS). It has a band gap of 1.37 eV and can act as an electron donor when paired with PCBM or C60 acceptor molecules.

In actual devices, however, the short-circuit current and open circuit voltages were lower than expected. In order to understand why, we use pump-probe spectroscopy to determine if electrons are being excited in the donor molecule and transferred to the acceptor molecules in solution.

Experimental Procedure:

We made three solutions of PDTNT-DPPOD dissolved in ortho-dichlorobenzene: PDTNT-DPPOD, PDTNT-DPPOD with PCBM, and PDTNT-DPPOD with C60. In all solutions, the concentration was 1 mg/mL. The mass ratio between PDTNT-DPPOD and PCBM/C60 was 1:1. For each pump-probe measurement, a 0.2 mm thick layer of one solution was flowed through a flow-cell using a 35 hz vibration pump. A pump pulse of 700 nm and a probe pulse of 670 nm were shone on the sample and the absorbance of the probe pulse was recorded. The delay between the two pulses was varied over a range of about 60 picoseconds. For the solutions of PDTNT-DPPOD alone and PDTNT-DPPOD with PCBM, the pump power was 10 mW and the probe power was 6 mW, at a repetition rate of 1 kHz. For the solution of PDTNT-DPPOD and C60, the pump power was 10 mW and the probe power was 4 mW at 1 kHz repetition, but the repetition was then lowered to 100 Hz to allow the system to return to the ground state between data point collection.

Results and Conclusions:

Pump-probe measurements of all three solutions showed a clear decrease in absorbance at zero delay between the pump and probe pulses. This indicates promotion of the ground state electrons to higher energy states, resulting in an absence of electrons that would have otherwise absorbed the probe pulse. We define the peak to steady-state ratio as the maximum decrease in absorbance over the end behavior decrease in absorbance (A/B in the figures).

PDTNT-DPPOD alone had the largest peak to steady-state ratio of 7.3, indicating most electrons excited by the pump pulse returned to the ground state 50 picoseconds later (Figure 1). The decay of the absorbance decrease was fitted by a two-exponential function with a fast portion corresponding to the singlet state decay and a slower portion corresponding to triplet state decay. PDTNT-DPPOD with PCBM had a lower peak to steady-state ratio of 4.9 indicating some electrons were captured by the PCBM acceptor and prevented from returning to the ground state (Figure 2). The decay still showed two separate exponential components corresponding to the singlet and triplet state decays however, indicating that many excited electrons were not captured. PDTNT-DPPOD with C60 had the lowest peak to steady-state ratio of 2.6, indicating a more efficient electron transfer than with PCBM (Figure 3). Additionally, the decay function had only a slow exponential component; the lack of an observed fast decay rate back to the ground state indicates efficient singlet charge transfer to the C60.

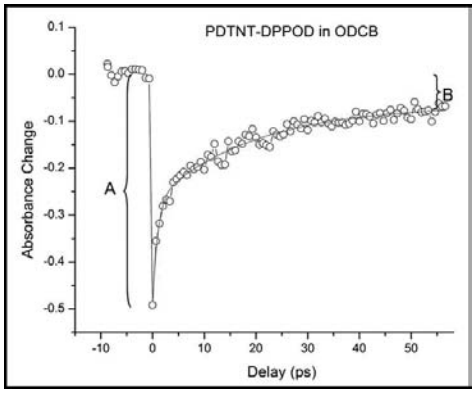

Figure 1: PDTNT-DPPOD undergoes rapid electron excitation, followed by a two-part exponential decay.

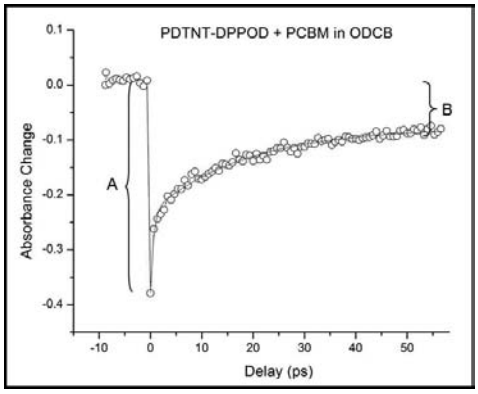

Figure 2: PDTNT-DPPOD with PCBM's moderate decrease in absorption indicates weak electron transfer.

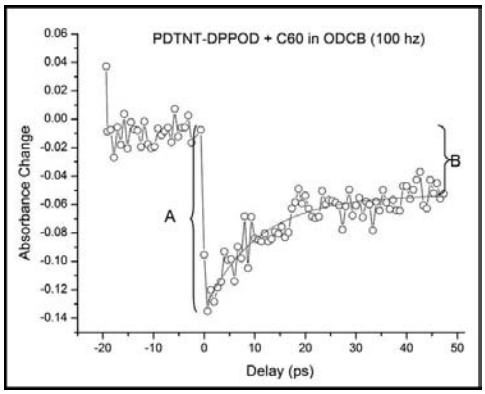

Figure 3: PDTNT-DPPOD with C60 has almost twice the absorption decrease of PCBM, indicating more efficient electron transfer.

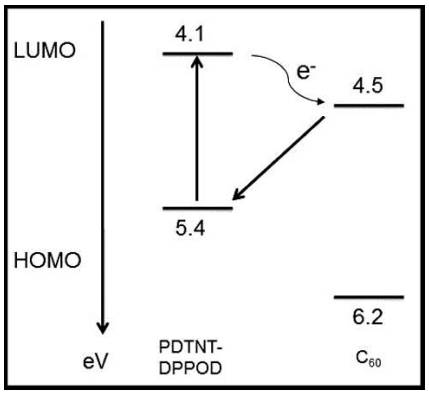

Figure 4: Electron excitation, charge transfer, and return to ground state/HOMO in PDTNT-DPPOD and C60.

PDTNT-DPPOD with C60 was originally measured at a repetition rate of 1 kHz, but that measurement never reached steady state. The measurement had to be repeated at 100 Hz because the absorbance of the system took longer to recover than for PDTNT-DPPOD alone. This indicates that charge transfer occurred from PDTNT-DPPOD's lowest unoccupied molecular orbital (LUMO) to C60's LUMO, which then had a longer recovery time back to PDTNT-DPPOD's highest occupied molecular orbital (HOMO) than from PDTNT-DPPOD's LUMO (Figure 4). This confirms device testing results that C60 served as a better electron acceptor than PCBM.

Future Work:

We have determined that the electron transfer process between PDTNT-DPPOD and PCBM is inefficient, likely because there is only a 0.1 eV difference in their LUMO energy levels. However, it is still unclear why solar cells made with PDTNT-DPPOD and C60 exhibit such low short-circuit current and open circuit voltage when compared with other molecules synthesized by Dr. Shirai's group. Fluorescence studies are needed to characterize the absorption wavelengths of different charge species for this molecule. To better understand device performance, nanosecond pump-probe measurements can be performed to determine carrier lifetime and recombination timescales. Solutions and films of thiophenes have also been known to exhibit different characteristics, so experiments should be performed with the film phase of this molecule.

Acknowledgments:

I would like to thank Dr. Kohei Uosaki, Dr. Hidenori Noguchi, Dr. Mikio Ito, Dr. Yasuhiro Shirai, NIMS, NSF, and the NNIN iREU Program for all their help and generosity.

References:

[1] Cook, S., Furube, A., and Katoh, R. Analysis of the excited states of regioregular polythiophene P3HT. Energy and Environmental Science, 1(2), 294-299. (2008).

[2] Guo, J. J., Ohkita, H. H., Benten, H. H., and Ito, S. S. Near-IR femtosecond transient absorption spectroscopy of ultrafast polaron and triplet exciton formation in polythiophene films with different regioregularities. Journal of the American Chemical Society, 131(46), 16869-16880. doi:10.1021/ja906621a (2009).

PROC

Gender and Nanoscientists: The Public Communication of Nanotechnology

Hannah Oros
Media and Communication, Global Health, Muhlenberg College

NNIN REU Site: Microelectronics Research Center, The University of Texas, Austin, TX
NNIN REU Principal Investigators: Dr. Anthony Dudo and Dr. LeeAnn Kahlor,
Department of Advertising and Public Relations, University of Texas at Austin
NNIN REU Mentor: Allison Lazard, Department of Advertising and Public Relations, University of Texas at Austin
Contact: hannah@oros.org, dudo@utexas.edu, kahlor@austin.utexas.edu, lazard@utexas.edu

Abstract:

The public communication of science and technology (PCST) — i.e., communication between scientists, the media, and society — is critical to enhance discourse about emerging technologies. The changing media landscape calls for a reexamination of PCST and nanotechnology. Although imperative, scant research has examined the role gender plays in nanoscientists' PCST engagement. Using a multi-wave online survey, this study examined how nanoscientists use new media to engage in PCST. The Theory of Planned Behavior was used to understand how subjective norms operate in predicting PCST engagement across gender [1]. Penultimate study results suggested that PCST perceptions and behaviors vary between male and female nanoscientists.

Introduction:

Nanotechnology is an emerging technology vulnerable to public opinion and shifts in discourse, which can influence its future applications. PCST allows for sources of scientific knowledge to inform the public, building a foundation for better decision-making regarding nanotechnology policies and regulations. Traditional forms of PCST, such as print media, have had limited success dispensing information to an audience through the deficit model [2]. Decision-making requires more than information dispersal; it should be dynamic, interactive, and include the voices of nanoscientists. The media landscape is changing; new media is arguably more interactive, which has the potential to empower the public to participate and be engaged. This paper provides an assessment of nanoscientists' PCST through new media technologies and examines the predictors of this behavior across gender. Studying gender is important within the nanotechnology because it is male-dominated.

The Theory of Planned Behavior is used to understand the PCST predictors by examining subjective norms, which are perceived social pressures and extrinsic rewards [1]. Subjective norms are perceptions of social influence encouraging one to act on or not act on a behavior and create normative beliefs, which are socially constructed codes of conduct. Normative beliefs are gendered and can thus influence behavior, potentially creating gender differences in PCST [1].

Methods:

Data was collected through a multi-wave e-mailed online survey. A list of 995 nanoscientists was provided by NNIN with contact information dated three years ago; we verified and corrected as much information as possible. The sample size was 65 nanoscientists; the response rate was 6.56% when the data was collected. Responses were excluded from the sample size if the respondents did not indicate their gender. One respondent selected their gender as "Not listed." Fifty respondents were male; fourteen were female. The gender ratio was representative. The data was analyzed using SPSS software.

Results:

The female nanoscientists' reported frequency of new media use (blogs, online forums, social networks, micro-blogging sites, and video-sharing) to communicate about science was generally higher than the male nanoscientists'. Female nanoscientists use social networking to communicate about science more than male nanoscientists. Female nanoscientists are almost twice as likely to use micro-blogging sites to communicate about science than male nanoscientists; however, the frequency of micro-blogging usage was low. There were almost no gender differences regarding PCST and video-sharing and blog usage.

Male nanoscientists were more likely than female nanoscientists to communicate using new media platforms to target the audience of media professionals, while female nanoscientists were more likely than male nanoscientists to

target non-scientists. All female nanoscientists, when using new media platforms to communicate about science, target a non-scientist audience. In contrast, almost one-third of male nanoscientists did not communicate using new media platforms toward a non-scientist audience. Female nanoscientists were approximately twice as likely to have helped plan or conduct a public information campaign than male nanoscientists. Almost one-quarter of male nanoscientists had written an article for the popular media, while zero female nanoscientists had done the same.

No female nanoscientists reported that when corresponding with the media or engaging in PCST related to their research, critical reactions from peers, heads of department or organization and the public were very unimportant. Female nanoscientists place greater importance on these critical reactions than their male counterparts. Female nanoscientists perceive a greater amount of job support and importance in the use of new media platforms to communicate about science. Enhanced personal reputation among peers when corresponding with the media or engaging in PCST was found to be statistically significant; almost three-quarters of female nanoscientists rated it as important and female nanoscientists did not assign any degree of unimportance.

Conclusions:

This study provides a preliminary understanding of nanoscientists' PCST activity using new media and it explores the relationships of gender and subjective norms. Female nanoscientists use new media platforms more often than their male counterparts and perceive more organizational support for using new media to communicate about science. Male nanoscientists have more contact with media professionals and place less importance on the critical reactions when engaging in PCST or corresponding with media professionals. Ultimately, PCST perceptions and behaviors vary between male and female nanoscientists.

Limitations and Future Research:

A limitation of this study was the low response rate and small sample size. This is due to several reasons: lacking up-to-date contact information on the provided list and including them on the e-mail list, time constraints of nanoscientists to finish the survey, and the ongoing nature of the survey.

In future research, the measurement of gender can be more inclusive and incorporate a box to type in one's gender. Future research includes examining the correlation between age, gender, and new media use. An area for future research is studying the relationships between other determinants of the Theory of Planned Behavior, e.g., attitude towards the behavior and perceived behavioral control. Finally, the societal implications of gender differences in PCST engagement should be researched.

Acknowledgments:

I thank my PI, mentor, research group members, site staff and coordinators for their support, and the NNIN REU Program and the NSF for funding.

References:

[1] Ajzen, I. The theory of planned behavior. Organizational behavior and human decision processes, 50(2), 179-211. (1991).

[2] Brown, S. The new deficit model. Nature Nanotechnology. Vol.4, 609-611. (2009).

A Multi-Method Approach to Understanding Knowledge Transfer Practices in the NNIN

Charles Yates
Psychology and Science, Technology and Society, Pitzer College

NNIN REU Site: Nanotechnology Research Center, Georgia Institute of Technology, Atlanta, GA
NNIN REU Principal Investigator: Dr. Jeongsik Lee, Scheller College of Business, Georgia Institute of Technology
NNIN REU Mentor: Hyun Jung, Scheller College of Business, Georgia Institute of Technology
Contact: cyates@students.pitzer.edu, jeongsik.lee@scheller.gatech.edu, hyun.jung@scheller.gatech.edu

Abstract:

While the National Nanotechnology Infrastructure Network (NNIN) attempts to foster knowledge transfers among researchers, there has not yet been documented evidence of the specific knowledge transfers that occur within the network. By observing the practices of the cleanroom, we identified the sources of the transfer and the type of knowledge present. The observational results, along with the surveys (n = 57) administered and interviews (n = 7) conducted, show that; 1) a significant amount of information originates from the staff members and equipment, while there is minimal evidence supporting that there is a significant number of transfers among users, and 2) the transfer of codified knowledge dominates that of tacit knowledge. The findings have implications concerning the future interactions within the NNIN and within other scientific networks.

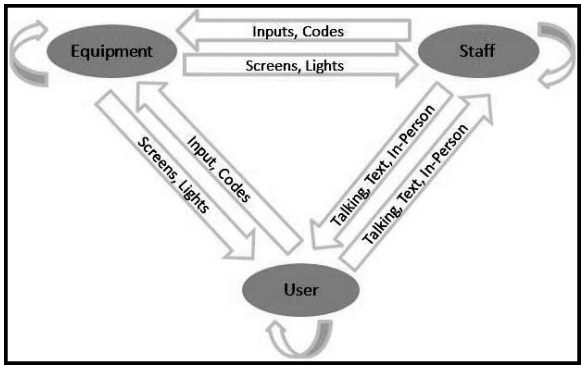

Figure 1: Actors and modes of the observed knowledge transfers.

Introduction:

A knowledge transfer in an organization describes the process through which one unit is affected by the experience of another [1]. This unit, be it an individual or a group, gains novel information from the original unit. It is simply not just a communicative process of transmission and reception, but rather, a process where the experience and information will be used or reused by the new unit [2].

Once acknowledging a knowledge transfer occurred, there are a few ways one can define it through its specific components. Namely, a knowledge transfer can be typically defined as either tacit or codified. While codified knowledge is explicit knowledge based on facts, tacit knowledge is based on experiential learning and accumulating tricks of the trade. Also, identifying where the knowledge is embedded in or originates from can define the transfer, whether it be human actors or inanimate agents. The question then arises on what kinds of knowledge transfers occur within a scientific network and what their natures are.

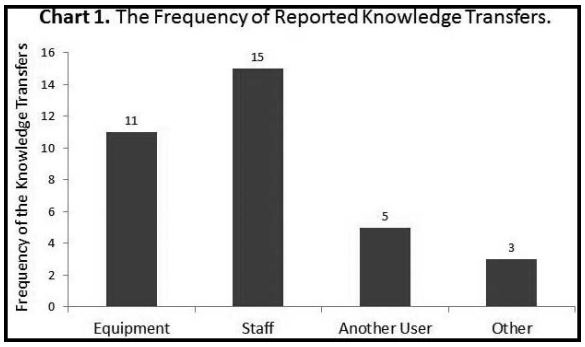

Figure 2: The frequency of reported knowledge transfers.

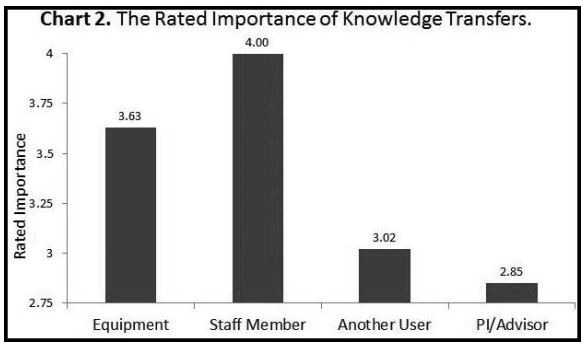

Figure 3: The rated importance of knowledge transfer sources.

Methods:

The ethnographic study included observation, surveys, and interviews. Fieldwork through participant observation allowed the documentation of the knowledge transfers that occurred in the cleanroom. This "fly

on the wall" technique objectively identified the source of the knowledge, what the knowledge was embedded to, and whether it was codified or tacit knowledge [3].

Surveys and interviews were also administered to support the fieldwork observation results. The active users of the Institute for Electronics and Nanotechnology were issued a pre-survey, as this is pilot experimental research. This voluntary survey inquired information about cleanroom usage and the knowledge transfers occurring in there. Out of the 57 users (8.2% yield rate) that participated, 18% were not solely affiliated to the Georgia Institute of Technology. The interviews (7) were conducted to include participant corroboration in the study.

Results and Conclusions:

There were 204 observed knowledge transfers in both the typical cleanroom environment and the training sessions. Codified knowledge transfers occurred five times more than tacit knowledge transfers. A majority of knowledge came from the staff and equipment, also known as the facility, when compared to the users and any other sources. This is interesting as the survey results indicated that both staff members and users prefer to have tacit knowledge transferred during training sessions, but there is still an overwhelming amount of codified knowledge transfers seen in the cleanrooms. The individuals interviewed also acknowledged the lack of communication among users and provided suggestions to foster future interactions.

The surveys indicated that the amount of recorded knowledge transfers coming from the equipment and staff were significantly higher than the transfers that came from the users and other sources. Furthermore, when the participants of the survey were asked to rate the importance of receiving knowledge from different sources, a similar pattern occurred: the importance of receiving knowledge from the facility, staff and equipment, was significantly higher than the reported importance from users and the other sources (rated on a scale from 1 to 5). The fact that users also rate the knowledge coming from the facility significantly higher than the other sources of knowledge is not coincidental; the cleanroom culture's dependence on the staff and equipment is more than evident in all three methods used in this project.

Future Work:

One of the NNIN's purposes is to foster knowledge among users at different nanotechnology sites and develop nanotechnology's interdisciplinary nature. While the NNIN has shown its merits through the depth of its current research, there are still many improvements that can be made by further studying network culture.

The current study immediately prompts further questions on the future of this network and of other scientific networks. Because this research targets topics that have not been fully developed, the next major step would be to look at strategies to increase the knowledge transfers in a more conducive manner as well as increasing the amount of tacit knowledge transfers, especially in the training session environment. Studying the patterns of any network or social group is meant to ultimately progress the work occurring in that network.

Acknowledgements:

I would like to thank my mentor, Hyun Jung, and my principal investigator, Dr. Jay Lee, for their invaluable and constant guidance with this research project. Funding was provided by the National Science Foundation and the National Nanotechnology Infrastructure Network Research Experience for Undergraduate Program. I would also like to thank Dr. Nancy Healy, Leslie O'Neill, Gary Spinner, my fellow interns and everyone else who gave me their unyielding support in this project.

References:

[1] Argote, L., and Ingram, P. Knowledge Transfer: A Basis for Competitive Advantage in Firms. Organizational Behavior and Human Decision Processes, Volume 82, Issue 1, p. 150-169, May 2000.

[2] Szulanski, G. The process of knowledge transfer: A diachronic analysis of stickiness. Organizational Behavior and Human Decision Processes, 82, p. 9-27. (2000).

[3] deMarrais, K., and Lapan, S. Foundations for Research: Methods of Inquiry in Education and the Social Sciences, Lawrence Erlbaum Associates, London. (2004).

NNIN Research Experience for Undergraduates (REU) Program

NNIN & Nanomanufacturing Systems for Mobile Computing and Mobile Energy Technologies (NASCENT) Program

NNIN International Research Experience for Graduates (iREG) Program

NNIN International Research Experience for Undergraduates (iREU) Program

Index of 2013 NNIN Interns (in bold), Mentors, and Principal Investigators

A

B

C

D

E

F

G

H

I

J

K

L

M

N

O

P

Q

R